The Diverse Environments of Gamma-Ray Bursts

by

Daniel Alan Perley

A dissertation submitted in partial satisfaction of the
requirements for the degree of
Doctor of Philosophy

in

Astrophysics

in the

Graduate Division
of the
University of California, Berkeley

Committee in charge:
Professor Joshua S. Bloom, Chair
Professor Reinhard Genzel
Professor Eliot Quataert

Fall 2011

The Diverse Environments of Gamma-Ray Bursts

Abstract

The Diverse Environments of Gamma-Ray Bursts

by

Daniel Alan Perley
Doctor of Philosophy in Astrophysics

University of California, Berkeley

Professor Joshua S. Bloom, Chair

I present results from several years of concerted observations of the afterglows and host galaxies of gamma-ray bursts (GRBs), the most energetic explosions in the Universe. Short gamma-ray bursts originate from a wide variety of environments, including disk galaxies, elliptical galaxies, galaxy haloes, and intracluster and intergalactic space. Long gamma ray bursts associate almost exclusively with star-forming hosts, but the properties of these galaxies also vary widely. Some are hosted in extremely small galaxies, difficult to identify directly in emission or infer from the absorption of afterglow light, but the host luminosity distribution extends up to very luminous ($> L_*$) systems as well. A significant fraction of long GRBs are observed along highly dust-obscured sightlines through their host medium. Some of these events are hosted within conspicuously dusty galaxies, although the hosts of other dust-obscured events show no outward signs of significant internal dust content. By measuring the wavelength dependence of dust absorption profiles using a few well-observed GRB afterglows, I provide evidence for ordinary dust with properties similar to those of dust in the Milky Way in a system at $z \sim 3$, but a very different absorption profile from the dust in a galaxy at $z \sim 5$, providing tentative evidence to support a transition in dust composition early in the history of the Universe. I present an observationally-determined redshift distribution for *Swift* GRBs, showing few to originate from high redshifts ($z \gtrsim 5$). I also provide the first photometric and spectroscopic catalogs from one of the largest GRB host-galaxy surveys ever conducted, including observations of almost 150 distinct GRB fields.

To my mother and father.

Contents

List of Figures

List of Tables

Acknowledgments

It is assuredly no coincidence that I am second-generation astronomer. Surely, there are many reasons to pursue astronomy as a profession: the excitement and challenge of searching for answers to the (literally) biggest questions in the Universe, the opportunity to travel and interact with a global community of intellectuals, the privelege of operating powerful telescopes to pursue one's own research goals, and the joy of sharing one's knowledge with the interested public community. Still, credit must go to my father (and National Radio Astronomy Observatory scientist) Rick Perley for providing the extra impetus to establish this field in particular as my life's work. Along with my mother, Peggy Perley, he has provided support, encouragement, and assistance at every step—an ample supply of books in my earlier years, assistance with my science fair ambitions throughout middle and high school (including the opportunity to begin working with Very Large Array data from the age of 15!), support for my undergraduate education (both morally and financially), and advice and assistance that continues to this day as I look towards the next generation of radio telescopes to continue to pursue my science goals in the postdoctoral world. Thoughout, he has been patient, understanding and unerringly positive: providing opportunity and encouragement but never any undue pressure. More than that, he has provided a shining example of the fact that professional astronomy (and life in general!) can be fulfilling, exciting, and even fun.

For the past six years, however, my scientific mentorship has been the task of my research advisor, Professor Joshua Bloom, to whom I owe an immense debt of gratitude. I came to Josh as a first-year student in April of 2005, initially looking for a short summer project in the world of GRB research—but quickly became absorbed in the subject and never looked back. From those first interactions through today, Josh has been tremenously supportive, providing opportunities to work with exciting data (in particular from the IR telescope PAIRITEL, the product, in part, of his own hard work in the years before his arrival at Berkeley; but also from Keck, Gemini, and many other telescopes which he helped train me to use and propose for during my years here), the encouragement and financial assistance to travel to and speak at major conferences, and strong support for my pursuit of my own ideas and projects. In each capacity he has gone above and beyond the advisor's call of duty in support of me and my efforts. I would not be where I am today without him.

Thanks are also owed to the other members of my qualifying and thesis committees. Eliot Quataert has provided useful theoretical and phenomenological insight into many of the

underlying issues motivating this thesis and the world of GRBs in general. Alex Filippenko has helped me connect my work on GRBs to the older, more established field of supernovae, and also has been an inspiration for my pursuits within undergraduate astronomy education early in my graduate career, when I had the privelege of working alongside him as head GSI for one of the nation's largest astronomy classes for two consecutive years. Reinhard Genzel has helped fill the gaps in my knowledge and training within the field of galaxy properties and evolution, which have obvious bearing on much of this work.

Many other colleagues have also supported and assisted me in the writing of this thesis. Gamma-ray burst astronomy is an immensively collaborative endeavor due to the need to compile data from many telescopes and many wavelengths and interpret the results to form a coherent picture, and I have leaned on (and learned from) a variety of experts at Berkeley and elsewhere throughout graduate school. Brian Metzger, my companion for five years in the office at the top of the stairwell in now-abandoned Old Campbell Hall, has provided many enjoyable and fruitful discussions (usually after midnight) about GRB research intersecting the boundaries of observation and theory. Bradley Cenko arrived in our group as a post-doc at a critical time to help unite the observational resources of Berkeley and Caltech, leading to some of the most important results in this work; his work in general has helped pave the way for my own studies. Nathaniel Butler, a post-doc at Berkeley for almost as long as I have been a student here, has provided critical expertise in the X-ray realm, answering my frequent questions and requests for help with interpreting X-ray data immediately and rigorously. The other graduate students in our group—Adam Miller, Christopher Klein, and Adam Morgan—have all helped to sort through the morasses of small-telescope GRB data, investing hours of their time in data reduction and photometry in support of my projects. And despite being half a world away, Alexander Kann has provided, during our lengthy and frequent e-mail correspondences, abundant insight into the the most exciting work in the world of GRBs (both past and present), not to mention prompt, thorough, and helpful commentary on my own papers.

Many of my department colleagues I have also had the pleasure of knowing as personal friends, to whom I also owe a great debt of gratitude for making my years in Berkeley without question the most enjoyable of my life so far and helping to provide balance to the years of devoted study. Charles Hansen has been a great friend of mine since our first year of solving problem-sets and continuing thorough to today, co-hosting our weekly "games nights" based around our shared appreciation of electronic- and cardboard-based forms of distraction throughout this period. Through him I also "inhereted" the two most entertaining friends and roommates I've ever known, William Klemm and (especially) Victor Acosta, who have helped teach me the fun of travel, of living life to the fullest, and of finding the hilarious upside in every character flaw or setback—not to mention an undending supply of wacky stories to tell my other friends. I hope our adventures near and far continue for many years yet. Adam Morgan, a wonderful friend both in reality and in the world of rufflable alter-egos, not only proofread most of this manuscript, but accompanied his comments with samples of brilliant artistic talent. Chris Klein has provided much-needed dessert support at every engagement imaginable, not to mention carefully considered insight about my post-

graduate school career options. Joseph Converse, fellow appreciator of theriological themes in the night sky, has been a valuable friend for many years. Katey Alatalo helped share the stresses of balancing GRB research, classes and teaching during our first few years at Berkeley and remains a friend, colleague, and invaluable resource today in her new capacity as a millimeter astronomer. And of course I have to give a shout-out to the fellow SNAGMRFs: Jeff Silverman, Mo Ganeshalingam, Adam Miller, and Ryan Chornock for many enjoyable "research meetings" at Triple Rock and Celia's.

Also essentially important but equally involved have been the efforts of the staff, both near and far, for their work behind the scenes to make our facilities. Particular thanks are owed to Dexter Stewart, whose friendly demeanor and long hours in the office of graduate affairs have solved every administrative problem I've had during my years here and helped make the department a more pleasant place. I also owe a debt of gratitude to the observing staffs at the many telescopes involved in providing the data which enabled this rearch. Paramount among these is Greg Wirth at Keck Observatory, a true instrument guru who we frequently tasked (and taxed!) with LRIS's problems over five years of observing runs. But credit is also owed to Marc Kassis, Andrew Stephens, and many others.

Thanks are also due to the funding agencies (and the taxpayers who support them) that make modern astronomy possible. NASA and the NSF have provided the resources than enabled, via a large number of successful grant and investigator programs, much of the research presented in this dissertation—not to mention years of my own salary! In these uncertain budgetary times, I hope that the public (and its elected representatives) will continue to recognize the value in the basic research in astronomy and other fields of science that these agencies (and others) allow us to pursue.

I would like to thank all the contributers to the various software packages and websites which have been invaluable in my graduate work: LaTeX, Python, IDL, IRAF, and packages developed for them: Gemini, mpfit, the GSFC IDL routines, pyephem, SciPy, AstLib, WCSTools, SWarp, and numerous other individual programs and packages too numerous to mention here. On the world-wide web, many other services have been of tremendous utility in my research: in particular NASA's Astrophysics Data System Bibliographic Services (ADS), the UK *Swift* Science Data Centre at the University of Leicester, the NASA/IPAC Extragalactic Database (NED, operated by the Jet Propulsion Laboratory at Caltech under contract with NASA), the United States Naval Observatory sky archive, astrometry.net, and especially Robert Quimby's GRBlog.

Acknowledgements are also due to the observational facilities themselves, and the organizations which support them and continue to make them available and successful. Much of the data presented in this thesis was obtained at Keck Observatory (operated as a scientific partnership among Caltech, UC, and NASA), which was made possible by the generous financial support of the W. M. Keck Foundation. Data was also provided by Gemini Observatory, which is operated by the Association of Universities for Research in Astronomy, Inc., under a cooperative agreement with the NSF on behalf of the Gemini partnership. I extend special thanks to those of Hawaiian ancestry on whose sacred mountain astronomers are privileged to be guests. PAIRITEL, operated by the Smithsonian Astrophysical Obser-

vatory (SAO) and made possible by the support of the Harvard University Milton Fund, a camera loan from the University of Virginia, and continued support the SAO, UC Berkeley, and Swift investigator grants, has been invaluable in providing much of the critical afterglow observations in this work, and its success is a result of the tireless work and effort of a large number of people that continues to this day. Finally, I wish to acknowledge the hard work and dedication of the *Swift* team, whose successful mission has made all of this work, and my graduate career, possible.

Chapter 1

Introduction

1.1 Preface

Shortly before the launch of the transformative *Swift* satellite in 2004 (and shortly before the start of my graduate career), one could be forgiven for concluding that gamma-ray bursts (GRBs) were nearly a "solved problem", in that most of the important questions appeared to be converging towards a surprisingly simple solution: specitifically, that all gamma-ray bursts were sudden, nearly impulsive releases of energy from the core collapse of a massive star into a black hole (a collapsar; MacFadyen & Woosley 1999), funnelling about 10^{51} erg of energy into a relativistic jet along the polar axis as the rest of the star explodes as a luminous type-Ic supernova (see the reviews of van Paradijs et al. 2000 and Mészáros 2002 for a summary of the state of GRB research at the time). Although this basic picture may remain illustrative of a "typical" GRB today, almost every element has been challenged in some way during the past seven years. We now know that GRBs have at least three distinct classes of progenitors (massive stars, an unknown older progenitor, and soft gamma repeaters in nearby galaxies; e.g., Bloom et al. 2008) and possibly more. GRBs can and do release energy well in excess of 10^{51} erg (Cenko et al. 2011). GRBs are not always accompanied by supernovae (e.g., Fynbo et al. 2006b). Finally, the behavior of an afterglow—the relativistic shock-wave that races out ahead of the explosion into the surrounding gas, gleaming brilliantly in synchrotron light (van Paradijs et al. 2000)—is far more complex than previously envisioned (e.g., Burrows et al. 2005a; Nousek et al. 2006), suggesting that the central engine must remain active for hours or longer (Lazzati & Perna 2007) and may even power a continuous wind as energetic as the initial explosion itself (Fan et al. 2006b; Zhang et al. 2006). Along the way, *Swift* shattered the record for the most distant object (GRB 090423; Salvaterra et al. 2009; Tanvir et al. 2009), most luminous object (GRB080319B; Bloom et al. 2009; Racusin et al. 2008), earliest observations of a supernova (GRB 060218 / SN 2006aj and XRO 080109 / SN 2008D; Soderberg et al. 2008; Modjaz et al. 2009) — and provided many other groundbreaking discoveries (see Gehrels et al. 2009 for a review).

In retrospect, the remarkable diversity and complexity now evident from these results should not have surprised us much. GRBs are notorious for their unpredictability, a fact that is reflected in the nature of follow-up observations: the GRB observer remains tethered to satellites in the sky via mobile phone or pager, ready to drop everything when the next burst happens. To those outside the field this may sound intimidating, but in fact this spontanaeity is one of the aspects that makes this work so exciting: regardless of how interesting (or not) one's task is at any given time, in an instant a new GRB can suddenly provide something even more interesting and potentially groundbreaking to work on. Six hundred bursts into the *Swift* era[1] the routine follow-up of a typical long-duration burst is no longer quite the all-hands affair it was in the heady days of the discovery of the first afterglow, but even now GRB satellites remain more than capable of dropping a major discovery into the lap of an attentive observer. This has happened countless times throughout my own career: I have had the incredible opportunity to play an active (and occasionally central) part in many of the major discoveries of the mission. Sometimes the remarkable features of a new burst are evident immediately; other times they are revealed only after detailed analysis.

As a result, my work has at times been motivated as much by the unpredictable nature of *Swift*'s latest discoveries as by my own best-laid plans for longer-term research! Nevertheless, as I have pursued my graduate study, a clear theme has emerged in my work: the study of GRB *environments*, meaning everything from the circumburst medium (the gas that the GRB literally explodes into) up to the integrated properties of the host galaxy itself. This theme—the diversity of cosmic environments which GRBs inhabit, and their connection to the greater cosmological story of the buildup of stars, galaxies, and heavy elements—will help guide the organization and goals of this thesis. I devote particular emphasis to the effects of dust: as I show, GRBs are (like so many other distant objects) often severely affected by interstellar extinction, but are nearly unique in their ability to act as excellent tracers to study the detailed properties of this obscuring dust out to the most distant parts of the observable universe.

Although *Swift* detects GRBs by the hundreds, the observational study of these events continues to revolve largely around detailed study of a relatively small number of individual objects. The reasons for this are not difficult to understand: due to observability constraints and other practical considerations, a small number of afterglows have received the lion's share of observations with available resources; furthermore, even with the picture of an "average" GRB now relatively well-established, attention is naturally further focused on the most exceptional cases. The early part of this thesis will similary be devoted to the intensive study of a few particularly notable events from the past five years. However, my goals are much broader than characterizing these bursts and the galaxies in which they occur as isolated examples: ultimately, one hopes to make generalizable statements about the broader population of environments in which GRBs explode—and from there, to use GRBs as tools to describe the universe generally. The tremendous (if evanescent) multi-

[1]More precisely, six hundred and three as of this writing: for an up-to-date count, see the official *Swift* GRB table at `http://swift.gsfc.nasa.gov/docs/swift/archive/grb_table.html`.

wavelength luminosity of a typical GRB certainly makes these events excellent point-probes of conditions in individual high-z galaxies, but (because of their direct association with star formation) they may be usable as cosmological probes in a global sense as well.

Any such study must involve particular attention to the sorts of GRBs that rarely appear in the typical single-burst observational paper—while the observer is naturally drawn to the nearest, brightest, and most luminous explosions due to the relative ease of acquiring excellent data, some bursts are known to be much more elusive. The rest of my attention, then, is devoted to these events: the short, the dim, and especially the "dark" bursts. What type of galaxies do these inhabit, if they even inhabit galaxies at all? Here, the ability to make conclusions from individual objects becomes much more limited: afterglow observations are of much poorer quality and, because of detectability limitations, the objects we see may not be representative of the greater population. However, thanks in a large part to *Swift*'s X-ray telescope, pinpointing these events on the sky and characterizing their environments is still feasible. GRB host galaxies are exceedingly faint, but by bringing the largest optical telescopes in the world to bear (in particular, the 10-meter Keck telescopes on Mauna Kea) I "fill in" these holes in our sample and finally shed light on these and other exotic classes of GRBs.

This project has been possible only due to the hard work of previous generations of astronomers, and before beginning the description of my own work, I will briefly summarize the history of the field from the 1960s up to the launch of *Swift* at the start of my graduate career, illustrating how my work builds on these previous studies. The discussion of my own research will be roughly divided into two general themes: studies focusing on the *afterglow* and on individual objects, and studies focusing on the *host galaxy* and entire categories of objects, in particular the "dark" bursts (events with unusually dim optical afterglow). This host/afterglow segregation only refers to the primary tool being employed and is not total: the afterglow discussion contains observations and analysis of host galaxies of the collection of bursts under study, and the host galaxy chapters similarly tie the properties of the hosts to the properties of the afterglows used to find them. Many of these chapters are based largely on previously published articles (cited at the start of chapter), although I have in places reworked the discussion to better represent the overall theme of this thesis or incorporated new observations. However Chapter 7, devoted to the Keck GRB Host Survey (the large observational project that has largely defined my graduate career) consists almost entirely of newer material not yet available in the scientific literature and is presented for the first time here.

1.2 Historical Background

The early history of gamma-ray bursts has many of the trappings of a good spy novel—Cold War rivalries, nuclear tests, covert satellites, unidentified signals from deep space—and the very discovery of GRBs was literally a fortuitous by-product of nuclear tensions between the Soviet Union and Western powers during the early part of the Cold War. The

first Soviet nuclear test in 1949 helped spark a series of escalating nuclear test explosions that continued for much of the 1950s. As the dangerous health effects of radiation and atmospheric fallout became known, however, it was eventually acknowledged that further above-ground testing could no longer be justified, and in 1963 the Partial Nuclear Test Ban Treaty was signed and ratified by the three powers, prohibiting most above-ground testing (underground testing remained permitted under the Treaty.) As part of verification efforts, the United States initiated a program known as Project Vela to search for illicit nuclear tests by the Soviet Union. This program was multi-tiered, including elements of seismic and atmospheric monitoring. Since nuclear tests in the upper atmosphere or in space could be missed by solely ground-based equipment, a third, satellite-based component, Vela Hotel, was also developed. Six satellite pairs (Vela 1a/1b, Vela 2a/2b, etc.) were developed by teams at Los Alamos and Sandia National Laboratories and launched between 1963 and 1970. (Reed et al. 1990; Bonnell 1995)

The tell-tale signature of a nuclear blast in space is high-energy radiation (X-rays and gamma-rays, as well as energetic particles), and the Vela satellites were outfitted with scintillators designed to detect these signals. While primitive by today's standards, the gamma-ray detectors on these early satellites[2] proved more than sufficient to detect the occasional, mysterious flashes of gamma-rays typically lasting a few seconds that became known as gamma-ray bursts. These events did not have the characteristics of a nuclear weapons test, and triangulation using the time-of-arrival of the burst signal at different satellites the ruled out the Earth, Sun and any other Solar System object, clearly identifying GRBs as an astronomical phenomenon. The birth of GRBs as a branch of astronomy was officially launched with the publication of the discovery paper (Klebesadel et al. 1973) by a team of Los Alamos scientists involved with the project.

Nothing matching the observed characteristics of GRBs had been previously predicted[3], and X-ray astronomy was still in its infancy at the time. This announcement of this unexpected natural phenomenon therefore provided ample grounds for theoretical speculation about their origins. Unfortunately, precious little observational evidence was available to constrain these theories, as is reflected in the diversity of different models proposed to explain them: comets colliding with neutron stars (Harwit & Salpeter 1973), the shock-breakout of a supernova (Colgate 1974), relativistic metal grains entering the Solar System (Grindlay & Fazio 1974), bright stellar flares (Brecher & Morrison 1974), "nuclear goblins"(!) (Zwicky 1974), runaway nucleosynthesis on a white dwarf (Hoyle & Clayton 1974), collisions of antimatter chunks with stars (Sofia & van Horn 1974), and evaporation of primordial black holes (Hawking 1974; Page & Hawking 1976)—to name only a few!

[2]Or at least, on the more advanced satellite pairs: the first known GRB was detected by Vela 4a/4b (and 3a/3b) but it was not until Vela 5a/b that the phenomenon could be studied scientifically, as these early satellites did not have sufficiently accurate timing information to determine the direction of the signal.

[3]Colgate (1968) had suggested that transient gamma-ray emission may originate from supernovae, but the timing of GRB explosions did not seem to match nearby supernovae, and this interpretation quickly fell out of favor. Of course, we now know that (many) GRBs are in fact directly associated with supernovae at much greater distances.

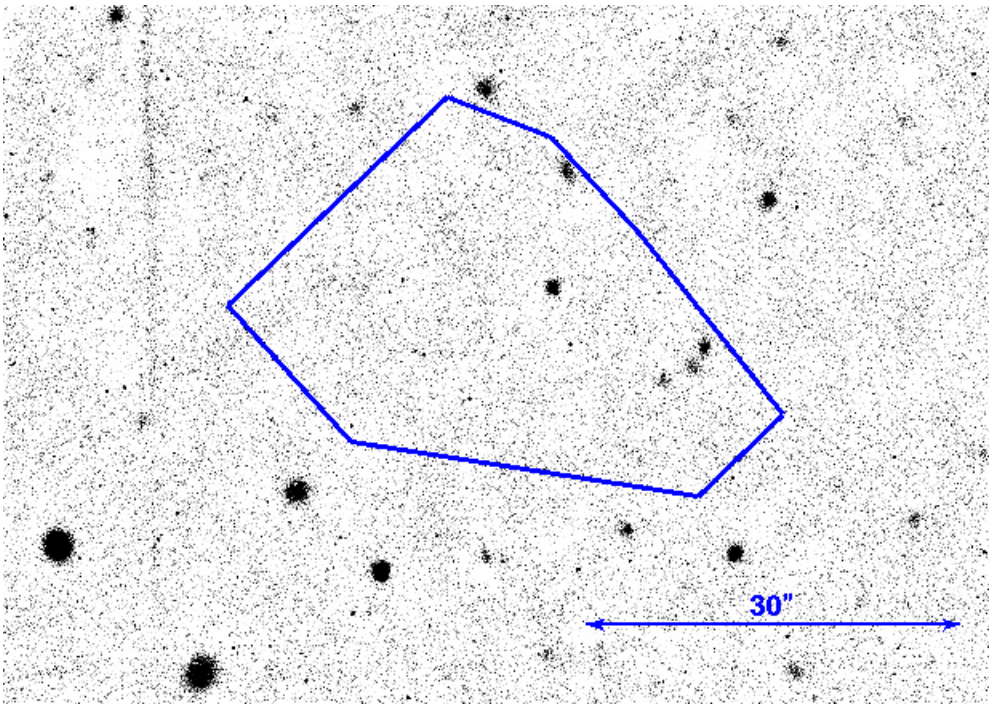

Figure 1.1 The uncertainty polygon of the bright gamma-ray burst GRB 790406, as constrained by the arrival times of the burst at different satellites in the interplanetary network (Laros et al. 1981). At less than 0.5 square arcminutes in total area, this was among the most accurately localized GRBs before the discovery of afterglows. Only a few, faint ($R \gtrsim 23$) objects are consistent with the burst position, demanding that the counterpart (if Galactic) be extremely faint in quiescence or (if extragalactic) have a very distant host, demanding that the explosion have tremendous energetics. (Imaging was conducted in 1992 with the NTT, and is taken from the ESO VLT archive.)

Some early theories could be ruled out based on the non-detection of line features in GRB spectra (Cline et al. 1973)—but beyond that, the observations were frustratingly nonconstraining. Paramount among the obstacles hindering progress in constraining this plethora of models was the inability of researchers to determine the distance to a GRB (and therefore its energetics). Gamma-rays cannot be reflected or refracted by most practical means (Aschenbach 1985), and as a result imaging of any gamma-ray source, a prerequisite for precisely determining its position, is extremely challenging. The first gamma-ray detectors provided almost no directional information whatsoever, and the only way to constrain the point of origin of an event was to reconstruct the passage of the gamma-ray signal through outer space using the time-of-arrival of the burst at different widely-spaced satellites (Giacconi 1972; Klebesadel et al. 1973). When restricted to satellites in Earth orbit this technique can provide only quite crude positions, but the launch of probes elsewhere in the Solar System (such as the Helios-2 solar probe or the Soviet Venera mission) greatly extended the spatial baseline, and therefore the accuracy, of this technique. This array of satellites and probes is usually referred to as the Interplanetary Network (IPN), and was the only means of providing GRB positions for several decades (e.g., Klebesadel et al. 1982; Atteia et al. 1987; Cline et al. 1999). Unfortunately, even the IPN produces only crude localizations; a "good" IPN error box is typically about an arcminute in width but tens of arcminutes in length. Furthermore, the long amount of time required to combine the data from this diverse array of different spacecraft to provide a position (typically, several days) essentially precluded rapid searches for a transient optical counterpart. In one or two cases a fortuitously small IPN error box (e.g., Laros et al. 1981) could be searched for a candidate *quiescent* counterpart (the progenitor star or host galaxy); with a few prominent and highly-nonrepresentive exceptions in which a large, nearby spiral galaxy was discovered to be consistent with the IPN position (GRB 790303, the famous March 5th event from the Large Magellanic Cloud [Evans et al. 1980], and much more recently GRBs 051003 and 070201 from M81/82 and M31, respectively [Perley & Bloom 2007; Frederiks et al. 2007; Mazets et al. 2008]) these uncertainty regions contained only faint stars and distant galaxies (Motch et al. 1985; Schaefer 1992); Figure 1.1. This suggested that the progenitor was associated with either an exceptionally low-luminosity Galactic star or was coming from cosmological ($z > 0.1$) distances.

Despite significant effort during the 1980s and early 1990s, astronomers remained unable to firmly resolve which of these two possibilities (the "Galactic" and "cosmological" hypotheses) was correct. Gradually, however, pieces began to fall into place. Observationally, the most significant development by far was the launch of the Compton Gamma-Ray Observatory (CGRO) and in particular its Burst and Transient Source Explorer (BATSE) experiment (Fishman et al. 1992), which consisted of a series of eight NaI scintillators studding the satellite on different sides. These detectors had no true imaging capability, but a GRB detected by multiple scintillators at once could be localized with a typical positional uncertainty on the sky of a few degrees. BATSE was also extremely sensitive, capable of detecting hundreds of GRBs per year (and thousands over its lifetime before finally being deorbited in 2000.) While these large uncertainty regions were still inadequate for identifying the host galaxy or quiescent counterpart of any event, BATSE positions were easily suffi-

cient to provide the first strong piece of evidence that GRBs originate beyond the Galaxy: the spatial distribution of these events on the sky showed no evidence of anisotropy, with no clustering towards the Galactic plane or the Galactic center (Fishman & Meegan 1995 and Figure 1.2). Until this time, the phenomenal energetics required if GRBs originated at cosmological distances (and the discovery of the soft gamma repeaters [SGRs], Local Group neutron stars which give off repeated high-energy flares similar in character to true gamma-ray bursts, but with a softer, thermal spectrum[4]) had pushed many towards the notion that GRBs come from from Galactic neutron stars (Lamb 1995). But as BATSE positions accumulated by the hundreds, the modifications necessary for this model to remain consistent became increasingly contrived (Paczyński 1995).[5]

Still, unambiguous proof of the distance scale (not to mention most other basic questions about GRBs) remained elusive. The technological limitations of gamma-ray detectors—specifically, their inability to pinpoint the location of a burst or measure its redshift—virtually guaranteed that only incremental progress was possible as long as GRB observations remained solely the province of gamma-ray astronomy. Detection of a counterpart at another wavelength would be necessary for a breakthrough in the field.

Efforts to detect such a counterpart had been ongoing for decades: it was thought that, should GRBs be a repeating phenomenon similar to the recently-discovered SGRs (soft gamma repeaters: soft-spectrum, recurring flashes of hard X-rays from local neutron stars;), detailed searches of historical plate archives covering the positions of known GRBs might eventually identify an optical flash originating from some previous bursting episode. Although associations were claimed in a number of cases (e.g., Schaefer 1981; Schaefer et al. 1984; Hudec et al. 1988, 1990), further analysis cast many of the reported associations into doubt, suggesting that the optical flashes were plate defects (Zytkow 1990) or unassociated sources (Laros 1988).

On the other hand, if GRBs were extremely distant objects, a very different behavior is predicted: the tremendous release of energy in such a small volume (of order 10^{52} erg released in a few seconds from a stellar-like object) should create a "fireball" (Cavallo & Rees 1978; Rees & Meszaros 1992; Piran et al. 1993): an extremely dense sphere[6] of nearly

[4]In fact, bright flares from SGRs were included among the early catalogs of gamma-ray bursts and not realized to be a separate phenomenon (on the basis of their repeatability and exclusive origin from the Galactic plane and LMC sources) for several years (Mazets et al. 1981; Laros et al. 1987); see Woods & Thompson (2006) for a review.

[5]While this narrative emphasizes the role of BATSE's positions in strengthening the case that GRBs were cosmological, CGRO and BATSE provided several other discoveries worthy of note, as BATSE also provided high-quality GRB *spectra* for enormous numbers of bursts. First by discovering a significant bimodality in the joint hardness-duration distribution, BATSE provided the first evidence that GRBs are composed of (at least) two distinct classes (see Section 1.3); second, high-quality BATSE spectra allowed the best constraints yet to be placed on the general mathematical form of GRB spectrum, known as the Band function after Band et al. (1993); finally, CGRO's high-energy instrument EGRET, the Energetic Gamma Ray Experiment Telescope [Kanbach et al. 1988], detected a small number of GRBs at very high energies, demonstrating that GRB explosions must be highly relativistic (otherwise, pair-production opacity would cut off the spectrum; Piran 1999; Ruderman & Sutherland 1975).

[6]Energetics considerations and other lines of argument now strongly indicate that the fireball is not an

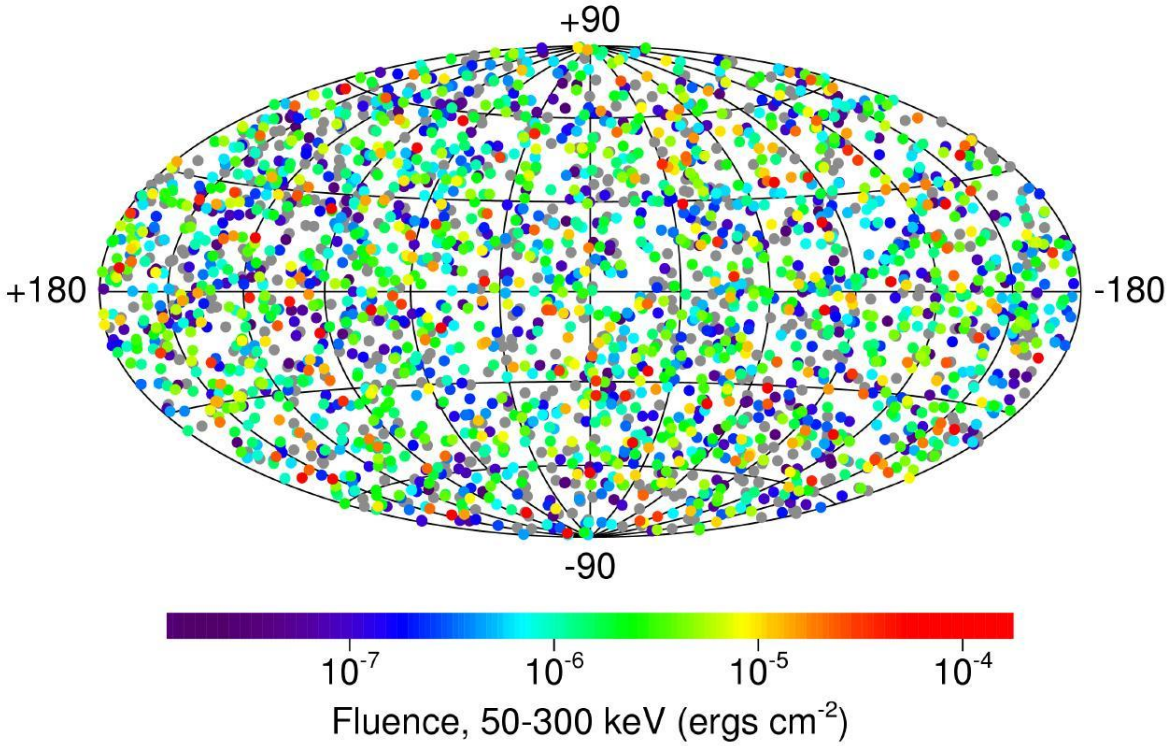

Figure 1.2 Sky positions, in an Aitoff projection using Galactic coordinates, of all 2704 GRBs detected during the BATSE mission, color-coded by the total fluence (flux integrated over the time of the event). The distribution is isotropic, with no concentration towards the plane of the Milky Way (independent of the fluence of the event). Image from `http://gammaray.msfc.nasa.gov/batse/grb/skymap/`.

pure energy (i.e., energetic gamma-rays, electron-positron pairs, and extreme magnetic fields, with a relatively limited amount of mass-energy in baryons) whose internal pressure quickly causes acceleration outward up to relativistic speeds. If the energy in this expanding fireball is not distributed or accelerated homogeneously, collisions between different shells of ejecta can create internal shocks that rapidly dissipate energy, explaining the GRB itself (Rees & Meszaros 1994).[7]

If GRBs originated in pure vaccuum, this would be the end of the story: any long-wavelength emission associated with the event would be just as fleeting as the burst itself. However, in reality, the expanding relativistic shell will quickly begin to accumulate matter from the circumstellar medium (CSM), slowing it down and creating a pair of shock waves: a *forward shock* that races forward into the CSM, and a *reverse shock* that travels backward (in the frame of the expanding shell) into the ejecta itself (Rees & Meszaros 1992; Katz 1994; Sari & Piran 1995). The forward shock is an (initially) highly relativistic blast-wave (Blandford & McKee 1976), carrying with it a strong magnetic field that causes accelerated electrons crossing the shock to quickly radiate their energy across the electromagnetic spectrum as synchrotron radiation. As the shock travels it slows and spreads out, and the bolometric luminosity falls as the characteristic frequencies of the emission move to longer wavelengths. The result, at most frequencies, is a light curve that looks like a fading power-law (Sari et al. 1998)[8]. The behavior of the reverse shock emission is similar (most of the same physics applies), but the fading rate is much faster (Sari & Piran 1999a). In all cases, the emission should be bright but short-lived: catching an afterglow while still detectable to a moderate-sized telescope would require observations within about a day (Meszaros & Rees 1997).

Given the large size of a BATSE error circle (degrees) relative to the fields of view of typical optical imagers and radio telescope beams (a few arcminutes), this was no easy task for ground-based astronomy. However, several major technological developments made the problem much more tractable. First, the technique of coded-mask imaging (Caroli et al. 1987)—effectively, placing a checkerboard-patterned block of metal over a large detector and using the location of its shadow to identify the source location—greatly improved the positional accuracy of gamma-ray detectors. At the same time, the development of sensitive,

isotropic sphere but a highly beamed jet of energy, probably released in a bipolar outflow (Rhoads 1997). However, because the event is ultra-relativistic, from the perspective of an observer along the line of sight, the observed evolution is essentially identical to that of a spherical explosion until the shock wave slows considerably, which does not occur for (usually) days to weeks.

[7]An alternative model associates the GRB with interaction with the external environment as the flow is decelerated by interstellar matter; i.e., an external shock (Meszaros & Rees 1993; Rees & Meszaros 1992; Katz 1994). The external shock model, however, has great difficulty explaining the short-timescale variability evident in GRB light curves—since external shocks occur far from the explosion site, any variation should be smoothed out by light-travel-time effects associated with emission from different regions of the shock (Fenimore et al. 1996; Sari & Piran 1997). Internal shocks occur much closer to the central engine and do not suffer this limitation (the internal shock model does, however, struggle to explain the high radiative efficiencies inferred for GRBs; citealtPanaitescu+1999,Kumar+1999.)

[8]Radio frequencies are a prominent exception: the radio luminosity actually rises for several days while the peak emission frequency moves from high to low frequencies. Once this peak frequency passes the radio band, the radio luminosity fades as well.

modern X-ray imagers made space-based afterglow searches in the X-rays practical (helpfully, the X-ray sky is much emptier of confusing sources than the optical sky). Finally, the development (and popularization) of the internet, and specifically of the Gamma-Ray Burst Coordinates Network (GCN; Barthelmy et al. 1994), allowed astronomers across the world to be rapidly notified about the locations of new GRBs.

Many years of hard work and frustration finally paid off in early 1997 with the discovery of the afterglow of GRB 970228[9]. This victory was shared by two groups of astronomers: the Beppo-SAX team who detected the burst itself (Boella et al. 1997) and later repointed the telescope to find a bright, fading X-ray afterglow consistent with the gamma-ray position (Costa et al. 1997), and the ground-based astronomers who discovered a fading optical transient at the same location (van Paradijs et al. 1997). Within a few days the transient disappeared and never recurred, leaving in its place a faint and distant galaxy. Three months later, the story was repeated with GRB 970508—but, this time, with successful detection of a radio transient (Frail et al. 1997) and, critically, an absorption spectrum (Metzger et al. 1997) of the optical transient that unambiguously demonstrated the cosmological ($z = 0.835$) nature of the object.

Within the span of a few months, the field had undergone a complete transformation. Progress in subsequent years was equally rapid: GRBs were shown to be highly beamed (based on the occurence of "jet breaks", steepenings in the light curve at late times as the relativistic blast-wave slows down and the observer sees the edge of the jet; Sari et al. 1999), helping to bring down what would otherwise be alarmingly high energetics (most explosions had a beaming-corrected output of only $\sim 10^{51}$ erg $\approx 0.001\ M_\odot c^2$ [Frail et al. 2001], a much more manageable quantity than the alarming $\sim 10^{54}$ erg $\approx M_\odot c^2$ that would be inferred from an isotropic explosion in some extreme cases; Piran 2000). Long-duration GRBs were shown with high certainty to be associated with regions of massive star-formation (Bloom et al. 2002)—and specifically to be coincident with type Ic supernovae (Galama et al. 1998; Hjorth et al. 2003), showing them to be a rare kind of stripped-envelope core-collapse event (even after correction for beaming, the GRB rate per galaxy is of order 10^{-5} year^{-1} [Podsiadlowski et al. 2004], many orders of magnitude lower than the Type II supernova rate and at least several orders of magnitude lower than the type Ib/c supernova rate [e.g., Cappellaro et al. 1997, 1999], indicating very special conditions must be required for a star to die as a GRB.)

This rennaissance in GRB research motivated the development and launch of the groundbreaking new satellite *Swift*[10] (Gehrels et al. 2004) in late 2004. *Swift* is remarkable for several reasons: its gamma-ray detector, the Burst Alert Telescope (BAT; Barthelmy et al. 2005), is extremely sensitive (detecting ~ 100 GRBs per year on average, compared to $\sim$10 for Beppo-SAX and HETE) and its X-ray Telescope (XRT; Burrows et al. 2005c) is able to

[9]GRBs are named based on the UT date on which they occur, in YYMMDD format: this famous burst, for example, occurred on 1997 February 28. Multiple events on the same day are distinguished with a letter suffix, starting with "A".

[10]In an uncharacteristic departure from the acronyms beloved of government agencies and astronomers alike, *Swift* was named for its unique capabilities—it is able to autonomously re-point itself in the direction of a new GRB within 1–2 minutes to study the afterglow—rather than via a prosaic acronym.

follow-up almost all bursts immediately and continue observing for days. *Swift* distributes accurate positions to ground-based observers almost immediately (the 3′ accuracy BAT position is distributed within seconds and a much more precise 2–5″ accuracy XRT position is distributed within minutes). *Swift* is also equipped with a UV/Optical Telescope (the UVOT; Roming et al. 2005), although this instrument has played a relatively smaller role in practice, as the UVOT is only able to detect about half of the bursts it observes (Roming et al. 2009) and because of its blue response, it is particularly insenstive to examples of the dusty, faint, and high-redshift objects around which most of this thesis revolves.

Swift's successes are almost too numerous to summarize (for a more complete overview, see Gehrels et al. 2009). Many groundbreaking studies have followed immediately upon discovery of individual keystone events (or occasionaly pairs of events): GRB 050509B first linked short GRBs to an older stellar population (Bloom et al. 2006f; Gehrels et al. 2005); GRB 060218 provided the first look at a supernova starting moments after the explosion; GRBs 060505 and 060614 suprised the community by *failing* to produce a detectable supernova (Fynbo et al. 2006b; Gehrels et al. 2006; Della Valle et al. 2006); GRB 080319B, the optically brightest and most luminous burst to date, provided the first (and, for now, only) truly simultaneous look at a GRB prompt-emission event in optical and gamma-ray energies simultaneously (Bloom et al. 2009; Racusin et al. 2008). Less spectacularly but equally important, *Swift* has also functioned as a powerful GRB afterglow-discovery machine, allowing bursts to be studied in detail in large numbers and making large, systematic demographical studies of the GRB population (Nousek et al. 2006; Kann et al. 2010; Gehrels et al. 2008; Nysewander et al. 2009a; Panaitescu & Vestrand 2008) finally possible.

1.3 Gamma-Ray Burst Classification

One of the most important discoveries of the *Swift* mission is that cosmological GRBs[11] separate into (at least) two physically distinct progenitor classes, corresponding roughly to the *phenomenological* dichotomy first recognized in BATSE data by Kouveliotou et al. (1993); Figure 1.3. The majority of observed GRBs belongs to the "long-soft" phenomenological class, which have typical durations[12] of $T_{90} \gtrsim 2$ s. An abundance of evidence associates these objects with the core-collapse of massive stars (there are invariably situated in star-forming environments and frequenly accompanied by supernovae (Bloom et al. 2002; Fruchter et al. 2006; Woosley & Bloom 2006; see section 1.4.2). Members of the "short-hard" class have typical durations shorter than 2 seconds (and, on average, harder spectra than their longer counterparts); their progenitor (or progenitors) is still unknown, but it almost certainly is *not* a massive star, based on the association of several short GRBs with "red and dead" galaxies with essentially no star formation (Prochaska et al. 2006b; see section 1.4.1).

A word of caution is in order before proceeding: although Kouveliotou's division of

[11] That is to say, GRBs excluding the small number lower-luminosity events from the nearby ($z \lesssim 0.01$) universe: the SGR hyperflares and enigmatic Galactic events like GRB 070610 (Kasliwal et al. 2008).

[12] T_{90} refers to the length of time over which 90% of the observed flux from a GRB is measured.

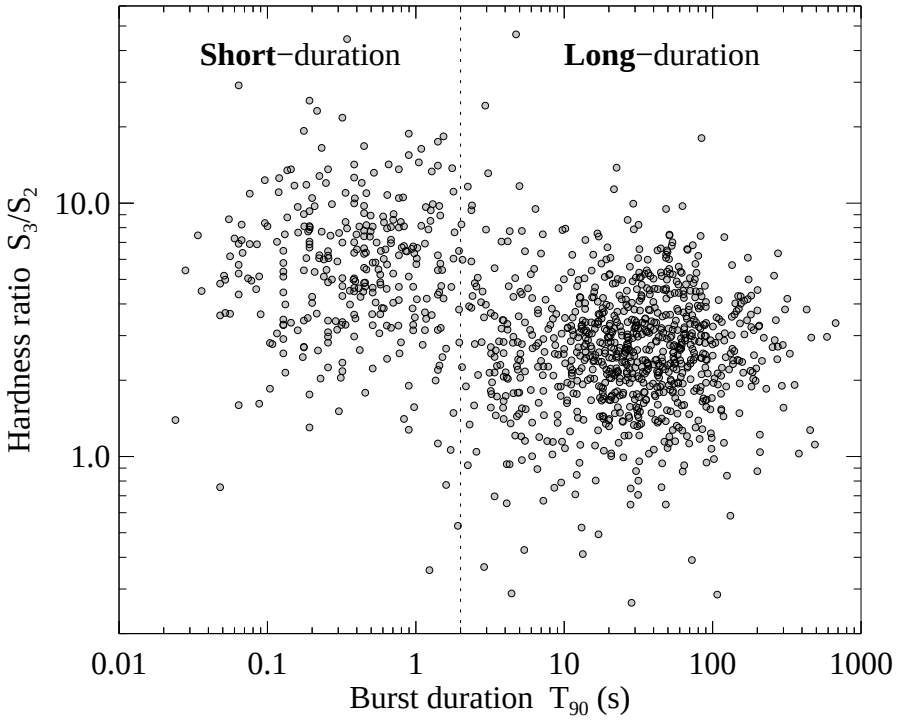

Figure 1.3 The duration versus spectral hardness of a large sample of BATSE bursts, using public BATSE data (Paciesas et al. 1999). A significant bimodality is evident, with two distributions of GRBs visible: a long-duration population with a mean durations of about a minute and a smaller short-duration population with durations of a fraction of a second. The long-duration bursts are softer, on average, than short-duration bursts.

GRBs into two classes on the hardness-duration diagram was remarkably prescient of what appears to be a real bifurcation in progenitor classes, this emphatically does *not* mean that all observationally "short-hard" bursts are one progenitor and "long-soft" bursts are another. Statistically, the two distributions overlap substantially, and GRBs close to the boundary (i.e., those with durations close to 2 seconds) cannot decisively be associated with either class.[13] T_{90} itself is a very crude metric of duration and does not take into account, among other things, the phenomenon of "short" GRBs with extended emission: events where an intense < 2 s pulse is then followed by gradual rise of softer emission lasting about a minute (Figure 1.4). Events with this profile seem to form a continuum between unambiguous short bursts with no extended emission, short bursts with very weak extended emission, and events with very bright (energetically dominant) extended emission and $T_{90} \sim 100$ s (Norris & Bonnell 2006). Finally, while there are physically reasonable justifications for why an old, degenerate progenitor without an envelope should release energy on a shorter overall timescale than a massive star (the accretion rate onto a black hole in a fully degenerate system is limited only by the viscous time of the disk [Paczyński 1991], whereas the accretion rate from a massive star is further limited by the gravitational free-fall time of the inner envelope of the star [Popham et al. 1999]; in the internal shock model these timescales manifets themselves directly in the prompt emission [Sari & Piran 1997]), GRB theory remains a long way from predicting *ab initio* the diversity of light-curve profiles and durations observed in GRBs (Kobayashi et al. 1997; Nakar & Piran 2002; Morsony et al. 2010).

Based on these considerations, then, it is fair to claim that duration, hardness, and other prompt-emission observables do not (yet) unambiguously distinguish the class of progenitor, and so the claim that something is phenomenologically a "short-hard" burst or a "long-soft" burst guarantees nothing more than that the burst is literally shorter (/harder) or longer (/softer) than the rest of the population as measured by a particular instrument. This is somewhat unsatisfying, and potentially misleading: the goal of the astronomer is to understand the underlying physical story producing the explosion (the progenitor and its history), and many other observables are now available that constrain the progenitor much more directly. As a result a certain amout of terminological confusion has developed in the literature, where it has become common practice to refer to bursts with bright extended-emission episodes and a $T_{90} > 60$ s, such as the defining GRB 070724, as "short". Zhang et al. (2007) have instead suggested a *physical* classification, using the more neutral terms "Type I" and "Type II" to refer to compact-star-progenitor GRBs and massive-star-progenitor GRBs, respectively, although this distinction could be criticized as premature given the relatively primitive state of understanding of the Type I "class" in particular. A similar, but even more detailed classification scheme has been suggested by Bloom et al. (2008).

In my personal view, the most logical way of constructing a classification system that

[13] A third parameter, the "lag" (the time-offset of the peak gamma-ray flux at different frequencies), has been introduced to attempt to further separate the two classes (Norris 1995; Norris & Bonnell 2006), but the degree to which it is able do so *independent* of the duration itself is controversial; correlation between lag and duration may be a property of individual pulses (e.g., Hakkila et al. 2008) and therefore indicative more of the radiation physics of the internal shocks than anything fundamental about the burst itself.

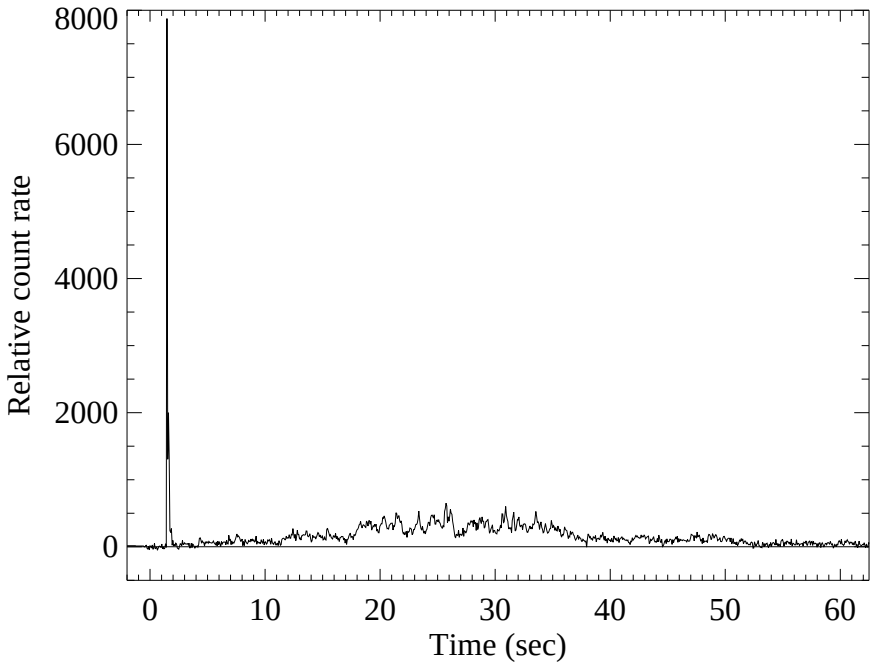

Figure 1.4 Light curve of BATSE GRB 921022B, a classic example of a short GRB with extended emission. After a brief (< 1 s), intense spike the flux fades to background level for a few seconds before recovering. Then another, much longer emission episode begins, lasting approximately one minute before fading away again. In this case, this long emission episode actually dominates the energetics of the burst. (Data is acquired from the BATSE FTP site: `ftp://cossc.gsfc.nasa.gov/compton/data/batse/ascii_data/64ms/`).

is both physically informative and observationally practical to implement is to borrow the concept of "type specimens" from biological taxonomy: choosing a few sterling individual events, which must be unambiguously physically *and* phemonenologically distinct from each other, as prototypes and evaluating the remainder of the sample based on their observational similarities to each (but with the ultimate *goal* of producing a classification that is physical rather than phenomenological). Specifically, I would hold out GRB 030329 as the prototype of what I will call the "LGRB" class and GRB 050724 as the prototype of what I will call the "SGRB" class[14]. Both of these prototype bursts are extremely well-observed and appear to be representive of other observed events (in terms of energetics, light curve, afterglow properties, etc.—they are not obvious "oddballs"[15]. Most importantly, however, the available observations lead to starkly opposite conclusions about the progenitors: GRB 030329 was followed by a luminous type Ic supernova that unambiguously labels this event as the explosion of a massive star(e.g., Price et al. 2003; Stanek et al. 2003); GRB 050724 definitely occurred in a galaxy with essentially no star formation and *cannot* be a massive star (e.g., Barthelmy et al. 2005; Berger et al. 2005b). Even if these were the only two GRBs in existence, we would be able to clearly recognize two distinct classes based on these observations, and they therefore represent an ideal starting point for classifying the rest of the sample based on all available evidence (including, but not limited to, the high-energy prompt-emission properties), starting with events that are most obviously similar to one prototype or another, then proceeding to the more ambiguous cases by comparing them with the two populations. I feel this classification system draws a reasonable middle ground between the purely statistical high-energy classifications (which risk placing GRB 050724, with its bright extended-emission episode, into the long "class" and generate only a probabilistic result for intermediate-duration events) and the more explicitly theory-laden classification schemes that explicitly invoke specific progenitor models. The downside is that there is no explicit prescription for assigning a member to one class or another; this procedure is entirely subjective and can blend both phenomenological and physical elements.

Despite the considerable attention paid here to classification, it is only occasionally a concern: Even a simple T_{90} cut seems to produce a self-consistent physical classification *most* of the time (for example, no event with $T_{90} < 1$ s has yet produced a supernova or otherwise been unambiguously associated with a massive star[16], whereas studies of populations of $T_{90} > 2$ s GRBs (e.g., Bloom et al. 2002; Fruchter et al. 2006) clearly point to a massive-star origin for the large majority of these events, with the exceptions generally being rare and

[14]Following a path previously treaded by the likes of KFC and BP, the acronym is conspicuously not spelled out.

[15]The prompt emission of GRB 030329 appears somewhat under-energetic compared to almost all other long-duration GRBs and therefore not completely typical, but an additional reservoir of energy emitted in a wide-angle jet may make up this difference; Berger et al. 2003b

[16]However, GRB 090426 has $T_{90}/(1+z) < 1$ s and is very likely associated with a massive star (e.g., Levesque et al. 2010b; Xin et al. 2011). Note also that the observational data for short-duration bursts tends to be much more limited than for long-duration bursts, since their afterglows are fainter (Nysewander et al. 2009a; Kann et al. 2011), making progenitor constraints much more challenging to provide.

isolated cases.) Only one SGRB event is discussed in detail in this thesis: the intriguing GRB 080503 in Chapter 2 (whose classification is very much up for debate, with a $T_{90} > 100$ s and a light curve reminiscent of 050724). As a result I will defer further discussion of the classification question to that chapter, and proceed to discuss the current understanding of the environments of the two classes I have defined.

1.4 Gamma-Ray Burst Environments

There is much more to the field of GRBs than the explosion itself. Gamma-ray bursts explode in galaxies, and (as the discussion above illustrates) understanding where a burst comes from, and what kind of environment it is exploding into, can be just as insightful regarding the nature of the phenomenon as studying their light curves and SEDs. Indeed, much of what is known about GRBs is based precisely on analysis of their environments in this way (e.g., Price et al. 2002; Bloom et al. 2002; Fruchter et al. 2006; Prochaska et al. 2006b).

1.4.1 SGRBs: An Enigmatic Population

As I have already mentioned, the prototypical event of the SGRB class is GRB 050724. This event, dating from early in the *Swift* era, occurred within $0.2''$ of the center of a bright, red elliptical galaxy at $z = 0.257$ (Barthelmy et al. 2005; Berger et al. 2005b). The spectrum of the host shows no detectable emission lines, limiting the star-formation rate to <0.05 $M_\odot$/yr (Prochaska et al. 2006b) despite a large population of old stars ($M_* \sim 5 \times 10^{10} M_\odot$, Gorosabel et al. 2006). This galaxy ceased forming new stars at any appreciable rate several billion years before the burst, and its progenitor star must therefore have formed hundreds of millions if not billions of years before exploding; it cannot have the same type of progenitor as the classical long-duration bursts. Furthermore, no supernova signature was seen despite sensitive observations in the ensuing weeks when such an event should have been peaking.

The next clearest case is GRB 050509B (Bloom et al. 2006f; Gehrels et al. 2005), which also seems to have occurred in a massive cluster elliptical with essentially no star-formation. This event, however, was exceedingly faint and the only detection of an afterglow is provided by a handful of X-ray photons recieved within a few minutes of the burst, so its position is relatively uncertain, and an association with one of several faint background galaxies is also possible—although a-posteriori arguments suggest this is quite unlikely. GRB 050813 had no coincident host but occurred within a high-redshift cluster of galaxies, suggesting a possible association with the intracluster light (Prochaska et al. 2006b).

Looking beyond this initial population, however, the picture quickly grows muddled. Many additional short GRBs (over 40) have been localized to better than $5''$ since 2005[17],

[17] A website tool I have developed, GRBOX (the Gamma-Ray Burst Online Index; Perley & Kemper 2008) makes determination of statistics like this simple.

but essentially none of them are clearly associated with old galaxies lacking any current star-formation (in the unambiguous manner of GRBs 050509B or 050724). Some are coincident with star-forming hosts, in all cases to date at redshifts of $z < 1$ (e.g., Graham et al. 2009). Some appear have no coincident host galaxy at all, suggesting that the explosion happened in the intergalactic or intracluster medium far from any galaxy; but in other cases, what at first appearances looks like a hostless system are shown after deeper imaging to be coincident with a much fainter, possibly high-redshift, host (Berger 2010a).

In recent years concerted effort has been devoted towards detailed characterization of the environments of short GRBs in detail with the Hubble Space Telescope (HST) and other major international facilities. Given the classificational ambiguities endemic to the field (it is worth noting again that our prototypical "short" burst, GRB 050724, has a T_{90} of 96 seconds—this GRB is a classic example of an extended-emission event), and the need for an optical afterglow to identify the precise site of the short GRB progenitor within its host, this effort is fraught with peril. Nevertheless, these studies continue to confirm a strong statistical difference with the environments of long-duration bursts: as a population, SGRBs happen in redder galaxies with lower star-formation rates and larger masses than LGRBs (Prochaska et al. 2006b; Berger 2009; Leibler & Berger 2010); and their locations within these galaxies do not follow the distribution of blue light emitted by the younger stars in the disk (Fong et al. 2010; Fruchter 2010).

Based on these results, the most popular progenitor model for the SGRBs is the merger of two neutron stars, or a neutron star and a black hole (Nakar 2007; Lee & Ramirez-Ruiz 2007). This theory has a long history; such a compact-object merger was one of the original models for (all) cosmological GRBs (e.g., Blinnikov et al. 1984; Eichler et al. 1989; Paczyński 1991; Narayan et al. 1992; Mochkovitch et al. 1993), and the rates and energetics seem quite consistent with most observations. However, this model is far from secure: the unambiguous observational markers of such an event (gravitational waves, or a faint, fast-evolving "mini-supernova"; Li & Paczyński 1998) have yet to be observed, and the long-lived activity (late X-ray flares) evident in some short GRBs presents a potential problem for what is expected to be a fast-accreting, short-lived system (see the review of Nakar 2007—however, modifications and extensions to the model such as the formation of a millisecond pulsar instead of a black hole [Dai et al. 2006] or fallback from tidally stripped material [Rosswog 2007] may alleviate this issue). Other models, such as the accretion-induced collapse of a neutron star (Vietri & Stella 1999; Katz & Canel 1996; MacFadyen et al. 2005), remain viable. Indeed, it is possible that the short class is actually split between several different progenitors: for example, Troja et al. (2008) have claimed that the presence or absence of extended emission might divide short GRBs into two physically distinct sub-classes (but c.f. Chapter 2 for a prominent counter-example).

1.4.2 LGRBs: Signposts of Star Formation

The LGRBs, typified by GRB 030329 (Hjorth et al. 2003; Stanek et al. 2003) with its luminous afterglow, clear association with a low-mass star-forming galaxy, and accompanying

type-Ic supernova, are much better understood. Many different lines of evidence associate this group, which constitutes the large majority of the observed GRB population[18] (using the phenomenological categorization, 75% of events from the BATSE sample and 90% of events from the *Swift* sample are long-soft bursts; Paciesas et al. 1999; Sakamoto et al. 2011), with star-forming regions and specifically with the core-collapse of massive stars in those regions. Many, perhaps most, LGRB hosts are extremely young, rapidly star-forming dwarf galaxies or bright, high-z starbursts with no appreciable evolved stellar population (e.g., Le Floc'h et al. 2003, 2006). The locations of the bursts within these galaxies are invariably close to the center and coincident with the stellar disk, consistent with a young stellar population but inconsistent with an old star or ejected progenitor (Bloom et al. 2002); not only do they trace the UV light from massive stars within these galaxies, but they appear to concentrate towards the very UV-brightest regions, suggesting association with the most massive stars (Fruchter et al. 2006). When an LGRB occurs sufficiently nearby for detection of supernova emission to be observationally practical ($z \lesssim 1$ for a photometric search or $z \lesssim 0.4$ for a spectroscopic search), a bright supernova is usually found (e.g., Galama et al. 1998; Malesani et al. 2004; Pian et al. 2006; Chornock et al. 2010; see Woosley & Bloom 2006 for a review). All such supernovae to date have been of the spectral type Ic, indicative of the core collapse of a very massive star which has lost its hydrogen and helium envelopes.[19]

What remains unclear, for now, is the channel by which this stripped-envelope star is produced, and what special conditions (if any) are required for its production. GRBs[20] are exceedingly rare (only one in $\sim 10^6$ stars will produce a GRB, and one in $\sim 10^4$ massive stars; Podsiadlowski et al. 2004) and the ingredients for producing one are clearly unusual: not only must the massive star be able to blow away its outer layers (as is necessary for the GRB jet to escape the stellar envelope; Matzner 2003), but theoretical arguments also demand

[18]If not necessarily the majority in a volume-limited sense: long GRBs are much brighter and can be observed to greater distances. The $z \sim 0$ volumetric rate of SGRBs may actually significantly exceed that of LGRBs (Nakar et al. 2006)

[19]However, two interesting cases in 2006 contradicted this expectation. GRB 060505, which occurred in an HII region in a $z = 0.08$ spiral galaxy, produced no detectable supernova to very deep limits (Fynbo et al. 2006b). GRB 060614 occurred in small galaxy with a very low star-formation rate at $z = 0.125$ and also produced no supernova (Fynbo et al. 2006b; Della Valle et al. 2006; Gehrels et al. 2006). The correct interpretation of these two events is controversial. First, their classification is unclear: GRB 060505 had a T_{90} of only 4 seconds, putting it within the overlap region of the duration-hardness diagram; GRB 060614 had a T_{90} of 102 seconds, but its light curve qualitatively resembles that of a short burst with extended emission and it has an unusually low "lag" (furthermore its host galaxy has a very low star-formation rate). As a result, one interpretation is that they are actually SGRBs (Zhang et al. 2007). (But, both of these judgements were made after the fact when the supernova nonassociation had been realized.) But if either or both are genuine LGRBs and are produced by the collapse of a massive star, this instead indicates that the core-collapse of such a star to a black hole can occur with minimal production of the radioactive Ni-56 that powers optical supernova emission; for example as was predicted by the original "collapsar" model of a failed supernova (Woosley 1993; Hartmann & Woosley 1995). Of course, it is also possible that one or both of these events belongs to neither progenitor class (Gal-Yam et al. 2006).

[20]For simplicity, we will often use "GRB" and "LGRB" interchangeably in sections such as this one where SGRBs are not being considered.

that it retain a rapidly-rotating core at the time of explosion (to produce the accretion disk and jet upon core collapse; Woosley 1993; MacFadyen & Woosley 1999). The most obvious such special ingredient is metallicity: metals provide the opacity of a star's envelope and make it more susceptible to losing mass as a result of radiation pressure (Eddington 1926). Therefore, one might naively expect that a high metallicity would be necessary to produce a GRB: after all, most stripped-envelope supernovae in the local universe originate from metal-rich galaxies (Modjaz et al. 2011). This is categorically *not* observed: in fact, there is evidence for the opposite conclusion, that GRBs originate primarily or even exclusively from very metal-poor galaxies (e.g., Stanek et al. 2006; Wolf & Podsiadlowski 2007; Modjaz et al. 2008). The solution probably lies in the fact that while winds do an excellent job of stripping away a massive star's outer layers, they also remove its angular momentum, thereby defusing the central engine. Alternatively, then, the star could actually *burn* the outer envelope if it is able to mix the outer material down into the core zone (Hirschi et al. 2005; Yoon & Langer 2005; Woosley & Heger 2006); theoretical work suggests that this may indeed be possible if the metallicity of the star is *very* low ($\lesssim$0.1 Solar). Or, even if the progenitor star does lose its envelope (and angular momentum), the core could be subsequently spun up again by mass transfer from or merger with a binary companion (Izzard et al. 2004; Podsiadlowski et al. 2004; Fryer & Heger 2005), in which case no strong metallicity dependence is expected.

Despite these uncertainties about the evolutionary history of the progenitor star, the association of long-duration GRBs with star-formation is sufficiently strong that their observational study is now motivated as much by their use for learning about the broader universe than by the goal of constraining their origins. Much attention in astronomy is currently devoted to understanding the history of star-formation in the early universe (e.g., Fan et al. 2006a; Bouwens et al. 2007; Reddy et al. 2008), and the sheer brightness of a long GRB and its afterglow combined with the direct association of the phenomenon with short-lived (and therefore recently-formed) massive stars makes GRBs extremely useful as probes of high-redshift star-forming galaxies and of star-formation generally.

GRBs can be used as tools in two distinct ways. First, GRB afterglows can be used as *backlights* to study the nature of the star-forming galaxies in which they reside in detail, as well as any other matter along the line of sight through which the radiation passes on its way to earth—usually via optical spectroscopy (e.g., Fynbo et al. 2009) but also potentially via broadband photometry (the primary technique employed in this work). GRBs and their afterglows are extremely luminous events (up to thousands of times more powerful than the most luminous quasars, another object frequently used as a cosmological backlight; Bloom et al. 2009), allowing them to be identified even at immense distances ($z > 8$ and beyond; Tanvir et al. 2009; Salvaterra et al. 2009; Cucchiara et al. 2011) or from within dust-enshrouded regions, sites where other observational techniques struggle. Also unlike quasars, GRBs are short-lived transient sources, and so their radiation does not alter the matter within their hosts before their explosion and, once the afterglow fades, its glare does not complicate detailed study of the host galaxy in emission.

Second, GRBs provide an excellent *beacon* for locating and sampling high-redshift galaxies as a population. The global distribution of a range of GRB observables (redshifts, host

colors and host morphologies) is directly controlled by cosmological properties (in particular the evolution of the global star-formation rate, the mass and luminosity function of high-z star-forming galaxies, the initial mass function, etc.). In particular, the detection of the high-energy radiation from a GRB (gamma-rays and X-rays) is unaffected by the luminosity or the dust content of the host galaxy, two major selection effects that complicate attempts to infer the demographics of star-formation in the early universe (e.g., Bouwens et al. 2007; Adelberger & Steidel 2000). If GRBs roduction is not strongly affected by the host-galaxy metallicity, a sample of host galaxies pinpoined by GRB afterglows would then provide a star-formation weighted sample of the sites of (massive) stellar birth in the universe independent of these traditional biases and up to almost any observable redshift (Lamb & Reichart 2000; Blain & Natarajan 2000). If the GRB rate is dependent on the host metallicity (as some evidence seems to indicate), the situation is obviously more complicated, as the stories of the conditions necessary to produce the GRB and of the evolution of cosmic star-formation become intertwined. Nevertheless, in conjunction with other diagnostics (including field-survey techniques, whose biases are quite different) we can hope to separate these effects and bring an answer to both questions.

1.4.3 A Biased Sample?

The hundreds of GRBs provided by *Swift* would seem to be an ideal data set to begin addressing these questions. However, extreme caution is warranted before proceeding—while the population of GRBs detected by the *Swift* BAT (or by other gamma-ray satellites) should *in principle* be independent of the environment and even (after some correction based on the GRB luminosity function and detector efficiency; e.g. Butler et al. 2010) redshift, the gamma-ray signal on its own carries almost no information about either redshift or environment.[21] In reality, then, essentially all useful information about the GRB environment is obtained from the afterglow, or from the host galaxy (which requires the positional accuracy provided by an afterglow detection to uniquely pinpoint.)

The detection of an afterglow is highly susceptible to observational biases of many different flavors. Numerous factors influence the observed flux (and therefore detectability) of an afterglow (e.g., Sari et al. 1998): the total energy of the shockwave, the density of the surrounding medium into which it explodes, the microphysics of the shock, as well as extrinsic

[21]This claim is subject to several caveats. A distant GRB *should*, in principle, appear fainter (due to distance), longer (due to cosmological time dilation), and softer (due to redshift) than a very close GRB. Unfortunately, the immense intrinsic diversity of GRBs—the isotropic energy-release, duration, and peak-photon energy ($E_{\rm iso}$, T_{90}, and $E_{\rm peak,rest}$) all vary over many orders of magnitude among GRBs—make this subject exceptionally difficult to approach, a problem that is only exacerbated by instrumental effects. While a great deal of effort has been invested in searching for correlations that may enable some of this intrinsic variation to be removed (e.g., Amati et al. 2002; Ghirlanda et al. 2004; Yonetoku et al. 2004; Firmani et al. 2006; Schaefer 2007) (and, perhaps, the results applied to cosmology) these results remain controversial (Butler et al. 2007, 2009). Finally, the assumption that the prompt emission is indeed independent of the burst environment is necessarily dependent on the notion that GRBs are internal shocks due to self-interaction of the ejecta, rather than external shocks produced by interaction of the ejecta with the environment.

effects (the distance of the burst from Earth and any absorption of the afterglow light along the sightline) and practicl considerations such as the response time of the telescope. All of these factors are potentially important, but few of them are of interest from the standpoint of constraining the burst *environment*, the developing theme of this study.[22] The two factors that should clearly give us pause are:

The *circumburst density*: The interstellar medium provides the material through which the forward shock travels and is therefore directly responsible for the afterglow emission.[23] The dependence is not strong (the observed flux below the cooling frequency varies with density as $F \propto n^{1/2}$; frequencies above the cooling break, such as X-rays, are not affected by the interstellar density at all—unless the density is so low that the cooling frequency itself is pushed beyond this band) and it takes a significant variation in density to appreciably dim an afterglow. Nevertheless, bursts occurring outside galaxies where the density is orders of magnitude below what is canonically observed ($n_{\rm IGM} \sim 10^{-4}$ cm^{-3}, instead of $n_{\rm ISM} \sim 1$ cm^{-3}) would have much fainter afterglows, even at X-ray wavelengths.

Host-galaxy absorption: Light from a GRB or other distant cosmic source can be absorbed by the matter through which it passes on the way to Earth. Optical-UV light is attenuated by interstellar dust (micron-sized granules in the ISM, composed mostly of unidentified molecular compounds of common refractory elements such as carbon, oxygen, and silicon; Draine 2003), while the soft X-rays are similarly attenuated by various metal species (mostly oxygen) in the gas phase. The host galaxy ISM also imprints absorption lines on the spectrum—most of which are insignificant in a broadband sense with the exception of the damped Lyman-α line, which in gas-rich hosts can absorb a significant fraction of the flux near a rest-frame wavelength of 1217 Å. Once the light escapes the host galaxy, ultraviolet light blueward of the Lyman-α break is further absorbed by neutral hydrogen in the intergalactic medium, should that be present in significant quantities (at $z \sim 1$ this effect is nearly negligible [Madau 1995]; at $z \sim 2-4$ the hydrogen is clumped into dozens of small clouds at varying redshifts along the line of sight that create a Lyman-α forest of deep absorption lines [e.g., Rauch 1998]; at $z > 4$ the IGM becomes so uniformly opaque that all light emitted blueward of 1217 Å in the host frame is almost totally absorbed, creating a sharp break in the spectrum [Gunn & Peterson 1965]) Finally, the light must pass through our own Galaxy, again subjecting it to the absorbing effects of dust and gas, although the Galactic dust and gas distributions are well-mapped (Schlegel et al. 1998) and, except near the plane, these effects can be easily corrected for (Cardelli et al. 1989).

Among the various absorption effects described above, only two are strong enough to

[22]Unless, of course, one of these factors correlates with the environment in a pernicious way: for example, if a sub-class of GRB is produced by a long-lived progenitor and for some reason produces a forward shock with a vastly weaker radiative efficiency than "ordinary" GRBs from massive stars. Such cases will be considered later.

[23]Alternately, the burst can shock on a circumstellar wind from the (massive star) progenitor itself. In this case the afterglow flux depends on the properties of the wind (specifically, the mass-loss rate and wind velocity), a characteristic of the progenitor star itself, and no longer depends on the environment at all. In any event, evidence for a wind environment is (somewhat surprisingly) rarely seen in GRB light curves.

explain the nondetection of an afterglow that would otherwise be bright (and therefore potentially bias an existing sample): host-galaxy dust extinction and Lyman-break absorption at $z > 4$.[24] At X-ray wavelengths, fortunately only *soft* X-rays are significantly absorbed by the host gas; the *Swift* XRT bandpass extends up to 10 keV at which the ISM is nearly transparent (even for a column density of $N_H \sim 10^{23}$ cm^{-2}—essentially unprecedented for GRBs—only 1% of the 10 keV flux is observed.)

Finally, independent of genuine selection biases, we must also consider simple incompleteness: before *Swift*, most conclusions about GRBs have been based on a relatively small number of events (43 with measured redshift). Even if these events are representative of nearly all gamma-ray bursts, we must remain open to the possibility that additional classes of events producing high-energy radiation could lurk within a larger or more general sample. An obvious example concerns SGRBs, which were not realized to be physically distinct from LGRBs until *Swift*'s capabilities finally enabled the detection of their extremely underluminous afterglows. As previously discussed, SGRBs are thought to usually be recognizable from LGRBs based on their high-energy emission, but this has never been firmly tested, and perhaps some canonically "long-duration" bursts are actually SGRBs in disguise, as has been speculated to be the case for GRB 060614 (Zhang et al. 2007). More exotically, the GRB population may harbor additional, rarer progenitor classes seprate from both SGRBs and LGRBs. This is not as speculative as it might seem at first glance: several other exotic classes of GRB that have been identified as lurking within the general GRB population include SGR megaflares from nearby galaxies (Frederiks et al. 2007; Mazets et al. 2008), an as-yet-unidentified rapidly-flickering transient within the Milky Way (Kasliwal et al. 2008), and an explosive eruption from a previously-quiescent supermassive black hole in a distant dwarf galaxy (Levan et al. 2011; Bloom et al. 2011). What other classes of GRBs might we able to recognize based on observations of their environments?

1.5 Goals and Outline

The goal of this thesis project is to directly address these possible deficiencies of the pre-*Swift* sample by specifically seeking out the kinds of events that are difficult to find. I employ a variety of different observational strategies towards this goal, but the large majority of the observations and data analysis revolve around two types of observational effort: the *multiwavelength analysis of GRB afterglows* using multi-color ground-based OIR observations in conjunction with *Swift* X-ray data (Chapters 2–6), and a multi-year program at Keck Observatory to *search for and characterize host galaxies* of a wide array of potentially "unusual" GRBs (Chapters 7–8).

Following this introduction, Chapter 2 of the thesis concerns short-duration bursts, and the particular case of GRB 080503. It has been previously claimed that despite the great difficulty in detecting short burst afterglows to date, this can be readily explained as a simple

[24] Of course, Galactic foreground extinction can be extremely significant, but these ∼10–20% of events can be easily recognized and excluded from the sample.

consequence of the fact that SGRBs are less energetic intrinsically (Nysewander et al. 2009a). I present an in-depth analysis of a particular event which defies this trend, showing that in at least one case a short GRB (with extended emission) likely exploded into a medium with very low density. Combined with the lack of coincident host galaxy in deep HST imaging, this provides strong evidence in support of the hypothesis that (some) GRBs are formed by the inspiral of compact-binary pairs that have been ejected far from their host galaxy by a supernova kick.

In contrast, only very few long GRBs seem consistent with occurring in an extragalactic environment. An interesting exception is discussed in Chapter 3, which focuses on GRB 071003, a long-duration gamma-ray burst with extremely weak Mg II absorption suggestive of formation in a Galactic halo or other environment. This GRB appears to have nevertheless originated from a massive star, suggesting that (as with GRB 070125, Cenko et al. 2008a; Chandra et al. 2008) its origin is most likely in an extremely low-mass galaxy or in tidal debris from a recent merger.

In Chapters 4–6 I present a detailed examination of the dust properties along the sightlines to a number of bright *Swift* GRBs for which good broadband photometry is available in the infrared from the robotic telescope PAIRITEL and in the optical from a variety of other telescopes. I will provide strong evidence for mild-to-moderate extinction columns affecting most of these events—and characterize the wavelength-dependence of this extinction (the extinction "law") in a variety of different cases, demonstrating that the cosmological diversity of extinction laws within GRB host galaxies is even greater than that seen within the Milky Way. I will also provide a minimum distance from the burst to the site of this dust by looking for evidence of dust destruction by radiation from the GRB.

In the remainder of the thesis, the focus switches from GRB afterglows to GRB host galaxies. Chapter 7 is an overview of our multi-year program at Keck observatory to identify these hosts, including the technical details of the data acquisition and reduction. With approximately 120 fields imaged to depths of $R > 25$ mag, this constitutes the largest GRB host-galaxy program ever conducted. The program as a whole does not constitute a uniform survey with strict target criteria designed to ensure a "fair" sample of all *Swift* GRBs. However, in Chapter 8, by combining a subset of our observations with the afterglow study of Cenko et al. (2009) we can provide a large (50-object) catalog that is nearly complete in redshifts and dust properties, which we use to quantify the causes of the so-called dark bursts and demonstrate them to be dust-extinguished.

Finally, in Chapter 9 I bookend this dissertation by briefly summarizing the major results presented elsewhere in the thesis. I will also attempt to summarize the state of the GRB field today, and the prospects for continued progress in the future.

Chapter 2

GRB 080503: A Short Gamma-Ray Burst in the Intergalactic Medium

An earlier version of this chapter was previously published as ApJ 696:1871–1885[1].

Abstract

Models for short GRBs which invoke the merger of degenerate objects (neutron stars or black holes) suggest that the progenitor of the explosion may be ejected from the disk of its host and flung into the galaxy's halo or even intergalactic space. The forward-shock model of GRB afterglows robustly predicts that this should result in a much fainter optical and X-ray afterglow in some cases, but none of the afterglows which have been studied in detail unambiguously show such a signature. In this chapter, I discuss the case of GRB 080503, a bright short-duration GRB with extended high-energy emission for which the optical counterpart is extraordinarily faint, never exceeding 25 mag in deep observations starting at ∼1 hr after the BAT trigger. The extreme faintness of this probable afterglow relative to the bright gamma-ray emission argues for a very low-density medium surrounding the burst (a "naked" GRB), consistent with the lack of a coincident host galaxy down to 28.5 mag in deep *Hubble Space Telescope* imaging. These observations reinforce the notion that short gamma-ray bursts generally occur outside regions of active star formation, but demonstrate that in some cases the luminosity of the extended prompt emission can greatly exceed that of the short spike, which may constrain theoretical interpretation of this class of events. This extended emission is not the onset of an afterglow, and its relative brightness is probably either a viewing-angle effect or intrinsic to the central engine itself. Because most previous BAT short bursts without observed extended emission are too faint for this signature to have been detectable even if it were present at typical level, conclusions based solely on the observed presence or absence of extended emission in the existing *Swift* sample are premature.

2.1 Introduction

Despite significant progress since the launch of the *Swift* satellite (Gehrels et al. 2004), the origin of short-duration, hard-spectrum gamma-ray bursts remains elusive. Evidence has been available since the early 1990s that these events constitute a separate class from longer GRBs on the basis of a bimodal distribution in duration (Mazets et al. 1981; Norris et al. 1984) and spectral hardness (Kouveliotou et al. 1993). The supposition that this phenomenological divide is symptomatic of a true physical difference in the origin of the events was supported by the first successful localizations of SGRB afterglows with the *Swift* X-ray telescope (Burrows et al. 2005c) coincident with or apparently very near low-redshift ($z < 0.5$) galaxies (Gehrels et al. 2005; Fox et al. 2005b). Several of these galaxies clearly lack significant recent star formation (e.g., Prochaska et al. 2006b; Gorosabel et al. 2006; Berger et al. 2005b), many events appeared at large offset from the candidate host (Bloom et al. 2006f, 2007b; Stratta et al. 2007), and in some cases the appearance of a bright supernova was definitively ruled out (e.g., Hjorth et al. 2005a). All of these circumstantial clues seem to suggest (Lee & Ramirez-Ruiz 2007; Nakar 2007) a progenitor very different from the one responsible for long-duration GRBs (LGRBs), which are predominately due to the deaths of massive stars (see Woosley & Bloom 2006 for a review).

The generally favored interpretation of SGRBs is the merger of two highly compact degenerate objects: two neutron stars (NS–NS, Eichler et al. 1989; Meszaros & Rees 1992; Narayan et al. 1992) or a neutron star and a black hole (NS–BH, Paczyński 1991; Narayan et al. 1992; Mochkovitch et al. 1993; Kluzniak & Lee 1998; Janka et al. 1999). However, other progenitor models (e.g., MacFadyen et al. 2005; Metzger et al. 2008b) can also be associated with galaxies having low star-formation rates (SFRs), and many SGRBs have also been associated with relatively low-luminosity, high-SFR galaxies (Fox et al. 2005b; Hjorth et al. 2005b; Covino et al. 2006c; Levan et al. 2006d) and at much higher redshifts (Berger et al. 2007c; Cenko et al. 2008a) than the better-known elliptical hosts of the first few well-localized SGRBs 050509B and 050724. (A review of SGRB progenitor models is given by Lee & Ramirez-Ruiz 2007.)

In addition, even the conventional distinction between SGRBs and LGRBs has been called into question by some recent events which poorly conform to the traditional classification scheme. A large number of *Swift* events which initially appeared to be "short" (based only on the analysis of the first, most intense pulse) were then followed by an additional episode of long-lasting emission with a duration of up to 100 s or longer. GRB 050724, which unambiguously occurred in an elliptical host, is a member of this class, creating a breakdown in the use of duration (in particular T_{90}, Kouveliotou et al. 1993) as a classification criterion. To further complicate the picture, long GRB 060614 exploded in a very low-SFR dwarf galaxy at $z = 0.125$ and despite an intensive follow-up campaign showed no evidence for a supernova, even if extremely underluminous ($M_V > -12.3$, Gal-Yam et al. 2006). Similar confusion clouds the physical origin of GRB 060505, which is of long duration ($T_{90} = 4 \pm 1$ s) and occurred in a star-forming region of a spiral galaxy (Thöne et al. 2008b), but also lacked supernova emission to very deep limits (Fynbo et al. 2006b). Two

earlier bursts, XRF 040701 (Soderberg et al. 2005) and GRB 051109B (Perley et al. 2006), may constitute additional examples of this subclass, though available limits in each case are much shallower and the alternate possibility of host-galaxy extinction is poorly constrained compared to the 2006 events. On the basis of these results and others, Zhang et al. (2007) have called for a new terminology for classification that does not refer to "short" and "long" but rather to Type I and Type II GRBs, in recognition of the fact that duration alone is likely to be an imperfect proxy for physical origin (see also Gehrels et al. 2006, Bloom et al. 2008, Kann et al. 2011).

The true "smoking gun" for the merger model, the detection of gravitational waves, is unlikely to occur before the completion of the next generation of gravity-wave detectors, as the sensitivity of current detectors (LIGO, Abbott 2004; and Virgo, Acernese 2004) is several orders of magnitude below what would be necessary to detect a merger at what appears to be a "typical" short GRB redshift of 0.2–1.0 (Abbott 2008). However, degenerate-merger models do offer additional observationally verifiable predictions.

First, merger progenitors are much older than massive stars and can travel far from their birthsites, especially if they are subject to kicks which in some cases could eject the binary system progenitor from the host galaxy entirely (Fryer et al. 1999; Bloom et al. 1999). Observationally, this should manifest itself in the form of large angular offsets between the burst position and the host galaxy or even the lack of any observable host at all. Such an trend has indeed been noted for many events (e.g., Prochaska et al. 2006b). The second prediction, however, has yet to be demonstrated: if some SGRBs explode in galactic halos, then the extremely low associated interstellar density will result in a much fainter afterglow associated with the external shock: a "naked" gamma-ray burst. And while the afterglows of SGRBs tend to be fainter in an absolute sense (Kann et al. 2011), relative to the gamma-ray emission (on average, SGRBs have much lower total fluences than long LGRBs) there appears to be no obvious difference between SGRB and LGRB afterglows (Nysewander et al. 2009a). Part of this may be a selection effect, but the brightest SGRBs to date have all been associated with bright afterglows and cannot be "naked".

Second, during the merger process, a significant amount of neutron-rich ejecta (including $\sim 10^{-3}\mathrm{M}_{\odot}$ of radioactive Ni, Metzger et al. 2008b) is believed to be ejected at nonrelativistic velocities into interstellar space. Nucleosynthesis in this matter and the resulting radioactive decay would be expected to produce a relatively long-lived optical counterpart, similar to ordinary supernovae (Li & Paczyński 1998). Unfortunately, the luminosity of the transient is generally much lower and the timescale of evolution is significantly faster than in a classical supernova. Detection of this signature remains one of the holy grails in the study of GRBs, though deep early limits for some SGRBs have allowed some limits to be set on the physical parameters of this phenomenon (Bloom et al. 2006f; Hjorth et al. 2005a; Kann et al. 2011).

In this paper, we present results from our follow-up campaign of GRB 080503, which we argue in §2.2.1 is a prominent example of the emerging subclass of SGRBs with extended episodes of bright, long-lasting prompt emission following the initial short spike. In §2.2.2–§2.2.7 we present additional space-based and ground-based observations of the event highlighting several extreme and unusual features of this burst, including extreme optical

faintness, a late light-curve peak, and a very deep late-time limit on any coincident host galaxy. In §2.3 we attempt to interpret the observed behavior in the context of existing models of emission from GRB internal shocks, an unusual afterglow, and light from radioactive decay (a Li-Pacynski mini-SN or kilonova), arguing that the latter is probably not a large contributor at any epoch. Finally, in §2.4 we discuss the implications of this event for GRB classification, and on the difficulties faced by future searches for mini-SN/kilonova light associated with SGRBs.

2.2 Observations

2.2.1 BAT Analysis and High-Energy Classification

The *Swift* Burst Alert Telescope (BAT) detected GRB 080503 at 12:26:13 on 2008 May 3 (UT dates and times are used throughout this paper). The GRB light curve (Figure 2.1) is a classic example of a short GRB with extended emission: a short, intense initial spike with a duration of less than 1 s followed by a long episode of extended emission starting at $\sim$10 s and lasting for several minutes. The overall T_{90} for the entire event is 232 s.

Similar extended emission has been seen before in many short bursts detected by both *Swift* and BATSE (Figure 2.3). All such events to date have remarkably similar general morphologies. However, the fact that the long component is so dominant in this case (factor of $\sim$30 in total fluence) raises the question of whether this is truly a "short" (or Type I) GRB and not an event more akin to the traditional LGRBs (Type II) in disguise. To this end we have reanalyzed the BAT data in detail and applied additional diagnostics to further investigate the nature of this event. We also downloaded and re-analyzed BAT data from all other SGRBs (and candidate SGRBs) with and without extended emission through the end of 2007. A summary of the results of our analysis is presented in Table 2.1.

The BAT data analysis was performed using the *Swift* HEAsoft 6.5 software package. The burst pipeline script, `batgrbproduct`, was used to process the BAT event data. In addition to the script, we made separate spectra for the initial peak and the extended emission interval by `batbinevt`, applying `batphasyserr` to the PHA files. Since the spectral interval of the extended emission includes the spacecraft slew period, we created the energy response files for every 5 s period during the time interval, and then weighted these energy response files by the 5 s count rates to create the averaged energy response. The averaged energy response file was used for the spectral analysis of the extended emission interval. Similar methods were employed for previous *Swift* SGRBs.

For GRB 080503, the T_{90} durations of the initial short spike and the total emission in the 15–150 keV band are 0.32 ± 0.07 s, and 232 s respectively. The peak flux of the initial spike measured in a 484 ms time window is $(1.2 \pm 0.2) \times 10^{-7}$ erg cm^{-2} s^{-1}. The hardness ratio between the 50–100 keV and the 25–50 keV bands for this initial spike is 1.2 ± 0.3, which is consistent with the hardness of other *Swift* SGRBs, though it is also consistent with the LGRB population. In Figure 2.2 we plot the hardness and duration of GRB 080503

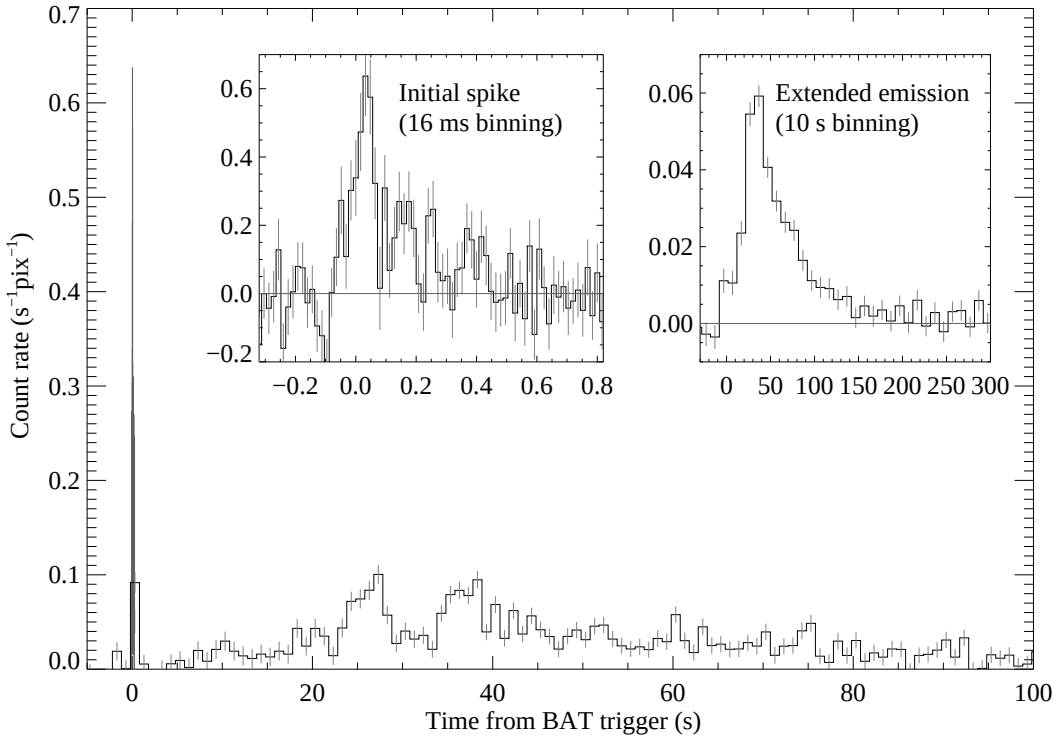

Figure 2.1 The BAT light curve of GRB 080503 with 1 s binning in the 15–150 keV band, with a 16 ms binning curve superposed for the duration of the short spike near $t = 0$. The short spike is also shown alone in the left inset. An extended, highly-binned (10 s) light curve is shown in the right inset, demonstrating the faint emission continuing until about 200 s.

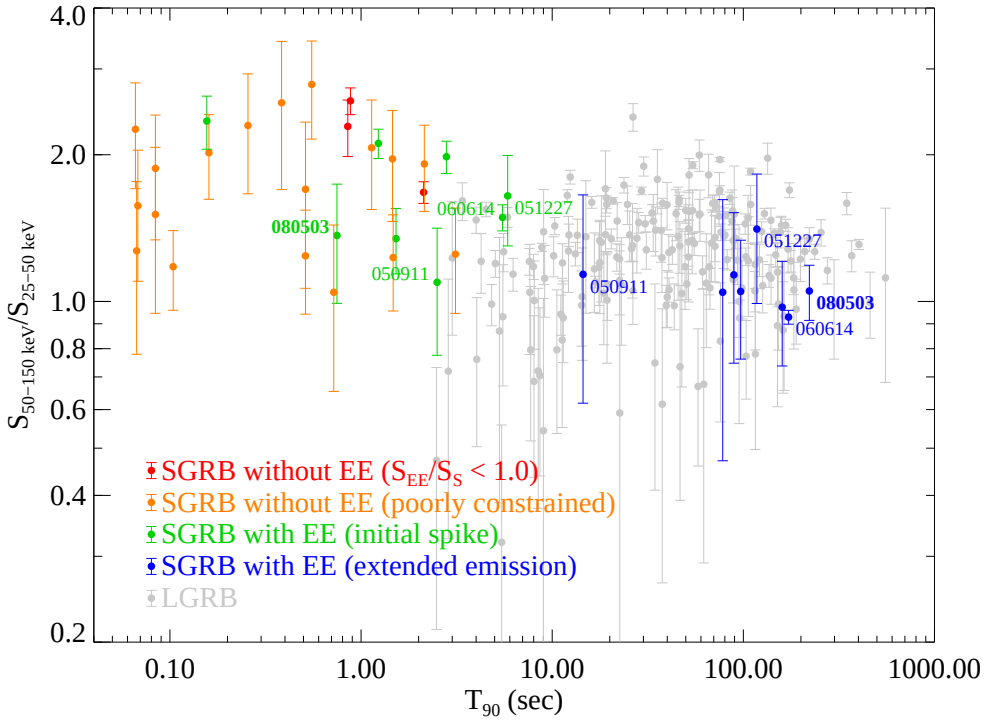

Figure 2.2 Duration-hardness plot for bursts detected by the *Swift* BAT. Long bursts are shown in gray. Short bursts (T_{90} < 2 sec) are colored based on the presence or absence of extended emission: bursts without extended emission are shown in red, faint bursts for which the presence of extended emission is poorly constrained are orange, and short bursts with observed extended-emission (including GRBs 050911, 060614, and 051227, whose classifications are controversial) are plotted with the short spike (green) shown separately from the extended emission (blue). The T_{90}s and hardness ratios measured for short-hard spikes in this population, including GRB 080503, are generally consistent with those measured for short bursts without extended emission. GRBs 060614 and 051227 may be consistent with both classes, but are unusually long compared to any short burst without extended emission. The extended-emission components of all three events display similar hardness and duration as the extended components of more traditional extended-emission events, which form a tight cluster (GRB 050911 is an outlier). In general, however, the hardness in the *Swift* channels is not a strong criterion for classification (Sakamoto et al. 2006; Ohno et al. 2008).

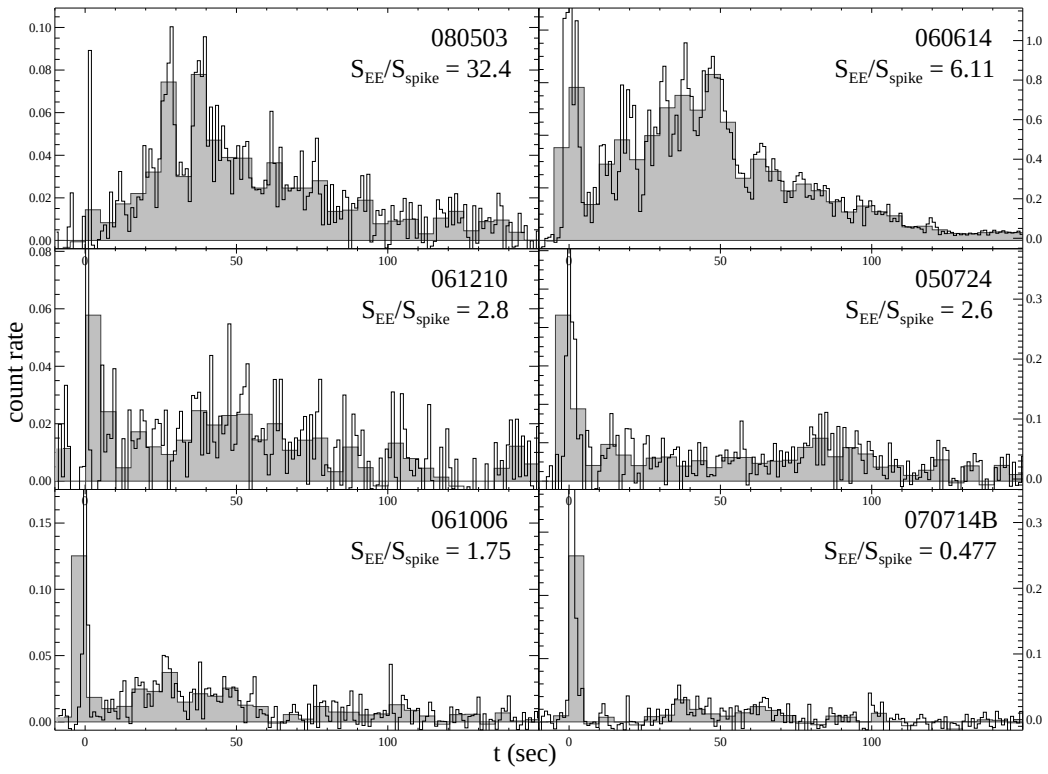

Figure 2.3 BAT 25–100 keV light curves of several different *Swift* short bursts with high signal-to-noise (S/N) extended emission, including GRB 080503 (top left), showing the similar morphology of these events. The 1 s binned curve is plotted as a black line; a 5 s binning is plotted in solid gray to more clearly show the longer-duration extended emission which for most events is near the detection threshold. Possible short GRB 060614 is also shown; it appears very similar to GRB 080503 except that the initial pulse is significantly longer.

against other *Swift* bursts, resolving this burst and other short events with extended emission separately into the spike and the extended tail. The properties of the initial spike of GRB 080503 match those of the initial spikes of other SGRBs with extended emission (and are consistent with the population of short bursts lacking extended emission), while the hardness and duration of the extended emission are similar to that of this component in other short bursts.

The fluence of the extended emission measured from 5 s to 140 s after the BAT trigger in the 15–150 keV bandpass is $(1.86 \pm 0.14) \times 10^{-6}$ erg cm^{-2}. The ratio of this value to the spike fluence is very large ($\sim$30 in the 15–150 keV band), higher than that of any previous *Swift* short (or possibly short) event including GRB 060614. It is not, however, outside the range measured for BATSE members of this class, which have measured count ratios up to $\sim$40 (GRB 931222, Norris & Bonnell 2006). In Figure 2.4, we plot the fluences in the prompt versus extended emission of all *Swift* SGRBs to date. BATSE bursts are overplotted as solid gray triangles; HETE event GRB 050709 is shown as a star. The two properties appear essentially uncorrelated, and the ratio has a wide dispersion in both directions. Although only two *Swift* events populate the high extended-to-spike ratio portion of the diagram (and the classification of GRB 060614 is controversial), the difference in this ratio between these and more typical events is only about a factor of 10, and the intermediate region is populated by events from BATSE and HETE[2], suggesting a continuum in this ratio across what are otherwise similar events.

Lag analysis (Norris et al. 2000) has also been used as a short-long diagnostic. For GRB 080503, the spectral lag between the 50–100 keV and the 25–50 keV bands using the light curves in the 16 ms binning is 1 ± 15 ms (1σ error), consistent with zero and characteristic of short-hard GRBs. Unfortunately, the signal is too weak to measure the spectral lag for the extended emission which dominates the fluence. While lag can vary between pulses in a GRB (Hakkila et al. 2008) and short pulses typically have short lags, even very short pulses in canonical long GRBs have been observed to have non-negligible lags (Norris & Bonnell 2006).

Based on all of these arguments, we associate GRB 080503 with the SGRB (Type I) class. Regardless of classification, however, the extremely faint afterglow of this burst appears to be a unique feature. In fact, as we will show, while the extremely low afterglow flux is more reminiscent of SGRBs than LGRBs, relative to the gamma-rays the afterglow is so faint that this event appears quite unlike any other well-studied member of either population to date.

2.2.2 UVOT Observations

The *Swift* UV-Optical Telescope (UVOT) began observations of the field of GRB 080503 at 83 s after the trigger, starting with a finding chart exposure in the White filter at $t = 85$–184 s. No source is detected within the XRT position to a limiting magnitude of >20.0

[2]However, the HETE fluence ratio is in a very different bandpass, and the actual ratio may be significantly lower than the plotted ratio.

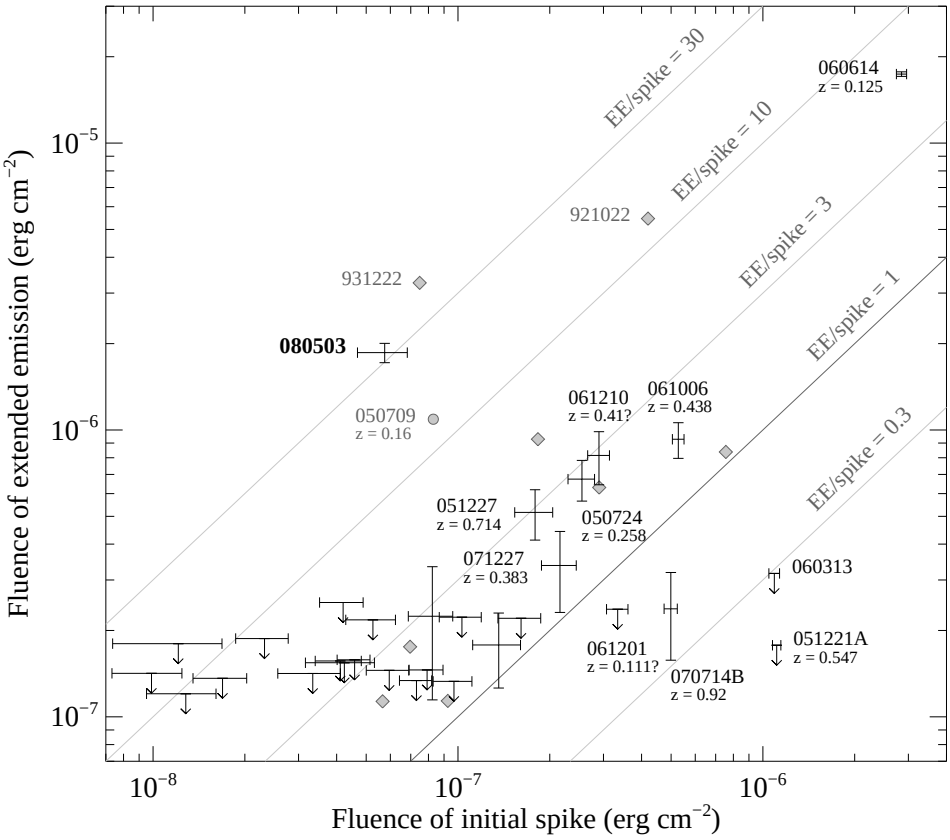

Figure 2.4 Fluences of the short initial spike versus the long extended-emission episode for SGRBs and candidate SGRBs. For *Swift* bursts this is measured in the 15–150 keV band. For BATSE bursts (diamonds) the values are calculated from the count rates in Norris & Bonnell (2006) and fluences (20–100 keV) on the BATSE website. HETE GRB 050709 (circle) is taken from Table 2 of Villasenor et al. (2005) and is in the 2–25 keV band, which is significantly softer than the *Swift* and BATSE bandpasses. In harder bandpasses the extended emission is likely to be much fainter; this point should therefore be treated as an upper limit. BATSE and HETE short bursts without extended emission are not shown. Several properties are worthy of note. First, the extended-to-prompt ratio shows large variance, quite unlike the observed T90 values and hardness ratios. Second, the large majority of *Swift* events without extended emission are very faint bursts — the limits on the extended counterpart are not strongly constraining, although strongly extended emission-dominated events like GRB 080503 do appear to be rare. Third, events with bright extended emission have a wide range of short-spike fluence; the two values are not correlated. Events with known redshift are labeled; no clear trends with distance are evident.

(Brown & Mao 2008). A sequence of filtered observations followed, and then additional White-band exposures. The transient is not detected in any exposure. Because of the deep Gemini data shortly thereafter, these additional limits do not constrain the behavior of the optical counterpart and are not reported or reanalyzed here. A summary of the the subsequent UVOT observations is given by Brown & Mao (2008).

2.2.3 Keck Observations

Shortly after the GRB trigger we slewed with the 10 m Keck-I telescope (equipped with LRIS) to the GRB position. After a spectroscopic integration on a point source near the XRT position that turned out in later analysis to be a faint star, we acquired (between 13:38:37 and 13:57:02) imaging in the B and R filters simultaneously. Unfortunately, because the instrument had not been focused in imaging mode prior to the target of opportunity, these images are of poorer quality and less constraining than Gemini images (see below) taken at similar times. The optical transient (OT) is not detected in either filter. Magnitudes (calibrated using the Gemini-based calibration, §2.2.4) are reported in Table 2.2.

On May 8 we used long-slit ($1''$ wide) spectroscopy with LRIS (Oke et al. 1995) on Keck I to obtain spectra of two relatively bright galaxies $13''$ SE of the afterglow position. We calibrated the two-dimensional spectra with standard arc and internal flat exposures. We employed the 600 line mm^{-1} grism (blue camera) and 600 line mm^{-1} grating blazed at 10,000 Å (red camera). The data were processed with the LowRedux[3] package within XIDL[4]. Both objects show the same emission lines, at common observed wavelengths of $\lambda_{\rm obs} \approx 5821$, 6778.8, 7592.2, 7745.6, and 7820 Å. The latter two are associated with the Hβ and [O III] λ5007 lines, respectively, identifying this system to be at $z = 0.561$.

While the placement of the slit in the target-of-opportunity spectroscopic observation on May 3 did not cover the location of the transient, a third, serendipitous object along the slit shows a single emission line at $\lambda_{\rm obs} \approx 6802.9$ Å and a red continuum. We tentatively identify this feature as unresolved [O II] λ3727 emission and estimate its redshift to be 0.8245. This source is far ($31''$) from the OT position, at $\alpha = 19^{\rm h}06^{\rm m}31^{\rm s}.1$, $\delta = +68^\circ48'04''.3$.

2.2.4 Gemini Observations

We also initiated a series of imaging exposures using GMOS on the Gemini-North telescope. The first image was a single 180 s r-band exposure, beginning at 13:24, 58 min after the *Swift* trigger. We then cycled through the g, r, i, and z filters with 5×180 s per filter. A second g epoch was subsequently attempted, but the images are shallow due to rapidly rising twilight sky brightness.

The following night (May 4) we requested a second, longer series of images at the same position. Unexpectedly, the transient had actually brightened during the intervening 24 hr,

[3] `http://www.ucolick.org/~xavier/LowRedux/index.html`; developed by J. Hennawi, S. Burles, and J. X. Prochaska.

[4] `http://www.ucolick.org/~xavier/IDL/index.html` .

so we continued to observe the source for several additional epochs. The next night (May 5), we acquired r-band images (9×180 s), followed by a long nod-and-shuffle spectroscopic integration, and concluded with 4×180 s exposures in each of the g and i bands. On May 6 and 7, we acquired long r-band imaging only (14×180 s on May 6 and 16×180 s on May 7). Finally, on May 8, we acquired a long K-band integration using NIRI, nearly simultaneous with the *HST* observations (§2.2.5) at the same epoch.

Optical imaging was reduced using standard techniques via the Gemini IRAF package[5]. Magnitudes were calculated using seeing-matched aperture photometry and calibrated using secondary standards. The standard star field SA 110 was observed on the nights of May 3, May 4, May 5, and May 8; catalog magnitudes (Landolt 1992) were converted to *griz* using the equations from Jester et al. (2005) and used to calibrate 23 stars close to the GRB position.

In an attempt to measure or constrain the redshift of GRB 080503, we obtained a nod-and-shuffle long-slit spectroscopic integration of the positions of the optical transient and the nearby faint galaxy S1 (Figure 2.6). Two exposures of 1320 s each were obtained starting at 12:20 on 2008 May 05. Unfortunately, even after sky subtraction and binning, no clear trace is observed at the position, and no line signatures are apparent. The redshift of the event is therefore unconstrained, except by the g-band photometric detection which imposes a limit of approximately $z < 4$.

We began near-infrared observations of GRB 080503 on 2008 May 08 at 12:46, roughly simultaneous with the *HST* measurement (§2.2.5). All images were taken in the K_s band with NIRI. We employed the standard Gemini-N dither pattern for each of the 30 s exposures. In all, 92 images were taken yielding a total time on target of ∼1.5 hr. The data were reduced and the individual frames were combined in the usual way using the "gemini" package within IRAF. There is no detection of a source at the location of the optical transient. The nearby faint galaxies (S1 and S4) are also undetected. Calibrating relative to the 2MASS catalog (excluding stars near the edge of the image), we derive an upper limit of $K_s > 22.47$ mag (3σ).

All optical photometry, in conjunction with the space-based measurements from *Swift* and Chandra, is plotted in Figure 2.5.

2.2.5 Hubble Space Telescope Observations

Given the unusual nature of the afterglow, and the indications of a Li-Paczyński-like light curve in the first two days, we proposed[6] to observe the field of GRB 080503 with the Wide-Field Planetary Camera (WFPC2) on *HST*. Filter changes, depth, and cadences were chosen to confirm or refute the basic predictions of the Li & Paczyński (1998) model (see §2.3.4). The localization region was observed in three epochs on 2008 May 8, May 12, and

[5]IRAF is distributed by the National Optical Astronomy Observatory, which is operated by the Association of Universities for Research in Astronomy (AURA) under cooperative agreement with the National Science Foundation.

[6]Program GO-DD 11551; PI Bloom.

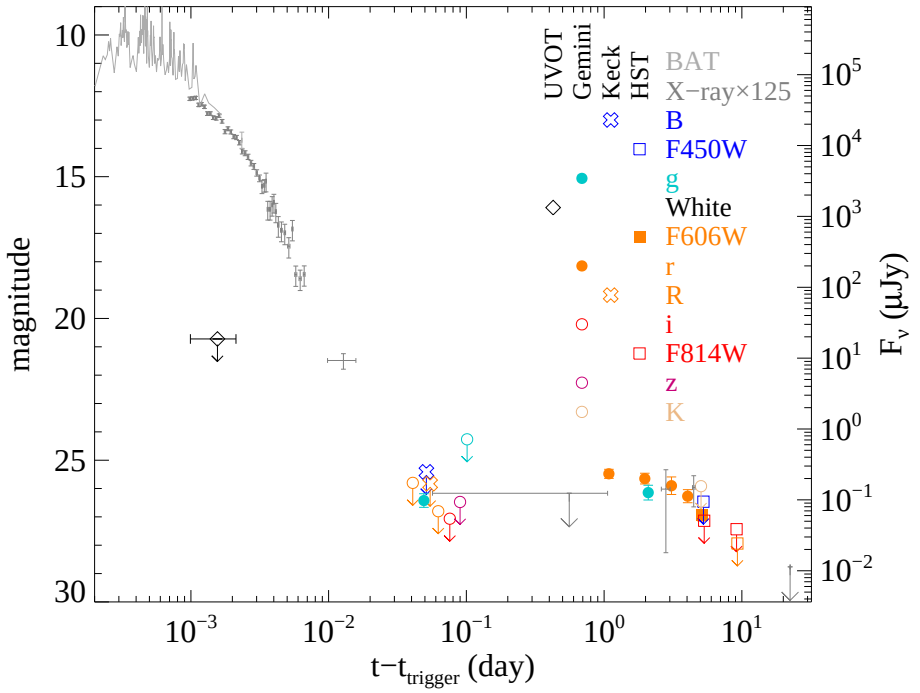

Figure 2.5 X-ray and optical light curves of GRB 080503. The optical bands have been shifted to the r band assuming an optical spectral index of $\beta = 1.2$; the X-ray light curve has been shifted by a factor of 125 to match the optical (corresponding to $\beta_{OX} = 0.75$). The BAT light curve is extrapolated into the X-ray band using the high-energy spectrum. 3σ upper limits are shown with arrows.

July 29. A set of F450W (1 orbit), F606W (2 orbits), and F814W (1 orbit) observations were obtained during the first visit, with F606W (2 orbits) and F814W (2 orbits) in the second visit, and finally a deep (4 orbit) observation in F606W in the third visit. Observations were dithered (a 3-point line dither for the first epoch of F450W and F814W, and a standard 4-point box for all other observations). The data were reduced in the standard fashion via `multidrizzle`, while the pixel scale was retained at the native $\sim 0.1''\text{pixel}^{-1}$.

At the location of the afterglow in our first-epoch F606W image we found a faint point source, with a magnitude of F606W = 27.01 ± 0.20 after charge-transfer efficiency correction following Dolphin (2000). Our other observations show no hint of any emission from the afterglow or any host galaxy directly at its position. We derived limits on any object at the GRB position based on the scatter in a large number (~ 100) of blank apertures placed randomly in the region of GRB 080503. The limits for each frame are shown in Table 2.2. In addition, a stacked frame of all our F814W observations yields F814W > 27.3 mag. A combination of all but our first-epoch F606W observations provides our deepest limit of F606W > 28.5 mag (3σ), in a stacked image with exposure time 13,200 s. Therefore any host galaxy underlying GRB 080503 must be fainter than that reported for any other short burst.

Although there is no galaxy directly at the GRB position, there are faint galaxies close to this position which are plausible hosts. In particular, our stacked image of all the F606W observations shows a faint galaxy $\sim 0.8''$ from the afterglow position, with F606W(AB) = 27.3 ± 0.2 mag (designated "S4" in Figure 2.6). Although faint, this galaxy is clearly extended, with its stellar field continuing to $\sim 0.3''$ from the GRB position. (It is plausible that deeper observations or images in redder wavebands may extend its disk further, but we have no evidence that this is the case.) Additionally, there is a brighter galaxy ("S1," F606W $\approx$ 26.3 mag) $\sim 2''$ to the north of the afterglow position, also visible in the Gemini images. Given the faintness of these galaxies and the moderate offset from the afterglow position, the probability of chance alignment is nontrivial (a few percent, following Bloom et al. 2002), and we cannot make firm statements about their association with GRB 080503.

The extremely deep limit on a host galaxy puts GRB 080503 in very rare company. Among short bursts, no comparably deep limit exists for any previous event except GRB 061201, although a study with deep *HST* imaging of short-burst hosts has yet to be published. However, ground-based searches for hosts of other SGRBs with subarcsecond positions have identified coincident host galaxies in 9 of 11 cases. The two exceptions are GRB 061201 (Stratta et al. 2007) and GRB 070809 (Perley et al. 2008a); both of these appear at relatively small physical offset from nearby spirals which have been claimed as host candidates. Short GRB 070707 has a coincident host with $R = 27.3$ mag (Piranomonte et al. 2008b), about the same as the magnitude of the nearest galaxy to the GRB 080503 OT position. In fact, even compared to long bursts, the lack of host galaxy is unusual; only five events have host-galaxy measurements or limits fainter than 28.5 mag.

There are two general possibilities to explain this extreme faintness. First, GRB 080503 could be at high redshift ($z > 3$), or at moderately high redshift in a very underluminous

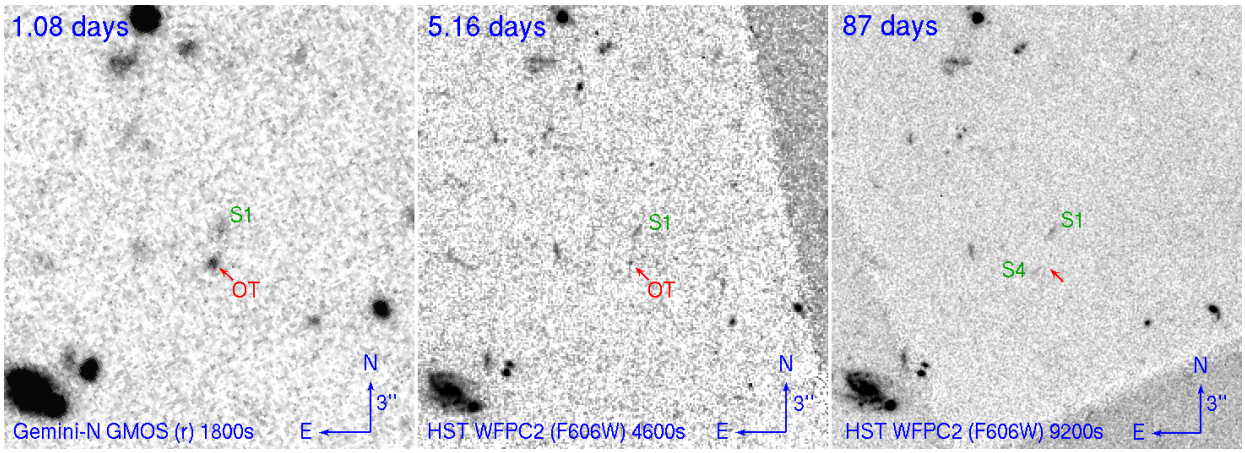

Figure 2.6 Ground-based and space-based images showing the evolution of the faint OT associated with GRB 080503. The transient peaked at about $t = 1$ d, shown in an image from Gemini-North at left. Thereafter it faded rapidly and is barely detected in the first *HST* epoch in F606W only. Later observations failed to reveal a galaxy coincident with the transient position. Two very faint nearby (but non-coincident) galaxies are designated "S1" and "S4."

galaxy (at $z \approx 1$, comparable to the highest-z SGRBs detected to date, $M_B < -15$ mag).[7] A bright "short" GRB at very high redshift would impose a much larger upper end of the luminosity distribution of these events than is currently suspected. An extremely underluminous host would also be surprising under a model associating SGRBs with old stars, since the bulk of the stellar mass at moderate redshifts is still in relatively large galaxies (Faber et al. 2007).

Second, GRB 080503 could be at low redshift but ejected a long distance from its host. To further examine this possibility, we have estimated the probabilities (following Bloom et al. 2002) of a statistically significant association with other bright galaxies in the field. A rather faint spiral galaxy is located 13″ SE of the afterglow position (J2000 coordinates $\alpha = 19^{\rm h}06^{\rm m}31^{\rm s}.7$, $\delta = 68°47'27''.9$; visible in the bottom-left corner of Figure 2.6) and has $r = 21.7$ mag and $z = 0.561$ (§2.2.3). The probability that this is a coincidence is of order unity. We also searched NED and DSS image plates for very bright nearby galaxies outside the field. The nearby ($D \approx 5$ Mpc) dwarf galaxy UGC 11411 is located at an offset of 1.5°; again the chance of random association is of order unity. There are no other nearby galaxies of note. While a low probability of random association does not rule out an association with one of these objects (a progenitor that escapes its host-galaxy potential well and has a sufficiently long merger time will be almost impossible to associate with its true host), it prevents us from making an association with any confidence.

[7] GRB 080503 could also be at moderate redshift $z = 1 - 3$ in a moderately large but extremely dusty galaxy. Even then, our K nondetection imposes strong constraints on the size of the object, and the relatively blue $g - r$ afterglow color suggests that the environment of the GRB is not particularly dust-obscured.

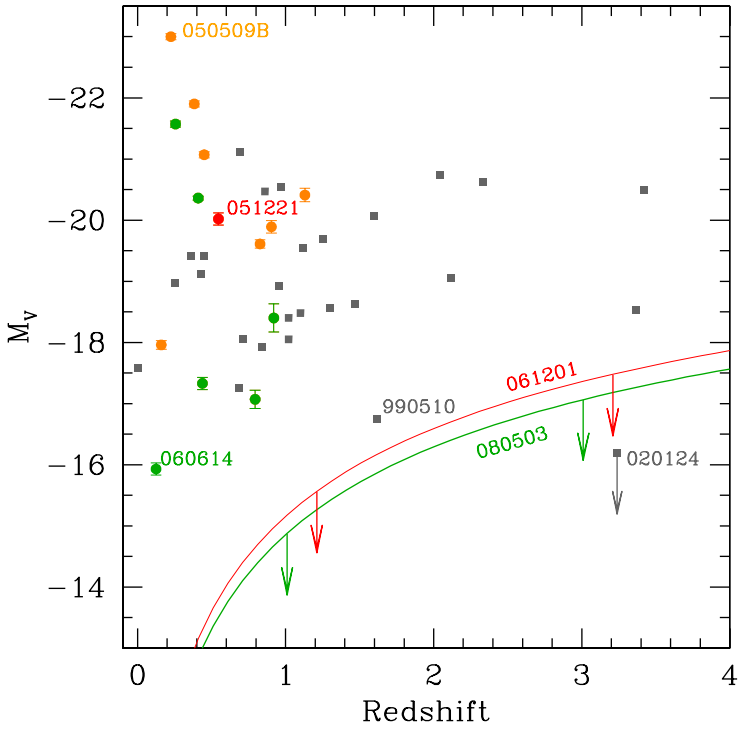

Figure 2.7 The absolute magnitudes and redshifts for a sample of both long (grey squares, from Fruchter et al. 2006) and short GRB hosts. Bursts with extended emission are marked in green and bursts without extended emission are red; orange denotes SGRBs too faint for a strong limit on extended emission fluence to be inferred. The two solid lines represent "host-less" SGRBs 061201 and 080503, and are extrapolated based on the observed limits. Due to the poor wavelength sampling of many faint GRB hosts the absolute magnitudes have been obtained assuming a flat spectrum K-correction $M_V = V - DM + 2.5\log(1+z)$, where DM is the distance modulus. We have assumed a ΛCDM cosmology with $\Omega_M = 0.27$, $\Omega_\Lambda = 0.73$ and $H_0 = 72$ km s^{-1} Mpc^{-1}. The nondetection of a host for GRB 080503 implies either that it lies at higher redshift than the majority of the SGRB population, that it originates from a host which is much fainter than the median, or that it has been ejected to a sufficient distance from its host that it can no longer be firmly associated with it. Such deep limits to hosts underlying GRBs are rare, with only a single LGRB (020124, Berger et al. 2002) undetected in deep HST imaging (out of a sample of ~ 50), while two SGRBs (of roughly 15 with good optical positions) are undetected to similar limits.

2.2.6 Swift XRT analysis

The *Swift* X-ray telescope began observing GRB 080503 starting ∼82 s after the burst, detecting a bright X-ray counterpart. Observations continued during the following hour and in several return visits.

The XRT data were reduced by procedures described by Butler & Kocevski (2007a). The X-ray light curve, scaled to match the optical at late times, is shown in Figure 2.5. Despite the bright early afterglow, the flux declined precipitously and no significant signal is detected during the second through fourth orbits. A marginally significant detection is, however, achieved during a longer integration a day later.

The X-ray hardness ratio decreases, as does the 0.3–10.0 keV count rate, during the course of the early observations (Figure 2.8a,b). Absorbed power-law fits to the evolving spectrum are statistically acceptable ($\chi^2/\mathrm{dof} \approx 1$) and yield a photon index Γ which increases smoothly with time and an H-equivalent column density N_H that apparently rises and then falls in time (Figure 2.8c,d). This unphysical N_H variation is commonly observed in power-law fits to the XRT emission following BAT GRBs and XRT flares (see, e.g., Butler & Kocevski 2007b); it suggests that the intrinsic spectrum, plotted on a log-log scale, has time-dependent curvature. In fact, we find that the combined BAT and XRT data are well fit by a GRB model (Band et al. 1993) with constant high- and low-energy photon indices and a time-decreasing break energy that passes through the XRT band during the observation.

The amount of physical column density that contributes to the effective N_H in Figure 2.8c can be estimated at early or late times, when the effective N_H is near its minimum, or from the Band et al. (1993) GRB model fits. We find $N_H = 5.5^{+1.5}_{-0.9} \times 10^{20}$ cm^{-2}, comparable to the Galactic value of $N_H = 5.6 \times 10^{20}$ cm^{-2}, indicating that the host-galaxy hydrogen column is minimal.

2.2.7 Chandra X-Ray Observatory Observations

Under Director's Discretionary Proposals 09508297 and 09508298, we conducted imaging using the Chandra X-Ray Observatory ACIS-S on two occasions. During the first integration (2008-05-07 19:18:23 to 2008-05-08 04:09:59) an X-ray source is detected at $\alpha = 19^{\mathrm{h}}06^{\mathrm{m}}28^{\mathrm{s}}.76$, $\delta = +68°47'35''.3$ (J2000, $0.5''$ uncertainty), consistent with the position of the optical afterglow. This source was not detected during the second epoch (2008-05-25 18:11:36 to 2008-05-26 03:04:28), limiting the decay rate to steeper than approximately $t^{-1.6}$.

Minimizing the Cash (1976) statistic, we find the Chandra spectrum to be acceptably fit by an absorbed power law with $\beta = 0.5 \pm 0.5$ and unabsorbed flux $F_X = (1.5 \pm 0.7) \times 10^{-14}$ ergs cm^{-2} s^{-1} (0.3–10 keV). We assume Galactic absorption only.

We attempted to use the photon arrival times to constrain the temporal index (α) assuming power-law brightening or fading behavior (Butler et al. 2005). The exposure time is short compared to the time elapsed since the GRB, precluding strong constraints. Although the data do marginally favor brightening behavior ($\alpha = -13 \pm 7$), in contrast to the well-established optical fading at this point, we do not consider this to be a strong conclusion.

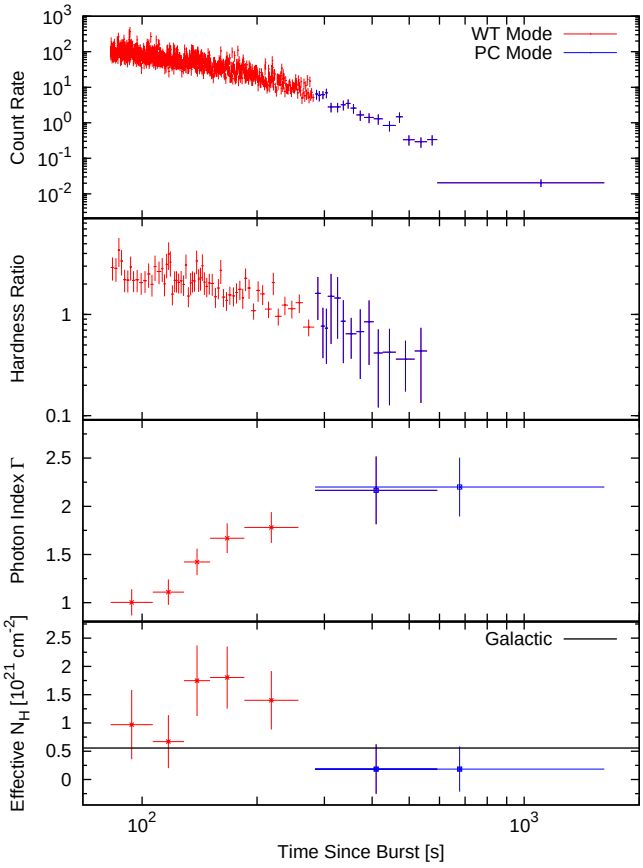

Figure 2.8 (a) The 0.3–10.0 keV X-ray flux measured by the XRT declines rapidly following the bursts. (b) The ratio of counts in the 1.3–10.0 keV to 0.3–1.3 keV bands also declines. (c,d) The spectrum is well modelled by an absorbed power law, although the effective column density N_H appears to unphysically rise and decline during the observations (see text).

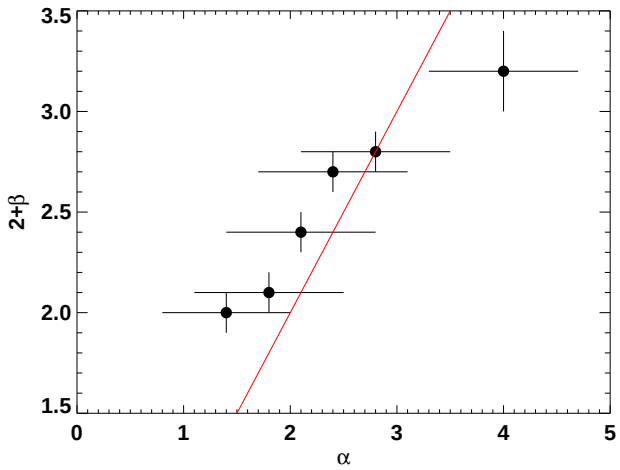

Figure 2.9 Decay index α versus spectral index β (+2) during the rapid-decay phase of the external power-law. For a purely power-law spectrum a closure relation $\alpha = 2 + \beta$ is predicted by the high-latitude (curvature) model; this is approximately obeyed as shown by the solid line. For more complicated spectra this relation may not be obeyed exactly.

2.3 Modeling and Interpretation

2.3.1 The Origin of the Rapid Decay Phase

Immediately after the prompt emission subsides, the X-ray light curve (Fig. 2.9) is observed to decline extremely rapidly ($\alpha = 2$–4, where α is defined by $F_\nu \propto t^{-\alpha}$), plummeting from a relatively bright early X-ray flux to below the XRT detection threshold during the first orbit. Although a similar rapid early decline is seen in nearly all GRBs for which early-time X-ray data are available (O'Brien et al. 2006), GRB 080503 probably constitutes the most dramatic example of this on record: the decline of ∼6.5 orders of magnitude from the peak BAT flux is larger by a factor of ~ 100 than observed for the reportedly "naked" GRB 050421 (Godet et al. 2006) and comparable to the decline of two other potentially naked *Swift* events described by Vetere et al. (2008). The lack of contamination of this phase of the GRB by any other signature (X-ray flares or a standard afterglow) affords an excellent test for models of this decay component.

An afterglow interpretation can be ruled out almost immediately. In addition to the difficulties faced by such a model in explaining the very sharp decay index, continuous spectral softening, and smooth connection with the prompt emission (all of which are commonly observed in the rapid decay phase of other GRBs), the early UVOT White measurement ($\lesssim$220 μJy at 85–184 s) imposes a limit on the X-ray to optical spectral slope of $\beta_{\rm OX} < -0.5$ (using the convention $F_\nu \propto \nu^{-\beta}$) that is very difficult to explain as afterglow emission, but is consistent with the low-energy tail of prompt-emission spectra.

While the origin of the rapid-decay phase observed in most X-ray light curves is still not settled, the most popular interpretation is high-latitude emission (Kumar & Panaitescu 2000), also referred to as the curvature effect. In this scenario, after the prompt emission ends some photons still reach us from increasingly larger angles relative to the line of sight (to the central source) due to a longer path length induced by the curvature of the (usually assumed to be quasi-spherical) emitting region (or shell). Such late photons correspond to a smaller Doppler factor, resulting in a relation between the temporal and spectral indexes, $\alpha = 2+\beta$, that holds at late times ($t - t_0 \gg \Delta t$) for each pulse in the prompt light curve (of typical width Δt and onset time t_0) where $\beta = -d\log F_\nu / d\log\nu$ and $\alpha = -d\log F_\nu / d\log(t-t_0)$. The total tail of the prompt emission is the sum of the contributions from the different pulses. At the onset of the rapid-decay phase the flux is usually dominated by the tail of the last spike in the light curve, and therefore can potentially be reasonably fit using a simple single-pulse model with t_0 set to near the onset of this last spike. At later times the tails of earlier pulses can become dominant. At sufficiently late times both $t - t_0 \gg \Delta t$ and $t \gg t_0$ (i.e., $t - t_0 \approx t$) for all pulses, and the relation $\alpha = 2 + \beta$ is reached for $t_0 = 0$ (i.e., setting the reference time t_0 to the GRB trigger time). In GRB 080503 the large dynamic range enables us to probe this late regime; as shown in Figure 2.9, which displays α versus $2 + \beta$ for the rapid-decay phase using $t_0 = 0$, the relation $\alpha = 2 + \beta$ roughly holds, as expected for high-latitude emission.

While the above discussion suggests that high-latitude emission is a viable mechanism for the rapid-decay phase in GRB 080503, a more careful analysis is called for, especially since assuming an intrinsic power-law spectrum during the rapid-decay phase requires an unphysical time-variable N_H; a better and more physical description is provided by using a fixed Galactic value for $N_{\rm H}$ and an intrinsic Band et al. (1993) spectrum whose peak energy passes through the XRT range (see §2.2.6). A more detailed analysis of this event (and others) in the context of the high-latitude model and possible alternatives using this model will be forthcoming in future work.

2.3.2 Constraining the External Density from Lack of Early Afterglow Emission

The faintness of the early afterglow is very striking. Any afterglow emission for this event was unlikely to be brighter than about ~ 1 μJy at optical wavelengths and 10^{-2} μJy in X-rays at any time after about 1 hr (and if the late afterglow peak were due to a non-afterglow signature, a possibility we consider in §2.3.4, these limits would be even more stringent.) Our early optical limits are the deepest for any GRB on record at this epoch (Kann et al. 2010). If the observed emission at $t > 1$ d is due to a mini-SN or other process, the absence of an afterglow is even more notable. Figure 2.10 shows the X-ray flux at 11 hr, $F_X(11\,{\rm hr})$, and the fluence of the prompt γ-ray emission, S_γ, for GRB 080503 together with a large sample of both LGRBs and SGRBs (data taken from Figure 4 of Nysewander et al. 2009a, but modified slightly as described in the caption.) GRB 080503 immediately stands

out as a dramatic outlier, with an F_X/S_γ several orders of magnitude below that of the general population, indicating a poor conversion of the energy left in the flow after the prompt gamma-ray emission into afterglow (emission from the external forward shock). A natural explanation for this difference is a very low external density.

A more thorough derivation of our limits on the circumburst density is presented in the original version of this Chapter (Perley et al. 2009b) and is only summarized here. Using the upper limit on the X-ray flux, $F_X(11\,\mathrm{hr}) < 8.4 \times 10^{-15}$ erg cm^{-2} s^{-1}, and the measured fluence, $S_\gamma = (1.7 \pm 0.1) \times 10^{-6}$ erg cm^{-2}, we derive constraints on the external density, $n = n_0$ cm^{-3} following Granot et al. (2006).

The "afterglow efficiency" ϵ_X, the ratio between the X-ray and gamma-ray fluence, generally does not depend on density—as discussed in Chapter 1, the density term drops out of the equations governing the brightness of the afterglow above the cooling break frequency ν_c (see Sari et al. 1998, Granot & Sari 2002, and Granot et al. 2006). It is also only weakly dependent on other factors (the microphysical parameters ϵ_e and ϵ_B, plus almost negligible dependence on $E_{\mathrm{k,iso}}$), and the remarkably low value observed for GRB 080503, $\epsilon_X(t = 11\,\mathrm{hr}) < 8.0 \times 10^{-5}\eta_{\mathrm{k}\gamma}^{-1}$, is difficult to explain. However, the frequency of the cooling break itself *is* dependent on density, and a very low circumburst density can push this frequency above the X-ray band, at which point the X-ray flux (and therefore ϵ_X) does become strongly dependent on the density.

Based on these considerations and using the expression for ν_c in Granot & Sari (2002), we impose a limit of:

$$n \lesssim 5 \times 10^{-6} E_{\mathrm{k,iso},52}^{-1/2} \epsilon_{e,-1}^{-1} \epsilon_{B,-2}^{-1/2}\ \mathrm{cm}^{-3}\ . \tag{2.1}$$

This dependence on the parameters is valid in the limit of $\epsilon_B \ll \epsilon_e$, where $Y \approx (\epsilon_e/\epsilon_B)^{1/2} \gg 1$ and $\nu_c \propto n^{-1} E_{\mathrm{k,iso}}^{-1/2} (1+Y)^{-2} \epsilon_B^{-3/2} \propto n^{-1} E_{\mathrm{k,iso}}^{-1/2} \epsilon_e^{-1} \epsilon_B^{-1/2}$. Therefore, the upper limit on the external density cannot easily be increased by a large factor. This suggests a very low external density compared to typical disk values ($n \approx 1$ cm^{-3}) or even a Galactic halo ($n \approx 10^{-3}$ cm^{-3}; Basu, Baidyanath 2003) but is of the same order as the intergalactic particle density ($n \approx 10^{-6}$ cm^{-3}, Hinshaw et al. 2009). This result therefore provides strong evidence that this explosion occurred far outside any galaxy. (An intriguing alternative to this, however, would be if the burst occurred in a low-density pulsar cavity inflated by one of the NSs in the precursor binary; Rosswog & Ramirez-Ruiz 2003.)

2.3.3 Afterglow Models: Why the Delay?

The counterpart rebrightened during the second night of observations, rising again above detectability in both the optical and X-ray bands. The optical is far better constrained than the X-rays in this case: the rise is at least 1.5 mag (a factor of ~ 3) and peaks between 0.1 and 2 d after the event, though most likely the peak is toward the end of this period as the optical observations at 1–2 d are consistent with constant flux. Although the faint afterglow and sparse observations preclude a careful search for chromatic behavior, the X-ray emission shows a broadly similar temporal behavior as the optical and is consistent with being on

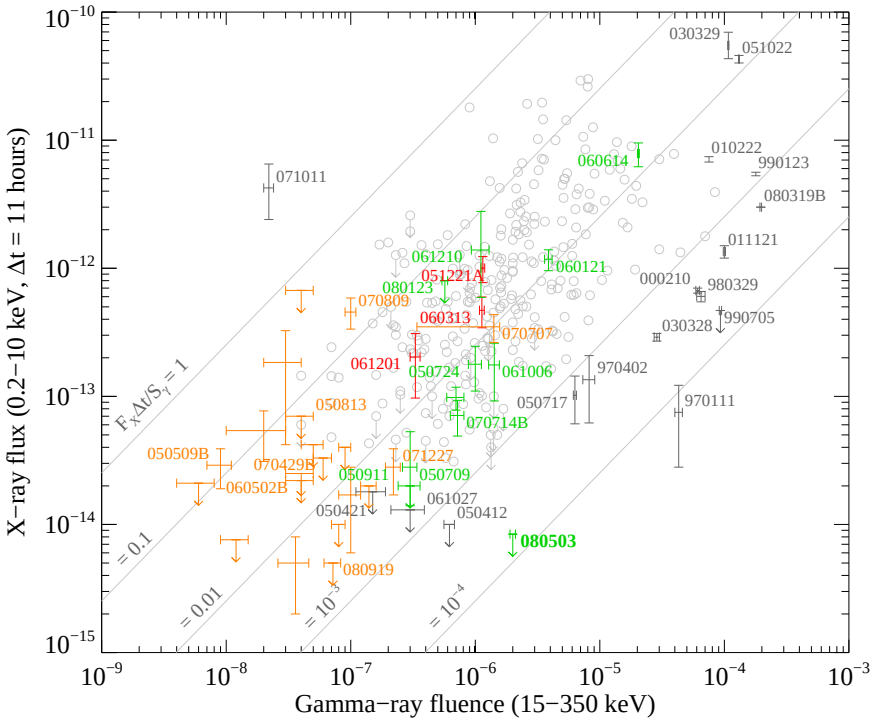

Figure 2.10 Comparison of the total gamma-ray fluence (15–150 keV) versus X-ray flux (0.2–10 keV) at 11 hr post-burst for GRBs with reported X-ray observations, based on Figure 4 and Tables 1–2 of Nysewander et al. (2009a) supplemented with our own re-evaluation of the upper limits on events without detections after ∼10 hr using the *Swift* XRT repository (Evans et al. 2007) and other primary references listed in Nysewander et al. (2009a). New SGRBs in 2008 have been added, along with the extremely bright GRB 080319B (Bloom et al. 2008). Long bursts are shown in gray, short bursts without extended emission in red, faint short bursts with poor constraints on extended emission in orange (as in Figure 2.2), and short bursts with extended emission (including the ambiguous GRB 060614) in green. Prominent events are labeled. Almost all events with detections fall along an approximately linear relation indicating a roughly constant prompt-to-afterglow ratio; most upper limits are not inconsistent with this. GRB 080503 (plotted as an upper limit, though the detection by Chandra at several days after trigger suggests that the flux cannot be much less than this) is strongly discrepant compared to nearly all previous events. GRB 970111 is the first burst for which rapid X-ray observations were conducted and its general faintness appears to be real (Feroci et al. 1998); however, based on the plot in the supplementary material of De Pasquale et al. (2006) the afterglow flux at 11 hr may be somewhat underestimated.

the same segment of a power-law spectrum ($F_\nu \propto \nu^{-\beta}$), with a very reasonable value of the optical to X-ray spectral slope for GRB afterglows, $\beta_{\rm OX} \approx 0.7$. This suggests that they arise from the same physical region, and probably also from the same emission mechanism (most likely synchrotron emission from the forward external shock, i.e. the afterglow; we will consider other models in §2.3.4).

A late peak ($t \approx 1$ d) is unusual for an afterglow but not unprecedented. Most such events are *rebrightenings* and not global maxima. The most prominent examples of this have been long bursts, though some modest X-ray flaring has been observed in a few short GRBs (Fox et al. 2005b; Campana et al. 2006), and notably the classification-challenged GRB 060614 peaked in the optical band between 0.3–0.5 d. Without deep imaging before our first Gemini exposure, we cannot constrain the nature of an optical afterglow in the earliest phases of GRB 080503. However, it is clear that since this behavior is consistent with that observed for at least some previous GRB afterglows, the observed light curve, like the SED, is consistent with an afterglow model. The cause of this delayed peak, however, remains an open question, which we will now turn our attention to.

The similar temporal behavior of the X-ray and optical flux around the observed peak argues against a passage of a spectral break frequency (e.g., the typical synchrotron frequency ν_m passing through the optical) as the source of the late time peak in the light curve, and in favor of a hydrodynamic origin. One possibility for such a hydrodynamic origin is the deceleration time, $t_{\rm dec}$. However, such a late deceleration time implies either an extremely low initial Lorentz factor of the outflow, Γ_0, or an unreasonably low external density

$$n_0 \approx \left[\frac{t_{\rm dec}}{42(1+z)\,{\rm s}}\right]^{-3} E_{\rm k,iso,51} \left(\frac{\Gamma_0}{100}\right)^{-8} \quad (2.2)$$

$$\approx 10^{-10} E_{\rm k,iso,51} \left(\frac{\Gamma_0}{100}\right)^{-8} \quad (2.3)$$

$$\approx E_{\rm k,iso,51} \left(\frac{\Gamma_0}{5.7}\right)^{-8} \quad (2.4)$$

(see, e.g., Granot 2005; Lee et al. 2005a), where we have used $t_{\rm dec}/(1+z) \approx 1$ d.

An initial Lorentz factor of $\Gamma_0 \gtrsim 100$ is typically required in order to overcome the compactness problem for the prompt GRB emission. This would in turn imply in our case an external density of $n \lesssim 10^{-10}$ cm^{-3} that is unrealistically low, even for the the intergalactic medium (IGM). An external density typical of the IGM, $n_{\rm IGM} \sim 10^{-6}$ cm^{-3} would require $\Gamma_0 \sim 30$. This may or may not be a strong concern in this case: the constraints on the high-energy spectrum of the extended-emission component of short GRBs are not yet well-established[8], and it is not yet certain that existing compactness constraints apply to this emission component, potentially allowing a lower minimum Lorentz factor than is required

[8]Note, however, that EGRET has detected high-energy emission including a ~ 1 GeV photon (Sommer et al. 1994) in the extended prompt emission (lasting ~ 50 s) of the short (< 1 s) GRB 930131 (Kouveliotou et al. 1994).

for SGRB initial spikes (*Fermi* has detected high energy emission up to ~ 3 GeV from the short GRB 081024B, Omodei 2008) or for classical LGRBs.

An alternative hydrodynamic explanation for the late peak is if the afterglow shock encounters a large and sharp increase in the external density into which it is propagating. However, it would be very hard to produce the required rise in the light curve up to the broad peak due to a sudden jump in the external density (Nakar & Granot 2007a) unless a change in the micro-physical parameters accompanies the sharp density discontinuity (as may occur inside a pulsar cavity inflated by one of the NSs in the precursor binary.) Below we discuss other possible causes for such a broad and largely achromatic peak in the afterglow light curve. The main features these models need to explain are the extremely low value of $F_X(11\,\mathrm{hr})/S_\gamma$ and the late-time peak (a few days) in the afterglow light curve.

Off-axis jet: The bulk of the kinetic energy in the afterglow shock might not be directed along our line of sight, and could instead point somewhat away from us. For such an off-axis viewing angle (relative to the region of bright afterglow emission, envisioned to be a jet of initial half-opening angle θ_0) the afterglow emission is initially strongly beamed away from us (this can be thought of as an extreme version of the "patchy shell" model – Kumar & Piran 2000a; Nakar et al. 2003). As the afterglow jet decelerates the beaming cone of its radiation widens, until it eventually reaches our line of sight, at which point the observed flux peaks and later decays (Rees 1999; Dermer et al. 2000; Granot et al. 2002; Ramirez-Ruiz et al. 2005). This interpretation can naturally account for the dim early afterglow emission (without necessarily implying an extremely low external density), as well as the rapid decay after the peak (if our viewing angle from the jet axis is $\theta_{\rm obs} \gtrsim 2\theta_0$). The possibility of a slightly off-axis jet is particularly intriguing given the fact that the initial spike is much fainter relative to the extended emission in this event (and in GRB 060614, which also exhibits a late light curve peak) than for most SGRBs; one may envision a unified short-burst model in which the short-spike component of the prompt emission is beamed more narrowly than the component associated with the extended emission. However, since a low circumstellar density is no longer needed, there is no natural means of supressing the early afterglow that should be created by the extended-emission associated component, and producing the large ratio of the gamma-ray fluence and early-time X-ray afterglow flux would require that the gamma-ray emission along our line of sight is bright and the gamma-ray efficiency is very large (Eichler & Granot 2006). Regardless of whether the jet is seen off-axis, there is good evidence that this GRB is significantly collimated, with a decay index $\alpha > 2$ at late times ($t > 3$ d) in both the optical and X-ray bands.

Refreshed shock: A "refreshed shock" (Kumar & Piran 2000b; Ramirez-Ruiz et al. 2001; Granot et al. 2003) is a discrete shell of slow ejecta that was produced during the prompt activity of the source and catches up with the afterglow shock at a late time (after it decelerates to a somewhat smaller Lorentz factor than that of the shell), colliding with it from behind and thus increasing its energy. This interpretation also requires a very large gamma-ray efficiency, ($\epsilon_\gamma \gtrsim 95\%$) corresponding to $\epsilon_\gamma/(1-\epsilon_\gamma) \sim \eta_{\rm k\gamma}^{-1} \gtrsim 30$. In this picture, the sharp decay after the peak (at least as steep as $\sim t^{-2}$) requires that the collision occur after the jet-break time.

The rather sparse afterglow data make it hard to distinguish between these options. Nevertheless, the overall observed behavior can be reasonably explained as afterglow emission in the context of existing models for afterglow variability.

2.3.4 Constraints on a Mini-Supernova

Under any scenario, the absence of a bright afterglow associated with GRB 080503, together with the late-time optical rise, suggests that a substantial fraction of this event's energy may be coupled to trans- and non-relativistic ejecta. Non-relativistic outflows from the central engine are sufficiently dense to synthesize heavy isotopes, which may power transient emission via reheating of the (adiabatically cooled) ejecta by radioactive decay (Li & Paczyński 1998). Since at most ~ 0.1 $M_\odot$ is expected to be ejected from any short GRB progenitor, the outflow becomes optically thin earlier and traps a smaller fraction of the decay energy than for a normal SN; these "mini-SNe" therefore peak earlier and at fainter magnitudes than normal SNe.

Current observational limits (Bloom et al. 2006f; Hjorth et al. 2005a; Castro-Tirado et al. 2005; Kann et al. 2011) indicate that any supernova-like event accompanying an SGRB would have to be over 50 times fainter (at peak) than normal Type Ia SNe or Type Ic hypernovae, 5 times fainter than the faintest known SNe Ia or SNe Ic, and fainter than the faintest known SNe II. These limits strongly constrain progenitor models for SGRBs. Unless SGRBs are eventually found to be accompanied by telltale emission features like the SNe associated with LGRBs, the only definitive understanding of the progenitors will come from possible associations with gravitational wave or neutrino signals.

The most promising isotope to produce bright transient emission is ^{56}Ni because its decay timescale of ~ 6 d is comparable to the timescale over which the outflow becomes optically thin. Compact object mergers, however, are neutron rich and are not expected to produce large quantities of Ni (Rosswog et al. 2003). Metzger et al. (2008a) estimate that in the best cases only $\leq 10^{-3}$ $M_\odot$ of Ni is produced by outflows from the accretion disk. On the other hand, neutron-rich material may be dynamically ejected from a NS–NS or a NS–BH merger. Its subsequent decompression may synthesize radioactive elements through the r process, whose radioactive decay could power an optical transient (Li & Paczyński 1998). Material dynamically stripped from a star is violently ejected by tidal torques through the outer Lagrange point, removing energy and angular momentum and forming a large tail. These tails are typically a few thousand kilometers in size by the end of the disruption event. Some of the fluid (as much as a few hundredths of a solar mass) in these flows is often gravitationally unbound, and could, as originally envisaged by Lattimer & Schramm (1976), undergo r-process nucleosynthesis (Rosswog et al. 1999; Freiburghaus et al. 1999). The rest will eventually return to the vicinity of the compact object, with possible interesting consequences for SGRB late-time emission. A significant fraction ($\sim$ 10–50%) of the accretion disk that initially forms from the merger will also be ejected in powerful winds (Lee et al. 2005b) from the disk at late times; this material is also neutron rich and will produce radioactive isotopes (Metzger et al. 2009).

In the case of GRB 080503, the amount (mass M) of radioactive material synthesized in the accompanying SGRB wind necessary to provide the observed luminosity is constrained to be $(M/\mathrm{M}_\odot)f \approx (1.5-1.8)\times 10^{-7}\,(z/1)^2$. A larger uncertainty is the value of f, which is the fraction of the rest mass of the radioactive material that is converted to heat and radiated around the optical near the peak of the light curve ($\sim$ 1–2 d). Generally $f \lesssim 10^{-4}$ since $\sim 10^{-3}$ of the rest mass is converted to gamma-rays during the radioactive decay, only part of the gamma-ray energy is converted to heat (some gamma-rays escape before depositing most of their energy), and only part of mass in the synthesized radioactive elements decays near the peak of the light curve (so that f can easily be much less than 10^{-4}, but it is hard for it to be higher than this value). We note here that the most efficient conversion of nuclear energy to the observable luminosity is provided by the elements with a decay timescale comparable to the timescale it takes the ejected debris to become optically thin (t_τ). In reality, there is likely to be a large number of nuclides with a very broad range of decay timescales. Current observational limits thus place interesting constraints on the abundances and the lifetimes of the radioactive nuclides that form in the rapid decompression of nuclear-density matter — they should be either very short or very long when compared to t_τ so that radioactivity is inefficient in generating a high luminosity.

Shown in Figure 2.11 are two different light-curve models for a Ni-powered mini-SN from GRB 080503 calculated according to the model of Kulkarni (2005) and Metzger et al. (2008a), based on two different assumptions about the burst redshift. Shown with asterisks and triangles are the r-band and F606W band detections and upper limits from Gemini and *HST*. The solid and dashed lines correspond to a low-redshift ($z = 0.03$) and high-redshift ($z = 0.5$) model, respectively. Qualitatively, both models appear to be reasonably consistent with the flux light curve. To reproduce the peak of the optical emission at $t \approx 1$ d as observed, a total ejected mass of ~ 0.1 $\mathrm{M}_\odot$ is required in either case; to reproduce the peak flux, the Ni mass required in the high- and low-redshift models is $M_{\mathrm{Ni}} \approx 0.3$ $\mathrm{M}_\odot$ and 2×10^{-3} $\mathrm{M}_\odot$, respectively. Since the former is unphysically large in any SGRB progenitor model, a high-redshift event appears inconsistent with a mini-SN origin for the optical rise.

If GRB 080503 originates at very low redshift ($z < 0.1$), a mini-SN model would still appear viable. However, most mini-SN models also predict that the spectrum should redden significantly with time and possess a negative spectral slope once the outflow becomes optically thin after the peak at $t \approx 1$ d; the *HST* detection in F606W and non-detections in F814W and F450W at 5.35 d, however, suggest that the spectrum is approximately flat at late times. While the detected optical emission may be attributed to a mini-SN type of event, the expected spectrum in such a case is quasi-thermal, resulting in no detectable emission in the X-rays. (Rossi & Begelman 2009 have proposed a fallback model in which X-rays can rebrighten days or weeks after the event, but the luminosity is extremely low, and to explain the Chandra count rate a very close distance of ~ 8 Mpc would be required; while not excluded by our data, this is orders of magnitude closer than any known non-magnetar short gamma-ray burst.) Therefore, the late X-ray detections a few days after the GRB are most likely afterglow emission.

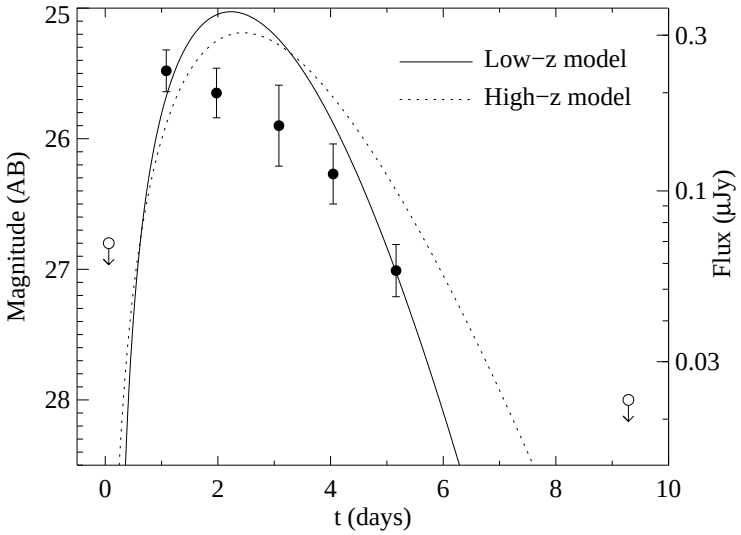

Figure 2.11 Two AB magnitude (Oke 1974) light-curve models for a Ni-powered "mini-SN" from GRB 080503, based on the model of Li & Paczyński (1998), Kulkarni (2005), and Metzger et al. (2008a). The solid line indicates a model at $z = 0.03$ with a ^{56}Ni mass $\approx 2 \times 10^{-3}$ M$_\odot$, total ejecta mass ≈ 0.4 M$_\odot$, and outflow velocity $\approx 0.1c$. The dotted line is for a pure Ni explosion at $z = 0.5$ with mass ≈ 0.3 M$_\odot$ and velocity $\approx 0.2c$. Also shown are our r-band and F606W detections and upper limits from Gemini and *HST*.

2.4 Conclusions

The very same faintness which makes GRB 080503 so remarkable unfortunately also makes it difficult to strongly constrain various physical interpretations of this event. However, the combination of the extremely low limit on the afterglow-to-prompt fluence ratio shortly after the burst and the lack of a coincident host galaxy provides strong evidence that this burst exploded in a very low-density (possibly even intergalactic) medium.

This result has several important implications for the nature of SGRBs and of GRB classification in general. For example, the interpretation of GRB 060614 (and whether it groups more naturally with canonical SGRBs events like GRB 050724, canonical LGRBs like 080319B, or in a new class entirely on its own) is clarified somewhat. GRB 060614, despite having a prompt-extended light-curve morphology (as well as negligible lag and no supernova to deep limits) was (like GRB 080503) strongly dominated by extended emission but also had a very long spike T_{90} (5.5 s), on the extreme end of the short class. The initial pulse of GRB 080503 was unambiguously short; furthermore, the faint afterglow and lack of host galaxy both provide evidence that this event occurred in an environment quite unlike those of canonical "long" GRBs. The existence of an apparent continuity between the appearance of the light curves of GRB 060614 and GRB 080503 and more traditional short bursts (in stark contrast to the bewildering diversity in the structure of longer GRBs) suggests that they originate from the same or similar progenitors, in spite of the apparent diversity in

environments and redshifts. The presence of bright extended emission in GRB 080503, and the prompt-like behavior of its fading tail in the X-ray band, is a counterexample to the inference that extended emission is an environment- or progenitor-correlated phenomenon (Troja et al. 2008). We note again that in the vast majority of cases observed by *Swift*, we cannot strongly constrain the presence of extended emission, and in only two events are limits sufficiently deep to constrain the extended-to-spike fluence ratio to less than the value observed for GRB 070714B.

This same result, however, may pose difficulties to the most popular model of short GRBs: NS–NS or NS–BH merger events. The possibility that the luminosity of the extended emission can exceed that of the initial spike by factors of 30 or more is problematic for a merger, in which the majority of the accretion disk is expected to accrete within a viscous timescale — not more than a few seconds (Rosswog 2007; Lee et al. 2004). This may strengthen the case for alternative models, such as accretion-induced collapse (Vietri & Stella 1999; Katz & Canel 1996; MacFadyen et al. 2005). On the other hand, the extremely low circumburst density is much more consistent with a merger event with its possibility of a natal kick than models such as accretion-induced collapse. One possible means of avoiding this difficulty in a merger scenario (but which could also apply to other models) would be if, for GRB 080503 and GRB 060614, the prompt spike were focused in a narrow jet seen nearly off-axis while the extended emission were more widely beamed. Such a scenario could occur in the case of compact object mergers if the relativistic jet is collimated by a neutrino-heated baryon wind from the accretion disk at early times (Levinson & Eichler 2000; Rosswog et al. 2003), but the collimating effect of the wind become less effective at later times as the neutrino flux and wind luminosity decreases.

The observed late peak in the optical light curve, which we suspected initially may have been the signature of a Li-Paczyński supernova, is explained reasonably by other models. The peak time of $\sim$1 d is too long to be explained by the deceleration timescale, even for a burst exploding into the extremely low-density intergalactic medium, unless the Lorentz factor associated with the extended episode is also very low. However, an off-axis jet, or alternatively a slower shell of ejecta that catches up with the initially very weak afterglow shock and energizes it (a "refreshed shock"), could produce a rebrightening and a late peak. A rather similar late peak has been observed before in several long bursts and in GRB 060614. Some contribution to the afterglow from a mini-SN is not ruled out but is not necessary to explain the available data.

Our failure to conclusively detect a mini-SN signature may also have significant observational implications. In spite of the "nakedness" of this event vastly suppressing the late-time afterglow flux, any possible mini-SN that may have been associated with this event was concealed by the late-time afterglow. Similar events in a higher-density environment (such as a galactic disk) will have even brighter afterglows. If mini-SN phenomena exist in nature, our observations suggest it will be extremely difficult to detect them over the glow of the relativistic shock created by the burst itself. Our best opportunity is likely to lie in observationally and intrinsically faint events like GRB 050509B, whose weak gamma-ray signal results from a low-energy flow insufficient to create a bright afterglow even in a relatively

dense medium, but is bright enough for localization.

Acknowledgments

We thank the *HST* and Chandra X-ray Observatory directors and scheduling teams for their extremely rapid turnaround time for observations of GRB 080503. We also thank the Gemini observing staff, in particular T. Geballe, for excellent support, and D. A. Kann for helpful commentary on the original manuscript.

Table 2.1: Prompt Emission Properties of Swift SGRBs and Candidate SGRBs

GRB	ambiguous?	z	$S_{\rm EE}/S_{\rm spike}$
050509B	N	0.2249	< 14.3
050724	N	0.258	2.64 ± 0.49
050813	N	0.722?	< 3.64
050906	Y[a]	-	< 14.87
050911	Y[b,c]	0.1646?	1.31 ± 0.43
050925	Y[d]	-	< 1.83
051105A	N	-	< 8.06
051210	Y[b]	0.114?	2.72 ± 1.33
051221A	Y[b]	0.5465	< 0.16
051227	Y[b]	-	2.87 ± 0.677
060313	N	-	< 0.29
060502B	N	0.287?	< 3.45
060801	N	1.131?	< 1.84
060614	Y[b,e]	0.125	6.11 ± 0.25
061006	Y[b]	0.4377	1.75 ± 0.26
061201	N	0.111?	< 0.71
061210	N	0.41?	2.81 ± 0.63
061217	N	0.827	< 3.81
070209	N	-	< 8.08
070429B	N	0.904	< 2.44
070714B	N	0.92	0.477 ± 0.163
070724A	N	0.457	< 4.24
070729	N	-	< 2.16
070731	Y[b]	-	< 1.37
070809	Y[b]	0.219?	< 1.37
070810B	N	-	< 9.40
070923	N	-	< 5.96
071112B	N	-	< 4.14
071227	Y[b]	0.383	1.56 ± 0.49[f]
080503	Y[e]	-	32.41 ± 5.7

[a] SGR flare in IC 328?
[b] Spike $T_{90} > 1$ s.
[c] Extended-emission episode is of much shorter duration than in all other events.
[d] Soft event; in Galactic plane.
[e] Fluence dominated by extended emission.
[f] Significance of the extended emission is $< 4\sigma$.

Table 2.2: Optical and Near-IR Observations of the Counterpart of GRB 080503[a]

$t_{\rm mid}$ (day)	Exp. (s)	filter	magnitude	λ (Å)	flux (μJy)	telescope
0.00156	98	white	> 20	3850	< 14.2	Swift UVOT
0.04083	180	r	> 25.80	6290	< 0.204	Gemini-N GMOS
0.04916	800	g	26.76 ± 0.24	4858	0.089 ± 0.018	Gemini-N GMOS
0.06250	800	r	> 26.80	6290	< 0.0811	Gemini-N GMOS
0.05125	300	B	> 26.00	4458	< 0.209	Keck I LRIS
0.05458	630	R	> 25.60	6588	< 0.208	Keck I LRIS
0.07583	800	i	> 26.80	7706	< 0.0779	Gemini-N GMOS
0.09000	800	z	> 26.00	9222	< 0.161	Gemini-N GMOS
0.10125	360	g	> 24.60	4858	< 0.650	Gemini-N GMOS
1.08333	1800	r	25.48 ± 0.16	6290	0.273 ± 0.037	Gemini-N GMOS
1.97500	1620	r	25.65 ± 0.19	6290	0.234 ± 0.038	Gemini-N GMOS
2.09167	720	g	26.48 ± 0.26	4858	0.115 ± 0.024	Gemini-N GMOS
3.08333	2700	r	25.90 ± 0.31	6290	0.186 ± 0.046	Gemini-N GMOS
4.04583	2880	r	26.27 ± 0.23	6290	0.132 ± 0.025	Gemini-N GMOS
5.20833	2760	K_s	> 22.47	21590	< 0.700	Gemini-N NIRI
5.35833	4600	F606W	27.01 ± 0.20	6000	0.067 ± 0.011	HST WFPC2
5.35833	2100	F450W	> 26.9	4500	< 0.080	HST WFPC2
5.35833	2100	F814W	> 26.8	8140	< 0.077	HST WFPC2
9.12917	4000	F814W	> 27.1	6000	< 0.058	HST WFPC2
9.12917	4000	F606W	> 28.0	6000	< 0.027	HST WFPC2

[a]SDSS magnitudes are given in AB, while B and R are under the Vega system. K_s is relative to the 2MASS system (Cohen et al. 2003). Flux values given are corrected for foreground extinction ($E_{B-V} = 0.06$, Schlegel et al. 1998) while magnitudes are uncorrected. Limits are 3σ values.

Chapter 3

GRB 071003: Broadband Follow-up Observations of a Very Bright Gamma-Ray Burst in a Galactic Halo

An earlier version of this chapter was previously published as ApJ 688:470–490[1].

Abstract

The optical afterglow of long-duration GRB 071003 is among the brightest yet to be detected from any GRB, with $R \approx 12$ mag in KAIT observations starting 42 s after the GRB trigger, including filtered detections during prompt emission. However, a high S/N ratio afterglow spectrum displays only extremely weak absorption lines at what we argue is the host redshift of $z = 1.60435$ — in contrast to the three other, much stronger Mg II absorption systems observed at lower redshifts. Together with Keck adaptive optics observations which fail to reveal a host galaxy coincident with the burst position, our observations suggest a halo progenitor and offer a cautionary tale about the use of Mg II for GRB redshift determination. We present early through late-time observations spanning the electromagnetic spectrum, constrain the connection between the prompt emission and early variations in the light curve (we observe no correlation), and discuss possible origins for an unusual, marked rebrightening that occurs a few hours after the burst: likely either a late-time refreshed shock or a wide-angle secondary jet. Analysis of the late-time afterglow is most consistent with a wind environment, suggesting a massive star progenitor. Together with GRB 070125, this may indicate that a small but significant portion of star formation in the early universe occurred far outside what we consider a normal galactic disk.

3.1 Introduction

Concurrent observations of long-wavelength afterglow and ongoing gamma-ray burst (GRB) activity should, in principle, yield important constraints on the nature of the physical processes of the emission (e.g., Kobayashi 2000). However, as a GRB typically lasts less than 100 s, it is challenging for large ground-based optical/infrared follow-up facilities to react to a GRB alert quickly and take data during the prompt phase. Multi-color observations, which provide vital information on the emission mechanism, are even more difficult to obtain during the prompt phase because of the added overhead associated with changing filters. Nevertheless, due to the coordinated efforts of recent space missions (*HETE-II*, Ricker et al. 2003; *Swift*, Gehrels et al. 2004) to detect GRBs and various ground-based optical follow-up programs, observations during the prompt phase of GRBs are no longer uncommon — the optical afterglows (OAs) of several dozen GRBs have been observed (e.g., Akerlof et al. 1999; Vestrand et al. 2006; Yost et al. 2007) during gamma-ray emission, and multi-color optical data have been obtained in a handful of cases (e.g., Blake et al. 2005; Nysewander et al. 2009b).

Observations of GRBs in the past several years have also revealed a rich demography in OA behavior. Some OAs have monotonic power-law decays (e.g., Li et al. 2003b; Laursen & Stanek 2003), while others have plateau (e.g., Rykoff et al. 2006) and rebrightening (e.g., Woźniak et al. 2006) phases. Even among GRBs with relatively simple behavior, however, short-timescale features not predicted in the basic shock models often appear in sufficiently well-sampled data. Various modifications to the standard picture have been proposed to explain such observations, including the presence of a jet with single (e.g., Sari et al. 1999) or multiple (e.g., Berger et al. 2003b) components, refreshed shocks (Zhang et al. 2006), central engine activity (Kocevski et al. 2007b; Chincarini et al. 2007), gravitational microlensing (Garnavich et al. 2000), and density irregularity in the GRB environment (Holland et al. 2003). Observationally, constraints on the change in the afterglow color and the spectral energy distribution (SED) play an important role in limiting the viability of models for a particular GRB.

The question of the nature of the GRB itself is intimately tied to the question of its environment and origins. At intermediate to late times, spectroscopy of the afterglow (e.g., Prochaska et al. 2007a; D'Elia et al. 2007) and deep imaging of the host environment (e.g., Bloom et al. 2002; Fruchter et al. 2006) can help establish the nature of the GRB's progenitor and environment, connecting what we learn about the burst itself to the larger question of its origins and place in the early universe.

In this Chapter, we report on our photometric and spectroscopic observations of GRB 071003 with various telescopes from the prompt phase to late times. In §2 we describe the observations, and in §3 we present the reductions. The analysis of the light curves and the constraints on the changes in the colors and SEDs are given in §4. The conclusions, including the implications of the extremely unusual spectrum of this event, are discussed in §5. We assume $H_\circ = 71$ km s^{-1} Mpc^{-1}, $\Omega_{\rm M} = 0.3$, and $\Omega_\Lambda = 0.7$ throughout.

3.2 Observations

3.2.1 BAT/XRT Observations

On 2007 October 3, 07:40:55 UT (defined as $t = 0$ in this Chapter; UT dates are used throughout), a bright GRB triggered the Burst Alert Telescope (BAT) onboard the *Swift* satellite. The first GCN notice was distributed within 16 s. Unfortunately, *Swift* was still returning to normal observations after its 2007 August gyro failure, but it did slew to the position after 22 ks and began observations using the X-Ray Telescope (XRT).

We downloaded the *Swift* BAT and XRT data from the *Swift* Archive[2] and quicklook data site.[3] The XRT and BAT spectra were fitted using ISIS[4].

The XRT data were processed with version 0.11.4 of the `xrtpipeline` reduction script from the HEAsoft 6.3.1[5] software release. We employ the latest (2007 December 4) XRT calibration files. Our reduction of XRT data from cleaned event lists output by `xrtpipeline` to science-ready light curves and spectra is described in detail by Butler & Kocevski (2007b). We use the latest calibration files from the 2007 September 24 BAT database release. We establish the energy scale and mask weighting for the BAT event mode data by running the `bateconvert` and `batmaskwtevt` tasks. Spectra and light curves are extracted with the `batbinevt` task, and response matrices are produced by running `batdrmgen`. To produce the BAT spectra, we apply the systematic error corrections to the low-energy BAT spectral data as suggested by the BAT Digest Web site[6], and fit the data in the 15–150 keV band. The spectral normalizations are corrected for satellite slews using the `batupdatephakw` task.

The burst exhibits one dominant emission episode of duration $dt \approx 30$ s, followed by a minor pulse ~ 150 s later of duration ~ 20 s. The total duration is $T_{90} = 148 \pm 1$ s, [7] placing it clearly into the long GRB class. The primary pulse is resolved into multiple pulses. The gamma-ray light curve is shown in Figure 3.1, overplotted with early-time photometry from KAIT and P60 (discussed in §3.2 and §3.5, respectively).

The time-integrated BAT spectrum from $t = -10.3$ to $t = 169$ s is acceptably fitted ($\chi^2/\nu = 47.64/55$, where ν is the number of degrees of freedom) by a power-law model, with photon index $\alpha = -1.3 \pm 0.1$ and energy fluence $S_\gamma = (1.7 \pm 0.1) \times 10^{-5}$ erg cm^{-2} (15–350 keV). The main emission episode ($t = -1.4$ s to $t = 22.8$ s) is harder ($\alpha = -1.08 \pm 0.03$, $S_\gamma = (1.51 \pm 0.03) \times 10^{-5}$ erg cm^{-2}, $\chi^2/\nu = 56.71/55$), while the final pulse ($t = 131$–169 s) is softer ($\alpha = -1.8 \pm 0.2$, $S_\gamma = 1.2^{+0.1}_{-0.2} \times 10^{-6}$ erg cm^{-2}, $\chi^2/\nu = 41.15/55$).

X-ray observations with the XRT began 6.2 hr after the BAT trigger. The X-ray light curve measured until $t \approx 5 \times 10^5$ s is well fitted by a power-law time decay $t^{-1.68 \pm 0.03}$. The time-integrated spectrum is well fitted ($\chi^2/\nu = 48.47/54$) by an absorbed power-law model

[2] `ftp://legacy.gsfc.nasa.gov/swift/data`

[3] `http://swift.gsfc.nasa.gov/cgi-bin/sdc/ql`

[4] `http://space.mit.edu/CXC/ISIS`

[5] `http://heasarc.gsfc.nasa.gov/docs/software/lheasoft/`

[6] `http://swift.gsfc.nasa.gov/docs/swift/analysis/bat\_digest.html`

[7] All uncertainties quoted in this Chapter are 1σ, except where specified otherwise.

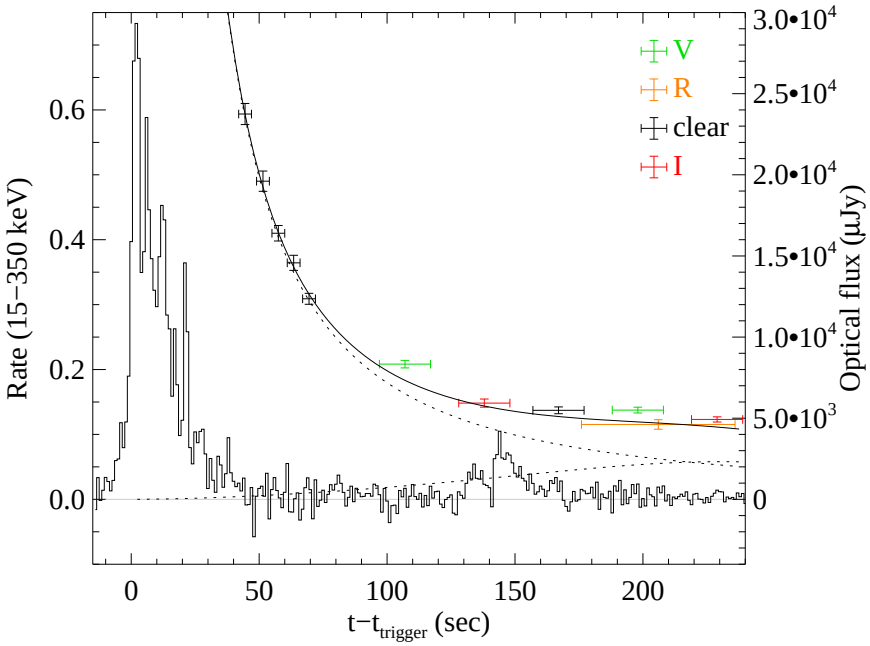

Figure 3.1 Light curve from the *Swift* BAT of GRB 071003, with optical photometry from KAIT and P60, and the optical light curve model discussed in Section 4.3, overplotted. The GRB is dominated by a complicated, spiky emission episode in the first 30 s, but a pulse is also observed much later, at 150 s. Optical data points (all from KAIT, except one R-band measurement from the P60), by contrast, show a power-law decay at early times followed by a slow-rising "bump." Here the V and I filtered observations have been offset to match the R and unfiltered points based on the relative colors at 2000 s.

[photon index $\Gamma = 2.14 \pm 0.12$, unabsorbed $F_X = (5.8 \pm 0.4) \times 10^{-13}$ erg cm^{-2} s^{-1}]. The equivalent H column density, $N_{\rm H} = (2.2 \pm 0.4) \times 10^{21}$ cm^{-2}, is marginally consistent with the expected Galactic column density in the source direction, $N_{\rm H} = 1.1 \times 10^{21}$ cm^{-2} (Dickey & Lockman 1990). Examining the X-ray hardness ratio (e.g., Butler & Kocevski 2007a), there is no evidence for spectral evolution during the XRT observation.

3.2.2 KAIT Observations

The Katzman Automatic Imaging Telescope (KAIT) is a 0.76-m robotic telescope at Lick Observatory that is dedicated to searching for and observing supernovae and monitoring other variable or ephemeral celestial phenomena. It is equipped with a Finger Lakes Instrument (FLI) ProLine PL77 back-illuminated CCD camera having a resolution of $0\farcs8$ pixel^{-1} and a total field of view (FOV) of $\sim 6\farcm8 \times 6\farcm8$. More information on KAIT can be found in Li et al. (2000), Filippenko et al. (2001), and Filippenko (2005), while the KAIT GRB alert system is described in detail by Li et al. (2003b). Notable KAIT observations of GRBs include GRB 021211 (Li et al. 2003a), GRB 051111 (Butler et al. 2006), GRB 060210, and GRB 080319B (Bloom et al. 2009).

Several improvements have been implemented for the KAIT GRB alert system since the description given by Li et al. (2003b). An FLI PL77 camera has replaced the Apogee AP7 camera, offering a much faster readout time (1.2 s for FLI vs. 11.0 s for Apogee). A new feature has been incorporated into the software so the system can easily terminate an ongoing exposure in preparation for the GRB response sequence. Most importantly, a real-time image-processing pipeline has been developed to compare the KAIT images to archival Digital Sky Survey (DSS) images to identify new objects. Astrometry solutions are derived for the KAIT images by matching the detected objects to the USNO B1 catalog (Monet et al. 2003), providing coordinates to any new objects to a precision of $\sim 0\farcs2$. Point-spread-function (PSF) fitting photometry is also performed on new objects, and calibrated to the red magnitudes of the stars in the USNO B1 catalog. The image-processing results are displayed in real time on a website.[8]

For GRB 071003, the KAIT GRB alert program received the GCN socket notice at $t = 16$ s. The system immediately terminated the ongoing supernova search program and began to slew the telescope to the GRB position. After slewing from close to meridian to an hour angle of 4.2 hr, a sequence of 5×5 s unfiltered images began at $t = 42$ s. KAIT then switched to a sequence that alternated with 20 s V, I, and unfiltered images. Finally, the sequence converted to 20 s I and unfiltered images. Because of the physical west hour angle limit of 4.7 hr, KAIT only finished part of this pre-arranged sequence. In total, 56 images were obtained in the V, I, and unfiltered passbands from $t = 42$ to 1628 s, with full width at half-maximum intensity (FWHM) of $\sim 3''$.

Visual inspection of the image-processing results revealed a true new object, measured at 12.8 mag at a position of $\alpha = 20^h07^m24^s.12$, $\delta = +10^\circ56'51''.8$ (equinox 2000.0; approx-

[8] `http://hercules.berkeley.edu/grbdata/grbfinder.gif`

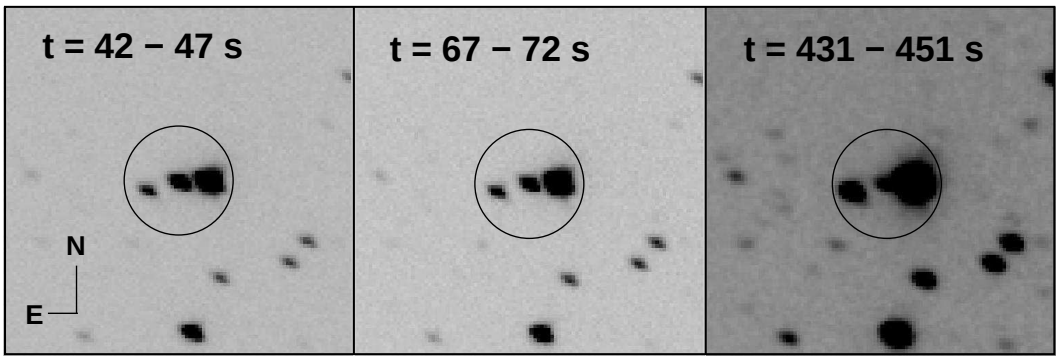

Figure 3.2 Sequence of KAIT images for the OA of GRB 071003. An $80'' \times 80''$ section is shown for the first and fifth unfiltered 5 s images and for a 20 s unfiltered image that started at $t = 431$ s. The OA is the central object in the circles. It is well detected in the early images and rapidly fades. The image quality is poor owing to the very high airmass of the object.

imate 1σ astrometric uncertainty $0''.3$). Our candidate OA was subsequently confirmed by observations from the automated Palomar 60-inch (1.5 m) telescope (P60). Figure 3.2 shows a sequence of the KAIT images for the OA of GRB 071003. An $80'' \times 80''$ section is shown for the first and fifth unfiltered 5 s image and a 20 s unfiltered image that started at $t = 431$ s. As seen in Figure 3.2, a bright ($R \approx 11$ mag) foreground star is located $6''.5$ west of the OA of GRB 071003. As discussed in §3, the presence of this bright star complicates the photometry for the OA, and various methods have been used to minimize its contamination.

3.2.3 P60 Observations

The Palomar 60-inch telescope (P60; Cenko et al. 2006h) automatically responded to the *Swift* trigger for GRB 071003, beginning a pre-programmed sequence of observations at 07:43:51 UT (176 s after the trigger). Observations were taken in the Kron R, Sloan i' and z', and Gunn g filters at large airmass (> 2.5). Individual images were reduced in real time by our automated reduction pipeline; the source is clearly detected in all four filters.

A second epoch of observations was manually scheduled for the night of UT October 4. In an attempt to lessen the contamination of the nearby bright saturated star, these observations were taken in the Johnson V-band filter in relatively short (30 s) exposures. A sequence of 30 images was obtained.

3.2.4 AEOS Observations

The 3.6-m US Air Force Advanced Electro-Optical System (AEOS) telescope, located at the Maui Space Surveillance System on Haleakala[9], observed the OA of GRB 071003 with the AEOS Burst Camera (ABC, Flewelling-Swan et al. 2006). ABC has a back-illuminated 2048×2048 pixel EEV chip, with a scale of $0''.189$ pixel^{-1} and a FOV of $\sim 6'.5 \times 6'.5$. Because there is no direct internet access to AEOS, after *Swift* detected the GRB, a FAX alert was automatically sent to the AEOS control room, to initiate a series of Target-of-Opportunity (ToO) observations.

The AEOS observations of GRB 071003 are all unfiltered 10 s exposures. The first batch of images started at ∼9 minutes after the BAT trigger, and 238 images were observed until $t \approx 83$ minutes, all with very good image quality (FWHM $\approx 0''.9$). The second batch of images started at $t \approx 205$ minutes, and 56 images were observed until $t \approx 222$ minutes. Due to the large airmass for these observations and the degraded seeing conditions, however, the images have rather poor quality. We have tried various methods to measure the brightness of the OA in these images but failed. Accordingly, only the first batch of 238 images is analyzed in this study.

3.2.5 Keck I/Gemini-S observations

In response to the detection of the OA of GRB 071003, we organized a campaign to obtain spectroscopy and late-time photometry with the 10-m Keck I and the 8-m Gemini-S telescopes. At $t \approx 2.6$ hr, we attempted to observe the OA with the HIRES spectrograph at Keck I, but the data are of poor signal-to-noise ratio (S/N) and no obvious lines were detected. Just before the HIRES spectroscopy started, we also obtained guider images for the OA, providing important photometric coverage during a gap in the photometry obtained elsewhere (see §3.4). The guider images have a scale of $0''.37$ pixel^{-1} with a FOV of $53''.5 \times 71''.3$.

On 2007 October 4, we observed the GRB 071003 OA with the Low Resolution Imaging Spectrometer (LRIS; Oke et al. 1995) on Keck I. Anticipating significant fading of the OA, a series of deep 300 s images was taken with the g and R filters under excellent seeing conditions (FWHM $\approx 0''.5$). Inspection of the images reveals that the OA was still bright and saturated in most of the images. Consequently, only a single image in each of the g and R bands, where the OA is not saturated, is analyzed in this study. LRIS uses a beamsplitter to separate the light between two arms, red and blue. Both the blue and red cameras have a usable FOV of $\sim 6'.0 \times 7'.8$. The red camera used a back-illuminated Tek 2048×2048 pixel chip with a scale of $0''.215$ pixel^{-1}, while the blue camera has a mosaic of two 2048×4096 pixel Marconi chips with a scale of $0''.135$ pixel^{-1}.

Encouraged by the brightness of the OA, we also performed LRIS spectroscopy of the OA. A detailed analysis of the spectroscopic observations is presented in §3.5.

[9]Based on data from the Maui Space Surveillance System, which is operated by Detachment 15 of the U.S. Air Force Research Laboratory's Directed Energy Directorate.

We performed more LRIS imaging for the OA of GRB 071003 on 2007 October 8, 9, 10, 11, and 15, using various combinations of u, g, V, and R filters. The presence of the very bright star presents a significant challenge to extracting useful data on the OA, as its diffraction spikes change positions and intensity according to the time and seeing conditions of the observations. Unfortunately, observations on 2007 October 8 were adversely affected by diffraction spikes and poor seeing, and were not usable. The data taken on 2007 October 15 are seriously affected by clouds, and do not provide an interesting limit to the brightness of the OA, so they are not used in this study.

We also triggered our TOO program (GS-2007B-Q-2; PI H.-W. Chen) for GRBs with the Gemini-S telescope and obtained g-, r-, i-, and z-band images with the GMOS camera on 2007 Oct. 5 and 6. The GMOS camera is equipped with three back-illuminated EEV 2048×4608 pixel chips. For our observations, the camera is used in a 2×2 binning mode with a scale of $0''.146$ pixel^{-1} and a FOV of $\sim5'.5\times5'.5$. Unfortunately, the 2007 October 5 images are badly affected by bleeding from the very bright star and are not used in this study.

As part of the efforts to follow the evolution of the OA of GRB 071003, we also performed adaptive optics (AO) observations with Keck I on 2007 October 19. The details of the AO observations can be found in §3.6.

3.2.6 Radio Observations

GRB 071003 was observed with the Very Large Array (VLA)[10] on various occasions. We made the observation in the B configuration array. We used VLA source 1950+081 as phase calibrator for 4.86 GHz (C) band observations and 2001+104 for 8.46 GHz (X) band observations. The data were analyzed using standard data reduction routines of the Astronomical Image Processing System (AIPS). The first observation took place on 2007 October 5 in the X band with flux density of 393 ± 55 μJy. Since then we made six observations in the X band and three observations in the C band (Table 3.1).

3.3 Data Reduction

The bright star in the neighborhood of the OA of GRB 071003 makes it a challenge to measure reliable photometry from the data described in §2. In this section we describe the methods used to minimize its contamination.

3.3.1 Photometric Calibrations

For photometric calibrations, the field of GRB 071003 was observed in B, V, R, and I on two photometric nights (2007 October 7 and 8) at Lick Observatory, using both KAIT

[10]The NRAO is a facility of the National Science Foundation, operated under cooperative agreement by Associated Universities, Inc.

and the Lick Nickel 1-m telescope. About a dozen Landolt standard-star fields (Landolt 1992) were observed at different airmasses throughout each photometric night. Photometric solutions to the Landolt standard stars yield a scatter of ∼0.02 mag for all the filters. The GRB 071003 field was also observed for several sets of $BVRI$ images with different depth on both nights. The photometric solutions are used to calibrate a set of local standard stars in the GRB 071003 field. Because the GRB 071003 field is quite crowded, the number of calibrated local standard stars is large, and the local standard stars in the field of GRB 071003 are well calibrated, with standard deviation of the mean (SDOM) of ∼0.01 mag for all the $BVRI$ bands. We refer to this calibration as the "Lick calibration" throughout the rest of the Chapter.

Several Landolt standard-star fields were also observed with LRIS at Keck I: in the u, g, and R bands on 2007 October 9, and in the V band on 2007 October 11. As the number of the observed standard-star fields is small, it is not possible to derive a complete photometric solution for either night. Since the GRB field was observed at similar airmasses with some of the standard-star fields, we can treat the LRIS filters as standard and derive the magnitudes for the local standard stars via differential photometry. Unfortunately, this procedure suggests that the 2007 Oct. 9 night was not photometric, as different standard-star observations yield somewhat different zero points. The 2007 October 11 night was photometric, but only the V-band standard stars were observed.

We elected to use the Lick calibration as the foundation for all the photometric calibrations, except in the case of the u band. The Lick-calibrated magnitudes are in $BVRI$, and can be reliably converted to the g, r, and i bands using color transformation equations (Jester et al. 2005). The conversion to the z band (Rodgers et al. 2006) is somewhat problematic, and as a result we adopt a relatively large uncertainty for the converted magnitudes. For the u band, only two standard-star fields were observed with LRIS on 2007 Oct. 9, and they give a difference of 0.30 mag in the zero points. We chose to calibrate the GRB 071003 field with the standard-star field that is closer in time of GRB observation, but we added an uncertainty of 0.30 mag to all the calibrated magnitudes. We note that the true error for the u-band calibration may be higher than 0.30 mag due to the nonphotometric conditions on 2007 October 9.

3.3.2 KAIT Data Reduction

The KAIT data were automatically processed with bias and dark current subtraction and flat-fielding. The PSF of the OA is seriously affected by the bright star which is less than 10 pixels away in the KAIT images. Consequently, normal PSF-fitting photometry cannot fit the peak and background of the OA simultaneously to produce a reliable measurement.

We use image subtraction to remove the contamination of the bright star. To generate template images for subtraction, KAIT imaged the GRB 071003 field in the unfiltered mode and in the V and I filters for the next several nights after the burst. To make sure the bright star is not saturated, short (5 s) exposures were used, and 50–100 images for each filter were acquired to ensure high S/N in the combined images. As discussed in §4, the GRB OA was

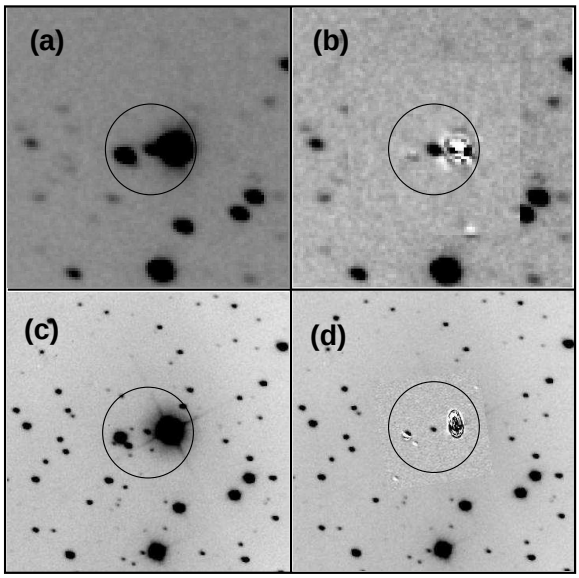

Figure 3.3 Illustration of using image subtraction to remove the contamination of the bright nearby star to the OA of GRB 071003. The KAIT image subtraction code is demonstrated here. (a) An $80'' \times 80''$ section of the original 20 s unfiltered KAIT image of the OA taken at $t = 431$ s; (b) the same section after image subtraction of the central $50'' \times 50''$ using an unfiltered template image after the OA has faded; (c) an $80'' \times 80''$ section of the combined unfiltered AEOS image at $t = 5002.6$ s; and (d) the same section after image subtraction of the central $30'' \times 30''$ using a hand-made template image. See text for more details.

still reasonably bright in the second night after the burst, so we used the images obtained at 4–6 days after the burst as the template for the field without significant OA contribution. Our image subtraction code is based on the ISIS package (Alard & Lupton 1998) as modified by B. Schmidt for the High-z Supernova Search Team (Schmidt et al. 1998). An illustration of the image subtraction is presented in the top panels of Figure 3.3.

The Lick calibration was used to transform the KAIT instrumental magnitudes to the standard Johnson V and Cousins I passbands, with proper color terms measured from the photometric nights. We also find that the combination of the KAIT optics and the quantum efficiency of the FLI CCD camera makes the KAIT unfiltered observations mostly mimic the R band. During the two photometric nights, unfiltered observations of the Landolt standard-star fields were also performed. Analysis of these images indicates that the KAIT unfiltered magnitudes can be effectively transformed to the R band, with a relatively large color term and an rms of $\sim$0.05 mag, similar to the earlier results we reported (Li et al. 2003b,a; Butler et al. 2006).

To increase the S/N, the late-time KAIT images of GRB 071003 were combined into groups of three to eight images. The final KAIT photometry for the GRB 071003 OA is listed in Table B.2 in the Appendix (along with all other photometry for this event).

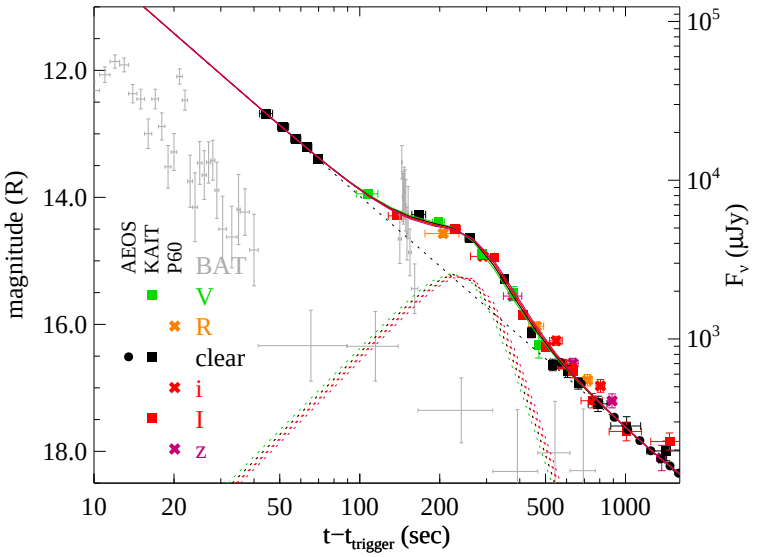

Figure 3.4 Early-time light curve of the optical afterglow of GRB 071003 using KAIT photometry, supplemented by observations from P60 and AEOS. The gamma-ray light curve from the BAT is overplotted in gray (scaled arbitrarily). A clearly additive "bump" at 100–500 s is apparent. Photometric follow-up observations continued after 2000 s with P60 and AEOS, as well as with Gemini and Keck in subsequent nights; the complete 16-day optical light curve is presented in Figure 3.9.

The reported error bars are the uncertainties in PSF-fitting photometry and those in the calibration process, added in quadrature. A plot of the KAIT photometry, along with measurements from other telescopes during the same timespan (with BAT data overplotted and fitted by a chromatic model described in § 4.3) is presented in Figure 3.4.

3.3.3 AEOS Data Reduction

The ABC images were processed using dark subtraction only. Because of highly variable stray light and vignetting, we did not apply a flat field to these images. We used SExtractor (Bertin & Arnouts 1996) to find all the sources in the images, from which we were able to determine the astrometry.

We employed the NN2 flux difference method (Barris et al. 2005; hereafter the NN2 method) for constructing the AEOS light curve. The NN2 method also uses image subtraction to measure the fluxes for a variable source, but it does not designate one particular image as the template. Instead, given N total observations, the NN2 method solves for the vector of fluxes from the individual images using the antisymmetric matrix of flux differences from the $N(N-1)/2$ distinct possible subtractions. Compared to the template image subtraction method, the NN2 method takes all the available information from the images into account,

and is less susceptible to possible noise associated with a single template image. To avoid a large number of image subtractions, we combined the original 238 AEOS observations into 39 images. For the first 228 images, each set of six consecutive images is combined into one. The last 10 images are combined into a single image. We compared the results from the NN2 method to those from a traditional template image subtraction method (bottom panels of Figure 3.3) and found them to be consistent with each other.

To calibrate the AEOS data to the standard photometry system, we used the KAIT R-band data during the overlap period and assume that the unfiltered AEOS data have no color term to the R band.[11] The reported error bars are only those output by the NN2 method, and do not include a possible large systematic error due to calibration. If the throughput of the AEOS telescope in the unfiltered mode is not drastically different from that of KAIT, we estimate the systematic error to be $\sim$0.07 mag when the GRB OA was bright ($t < 20$ minutes), and $\sim$0.15 mag when the GRB became faint ($t > 40$ minutes). The systematic errors can be much higher if the unfiltered throughput is very different for the two telescopes.

3.3.4 Keck I/Gemini-S Data Reduction

Due to the large aperture of the Keck I and Gemini-S telescopes, the bright star close to the GRB 071003 OA produces numerous diffraction spikes, as well as two large blooming spikes along the readout direction. Because the orientation, width, and intensity of the spikes change with the seeing conditions, the exposure duration, and the time of the observations, it is difficult to cleanly remove them using the template image subtraction or the NN2 method. However, due to the high resolution of these images, the spikes are well sampled and show distinct axial symmetry. We developed a saturation spike subtraction method, in which we divide the image of the bright star in half, flip the right side, and subtract it from the left side. Due to the symmetry in the spikes, this subtraction process leaves a reasonably clean region around the GRB OA. PSF-fitting photometry was then performed on the GRB OA in the spike-subtracted images, and on a series of local standard stars. The Lick calibration is used to calibrate the Keck I and Gemini-S instrumental magnitudes to the standard system.

The final Keck I and Gemini-S photometry is reported in Table B.2. The error bars of the magnitudes are the uncertainties from the PSF-fitting photometry and those in the calibration process added in quadrature. One special data point is the Keck I HIRES guider image at $t = 9523.7$ s because it bridges the early KAIT/AEOS data to the late-time Keck I and Gemini-S observations. The GRB OA was well detected in the guider image, but because the image has a small FOV and is unfiltered, photometric calibration becomes particularly difficult.

We have used three methods to calibrate the measured instrumental magnitude of the OA after the guider images were processed with the saturation spike subtraction method:

[11] We attempted to quantify the color term of the unfiltered AEOS data to the standard R system using the local standard stars in the field of GRB 071003, but found no apparent correlation between the scatter of the (unfiltered $-$ R) differences versus the colors of the stars.

differential photometry between the AEOS unfiltered data and the guider images, photometric calibration to about half a dozen stars in the HIRES guider images using the KAIT unfiltered images, and photometric calibration to these stars using the Keck I R-band images. The measured R-band magnitudes from these three methods show a scatter of $\sim$0.25 mag, and their average value and uncertainty are listed in Table B.2.

3.3.5 P60 Data Reduction

The P60 data reduction is presented in this section because it employs several methods (illustrated in Figure 3.3) discussed earlier in the Chapter. We obtained template images for the field after the OA of GRB 071003 has faded. However, the saturation spikes of the bright star close to the GRB ruined the template images in the R and i' bands, so we were only able to run image subtraction for the data in the g and z' bands. We also employed the saturation spike subtraction methods as described in §3.4. Although P60 does not have the resolution of the Keck I and Gemini-S telescopes, subtraction of half of the saturation spikes helped to clean up the background of the OA considerably.

We also applied a third method to reduce the P60 data. Due to the richness of stars in the GRB 071003 field and the large field of view of the P60 camera ($12'.9 \times 12'.9$), we were able to pick a star that is close in brightness (within 0.1 mag in all filters) and thus has similar saturation spikes to the bright star close to GRB 071003. The chosen star is located at $\alpha = 20^h07^m14^s.84$, $\delta = +10°53'59''.8$ (equinox J2000.0), which is $136''.7$ west and $172''.0$ south of the GRB 071003 OA. By slightly scaling the PSF of this bright star and subtracting it from the star close to the GRB, we were able to largely remove the complicated background around the GRB OA.

PSF-fitting photometry is applied to the images after different ways of image subtraction, and the Lick calibration is used to calibrate the instrumental magnitudes into the standard system. The final photometry from the P60 data is listed in Table B.2, which is the average of the spike and bright star subtraction methods. The results from the template image subtraction method are not considered because the method can only be applied to a subset of filters, but they are consistent with the other two methods within measurement uncertainties.

3.3.6 Keck AO Data Reduction

On 2007 October 19 (starting at UT 05:14) we observed the GRB 071003 OA with the NIRC2 (Van Dam et al. 2004) narrow-field camera ($0''.01$ pixel^{-1}) on Keck II using natural guide star adaptive optics (NGS AO). While the extremely bright nearby star greatly complicated the optical analysis, it was ideal to be used as the natural guide star during NGS AO imaging. We took 15 science exposures, each of 60 s and 2 coadds, resulting in a total integration time of 30 minutes. The images were reduced using standard techniques, including dark subtracting, flat fielding, and filtering for deviant pixels. Each frame was dewarped

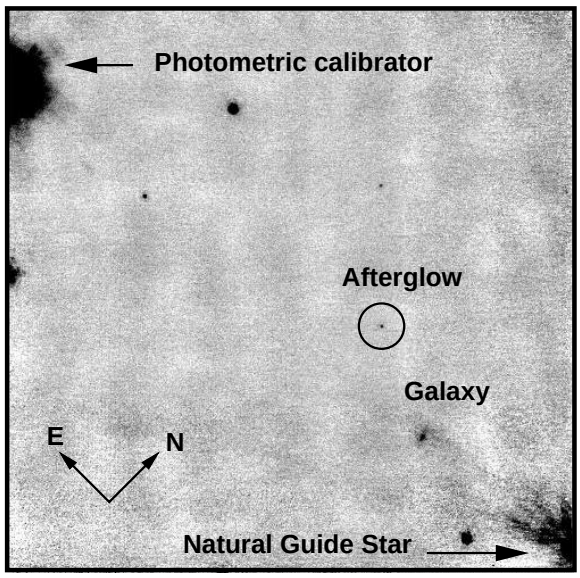

Figure 3.5 NGS AO image of the GRB 071003 field taken with Keck II on 2007 October 19, 16 days after the burst. The FOV is approximately $12'' \times 10''$. The afterglow is well detected with $K' = 21.58 \pm 0.03$ mag. No host-galaxy emission is detected.

using the recommended method for NIRC2, and the resulting images were registered to a common origin and combined.

The GRB OA is well detected 2 weeks after the burst, as shown in the final combined image in Figure 3.5. To measure the brightness of the OA, we created a model of the PSF using short-exposure, unsaturated images of a nearby Two Micron All Sky Survey (2MASS) star ($K_s = 12.011 \pm 0.024$ mag, $d = 7.8''$), taken immediately prior to the science exposures. We then subtracted this model PSF from the OA. With the same 2MASS star as the photometric calibrator, we measure the OA to have $K' = 21.65 \pm 0.10$ Vega mag. (Galactic reddening of $A_{K'} \approx 0.05$ mag is negligible along this sightline and has not been applied.)

3.3.7 Keck LRIS Spectroscopy Reduction

We obtained low-resolution optical spectroscopy of the optical afterglow of GRB 071003 on 2007 October 4.335 using the LRIS on the Keck I telescope. A pair of 600 s dithered exposures was taken under clear conditions at airmass 1.2 with $0.6''$ seeing. We used both the blue and red arms of LRIS, with the light split by the D680 dichroic. The 300/5000 grism on the blue side gave a spectral resolution of 8.4 Å over the range 3300–6500 Å. We used the 600/10000 grating to achieve 4.1 Å resolution over the range 6500–8630 Å. The spectrophotometric standard star Feige 110 (Stone 1977) was observed the following night in the same setup. Intermittent clouds were present the night of the standard-star observation, so the absolute flux scale is unreliable.

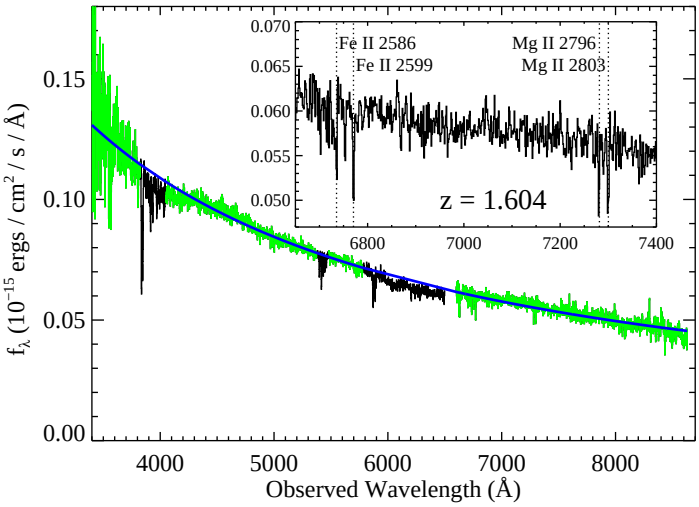

Figure 3.6 Spectrum of the GRB 071003 afterglow covering the full observed spectral range. The spectrum has been flux-calibrated and corrected for Galactic reddening of $E(B-V) = 0.148$ mag. The inset shows an expanded view of the region surrounding the Fe and Mg absorption system at the burst redshift. A power-law continuum was fitted to the regions of the spectrum shown in green, chosen to avoid strong absorption lines and the wavelength range contaminated by second-order blue light. The thick solid blue line shows the resultant fit ($f_\lambda \propto \lambda^{-1.13}$, or $f_\nu \propto \nu^{-0.87}$), but it differs in slope from our more reliable fit to the broadband photometry; thus, it is used only to normalize the spectrum.

The long, 1.0″-wide slit was oriented at a position angle of 10° for the afterglow observations, which was not the parallactic angle (Filippenko 1982). However, the Cassegrain Atmospheric Dispersion Compensator module (Phillips et al. 2006) was mounted, so the derived spectral shape should be reliable. The exception is in the spectral range of 6000–6500 Å, where second-order blue light contamination is prominent in the spectrum of the standard star. An attempt was made to correct for the contamination, but the spectral slope in this section is more uncertain than in the rest of the spectrum. We also fitted an extinction-corrected power law to the flux-calibrated spectrum (excluding line and second-order contaminated regions) in an attempt to estimate the spectral slope, but the estimated slope of $f_\nu \propto \nu^{-0.87}$ differs significantly from the spectral slope estimated from multi-band late-time photometry (§4.7). This may be due to continuum contamination from the nearby star in the spectrum (which is difficult to properly remove), so we do not further consider this spectroscopic spectral index.

The largely featureless spectrum (Figure 3.6) has a S/N > 5 pixel^{-1} down to ∼3500 Å. There is no apparent absorption by the intergalactic medium at these wavelengths, yielding an upper limit to the redshift of the burst of $z_{GRB} < (3500/1216) - 1 = 1.88$. Numerous metal-line absorption lines (but no emission lines) are visible in the spectrum. We have fitted

the equivalent widths of all $\gtrsim 5\sigma$ features in the normalized spectrum using a Gaussian profile and report the rest-frame values in Table 3.2.

We previously presented (Perley et al. 2007e) analysis of this spectrum, identifying Mg II absorption systems at $z = 0.372$ and $z = 1.100$. A VLT spectrum acquired the same night (Fugazza et al. 2007) identified a third absorption system at $z = 0.937$, which is confirmed by our observations. These are the only strong absorption systems in the data, and previously we considered it likely that the $z = 1.100$ system originated from the host galaxy (Figure 3.7). Surprisingly, however, a more thorough investigation revealed a fourth, weak absorption system at a higher redshift of $z = 1.604$ (Figure 3.8). Contrary to our expectation, the gas at this redshift has the weakest Mg II absorption of the four systems.

This is remarkable: absorption lines associated with GRB environments are generally very strong with rest-frame equivalent widths exceeding several angstroms (Savaglio et al. 2003; Prochaska et al. 2008a). Figure 3.7 also indicates, however, the presence of fine-structure Fe II transitions at this redshift. With the exception of active galactic nucleus environments, these transitions have only been identified in gas surrounding the GRB phenomenon (Prochaska et al. 2006a). These transitions are excited by the GRB afterglow itself through indirect ultraviolet pumping (Prochaska et al. 2006a; Vreeswijk et al. 2007) of gas in the interstellar medium (ISM) of the host galaxy. Altogether, the coincidence of (1) the absence of any higher-redshift absorption systems in our spectrum, (2) the positive detection of fine-structure Fe II transitions, and (3) the absence of intergalactic medium absorption at $\lambda > 3500$ Å establishes $z = 1.604$ as the redshift of GRB 071003.

It might seem unusual to have detected fine-structure Fe II transitions in such a late-time spectrum ($t \approx 24.3$ hr). Because the lines are excited by the GRB afterglow, they will decay as the afterglow fades on hour-long timescales (Dessauges-Zavadsky et al. 2006; Vreeswijk et al. 2007; D'Elia et al. 2009a). The presence of fine-structure transitions in our spectrum, however, is consistent with the late-time rebrightening of GRB 071003 provided that the gas lies within a few kiloparsecs of the GRB. In Figure 3.8 we present a velocity plot of strong resonance-line transitions for $z = z_{GRB}$. We report the positive detections of C IV λ1548, Fe II $\lambda\lambda$2382, 2586, 2600, and Mg II λ2803, and we note probable but statistically insignificant absorption at Al II λ1670 and Mg II λ2796. The rest-frame equivalent widths are among the lowest ever recorded for the ISM surrounding long-duration GRBs. The equivalent width of Mg II, for example, is fully an order of magnitude below the general population (Cenko et al. 2008a), with the sole exception of GRB 070125, and the equivalent width for the C IV gas ($W_{1548} = 0.22 \pm 0.06$ Å), represents the lowest measurement to date (Prochaska et al. 2008a).

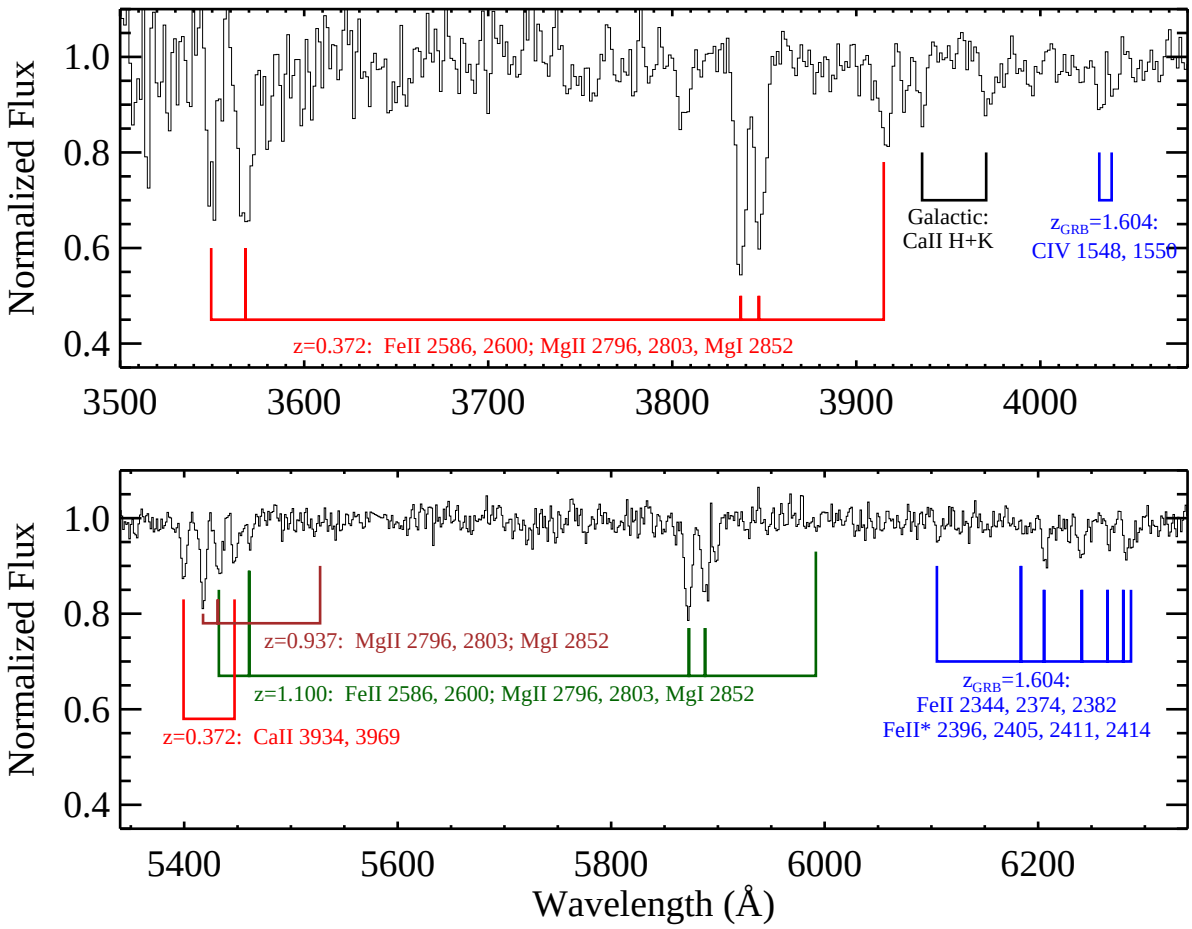

Figure 3.7 Portions of the normalized Keck LRIS spectrum of the GRB 071003 afterglow. We mark the positions of several metal absorption-line features from four distinct extragalactic systems including a series of Fe II and Fe II* transitions associated with the host galaxy of GRB 071003 ($z_{GRB} = 1.604$). Note that the Ca II doublet marked as Galactic may be due to the very bright Galactic star offset by 6.5″ from GRB 071003 as opposed to the Galactic ISM.

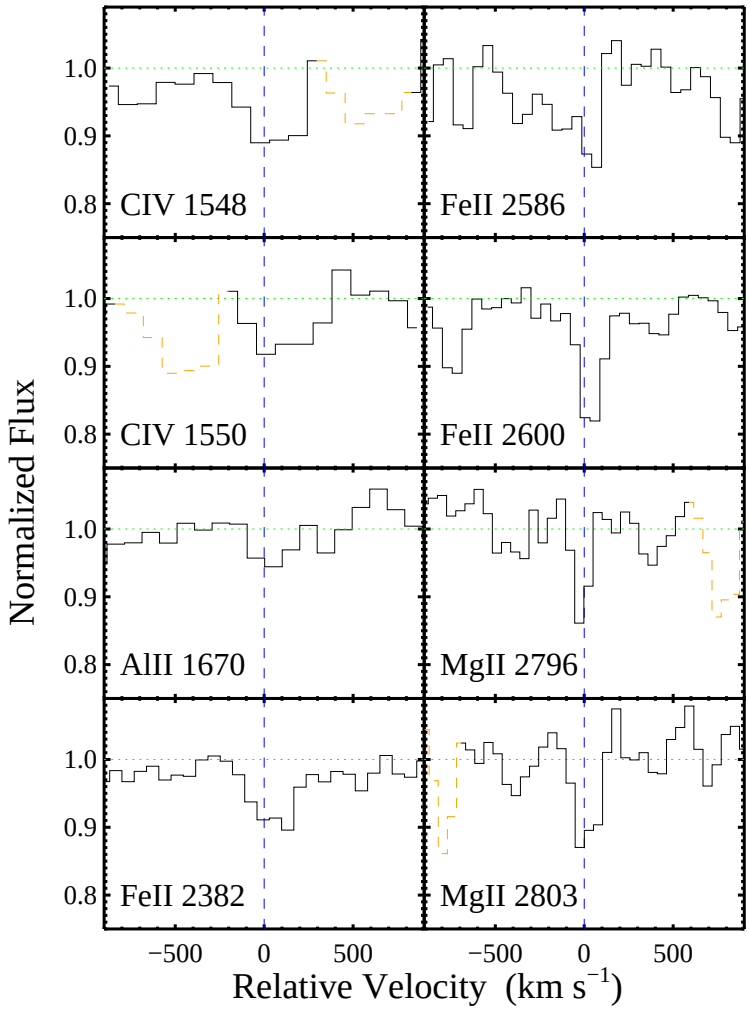

Figure 3.8 Velocity plot of strong, resonance-line transitions for gas associated with GRB 071003 ($z_{GRB} = 1.60435$). These lines are very weak (note the ordinate scale) with rest-frame equivalent widths of 100–200 mÅ (Table 3.2). Indeed, the C IV absorption is the weakest yet reported for a GRB afterglow (Prochaska et al. 2008a).

3.4 Results and Modeling

3.4.1 Light Curve: General Observations

The multi-color photometric evolution of the GRB 071003 OA is shown in Figure 3.9, fitted by our preferred model (described later). Visual inspection of the light curves reveals what appear to be three distinct components: an overall power-law decline that has already set in by the very first measurement at 42 s, a small "bump" feature at ∼120–600 s, and then a dramatic, but unfortunately not well sampled, rebrightening starting around 3000 s that dominates the remainder of the evolution.

The bump feature appears to be additive only: fitting a single power law to measure the decay index ($t^{-\alpha}$) for the clear-band data both before this period and after it, the power-law indices ($\alpha = 1.47$ and $\alpha = 1.49$, respectively) are fully consistent with each other and with the overall decay index over both periods ($\alpha = 1.48$).

The rebrightening is more difficult to characterize. We have no observations between the Keck I HIRES guider point at $t \approx 2.6$ hr and our observations the second night; moreover, the points reported in the GCNs are highly discrepant. An optical R-band limit is reported at $t \approx 4$ hr by Shih et al. (2007), which seems to contradict the rebrightening trend suggested by the AEOS data and guider point. It is unlikely that the OA would show such a dramatic drop (> 3 mag) in a short time interval at such late times, so we suspect that the OA might be heavily contaminated by the bright nearby star and was not resolved in the Lulin 1-m telescope images of Shih et al. (2007). On the other hand, the U-band detection at $t \approx 7.5$ hr reported by Misra et al. (2007) supports a rebrightening but is several magnitudes above the extrapolated light curve at this time, seemingly far too bright to be consistent with our observations. Calibration and the contamination from the bright star are the likely causes of the discrepancy.

3.4.2 Optical to Gamma-Ray and X-Ray Comparison

The BAT and XRT light curves we derive for GRB 071003 are also shown in Figure 3.9. Unfortunately, because *Swift* was still in the process of returning to normal operations after its gyro failure (Gehrels 2007), automatic slewing to GRB 071003 was disabled at the time when the GRB was detected. As a result, there were no prompt XRT observations for GRB 071003, leaving a long gap in the gamma-ray/X-ray light curve at $t = 200$–20000 s. In particular, there are no X-ray observations until approximately the peak of the rebrightening in the optical band. Nevertheless, direct comparison of the data available reveals three relevant facts.

First, there is no obvious optical prompt counterpart to the last spike of the gamma-ray light curve. However, this spike is nearly contemporaneous with the much more slowly rising optical bump feature; we return to this possible connection in our later modeling (§4.5).

Second, at late times the X-ray light curve declines as a power law with decay index consistent with that observed in the optical. A simple power law fits the data well, with

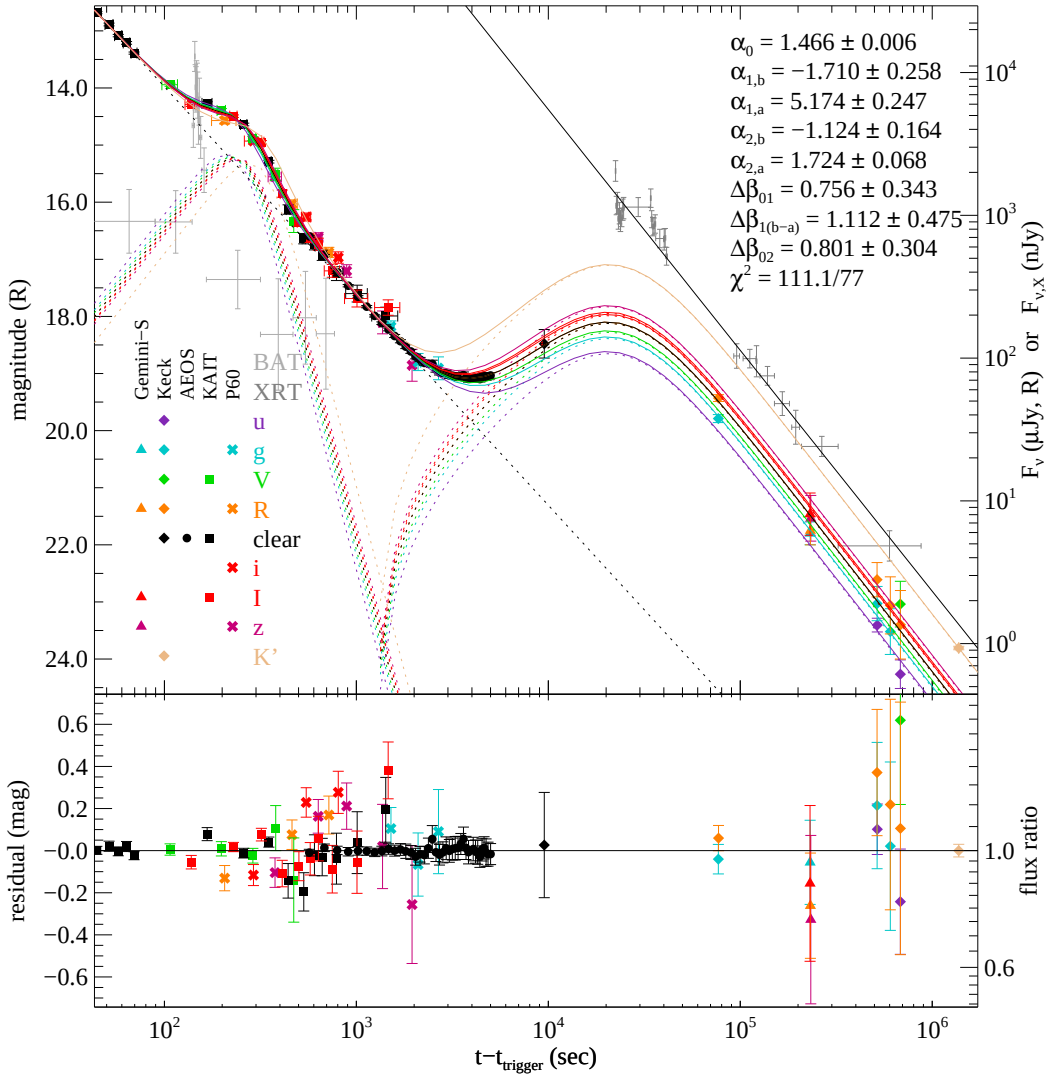

Figure 3.9 Multi-color, early through late-time light curves of the OA of GRB 071003. The magnitudes are offset according to their early-time colors, showing the color evolution between early and late times. Overplotted colored curves indicate the best-fit three-component, color-evolution model described in the text; the dashed lines represent the individual components that compose this model (a uniform power-law decay, a chromatic early-time bump, and a monochromatic late-time rebrightening). The X-ray and gamma-ray afterglows are also overplotted for comparison. The gamma-ray light curve is scaled arbitrarily; if scaled based on the likely gamma-to-X-ray spectral index it would fall on or near the extrapolation of the X-ray light curve back to early times.

a best-fit decay index of $\alpha_X = 1.68 \pm 0.04$. In addition, the late-time OA behavior (after $t \approx 5 \times 10^4$ s) is consistent with a single power-law decay with an index of $\alpha_O = 1.72 \pm 0.07$, fully consistent with this value. As we note later, an extrapolation of the X-ray spectral index is also consistent with the optical observations, suggesting that at late times there is no need for an additional X-ray contribution (such as inverse Compton) or large amounts of host-galaxy extinction.

Finally, while the gamma rays are scaled arbitrarily in Figure 3.9, we note that if we extrapolate the gamma-ray spectrum into the X-rays to compare the BAT and XRT light curves, the evolution between the end of the prompt emission and the start of the XRT observations is nearly consistent with a simple extension of the late-time XRT power law back to earlier times, without a need for a rebrightening or break. However, *Swift* has shown previously (Nousek et al. 2006) that early-time X-ray light curves can conceal a wide variety of complex features, so we will not speculate further as to whether or not this was actually the case.

3.4.3 Detailed Optical Modeling

The fitting procedure used to model the light curve for this burst is outlined in detail in Appendix A. For this particular event, I use three separate components: an unbroken power-law decay starting from the earliest measurements (component 0), a fast-rising, fast-falling early "bump" component (component 1), and a late-time rebrightening component (component 2). I perform a variety of fits under varying combinations of assumptions regarding the relations of the fit parameters. Some of the possibilities considered include the following:

1. Forcing the bump (component 1) to have the same color as the uniform decay (component 0), or allowing it to be a different color overall.

2. Forcing the bump itself to be achromatic over its evolution, or allowing it to contain a chromatic break.

3. Forcing the late rebrightening (component 2) to have the same color as the uniform decay, or allowing it to have a different color.

4. Fixing dt_0 for the early steep decay to be zero (the BAT trigger time), or allowing it to be free to vary.

5. Fixing dt_1 for the bump component to be zero, to be equal to the beginning of the prompt-emission pulse that is nearly contemporaneous with it, or allowing it to be free to vary.

6. Fixing dt_2 for the late rebrightening to be zero, or allowing it to be free to vary.

The results under various combinations of these assumptions are presented in Tables 3.3 and 3.4. We discuss the implications of these results in the remainder of the Chapter.

3.4.4 Color Change

Detection of a GRB afterglow in filtered observations during prompt emission, as was the case here, is rare. The situation is even more intriguing since our multi-color prompt OA observations show an apparent bump feature (component 1) that is nearly contemporaneous with a rebrightening pulse in the gamma-ray light curve. Therefore, it is of great interest to attempt to measure the color of Component 1. By the same token, we have good spectral coverage of the afterglow both during the primary normal decay and during the fading of the dramatic late rebrightening, and any color difference may shed light on the origin of these features.

We tested for color differences in three places: between component 0 (rapid decay) and component 1 (bump), between component 0 and component 2 (rebrightening), and over the break of component 1 itself (since the rising spectral index may differ from the falling spectral index). In all cases we find evidence for color variation, although in each case only at the $\sim 2\sigma$ level. The fading component of the bump is redder than the fading component of the uniform decay by $\Delta\beta = 0.75 \pm 0.34$, the bump feature is chromatic with a shift from the rising to falling component of $\Delta\beta = 1.11 \pm 0.47$, and the rebrightening (for which we only have color information during the fading component) is also redder, by $\Delta\beta = 0.84 \pm 0.31$.

One must be somewhat cautious in interpreting these results — since different filters sample the data differently, systematic errors that affect only one portion of the light curve can masquerade as color change. Data reduction for GRB 071003 was also challenging due to the presence of the nearby bright star, as detailed in §3. In addition, we note that the degree of spectral index shifts noted is dependent on the model. In spite of these considerations, however, we feel that our conclusion of color change is reasonably secure in each case.

3.4.5 Energy Injection Times

It is often unclear what time is most appropriate to use as t_0 when fitting a power law to a GRB afterglow. Thanks to the extremely early-time clear-band data, it is possible to fit t_0 and constrain this within a few seconds in the case of GRB 071003. This fit, notably, gives a t_0 of almost exactly the trigger time ($dt_0 = -0.01 \pm 3.01$ s). The gamma-ray light curve (Figure 3.1) fluence is strongly dominated by the initial pulse, which rises sharply and peaks within a few seconds, so this is not necessarily surprising.

Some authors (Blake et al. 2005; Vestrand et al. 2005, 2006; Yost et al. 2007) have presented evidence of an optical component rising coincident with the prompt emission, although significantly longer lasting. We can analyze whether the bump component observed in GRB 071003 may be such a feature by determining whether or not it can be fitted with a pulse that rises abruptly, contemporaneous with the prompt emission. While our power-law model is somewhat simplified and the sampling of the rise is extremely poor, we find that it generally does not: the best-fit t_0 is intermediate between the trigger time and the time of the prompt emission spike ($\sim$125 s) at $dt_1 = 60 \pm 20$ s. This is a model-independent result, although it rests mostly on one data-point: the initial V-band measurement, representing

an integration from 97 to 117 s after the BAT trigger (∼18 s before the rise of the prompt emission spike), lies 0.14 mag above a simple power-law extrapolation from regions of the data excluding the bump, compared to a photometric error of only 0.03 mag. While it is possible to envision scenarios where a relatively slow optical rise might follow a gamma-ray pulse (any broadband feature with hard-to-soft evolution, or perhaps a late internal shock that later collides with and energizes the external shock), no model to our knowledge can explain why an optical flare would precede a gamma-ray pulse, so we take this as evidence that the two features are physically unconnected.

While our sampling around the rise and peak of the late-time rebrightening is poor (and dominated by the difficult-to-calibrate AEOS and HIRES guider images), we can also attempt to fit the t_0 for the rebrightening component. This is significantly different from $t = 0$, with a best-fit initial time of $dt_2 = 1245 \pm 311$ s. (This is well short of its peak time of approximately 20 ks, so the effect on the light curve is minor.) No prompt-like fluctuations or other features are observed in the light curve in this region.

3.4.6 Radio Modeling

GRB 071003 is rare among *Swift* bursts for having a bright radio afterglow. We were able to successfully detect the afterglow at two frequencies and several epochs spanning ∼2–20 days after the burst, including observations nearly contemporaneous with our optical data. The data are plotted in Figure 3.10.

This GRB is not far off the Galactic plane, and the radio observations are affected by scintillation. Following Walker (1998, 2001), the afterglow is in the strong scattering regime for both X and C bands. An approximate modulation index (which estimates the fractional rms variation) is 0.4 in the C band and 0.6 in the X band, over a refractive timescale of ∼0.5 days in the X band and 2 days in the C band. This is longer than any integration (so the error is not reduced by integration time) but shorter than the interval between exposures (so errors are uncorrelated).

Radio data were fitted using both an unbroken power-law model and a singly broken power-law model. We attempted the fit both before including uncertainties due to scintillation and with an additional 40% flux error added to all C-band points and 60% error added to all X-band points.

Without the additional flux errors, the unbroken model is a poor fit, with $\chi^2/\nu = 15.32/6$. A single, monochromatic break improves the fit dramatically ($\chi^2/\nu = 2.45/4$). This improvement is significant at 97.4% confidence. A monochromatic radio break of this nature is very difficult to explain physically. However, with scintillation flux errors folded into the light curve, we find that a simple power law is a more than adequate fit to the data ($\chi^2/\nu = 1.4/6$), which may suggest that we have overestimated the degree of modulation somewhat. (This is to be expected: the modulation index calculated is an upper limit as it strictly applies only for a point source. The afterglow has a physical size, which quenches the scintillation modulation somewhat.) Therefore, as a final modification, we scaled down this additional error until the final $\chi^2/\nu \approx 1$. Properties of the temporal fits are given in

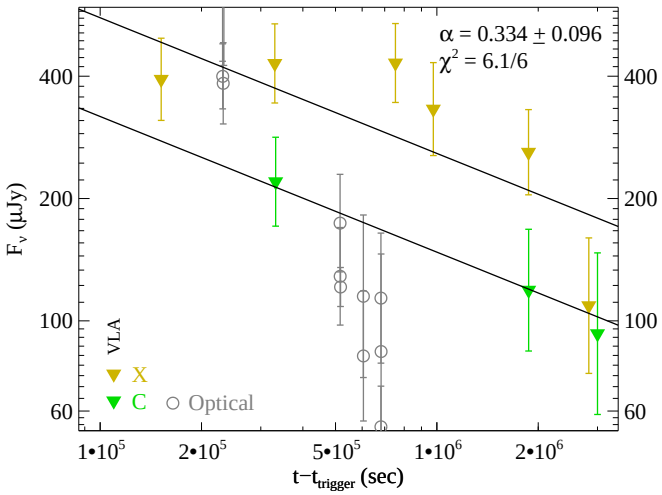

Figure 3.10 VLA radio light curve fitted to an unbroken power law. The uncertainties in the measurements have been increased compared to their statistical values to take into account the effect of interstellar scintillation. Some contemporaneous late-time optical points (scaled arbitrarily) are shown for comparison.

Table 3.5.

The uncertainty due to scintillation is in any event too large to allow any firm conclusions about the light curve. However, since only refractive scintillation is expected to be significant, the refractive timescale is much longer than the several-hour timescale of individual observations, and the C-band observations were in all cases taken immediately after the X-band observations, we do consider the measurement of the radio spectral index ($\beta_R = -1.15 \pm 0.42$) to be trustworthy regardless of any scintillation uncertainty.

3.4.7 Spectral Energy Distribution and Extragalactic Extinction

If our modeling assumptions are accurate (or nearly so), we can use our model to calculate the SED at any time using a combination of all the data available, rather than restricting the measurement to a small subset of the photometry and filters, even if the data were acquired at very different times in the evolution of the GRB and the color is not constant.

We calculate the SED at two epochs. First, we calculate the SED at $t = 2.67$ days after the burst, the time of our four-color Gemini-South observations. In calculating this SED, we perform a slightly modified light-curve fit: we do not perform any filter transformations (e.g., to convert r to R), but we fix all non-SED parameters to that derived from the light-curve analysis. In addition, we add in quadrature a calibration uncertainty equal to 5% in all filters, with a few exceptions. For z, we use a 15% uncertainty. For u, we use a 30% uncertainty, for reasons described earlier. Finally, for K', we use a large extra uncertainty of 50% due to

the possibility of a temporal break sometime between our last optical observations and the AO observations. (However, if such a break is absent, then the K' observation is much more precise than is given on the plots.) Unfiltered observations are not used. We also calculate an early-time SED during the "normal" power-law decay at $t = 1000$ s, using a fit excluding late-time measurements and measurements during the (possibly chromatic) bump. Addition of uncertainties is as for the late-time SED.

The resulting SEDs are plotted in Figures 3.11 and 3.12. After removing the effects of Galactic extinction (but not yet considering non-Galactic extinction), both SEDs are a reasonable fit to a power law, providing a general confirmation of our assumptions as well as indicating that the host or intervening galaxies do not impose a great deal of frequency-dependent extinction. In support of our analysis from the light-curve modeling, the spectral indices appear to differ from early to late times: $\beta_{1000s} = 0.62 \pm 0.33$, while $\beta_{2.67d} = 1.25 \pm 0.09$. (These values are direct fits to the data and do not include the effects of the small amount of extragalactic extinction we do believe to be present, which we discuss shortly.)

Unfortunately there were no early-time observations outside the optical band, since *Swift* was unable to slew rapidly. However, this GRB was observed nearly simultaneously in X-rays, optical, and radio during the declining phase of the late rebrightening. Therefore, it is possible to calculate a coeval late-time spectrum at all wavelengths simultaneously. The values at 2.67 days (the same as the first optical-only SED, above, which is also contemporaneous with XRT observations and within about half a day of the first VLA observation) are given in Table 3.6 and plotted in Figure 3.13.

Even without considering host-galaxy extinction, the optical and X-ray observations are nearly consistent with a common spectral index: $\beta_O = 1.25 \pm 0.09$, $\beta_X = 1.14 \pm 0.12$, and $\beta_{OX} = 0.90 \pm 0.03$. This consistency, plus the fact that the optical and X-ray temporal decays are identical ($\alpha_O = 1.72 \pm 0.31$, $\alpha_X = 1.68 \pm 0.05$), argues that both X-ray and optical are in the same synchrotron regime and the spectrum across this range is a simple power law. We assume this throughout the remainder of the analysis.

The deviations in the observed spectral index suggest the presence of a small amount of extragalactic extinction. Because of the presence of numerous absorbers and the unusually weak nature of the highest-redshift absorption system, however, the appropriate assumptions for modeling the extinction contribution are not clear. Although Mg II is not an exact tracer of the presence of dust, the extremely weak line absorption at the likely host-galaxy redshift of $z = 1.604$ suggests that the dust column at that redshift is nearly negligible. Among the remaining absorbers, the Mg II system at $z = 0.372$ is by far the strongest (by a factor of $\sim$3 in equivalent width compared to the next strongest system at $z = 1.10$), and is likely to be the dominant contributor to any observed dust absorption. However, this is partially offset by the fact that dust at higher redshift is much more opaque (since the observed optical frequencies are in the rest-frame UV at $z > 1$), so for the moment we remain agnostic as to the actual redshift of the absorbing dust.

We fit the optical spectrum simultaneously with the normalized X-ray flux of $F_{1\mathrm{keV}} = 0.036 \pm 0.004$ μJy at 2.67 days. This value has already been corrected for photoelectric absorption (§2.1), and X-ray absorption is not considered in the fit, allowing the gas-to-dust

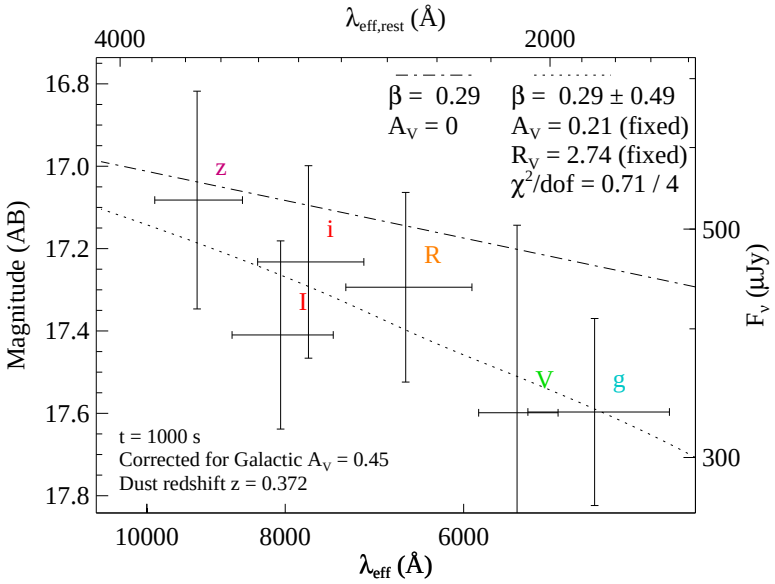

Figure 3.11 Optical SED of the GRB 071003 OA at 1000 s after the burst, fitted using the extinction constraints derived using the late-time SED. The intrinsic (pre-extinction) model spectrum is also shown.

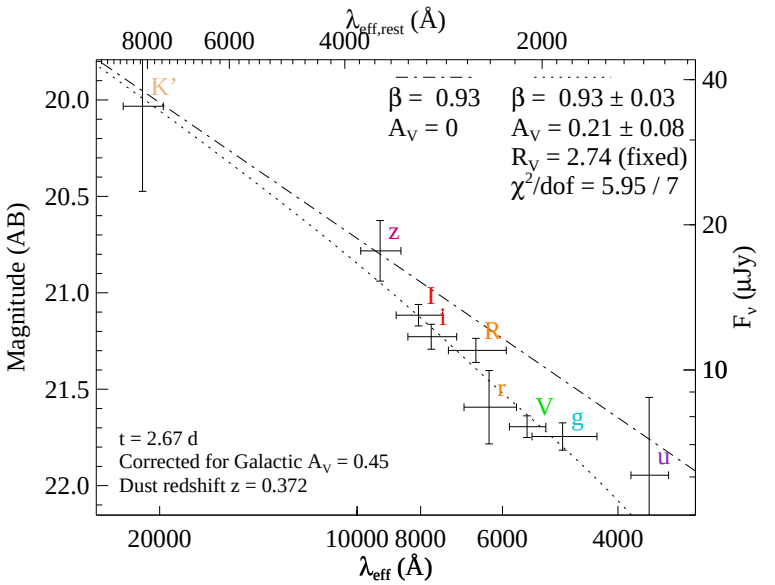

Figure 3.12 Same as Figure 3.11 but for $t = 2.67$ d after the burst. The data (plus an X-ray normalization, not shown) have been fitted with an SMC-like extinction law, with the best-fit curve overplotted. The intrinsic (pre-extinction) model spectrum is also shown.

ratio to be independent of the amount of extinction, A_V.

Four different extinction models were tested. In addition to a control fit with no extinction, we fit for Milky Way-like, Small Magellanic Cloud (SMC)-like, and Large Magellanic Cloud (LMC)-like extinction using the parameterization of the Fitzpatrick & Massa (1990) ("FM") model, and a model for extinction in starburst galaxies parameterized by Calzetti et al. (2000). In all cases the standard average value of the ratio of total-to-selective extinction R_V in the reference galaxy in question was used. (Fits with varying R_V were attempted, but lacking infrared or ultraviolet measurements we were unable to constrain this parameter.) We performed separate fits assuming dust at $z = 0.372$, 1.100, and 1.604.

Results are given in Table 3.7. We find significant evidence (f-test: 96% confidence) for a small amount ($A_V = 0.1$–0.3 mag, depending on the model) of extinction along the light of sight. We cannot strongly constrain its nature; all four extinction laws, at each of the three possible redshifts, give reasonable fits to the observations. The intrinsic (pre-extinction) spectral slope β is strongly constrained to be 0.94 ± 0.03, averaged across the different models. This is consistent (although marginally, at about the 90% confidence level) with the absorption-corrected X-ray measurement of $\beta = 1.14 \pm 0.12$.

As expected, the spectrum turns over dramatically somewhere redward of the optical and is declining with decreasing frequency by the radio band. The radio results are discussed further in §5.4.

3.4.8 Photometric Limits on a Host Galaxy and Intervening Absorbers

Neither our LRIS imaging nor our late-time NGS AO imaging show any evidence of extension or host-galaxy emission consistent with the afterglow position. We searched for emission from a host coincident with the OA position by smoothing and binning the PSF-subtracted AO image. No host emission was detected to a conservative upper limit of $K' \approx 23$ Vega mag.

In our first-night LRIS image (when the seeing was best and contamination from the bright nearby star relatively minimized), a faint, extended source is visible slightly southwest of the OA. The same source is also visible in the AO image, clearly resolved into a faint galaxy with $K' \approx 19$ mag at an offset of $2.07''$ southwest of the OA.

We know from the spectral analysis that there are at least four systems that intersect the sightline between the $z = 1.604$ GRB and Earth, including the host itself. Of these, the strongest candidate for association with the observed galaxy is clearly the $z = 0.372$ system, which both is closest and exhibits the strongest absorption signature. (Unfortunately, we have no spectra of the galaxy to confirm this.) This source appears to be a small irregular galaxy, which at this redshift would be offset by ~ 10 kpc (a reasonable distance to explain the observed absorption) and approximately 0.5 kpc in half-light radius.

No other extended sources are detected within $3''$ of the afterglow, so our upper limit rules out detection of both a host galaxy and any absorbing systems within this distance.

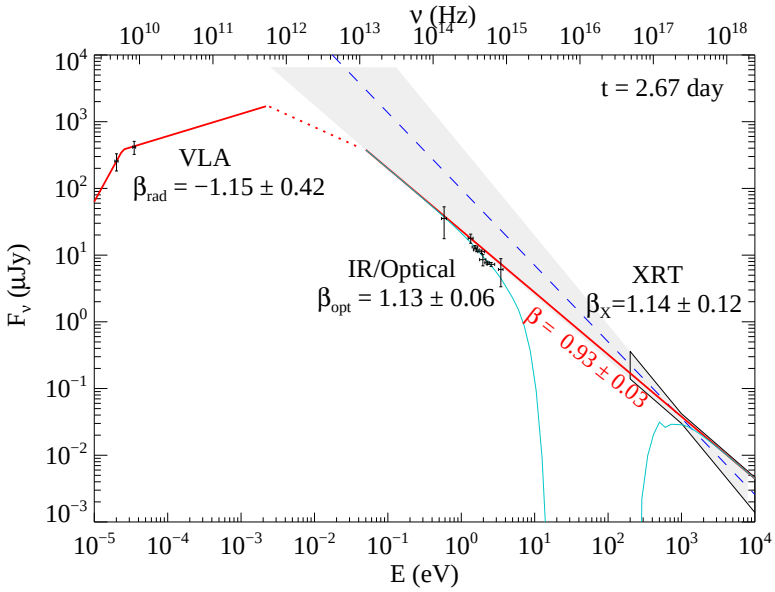

Figure 3.13 Broadband SED at $t = 2.67$ days from radio through X-ray observations. The shaded region shows an unbroken extrapolation of the X-ray fit (90% confidence region), which is consistent with the optical measurements. The optical points are corrected for Galactic but not extragalactic extinction; a best-fit model for the effects of host-galaxy and intervening-galaxy extinction is shown (thin cyan line). The locations of the cooling break and peak frequency shown are arbitrarily chosen; the actual frequencies are not constrained by the available data except that both are located between the radio and optical bands.

The corresponding limit on a galaxy luminosity is only mild, compared to the known GRB host distribution. At the presumptive GRB redshift of $z = 1.6$, any host galaxy is limited to a K-band absolute magnitude of $M(K') = -22.2$ Vega mag. This value falls roughly in the middle of the typical range of previously studied GRB hosts, which appear to have K-band luminosities on the order of 0.1 L_*, and are bluer and fainter than typical SCUBA galaxies (Le Floc'h et al. 2003).

3.4.9 Spectroscopic Constraints on the Host Galaxy and Intervening Absorbers

The very weak absorption at the host redshift in our spectrum suggests a lower than average H I column density along the sightline and/or a metal-poor gas. Because of our low spectral resolution, however, the absorption is unresolved and the line profiles may be saturated (Prochaska 2006). We may conservatively report a lower limit to the column densities by assuming the weak limit. In this manner, we estimate $N_{\rm Mg^+} > 10^{12.6}$ cm^{-2} based on the equivalent width of Mg II λ2803. For a solar metallicity gas, this implies $\log N_{\rm HI} > 10^{17}$ cm^{-2}. This is a conservative estimate because the gas metallicity is presumably subsolar. Nevertheless, it is unlikely that the gas has an H I column density matching the values typical of most GRBs.

In addition to the gas associated with GRB 071003, the afterglow spectrum reveals three foreground Mg II absorbers. Two of these have moderate rest-frame equivalent widths ($W_{2796} \approx 0.7$ Å), but the lowest redshift system exhibits a very large value ($z = 0.3722$, $W_{2796} = 2.5$ Å). The incidence of such strong Mg II absorption at $z < 0.5$ has not yet been established along quasar sightlines. These absorbers are very rare at $z \approx 0.5$ however, and the incidence is declining with redshift (Nestor et al. 2005; Prochter et al. 2006a). The number of absorbers with $W_{2796} > 1$ Å per unit redshift is $\ell(z) = 0.13$ at $z = 0.5$, and the incidence of absorbers with $W_{2796} > 2$ Å is an order of magnitude lower. This implies that one would need to observe of order 100 quasar sightlines to detect a single absorber with $W_{2796} > 2$ Å at $z < 0.5$. Although these are *a posteriori* statistics, this analysis reminds one of the apparent enhancement of strong Mg II absorbers along GRB sightlines (Prochter et al. 2006b). Given its low redshift, this system will be an excellent case to perform follow-up observations and examine the properties of the galaxies hosting such systems (Pollack et al. 2008, submitted) The bright nearby star, however, poses a formidable obstacle for non-AO ground-based observations.

3.4.10 Energetics

The measured gamma-ray fluence of 5.32 (-0.67, $+0.30$) $\times 10^{-5}$ erg cm^{-2} (Konus, 20 keV–4 MeV: Golenetskii et al. 2007) can be converted to an isotropic-equivalent total energy release in the host frame: $E_{\rm iso} = 3.4$ (-0.6, $+0.2$) $\times 10^{53}$ erg — well in the upper range of *Swift* events.

No clear jet break is observed over the course of our observations, in either the optical bands or the X-ray, out to at least 6×10^5 s. There is a possible monochromatic break in the radio bands at around 8 days (7×10^5 s), but it appears likely to be a scintillation artifact (see §4.6).

Using this limit, and following Sari et al. (1999), for a uniform circumburst medium we can calculate the minimum jet opening angle and minimum collimation-corrected energy. Using standard values for the radiative efficiency ($\eta = 0.5$) and circumburst density ($n = 3.0$ cm^{-3}) (the end result is nearly insensitive to these parameters), we have

$$\theta_{\rm jet} = 6.5^\circ (\frac{t_{\rm jet}}{\rm d})^{3/8} (\frac{n}{3\ {\rm cm}^{-3}})^{1/8} (\frac{1+z}{2})^{-3/8} (\frac{E_{\rm iso}/\eta}{10^{53}\ {\rm erg}})^{-1/8}. \quad (3.1)$$

However, as we discuss later, the late-time afterglow behavior in this case favors a wind model. Thus, following Li & Chevalier (2003) we have

$$\theta_{\rm jet} = 5.4^\circ (\frac{t_{\rm jet}}{\rm d})^{1/4} (A_*)^{1/4} (\frac{1+z}{2})^{-1/4} (\frac{E_{\rm iso}/\eta}{10^{53}\ {\rm erg}})^{-1/4} \quad (3.2)$$

The upper limit on $t_{\rm jet}$ of 7 days gives a limit on the opening of at least 3.1 $(A_*/0.1)^{1/4}$ deg. (As discussed later in §5.4, we estimate $A_* \approx 0.1$ from the broadband spectrum.) Therefore the collimation-corrected energy is at least $E_\gamma \gtrsim 2 \times 10^{50}$ $(A_*/0.1)^{1/2}$ erg.

It is also possible that the jet break is hidden by the complicated evolution of the burst, including the rebrightening, which would imply more modest energetics for this burst. However, as the late-time slope is still relatively shallow ($\alpha = 1.72$; generally we expect $\alpha \geq 2$ after a jet break) we consider this relatively unlikely.

3.5 Discussion

3.5.1 Initial Power-Law Decline

We first turn our attention to the rapidly declining power law. The temporal behavior of this feature is quite simple, with a decay constant $\alpha = 1.466 \pm 0.006$ and no evident substructure before the "bump" or after it. There is no evidence of a rising component or any early break. The observed spectral index $\beta = 0.62 \pm 0.33$, although if the extinction measured at late times is also present at early times (as we expect), the intrinsic index is actually shallower; correcting this using our preferred extinction model, we derive $\beta = 0.29 \pm 0.49$.

Especially when the decay is observed to flatten later, very early-time decay of this nature is often interpreted as a reverse shock. This seems possible — the spectral and temporal indices are within the range of predictions for reverse-shock models (specifically, the thick-shell case of Kobayashi 2000). However, a forward-shock origin is also consistent. Examining the standard closure relations between α and β (as in, for example, Price et al. 2002), all environment models (ISM, wind, and jet) are consistent with the constraints

derived from the data, largely because the early-time constraint on β is poor. (We discuss the forward vs. reverse-shock models for this emission again in §5.3, in connection with the late-time rebrightening.)

3.5.2 The Bump: Internal Shock Origin Without a Prompt Emission Connection

The bump feature is of considerable interest, since it is nearly simultaneous with a prompt-emission pulse. However, as discussed earlier, the temporal analysis seems to disfavor the interpretation as a prompt reverberation: the bump seems to be already rising even before the prompt spike.

Another possible explanation for the origin of this feature is a large density variation in the surrounding medium (a large clump or other discrete physical feature in the path of the expanding shock). The observed pulse width $\Delta t/t \approx 1$ is consistent with a density variation, and the general appearance of the light curve over this region is reminiscent of simulations of a GRB forward shock intersecting ISM density enhancements (e.g., Figure 3 of Nakar & Piran 2003). However, our observation of possible color change across the bump would (if real) disfavor this hypothesis, at least in the simplest models: density variation will not change the intrinsic spectrum, unless either the microphysical parameters or cooling frequency suddenly and significantly change. We consider this unlikely, although some authors (e.g., Yost et al. 2003; Granot & Kumar 2006) have discussed the role of variable microphysics in previous GRB afterglows.

Alternatively, the observation that the fast-declining component seems completely unaffected by the afterglow (the temporal indices before and after are effectively identical) leads us to interpret the bump as originating from a distinct emission episode — given the rapid rise and fall and the hint of blue-to-red evolution we suggest that it arises from internal-shock emission. Hard-to-soft evolution and an underlying power-law decay not affected by the flare have also been seen in X-ray flares (Butler & Kocevski 2007b; Chincarini et al. 2007). We also note that earlier studies of GRB prompt emission have shown pulses observed at lower energy to be broader than those at higher energy (Fenimore et al. 1995); this trend may continue into the optical band. The broader, smoother profile of this pulse relative to the much faster-evolving X-ray flares may in this case illustrate important attributes of the emission — either from viewing effects or resulting from the physics of the emission itself.

3.5.3 The Late Rebrightening

The rebrightening phase of this burst is quite dramatic. While our observations do not sample the peak of the emission, a fit with a reasonable assumption of the sharpness parameter suggests that the flux increased by approximately 1 mag, and the amount of integrated optical flux released during the rebrightening is comparable to or more than that emitted by the early afterglow. A rise in optical flux of more than a magnitude at intermediate times (well after the end of prompt emission, but before any supernova component) has to our

knowledge been seen in only a handful of previous cases: GRBs 970508 (Castro-Tirado et al. 1998), 041219A (Blake et al. 2005), 060729 (Grupe et al. 2007), 070420 (Jelínek et al. 2007), and 070311 (Guidorzi et al. 2007a).

The rebrightening is also notable because it appears to differ subtly from the early decay, even though the evolution of both curves is generally quite simple. The decay index and spectral index both steepen, by $\Delta\alpha = 0.25 \pm 0.14$ and $\Delta\beta = 0.80 \pm 0.30$, respectively. Assuming a synchrotron spectrum, there are only two possible origins for this — the optical band is in different synchrotron regimes at different times (specifically, $\nu < \nu_c$ before cooling, and $\nu > \nu_c$ after cooling, consistent with the changes observed), or because of a shift in the electron index p by approximately $\Delta p = +0.4$.

We consider several physical origins for the rebrightening feature: the appearance of the forward shock when the burst ejecta first decelerate against the ISM, the late-time peak of a pre-existing forward shock due to evolution of the critical frequencies, impact of the forward shock through a density variation, and rebrightening caused by a refreshed shock.

Appearance of forward shock — When the GRB ejecta first begin to sweep up an amount of matter from the ISM comparable to the energy in the ejecta, they begin to decelerate, and reverse and forward shocks are propagated back into the ejecta and forward into the ISM, respectively; depending on the Lorentz factor, both shocks can then rise very quickly. We consider this scenario extremely unlikely to be relevant, since by necessity the forward and reverse shocks must rise simultaneously, and there is no explanation for the bright early-time component in the burst — save for a prompt model connected with internal shocks, but as we have already shown, there is no evidence linking the early optical behavior with the high-energy emission.

Spectral peak of existing forward shock — A more reasonable model postulates that the reverse and forward shocks both formed extremely early, but because they evolve differently (the reverse shock, whose synchrotron parameters are boosted down by factors of γ^2, begins to fade immediately, while the forward shock will rise at lower frequencies), the reverse shock fades rapidly, while the forward shock can rise and peak when the synchrotron frequency ν_m passes through the optical band. This model has, for example, been invoked to explain early-time bumps in the light curves of GRB 021004 (e.g., Kobayashi & Zhang 2003), GRB 050525A (Shao & Dai 2005), and GRB 080319B (Bloom et al. 2008), which level off significantly (but do not rebrighten) at around 10^4 s. However, this model is problematic here: although we have only sparse observations of the rebrightening, the observed rising temporal index of $\alpha = -1.12 \pm 0.16$ is far too fast to be consistent with a rising phase of a forward adiabatic shock, which predicts $F \propto t^{(2-s)/(4-s)}$ ($= t^{1/2}$ for a constant-density ISM and constant for a wind). Therefore, the synchrotron peak of the forward shock alone cannot explain this feature.

Density variation — A third possibility, not invoking the transition between reverse and forward shocks, might be a dramatic density variation: for example, the impact of the shock wave into a previously ejected circumstellar shell, or emergence of the shock from a low-density cavity into a dense external medium. Density fluctuations have been successfully invoked to explain low-level variations in several previous studies (e.g., Lazzati et al. 2002b)

and the timescale of the rebrightening ($\Delta t/t \approx 1$) is consistent with a density-fluctuation origin (Nakar & Piran 2003). However, in this case we would expect neither a change in the spectral index (as is probably observed) nor such a slow decline after the peak, with a temporal index that differs significantly but only slightly from the value of the initial decay. Furthermore, detailed numerical studies by numerous authors (Huang et al. 2006; Nakar & Piran 2003; Nakar & Granot 2007b) have failed to reproduce anything but the smallest rebrightening signatures in previous GRBs using density variations.

Multi-component jet — The complicated light curve of GRB 030329 has been interpreted (Berger et al. 2003b) as the result of two separate forward shocks, arising from two different jet components: a narrow, highly relativistic jet whose emission peaks extremely early, plus a wide, more mildly relativistic jet that dominates the late-time and radio evolution. Could this model conceivably explain the observations of GRB 071003? While a complete analysis is beyond the scope of this work, we note that the observations do seem consistent: the similarities of late-time decay of both rapid and late-time components are naturally explained, the timescale of our rebrightening is similar to that observed in GRB 030329, and (notably) the most significant criticism of the two-jet interpretation of GRB 030329 (that the rebrightening rose too rapidly and peaked too sharply — Huang et al. 2006) does not apply here: the rebrightening in this case is much smoother than that observed for GRB 030329.

Refreshed shock — Finally, we consider the possibility that this feature is due to a discrete energy reinjection energizing the forward shock, such as via a slow-moving shell that catches up to the forward shock at late times after it decelerates. This seems consistent with all observations, although largely by virtue of not making strong predictions; by invoking a customized pattern of energy reinjection at the right times, a very broad space of light curve behavior can be modeled (Huang et al. 2006). We do note that a large, sudden rebrightening of this nature may also produce a (second) reverse shock, which would be observable in radio and decline rapidly with time. The radio flux does in fact decay somewhat (in contrast to the expectation from a forward-shock model, where the radio flux is constant or rising), and the measured $\alpha = 0.33 \pm 0.10$ is not far from the predicted decay constant for a reverse shock of $\alpha \approx 1/2$ in the $\nu < \nu_m$ frequency regime (Kobayashi 2000). However, the radio decay could conceivably be due to other effects (e.g., late jet break), and without an independent measurement of the synchrotron peak frequency ν_m and late-time Lorentz factor Γ we are unable to further constrain the presence or absence of such a feature with the limited observations available.

We therefore find that only the multi-component jet and refreshed shock models are consistent with all available data. Unfortunately, we do not have sufficient observations during the rising phase of the rebrightening to distinguish the two models; in particular, we can set no constraints on the color evolution and lack a detailed light curve of the rise to peak of the rebrightening. We do note that the X-ray observations are already decaying well before the (probable) optical peak by an extrapolation of our observations (Figure 3.9), which may suggest hard-to-soft evolution in this feature as well. However, as noted earlier, the X-ray decay extrapolates back to the BAT light curve without explicit need for a rebrightening, so

without earlier X-ray measurements this association is speculative.

3.5.4 Environmental Constraints

In the simplest models, the late-time light curve of any GRB is fixed by a number of basic parameters: microphysical parameters ϵ_B (the fraction of energy in magnetic fields), ϵ_e (the fraction of energy in electrons), and p (the electron energy index); macroscopic parameters E_K (the blastwave energy) and θ_j (the jet opening angle); and a parameter quantifying the density of the surrounding medium, n (for a uniform density) or A_* (for an r^{-2} density profile). Our broadband observations (spanning from radio to X-rays) should, in principle, allow us to firmly constrain most of these parameters for GRB 071003 — or, more accurately, to its late rebrightening phase, as this component is dominant at late times.

The indices α and β are both well constrained at late times in the optical through X-ray bands, thanks to the wide range of temporal and spatial sampling: $\alpha_{O+X} = 1.71 \pm 0.14$, $\beta_{OX} = 0.93 \pm 0.03$. Two environment models satisfy these constraints within 90% confidence: a wind-driven medium ($\rho \propto r^{-2}$) in which $p \approx 2.9$, and a model in which the jet break has already occurred with $p \approx 1.9$ (but consistent with $p = 2$). Notably, ISM models are a poor fit: the late-time decay rate is too fast for the shallow spectral index. The radio observations appear to support this conclusion: the rising light curve predicted by the ISM model is clearly ruled out, and while the slow radio decay ($\alpha_R = 0.33 \pm 0.1$) is inconsistent in detail with the wind prediction of constant evolution as well, it is conceivable that variations from an exact $s = -2$ profile, an additional source of radio emission at early times (e.g., a reverse shock), or a soft jet break at $t \approx 5$ days may explain this difficulty.

The apparent spectral index of $\beta \approx -1.1$ observed in the radio is notable. A synchrotron spectrum is expected to have a self-absorbed $\beta = -2$ spectrum below the self-absorption frequency ν_a and a spectrum of $\beta = -0.5$ above it. The fact that the observed spectral index is intermediate between these values and consistent with neither (to ∼90% confidence) tells us that, if the spectrum is really synchrotron, the absorption break is likely to be very close to these frequencies, although exact constraints are difficult with only two frequencies since the break is likely to be quite soft. The radio evolution appears nearly achromatic, which would argue against this interpretation, but considering the relatively narrow time and frequency window of the observations and unknown break sharpness, we feel that this is not a major concern.

Because the ISM model is notably discrepant with the measured values of α and β, we unfortunately cannot use the afterglow as a probe of the ambient density. If the wind model, which is more consistent with the observations in this case, is correct, we can calculate the parameter A_* using (for example) equation 2 in Chevalier & Li (1999):

$$F_{\nu_m} = 20 \text{ mJy} \left(\frac{d_L}{5403 \text{ Mpc}}\right) (1+z)^{1/2} \left(\frac{\epsilon_B}{0.1}\right)^{-1/2} E_{52}^{1/2} A_* t_{\rm d}^{1/2}. \quad (3.3)$$

While we have no direct measurement of F_{ν_m}, it is constrained by the radio and optical observations (see Figure 3.13) to be ∼1 mJy (within a factor of ∼3). We therefore measure

$A_* = 0.07(\epsilon_B/0.1)^{1/2}$, an interestingly low value regardless of the value of ϵ_B. While ϵ_B is not strongly constrained, the absence of a cooling break between the X-ray and optical bands during the first 5 days (the cooling frequency ν_c increases in a wind model) requires $\epsilon_B \gtrsim 0.3$.

It is possible that the wind model is inappropriate and the rapid optical decay is due to a jet that broke before our multicolor late-time observations. (One possible criticism of the wind model is that in this case, the color transition between early and late times is hard to explain; because the cooling frequency rises with time, if $\nu > \nu_c$ late it must have been early as well under standard synchrotron evolution. However, because the rebrightening appears to be either a separate phenomenon or a large energy impulse that could conceivably have "reset" the synchrotron parameters [including ν_c] to new values, this may not be a major concern.) No jet break is observed in the light curve, but it is possible that a jet signature was concealed by the rebrightening. This case would certainly rule out the wide-angle jet interpretation of the secondary peak and would significantly reduce the energetics.

3.5.5 Spectral Implications on the Environment and Host Galaxy

The late-time spectroscopy and imaging tell a coherent story: unlike the vast majority of GRBs (Wainwright et al. 2007; Prochaska et al. 2008a), GRB 071003 did not occur in a gas-rich[12] galaxy. The environment is more consistent with a progenitor located in an outer galactic halo, or in an extremely small (even compared to "normal" long-duration GRB hosts) and gas-poor galaxy. While the possibility of line saturation prevents us from setting definitive upper limits, the column density through any host is consistent with being 3 orders of magnitude below typical GRB-derived values, and the contrast to the overall GRB population - which is dominated by subluminous galaxies to begin with (e.g., Fruchter et al. 2006; Fynbo et al. 2008), is dramatic.

While it is well established that long-duration GRBs generally originate from massive stars, we should be careful to ensure that our prior experience does not blind us to the existence of rarer subclasses of events. We note that one other GRB on record, GRB 070125, had very similar properties: extremely low Mg II absorption and no coincident host (Cenko et al. 2008a), as well as a very bright afterglow and extreme energetics ($E_\gamma = 3 \times 10^{52}$ erg; Chandra et al. 2008), and even a (mild) late-time rebrightening (Updike et al. 2008b). Both are also among the few *Swift* bursts detected at radio wavelengths.

However, GRB 070125 and GRB 071003 show evidence from their broadband light curves of origins typical of ordinary long GRBs. In the case of GRB 070125, a constant but very high circumstellar density suggested that it occurred in what was locally a dense environment, not an empty galactic halo, despite the near absence of a large-scale gas signature in the spectrum. In our case, for GRB 071003, we find evidence of a wind-like stratified

[12]Since our measurement is based on magnesium, we are directly measuring the metal column, not the gas column. An alternate possibility, therefore, is that the host is "normal" but extraordinarily metal-poor, less than 10^{-2} of the average solar abudance. However, we consider a highly subluminous host a more likely possibility. Both effects may be in play: low-luminosity galaxies, and those with low equivalent widths, tend to be relatively metal-poor (Prochaska et al. 2008a).

environment, a characteristic of a massive star. Together, these events appear to suggest an origin for these "halo" bursts similar to those of all other GRBs.

If GRB 071003 did occur in a star-forming region, then there are two possibilities consistent with the extremely small metal absorption in the spectrum. First, the burst may simply have formed in an extremely subluminous galaxy — necessarily, the number or distribution of such objects at very high redshift is not observationally constrained, but most simulations predict an abundance of small, highly sub-Galactic halos in the universe that could very well harbor limited star formation. Alternatively, GRB 071003 may have occurred in a tidally stripped tail from another, larger galaxy. In this case, further follow-up observations should reveal a disturbed, star-forming host in the close vicinity of the burst.

Either scenario seems plausible to explain the constraints derived on the burst environment. In either case, if GRBs are shown to be reasonable tracers of star formation at high redshift, then future large-sample GRB spectroscopy missions may be able to place important constraints on the star-formation history of the universe not possible by any other means. While the sample size of such low-column-density GRBs is now small [13], these results are already suggestive that this fraction may be significant (on the order of a few percent), and systematic rapid afterglow spectroscopy should continue to increase the number considerably over the years and decades to come. It would be an interesting discovery if the distribution of Mg II equivalent widths turns out to be bimodal.

On a related note, the existence of GRB 071003 and GRB 070125 may have important implications regarding the escape fraction of ionizing photons and the reionization history of the universe. Although the relatively low redshift of these systems keeps the Lyman-α and Lyman-break absorption features out of our spectral range and prevents us from measuring the H I column density directly (Chen et al. 2007d), these GRBs provide evidence that massive stars can form well outside of gas-dense hosts, where there is little to shield the intergalactic medium from their ionizing UV radiation. If the fraction of these events is more than a few percent at $z > 7$, then such "halo" stars may in fact be primarily responsible for the reionization of the universe. Observationally, spectroscopy of such events at these high redshifts may allow accurate measurement of the neutral gas fraction $\bar{x}_{\rm H}$ (e.g., McQuinn et al. 2008) without the interference of saturated line profiles originating from the host galaxy.

3.6 Conclusions

Although the temporal evolution of the optical afterglow of GRB 071003 is complicated, our early through late-time photometric follow-up data clearly resolve the optical light curve into separate components. Observations from KAIT during the prompt phase of the GRB revealed a slowly rising, slowly falling bump or flare component, superimposed on a simple

[13] In the previously published version of this manuscript, GRB 061021 (Thöne et al. 2006a) was mentioned as a third possible example, but subsequent analysis demonstrates this event to be simply at low redshift, placing the Mg II lines at the edge of the spectral range where they were missed in the preliminary reduction (Fynbo et al. 2009).

fading power law that has no observable correlation with the prompt emission, suggesting that while early internal-shock flares can be observed in the optical, they are not necessarily the same as those producing the high-energy signatures. Our late-time observations revealed one of the most dramatic late rebrightenings ever recorded in a GRB light curve, and suggest that this feature is not due to a reverse-forward shock transition or density variation, requiring either angular jet structure or very discrete late-time re-energizing of the optical afterglow. This may have important implications for the interpretation of other, less dramatic bumps and rebrightenings at similar timescales that appear to be common features in GRB afterglows.

The spectroscopic study of GRB 071003 offers a cautionary tale about the standard use of Mg II to infer a redshift: while it is common practice to use the highest-redshift Mg II system observed (especially in the cases when the absorption is quite strong) under the assumption that the GRB host system should show significant metal absorption, here we have a clear case where this assumption is fundamentally flawed. Were the S/N of the spectrum worse, or the host-galaxy absorption even weaker by a factor of only 2–3, it is likely that we would have missed the higher-redshift system entirely and proceeded with the assumption that this burst was at a redshift of 1.100 instead of 1.604. In light of this fact, previous and future GRB redshift claims based solely on identification of Mg II absorption should be regarded with increased skepticism.

The intervening absorption systems are nevertheless also remarkable. With three completely independent Mg II systems along the line of sight, GRB 071003 is among the most dramatic examples yet of the bizarre overabundance of these systems in GRB afterglows relative to those of quasars. Further study of this sightline, especially using AO systems, may help shed light on this mysterious result.

Acknowledgments

KAIT and its ongoing operation were made possible by donations from Sun Microsystems, Inc., the Hewlett-Packard Company, AutoScope Corporation, Lick Observatory, the NSF, the University of California, the Sylvia & Jim Katzman Foundation, and the TABASGO Foundation.

Table 3.1 Radio observations of GRB 071003

$t_{\rm mid}$ (h)	Frequency (GHz)	Flux density (μJy)	Error (μJy)
42.168	8.46	393	55
91.698	8.46	430	50
92.238	4.86	220	54
209.248	8.46	431	51
271.158	8.46	332	67
519.898	8.46	260	42
520.358	4.86	119	46
785.328	8.46	109	45
833.336	4.86	93	52

Table 3.2 Absorption Lines in the Afterglow Spectrum of GRB 071003

λ (Å)	z	Transition	W^a (Å)	$\sigma(W)^b$ (Å)
3549.69	0.37223	FeII 2586	< 2.51	
3568.06	0.37223	FeII 2600	2.33	0.59
3837.72	0.37223	Mg II 2796	2.48	0.20
3847.65	0.37223	Mg II 2803	2.14	0.19
3915.45	0.37223	MgI 2852	1.02	0.17
4032.63	1.60435	CIV 1548	0.22	0.06
4039.88	1.60435	CIV 1550	< 0.28	
4351.92	1.60435	AlII 1670	< 0.14	
5003.26	1.10019	FeII 2382	0.20	0.05
5276.54	1.60435	ZnII 2026	< 0.08	
5399.79	0.37223	CaII 3934	0.61	0.07
5417.99	0.93740	Mg II 2796	0.61	0.05
5432.79[c]	1.10019	FeII 2586	0.46	0.05
5447.85	0.37223	CaII 3969	0.46	0.07
5872.31	1.10019	Mg II 2796	0.80	0.05
5888.27	1.10019	Mg II 2803	0.68	0.06
6105.90	1.60435	FeII 2344	< 0.17	
6206.91	1.60435	FeII 2382	0.26	0.04
6240.46	1.60435	FeII* 2396a	0.25	0.04
6265.95	1.60435	FeII* 2405	< 0.16	
6282.68	1.60435	FeII* 2411b	0.18	0.03
6284.57			0.72	0.12
6734.47			0.97	0.15
6737.28	1.60435	FeII 2586	0.16	0.04
6772.60	1.60435	FeII 2600	0.27	0.05
7301.58	1.60435	Mg 2 2803	0.17	0.05
7430.06	1.60435	MgI 2852	< 0.24	
8091.56			0.92	0.13
8436.10[d]			0.86	0.26
8534.91[d]			0.72	0.17
8599.02[d]			1.34	0.17

[a] Equivalent widths are rest-frame values and assume the redshift given in Column 2.

[b] Limits are 2σ statistical values.

[c] Blended with Mg II λ2803 at $z = 0.937$.

[d] These features may be residuals from sky subtraction.

Table 3.3 Optical Light-Curve Fits: Color Change

Model Description	$\Delta\beta_{0-1}$	$\Delta\beta_{1(b-a)}$	$\Delta\beta_{0-2}$	β_2	χ^2/ν
Fully monochromatic	0	0	0	0.72±0.10	125.8 / 81
Uniformly chromatic bump	0.22±0.27	0	0	0.68±0.10	125.1 / 80
Variably chromatic bump	0.66±0.33	1.05±0.47	0	0.70±0.10	120.3 / 79
Chromatic rebrightening	0	0	0.77±0.31	1.26±0.11	120.0 / 80
Chromatic bump+rebrightening	0.75±0.33	1.09±0.47	0.84±0.31	1.26±0.11	113.7 / 78

Summary of relevant parameters and χ^2 for models allowing or disallowing color transitions and chromatic breaks between the various components. Values without uncertainties are fixed. Component 0 is the fast-decay component, Component 1 is the bump, and Component 2 is the late rebrightening. The absolute late-time spectral index β_2 is not a model parameter, but is fit externally after completion of the fit.

Table 3.4 Optical Light-Curve Fits: t_0

Model Description	dt_0 (s)	dt_1 (s)	dt_2 (s)	χ^2/ν
Reference	0	0	0	113.713 / 78
Decay	-0.01 ± 3.01	0	0	113.713 / 77
Bump	0	60.5±20.4	0	112.700 / 77
Bump (prompt pulse)	0	125.0	0	115.118 / 78
Rebrightening	0	0	1245±311	111.149 / 77

Summary of relevant parameters and χ^2 for models using a t_0 different from the trigger time. In all cases, the favored color-change model (chromatic bump and rebrightening) was used. Values without uncertainties are fixed. Component 0 is the fast-decay component, Component 1 is the bump, and Component 2 is the late rebrightening.

Table 3.5 Radio Modeling of GRB 071003

Parameter	Value (broken power law)	Value (unbroken)	Value (unbroken w/scintillation[a])
α_b	-0.11 ± 0.21	0.27 ± 0.06	0.34 ± 0.10
α_a	0.81 ± 0.25	–	–
t_{break}	8.51 ± 3.78	–	–
β	-1.11 ± 0.34	-1.15 ± 0.44	-1.15 ± 0.42
χ^2/ν	2.45 / 4	15.32 / 6	6.07 / 6

Best-fit parameters of a fit to the radio afterglow of GRB 071003 using a Beuermann et al. (1999) broken power-law model versus an unbroken power-law model. The improvement for the broken power-law fit is significant given the flux uncertainties, but due to interstellar scintillation may be coincidental. If a small amount of interstellar scintillation uncertainty is added in quadrature, an unbroken power-law fit is reasonable.

[a] In this model, we added a 15% error to all X-band points and a 22% error to all C-band points.

Table 3.6 Model fluxes at $t = 2.67$ days

Band/Filter	E eV	Flux μJy	Uncertainty μJy
X-ray	1000	0.036	0.006
u	3.46	3.17	1.42
g	2.55	4.47	0.30
V	2.25	5.07	0.27
r	1.97	5.97	1.14
R	1.88	8.01	0.47
i	1.61	9.16	0.56
I	1.54	10.34	0.54
z	1.34	14.74	2.29
K'	0.584	33.59	16.8
X	3.5e-5	414.6	91.8
C	2.0e-5	256.1	73.9

Fluxes of the afterglow interpolated to $t = 2.67$ d after the BAT trigger using all available X-ray, optical, and radio data. Galactic extinction ($E(B-V) = 0.148$ mag) is not accounted for; however, the X-ray flux is corrected for photoelectric absorption.

Table 3.7 Extinction models for optical/X-ray fits of GRB 071003

model	A_V	R_V	β	χ^2/ν
none	0	-	0.913 ± 0.029	12.4 / 8
$z = 0.372$				
Milky Way	0.239 ± 0.093	3.09	0.939 ± 0.028	5.80 / 7
SMC	0.209 ± 0.082	2.74	0.934 ± 0.028	5.95 / 7
LMC	0.256 ± 0.099	3.41	0.941 ± 0.029	5.87 / 7
Calzetti	0.279 ± 0.108	4.05	0.945 ± 0.029	5.80 / 7
$z = 1.10$				
Milky Way	0.133 ± 0.058	3.09	0.935 ± 0.029	7.16 / 7
SMC	0.127 ± 0.052	2.74	0.935 ± 0.028	6.38 / 7
LMC	0.132 ± 0.057	3.41	0.934 ± 0.028	7.16 / 7
Calzetti	0.247 ± 0.095	4.05	0.957 ± 0.032	5.78 / 7
$z = 1.60$				
Milky Way	0.139 ± 0.048	3.09	0.943 ± 0.028	3.94 / 7
SMC	0.096 ± 0.037	2.74	0.934 ± 0.028	5.77 / 7
LMC	0.131 ± 0.045	3.41	0.940 ± 0.028	3.98 / 7
Calzetti	0.240 ± 0.093	4.05	0.965 ± 0.033	5.84 / 7

Results of various fits to the contemporaneous optical and X-ray fluxes for extinction due to either the host galaxy or the intervening absorbers at $z = 0.372$ and $z = 1.10$. A small amount of extinction is required to accurately fit the data, but its nature is not strongly constrained. We adopt SMC-like extinction at $z = 0.372$ in the discussion and plots based on the relative strength of the intervening absorber at this redshift in the spectrum.

Chapter 4

GRB 061126: Does a Grey Burst Imply Grey Dust?

An earlier version of this chapter was previously published as ApJ 672:449–464[1].

Abstract

We report on observations of a gamma-ray burst (GRB 061126) with an extremely bright ($R \approx 12$ mag at peak) early-time optical afterglow. The optical afterglow is already fading as a power law 22 seconds after the trigger, with no detectable prompt contribution in our first exposure, which was coincident with a large prompt-emission gamma-ray pulse. The optical–infrared photometric spectral energy distribution is an excellent fit to a power law, but it exhibits a moderate red-to-blue evolution in the spectral index at about 500 s after the burst. This color change is contemporaneous with a switch from a relatively fast decay to slower decay. The rapidly decaying early afterglow is broadly consistent with synchrotron emission from a reverse shock, but a bright forward-shock component predicted by the intermediate- to late-time X-ray observations under the assumptions of standard afterglow models is not observed. Indeed, despite its remarkable early-time brightness, this burst would qualify as a dark burst at later times on the basis of its nearly flat optical-to-X-ray spectral index. Our photometric spectral energy distribution provides no evidence of host-galaxy extinction, requiring either large quantities of grey dust in the host system (at redshift 1.1588 ± 0.0006, based upon our late-time Keck spectroscopy) or separate physical origins for the X-ray and optical afterglows.

4.1 Introduction

While the study of the early-time X-ray afterglows of gamma-ray bursts (GRBs) has seen enormous strides since the launch of the *Swift* satellite (Gehrels et al. 2004), progress in the

understanding of the longer-wavelength emission has been somewhat more measured. This is unfortunate, as a complete understanding of *Swift* afterglows can only come from a combined broadband picture that allows us to systematically investigate whether the peculiarities seen in X-ray data carry over into the optical domain. Many of the same questions raised by recent X-ray results can also be asked about the optical. Is there a prompt optical component, analogous to the steeply decaying component seen in X-rays (Barthelmy et al. 2005)? Does the optical light curve show unusual features suggestive of energy injection, such as the nearly ubiquitous X-ray shallow-decay phase (Nousek et al. 2006)? Are there achromatic optical and X-ray breaks? Do the optical and X-ray afterglows even have a common origin at early times?

Previous studies have provided important hints. Most observations have been interpreted to support the consensus picture of synchrotron emission originating from a forward shock as it sweeps through the interstellar medium (e.g., Dai & Lu 1999; Vrba et al. 2000), or less commonly through a stellar wind (Price et al. 2002; Nysewander et al. 2006) — see Chevalier (2007) for a review. In a smaller number of cases (Akerlof et al. 1999; Li et al. 2003a; Kobayashi & Zhang 2003; Shao & Dai 2005), very early-time data have provided tentative evidence for an additional emission component originating from the reverse shock as it travels backward into the shocked material in the frame of the forward shock. Recently, studies of early-time light curves have also shown evidence of significant delay between the onset of the prompt emission and the afterglow (Rykoff et al. 2004), and in at least one case complicated energy injection activity as late as nearly an hour after the gamma-ray burst (Woźniak et al. 2006), long after the gamma-ray emission has faded away. However, simultaneous, correlated optical and gamma-ray emission has also been reported (Blake et al. 2005; Vestrand et al. 2005, 2006; Yost et al. 2007) for some events. In the *Swift* era, comparison to the very early X-ray afterglow has also been of great interest (e.g., Quimby et al. 2006).

Most interpretations of the early afterglow have been based on unfiltered observations, or observations in a single filter. Without information about the frequency domain, the reported early-time behaviors discussed above are difficult to definitively associate with any single physical interpretation. Fortunately, the increasing number of fast-responding robotic ground-based observatories, the maturation of existing ones, and the rapid-response capabilities of *Swift* are beginning to address this observational gap.

In the following discussion, we report on one of the brightest bursts of the *Swift* era, GRB 061126. The breadth and rapidity of the ground-based response to this burst were remarkable, including unfiltered detection during the prompt emission and multi-color simultaneous detections in filters from U through K_s (ranging a full decade in frequency) starting less than one minute after the burst trigger. This data set provides the opportunity to examine in unprecedented detail the time-dependent color properties of an early GRB afterglow.

In §4.2 we present our observations from infrared (IR) through gamma rays of the early afterglow and our late-time Keck spectrum of the host, establishing the probable redshift of this system to be $z = 1.1588$. In §4.3.1 we examine the properties of the prompt emission, and show that the high-energy and optical emission are observationally uncorrelated temporally

or spectrally, even at very early times. In §4.3.2–4.3.3 we examine the properties of the optical–IR light curve, and provide evidence for a red-to-blue change in the spectral index of $\Delta\beta \approx 0.3$ at early times. We investigate the X-ray behavior in §4.4.1, and show that no standard adiabatic model can fully explain the behavior seen by the X-Ray Telescope (XRT). Finally, while in §4.4.2–4.4.3 we show that the earliest afterglow appears reasonably fit by a reverse shock and the later afterglow by a forward shock based on the optical data alone, in §4.4.4 we demonstrate that an extrapolation of the X-ray spectrum overpredicts the contemporaneous optical flux by a factor of 5–20. We demonstrate using the optical–IR spectral energy distribution (SED) that this discrepancy cannot be due to any known dust extinction law. Unless we appeal to large quantities of grey dust, a possibility we discuss in §4.5.1, we argue in §4.5.2–4.5.3 that the X-ray and optical afterglow emission from this burst have separate physical origins.

4.2 Observations

4.2.1 Swift BAT and XRT

At 08:47:56 on 26 November 2006 (UT dates are used throughout this paper), the *Swift* Burst Alert Telescope (BAT) triggered and located GRB 061126. Unfortunately, due to an Earth-limb constraint, *Swift* was unable to slew promptly to the target for 23 minutes and could not begin observations with the XRT or the Ultraviolet/Optical Telescope (UVOT) before that time. After 23 minutes, *Swift* slewed to the burst position and detected a fading X-ray afterglow.

We download the *Swift* BAT and XRT data from the *Swift* Archive[2]. The XRT data are processed with version 0.10.3 of the `xrtpipeline` reduction script from the HEAsoft 6.0.6[3] software release. We employ the latest (19 December 2006) XRT and BAT calibration files. We establish the BAT energy scale and mask weighting by running the `bateconvert` and `batmaskwtevt` tasks, also from the HEAsoft 6.0.6 software release. BAT spectra and light curves are extracted with the `batbinevt` task, and response matrices are produced by running `batdrmgen`. We apply the systematic error corrections to the low-energy BAT spectral data as advised by the BAT Digest website[4]. The spectral normalizations are corrected for satellite slews using the `batupdatephakw` task.

The reduction of XRT data from cleaned event lists output by `xrtpipeline` to science-ready light curves and spectra is described in detail in Butler & Kocevski (2007b). The XRT, BAT, and RHESSI (Reuven Ramaty High Energy Solar Spectroscopic Imager) data are fit using ISIS[5].

The XRT light curve is converted to unabsorbed spectral flux at 1 keV using a scaling

[2] `ftp://legacy.gsfc.nasa.gov/swift/data`

[3] `http://heasarc.gsfc.nasa.gov/docs/software/lheasoft/`

[4] `http://swift.gsfc.nasa.gov/docs/swift/analysis/bat_digest.html`

[5] `http://space.mit.edu/CXC/ISIS/`

of 7.5 μJy/cps. The conversion from count rate to 0.5-10 keV (unabsorbed) flux can be accomplished by scaling the count rate by 5.4×10^{-11} erg cm^{-2} s^{-1}/cps.

4.2.2 RHESSI

RHESSI (Lin et al. 2002) is a dedicated solar observatory which uses nine germanium detectors to image the Sun at hard X-ray to gamma-ray energies (3 keV – 17 MeV). These detectors are unshielded and therefore frequently detect emission from off-axis GRBs. GRB 061126 was detected by RHESSI, which with its large spectral range allows us to complete the high-energy spectrum of this event.

To model the RHESSI response to off-axis photons, we have used Monte Carlo simulations and a detailed mass model. Since RHESSI rotates about its axis with a 4 s period, we have generated azimuthally averaged responses spaced 15° apart in polar angle. These responses are two-dimensional matrices of effective area: input photon energy vs. detected count energy bins. At present both energy axes are 64 logarithmic bins from 10 keV to 10 MeV. We generate the response matrices with `MGEANT` (Sturner et al. 2000) simulations: each response requires 64 simulations of a monoenergetic input spectrum, one for each photon energy bin. For an individual GRB, we generate and subtract a background count spectrum using data intervals before and after the burst. We generate a burst-specific response matrix with a weighted average of the two adjacent 15° responses. Convolving a spectral model with the response yields a model count spectrum for fitting to the GRB data.

4.2.3 RAPTOR

The RAPTOR (Rapid Telescopes for Optical Response) experiment (Vestrand et al. 2002) consists of a series of small telescopes used to conduct transient surveys as well as perform rapid followup of GRBs and other events. One of these telescopes, RAPTOR-S, is a 0.4 m fully autonomous robotic telescope, typically operated at focal ratio $f/5$. It is equipped with a 1k × 1k pixel CCD camera employing a back-illuminated Marconi CCD47-10 chip with 13 μm pixels. The telescope is owned by Los Alamos National Laboratory and located at the Fenton Hill Observatory (106.67° W, 35.88° N) at an altitude of ∼2500 m in the Jemez Mountains of New Mexico.

RAPTOR-S responded to the *Swift* trigger at 08:48:17.29, or 20.87 s after the trigger and 4.3 s after receiving the GCN (Gamma-ray Burst Coordination Network) packet. The telescope took a series of nine unfiltered 5 s exposures (the first two of which occurred while detectable gamma-ray emission was still ongoing), followed by a series of 10 s and 30 s exposures. The optical transient is detected in all these frames. Preliminary photometric calibration was performed using the R-band magnitudes from the USNO (United States Naval Observatory) B1.0 catalog. However, for consistency with the unfiltered KAIT (Katzman Automatic Imaging Telescope) observations, which were calibrated using the more precise SDSS (Sloan Digital Sky Survey) measurements, we subtract a constant offset of 0.16 mag

post-calibration. The RAPTOR photometry (not including this final offset) is given in Table B.1.

4.2.4 PAIRITEL

Starting in 2003, we began to automate the 1.3-m Peters Telescope, formerly used for the Two Micron All Sky Survey (2MASS; Skrutskie et al. 2006), on Mt. Hopkins, Arizona. The telescope was re-outfitted with the southern 2MASS camera, and all of the control and data acquisition systems were rewritten (Bloom et al. 2006e). The Peters Automated Infrared Imaging Telescope (PAIRITEL) has been obtaining useful IR observations of GRBs since 2004.

At 08:48:18 ($t = 22$ s), PAIRITEL was triggered with the GCN BAT position notice of GRB 061126. The autonomous slew of the telescope and dome began at 08:48:22 and ended at 08:48:47; the slew time was short since we had been observing M82 (23.9° to the east of the GRB) immediately prior to the GRB. After an initial reset of the camera, the first 7.8 s images in J, H, and K_s bands were obtained starting at 08:48:54.35 ($t = 58$ s). We continued with a dense sampling of observations over the next three hours as well as several hours of imaging the following night.

Reductions of the individual images were performed using a set of customized scripts written in PYRAF and Python. The afterglow was well detected with signal-to-noise ratio (S/N) > 10 in individual images for the first 20 min of observations (Figure 4.1). In fact, the H- and K_s-band fluxes of the afterglow are so bright in the first few minutes that the pixel responses were in the nonlinear regime. Unfortunately, the cloud cover in Arizona was highly variable during the first 30 min of GRB 061126 observations, leading to variable transmission on 10 s timescales. As such, in our analysis we refit the zeropoint in every individual exposure to the 2MASS catalog. The typical root-mean-square (rms) uncertainties in the zeropoints are 2–3%. Given the large variations in the sub-pixel response function for NICMOS3 arrays, we have found that aperture photometry on individual exposures suffers a roughly 3% systematic uncertainty from image to image (Blake et al. 2008). Table B.1 in the Appendix gives the aperture magnitude measurements from the PAIRITEL observations. In this table and in all plots and modeling, we exclude exposures in which the CCD response was nonlinear, as well as H-band observations during periods of poor transmission.

We determined the position of the afterglow to be $(\alpha, \delta) = (05^h46^m24.47^s \pm 0.16'', +64°12'38.60'' \pm 0.18'')$ (J2000) from a stacked J-band image covering the first 30 min after the trigger. The quoted uncertainties are 1σ, dominated by the astrometric mapping error from our stacked image to the catalog positions of 90 2MASS sources.

4.2.5 NMSU 1 m Telescope

Optical observations in the Johnson-Cousins *UBVRI* filters were obtained using the New Mexico State University robotic 1 m telescope located at Apache Point Observatory. Because the telescope happened to be pointed relatively near the burst location, the first

observations were started only 47 s after the burst trigger, and only 31 s after the alert. The telescope took five sequences of observations in the order I, R, V, B, U with exposure times of 10, 10, 20, 40, and 60 s, respectively, and then took another five sequences of observations with exposure times of 20, 20, 40, 80, and 120 s. With overhead, these ten sequences took about an hour to complete. The afterglow was detected in all of the observations, with random errors ranging from better than 0.01 mag in the first series to 0.1–0.2 mag in the last series.

The afterglow brightness was measured using aperture photometry with an aperture of $3''$ radius; several reference stars in the field were also measured. Calibration was achieved via observations of these reference stars, along with *UBVRI* standard stars, on 22 December 2006. A standard photometric solution was derived for this night, yielding calibrated magnitudes for the reference stars. On the calibration night, the standard-star solution yielded rms deviations of about 0.03 mag in each bandpass, so the calibration zeropoints are accurate only to this level. The final photometry is given in Table B.1.

4.2.6 KAIT and the Lick Nickel Telescope

The 0.76 m robotic Katzman Automatic Imaging Telescope (KAIT; Filippenko et al. 2001) and its GRB alert system (Li et al. 2003b) responded to the GCN notice with the position of GRB 061126 at $t = 16$ s after the trigger, and attempted to execute a pre-arranged observation sequence. Unfortunately, the weather conditions were poor, so KAIT did not acquire a useful image until $t = 305$ s. Also, the telescope did not have a successful focusing procedure before the GRB observations (again due to bad weather), so the images were not fully in focus. Nevertheless, a sequence of V, I, and unfiltered observations was made, and the GRB afterglow was detected in most images. A successful focusing procedure was executed during the middle of the GRB observations, and KAIT followed the GRB until humidity forced the system to shut down at $t \approx 1.8$ hr. The images were automatically processed with the proper dark current, bias, and flat fields before measuring photometry and calibrating relative to ten SDSS stars (Cool 2006; Adelman-McCarthy et al. 2006). The reference magnitudes of these stars were converted to *VRI* using the transformation equations of Lupton (2005)[6]. Unfiltered observations were calibrated using the R-band magnitudes.

A sequence of 300 s R-band images was also manually obtained at the Lick Observatory Nickel 1 m telescope from $t \approx 1.0$ hr to 1.7 hr. The observations were again terminated prematurely due to the weather conditions. The images were manually reduced with the proper calibration files (bias, dark current, and flat-field images), and calibrated relative to our SDSS reference stars. The photometry is given in Table B.1.

[6] `http://www.sdss.org/dr4/algorithms/sdssUBVRITransform.html\#Lupton2005`

4.2.7 *Swift* UVOT

Swift began follow-up observations of GRB 061126 at 1605 s after the burst trigger, its slew having been delayed as a result of the Earth-limb constraint. Despite this time delay the afterglow was still detected, albeit marginally, in all of the UVOT filters except for UVW2.

We acquired the UVOT imaging data from the NASA archive[7]. Unfortunately the afterglow had already become quite faint by the beginning of the observations, and is not well detected except in stacked exposures. To calculate the most accurate photometry possible, we therefore bin observations obtained at similar epochs, and perform aperture photometry using the optimal aperture size as given in the prescription of Li et al. (2006) for the V, B, and U data. For the UV filters, we use the photometry reported by the UVOT team in the most recent GCN Report for this burst (Sbarufatti et al. 2006). Our photometry is given in Table B.1.

Despite our small-aperture analysis, the UBV photometry has large uncertainties, and some points are not formally consistent with effectively simultaneous ground-based observations in the same filters. This is not necessarily surprising; due to the extremely faint nature of the afterglow by the time that *Swift* completed its slew, the actual uncertainty on these measurements may be significantly larger than the nominal photometric error. We do not use these points in our modeling, but we do include them in our plots. The UVW1 and UVM2 points have even larger uncertainties (0.4–0.8 mag), and no ground-based calibration is available; moreover, Galactic extinction (which is significant in this direction: $A_{UVM2} \approx 1.8$ mag) is increasingly uncertain toward these wavelengths. Therefore, we exclude these points from the formal fits as well, and restrict our modeling to the much more precise ground-based photometry. However, we do include the UV points in our SED plots for comparison.

4.2.8 GCN Circulars

For comparative purposes, our plots also include points from the GCN Circulars[8], but we do not actually use these points in our fitting. Most early-time data were calibrated against the USNO B1.0 survey (Monet et al. 2003), which does not contain very accurate photometry. Some data points were also calibrated against a preliminary release of an SDSS pre-burst observation of this field (Cool et al. 2006) which was later found to be incorrectly calibrated (indeed, our own use of these observations for our preliminary calibrations exposed the problem and motivated the re-release of the SDSS calibration used for the KAIT reductions, Cool 2006.)

4.2.9 Keck Host Imaging and Spectroscopy

The galaxy hosting GRB 061126 was observed on 18 January 2006 with the Low Resolution Imaging Spectrometer (LRIS; Oke et al. 1995) on the Keck I 10 m telescope. A

[7] `http://heasarc.gsfc.nasa.gov/docs/swift/archive/`

[8] `http://gcn.gsfc.nasa.gov/gcn3_archive.html`

total of 3 × 300 s of imaging was obtained simultaneously in R_c and g' filters, followed by two long-slit spectroscopic exposures of 20 min each over the host location identified in our images (Figure 4.2).

Imaging data were reduced using standard techniques. In the final, reduced images we identify an extended source consistent with the GRB afterglow position, apparent in both our g' and R imaging. This source, which we identify as the GRB host, has significant substructure, with two clearly distinct elongated knots, each of which may have further substructure. The afterglow is offset by $< 1''$ from the brightest knot. The magnitude of the whole complex, using a large ($2.55''$ radius) aperture fixed at the position $(\alpha, \delta) = 05^h46^m24.53^S, +64°12'39.31'')$ and performing photometric calibration using the subset of our SDSS stars that are unsaturated in the Keck images, is $g = 25.13 \pm 0.16$ and $R = 24.10 \pm 0.11$ mag. After correcting for Galactic extinction, the $g - R$ color is 0.88 ± 0.19 mag.

Using the long slit of width $1.0''$, the 600 line mm^{-1} grating blazed at 7500 Å, and the 300 line mm^{-1} grism blazed at 5000 Å, we obtained spectra covering the wavelength range 6680–9266 Å and 3200–7649 Å with the red and blue cameras, respectively. The spectroscopic data were processed with an IDL package[9] customized for LRIS long-slit reductions developed by J. Hennawi and J. X. Prochaska. The observed PA of -69.35° is significantly different from the parallactic angle, but as we are only seeking a line identification the effects of differential slit losses (Filippenko 1982) are not very significant.

The two-dimensional reduced spectra show a faint blue continuum and a sole emission feature at a vaccuum wavelength of ~ 8050 Å (Figure 4.3). From the one-dimensional spectrum it is clear that the emission feature is slightly resolved; it has a full width at half-maximum intensity (FWHM) of roughly 10 Å, while the spectral resolution in that wavelength range, as determined by the FWHM of arc-line profiles, is 5.8 Å. As we detect only one emission feature, it is impossible to definitively report the redshift of the GRB host. However, the width of the line and the presence of obvious continuum blueward of this feature suggest that it likely corresponds to the [O II] $\lambda\lambda$ 3727.11, 3729.86 Å doublet. Using our best-fit observed line centroid of 8049.0 ± 2.0 Å and assuming an intrinsic doublet centroid of 3728.5 ± 0.5 Å, this would imply that the GRB host lies at a redshift of $z = 1.1588 \pm 0.0006$. The width of the emission feature is consistent with an [O II] doublet at this redshift (3.19 Å separation at $z = 1.159$) when convolved with the instrumental resolution. Furthermore, if the emission is from [O II] we would not expect to see any other spectral lines; the most common, redder lines would fall redward of our red spectrum, and the only strong emission line blueward of [O II] is Lyα which lies below our spectral coverage.

Adopting the 8050 Å emission feature as the [O II] doublet, we can estimate the star-formation rate (SFR) of the host galaxy based on the line flux. We measure the total flux from the extracted, one-dimensional spectrum in the region 8042.0–8056.0 Å. We measure the continuum by computing the median flux in two regions free of sky lines (regions "C" in Figure 4.3). The total flux in these lines is $(1.6 \pm 0.2) \times 10^{-17}$ erg s^{-1} cm^{-2} (or). Using

[9]Specifically, the Longslit codes now bundled within XIDL, `http://www.ucolick.org/~xavier/IDL/index.html`

the relation between [O II] luminosity and SFR described by Kennicutt (1998), we find that the GRB host galaxy is undergoing star formation at a rate of 1.6 ± 0.2 $M_\odot$ yr^{-1} (assuming $H_\circ = 71$ km s^{-1} Mpc^{-1}, $\Omega_M = 0.3$, $\Omega_\Lambda = 0.7$, as is done throughout this paper), or 2.2 ± 0.3 $M_\odot$ yr^{-1} after correcting for Galactic extinction. The intrinsic uncertainty in the calibration converting [O II] line luminosity into SFR is approximately 30% (Kennicutt 1998); this uncertainty is not included in our quoted error. Though our measured SFR must be considered a lower limit because we have not accounted for dust extinction, it is interesting to note that the rate of star formation in the host galaxy of GRB 061126 is comparable to the SFRs found in other GRB hosts, measured using dust-corrected UV fluxes as well as [O II] luminosities (Christensen et al. 2004).

4.3 Data Analysis and Modeling

4.3.1 Prompt Emission

The prompt emission from GRB 061126 displays a complex, multi-peaked profile dominated by two large pulses (Figure 4.4). After a gradually increasing component starting at 7 s before the trigger and a small precursor spike at $t \approx 1$ s after the trigger, the first and largest pulse ("Pulse A") begins at $t \approx 3$ s, and fades to about twice the background level by $t \approx 15$ s. A second pulse ("Pulse B") begins at $t \approx 19$ s, lasting until $t \approx 25$ s. There is short-timescale microstructure in both of these pulses. The full burst has a T_{90} (Kouveliotou et al. 1993) of 26.8 ± 0.8 s in the full *Swift* 15–350 keV band (Butler et al. 2007).

Using the combined *Swift* BAT and RHESSI spectrum, we fit a Band model (Band et al. 1993) over several different time regions: The entire burst, the first pulse, and the second pulse. Results are summarized in Table 4.1. For the full burst, we measure an average peak energy $E_{p,obs}$ of 620 keV, though there probably is hard-to-soft spectral evolution, as evidenced by the significantly different values of $E_{p,obs}$ during the two pulses. The total fluence over the full spectral range is $(3.0 \pm 0.4) \times 10^{-5}$ erg cm^{-2}, which at the putative host redshift of 1.16 corresponds to an isotropic release of energy of $E_{iso} = (1.06 \pm 0.14) \times 10^{53}$ erg over a 1–1000 keV host-frame bandpass, assuming our standard cosmology.

Given this value of E_{iso}, the Amati relation (Amati et al. 2002) predicts $E_{p,obs} = 130 \times 10^{0.0 \pm 0.3}$ keV, which is 2σ from the measured value. Given E_{iso} and $E_{p,obs}$, the Ghirlanda relation (Ghirlanda et al. 2004) predicts a jet break at $t = 10^{1.41 \pm 0.27}$ d (13–49 d). The beaming-corrected energy release is $10^{51.6 \pm 0.2}$ erg, for a jet opening angle of $10^{1.21 \pm 0.10}$ degrees (13–20°).

RAPTOR detected GRB 061126 contemporaneously with the BAT emission. Fortuitously, the first unfiltered exposure (which took place 20.87–25.87 s after the BAT trigger) matches quite well the second pulse of the GRB (peak time of 22.5 s and a T_{90} of about 5 s) — see the first optical point of Figure 4.4.

Comparing this first, contemporaneous data point to later exposures in which the prompt emission has faded, the early-time RAPTOR data are seen to fade as a simple

power law ($F_\nu \propto t^{-\alpha}$), with the decay index $\alpha \approx 1.5$ (using the GRB trigger time as t_0). There is no evidence for an additional prompt flux component based on an extrapolation backward from later measurements. Consistent with this observation, if we extrapolate the best-fit Band (Band et al. 1993) model of the second GRB pulse into the optical (Figure 4.5), the predicted optical flux is only 250 μJy, significantly less than what is observed. Finally, if we extrapolate the Band model of the prompt emission in time to 60 s (assuming continued hard-to-soft spectral evolution and fading), it both falls far short of our multi-color data at that time and also has a different spectral slope (open circles and dashed line in Figure 4.5). For this burst, there is no clearly observable association between the prompt emission and the long-wavelength afterglow, even as early as 20 s after the burst. This is not inconsistent with earlier reports of a link (e.g., Blake et al. 2005; Vestrand et al. 2006; Yost et al. 2007): more likely, as our SED shows, for this burst the prompt component is simply dominated by an extremely bright early-time afterglow.

4.3.2 Optical Light Curve

While the very early optical light curve appears to follow a power-law behavior, the light curve enters a more complex phase within a few minutes. A brief visual inspection of the overall afterglow light curve (Figures 4.6 and 4.7) shows several interesting features of this burst. The early decay that began in our earliest data continues with the same trend for several decades in time, fading roughly as a power law with an average decay index α of about 1.5. A simple power law is clearly a poor fit, however, due to the presence of of a prominent "bump" feature at around 120 s.

Rapid early decay gives way to a shallower-decaying ($\alpha < 1$) component starting at about 10^3 s that dominates for the rest of our observations.

In our modeling, we construct the light curve as a sum of several broken power-law components, each of generally different color as well as different decay indices. As with the other events presented in this thesis, we use the procedure outlined in the Appendix of constructing the overall light curve from a sum of (potentially chromatic) Beuermann functions. We use three total summed components, though two of them are tightly linked: a "fast" early-time component, with no break ($\alpha_{F,a} = \alpha_{F,b}$), a "bump" component, fixed to have the same color as the fast component ($F_{\nu,B} \propto F_{\nu,F}$), and a "slow" component, also with no break ($\alpha_{S,a} = \alpha_{S,b}$). (Note that, for this burst, we use the letter subscripts F, B, and S instead of numerals to designate the different components.)

The constraints on the slow component depend on the specific model tested. In all cases, the decay index (α_S) is free to vary. We do not directly constrain the spectral index (defined here using the convention $F_\nu \propto \nu_{eff}^{-\beta}$) or require a power-law SED. However, in some models we do constrain the change in the spectral properties. In our different models, these color constraints are as follows:

- Unconstrained, allowing the linear flux factor $F_{\nu,S}$ to take arbitrary values for each filter.

- Constrained to allow no spectral evolution: $F_{\nu,S} = CF_{\nu,F}$, where C is a fitted constant.
- Constrained in such a way as to permit the spectral index of the slow component to differ from that of the fast component by $\Delta\beta_{F-S}$. This *difference* in the spectral index can be fit directly regardless of Galactic extinction (which is significant) or host-galaxy extinction as long as the extinction can be assumed to be a constant in time.

We also attempt two other, somewhat more specialized models:

- A fourth, physically motivated model in which the slow component is treated as an adiabatic forward shock whose flux peaks at some time during our multi-color observations. In this case the slow component is broken, where the rising and decay indices ($\alpha_{S,b}$ and $\alpha_{S,a}$, respectively) and the change in spectral index across the break ($\Delta\beta_S$) are fixed using the constraints from the X-ray spectrum discussed in §4.4.1.
- Solely for the purposes of estimating the "average" early-time optical decay index, we also fit a model with no bump component at all. (This is a very poor fit, and because most of the IR observations were performed during the bump any photometric SED generated would be highly biased. Therefore we do not use this model for any other purpose.)

Our data only trace the light curve with no gaps in coverage until $\sim$ 7000 s, and we have no color information past 4000 seconds aside from a marginal J-band detection and H and K_s limits from the second night. Later-time measurements are present in the GCN Circulars, but different authors report different and somewhat contradictory behavior, suggesting either a problem with some of the public data or complex behavior of the light curve at late times. Consequently, we do not include any optical points after 10^4 s in our fits, anticipating that the late-time optical evolution will be discussed in greater detail in upcoming work by Mundell and collaborators. Instead, we focus on the properties of the early and intermediate afterglow.

After fitting, we correct for Galactic extinction of $E_{B-V} = 0.182$ mag (using the NED extinction calculator[10], Schlegel et al. 1998) and fit a simple power law to estimate the observed spectral index for different components. (This neglects the possibility of host extinction, but as we will show in §4.4.4, if host extinction is present it does not cause significant deviation from a power law.)

Despite the complexity of the models, no fit is observed to give a value of χ^2 per degree of freedom (dof) ≈ 1. The most successful model, using unbroken power laws and arbitrary filter-dependent color change, gives $\chi^2/\mathrm{dof} \approx 6$. This is not surprising; modulations in afterglow flux have been observed in many previous cases (for example, Lipkin et al. 2004). Accordingly, we add in quadrature an extra uncertainty of 0.08 mag to all the photometric measurements. With this adjustment, our different models produce fit results

[10]The NASA/IPAC Extragalactic Database (NED) is operated by the Jet Propulsion Laboratory, California Institute of Technology, under contract with the National Aeronautics and Space Administration.

as given in Table 4.2. There is strong evidence for color change — a fit allowing no change in the relative fluxes of different components has a value of $\chi^2/\mathrm{dof} = 261.9/193$, while an equivalent fit allowing the early fast-fading and later slow-fading components to have different spectral indexes (Figure 4.8) gives $\chi^2/\mathrm{dof} = 231.3/192$. (The f-test significance of this improvement is 10^{-6}.) Under this model, β shifts toward the blue across the transition by $\Delta\beta_{F-S} = -0.383 \pm 0.075$.

4.3.3 Optical Color Evolution

The above results indicate color evolution across the steep-to-shallow transition. To confirm this behavior and ensure this is not an artifact of the modeling, we construct truly contemporaneous SEDs using simultaneous PAIRITEL and NMSU 1.0 m observations by mosaicing only those individual PAIRITEL exposures taken during the NMSU exposure time range. In cases where the exposure time is much less than the time since the burst, we increase the effective PAIRITEL exposure time by also including exposures shortly before the beginning or after the end of the optical exposures (otherwise the S/N for the late-time PAIRITEL measurements is quite low). After correcting for Galactic extinction, we fit the three J/K_s/optical data points with a basic power law, and determine the best-fit value and uncertainty for the spectral index β. (We omit H-band measurements from this fit, since the variable transmission introduces a significantly larger scatter in that band compared to J and K_s.) The results are plotted in Figure 4.9.

The early-time colors from the first NMSU filter cycle are consistent with a spectral index of $\beta = 1.2 \pm 0.1$, but starting at around 500 s the colors shift notably blueward and at later times the index is typically $\beta = 0.95 \pm 0.10$. This provides model-independent support of our fit conclusion that the afterglow has undergone a color change.

4.3.4 X-ray Light Curve and Spectrum

The XRT light curve (Figure 4.6) fades as a purely unbroken power law with a decay index $\alpha_X = 1.31 \pm 0.01$ over the entire span of the *Swift* observations, from ∼2 ks out to nearly 10 d. There is some suggestion that the decay rate is slightly faster during the first orbit, but the unbroken fit is still good ($\chi^2/\mathrm{dof} = 668.2/550$) and joins with an unbroken extrapolation of the fading BAT light curve.

After removing the effect of neutral hydrogen[11] absorption [both Galactic, for which we estimate $N_{\mathrm{H,Galactic}} = 0.103 \times 10^{22}$ cm^{-2} from Dickey & Lockman (1990), and at the host redshift, for which we calculate a best-fit value of $N_{\mathrm{H,host}} = (1.1 \pm 0.3) \times 10^{22}$ cm^{-2}], the X-ray spectrum is a good fit ($\chi^2/\mathrm{dof} = 213.9/238$) to a simple power law, with a spectral index $\beta_X = 1.00 \pm 0.07$. There is no evidence for spectral evolution during the observations: using the X-ray hardness ratio (see Butler et al. 2007); we constrain the change in the X-ray

[11] More accurately, the X-ray absorption is dominated by light metals, rather than hydrogen. However, we will use the standard terminology and refer to the absorption column in terms of the hydrogen density.

spectral slope to be $\Delta\beta_X < 0.4$ (90% confidence). Our analysis is consistent with that from the most recent GCN report for this event (Sbarufatti et al. 2006). [12]

4.4 Discussion

4.4.1 Constraints on Synchrotron Model Parameters

Due to the complex behavior of the optical light curve and the possibility of host extinction, it is difficult to apply any constraints on the physical parameters of this burst (p, ϵ_B, ϵ_E, etc.) from the optical observations alone. However, in principle the degeneracy can be broken using the XRT data.

The fits to our data unambiguously show that the optical flux and X-ray flux are decaying at different rates during the period when we have contemporaneous data in both bands (1800–6000 s): $\alpha_{opt} = 0.75 \pm 0.05$ and $\alpha_X = 1.31 \pm 0.01$. Assuming a normal synchrotron spectrum (Sari et al. 1998), this allows only two possibilities for the ordering of the spectral breaks: $\nu_c < \nu_{opt} < \nu_m < \nu_X$(fast cooling), or $\nu_m < \nu_{opt} < \nu_c < \nu_X$ (slow cooling). In either case, the X-ray spectral index is predicted to be $\beta = p/2$. The observed spectral index is $\beta = 1.00 \pm 0.07$, so we can confidently calculate an electron index of $p = 2.00 \pm 0.14$, the minimum value for a distribution that is unbroken at high energies.

However, this conclusion is problematic in light of the observed X-ray light curve. Independent of environment, the decay index of emission from an expanding adiabatic forward shock in the regime $\nu_c, \nu_m < \nu$ should obey $\alpha = 3\beta/2 - 1/2$, which for our spectral data would imply $\alpha = 1.00 \pm 0.10$, disagreeing by about 3σ from the measured value.

The discrepancy is significant and indicates that at least one standard assumption does not hold. We consider several possibilities:

1. Our conclusion of $\nu_c, \nu_m < \nu_X$ is incorrect. But, this is unlikely: no other ordering can produce optical and X-ray light curves that decay at different rates. Furthermore, the X-ray light curve remains unbroken out to very late times ($t \gtrsim 10^6$ s). Such a late cooling break in the X-ray band would imply an extremely low density and ϵ_B (specifically, $\epsilon_B n < 1.5 \times 10^{-6}$ cm^{-3}), which we consider to be unlikely.

2. The afterglow evolution is dominated by radiative losses and has not yet transitioned to an adiabatic phase, even out to ~ 9 d. This case (Sari et al. 1998) would predict that $\alpha = 12\beta/7 - 2/7 = 1.42 \pm 0.12$, within 1σ of the observed value. However, this requires that the synchrotron spectrum still be fast-cooling, which demands that the optical band be above the synchrotron critical frequency ($\nu_c < \nu_{opt} < \nu_m$) to produce a fading optical light curve in a constant-density medium. The specific, predicted value of $\alpha = 4/7 = 0.57$ is not statistically consistent with our observations of the optical

[12]Note, however, that the GCN report quotes the photon spectral index, instead of the flux spectral index, and that since they fit neutral hydrogen absorption only at $z = 0$ instead of the host redshift, their N_H excess is significantly less than our $N_{\rm H,host}$.

decay index in this region, but it is possible that the measurement may be confused somewhat by the presence of soft breaks or other systematic effects.

3. The X-ray light curve is affected by synchrotron self-Compton (SSC) losses, which would steepen the decay slightly relative to that predicted by a no-Compton model (Sari & Esin 2001). The amount of predicted steepening is, unfortunately, relatively low: $\Delta\alpha \approx 0.5(p-2)/(4-p)$, which for the X-ray inferred value of $p = 2\beta = 2.0 \pm 0.14$ gives a constraint of the SSC-corrected decay index of 1.0 ± 0.14, still off by 2σ from the observed value of 1.31 ± 0.01.

4. The X-ray emission is not due to a forward shock, or not due to synchrotron radiation.

Some combination of factors may also be at work. In any event, the specific resolution to this problem is not critical at this stage, and we will proceed assuming $p = 2$, which is independent of any assumptions about the burst environment and requires only that the source of the X-ray light be synchrotron radiation, where the X-ray band is above the cooling and minimum-energy breaks.

In addition to identifying the spectral regimes, we also seek to identify the burst environment (constant-density, wind-stratified, or a spreading jet). A spreading jet has a rapidly decaying light curve and can be immediately ruled out. A wind can also be ruled out, since it would predict that the optical flux should decay faster than the X-ray flux, yet we observe the opposite. However, a constant-density (interstellar medium) environment is consistent with all of the qualitative features of the light curve.

4.4.2 The Very Early Afterglow Decay — A Reverse Shock?

For any assumption about the X-rays, the behavior of the fast-decaying optical component cannot be reproduced as originating from a forward shock. The early optical decay index is $\alpha_F \approx 1.5$ if we fit a single component (no bump), though in our fits with a bump component the decay rate is steeper. (However, if we interpret the bump as a density variation or other modulation of a single power law, rather than a truly separate component, the value of $\alpha_F \approx 1.5$ is most appropriate. For our discussion of the interpretation, we use the constraint $\alpha \gtrsim 1.5$, which is certainly true independent of the number of components used in our model.)

This decay is steeper than the $\alpha_X = 1.31$ decay slope observed in the X-rays at late times. In no regime of the forward-shock interstellar-medium model can the longer-wavelength emission decay faster than the X-rays at the same or later times (Sari et al. 1998).[13] Furthermore, the subsequent passage of ν_m or ν_c through the optical bands should produce breaks in the optical light curves which can only accelerate the temporal decay, not decelerate it.

The lack of flux excess in the first RAPTOR measurement, and the extrapolation of the Band model into the visible frequency range, argue against association with this emission to

[13] It is possible in a wind-stratified medium, but even then, the observed value of α_F is too steep for $p = 2$.

a prompt optical component from the internal shocks that (presumably) produced the high-energy emission. Therefore, the most likely candidate to be responsible for this early optical emission is an external reverse shock which is produced when the forward shock begins to interact with the surrounding medium. Such an explanation has been previously used by several authors to explain observed peculiarities in the early-time light curves of a number of GRB afterglows (Sari & Piran 1999a; Kobayashi & Zhang 2003; Wei 2003; Shao & Dai 2005).

Kobayashi (2000) derived the temporal behavior of reverse-shock light curves for two different regimes: the thick shell (corresponding to cases in which the reverse shock is able to become relativistic as it crosses back through the ejecta) and the thin shell (for cases where the shock always remains nonrelativistic). The thick shell case is associated with relatively long bursts, and in particular predicts that the peak of the reverse-shock emission will happen at about the same time as the burst itself, whereas the thin-shell case predicts an optical peak after the GRB. As the RAPTOR data indicate an optical light curve that is already rapidly declining during the prompt emission, we apply the thick-shell case here. (However, the thin-shell case gives identical numerical predictions for the region of interest for $p = 2$.)

Before the shock crossing time T, the reverse-shock light curve is expected to rise as $t^{1/2}$, which as already discussed is not observed. The light curve peaks at T and then decays: for frequencies $\nu_m < \nu < \nu_c$ the flux decays as $t^{-(73p+21)/96}$, while for $\nu < \nu_m$ it decays as $t^{17/36}$. (For $\nu_c < \nu$ the light curve shuts off and rapidly dives to zero, and for fast cooling the light curve either declines as $\alpha = 17/36$ or is shut off after T.)

Observationally, the early-time average decay index is $\alpha_{F,av} \approx 1.52 \pm 0.02$ if we fit only a single component with no bump, though because of the bump feature the exact decay rate clearly varies; given this complexity, a rigorous statistical comparison with the simplistic predictions is not possible. However, we can unambiguously rule out all cases except for the slow-cooling case in which $\nu_m < \nu < \nu_c$, where, if we use the value of p from the late-time X-ray spectrum, we predict $\alpha = 1.74 \pm 0.11$, which is generally consistent with our observations.

Our early-time multi-color photometry provides us with a rare opportunity to test the spectral predictions of reverse-shock models, in addition to the time-domain predictions. The synchrotron spectrum of a reverse shock is predicted to be identical in its general form to that from a forward shock, with the exception that after the reverse shock crosses the shell (at time T), there is no emission from frequencies above some cutoff frequency $\nu_{\rm cut}$. The spectral power-law indices are the same (for the same value of p), although the break frequencies ν_m and ν_c are generally not.

For the reverse shock, the only regime consistent with the data is $\nu_m < \nu < \nu_c$. The prediction for the spectral index in this region (from Sari et al. 1998) is $\nu^{-(p-1)/2}$. Again assuming $p = 2.00 \pm 0.14$ from the late-time X-ray observations, we predict that the spectral index should be $\beta = 0.50 \pm 0.07$. This is significantly less than the observed value (after correcting for Galactic extinction) of $\beta_F \approx 1.25$. This very large discrepancy may be due to host-frame extinction. However, as we will discuss in §4.4.4, the lack of observable curvature

in the SEDs of either the fast-decaying or the slow-decaying components impose strong constraints on the amount and nature of any extinction.

4.4.3 Transition to Forward Shock

The fast-decaying early-time optical component is subsumed by the shallower late-time component at around 10^3 s. The natural inclination is to assume that the reverse-shock emission has been replaced by that from a forward shock.

As already discussed, the different decay rates of the X-ray and optical light curves rule out the possibility that they are in the same synchrotron regime, so we expect the optical band to be below a spectral break. For adiabatic evolution, if the optical band is below the cooling break, we expect (assuming $p = 2.0$) an optical decay index of $\alpha_{opt} = 0.75$. This is consistent with the data, both in the empirical model where we assume a power law that fades throughout the observations (for which we calculate $\alpha_S = 0.75 \pm 0.06$) and the more realistic fit in which the slow component rises, experiences a (chromatic) break, and then fades ($\chi^2/\mathrm{dof} = 228.0/197$ for this model, slightly better than the best model assuming an unbroken slow decay.) For radiative evolution and the case that the optical band is below the minimum-energy break (but above the cooling break and the critical frequency), $\alpha_{opt} = 4/7$, which is only consistent within 2.5σ.

If the slower decay component is due to an adiabatic forward shock and the optical band is in the range $\nu_m < \nu_{opt} < \nu_c$ then the predicted intrinsic optical spectrum is $F_\nu \propto \nu^{-(p-1)/2}$, which for $p = 2.0 \pm 0.14$ suggests $\beta = 0.5 \pm 0.07$. If the forward shock is radiative, the prediction is the same but with no statistical uncertainty ($\beta = 1/2$). The observed spectral index of the possible forward-shock component is somewhat redder than this value, $\beta_S = 0.92 \pm 0.08$ — or, using our physical model, the post-peak $\beta_S = 1.11 \pm 0.09$. Again, one may appeal to host-galaxy extinction to make up the difference.

We will examine this possibility in greater detail in the next section. For now, however, we can sidestep the host extinction question completely if we look only at the *change* in spectral index between the early (reverse shock) and late (forward shock) components, as long as we can assume that the extinction is constant with time.

As discussed earlier, the only reverse-shock model consistent with the observed early-time light curve requires that either $\nu_m < \nu_{opt} < \nu_c$ (adiabatic) or $\nu_c < \nu_{opt} < \nu_m$ (radiative), both of which predict the same value for the spectral index for $p \approx 2$. We reach the same conclusion with the later-time data, meaning that the reverse and forward shocks are in the same synchrotron regime and should therefore have the same color as long as p is the same.

However, we do in fact observe a color change between the two components, of $\Delta\beta = -0.38 \pm 0.08$ in our model. There are several possible interpretations for this.

Most likely, the forward shock is not strictly in the $\nu_m < \nu_{opt} < \nu_c$ regime at the transition time, but is in fact still in the process of breaking from its very blue rising portion (that is, $\nu_m \approx \nu_{opt} < \nu_c$), and does not attain its "true" color until significantly later, when it will shift back to the reverse-shock color. Our data are quite consistent with this possibility; the physically motivated fit which models the reverse shock as a rising and falling with the

appropriate change in spectral index over its peak is equally sound as the fit assuming no rising portion; the ultimate change in spectral index in this model is $\Delta\beta_{F-S,b} = -0.12 \pm 0.08$, consistent with no change within 2σ. If this is the case, we predict that the afterglow color will shift back towards the red after the end of our observations.

Alternatively, one of our assumptions could be in error. It is possible that the value of p is different between the forward and reverse shocks; in this case a difference of $p_{rev} - p_{fwd} = 0.7 \pm 0.1$ would be required. Also, the amount of extinction could in fact be variable due to dust destruction by the GRB, though the general constancy of the early-time spectral index in Figure 4.9 before the transition time seems to speak against this possibility. Finally, if the optical or X-ray emission is strongly affected by another process such as Compton scattering, this could also produce spectral variability.

Of course, a combination of two or more of these factors is also possible.

4.4.4 Broadband Spectral Fits and Constraints on Extinction

The light curve fits performed in our analysis naturally give rise to spectral fits. The filter-dependent flux parameters $F_{\nu,j}$ give the relative fluxes in each filter for both components of the light curve, and can be used to calculate the observed SED and look for signs of host extinction. We have already referred to the best-fit spectral indices β for the fast and slow components, all of which were fit assuming no host extinction. Here we will use different extinction models to constrain the properties of any host-frame dust in greater detail.

Large amounts of extinction are implied by the X-ray to optical SED. In Figure 4.10 we plot the SED of the "slow" component as computed at $t = 2000$ s, shortly before the end of our multi-filter observations and after the beginning of the XRT observations.[14] A model for Galactic extinction of $E(B-V) = 0.182$ mag has been subtracted. The predicted X-ray to optical slope, and the predicted slope in the optical–IR frequency window, is $\beta = (p-1)/2 = 0.5$ in the adiabatic case and also $\beta = 1/2 = 0.5$ in the radiative case, so the prediction is the same. In fact, however, we measure a nearly flat X-ray to optical slope of $\beta_{OX} = 0.23$ (using the R-band and 1 keV fluxes), and an IR-optical slope of $\beta_{opt} \approx 0.95$. This value of β_{OX} is enough to unambiguously label this event as a "dark burst" by the criterion of Jakobsson et al. (2004a) (that is, any burst with β_{OX} less than the $p = 2$ synchrotron limit of 0.5) at this time, in spite of this being in fact one of the optically brightest bursts ever observed by *Swift*! This surprising fact is a consequence of a combination of the unusual late-time X-ray brightness and the rapid early fading of the optical afterglow. (We could, perhaps, incorporate both this burst's early-time brightness and its later-time faintness with the

[14] Our physical model of the light curve in terms of a reverse-to-forward shock transition indicates that the intrinsic SED of the slow component may be variable due to the passage of a shallow minimum-energy break somewhat before this time, and so changes slightly after the end of our optical observations. However, to keep the discussion on firm observational footing without extrapolating our measurements beyond the range of our available data or favoring any particular model, we choose the simple empirical model (with no rising component) for discussion of extinction. These results are not significantly affected by choosing the physical model instead.

moniker "grey burst," since "dark burst" seems inappropriate to the burst's entire evolution.)

The most commonly invoked interpretation for these dark bursts, and for X-ray/optical flux mismatches generally (e.g., Schady et al. 2007), is that the optical flux has been suppressed by dust extinction (or, for very high-redshift bursts, hydrogen absorption). A large amount of extinction would be necessary to apply this explanation here. To calculate a minimum amount of extinction, we assume the case that the cooling break (or for radiative evolution, the minimum-energy break) is just redward of the X-ray band, and take the minimum value of the intrinsic $\beta_{OX} = 0.43$ permitted by our uncertainty in β_X (this would imply $p < 2$, which is within our errors). For this case, the optical flux is overpredicted by more than a factor of 5.3 in the observed V band, requiring > 1.8 mag of host extinction in this band, or $A_V = 1$ mag in the host-galaxy frame. This is an absolute minimum: requiring an intrinsic $\beta_{OX} = 0.5$ ($p = 2$ or a radiative regime) increases this to 2.2 mag in the observed V, and placing the break at a more general point between the X-ray and optical bands increases it even further.

Assuming a Milky Way metallicity and extinction law, our measurement of the host-frame hydrogen column of $N_{\rm H,host} = (1.1 \pm 0.3) \times 10^{22}$ cm^{-2} would correspond to a large host-frame extinction column of $A_V \approx 6$ mag, even greater than that indicated by the X-ray/optical discrepancy. However, this assumption is unlikely to be appropriate. For a more realistic choice of the gas-to-dust ratio in the Small Magellanic Cloud (SMC; about 8.4 times the Galactic value; Gordon et al. 2003) or a starburst galaxy (~ 10 times Galactic; Lisenfeld et al. 2002), we expect a proportional reduction in A_V, predicting $A_V \approx 0.6$–0.9 mag, roughly consistent with the minimum necessary suppression.

The wide frequency coverage, photometric accuracy, and contemporaneous nature of our optical data gives us the opportunity to firmly constrain the extinction properties of this event. As such, we fit a power law plus an extinction component to our optical–IR SED, allowing the intrinsic unabsorbed spectral index β to vary as a free parameter. We try numerous extinction profiles, including the Fitzpatrick & Massa ("FM") model (Fitzpatrick & Massa 1990), which has parameterizations for a wide range of galaxy types, of which we fit both a Milky Way extinction profile and a SMC profile using the parameters measured by Gordon et al. (2003). We also fit the Pei extinction profile (Pei 1992) for the SMC, and the Calzetti extinction profile (Calzetti et al. 2000) measured from observations of starburst galaxies. We use the flux parameters from our model of the slow component, and assume a systematic error of 2% in the IR filters, 3% in the optical filters, and 5% in U-band. The different extinction curves are plotted in Figure 4.11.

In every case, the best-fit model is that of no host-frame extinction ($A_V = 0$ mag; our fits restrict A_V to be non-negative) or a very low value consistent with 0, indicating an intrinsic early-time spectral index equal to the observed spectral index of $\beta = 0.93 \pm 0.02$. This extinction-free fit is good, with $\chi^2/{\rm dof} = 1.91/6$, and is plotted in Figure 4.12.

The limit on A_V depends largely on the model adopted: greyer dust-extinction models (and larger values of R_V, indicating larger grain sizes, within those models) permit more A_V. However, all "normal" dust-model fits strictly limit the observed extinction to $A < 0.2$ mag in the observed V band. The relatively grey Calzetti model allows more extinction, but even

for this case, the amount of observed extinction can only be achieved for extremely large ratios of the total-to-selective extinction ($R_V \gtrsim 8$) and the fit is degraded, $\chi^2/\mathrm{dof} = 4.70/6$ (Figure 4.12), though still acceptable. The χ^2 confidence contours for a few different fit models are plotted in Figure 4.13.

This is, furthermore, for the contrived "optimistic" case where the X-rays are just above the break; for the more general case where the break is at lower energy, the required extinction is greatly increased. There is evidence to believe that this break is relatively near the optical at this time — the observations in the GCN Circulars suggest a break around $t \approx 3 \times 10^4$ s, and despite some discrepancies all observations (including our single-epoch late-time PAIRITEL observations) agree that the optical flux by the second night has fallen well below the predicted value from the $\alpha < 1$ decay we measure at intermediate times. If we assume that this break in the light curve were due to a spectral break passing through the R band, at $t = 2000$ s the break would be at $\sim$40 eV, predicting an optical flux 4 times (1.5 mag) higher even than the above "minimum" prediction would suggest, or 3.3 mag total ($A_V \approx 1.8$ in the host frame.)

4.5 Implications and Alternative Models

The standard assumptions of the fireball synchrotron model fare poorly when confronted with the available early-time data on GRB 061126. The most striking failure is the large discrepancy between optical and X-ray fluxes, though the unexplained bump feature in the early optical light curve and the lack of agreement between theoretical predictions for α and β in X-rays are also unsettling.

It is beyond the scope of this paper to fully resolve this quandary. Nevertheless, we present some possible solutions and briefly analyze their relative merits and failings in light of our available observations.

4.5.1 Grey Dust?

We have demonstrated that no standard extinction law can fully explain the discrepancy between the X-ray and optical fluxes at late times. Sufficiently high values of R_V (8–12) — corresponding to relatively grey dust laws, and physically to large grain sizes — do provide a respectable fit, but since even in the starburst galaxies studied by Calzetti, and in the molecular clouds in the Milky Way, R_V is generally in the range of only 2–5, it is worth asking if this is physically reasonable.

There is ample reason to suspect that GRB host galaxies, and the GRB progenitor sites within those galaxies, will have dust properties that do not resemble the local universe. GRBs in general (and GRB 061126 is no exception) occur at high redshift and in very low-mass, high star-formation galaxies, and dust properties may evolve with time and almost certainly do correlate with host-galaxy type. Furthermore, if GRB progenitors are very massive stars, they should occur near their birth sites (probably within dense clouds); in

the Milky Way, such environments are known to be correlated with anomalous extinction curves and high values of R_V (Cardelli et al. 1989). Finally, the GRB itself is expected to destroy dust within several parsecs of its progenitor, which can preferentially affect certain types of dust — for example, destroy smaller grains while leaving the larger grains relatively untouched (Waxman & Draine 2000; Perna et al. 2003).

Furthermore, this is not the first GRB in which the observed optical flux has been deficient relative to the X-ray flux, or relative to a late-time synchrotron prediction using the optical decay rate. In many cases a relatively normal extinction law [except, in nearly all cases, for the lack of the characteristic 2175 Å bump feature seen in the Milky Way and the Large Magellanic Cloud (LMC)] has successfully explained the suppression (e.g., Schady et al. 2007), although we caution that without broadband photometry (including IR measurements) it can be difficult to accurately distinguish different models, and extinction laws other than the standard Milky Way, LMC, and SMC laws are often not tested. Even so, in many other cases (e.g., Stratta et al. 2005; Chen et al. 2006) the low-redshift dust models clearly do not work — in these cases, the optical data are consistent with an unabsorbed power-law, but one that disagrees with an extrapolation from the X-ray band. Most of these authors favor a grey-dust interpretation of one manner or another. Unusual reddening laws have also been reported from observations of supernovae (Wang et al. 2006c; Elias-Rosa et al. 2006) and high-redshift quasars (Maiolino et al. 2004).

Unusual dust probably remains the simplest explanation for the flux discrepancy. Nevertheless, at least two factors give us pause when considering this explanation. First, our fits to the optical data alone simply do not require it. There is no physically compelling reason that we can think of why dust should exhibit an extinction law that simply transforms one power law to another, requiring $A_\lambda \propto (0.5 \pm 0.1)\log(\nu/\nu_o) + C$ or something mimicking it within our observational uncertainties. From the optical data alone, it is more natural to assume that the excellent power-law SED is intrinsic, and look elsewhere to explain the disagreement with the X-ray data.

Second, the observed dust-to-gas ratio, while seeming to favor large amounts of extinction, actually greatly overpredicts the extinction if we assume a physical interpretation of the relatively grey extinction law in terms of dust that is mostly bound up in large grains. The grain size distributions presented by Weingartner & Draine (2001), for example, are already biased (as weighted by the grain volume) toward the largest grains, so for the same dust-to-gas ratio, skewing the grain distribution further toward large grains will significantly decrease the opacity at long wavelengths but also decrease it at short wavelengths. When the anticipated low dust-to-gas ratio of the GRB host galaxy is considered, the observed X-ray N_H column is already only just enough to explain the observed extinction; suppressing it further by binding the available dust into very large grains becomes problematic.

Nevertheless, without a detailed physical modeling of the potential dust in the GRB environment (including the possible effects of time-variable opacity due to dust destruction), we can neither firmly confirm nor rule out the presence of grey dust in this burst. Such an examination is beyond the scope of our present analysis; however, we encourage dust modelers to make use of our observations of the minimum extinction required (Figure 4.11)

to help determine the viability of grey-dust models for this event. Our early-time infrared and optical photometry should strongly constrain any models involving dust destruction.

4.5.2 Synchrotron Self-Compton as the Origin of the X-ray Afterglow

We now turn to interpretations in which the optical SED is treated as intrinsic, and instead look to processes primarily affecting the X-rays to explain the anomalous behavior. The discrepancy between the X-ray α and β independently argues that the X-ray emission for this burst may not obey the normal assumptions about GRB afterglows.

The SED in Figure 4.10, if intrinsic, has two peaks, reminiscent of the spectrum created by inverse-Compton scattering from a synchrotron source. Furthermore, it is interesting that the observed optical spectral index is consistent with the X-ray spectral index: perhaps the X-ray afterglow is dominated by inverse synchrotron self-Compton flux boosted from the optical band. Compton scattering has not commonly been invoked in interpreting GRB afterglow observations, but it has been used to explain X-ray/optical flux discrepancies similar to this one in at least two previously published cases: GRB 000926 (Harrison et al. 2001) and GRB 030227 (Castro-Tirado et al. 2003).

However, we consider SSC unlikely to be the solution to our discrepancy for several reasons.

1. Even admitting for the effect of Compton scattering on the light curve, the optical data do not obey the predictions of any model without an extinction correction. The optical and X-ray have very similar spectral slopes ($\beta_{opt} = 0.93 \pm 0.02$, $\beta_X = 1.00 \pm 0.07$), suggesting that the X-ray photons are in fact upscattered optical photons, and that (nongray) extinction is minimal, so this value of β must be treated as intrinsic. This restricts us to two synchrotron regimes: $\nu_c < \nu_{opt}$ or $\nu_m < \nu_{opt} < \nu_c$. The former case would imply $p = 2$ and requires a light curve that falls off as $\alpha = (3p-2)/4 + (p-2)/(2(4-p)) = 1.0$, which is ruled out by the observations. (The optical light curve decays quite slowly: $\alpha = 0.75 \pm 0.06$ during our observations, though it steepens later.) The latter case would imply $p = 3$, and predict $\alpha = 3(p-1)/4 = 1.5$, which is also ruled out.

2. Inverse-Compton scattering does not produce a broken power-law SED at high energies; Sari & Esin (2001) have shown that in reality the breaks are significantly softened, in disagreement with the X-ray observations which indicate a simple power-law spectral slope.

3. Finally, it is difficult to construct the Compton-scattered portion of the broadband SED without "contaminating" the optical bands with Compton-scattered flux from lower energies in a way that would noticeably bias the blue end of our photometric SED. (However, this effect may be alleviated somewhat if the Compton-boosted

self-absorption frequency $\nu_{a,IC}$ is not much less than the Compton-boosted cooling frequency $\nu_{c,IC}$, since this would make the low-energy side of the Compton-scattered spectrum much steeper than what is otherwise a very slowly falling ($\beta = -1/3$) low-energy tail.)

4.5.3 Physically Separate X-Ray and Optical Emission Regions

Finally, we consider the possibility that the emission regions for the optical and X-ray emission are spatially distinct. There may be two forward shocks (each peaking in a different energy range) resulting from a two-component jet (e.g., Berger et al. 2003b; Peng et al. 2005), or the entire optical afterglow may be due to a reverse shock with an erratic profile extending out to late times (as in Uhm & Beloborodov 2007), while the X-ray light curve may be due to a more well-behaved radiative forward shock.

The notion of finding a way to physically separate the optical and X-ray emission has recently found support in other contexts, in particular to try to resolve the apparent lack of correlation between *Swift* X-ray and optical breaks (Oates et al. 2007) and to explain *Swift* X-ray breaks generally (Panaitescu 2007). Unfortunately, the relatively short period of overlap between the optical and X-ray data for GRB 061126 prevents us from being able to constrain this possibility in any detail for this event. However, we will note that any two-origin explanation shares the difficulty just discussed in the context of whether inverse Compton may explain the X-ray flux excess — that is, how to avoid contaminating the blue end of the observed optical spectrum with emission from the low-energy tail of a synchrotron-like spectrum peaking at X-ray wavelengths.

4.6 Conclusions

We have presented multi-wavelength, early-time observations of the recent, bright GRB 061126. In our favored model, the early optical data appear to be well explained by a reverse shock. The reverse-shock emission fades rapidly and is dominated by emission from the forward shock from $\sim$500 s onward. A small color change is observed at this transition, likely due to the peak of the forward-shock synchrotron spectrum passing through the optical band at roughly the same time.

However, only with significant contrivance can this model also explain the X-ray observations from the *Swift* XRT, which are much brighter than an extrapolation of the optical flux would predict. The optical flux may be suppressed by host-galaxy extinction, but this would require a remarkably grey dust law, capable of generating 1.5–3 mag of optical extinction without causing the observed U–K_s SED to deviate from a power law. Alternatively, the X-ray and optical emission may be due to two physically or spatially distinct emission processes, but our observations strongly restrict the positions and sharpness of any spectral breaks and cast doubt on the viability of this model.

In either case, we advise caution in interpreting future early afterglows in the absence of

data sets that are not well sampled both spectrally and temporally. Many previous studies, by necessity, have been restricted in either their temporal properties (sampling), frequency coverage (available filters and wavebands), or both. Under the standard fireball model these assumptions seemed valid, as only a single parameter set would fit them. Here we show that when a more complete picture is available, no parameter set seems to fit the data, unless we invoke large quantities of grey dust or separate origins for the X-ray and optical afterglows.

The very bright X-ray afterglow and late-time optical faintness are enough to qualify this event under some definitions as a dark gamma-ray burst in spite of the extraordinary bright early afterglow. Had the event been intrinsically fainter or at higher redshift, or had the optical follow-up observations been delayed significantly, the optical afterglow may have been missed entirely. Therefore, it is possible that events like GRB 061126 may represent a significant fraction of dark bursts.

The most common interpretation of dark bursts is that they are due to absorption of the optical flux by host-galaxy dust or by neutral hydrogen at very high redshift. Our study presents tentative evidence for a third possibility, which is that the optical faintness may be intrinsic to the GRB itself, due to enhancement of the X-ray flux or intrinsic suppression of optical flux, or both. If the optical faintness is due to dust, our results suggest that near-IR and optical observations alone may not be as constraining as once hoped, since any extinction must not cause significant deviations from a power law, even across a decade in frequency from the near-IR to the UV. However, the combination of near-IR, optical, and X-ray observations remains a potent tool for understanding GRBs, and we anticipate that additional multi-wavelength observations in the coming years will continue to shed light on "anomalous" events like GRB 061126.

Acknowledgments

RAPTOR is primarily supported by Laboratory Directed Research and Development funding at Los Alamos National Laboratory. KAIT was made possible by donations from Sun Microsystems, Inc., the Hewlett-Packard Company, AutoScope Corporation, Lick Observatory, the National Science Foundation, the University of California, the Sylvia & Jim Katzman Foundation, and the TABASGO Foundation. We are grateful to Erin McMahon for her critique of the synchrotron model presented in our first version of this manuscript, and to the anonymous referee for a very thorough and helpful commentary.

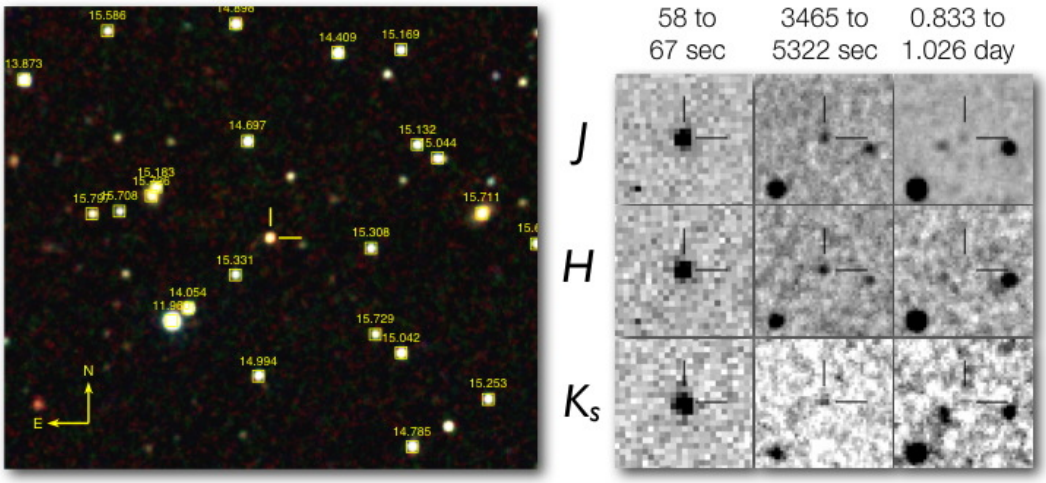

Figure 4.1 False-color PAIRITEL finding chart ($260'' \times 260''$) of the afterglow of GRB 061226 (left). The 2MASS catalog stars used for the photometric calibration are denoted with boxes at the catalog positions and labeled with J-band (2MASS) magnitudes. At right, IR images show the fading of the afterglow from 58 s to 1 d after the GRB; the images are progressively deeper at later epochs.

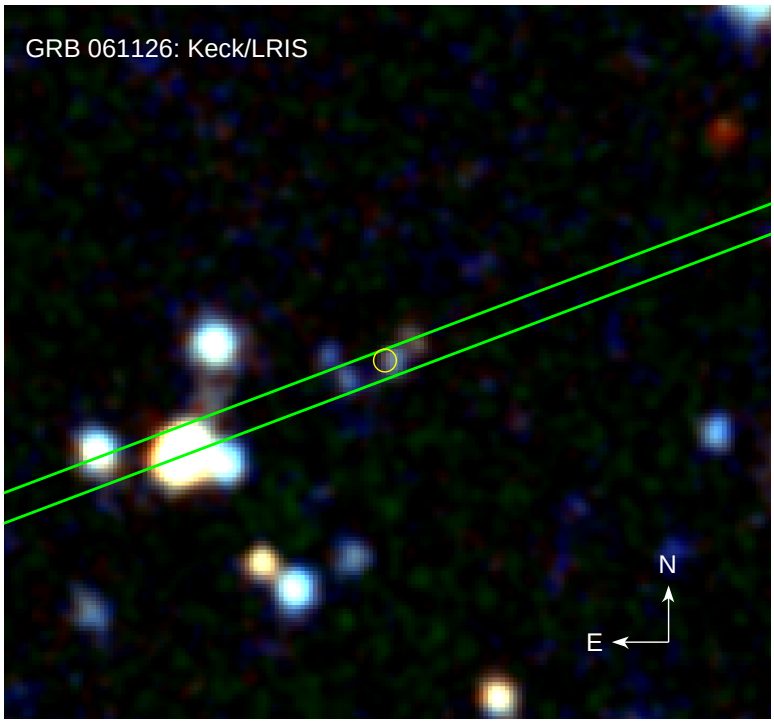

Figure 4.2 Keck I (LRIS) late-time finding chart. The image is 25″ on a side and represents the stacked g' and R bands. The placement of the 1″-wide slit is shown in green. The white circle is the 2σ position of the afterglow as measured from PAIRITEL images. The probable host galaxy is visible at this location. The object is blue and extended, appearing to have a complicated morphology. Further down the slit 21.1″ to the southeast is a relatively bright galaxy with $z = 0.6225 \pm 0.0004$, based on emission from [O III] $\lambda\lambda$4960.2, 5008.2, $H\beta$, and [O II] $\lambda\lambda$3727.11, 3729.86. (This second galaxy is not associated with the GRB.)

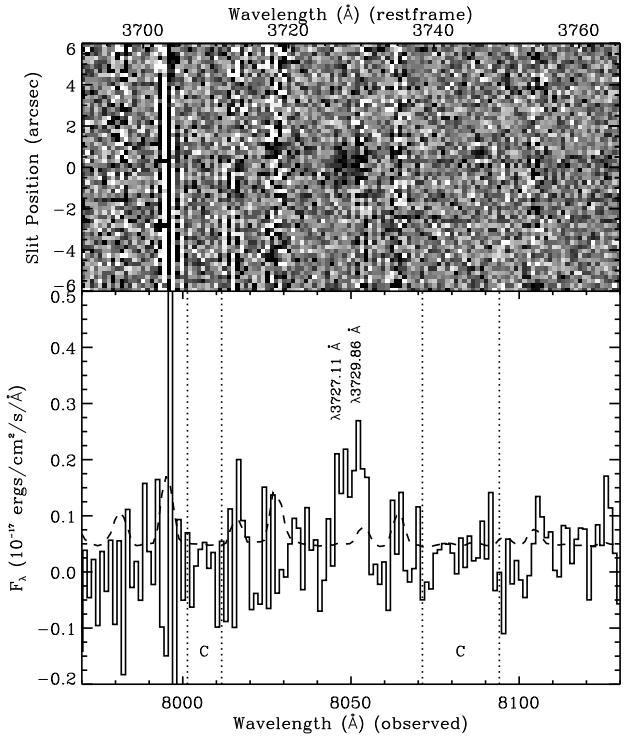

Figure 4.3 Spectrum of the host galaxy of GRB 061126 in the vicinity of the sole emission line, interpreted as the [O II] doublet. The data were taken with LRIS on Keck I using the $1''$ slit and the 600/7500 grism. Top: Background subtracted, two-dimensional spectrogram showing the weighted mean of two 1200 s exposures. Pixels contaminated by cosmic rays in one exposure are excluded from the mean. Bottom: One-dimensional, coadded spectrum. The profile fit from a bright, nearby source was used to extract a spectrum at the known location of the GRB host galaxy. The dashed line represents the 1σ uncertainty at each pixel. The width of the emission feature is comparable to the spacing of the [O II] doublet at a redshift of 1.16. The doublet spacing is approximately equal to the instrument's resolution element at 8050 Å, so we expect the doublet to be barely resolved. We measure the galaxy's continuum by computing the median flux in two regions free of night-sky lines (regions "C"). Using this continuum value, and measuring the signal between 8042.0 and 8056.0 Å, we find that the total flux in this emission feature is $(1.6 \pm 0.2) \times 10^{-17}$ erg s^{-1} cm^{-2}.

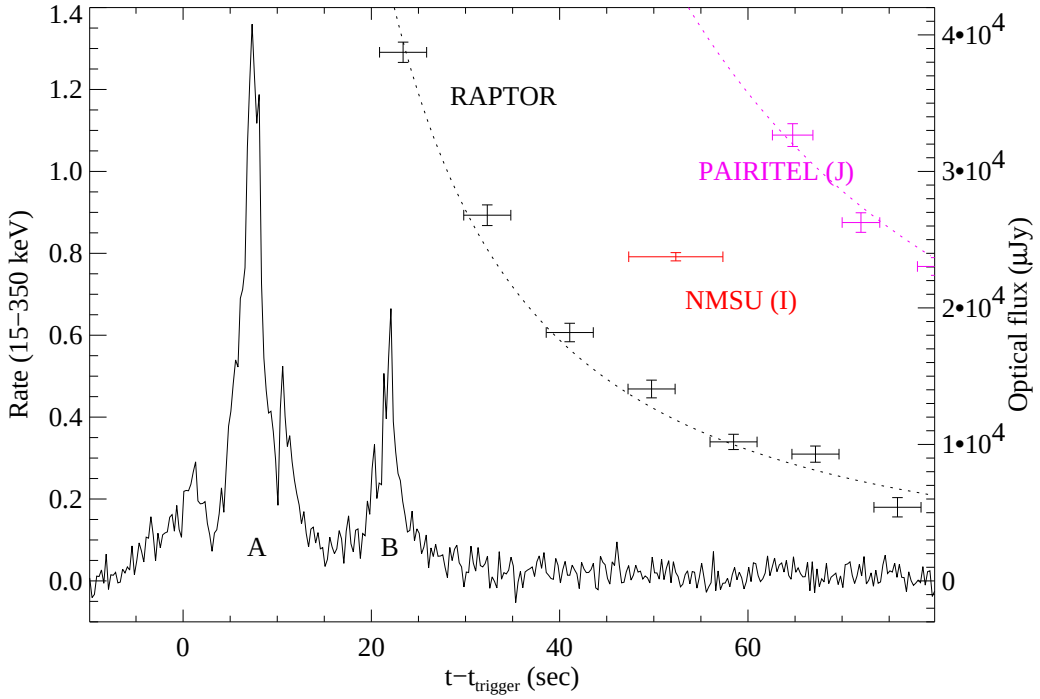

Figure 4.4 BAT 15–350 keV light curve of GRB 061126, showing the profile of the main burst (dominated by two primary pulses, labeled "A" and "B") as well as the rapid response from the robotic telescopes RAPTOR, the NMSU 1.0 m, and PAIRITEL. At this early time the light curves are well fit by a simple power law ($F_\nu \propto t^{-1.5}$) with t_0 simply set to the trigger time. There is no evidence for a rising component or any correlation of the optical emission with the prompt emission.

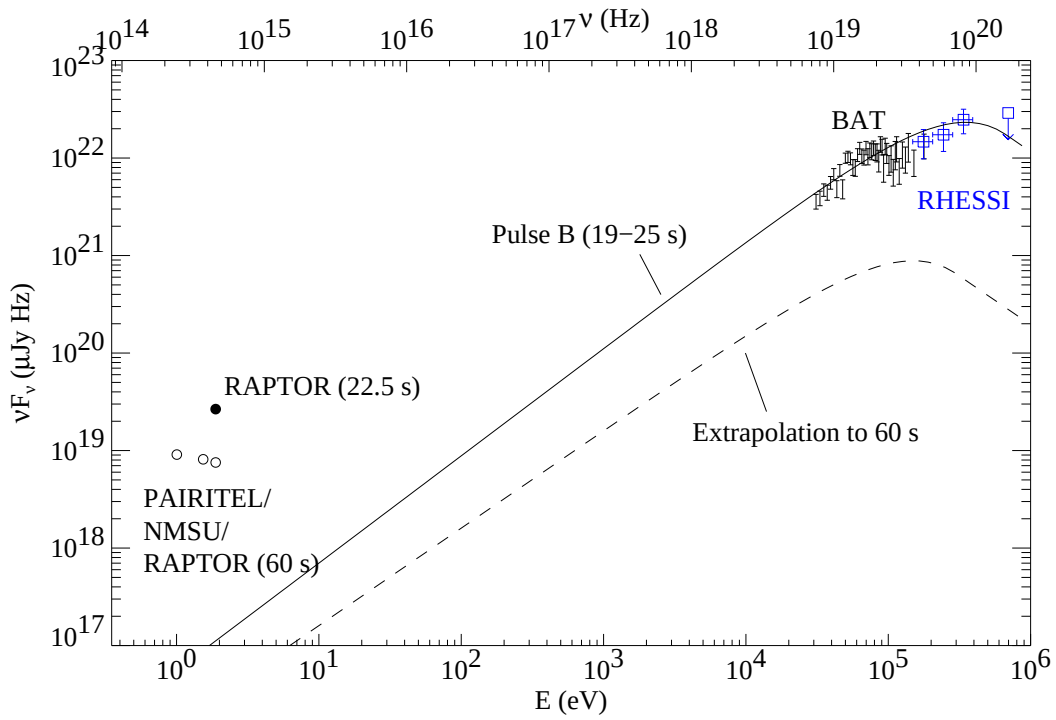

Figure 4.5 High-energy SED during the second main pulse of the prompt emission ("Pulse B"), with the contemporaneous RAPTOR measurement superimposed. An extrapolation of our best-fit Band (Band et al. 1993) model (Table 4.1) into the optical is shown to underpredict the optical flux by several orders of magnitude, suggesting that even at this very early time the optical afterglow is already present at 20 s post-trigger, dominating the early-time flux at long wavelengths. A temporal extrapolation of the BAT light curve to 60 s similarly underpredicts our multi-color data at that time.

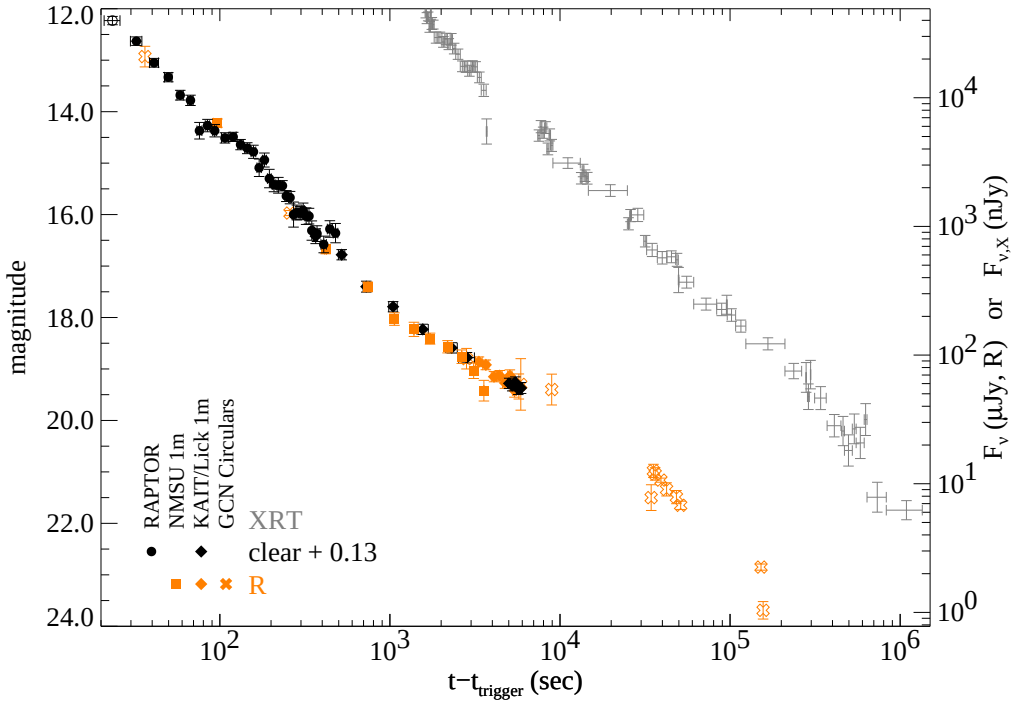

Figure 4.6 *R*-band and X-ray light curves of the afterglow of GRB 061126 showing the basic features of the early-to-late optical and X-ray afterglow light curves. Unfiltered data are also included, offset by 0.13 mag to match the *R*-band calibration. Optical data are shown as filled (used in modeling) or unfilled (not used) symbols; X-ray data are shown as error bars with no central symbol. There is a rapid decay with a bump at early times, transitioning to a significantly slower decay that probably breaks at late times. Due to a delayed slew the X-ray afterglow was not observed until 1600 s, but from then until it faded below the detection threshold at ~ 9 d it decays as an unbroken power law. The 1 keV normalized flux is plotted.

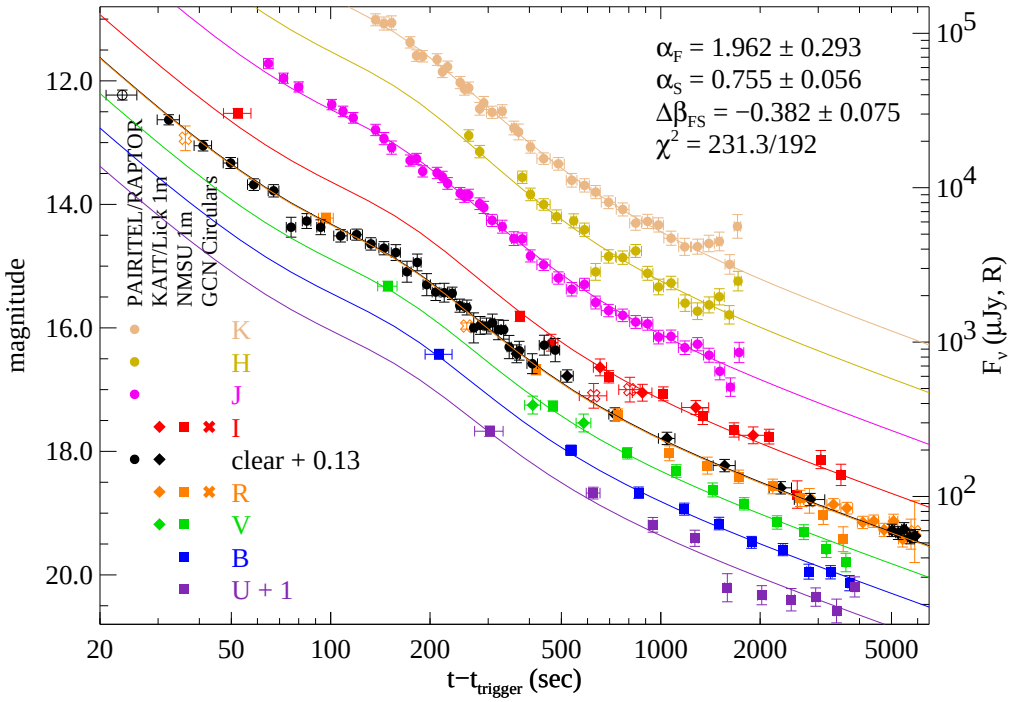

Figure 4.7 Broadband light curves of our early-time, multi-color photometry of the afterglow. The light curves are fitted with a three-component broken power-law model, assuming that the third component (with the slowest decay) has a spectral index that differs from that of the early component by an amount $\Delta\beta$.

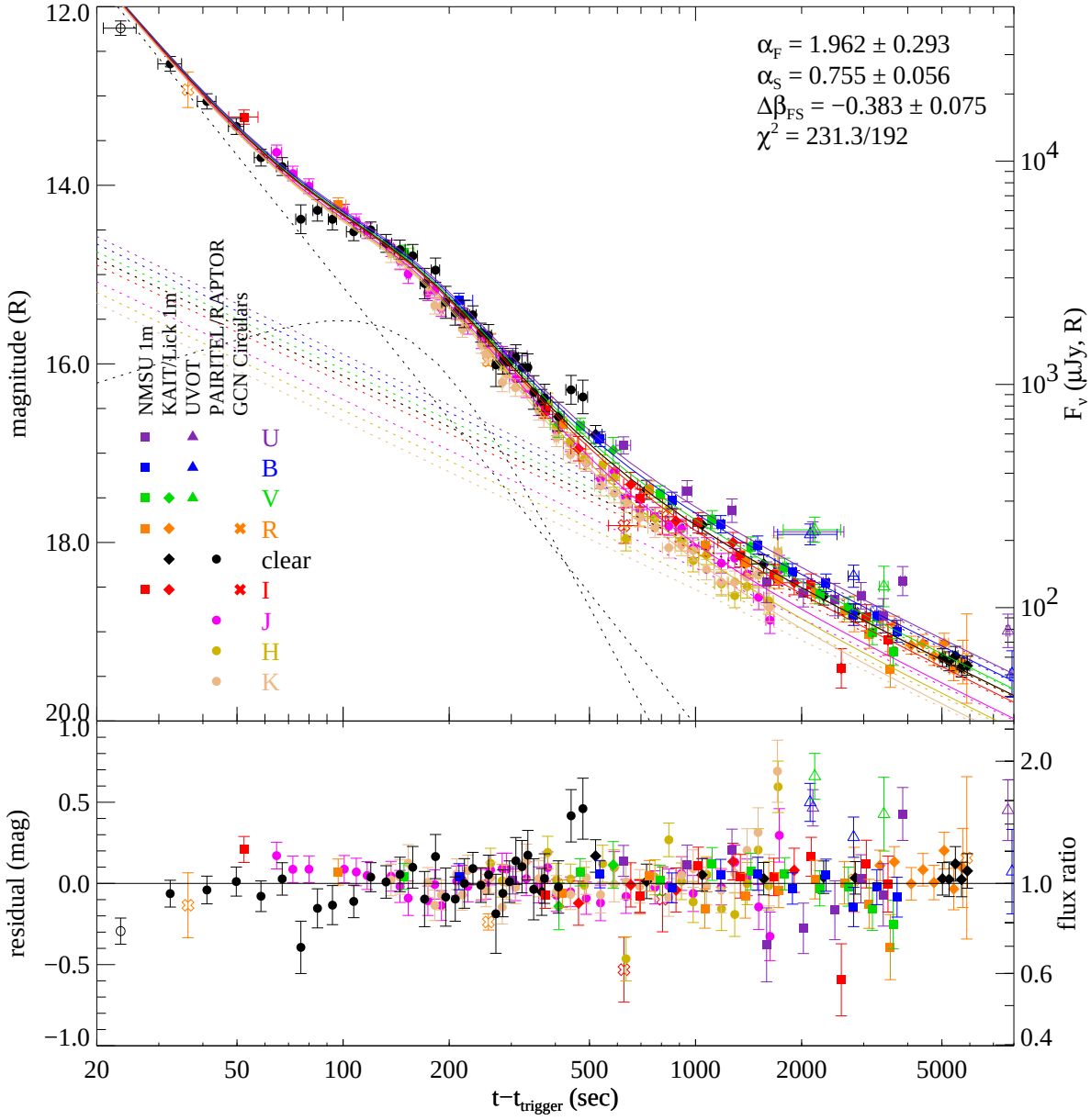

Figure 4.8 Broadband light curves of the afterglow with the curves aligned based on the early-time flux, emphasizing the red-to-blue color change. The model is the same as in Figure 4.7.

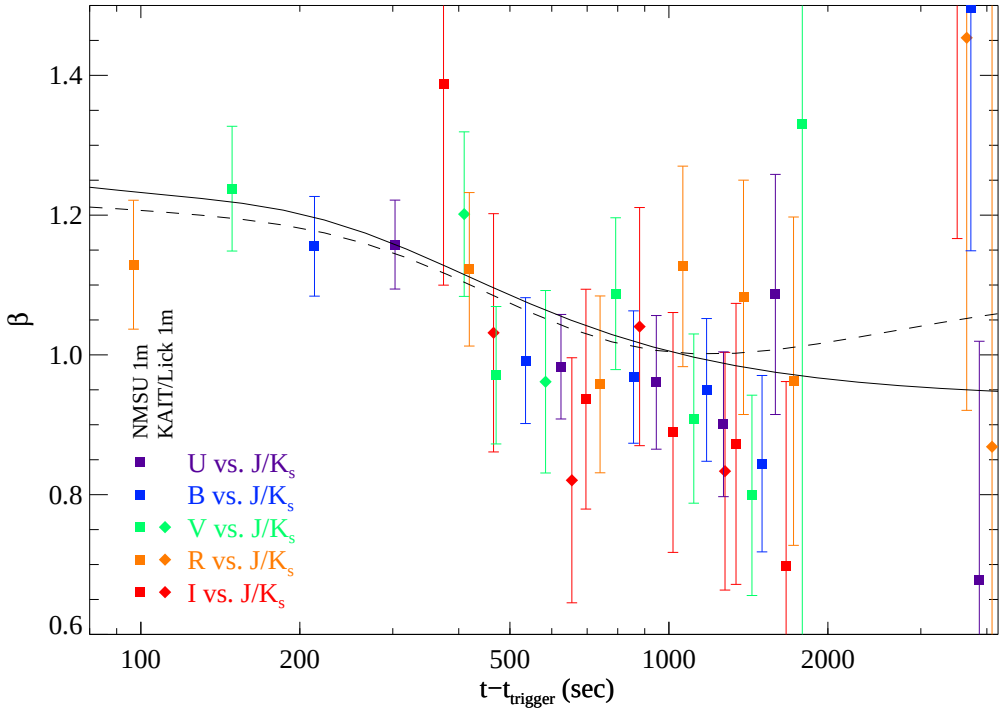

Figure 4.9 Evidence for color change across the transition from the rapidly decaying component to the slowly decaying component. We fit a power law to simultaneous J/K_s PAIRITEL exposures and optical exposures (in U, B, V, R, or I; color-coded appropriately) from the NMSU 1.0 m telescope. The solid curves are not direct fits to these data, but represent the spectral index that would be observed at each time if fit to $K_s - U$ photometry based on two of our models. The solid line is for a model where the late-time component of the afterglow is modeled as a simple power law; the dashed line represents a model of a forward shock undergoing a minimum-energy break at approximately the transition time.

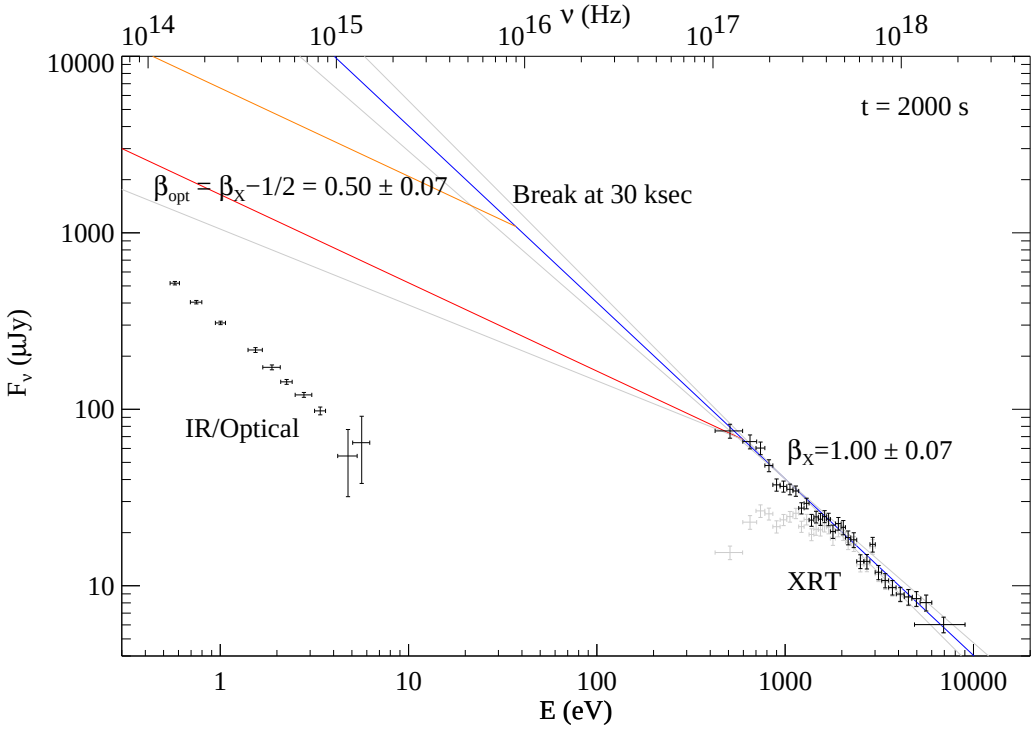

Figure 4.10 Broadband SED from optical to X-ray at $t = 2000$ s after the trigger. The steep X-ray decay and apparent shallow optical decay places the cooling break between the X-ray and optical bands. Even if we make the maximally generous assumption and place the cooling break at 1 keV, the optical flux is seen to be overpredicted (red line) by a factor of about 5. If we are less generous with our assumption, and choose to interpret the late-time break in the optical afterglow seen in the GCN Circulars as the effect of the spectral break passing through the R band at that time, the discrepancy is even larger. The optical data are a good fit to a power law, and it is difficult to appeal to extinction to make up the difference. The black X-ray points are corrected for Galactic absorption plus a best-fit model of the host hydrogen column; grey points are corrected for Galactic absorption only (no host-galaxy absorption). Optical data are corrected for Galactic extinction only.

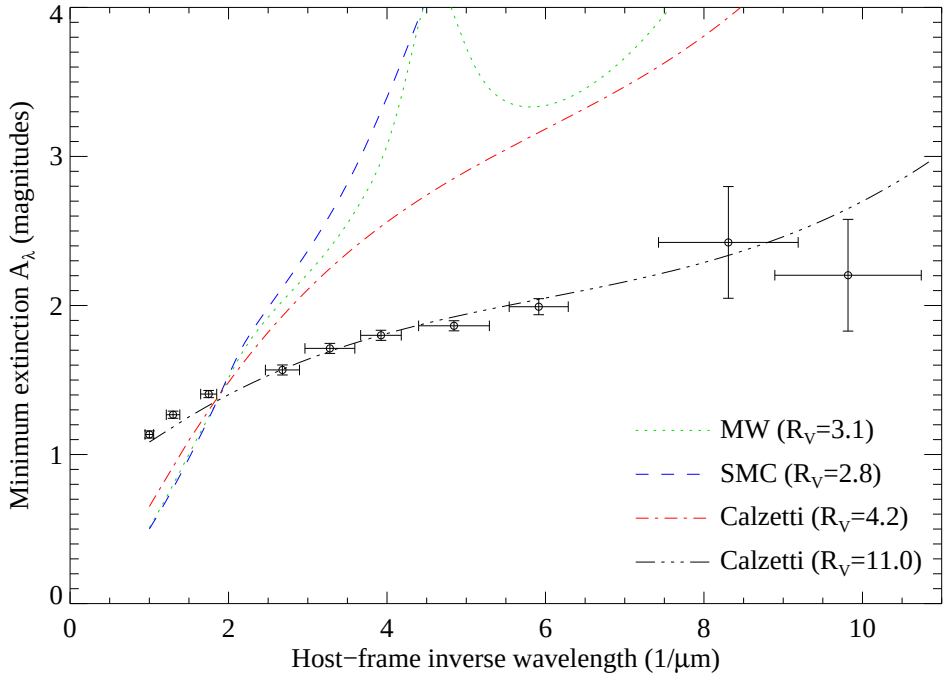

Figure 4.11 Plot of the minimum amount of extinction necessary in each band to resolve the discrepancy with the X-ray flux measurements (assuming $p = 2$), compared to several representative extinction curves. A_V is fixed at 1.35 mag for all models. The Milky Way and SMC models use the formulation of Fitzpatrick & Massa (1990); the Calzetti model is a model for extinction in starbursting galaxies from Calzetti et al. (2000).

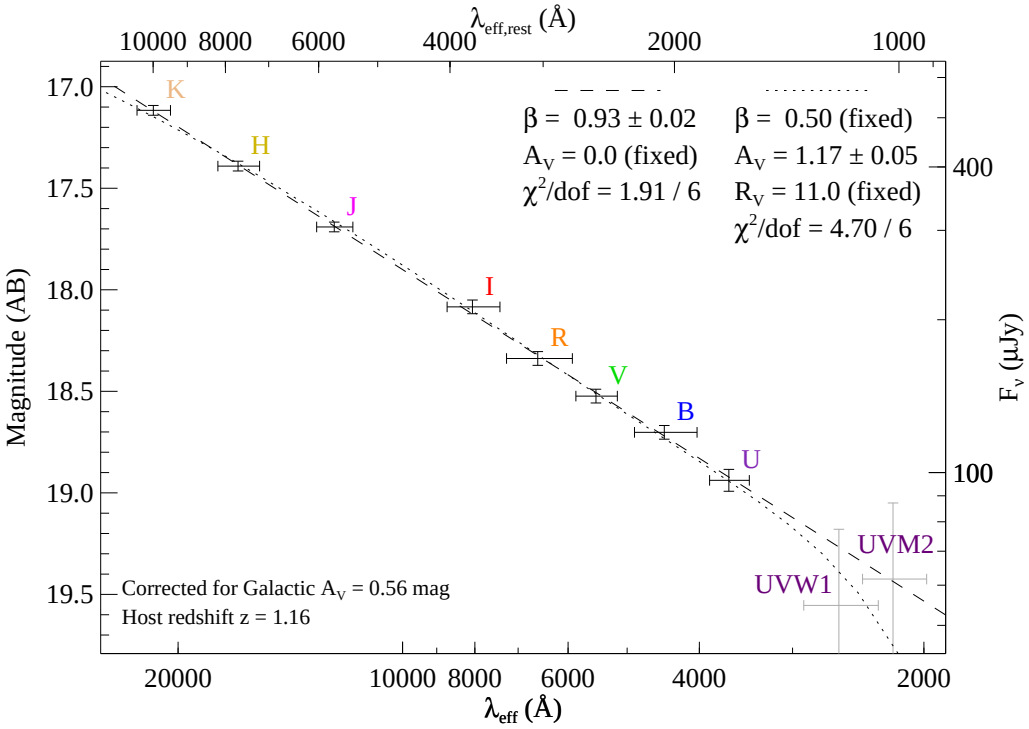

Figure 4.12 Spectral energy distribution of the slowly decaying component of the afterglow at 2000 s, fit both to a model assuming no host-galaxy extinction (dashed line) and a model assuming host-frame extinction is present in sufficient quantity to provide the observed minimum discrepancy between these optical measurements and the X-rays. We use the Calzetti et al. (2000) extinction model of starburst galaxies, with R_V in this case set very high, to 11. The uncertainties of the UVOT measurements are very large and we do not include them in our fits.

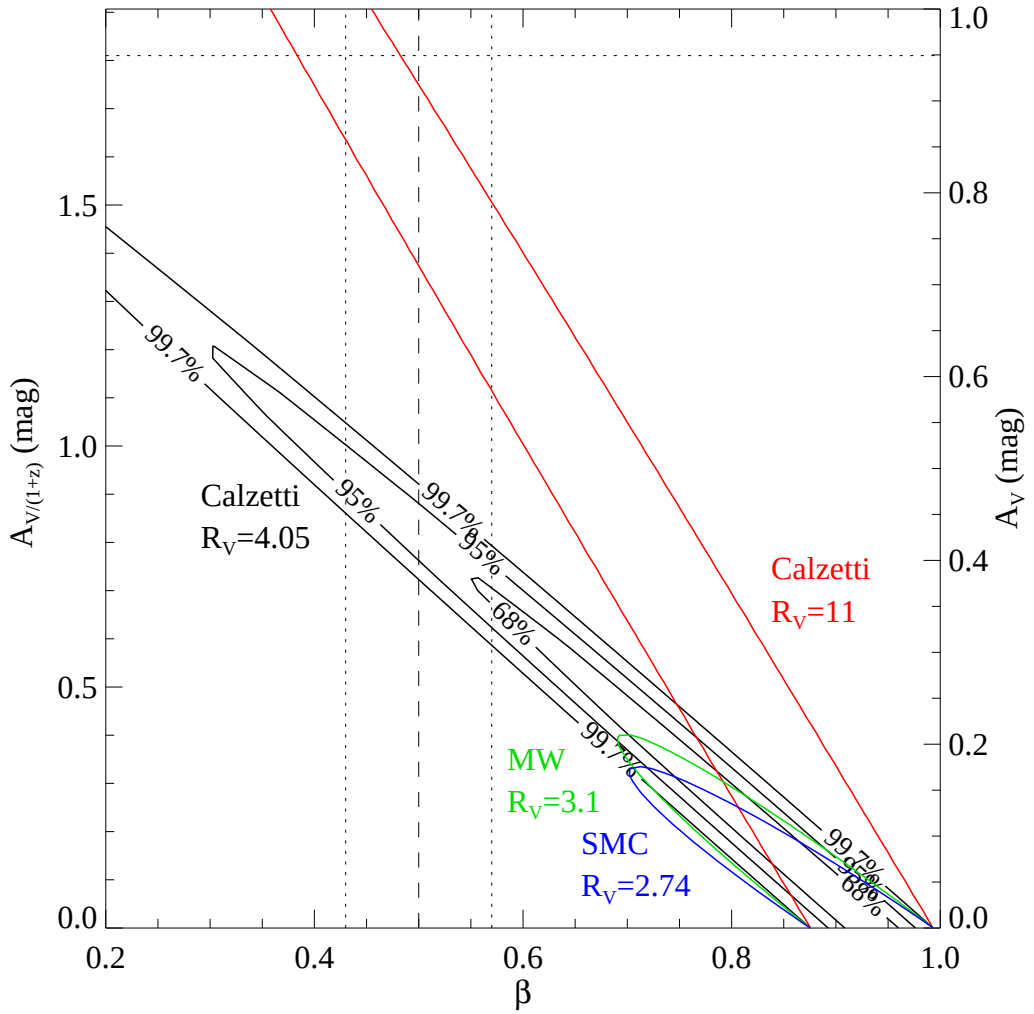

Figure 4.13 Plot of χ^2 as a function of A_V and the intrinsic unabsorbed β for different models. Extinction is strongly limited for standard extinction laws. The Calzetti et al. (2000) extinction law allows slightly larger amounts of extinction, but still short of the amount required (an absolute minimum of 1.8 mag, represented by the dotted line near the top). The vertical bars indicate the range of β predicted by the X-ray observations if the optical emission is due to a forward shock, though if the forward shock is still peaking the intrinsic β is allowed to be blueward (lower β) of this range.

Table 4.1 Band model fits to the BAT+RHESSI spectrum of GRB 061126

Region	α	β	$E_{\rm peak}^{\rm obs}$ [keV]	100 keV Norm. [ph cm^{-2} s^{-1}]	χ^2_ν (DOF)
Full ($t = -6$–35s)	-1.06 ± 0.07	< -2.3	620^{+220}_{-160}	$7.8^{+0.7}_{-0.5} \times 10^{-3}$	0.733 (106)
Pulse A ($t = 3$–14s)	-0.94 ± 0.06	< -2.5	790^{+160}_{-130}	$1.8 \pm 0.1 \times 10^{-2}$	1.042 (105)
Pulse B ($t = 19$–25s)	$-0.9^{+0.2}_{-0.1}$	...	350^{+190}_{-110}	$1.1^{+0.4}_{-0.1} \times 10^{-2}$	1.179 (100)

The quoted uncertainties correspond to the 90% confidence region. The data in each time region are acceptably fit by an exponential times a power-law model. The high-energy power-law component (with photon index β) is not required in the fits but can be constrained for regions "Full" and "Pulse A." Using $\alpha \approx -1$ and the declining $E_{\rm peak}$ and normalization values between pulses A and B, we estimate an approximately energy-independent GRB spectral flux of $0.1^{+0.1}_{-0.5}$ mJy below 1 keV at $t = 60$ s (Figure 4.5).

Table 4.2 Optical Light-Curve Fits

α_F	β_F	$\alpha_{S,b}$	$\alpha_{S,a}$	$\Delta\beta_{F-S}$	χ^2/dof
2.09 ± 0.29	1.28 ± 0.01	-	0.80 ± 0.05	-0.32 ± 0.03[a]	212.0/185
1.76 ± 0.22	1.07 ± 0.02	-	0.58 ± 0.12	0[b]	261.8/193
1.96 ± 0.29	1.31 ± 0.02	-	0.75 ± 0.06	-0.38 ± 0.08	231.3/192
1.70 ± 0.09	1.23 ± 0.02	-0.50[b]	0.75[b]	-0.12 ± 0.09[c]	227.6/197

Summary of key parameters and χ^2 from the various models fit to the data. The model with no color change is strongly ruled out. The nature of the color change depends on the assumed model.

[a] Not a formal fit parameter in this model — the flux amplitude parameters in each filter are allowed to assume their arbitrary best-fit values. In other models the change in these parameters is constrained to be due to variation in the spectral index β.

[b] Fixed parameter.

[c] Change between the spectral index of the fast component and the index fit to the slow component after its peak ($\beta_{S,b}$). The slow component undergoes a chromatic break from $\beta_{S,b}$ = 0.284 to $\beta_{S,b}$ = 1.11.

Chapter 5

GRB 071025: Evidence for Supernova-Synthesized Dust at $z \sim 5$

An earlier version of this chapter was previously published as MNRAS 406:2473–2487[1].

Abstract

We present observations and analysis of the broadband afterglow of *Swift* GRB 071025. Using optical and infrared ($RIYJHK$) photometry, we derive a photometric redshift of $4.4 < z < 5.2$; at this redshift our simultaneous multicolor observations begin at ∼30 s after the GRB trigger in the host frame, during the initial rising phase of the afterglow. We associate the light curve peak at ∼580 s in the observer frame with the formation of the forward shock, giving an estimate of the initial Lorentz factor $\Gamma_0 \sim 400$. The red spectral energy distribution (even in regions not affected by the Lyman-α break) provides secure evidence of a large dust column. However, the inferred extinction curve shows a prominent flat component between 2000-3000 Å in the rest-frame, inconsistent with any locally observed template but well-fit by models of dust formed by supernovae. Time-dependent fits to the extinction profile reveal no evidence of dust destruction and limit the decrease in the extinction column to $\Delta A_{3000} < 0.54$ mag after $t = 50$ s in the rest frame. Together with studies of high-z quasars, our observations suggest a transition in dust properties in the early universe, possibly associated with a transition between SN-dominated and AGB-dominated modes of dust production.

5.1 Introduction

Starting with the discovery of the 9th magnitude afterglow of gamma-ray burst (GRB) 990123 (Akerlof et al. 1999), the early-time study of GRB afterglows has presented great

promise to elucidate both the nature of the gamma-ray burst phenomenon itself and of the medium surrounding these objects in extremely distant galaxies. Fast-responding telescopes, slewing to the burst location in time to catch the afterglow at or near the time of peak luminosity, can probe the physics of the explosion in the initial seconds as the ultrarelativistic outflow is decelerated by the interstellar medium. Continued observations can then follow the evolution of the reverse and forward shocks for many hours as the afterglow fades away, providing constraints on the still poorly-understood early-time emission processes. In addition, the extreme luminosities at early times (e.g., Kann et al. 2007; Bloom et al. 2009; Racusin et al. 2008) enable even very small telescopes to provide precise photometric and occasionally spectroscopic measurements of the afterglow spectral energy distribution (SED) and act as a probe of interstellar gas and dust out to the epoch of reionization (Kawai et al. 2006; Totani et al. 2006; Gallerani et al. 2008; McQuinn et al. 2008; Greiner et al. 2009b; Tanvir et al. 2009; Salvaterra et al. 2009). And while the usage of early-time SEDs as probes of the interestellar environment is hindered to some extent by the uncertain emission processes acting at these times, they nevertheless can provide constraints on the direct influence of a GRB on its surrounding medium in the form of dust destruction and photoionization (Waxman & Draine 2000; Fruchter et al. 2001; Draine & Hao 2002; Perna & Lazzati 2002; Perna et al. 2003).

At the same time, however, the fleeting and time-variable nature of GRB afterglows poses several challenges for these early-time diagnostics. To maximise sensitivity, the smallest telescopes typically do not employ filter systems and therefore give minimal frequency-domain information. When filters are employed, ordinary telescopes are forced to employ a filter cycle, creating the possibility of confusion between spectral and temporal evolution of the event. Nevertheless, progress has advanced steadily with the commissioning of several simultaneous-color robotic telescopes. The Peters Automatic Infrared Imaging Telescope (PAIRITEL; Bloom et al. 2006e), online since late 2004, provides simultaneous measurements in the J, H, and K_s-bands every 7.8 s starting within 1–3 minutes of a typical GRB and is the primary subject of this chapter. More recently, the seven-channel Gamma-Ray Burst Optical/Near-Infrared Detector (GROND, Greiner et al. 2008) has also produced simultaneous SEDs of afterglows at over the wavelength range 4000-24000 Å, including in several cases time-dependent SEDs during the afterglow rise and fall (Krühler et al. 2008, 2009b) and short-timescale flares (Krühler et al. 2009a; Greiner et al. 2009a), and RAPTOR-T has tracked spectral changes during the fading of GRB 080319B in several optical bands simultaneously (Woźniak et al. 2009). In all cases, color evolution appears to be absent or modest, consistent with the lack of strong color evolution in the generally less constraining measurements by filter-cycling instruments such as the *Swift* UVOT (Oates et al. 2009). Correlation with the gamma-ray prompt emission and with X-ray flares (also thought to be associated with the prompt phase: Kocevski et al. 2007b, Chincarini et al. 2007) is rare (Yost et al. 2007), but has been observed in some cases (Vestrand et al. 2005, 2006; Page et al. 2007; Krühler et al. 2009a; Racusin et al. 2008; Klotz et al. 2009). These multi-band observations are particularly important for distinguishing the predictions of different models for the large variety of light curve behaviors observed at early times: reverse shock (Sari &

Piran 1999a), energy reinjection (Rees & Meszaros 1998), prompt emission (e.g., Kumar & Panaitescu 2000, 2008), outflow deceleration (Sari & Piran 1999b; Mészáros 2006), spectral breaks moving through the optical bandpass (Sari et al. 1998), and many others.

GRB 071025, detected by the *Swift* mission (Gehrels et al. 2004), provides among the best probes of the early-time behavior of a gamma-ray burst to date. While no secure spectroscopic redshift was attained ($z \sim 5.2$ was estimated from a low-quality HIRES optical spectrum at Keck; Fynbo et al. 2009), the photometric SED presented here shows clear evidence of a Lyman-α break in the observer-frame R-band and indicates a photometric redshift of $4.4 < z < 5.2$ (§5.3.2), making this among the highest-redshift bursts to date and one of only a few observed in simultaneous colors during prompt emission. Our infrared and optical observations start at ∼30 s after the burst in the rest frame and follow the rise, peak, and fall of an afterglow in simultaneous rest-frame optical colors. In this paper, we use this unique data set to test various models for the origin of the early emission and conclude it is likely due to the deceleration of the burst outflow into a uniform-density interstellar medium, allowing estimation of the Lorentz factor Γ (§5.4.1). The $IYJHK$ spectral energy distribution demonstrates the existence of a significant dust column obscuring a star-forming region at $z > 4.4$ and provides evidence that the dust at this epoch had different properties from dust that prevails along sightlines in the more nearby universe, in agreement with the study of a high-z QSO by Maiolino et al. (2004). We suggest that this difference is reflective of an absence of evolved AGB stars in these earliest epochs, and search for (and place stringent limits on) signs of destruction of this dust by radiation from the GRB (§5.4.2). Throughout the paper we use the convention $F \propto t^{-\alpha}\nu^{-\beta}$ and assume cosmological parameters $h = 0.71$, $\Omega_\Lambda = 0.7$, $\Omega_M = 0.3$.

5.2 Observations

5.2.1 Swift

At 04:08:54 UT on 2007 October 25[2], the Burst Alert Telescope (BAT, Barthelmy et al. 2005) on-board *Swift* detected GRB 071025 and performed a rapid slew to the GRB location, beginning observations with the XRT (Burrows et al. 2005c) at 146 s after the trigger. The BAT light curve is broad and only slowly variable: the flux rises slowly during the first ∼80 s and peaks several times before beginning a steady decay at approximately ∼130 s. The GRB remains detectable above the background until *Swift* was forced to slew away from the position due to an Earth constraint at 422 s after the initial trigger. Observations resumed at 3500 s, and tracked the afterglow using the XRT with no further large gaps in temporal coverage for the next ∼3 days, after which it became too faint to be detected. Details of our high-energy reduction pipeline are described in detail by Butler et al. (2007)

[2]This trigger time will be used as the reference time in the remainder of the paper.

for the *Swift* BAT and by Butler & Kocevski (2007a) for the *Swift* XRT[3].

Swift's Ultra Violet-Optical Telescope (UVOT, Roming et al. 2005) observed the field starting at 155 s, but detected no significant afterglow signal in any of its seven filters (Pagani et al. 2007). The non-detection is consistent with our photometric redshift, as outlined in §5.3.2.

5.2.2 PAIRITEL Observations

The robotic infrared observatory PAIRITEL consists of the 1.3-m Peters Telescope at Mt. Hopkins, Arizona, formerly used for the Two Micron All Sky Survey (2MASS; Skrutskie et al. 2006), re-outfitted with the southern 2MASS camera. PAIRITEL, like 2MASS, makes use of two dichroics to image in the J, H, and K_s filters simultaneously.

PAIRITEL responded to the initial Gamma-ray Burst Coordinate Network (GCN, Barthelmy et al. 1995) alert at 74.3 s and slewed immediately to the source. Observations began at 162 s and continued uninterrupted until 3812 s, when due to a problem with the observing queue PAIRITEL temporarily slewed to another location. Observations resumed at 9108 s and continued for another two hours. Raw data files were processed using standard IR reduction methods via PAIRITEL Pipeline III and resampled using SWarp (Bertin et al. 2002) to create final 1.0-arcsec/pix images for final photometry. PAIRITEL's standard observing cycle is to take three 7.8 second exposures in immediate succession at each dither position. While the early afterglow is detected in even the shortest 7.8 second frames, the S/N was too low for reliable photometry, so the shortest exposures reported here consist of 23.4-second "triplestacks", the sum of all three images at each dither position. These images were further binned at successively later times to further improve the S/N. The afterglow position, relative to 2MASS astrometric standards, is $\alpha = 355.0711583$, $\delta = +31.778575$ (J2000).

Photometry was performed in IRAF[4] using the `phot` task. Best results were achieved using aperture photometry with an aperture radius of $2.25''$ in J-band, $2.5''$ in H-band, and $2.75''$ in K_s-band. Unfortunately, while conditions during the observations were generally clear, the night was not fully photometric, with variations in the transmission of up to 0.3 mag during the course of observations and additional significant fluctuations in the seeing. Calibration was therefore performed by re-determining the zeropoint for each image individually by comparison to our secondary field standards (§5.2.11). Fortunately, the field of GRB 071025 is rich in bright field stars, and a total of eight nearby stars (present and well-detected in even short exposures with reference uncertainties of <0.05 mag) were used to determine the zero-point. The statistical uncertainty on the zero-point (never more than 0.05 mag) is essentially negligible relative to other sources of error in all cases. Systematic

[3] *Swift* bursts occurring after these publications, including GRB 071025, have been processed using the same methods; these results are available online at `http://astro.berkeley.edu/~nat/swift/`

[4] IRAF is distributed by the National Optical Astronomy Observatory, which is operated by the Association of Universities for Research in Astronomy (AURA) under cooperative agreement with the National Science Foundation.

sources of error are addressed in §5.3.4.

The large plate scale of PAIRITEL (2.0 ″/pix) and the variable sub-pixel response function of the NICMOS3 arrays creates a significant additional uncertainty in each position beyond ordinary photometric errors, estimated at ∼3 percent by Blake et al. (2008). To quantify this uncertainty as accurately as possible, we constructed light curves for standard stars of different magnitudes in regions of the image free of defects by measuring the image-to-image magnitude variations of bright (source-dominated) stars. An additional uncertainty of approximately ∼0.02 mag per position was required to incorporate the observed scatter in the photometry of these objects. Additionally, we examined fainter (sky noise-dominated) stars to compare the IRAF-generated uncertainty to that observed in the zero-pointed light curve, finding the IRAF uncertainties to be too low by about 20% in each filter. Therefore the final uncertainties on our photometry, reported in Appendix B, were determined by increasing the IRAF uncertainty by 20% and adding the result in quadrature with $0.02/\sqrt{N_{\rm pos}}$ mag, where $N_{\rm pos}$ is the number of unique dither positions per stacked image.

5.2.3 REM Observations

GRB 071025 also triggered REM (Rapid-Eye Mount; Zerbi et al. 2001), a robotic (Covino et al. 2004) telescope located at the ESO Cerro La Silla observatory (Chile). The REM telescope has a Ritchey-Chretien configuration with a 60 cm f /2.2 primary and an overall f /8 focal ratio in a fast moving alt-azimuth mount providing two stable Nasmyth focal stations. At one of the two foci, the telescope simultaneously feeds, by means of a dichroic, two cameras: REMIR (Conconi et al. 2004) for the NIR and ROSS (Tosti et al. 2004) for the optical. Both cameras have a field of view of 10x10 arcmin and imaging capabilities with NIR (1μ, J, H, and K) and Johnson-Cousins VRI filters. Observations of the GRB 071025 field began at 144 s after the trigger, although this initial H-band exposure did not detect the afterglow. The optical camera was unfortunately not operational due to maintenance, so exposures were acquired only in 1μ, J, H, and K.

The raw frames were corrected for dark, bias, and flat field following standard procedures. Although the burst was at low elevation at the trigger time, seeing conditions were good and photometry was performed using a 3.5 pixel (1.2″) aperture. Conditions were not photometric, and so the zeropoint was determined for each image individually in JHK bands using a subset of 2MASS-based standards. The 1μ-band (often referred to as z in previous work, though this filter has almost no overlap with the traditional SDSS z-band), after taking into account the transmission of the ROSS/REMIR dichroic, is close to the MKO Y-band[5] and so we treated this filter as a Y measurement (see §5.2.11) and basing the calibration on four reference stars well-detected in all images.

[5] `http://www.ukidss.org/technical/instrument/filters.html`; see also Hillenbrand et al. (2002)

5.2.4 RAPTOR Observations

The RAPTOR (Rapid Telescopes for Optical Response) experiment (Vestrand et al. 2002), operated by Los Alamos National Laboratory, consists of a series of small telescopes at the Fenton Hill Observatory in New Mexico. RAPTOR-S is a fully autonomous robotic telescope with a 0.4-m aperture and typical operating focal ratio f/5. It is equipped with a 1000×1000 pixel CCD camera employing a back-illuminated Marconi CCD47-10 chip with 13μ pixels.

RAPTOR-S responded automatically to the localization alert and was on target at 04:10:14.95 UT, 81.3 s after the trigger time (4.2 s after receiving the GRB position). The rapid response sequence of RAPTOR-S consists of nine 5-second images followed by twenty 10-second images and finally 170 30-second images for a total of ∼2 hours of coverage (including 5-second intervals between exposures used primarily for readout). In order to improve the S/N ratio, photometry was performed on coadded images. Aperture photometry was performed using the SExtractor package (Bertin et al. 2002), and the magnitude offsets between epochs were derived using several dozen field stars.

Because of the extreme redness of this afterglow, the unfiltered RAPTOR-S observations required a special calibration procedure. Although the effective wavelength of the response curve for RAPTOR-S is close to that of the standard R band, the spectral energy distribution of this burst (§5.3.2) indicates a sharp drop in the flux between I and R bands, likely due to the onset of the Lyman-α forest. As a result, most photons detected by RAPTOR-S actually fall in the spectral region covered by the standard I filter.

Therefore, we tie the unfiltered data to I-band standards from the Lick calibration (§5.2.11). The offset $(m_{\rm C} - I)_{\rm star}$ between the unfiltered magnitudes and standard I was derived using 7 well-measured stars in the vicinity of the GRB covering a narrow range of colors $0.5 < (R - I) < 0.66$. Assuming that the SED of the burst emission did not change significantly between the time of RAPTOR-S observations and the time when it was measured, we derived an approximate correction to $(m_{\rm C} - I)_{\rm star}$ to account for the extremely red color of the GRB. We used a K5V model spectrum from Kurucz (1979) as a proxy SED matching the mean color of our comparison stars. By folding both SEDs with response curves of RAPTOR-S and the standard I-band filter we find $(m_{\rm C} - I)_{\rm GRB} = (m_{\rm C} - I)_{\rm star} + 0.74$ mag. The uncertainty of the derived zero point is about 10%; consistent with this, we measure a relatively small offset of -0.08 magnitudes between the calibrated RAPTOR magnitudes and an extrapolation from later, filtered I-band observations using our light curve model (see §5.3.1). Table B.3 lists the final RAPTOR-S photometry.

5.2.5 Super-LOTIS Observations

Super-LOTIS (Livermore Optical Transient Imaging System) is a robotic 0.6-m telescope dedicated to the search for optical counterparts of gamma-ray bursts (Williams et al. 2004, 2008). The telescope is housed in a roll-off-roof facility at the Steward Observatory Kitt Peak site near Tucson, Arizona. Super-LOTIS triggered on GRB 071025 and began observations at

04:10:29 UT (95 s after the trigger), acquiring a series of R-band frames, which were reduced using standard methods. Unfortunately, because of the optical faintness of the afterglow and high sky background, the quality of the images is poor and even after extensive stacking the detection is marginal, particularly in the earliest few stacks. Photometry was performed using aperture photometry and our Lick R-band field calibration as detailed in §5.2.11.

5.2.6 Lick Infrared Observations

We acquired an additional series of infrared observations using the 3m Shane telescope at Lick Observatory equipped with the UCLA GEMINI IR camera (McLean et al. 1993, 1994). A total of nine exposures were acquired in J and K' bands simultaneously starting at 04:52:23 UT, integrating for 11 coadds of 20 s each in J and 35 coadds of 6 s each in K'. The IR afterglow was still very bright at this time, and is clearly detected with signal-to-noise $S/N > 50$ in individual exposures. Reduction was performed via direct subtraction of temporally adjacent exposures followed by division by a twilight flat. Photometry was performed using IRAF and an aperture of 2 pixels (1.4″); images were calibrated relative to the PAIRITEL magnitudes of five nearby bright field stars.

The response of the K' filter is significantly different from K_s and the GRB exhibits an apparent color ($H - K \approx 1.0$ that is much redder than any field star used for comparisons (ranging between $H - K = 0.04 - 0.18$). To correct to K_s for direct comparison to the PAIRITEL data, we use an approximate correction of $K_s \approx K \approx K' - 0.07$ (Wainscoat & Cowie 1992), with this correction inferred from the reddest star in Table 1 of that work (Oph S1, $H-K = 0.94$, $K'-K = 0.07^{+0.015}_{-0.025}$). The K to K_s color term is assumed to be negligible. This is found to produce good agreement between Lick data and coeval PAIRITEL points. However, due to uncertain differences between the Lick, MKO, and other filter sets and the intrinsic GRB spectrum itself the overall calibration offset could be as much as 0.05 mag, and as a result the Lick K' photometry is not used in fitting.

5.2.7 MAGNUM Observations

The MAGNUM (Multicolor Active Galactic NUclei Monitoring) 2.0 m telescope on Haleakala has been carrying out observations of AGN and other variable objects (including GRBs) since 2001 (Yoshii 2002; Yoshii et al. 2003; Kobayashi et al. 2003). The telescope is equipped with dual optical and infrared channels, allowing simultaneous observations in two bands.

We initiated MAGNUM observations starting at 06:59 UT, acquiring a sequence of dithered exposures over the next ∼2 hours in a large number of filters, including RI in the optical channel and $YJHK$ in the infrared channel. The MAGNUM FOV is small, and generally only one star was present in the field and away from the chip edge at all dither positions. Therefore only a single star was used to establish the calibration in each filter. In the H, K, and Y-band observations the star at α=355.066002°, δ=31.793428° was used for this purpose; for R, I, and J the star at α=355.058815° δ=31.780569° was used. The second

Y-band exposure unfortunately contained no usable reference star. However, comparison of exposures in other filters and at other points in the night suggest that conditions were photometric, and so calibration was achieved by comparison to the first Y-band exposure (with a small aperture correction.)

5.2.8 Kuiper Observations

Shortly after the GRB trigger, we initiated imaging observations at the 1.54m Kuiper telescope, operated by Steward Observatory and located on Mt. Bigelow. Observations began at 04:37:08 UT and continued until 08:55:41 UT, mostly in the R and I filters with some additional observations in V. Images were reduced and combined in IRAF using standard techniques. The I-band images were not dithered and so an archival fringe frame was used to subtract the fringe pattern. Photometry was performed in IRAF using secondary standards.

5.2.9 Late-Time Afterglow Observations

To try to constrain the late-time ($t > 12$ hr) behavior of this burst, additional follow-up was carried out on the 3.6-m New Technology Telescope and at GROND. We observed the burst location on NTT using the infrared imager SOFI in a series of J, H, and K-band exposures, and additionally in H-band only on the following night. Photometry was calibrated relative to our IR secondary standards.

GROND is a seven-channel instrument which has been mounted on the ESO 2.2-m telescope at La Silla, Chile, since April 2007. GROND began observations of GRB 071025 on 2007 Oct 26 at 01:50 UT and completed one 8 minute observing block and two 20 minute observing blocks. In total, 9 images were taken in the $g'r'i'z'$ bands and 216 were taken in the NIR. Each NIR image was 10 s long; the optical images varied in length from 137 to 408 s. The images were reduced using the GROND pipeline (Küpcü Yoldaş et al. 2008), with all images combined into a single stack for each filter. For consistency with other measurements, photometry was performed using aperture photometry calibrated to our secondary standards in JHK. For $g'r'i'z'$ bands, images are calibrated directly relative to spectroscopic standard stars SA 114-750 and SA 114-656.

Poor agreement is observed between the NTT and GROND observations (and between the overall SED at this time and earlier data) using a standard 1″aperture, even though these epochs are effectively coeval. We have re-examined these data and find no clear evidence of problems in the reduction or photometry, although the afterglow appears extended in the N-S direction in the GROND H-band frame, suggesting that it might be blended with a nearby source or image artifact. No neighboring source is observed in the NTT imaging, and the deep Keck optical imaging shows no object within $\sim 3''$ of the afterglow position (§5.2.10). However, to guard against this possibility we performed the photometry in the GROND J and H channels and all NTT channels using a small aperture ($0.5''$) in all bands.

This smaller aperture provides good consistency between the two observations and is used in our analysis.

5.2.10 Keck Observations

To help rule out a low-redshift origin for this burst we imaged the field around the GRB with LRIS (Oke et al. 1995) on the Keck I telescope on 2008 Aug 02 using the g and R filters simultaneously under excellent conditions. Total exposure times were 1050 s in R-band and 1140 s in g-band. Consistent with the large photometric redshift inferred from the SED, no significant flux due to a host galaxy was detected at the location of the optical/IR afterglow (the nearest object is a pair of faint point-like sources located $3''$ to the northeast). Forced photometry at the position of the optical afterglow, calibrated using unsaturated secondary standards, gives a limit (3-σ) of $R > 26.5$ mag, $g > 27.2$ mag.

5.2.11 Field Calibrations

To improve upon the photometric accuracy of 2MASS, we stacked together all observations of the GRB field acquired by PAIRITEL during the night of 2007 October 25 UT and calibrated a set of isolated, high-S/N stars present in the field in all or nearly all dither positions relative to 2MASS. These magnitudes were used in place of 2MASS magnitudes directly.

For the optical filters, on the night of 2009 June 19 we observed the field of GRB 071025 using the Nickel 1m telescope at Lick observatory. Conditions were photometric throughout the night. Three exposures were acquired in R-band and one each in I and g band and stars within the field were calibrated by comparison to repeated observations of PG 1633 and PG 2336 (Landolt 1992) at varying airmass, calibrating reference stars within the field. A second calibration was conducted on 2009 Sept 28 using repeated observations of standard fields PG 1633, PG 2336, PG 0213, and SA 110; the results were found to be completely consistent with the June calibration.

No field calibration was performed in the Y-band. To calibrate the observations in this filter, we derived our own transformation equation for calculating Y magnitudes of reference stars given photometry in nearby bands by fitting a simple linear regression model to the photometry available online at the UKIRT webpage[6]. (The $Y - J$ color was fit as a linear function of $J - H$, and the residuals were then fit to a linear function of $I - J$.) The transformation equation $Y = J + 1.104(J - H) - 0.11(I - J) - 0.03$ was found to accurately describe the observed Y-band magnitudes for the available standards (with photometry in all four bands) with an RMS of < 0.03 mag. We therefore applied this equation to calculate the Y magnitudes for secondary standards in the GRB 071025 field using the calibrated IJH photometry.

[6] `http://www.jach.hawaii.edu/UKIRT/astronomy/calib/phot_cal/fs_izyjhklm.dat`

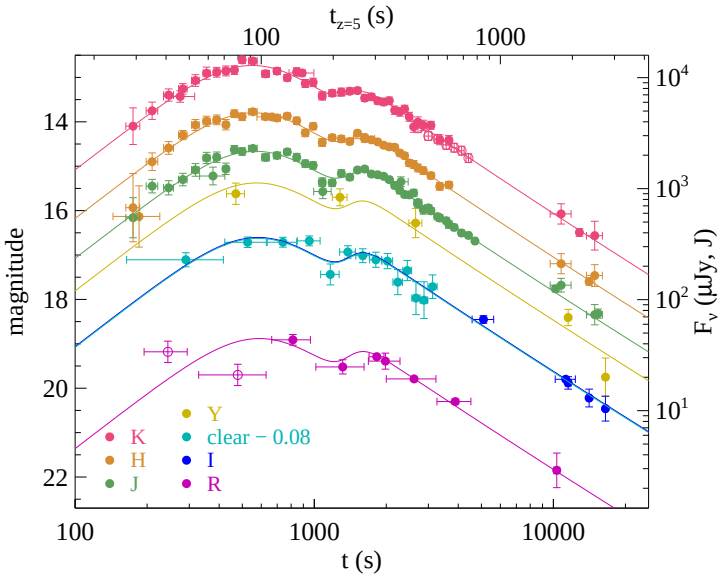

Figure 5.1 Early-time multiband optical and infrared light curves of GRB 071025 fit to our empirical light curve model. The afterglow is caught during its rise at ∼30 s in its rest frame (assuming $z = 5$), and exhibits a double-peaked structure before fading again as a simple power-law. The RAPTOR unfiltered data has been shifted to match the I-band data. Magnitudes are Vega-based and not corrected for extinction.

5.3 Analysis

5.3.1 Early-Time Afterglow Evolution: Rise, Fall, and Reddening

All photometric observations of GRB 071025 during the first night are presented in Figure 5.1. Several features are immediately apparent. First, the afterglow was caught during what appears to be its initial optical rise, brightening by ∼1.5 mag from the first detections to the peak in all filters. Second, the evolution is not single-peaked: a limited rebrightening is observed at ∼1800 s. Third, the burst is extremely red, with $R - K \sim 6.5$ mag. Finally, no dramatic color change is evident. This is not to say that there is not finer-scale color evolution, however—as will be discussed later, the best-fit curves plotted in Figure 5.1 correspond to a chromatic model which is shown to produce a large improvement in χ^2 relative to the monochromatic case.

The empirical model used to fit this burst is described in Appendix A. For this GRB, we employ two summed Beuermann et al. (1999) functions. The sharpness parameter s was fixed at 1 (allowing it to vary resulted in insignificant improvement to χ^2). The overall flux-normalization factor in each filter is arbitrary, determined by the best fit to the data. Color is allowed to vary between components and between rising and falling segments of an individual component. As explained in more detail in Appendix A, it should be emphasised that this method makes no assumptions about the overall SED, since only the *variation* in β

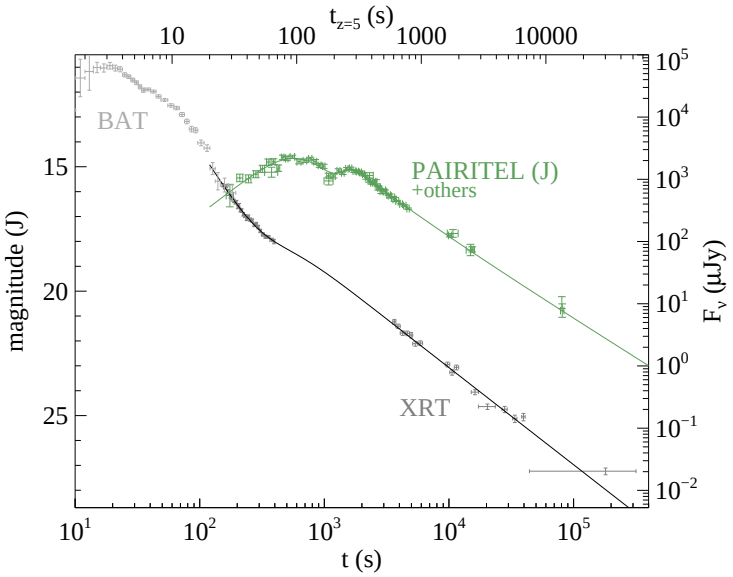

Figure 5.2 The gamma-ray (*Swift* BAT) and X-ray light curves (*Swift* XRT) of GRB 071025, compared to the J-band light curve out to late times. The X-ray light curve is rapidly fading during the optical-IR rise, probably due to high-latitude prompt emission (the light curve connects smoothly with the BAT light curve at these times if scaled to the X-ray flux, as shown.) Both optical and X-ray light curves fade with an unbroken decay at late times but with different decay slopes: $\alpha_{\rm opt} = 1.27 \pm 0.04$ versus $\alpha_{\rm X} = 1.56 \pm 0.03$.

is constrained. Indeed, the fitting method can be used to generate a best-fit observed SED in all available filters, using all available data, at any chosen time (§5.3.2).

Two components (best-fit parameters are summarized in Table 5.1) are found to provide an excellent fit to the data.[7] The light curve brightens quickly between our first detections at 180 s with a power-law of approximately $\alpha_{1,\mathrm{r}} = -1.66 \pm 0.15$ to a smooth peak at 580 s, then fades until about 1200 s. At that point the afterglow briefly rebrightens, peaking again at ∼1400 s before fading as a simple power-law ($\alpha_{2,\mathrm{f}} = 1.27 \pm 0.04$) for the remainder of our observations. The χ^2 residual, assuming no color change, is 222.4 per 154 degrees of freedom (dof). Permitting color change improves the fit significantly: allowing the parameters $\Delta\beta_{12}$ (describing the change in intrinsic spectral index between the first and second component after peak) and $\Delta\beta_{1(\mathrm{rf})}$ (describing the change in intrinsic index between rising and falling portions of the first component) to both vary, χ^2/dof improves to 197.4/152 which (according to the f-test) is significant at $> 99.9\%$ confidence. Most of this change is associated with the transition to the second component ($\Delta\beta_{12} = -0.26 \pm 0.12$, versus a not-significant color change across the first peak of $\Delta\beta_{1(\mathrm{rf})} = -0.20 \pm 0.14$) but unfortunately, although the need for overall red-to-blue color change is clear, its nature cannot be clearly distinguished by this methodology. We will further examine scenarios for this possible color change in §5.4.2.

The X-ray light curve (Figure 5.2) was fit using a similar method (but with only a single "filter", simplifying the process significantly). Again, two summed functions are found to provide an acceptable fit to the data. However, the first component is a rapidly-declining, unbroken power-law with $\alpha_{\mathrm{X,init}} = 3.1 \pm 0.2$. This initial segment connects smoothly with the BAT prompt emission, as has been seen for a large majority of *Swift* bursts (O'Brien et al. 2006). The optical peaks unfortunately fall during an orbital gap in the XRT coverage, but by the end of the first observations the power-law is already clearly flattening, almost certainly due to the transition from the rapid decay phase (O'Brien et al. 2006) to a standard afterglow (Nousek et al. 2006). Coverage resumes approximately an hour later, by which time the X-ray light curve is fading rapidly in an unbroken decay with $\alpha_{\mathrm{X}} = 1.56 \pm 0.03$.

5.3.2 SED and Photometric Redshift

At 10000 s after the burst, the evolution of the light curve has given way to a simple power-law decay dominated by only a single component. Moreover, thanks to the MAGNUM observations, photometry is available in all colors within a relatively short time span surrounding this epoch with high S/N in JHK. We therefore choose this time as the extraction point for the overall spectral energy distribution (SED) of this burst, using the model fluxes from our fit as described above. (These fluxes are consistent with the MAGNUM and PAIRITEL photometry measured at this epoch specifically.) All fluxes are corrected for

[7] The first two Super-LOTIS points are an exception, both of which deviate from the fitted model by 2–3 σ. Given the low signal-to-noise detections and large degree of time-binning in both cases, these points are not included in the fit, although the low flux observed in the second observational window, which covered the peak of the light curve, is nevertheless surprising given the behavior in all three PAIRITEL bands and in RAPTOR data at that time.

Galactic extinction (relatively small at $E_{B-V} = 0.07$ mag in this direction; Schlegel et al. 1998.)

The 1σ uncertainty on the fit parameter was combined in quadrature with an estimate of the calibration uncertainty in each filter. In the J and H filters, where the afterglow is comparable in color to reference stars (which show negligible scatter), we use an uncertainty of 0.04 mag; in K where the afterglow color is much redder than our reference stars we conservatively increase this to 0.06 mag. This incorporates both the absolute and relative calibration accuracy of 2MASS (estimated at $\sim$0.02 and 0.011 mag, respectively; Cohen et al. 2003 and 2MASS online documentation[8]), effects of variation of the effective wavelength $\lambda_{\rm eff}$ from its reference value due to a non-standard spectrum (< 0.02 mag), the possibility of strong absorption from ISM or IGM lines (very likely < 0.02 mag), and uncertainties in the extinction correction (< 0.01 mag). In Y-band, we use an estimate of the photometric scatter of the high-S/N REM reference stars to the interpolated secondary standards (0.1 mag). We also use 0.1 mag in I-band due to the redness of the afterglow in this band and the possibility that Lyman-α may be affecting the flux towards the blue filter edge if the redshift is $z > 5.0$. In R-band a large uncertainty of 0.2 mag is used, although because R is almost certainly heavily blanketed by the Ly-α forest we use this filter only to place a limiting value on the redshift and exclude it from fits to the extinction profile. The resulting SED (fit with various models, explained below) is plotted in Figure 5.3.

The sharp dropoff towards the R-band is suggestive of high redshift. However, the spectral slope observed even well redward of this apparent break is quite red ($\beta \sim 1.64$, as shown by the dashed straight line in Figure 5.3), suggesting that significant extinction is likely present as well. In order to quantitatively constrain the redshift z, we fit the data set with a large number of different extinction models (detailed in §5.3.3) at varying redshifts. Absorption due to the Lyman-α forest is taken into account using a simple model of the average opacity of the IGM as a function of z and λ from Madau (1995). The extinction column A_V and the spectral index β were constrained to be positive: negative extinction is unphysical, while a negative spectral index would be both much bluer than any previously observed afterglow and in disagreement with standard afterglow theory (Sari et al. 1998).

The HIRES spectrum discussed in Fynbo et al. (2009) shows a trace extending from the limit of the spectral range at 7950 Å down to 7550 Å, blueward of which no flux is detected. While the quality of this spectrum is poor, the nondetection of Lyman-α puts a robust upper limit on the redshift of $z < 5.2$, so this was treated as the maximum redshift. Regardless of the extinction law, no known dust curve is able to reproduce the extremely steep $I - R$ slope without invoking Lyman-α blanketing of the R-band, which becomes significant at $z \sim 4.0$. Even after including a variety of extinction templates (below), the lower limit on the redshift (95% confidence) is $z > 4.4$. Treating redshift as a free parameter, the best-fit z is dependent on the extinction law but is approximately $z = 4.8 \pm 0.2$ (1σ). In the remaining discussion we will assume a fiducial value of $z = 5.0$; however, similar conclusions apply to other redshifts within the constrained range ($4.4 - 5.2$).

[8] `http://www.ipac.caltech.edu/2mass/releases/allsky/doc/sec4_8.html`

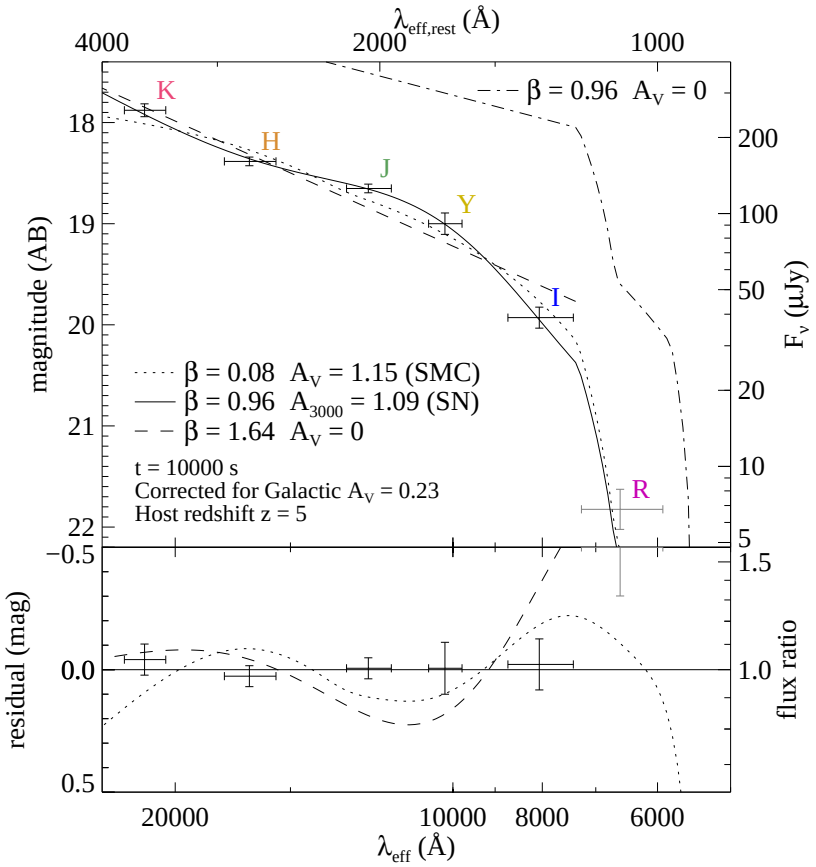

Figure 5.3 Spectral energy distribution of GRB 071025 inferred from our broadband photometry, fit with different extinction models. Note the spectral flattening between J and H that contrasts with red $H-K$ and $I-Y$ colors. (The $R-I$ color is due to absorption by the Lyman-α forest.) Traditional models (such as SMC-like extinction, shown here as a dotted line) cannot reproduce this feature and give poor fit residuals (χ^2/dof= 20.8/2). The supernova-dust model of Maiolino et al. (2004), shown as the solid line, is an excellent fit (χ^2/dof= 0.81/2). The dot-dashed line represents the intrinsic afterglow SED (for the SN model) without extinction applied but including our model of the IGM opacity at this redshift.

5.3.3 Extinction Profile

Qualitatively, the SED presented in Figure 5.3 is unusual among GRB afterglows due to the presence of an apparent inflection: while the $K-H$ and $Y-I$ colors are very red, between H and J bands the slope is quite flat. This flattening is quite significant (e.g., the H-band point is more than 0.2 mag below an interpolation between J and K) and suggests that the afterglow of GRB 071025 is subject to a complex reddening profile. To try to distinguish different possible models, we therefore fit many different extinction laws to the photometric SED, including Milky Way, LMC, and SMC curves estimated using the parametrization of Fitzpatrick (1999) as implemented in the GSFC IDL astronomy user's library, the starburst-galaxy Calzetti curve (Calzetti et al. 2000), and the high-z QSO extinction law from Maiolino et al. (2004). The intrinsic spectral index β is free but limited to be $\beta > 0$. A summary of the goodness-of-fit χ^2 for each fit model is presented in Table 5.2.

A large family of models, including the Milky Way and Large Magellenic Cloud curves as well as the extinction curves derived from a few recent highly reddened GRBs (Krühler et al. 2008; Prochaska et al. 2009; Elíasdóttir et al. 2009), display a prominent 2175 Å bump. We can strongly rule out such a feature: at the observed redshift, the broad absorption signature would fall in or near the J-band. Formal fits using these extinction templates (regardless of R_V) return A_V of zero in all cases (our fits do not permit negative extinction.)

An SMC-like extinction curve (dotted line in Figure 5.3) provides a visually reasonable-looking fit to our data, but the χ^2/dof is unacceptable at 20.8/2. This is again no surprise: the SMC extinction curve increases rapidly and monotonically with decreasing wavelength and cannot produce the flattening in our SED. The featureless Calzetti law similarly produces a poor fit because it cannot produce the deviations from a power-law evident in the photometry.

We also attempted a general fit using the full parameterization of Fitzpatrick (1999), but even if the γ and x_0 parameters of this model are fixed and the c_1 and R_V parameters are tied c_2 using e.g. the correlations of Reichart (2001), the solution is underdetermined. If the intrinsic spectral slope β is fixed, the solution is exactly determined; for e.g. $\beta = 0.65$, we derive $R_V = 5.26 \pm 0.53$, $c_2 = 0.17 \pm 0.12$, $c_3 < 0.2$, $c_4 = 1.03 \pm 0.32$, $\chi^2/\mathrm{dof} = 1.49/0$. However, this combination of parameters (small c_2 and low or zero c_3, indicating a shallow near-UV extinction law and negligible 2175Å bump) is unlike any sightline in the local universe observed to date. We also fit the data to the general extinction curve of Li et al. (2008a), fixing $\beta = 0.65$ and $c_4 = 0$ to avoid underdetermination, but the c_1 and c_3 parameters did not converge.

However, one previously observed extinction law performs extremely well at matching the observed features. Maiolino et al. (2004) presented observations of the reddened $z = 6.2$ broad absorption line quasar SDSSJ104845.05+463713, comparing NIR spectroscopy of the source to optical spectra of low-redshift quasars of the same class to estimate the extinction law. The inferred curve of this object is notable for a distinct flattening between 1800−3000Å, and was interpreted (and modeled quantitatively) by that paper as the signature of dust synthesised in supernova explosions. We fit a polynomial to the solid ($Z = 10^{-4} Z_\odot, M = 25 M_\odot$) curve displayed in Figure 2 of that paper and used the resulting extinction curve

to fit our observed photometry.[9] The result is an excellent match ($\chi^2/\mathrm{dof} = 0.81/2$) and is shown as the solid line in Figure 5.3. The associated extinction column is $A_{3000} = 1.09 \pm 0.20$ mag.[10]

The best-fit value of the intrinsic spectral index $\beta_{\rm IR}$ as inferred at the SED extraction epoch is $\beta_{\rm IR} = 0.94 \pm 0.14$, quite typical of other afterglows at this stage. This value is also consistent (albeit only marginally) with the theoretically expected value based on the observed X-ray spectral index (intrinsic $\beta_{\rm X} = 1.15 \pm 0.12$) if a cooling break is present between IR and X-ray bands: in this case $\beta_{\rm IR} = \beta_{\rm X} - 0.5 = 0.65 \pm 0.12$.) Imposing this constraint as a prior on the fit to A_V and βIR, we measure $A_V = 1.27 \pm 0.20$ mag.

Alternatively, the SED is also consistent with the presence of no cooling break: at the extraction epoch the combined IR-through-X-ray SED is well-fit ($\chi^2/\mathrm{dof} = 1.14/3$) by a single power-law with $\beta_{\rm IR,X} = 0.88$ and $A_V = 1.19 \pm 0.20$ of Maiolino dust, both consistent with the values inferred from the optical data alone. However, the X-ray flux at this time is clearly fading faster than the optical light curve (Figure 5.1): if this is not due to the presence of a moving spectral break such as a cooling break, the spectral index itself would have to be slowly evolving (implying evolution in the electron index p).

In support of our general conclusion of a significant amout of dust extinction, we note that a large amount of absorption is inferred from the X-ray spectrum also: we measure an equivalent column of $N_{\rm H} = (3.2 \pm 0.8) \times 10^{22}$ cm^{-2}. Although the scatter in the ratio of $A_V/N_{\rm H}$ for *Swift* bursts is nearly an order of magnitude, using the average value from Schady et al. (2007) this column corresponds to an extinction of $A_V \sim 4$ mag.

5.3.4 Further Investigations of the IR Calibration

The inferrence of SN-type dust for this object depends sensitively on the accuracy of our photometric calibration, and statements of its significance relative to the SMC fit depend equally critically on the precision in the JHK bands being as good as we claim: the Maiolino model is no longer preferred at $> 95\%$ confidence if, for example, additional uncertainty of >0.075 mag (in addition to the systematic uncertainties already applied; §5.3.2) is added in quadrature to all SED data points, or if >0.1 mag is added to just the H-band point (dependence on the other data points is much more robust: an addition of >0.2 mag to K is required, and any one of the J, Y, or I points could be removed completely). Therefore we have scrutinised in detail our infrared calibration procedures with particular emphasis on the PAIRITEL data. Because of the large number of exposures and large number of calibration stars detected at high S/N, the statistical errors on the zeropoint are small. Possible sources of systematic uncertainty (beyond the minor effects we have already discussed and included) we have considered include:

[9] Our K-band point is not covered by this figure, as the corresponding rest wavelength is shifted out of the IR window at $z = 6.2$. We assume an approximately linear extinction law in $1/\lambda$ below $\lambda_{\rm rest} < 3300$ Å.

[10] The Maiolino extinction curve is normalised to A_{3000} instead of A_V (the V-band at $z > 5$ is shifted into the mid-IR).

Instrumental color terms. PAIRITEL uses the same telescope, filter, and camera system as the 2MASS survey, and so there is no reason to expect color terms associated with the optics to be present. However, the presence of a significant bandpass difference could cause systematic discrepancies in calibration relative to field stars (see also §5.2.6), in particular in H and K bands where the afterglow color is much redder than any of the bright stars used for calibration. We inspected the magnitudes derived from stars in our deep stack as compared to the stars in 2MASS to search for a correlation between the magnitude offset and color; none was found.

Strong atmospheric variations in the effective filter bandpass. The infrared absorption bands associated with water in Earth's atmosphere exhibit time-variability, even within the observational windows. In particular, the exact shape of the J-band transmission function depends on the amount of precipitable water vapor (Cohen et al. 2003; however, the effect is small, with less than 2% variation in relative magnitudes), and the H-band contains a water ice absorption band which could introduce similar variations. Time-dependent absorption may therefore introduce temporary color terms not evident in the all-night stack. Therefore, we carefully inspected the time evolution of the observed zeropoints in all three bands. A small amount (up to 0.3 mag) of total transmission variability is indeed observed during the first 20 minutes, after which the zeropoint in all three bands is nearly constant within uncertainties. No significant variation is observed in the difference between zeropoints in different PAIRITEL bands, nor is any correlation observed between the overall zeropoint and the difference in zeropoints between two bands that would suggest chromatic variations in the transmission. Furthermore, the zeropoint appears constant (within our uncertainties) after $\sim$1400 s (the SED is determined at 10000 s). The MMTO cloud camera [11] shows no evidence of significant cloud cover at any point during the night, and weather archives indicate warm and stable conditions during the observation. Furthermore, in addition to PAIRITEL (Arizona), the Lick J-band (California) and MAGNUM (Hawaii) coeval measurements both give consistent results for the infrared magnitudes, giving additional confidence in our results; in particular both PAIRITEL and MAGNUM JHK data sets show the putative extinction feature independently. Therefore, we have no reason to believe that our SED is significantly affected by absorption features in Earth's atmosphere.

Intrinsic deviation of the GRB spectrum from a power-law. We have assumed in our fits that the intrinsic spectrum of the GRB was a simple power-law, as generally predicted by synchrotron theory. This assumption could, in principle, be violated. However, the most natural deviation from a power-law SED that might be expected (a spectral break within the optical/IR band) would create downward curvature in the intrinsic SED and actually require additional dust to produce the upward inflection feature that is observed. An SED modeled as the sum of two components (a steep power-law dominating $K-$band and a shallower power-law dominating J-band) would produce upward curvature, but cannot reproduce the sharpness of the observed feature unless the spectral index of the steep power-law is unrealistically red ($\beta > 4$). Additionally, it would be surprising that both components

[11] `http://skycam.mmto.arizona.edu/`

would rise and fall in synch with each other throughout the complex early evolution of the light curve, as is observed. Indeed, evidence for Maiolino-like dust is observed at every epoch with no significant variation in its strength or wavelength (Figure 5.4; also §5.4.2) with the exception of the final (GROND+NTT) SED, when the photometic uncertainties are too large to place any strong constraints on the extinction law.

Absorption from a DLA host system or Lyman-α forest. If the host galaxy is at the maximum redshift of z=5.2, our mean-opacity model of the Lyman-α forest may significantly underestimate the impact of hydrogen absorption on the I-band. To represent the most extreme possible case, we reran our dust models after adjusting the I-band flux upward by 20% (the approximate maximum dimunition expected in the Kuiper I-band filter assuming 100% opacity blueward of 7550Å, the limit on any DLA imposed by the HIRES spectrum) at $z = 5.2$. Even in this case, the Maiolino dust profile is strongly preferred (χ^2/dof = 2.5/2, versus 11.9/2 for SMC-like dust.)

5.4 Discussion

5.4.1 Rise of the Forward Shock and Constraints on the Lorentz Factor

The nearly achromatic first peak in the light curve shows the major hallmarks of the initial rise of the afterglow due to hydrodynamic deceleration of the fireball: a steep rise with no significant evidence of color change across the peak. Alternative possibilities can be generally ruled out: for example, the transition of the synchrotron peak frequency (which would also produce a peak were it to occur after the initial deceleration) would rise slowly and exhibit a blue-to-red color shift of $\Delta\beta = (p-1)/2 - (-1/3) = p/2 - 1/6$, completely incompatible with the observations of no color change or even limited red-to-blue evolution at this time. If the peak were due to dust destruction we would also expect significant color change during the rise itself, which is not apparent in the data. (We will examine the possibility of dust destruction in more detail in §5.4.2).

Within the category of hydrodynamical effects, there are then three possibilities for the rise of the afterglow: peak of the reverse shock, peak of the forward shock, or an off-axis jet.

We will consider the jet model (Granot et al. 2002; Granot 2005) first. In this case, the outflow is assumed to be strongly collimated with an observer located outside both the jet opening angle θ (observing angle $\theta_{\rm obs}$) and Lorentz cone $1/\Gamma$ (for a uniform jet; the theory can be suitably modified for a structured outflow: Kumar & Granot 2003). As the jet decelerates, a peak in the light curve will be observed once the flow has decelerated sufficiently for the $1/\Gamma$ cone to expand past the observer line of sight; this model has shown reasonable success representing the rising light curves of e.g. XRF 080330 (Guidorzi et al. 2009) and GRB 080710 (Krühler et al. 2009b). However, we are disinclined to favor this model on the grounds that it is expected to produce a very rapid post-break decay ($\alpha > 2$), which is not observed at late times ($\alpha_{2,f} = 1.27 \pm 0.04$). This could be accounted for by

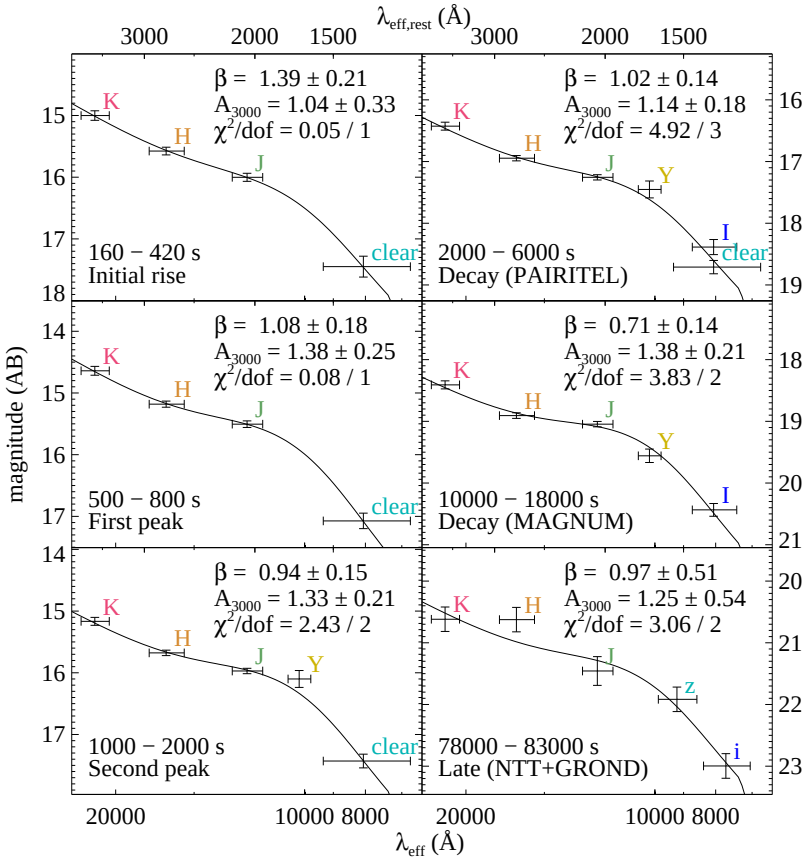

Figure 5.4 Time-dependent spectral energy distribution of GRB 071025 inferred after dividing the data into six different windows and re-fitting the flux parameters at each epoch using the light curve model. The resulting SED is then fit for spectral index β and extinction column A_{3000} at each epoch individually using a Maiolino extinction profile. The characteristic flattening between J- and H-bands is observed at every epoch (except at late times, when photometric errors are large) with no significant variation in its strength, increasing our confidence that it is a feature extrinsic to the GRB.

associating the second component (which dominates the late-time decay) with an on-axis wide jet undergoing its initial rise (as in Krühler et al. 2009b), but this model is somewhat contrived in our case, requiring fine-tuning of the physical properties of the two jets to accommodate the large variation in their jetting times while still ensuring that they peak within a factor of $\sim$2 in time and flux. Alternatively, refreshed shocks and continuous energy injection out to late times could also be invoked to explain the two-peaked structure and lack of late decay within this model. Even in that case, another criticism of this model is that the isotropic energy release observed for this burst ($E_{\rm iso} = 6.5 \times 10^{53}$ erg) is not expected for a burst seen off-axis.

Next, we consider if the initial rise could be due to the reverse shock (Sari & Piran 1999a). This model is particularly attractive, as the overall light curve qualitatively looks impressively similar to the theoretical curve of Zhang et al. (2003): the first peak corresponds to the reverse shock and the second peak to the forward shock. However, the initial rise is somewhat slower than expected from simple analytic models. The assumed reverse shock rising index $\alpha_{1,r}$ depends on the assumed zero time t_0 (which was set to the trigger time in the above fits), but t_0 would need to be shifted back in time by an amount greatly in excess of the duration of the burst itself to match the predicted $t^{3p-5/2}$ predicted for the reverse shock rise in the slow-cooling case (Kobayashi 2000). The alternate fast-cooling case predicts a slower rise (too slow: $t^{13/16}$) and also a bluer spectrum than is preferred by our extinction modeling. A wind model also requires fast-cooling and a blue spectrum, and an even slower rise ($t^{1/2}$). Therefore a reverse shock is not our preferred paradigm either, though we are hesitant to rule it out on the basis that the known complexity of early afterglows and the failure of even late-time closure relations to properly predict the decay rate α (e.g., Rykoff et al. 2009) suggest that the quantitative details of light curve behavior may not be an especially reliable way to evaluate different models.

The most straightforward scenario for the initial rise is the formation of the forward shock as the burst ejecta decelerates into the surrounding medium (e.g., Rees & Meszaros 1992). In this case $\alpha = -2$ for $\nu < \nu_c$, which is still somewhat too fast but still consistent with the data within 2σ if t_0 is moved backwards in time by about 30 s. In this model, the second peak is presumably due to additional energy input from the central engine into the forward shock, perhaps in the form of a slow-moving shell that catches up at around 1 ks (Rees & Meszaros 1998). This model is generally consistent with all available observations including the apparent rapid rise of the second component, though the observed significant (albeit minor) color change is not predicted. It could be due to the passage of a cooling break (though would imply $\nu > \nu_c$ initially and a too-steep $\alpha = -3$ during the rise) or another effect such as variation in the electron index p.

Interpreting this feature as a forward shock enables us to measure the initial Lorentz factor of the explosion. Following e.g. Mészáros (2006) and Rykoff et al. (2009), this can be estimated from observable parameters via the following relationship:

$$\Gamma_0 = 2\Gamma_{\rm dec} = 2\left(\frac{3E_{\rm iso}}{32\pi n m_{\rm p} c^5 \eta t_{\rm pk,z}^3}\right)^{1/8}$$

$$= 560(\frac{E_{\rm iso,52}}{\eta_{0.2} n_0 t^3_{\rm pk,z,10}})^{1/8}$$

Here $E_{\rm iso,52}$ is the isotropic-equivalent energy release in units of 10^{52} erg, $\eta_{0.2}$ is the radiative efficiency in units of 0.2, n_0 is the circumburst density in units of cm^{-3}, and $t_{\rm pk,z,10}$ is the afterglow peak time as observed at the burst redshift z in units of 10 s. For GRB 071025, using $E_{\rm iso} = 6.5 \times 10^{53}$ erg from our spectral model of the BAT data (at $z = 5$), we derive:

$$\Gamma_0 \sim 404 \eta_{0.2}^{-1/8} n_0^{-1/8}$$

Compared to direct pair-opacity lower limits inferred by the *Fermi* LAT (Abdo et al. 2009c,b), this is a relatively low value of Γ. However, it is fairly typical of afterglow-inferred values (100-1000, Rykoff et al. 2009, Molinari et al. 2007, Oates et al. 2009, Krühler et al. 2009a,b). This may indicate a difference in the types of populations probed by the two methods: the intrinsic delay in optical follow-up can measure Γ only for bursts for which the peak is quite late (low Γ), while high-energy photons themselves escape only if Γ is large. Hopefully, in the near future a joint *Swift-Fermi* burst with a luminous afterglow will allow both methods for estimation of the Lorentz factor to be compared.

5.4.2 Color Evolution: Limits on Dust Destruction

Because of the need for $\nu_{\rm IR} < \nu_c$ to explain the slow rise, there is no explanation within the standard assumptions of afterglow theory for the color change observed during the afterglow. One possible solution would be to invoke a time-variable electron index p at early times; a softening of the electron distribution during the complex early evolution would cause a corresponding softening of the afterglow emission.

Another intriguing possibility, however, is the photodestruction of dust along the GRB line of sight (Waxman & Draine 2000; Draine & Hao 2002). While we have ruled out this model as being the predominant origin of the rise of the light curve based on the modest or absent color change during the rising phase, it is still possible that it is occurring on a more subtle level. Because our light curve model assumes any color change is associated with a temporal break, it is not clear that such a change would be manifest in those models. As a result, we have scrutinised the overall color evolution of this GRB in significant additional detail to search for time-evolution in the extinction column A_V.

The large flat (grey) component of the Maiolino SN-type extinction law has the useful feature that the observed spectral slope of an SED measured over this region will closely match the intrinsic spectral slope even for a large extinction column, breaking the degeneracy between the intrinsic spectral index β and amount of reddening A_{3000}. At $z \sim 5$, the $J - H$ color (where the extinction law is grey) is affected only by the intrinsic spectral index and is nearly independent of A_{3000}, while $H - K$ and $J - I$ are affected by both the intrinsic index and reddening. This allows us to fit for β and A_{3000} independently with reasonable reliability, even with only a small number of points in the SED.

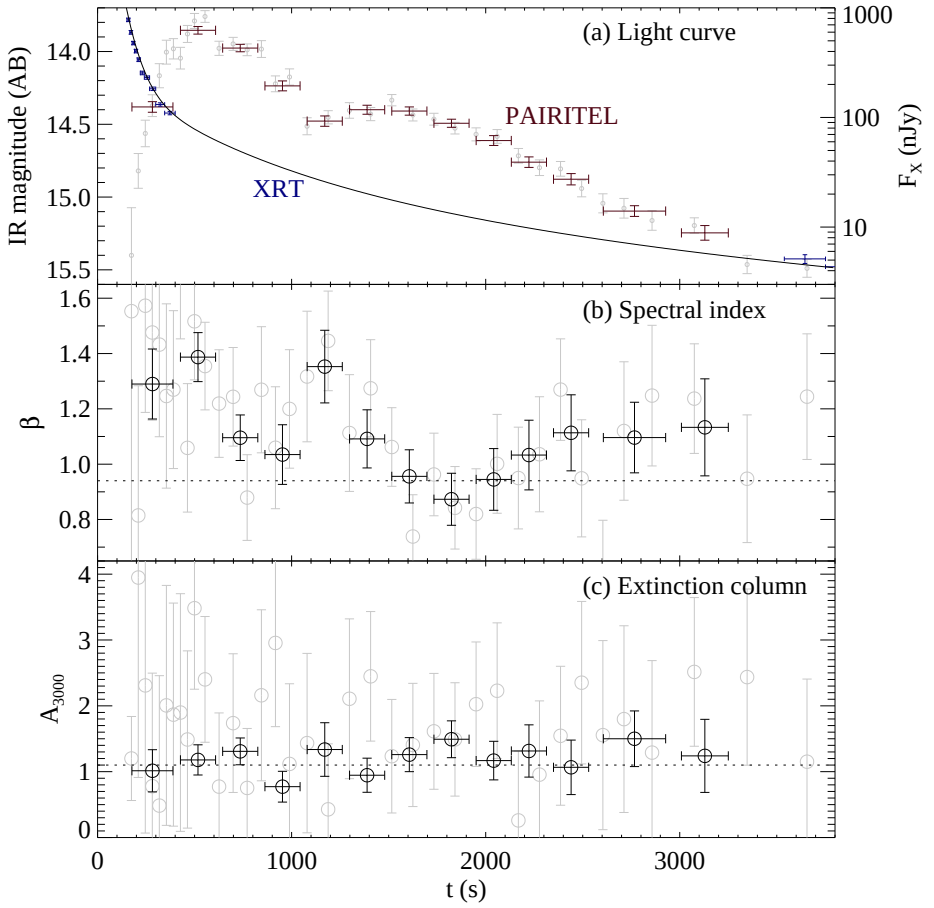

Figure 5.5 Models of color evolution in the afterglow of GRB 071025. (a) Infrared and X-ray light curves of GRB 071025 from PAIRITEL and the *Swift* XRT showing the divergent behavior in the two bands at these times. The early X-ray light curve is probably dominated by prompt emission, which is continuing in the BAT as well during this early decay phase. (b) The infrared/optical spectral index β, as measured by a fit to PAIRITEL JHK and RAPTOR unfiltered data. Fixed extinction $A_{3000} = 1.1$ mag is assumed. The SED is observed to redden significantly during the obervations. Grey points indicate fits to PAIRITEL JHK photometry only. (c) The time-dependent extinction column A_{3000} as measured by PAIRITEL and RAPTOR. The spectral index β is also free to vary in these fits. No evidence for variation in the extinction column is observed, ruling out dust destruction after ∼150 s.

We have, therefore, undertaken time-variable extinction fits using simultaneous measurements by mosaicing the PAIRITEL JHK data to temporally match the early-time RAPTOR points, which are a good approximation of the I-band (after a small adjustment of -0.08 mag: see §5.2.4 and Figure 5.1). Dust models were fit to this four-point SED as in section §5.3.3. Results are plotted in Figure 5.5.

As in the case of the complete data set, a Maiolino dust model is significantly preferred, with no evidence of evolution. In particular, the first mosaic (the only one contemporaneous with bright X-ray prompt emission, which is probably the dominant contributor to dust destruction: Fruchter et al. 2001) gives a modest value of $A_{3000} = 1.03 \pm 0.31$, fully consistent with our measurement at 10000 s. The corresponding 95% confidence limit on the decrease in the extinction column is $\Delta A_{3000} < 0.54$ mag. As we observe the H-band ($\lambda_{\rm eff} \sim 2770$Å in the host frame) rising by at least 1.5 mag between our first REM and PAIRITEL observations and the peak, this clearly rules out dust destruction as the cause of the early peak, consistent with our conclusions of the chromatic light curve modeling in §5.4.1. The entirety of the color variation appears to be due to variation in the intrinsic spectrum.

The significant dust column, combined with the lack of variability even during the end of the prompt phase, places a limit on the proximity of this dust to the GRB. The simulations of e.g. Perna et al. (2003) suggest that for a bright GRB virtually all dust within about 10 pc of the GRB will be destroyed, and significant destruction will be observed even out to 100 pc. While the exact constraints for this event will likely depend on detailed modeling of GRB 071025 specifically, this gives an approximate limit on the distance of the inferred absorbing dust column from the progenitor of at least $\gtrsim 10 - 100$ pc.

5.5 Conclusions

GRB 071025 joins a growing list of gamma-ray bursts caught early enough in their evolution to observe the rise and peak of the optical afterglow. Interpreting this as the initial rise of the forward shock, we estimate $\Gamma \sim 400$ for typical ISM densities. The mild red-to-blue color evolution of the afterglow appears to be due to unknown intrinsic properties of the forward shock, rather than dust destruction due to irradiation of the burst environment. All of these properties are similar to those inferred from early-time observations of other GRB afterglows.

However, the extinction law we measure is nearly unique. Most afterglows with well-characterised SEDs show little extinction (Kann et al. 2010), and events for which significant extinction has been observed have most commonly shown simple SMC-like profiles (e.g., Kann et al. 2006a; Schady et al. 2007), characterised by significant curvature (strong wavelength dependence) but no spectral features. More rarely, featureless or even grey light curves with no significant curvature have been inferred for some bursts (e.g., Savaglio & Fall 2004; Stratta et al. 2005; Chen et al. 2006; Perley et al. 2008e; Li et al. 2008d), and recently a small number of events have been discovered containing the clear signature of the 2175-Å bump present in the Milky Way and LMC (Krühler et al. 2008; Prochaska et al. 2009;

Elíasdóttir et al. 2009), though the details of these extinction curves show some differences from the average Milky Way ISM law. But to our knowledge, no other GRB sightline has shown clear evidence of dust not well-fit either by a local extinction template or by a simple, featureless law.

A possible exception is z=6.3 GRB 050904. For this GRB, an analysis by Stratta et al. (2007) favored the supernova-type dust of Maiolino et al. (2004) over standard SMC, Milky Way, and Calzetti models. Taken together, these two bursts would represent compelling evidence of an association between the observed dust model and the chemical evolution of the universe itself: to date, these events are the only bursts at $z \gtrsim 4.5$ showing evidence for significant extinction (all other bursts for which useful constraints on the extinction law have been possible are at $z \lesssim 4$: Kann et al. 2010).[12]

Strong chemical evolution of the dusty ISM is to be expected at $z \sim 5-6$: while most dust at low-to-moderate redshifts is thought to have been produced in AGB stars, during the first ∼1 Gyr following the Big Bang there had not yet been time for these stars to form in large numbers (Morgan & Edmunds 2003). The cosmic age of $1.1-1.4$ Gyr (assuming standard cosmological parameters with ΛCDM) allowed by our photometric redshift suggests that SN-like dust[13] is still the predominant source of obscuration in galaxies at this epoch and could provide important constraints on the evolution of the first galaxies and the production of early dust grains (e.g., Dwek et al. 2007). We note that the extinction column inferred from this galaxy is even larger than that inferred from the $z = 6.2$ QSO ($A_{3000} = 0.4-0.8$ mag, Maiolino et al. 2004), suggesting that even at this epoch, significant amounts of dust are present near sites of active star formation. Alternatively, the unusual dust could be associated with the relatively nearby environment of the GRB only and not necessarily representative of the galaxy itself. However, the survival of this late dust limits the distance from the progenitor to at least $10-100$ pc, suggesting that its association with the progenitor star-forming region cannot be too close.

The case of GRB 071025 is illustrative of the potential for early-time broadband photometry of GRBs to reveal the chemical history of the early universe (Hartmann et al. 2009). Well-characterised high redshift bursts are unfortunately rare (five years into the *Swift* mis-

[12]Unfortunately, the case of GRB 050904 is still ambiguous. Numerous other papers have investigated the dust properties of this event (Kann et al. 2007; Gou et al. 2007) and none of these other authors presented evidence favoring the Maiolino curve. Liang & Li (2009) have claimed detection of the 2175 Å feature. Therefore, we downloaded the available data on this source (Haislip et al. 2006; Tagliaferri et al. 2005; Kawai et al. 2006; Boër et al. 2006) and attempted to model the dust profile of this event using the same tools applied to GRB 071025, and found no evidence for a featured extinction curve. Indeed, the data are fully consistent with no extinction at all: our extinction fits converged to a simple power-law with $\beta \sim 1.0$, in agreement with the comprehensive analyses of Kann et al. (2007) and Gou et al. (2007) and—after the original publication of this work—the dedicated reanalysis of Zafar et al. 2010.

[13]Although the extinction profile observed is an excellent match to the models of dust produced in supernovae provided by Maiolino et al. (2004), we note that this does not demonstrate conclusively that this dust was formed in the supernova explosion itself. Alternatively, the dust could be formed in the ISM (Draine 2009) from refractory elements produced in SNe, from early carbon stars (Sloan et al. 2009), or from an unknown pre-AGB formation mechanism.

sion, only five other bursts to date have been confirmed to be at $z > 5$), and high-redshift events showing significant dust columns are even rarer (with the exception of the controversial 050904, above, none of the other $z > 5$ events show evidence for significant reddening: Greiner et al. 2009b; Ruiz-Velasco et al. 2007; Tanvir et al. 2009; Kann et al. 2010.) However, future GRB missions are likely to produce a large advancement in our understanding of these events. While several missions in development (e.g., JANUS and LOBSTER, Burrows et al. 2010) are designed to search for GRBs at the redshift extremes ($z > 7$) and characterise these events spectroscopically, infrared photometry acquired of the much more frequent moderate-redshift events ($z = 4 - 7$) will place important constraints on the abundance and composition of dust during these early stages of cosmic evolution, when galaxies were in the active phase of assembly and the first generations of stars led to a rapid build up of the metal content of the universe.

Acknowledgments

We thank C. Melis at UCLA for acquiring the Lick infrared photometry. Part of the funding for GROND (both hardware as well as personnel) was generously granted from the Leibniz-Prize (DFG grant HA 1850/28-1) to Prof. G. Hasinger (MPE).

Table 5.1 Light Curve Best-Fit Parameters

Parameter	symbol	value
C1 rising index	$\alpha_{1,\mathrm{r}}$	-1.66 ± 0.15
C1 fading index	$\alpha_{1,\mathrm{f}}$	1.73 ± 0.21
C2 rising index	$\alpha_{2,\mathrm{r}}$	-11.0 ± 2.1
C2 fading index	$\alpha_{2,\mathrm{f}}$	1.27 ± 0.04
C1 peak time (s)	$t_{\mathrm{pk},1}$	575 ± 42
C2 peak time (s)	$t_{\mathrm{pk},2}$	1437 ± 17
Ratio of C2/C1 peak flux	F_2	0.24 ± 0.03
Color change across C1 peak	$\Delta\beta_{1(\mathrm{rf})}$	-0.20 ± 0.14
Color change between C1/C2	$\Delta\beta_{12}$	-0.26 ± 0.12
Flux at $t = 10000$s	F_R	5.76 ± 1.15
	F_I	34.4 ± 3.48
	F_Y	84.45 ± 8.66
	F_J	118.9 ± 4.79
	F_H	155.4 ± 6.26
	F_K	250.4 ± 15.1

Summary of free parameters fit in the light curve model. Peak times are for the J-band filter. Flux parameters are not corrected for Galactic extinction; uncertainties include added systematics. "C1" refers to the first light-curve component; "C2" refers to the second component.

Table 5.2 Results of Extinction Fits

Dust Model	β	A_V mag	R_V	χ^2 / dof
none	1.64 ± 0.08	0		33.3 / 3
SMC	0.08 ± 0.42	0.12 ± 20.6	2.73	20.8 / 2
MW	1.64 ± 0.08	< 0.07	3.1	33.3 / 2
LMC	1.64 ± 0.08	< 0.07	3.2	33.3 / 2
GRB080607	1.64 ± 0.08	< 0.12	4.0	33.3 / 2
Calzetti	0.00 ± 0.80	1.42 ± 0.68	4.0	25.3 / 2
Fitzpatrick	0.65	2.52 ± 0.97	5.26 ± 0.53	1.49 / 0
Maiolino SN	0.96 ± 0.14	1.09 ± 0.20[14]		0.81 / 2

Summary of key parameters from fits of various dust models to the SED of GRB 071025 as modeled at t=10000 s. A redshift of $z = 5$ is assumed in all cases.

Chapter 6

GRB 080607: An Ultraluminous Burst Behind a Dusty Molecular Cloud

An earlier version of this chapter was previously published as AJ 141:36–49[1].

Abstract

We present early-time optical through infrared photometry of the bright *Swift* gamma-ray burst (GRB) 080607, starting only 6 s following the initial trigger in the rest frame. Complemented by our previously published spectroscopy, this high-quality photometric dataset allows us to solve for the extinction properties of the redshift 3.036 sightline, giving perhaps the most detailed information to date on the ultraviolet continuum absorption properties of any sightline outside our Local Group. The extinction properties are not adequately modeled by any ordinary extinction template (including the average Milky Way, Large Magellanic Cloud, and Small Magellanic Cloud curves), partially because the 2175 Å feature (while present) is weaker by about a factor of two than when seen under similar circumstances locally. However, the spectral energy distribution is exquisitely fitted by the more general Fitzpatrick & Massa (1990) parameterization of Local-Group extinction, putting it in the same family as some peculiar Milky Way extinction curves. After correcting for this (considerable, $A_V = 3.3 \pm 0.4$ mag) extinction, GRB 080607 is revealed to have been among the most optically luminous events ever observed, comparable to the naked-eye burst GRB 080319B. Its early peak time ($t_{\rm rest} < 6$ s) indicates a high initial Lorentz factor ($\Gamma > 600$), while the extreme luminosity may be explained in part by a large circumburst density. Only because of its early high luminosity could the afterglow of GRB 080607 be studied in such detail in spite of the large attenuation and great distance, making this burst an excellent prototype for

the understanding of other highly obscured extragalactic objects, and of the class of "dark" GRBs in particular.

6.1 Introduction

The most extreme gamma-ray bursts (GRBs) have often been the most illuminating — both literally and figuratively. The enormous isotropic-equivalent energy of GRB 971214 (redshift $z = 3.43$, $E_{\rm iso} = 3 \times 10^{53}$ erg; Ramaprakash et al. 1998; Odewahn et al. 1998; Kulkarni et al. 1998) emphatically demonstrated the need for collimation to bring the energy budget of long-duration GRBs within physically reasonable values. Observations of the mag 9 optical flash of GRB 990123 ($z = 1.61$, $E_{\rm iso} = 3.4 \times 10^{54}$ erg; Akerlof et al. 1999; Kulkarni et al. 1999) anticipated the utility of GRBs to probe the high-redshift universe: similar events would be easily detectable even at $z > 6$. This possibility was first vindicated by GRB 050904 ($z = 6.29$, $E_{\rm iso} = 1.2 \times 10^{54}$ erg; Kawai et al. 2006; Sugita et al. 2008), which for three years remained the most distant GRB known and, at the time, was also the most luminous optical transient observed in the Universe (Kann et al. 2007). The latter record has since been surpassed dramatically by GRB 080319B ($z = 0.937$, $E_{\rm iso} = 1.3 \times 10^{54}$ erg), whose optical afterglow peaked at $V \approx 5$ mag (Racusin et al. 2008; Bloom et al. 2009; Woźniak et al. 2009). The current record for the bolometric isotropic-equivalent energy is held by the *Fermi* burst GRB 080916C ($E_{\rm iso} = 6.5 \times 10^{54}$ erg; Abdo et al. 2009c; Greiner et al. 2009c).

Joining this list of record setters is GRB 080607 ($z = 3.036$; Prochaska et al. 2009), with $E_{\rm iso} = 1.87 \times 10^{54}$ erg (Golenetskii et al. 2008c). This event is remarkable not only for its intrinsic properties, but also because of its unusual environment: a Keck spectrum obtained starting only 20 min after the burst (Prochaska et al. 2009) reveals that the sightline penetrates a giant molecular cloud in the host galaxy, obscuring the rest-frame visible light by $A_V \approx 3$ mag of extinction (or ~ 6 mag at 1600 Å, corresponding to the observed R band) before it even began its journey through intergalactic space.[2] In spite of this extreme attenuation, the event was bright enough to be detected by small optical telescopes for over an hour.

The spectroscopic properties of this event have been previously discussed by Prochaska et al. (2009), along with a preliminary analysis of its extinction properties; further analysis of the spectra was also presented by Sheffer et al. (2009). In this Chapter, we analyze several other aspects of this burst, from the prompt emission (and simultaneous optical detection) through a late-time search for the host galaxy, and we present a significantly expanded discussion of its extinction properties. In §6.2 we describe our early-time multicolor observations of the afterglow with several different robotic telescopes. We analyze the optical light curve in §6.3.1–6.3.2 and show no correlation between the prompt emission behavior and the early optical observations, starting at only 6 s post-trigger in the host frame, and we present limits on color variations at early times. In §6.3.3–6.3.4 we examine in more

[2]Dust extinction is limited or absent for the vast majority of well-studied GRBs (Schady et al. 2007; Kann et al. 2010), and no other GRB displays firm evidence for molecular lines.

detail the combined photometric and spectroscopic spectral energy distribution (SED) and place our final constraints on the host-galaxy extinction properties, demonstrating the firm detection of a 2175 Å bump, the highest-redshift detection of this signature to date. The X-ray light curve is analyzed in §6.3.5 to search for evidence of dust scattering in the host at these wavelengths. In §6.4 and §6.5 we place GRB 080607 and its environment in the context of other GRBs, both ultraluminous and bright events like GRB 080319B as well as the poorly understood class of extremely dark bursts (Jakobsson et al. 2004a).

6.2 Observations

6.2.1 Swift

GRB 080607 triggered the Burst Alert Telescope (BAT, Barthelmy et al. 2005) on the *Swift* satellite (Gehrels et al. 2004) at 06:07:27 on 2010 June 7 (UT dates are used throughout this work; times are referenced to this trigger time, although it is important to note that there was significant emission before this trigger). The light curve (Figure 6.1) is spiky and erratic, exhibiting a dominant peak at ~ 4 s as well as numerous other, fainter peaks ranging from a few seconds before the trigger out to $\sim$130 s after, when the signal falls below the background level. *Swift* slewed immediately to the source and began pointed observations with the X-ray Telescope (XRT, Burrows et al. 2005c) at 82 s, followed by observations with the Ultraviolet Optical Telescope (UVOT; Roming et al. 2005) beginning at 100 s. Observations continued until 1049 s, after which *Swift* slewed away temporarily, returning to the field at 4226 s. From then, observations continued intermittently over the next four days, after which the X-ray flux was too faint for *Swift* to detect.

The BAT observations were processed using the *Swift* HEAsoft 6.5 software package via the burst pipeline script, `batgrbproduct`. We calculated spectral parameters both directly and using the Bayesian formalism described by Butler et al. (2007). Fit to this burst alone, a Band et al. (1993) model provides no significant improvement over a basic power-law fit over BAT's 15–350 keV energy range (photon index $\Gamma = 1.16$), suggesting a peak energy above the BAT range. Using the Band model Bayesian estimate of $E_{\rm peak,obs} = 902^{+1170}_{-460}$ keV and the measured redshift ($z = 3.036$), we estimate a broad-band isotropic-equivalent energy of $E_{\rm iso} = 2.8^{+1.3}_{-0.9} \times 10^{54}$ erg. These values place GRB 080607 second in $E_{\rm iso}$ rank among all *Swift* GRBs to date and in the same regime as extreme GRBs 080319B and 990123.

GRB 080607 was observed by other satellites as well (Konus-Wind and Super-AGILE), enabling a precise measurement of the spectral parameters. An in-depth analysis of the Konus data will be presented in future work by Sbarufatti et al., but preliminary calculations from Golenetskii et al. (2008c) give the following values: $E_{\rm peak,obs} = 394^{+58}_{-54}$ keV and $E_{\rm iso} = 1.87^{+0.11}_{-0.10} \times 10^{54}$ erg. These are at the low end of, but generally consistent with, the Bayesian *Swift* result, and confirm that GRB 080607 was among the most luminous and intrinsically hardest (highest $E_{\rm peak,rest}$) GRBs observed by any satellite.

The X-ray afterglow was detected throughout the XRT observations; XRT data were

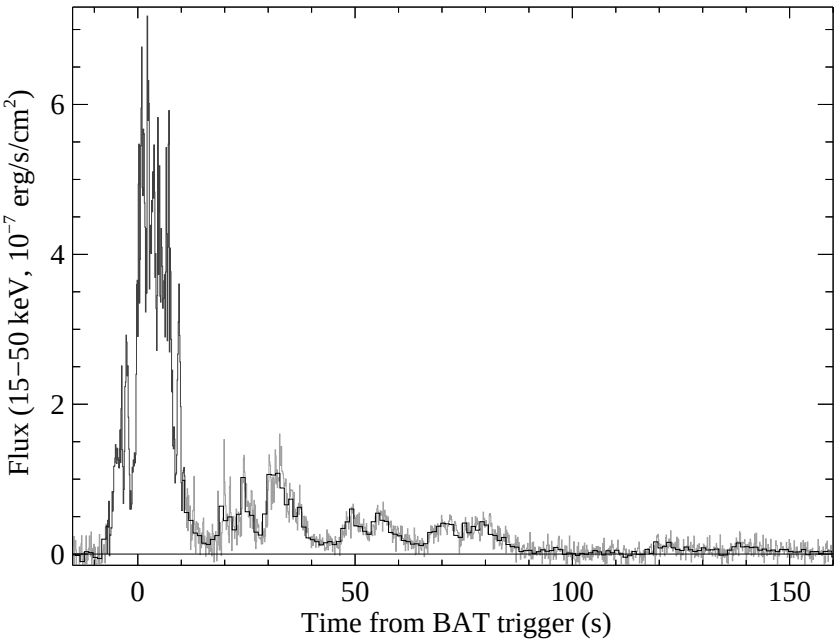

Figure 6.1 Gamma-ray light curve of GRB 080607 (at a combination of 128 ms and 1 s binning), showing the bright initial pulse complex followed by an additional series of pulses lasting for the next several minutes. Original data for the light curve are taken from the *Swift* Burst Analyser (Evans et al. 2010).

reduced by the procedures of Butler & Kocevski (2007a). The UVOT afterglow, by contrast, is only marginally detected in the earliest epoch, and only in White and V filters (Schady & Mangano 2008). Both filters are heavily impacted by damped Lyman-α absorption at $z = 3.036$, and so are not used in our analysis.

6.2.2 ROTSE

The ROTSE-III (Robotic Optical Transient Search Experiment) array is a worldwide network of 0.45 m robotic, automated telescopes, built for fast responses to GRB triggers (Akerlof et al. 2003). ROTSE-IIIb, located at the McDonald Observatory, Texas, responded immediately to the initial Gamma-ray Burst Coordinate Network (GCN, Barthelmy et al. 1995) alert. The first image started at 06:07:49.0 (22 s after the burst), clearly detecting a bright afterglow at the XRT position in this exposure. All ROTSE-III images were processed with our custom RPHOT photometry program based on the DAOPHOT (Stetson 1987) point-spread function (PSF) fitting photometry package (Quimby et al. 2006). The unfiltered, thinned ROTSE-III CCD has a peak sensitivity in the wavelength range of the R band. The ROTSE magnitudes were thus adjusted using the median offset from the USNO B1.0 R-band measurements of selected field stars. Observations are presented (along with photometry from all other telescopes, below) in Table B.4.

6.2.3 Super-LOTIS

Super-LOTIS (Livermore Optical Transient Imaging System) is a robotic 0.6 m telescope dedicated to the search for optical counterparts of GRBs (Williams et al. 2004, 2008). The telescope is housed in a roll-off-roof facility at the Steward Observatory Kitt Peak site near Tucson, AZ. Super-LOTIS triggered on GRB 080607 and began observations at 06:08:03 (36 s after the trigger), acquiring a series of frames in the R band. The images were reduced and photometry performed using standard techniques, calibrated relative to nearby Sloan Digital Sky Survey (SDSS) standard stars.

6.2.4 KAIT

The Katzman Automatic Imaging Telescope (KAIT) at Lick Observatory (Li et al. 2003b) also responded automatically to the *Swift* alert and began taking observations, the first starting at 06:09:25, 118 s after the BAT trigger. The KAIT filter sequence consists of a series of unfiltered observations, followed by a cycle through V, I, and unfiltered exposures. The optical afterglow was detected in all filters, although it is quite faint in the V band. Following this sequence, a series of unfiltered and I-band exposures was manually added, although the afterglow was not detected in the I band and only marginally detected in our unfiltered exposures at that time (even after stacking).

Images were reduced using standard techniques. This left some residual variation in the background sky, which was removed by subtraction of an illumination frame. We used

aperture photometry to measure the afterglow flux, calibrating relative to SDSS stars in the field transformed to the Johnson/Cousins system using the equations of Lupton (2006). The unfiltered exposures were calibrated to the R band (Li et al. 2003b).

6.2.5 PAIRITEL

The robotic Peters Automatic Infrared Imaging Telescope (PAIRITEL; Bloom et al. 2006e) consists of the 1.3 m Peters Telescope at Mt. Hopkins, AZ — formerly used for the Two Micron All Sky Survey (2MASS; Skrutskie et al. 2006) — refurbished with the southern 2MASS camera. PAIRITEL uses two dichroics to image in the infrared (IR) J, H, and K_s filters simultaneously every 7.8 s.

PAIRITEL responded to the initial BAT alert and slewed immediately to the source. Observations began at 06:08:44, 77 s after the trigger, and continued for the next 1.3 hr until the source reached its hour-angle limit.

The early-time (<0.3 hr) raw data files were processed using standard IR reduction methods via PAIRITEL Pipeline III (Klein et al., in prep) and resampled using SWarp (Bertin et al. 2002) to create $1.0''$ pixel^{-1} images for final photometry. Due to changing sky conditions that complicated the otherwise superior Pipeline III reductions in the K_s band as the source approached the horizon, the remainder of the raw data were reduced using an older pipeline which utilized a "dark bank" that more robustly handles flat-fielding in such cases.

PAIRITEL's standard observing cycle is to take three 7.8 s exposures in immediate succession at each dither position. While the early afterglow is detected in even the shortest 7.8 s frames, for signal-to-noise ratio (S/N) and calibration considerations, we report 23.4-s "triplestacks" (the median of all three images at each dither position) as our shortest exposures. These images were further binned at successively later times to further improve the S/N.

Aperture photometry was performed using custom Python software, utilizing Source Extractor (SExtractor; Bertin & Arnouts 1996) as a back end. Four calibration stars present in all images were chosen based on brightness, proximity of nearby contaminating sources, and location relative to bad pixels. The optimal aperture of $\sim 3''$ radius was determined by minimizing the absolute error relative to 2MASS magnitudes of our four calibration stars.

Calibration was performed by redetermining the zero-point for each image individually by comparison to 2MASS magnitudes using these four stars. The resulting statistical uncertainty in the zero-point is negligible relative to other sources of error. Additional, systematic sources of error are addressed in detail by Perley et al. (2010); we use a similar procedure here to determine the total uncertainty of each point.

6.2.6 P60

The robotic Palomar 60 inch telescope (P60; Cenko et al. 2006h) automatically responded to the *Swift* trigger for GRB 080607, executing a predefined sequence of observa-

tions in the Kron R and Sloan i' and z' filters beginning 174 s after the burst trigger time. Individual images were reduced in real time using standard IRAF[3] routines. The images were calibrated with respect to several dozen field stars from the SDSS Data Release 7 (Abazajian et al. 2009), using the filter transformations of Jordi et al. (2006) for the Kron R filter.

6.2.7 UKIRT

The United Kingdom Infrared Telescope (UKIRT) becan observations of GRB 080607 starting at approximately 39 min after the GRB trigger. An initial series of three K-band exposures was acquired, followed by a $JHJK$ sequence, repeated three times. The afterglow is detected at very high significance ($> 10\sigma$) in all coadded frames.

Observations were reduced using standard IR techniques and calibrated relative to 2MASS standards in the field. In the case of the K observations, we convert K to K_s using color terms derived from bright 2MASS standards in the field, but because the afterglow is extremely red and the field stars are all much bluer (with very limited dispersion in color), this term is quite uncertain, and the K observations are not used in fitting.

The telescope was dithered only once during the exposure sequence (after the first three K-band exposures). A pixel-sampling uncertainty (0.025 mag, derived from the median absolute offset of bright stars before and after the dither) was added in quadrature to all data points, but it should be noted that this uncertainty is correlated (points before and after the dither are all affected in nearly the same way; indeed, a small shift is evident between the first and last three K-band exposures.)

Although we do not find significant evidence of color change for this GRB afterglow (§6.3.1), given that the UKIRT points are nonsimultaneous with all other filters we do not include them when deriving the broad-band SED used for modeling (§6.3.3). On the other hand, we do use them to constrain the late-time evolution of the light curve.

6.2.8 Keck Spectroscopy

We initiated spectroscopic observations of the afterglow with the Low Resolution Imaging Spectrometer (LRIS; Oke et al. 1995) on the Keck I 10 m telescope at 13 min after the *Swift* trigger, although due to poor guiding this first frame was not usable. The first exposure used in our analysis began at 20.1 min following the trigger. Several additional exposures were taken over the next 2 hr using the B600 grism and both the R400 and R1200 gratings; our final observations span a wavelength range of 3000–9000 Å. Observations were flux calibrated relative to the spectroscopic standard HZ 44. More details on these spectroscopic observations and our reductions are given by Prochaska et al. (2009).

[3]IRAF is distributed by the National Optical Astronomy Observatory, which is operated by the Association for Research in Astronomy, Inc., under cooperative agreement with the National Science Foundation (NSF).

6.2.9 Keck Host-Galaxy Imaging

The field of GRB 080607 was imaged in several deep integrations at Keck through various optical/IR filters (g, I, and K_s). A likely host galaxy is marginally detected in each of these observations. A log of our ground-based host observations is reported in Table 6.1.

The host galaxy is, however, well detected at 1.6 μm in a deep *Hubble Space Telescope (HST)* image using WFC3, as well as in both of the warm *Spitzer* IRAC channels (3.6 μm and 4.5 μm). The extreme optical faintness of this system, while partially due simply to its high redshift ($z = 3.036$), makes this galaxy of particular interest: determination of the redshift would be exceptionally difficult using traditional field-survey techniques, illustrating the unique ability of GRBs to select and study optically faint galaxies at high redshift. Its red color, likely reflective of large internal dust content, is also noteworthy. Further discussion of the host galaxy, including detailed analysis of both the ground- and space-based imaging, is presented by Chen et al. (2010).

6.3 Analysis

6.3.1 Light Curve

The multi-band light curve of GRB 080607 is plotted in Figure 6.2. After an initially slow decay the light curve steepens (decay index $\alpha = 1.6$, using the convention $F \propto t^{-\alpha}$) before flattening out at 1000 s to a temporarily flat decay. This slow decay lasts for approximately another hour before fading rapidly, falling below the detection threshold of subsequent KAIT images, but still well detected by UKIRT.

The light curve was fitted using the techniques described by Perley et al. (2010) and previous works by our group, modeling the light curve as the sum of several broken power laws. Our temporal coverage of this event is limited (ending at 10^4 s), making the analysis simple: we employ two Beuermann et al. (1999) broken power laws, one to describe the early behavior and a second to describe the later flattening. Because we do not detect the rising phase of the afterglow, the pre-break index of the first power-law component is not usefully constrained by our data and is fixed arbitrarily to -0.5. The X-ray light curve (after 130 s) was fitted using similar techniques, but with unbroken power laws. We do not attempt to model the low-level late-time X-ray flaring that appears to be present in the data.

Modest but significant color change has been previously observed in early-time GRB afterglows (see Chapters 3 and 5 for prominent examples), a possibility which we model by allowing the intrinsic spectral power-law index β ($F \propto \nu^{-\beta}$) to vary between components or across breaks. However, in the case of GRB 080607, any such color change is not significant: the change in intrinsic index between the fast-decay and flat components is just $\Delta\beta = 0.05 \pm 0.07$ and only modestly improves the goodness of fit. Therefore, for simplicity we assume no color change during our observations of this burst.

Because of the relatively short temporal coverage and lack of overlap between the X-ray and optical light curves (except at the earliest times; see §6.3.2), it is difficult to unambigu-

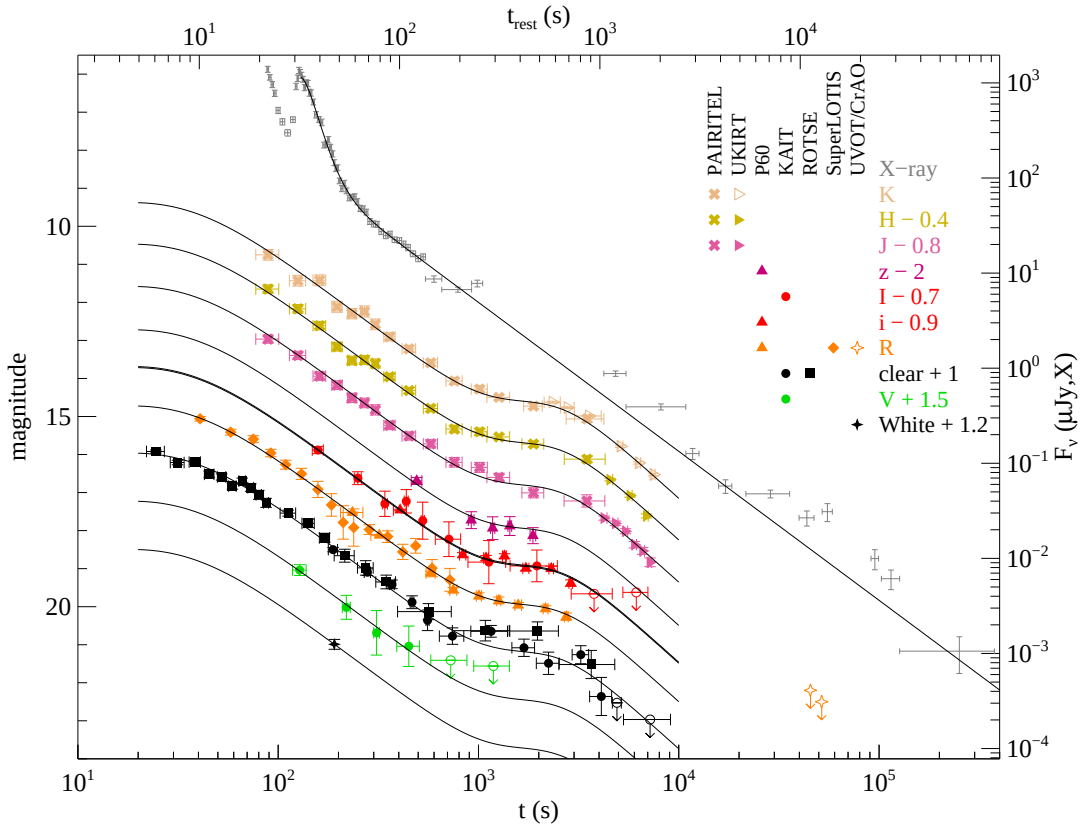

Figure 6.2 Multi-band light curve of GRB 080607 from a variety of ground-based telescopes as well as the *Swift* XRT, fit to a sum of two broken power laws. (XRT data are fit to a sum of two unbroken power laws.) Magnitudes are in the Vega (VRI), SDSS (ri), or 2MASS (JHK) systems and (with the exception of R and K_s) have been shifted as indicated for clarity; these magnitudes are *not* corrected for Galactic extinction (which is nearly insignificant) or host-galaxy extinction (which is very large). The afterglow initially fades slowly, then steepens; it briefly levels out at 10^3 s before breaking again and is not detected after 5000 s. The late-time R-band limits are from Rumyantsev & Pozanenko (2008). We use the BAT trigger time for t_0 (06:07:27 on 2010 June 7), which corresponds to the start of the largest prompt-emission pulse; using the start of gamma-ray emission instead does not significantly change the qualitative results.

ously associate the features of the light curve with intrinsic properties of the burst itself. The moderately rapid early decay ($\alpha_{\rm opt} \approx \alpha_{\rm X} \approx 1.6$) is suggestive of a reverse shock or possibly a wind-driven medium (see also §6.4.2), although we cannot distinguish between these cases with the data available, and a constant-density environment is also plausible if both optical and X-ray bands are above the cooling break. The achromatic flattening (and subsequent rapid falloff) may be produced by a density variation, energy reinjection episode, or other feature. Interestingly, the X-ray flux increases significantly just before the end of the first-orbit observations (and just before the start of the optical flattening), but because the flattening itself corresponds to the *Swift* orbit gap it is difficult to determine whether the two features share a common origin.

6.3.2 Absence of Optical/High-Energy Correlations

Our optical follow-up observations of this burst begin extremely early. The ROTSE coverage begins at only 21 s after the BAT trigger, corresponding to less than 6 s in the GRB rest frame. The prompt emission was still extremely active at this time: at least five major gamma-ray flares occurred during our optical observations, the last of which was also caught at X-ray wavelengths by the XRT. PAIRITEL, KAIT, and SuperLOTIS were all observing during this last flare.

Even in this rich overlapping dataset, there is no correlation visible between the optical and high-energy light curves of the type seen by, for example, Vestrand et al. (2005), Blake et al. (2005), and Beskin et al. (2010). In Figure 6.3 we overplot the gamma-ray, X-ray, and optical light curves using the same relative scaling. In spite of the erratic, flaring high-energy behavior, we see no sign of significant deviation of the optical light curves from their smooth power-law behavior at any point. This is consistent with other ROTSE-followed bursts (e.g., Yost et al. 2007; Rykoff et al. 2009) and provides another clear example of a burst whose afterglow behavior is clearly divorced from that of the prompt emission.

The lack of even modest influence of the prompt emission on the afterglow may initially seem surprising: even if truly prompt (internal-shock) emission is absent in this band, one might expect that some of the energy being released so liberally by the central engine might end up in the external shock, causing a less dramatic but still observable rebrightening of the afterglow (a refreshed shock; Panaitescu et al. 1998). We note, however, that despite the intense flaring shown in Figure 6.3, this emission is actually dwarfed by an earlier episode: the initial pulse of the prompt emission (see Figure 6.1) exceeds any of the later spikes by an order of magnitude in both intensity and energy, and it is this initial pulse that dominates the energetics of the burst. The later flares are much more modest by comparison, so even presuming direct input from outflow (revealed by the prompt emission) to external shock (revealed by the afterglow), the absence of further brightening is not necessarily surprising.

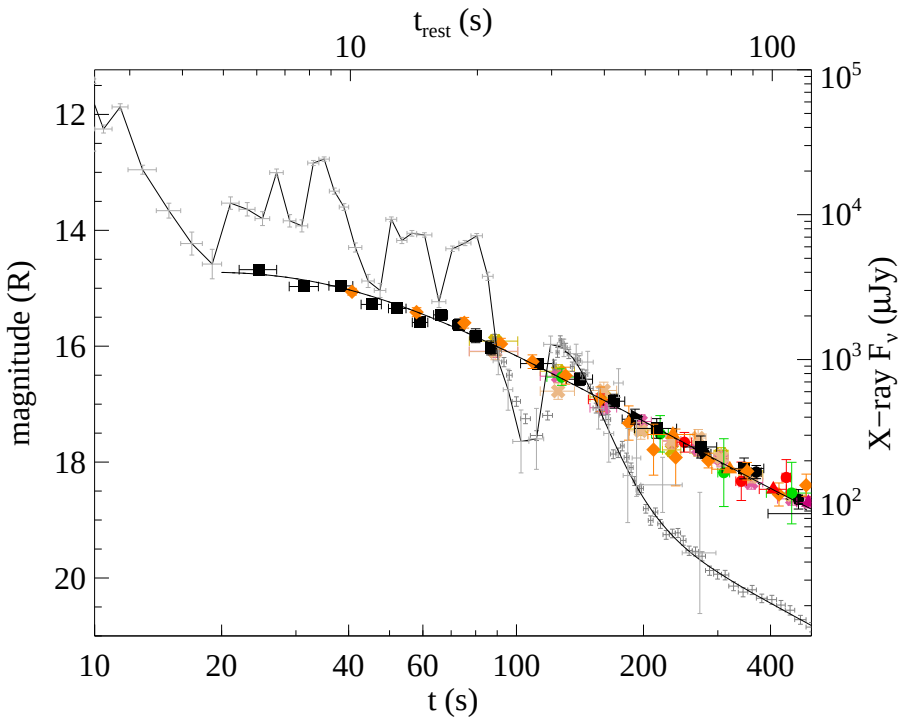

Figure 6.3 Early-time optical and gamma-ray/X-ray light curves of GRB 080607, demonstrating the extremely early peak $t_{\rm rest} \lesssim 6$ s as well as the absence of any visible correlation between the optical and high-energy light curves. (Optical fluxes in other bands have been scaled to match the R band; the gamma-ray light curve is scaled to match the X-ray curve.) Symbols are the same as in Figure 6.2.

6.3.3 Spectral Energy Distribution

Our light-curve fits naturally provide values for the afterglow flux in each filter at any given time, allowing us to model the SED at any time during our observations. Because of the absence of significant color change, the choice of extraction epoch is arbitrary; 300 s is chosen in this case (when all ground-based robotic telescopes were observing and the afterglow was still bright enough to be well detected in all bands).

The Keck optical spectroscopy covers a wide range of wavelengths and was carefully flux calibrated: photometric standard stars were observed immediately after our observations at similar airmasses and the night was photometric throughout. Accordingly, we couple our spectrum to the photometry to improve the precision of our broad-band modeling.

The optical spectrum is replete with lines from a variety of elements and molecules at the host-galaxy redshift of 3.036. The analysis of these line features is discussed extensively by Prochaska et al. (2009) and Sheffer et al. (2009), and we will not repeat it here; our primary interest is in the continuum. Although the contribution of absorption lines is usually ignored in GRB photometric dust modeling, the lines in the spectrum of GRB 080607 are so abundant and so strong that ignoring them would create systematic errors significantly larger than our photometric uncertainties in both the spectrum itself and in the broad-band photometry. In addition, nearly the entire spectrum at wavelengths shorter than ∼6900 Å is affected by a forest of weak lines from vibrationally excited H_2^*, further complicating the analysis.

Fortunately, we are able to correct for these effects. We use the line list presented in Table 1 of Prochaska et al. (2009) to identify all regions of the spectrum affected by ionic lines, including the entire spectrum blueward of 5400 Å, which is affected by the host damped Lyman-α and the Lyman-α forest. In addition, the spectrum is corrected for the subtler but more widespread H_2^* absorption using the model developed by Sheffer et al. (2009). We then fit a sixth-order polynomial to the ionic line-free regions of this corrected spectrum to create a continuum model and perform synthetic photometry using both the model spectrum and the observed, uncorrected spectrum (and take the ratio) to calculate an adjustment factor with which to convert the observed (line-affected) fluxes to continuum (line-free) fluxes for each of our broad-band filters covering the optical spectrum (R, I, i, and V; we assume the line contribution is small further to the red). We also wish to use the flux-calibrated spectrum itself in later analysis, so we scale the spectrum to the photometric SED extraction epoch of 300 s (the scale factor is determined by the value that minimizes χ^2 for our extinction fits; see §6.3.3) and bin the flux in blocks of 200 Å (excluding line-affected regions). Uncertainties are determined by combining the statistical uncertainties from the spectrum with a systematic term of 3% per bin to incorporate any uncertainty in the flux calibration (10% is used for <5500 Å and >9000 Å, which are especially uncertain.) Using this technique, we generate a line-corrected narrow-band SED spanning 5400–9200 Å to complement our line-corrected photometry. The afterglow fluxes from direct and synthetic photometry are presented in Tables 6.2 and 6.3, respectively.

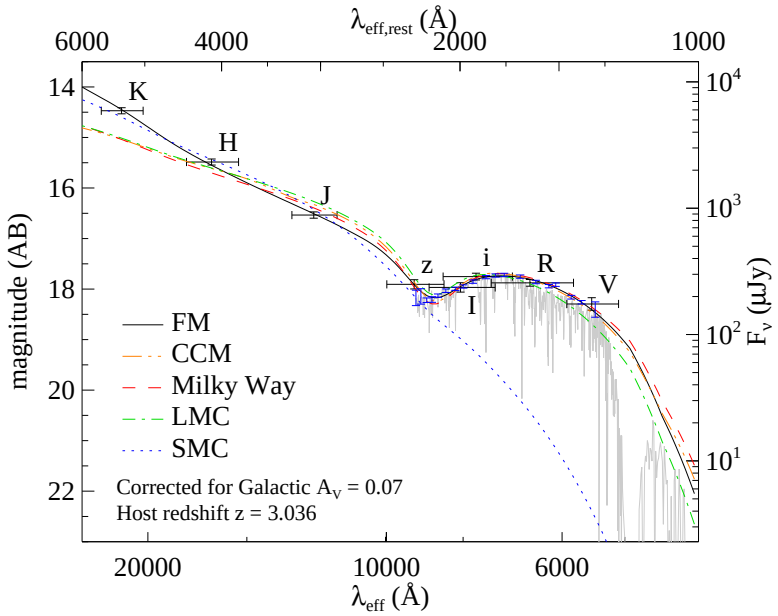

Figure 6.4 The combined photometric and spectroscopic SED of GRB 080607 fitted with several different extinction models. (FM = Fitzpatrick & Massa 1990, CCM = Cardelli, Clayton, & Mathis 1989). Black error bars indicate broad-band photometry; blue error bars show the binned pseudo-photometry as derived from the Keck spectrum and corrected for line absorption (including H_2^*). The light-grey line shows the spectrum (mostly unbinned and including all lines). Several different extinction fits are shown; only the general FM model (solid black) is an acceptable fit to the data. The SMC curve shown is a fit to the IR data only (an SMC fit to all data converges to $A_V = 0$ mag).

Extinction Fitting

The combined photometric and spectroscopic SED is plotted in Figure 6.4. It is immediately evident that this curve is unlike almost any other GRB SED that has been observed in detail to date. First, the color is extremely red: a power-law fit to the broad-band photometry would give a spectral slope ($F \propto \nu^{-\beta}$) of $\beta \approx 3$, at odds with the theoretically expected value of $\beta = 0.5$–1.2 for a fading early afterglow (Sari et al. 1998). Second, it is not monotonic: the flux drops sharply from the K_s band until ∼2200 Å in the rest frame before actually recovering, showing a local maximum at ∼1600 Å before falling again further to the blue.

These properties are immediately recognizable as signatures of dust extinction, and particularly of Milky-Way like extinction with its broad 2175 Å absorption band. This strong extinction imprint, in combination with our high-S/N afterglow observations spanning the entire optical/near-IR window, permits analysis of the rest-frame UV extinction properties at a level of detail that is almost never possible with GRBs (or indeed, with any other technique at this redshift range).

To constrain the dust properties, we initially followed the standard procedure (e.g., Jakobsson et al. 2003; Schady et al. 2007; Heng et al. 2008; Kann et al. 2010) for GRB extinction measurements by fitting the average Milky Way (MW), Large Magellanic Cloud (LMC), and Small Magellanic Cloud (SMC) curves, assuming an intrinsic power-law sectrum. (Here, and elsewhere unless otherwise specified, the intrinsic spectral slope over the optical range is fixed at $\beta = 0.7$. Fortunately, because the amount of extinction for this burst is so large, deviations from this assumption do not significantly affect our results, except to slightly increase the uncertainties in the derived parameters, as we will discuss in §6.3.4.) In all three cases we use the Fitzpatrick (1999) parameterization of Local-Group extinction as implemented in the GSFC IDL package, with R_V fixed to their average value for each galaxy; for SMC extinction we use the Fitzpatrick parameters from Gordon et al. (2003) (SMC bar average). SMC extinction is ruled out (it converges to $A_V = 0$ mag with $\chi^2/\mathrm{dof} = 1159/24$), as it rises steeply to the far-UV (FUV) and does not allow for the 2175 Å bump feature that is so prominent in our data. The LMC and MW curves fit the data much better, but nevertheless they are not statistically acceptable either. Both curves are too flat in the observed IR; the MW curve also significantly overestimates the strength of the 2175 Å bump.

This should not be a surprise: even within our own Galaxy a significant diversity of extinction laws is evident. The majority of observed Galactic sightlines are consistent with variation in a single parameter R_V, which describes the relative "greyness" (wavelength independence) of the extinction at optical through UV wavelengths (Cardelli et al. 1989; hereafter CCM). A small number of sightlines in the MW (and all sightlines within the LMC and SMC) require additional parameters to fit accurately. A more general Local-Group extinction law, developed by Fitzpatrick & Massa (1990; hereafter FM), is able to fit essentially all local sightlines by adding an additional family of parameters: c_2 for further variations in steepness in the UV, c_3 for the strength of the 2175 Å bump, γ for the bump's width, and c_4 for the strength of the FUV rise. (The parameter c_1 is also present in principle, but it is essentially degenerate with c_2 and R_V, and in practice it is fixed based on those values. In addition, the parameter x_0 describes the central wavelength of the 2175 Å bump, but it has not been conclusively shown to vary and is fixed to the average value.)

We first attempted to fit using the general FM law (joined to the standard CCM law in the rest-frame optical with a spline), leaving all parameters free (except c_1 and x_0 as described above). Unfortunately, because our observations do not extend far enough into the rest-frame optical to properly constrain the optical/IR extinction properties independent of the UV, the R_V parameter is effectively unconstrained in this case. Fortunately, R_V and c_2 also are tightly correlated locally and can be tied together — using, for example, the correlation of Fitzpatrick (1999) (linear) or that of Reichart (2001) (quadratic, allowing for the optically flat, steep-UV SMC-like curve). Both correlations give acceptable (and very similar) fits to our data, and the Fitzpatrick-constrained curve is shown in Figures 6.4-6.5.

We also attempted a range of non-FM models, such as those of Calzetti et al. (2000), Maiolino et al. (2004), and Gaskell et al. (2004). These curves all lack the 2175 Å bump and do not fit the data well. In addition, we tried to fit the multi-parametric extinction curve from Li et al. (2008a), which can incorporate the 2175 Å bump and gives a fairly reasonable

fit (however, the c_1 parameter diverges and had to be fixed manually, and the result is significantly worse than the FM curve). As the Li curve has not been used extensively on local sightlines, it is difficult to interpret the results, and we will not discuss it further.

The results from our various fits are presented in Table 6.4. Note that despite the qualitative similarity of the curve to MW and LMC sightlines, three major parameters ($R_V = 4.17 \pm 0.15$, $c_3 = 1.70 \pm 0.29$, and $c_4 = 0.28 \pm 0.07$) differ significantly from the average MW and LMC values (γ is consistent with the average MW value). In general, the GRB 080607 sightline is UV-greyer, and its 2175 Å bump weaker, than the average MW sightline. Still, all these properties are in the *range* seen along different sightlines locally (e.g., from Fitzpatrick & Massa 1990: $2.3 < R_V < 6.6$, $1.2 < c_3 < 4.5$, $0.15 < c_4 < 0.90$). No single local analog appears to match the properties seen toward the GRB exactly, but it is nevertheless notable that our data are so well fit by the standard, locally derived laws without the need for any unusual parameters.[4] We will further discuss the implications of the FM parameters in §6.4.3.

Assuming any particular extinction model is not strictly necessary for this GRB: the large extinction column actually allows us to directly *measure* the wavelength-dependent extinction without need for fitting. Traditionally, UV extinction curves are presented as $E(\lambda - V)$ (i.e., $A_\lambda - A_V$; the optical extinction itself A_V need not be known). Our K_s-band measurement corresponds to the rest-frame V band, and so if the intrinsic slope can be assumed, one can simply measure this value for each filter (or wavelength bin) by comparing the observed $\lambda - V$ color to the predicted color for the assumed intrinsic spectrum. The results are plotted in Figure 6.5, illustrating the intrinsic differences between the curves and the inability of most of them to fit the data.

6.3.4 Effect of Varying Intrinsic β

The above quoted results all assume $\beta = 0.7$. In reality, we do not know the exact intrinsic spectral index, which varies from burst to burst.[5] As previously mentioned, the extinction of this burst is sufficiently large, and the intrinsic variation in β between events relatively small, that the errors introduced from variation in the spectral index are small. Here we quantify that statement and propagate the effects into our parameter uncertainties.

[4]This is not simply a matter of the flexibility of the fitting function: the model is quite limited in scope, with only four free parameters, each of which is constrained to a small allowable range. Indeed, some reported extragalactic sightlines, e.g., the high-z QSO sightline of Maiolino et al. (2004), cannot be accurately fitted within this model.

[5]In theory, closure relations (e.g., Price et al. 2002) allow β to be calculated from the light-curve decay slope α. However, as discussed in §6.4.2, we are unable to unambiguously determine whether the burst medium is in an interstellar medium or wind environment, or whether the early observations are reverse-shock dominated, so it is not clear which relation is most appropriate. Furthermore, even for bursts where no extinction is present and β can be measured directly, closure relations sometimes fail to accurately relate the observed parameters (e.g., Racusin et al. 2009). To avoid dependency of our conclusions on the details of the uncertain early-time afterglow physics, we therefore adopt the entirely empirical treatment of β described in this section.

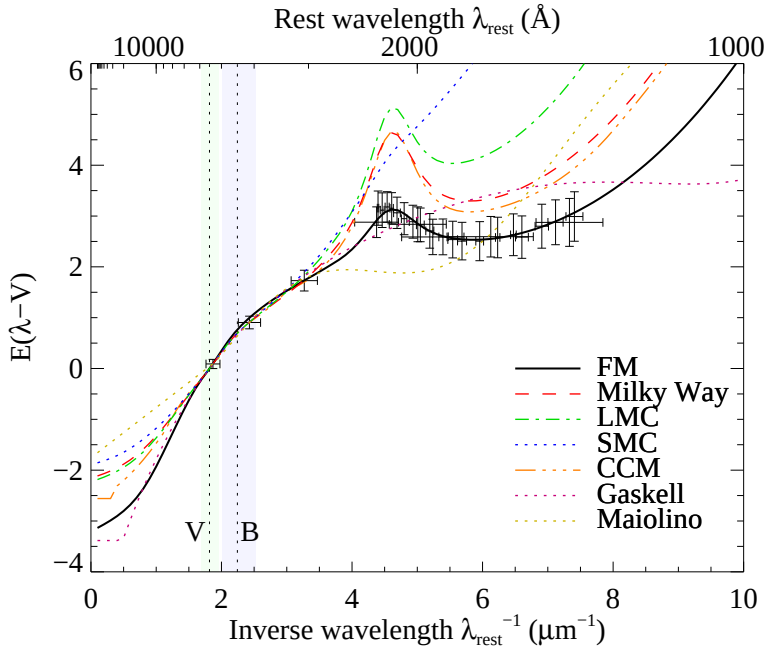

Figure 6.5 Different extinction curves compared with our afterglow data, shown as the selective extinction $E(\lambda - V) = A_\lambda - A_V$. All curves are normalized to match the observed $B - V$ color (traditionally, UV extinction curves are plotted as $E(\lambda - V)/E(B - V)$). This illustrates the flatter nature of the derived extinction curve (higher R_V) and weaker 2175 Å bump required along the GRB sightline relative to the average MW or LMC sightlines.

Kann et al. (2010) have compiled photometry for a large number of bright, well-observed, *Swift* -era GRBs and performed fits to the extinction (using the standard MW/LMC/SMC method) and spectral index of each event. We downloaded the data in Table 2 of that work and removed all events which did not have a best-fit (among the three models) $A_V < 0.2$ mag within 2σ to exclude events with significant or poorly determined extinction. We further removed any events reporting an unphysical $A_V < 0$ mag at more than 2σ and any event with an uncertainty in its derived spectral index $\sigma_\beta > 0.2$. The intrinsic spectral indices of this final sample of 21 low-extinction, well-constrained bursts have an average spectral index of $\beta = 0.70$ and standard deviation $\sigma_\beta = 0.26$. We take this as a representative sample with which to determine a prior on the intrinsic (unextinguished) spectral index β.

The observed spectral index between the J and K_s bands for this GRB is $\beta = 3.5$, so the impact of reddening (between these wavelengths) from dust is clearly much larger (by about an order of magnitude) than the typical variation in the intrinsic spectral index. This variation in the intrinsic index is, however, the largest source of uncertainty in the measurement of the extinction parameters. To take this into account, we refit our preferred extinction models for the $\pm 1\sigma$ cases and combined the resulting variation of the best-fit value in quadrature with the statistical uncertainties on the $\beta = 0.7$ fit. The final values for all extinction parameters (using the Fitzpatrick $c_2 - R_V$ correlation; the Reichart correlation is not significantly different) are presented in Table 6.5.

As an alternative to assuming an intrinsic optical β, we also attempted our fits by including the X-ray flux value at the extraction epoch and assuming an unbroken power law over the full range between the optical and X-ray data (which allows for a much more precise derivation of β as well as a constraint on the overall flux normalization, though it is strongly dependent on this assumption of an unbroken intrinsic index). This gives generally quite consistent values with our optical-only fit, in further support of our assertion that the derived dust properties are not strongly affected by our assumptions about the intrinsic spectrum.

6.3.5 X-ray Scattering?

Of particular note in Table 6.5, and consistent with our previous work (Prochaska et al. 2009), is the conclusion of a large extinction column ($A_V = 3.26 \pm 0.35$ mag). This identification of GRB 080607 as a highly extinguished event makes it a potentially useful test case of the X-ray scattering model for early-time afterglows (Shen et al. 2009). However, even $A_V = 3$ mag is generally inadequate to expect any significant effects on the X-ray light curve in this case. Following the discussion by Shen et al. (2009), we calculate the 1 keV specific fluence from the prompt emission using the parameters given by Golenetskii et al. (2008c) and integrate the X-ray afterglow flux (starting at 100 s, and ignoring the X-ray flare) using our power-law fit. The resulting ratio of $S_{\rm AG}/S_{\rm prompt} = (1.0 \times 10^{-6})/(1.6 \times 10^{-7}) = 6.3$ places an upper limit on the scattering opacity at this wavelength (i.e., $\tau_{\rm scat} < 6.3$). Translating this to a limit on the optical opacity using Equation (8) of Shen et al. (2009), the limiting dust extinction for this case is the thoroughly unconstraining $A_V < 686$ mag, a value about 200 times higher than our direct measurement. Equivalently, the total fluence of

the dust-scattered X-rays for this event is anticipated to be 200 times lower than the actual afterglow fluence observed, and therefore undetectable. Indeed, for this event, the X-ray light curve follows a simple unbroken power law and (with the exception of the early X-ray flare, a prompt-emission feature; Kocevski et al. 2007b; Chincarini et al. 2007) no significant hardness variations of the type predicted by Shen et al. (2009). We conclude that, despite the large surrounding dust column, X-ray scattering is not significant for this GRB.

6.4 Discussion

6.4.1 Afterglow Luminosity in Context

The impressive optical brightness for an event at $z = 3$ has already been noted. In fact, as we shall show, after the effects of extinction are taken into account, GRB 080607 is among the most optically luminous GRBs (and therefore objects of any sort) to date, second only to GRB 080319B.

Following Kann et al. (2007, 2010), we select as our comparison filter the $z = 1$ R-band (that is, the wavelength which is shifted to the observed R band if at $z = 1$); this corresponds roughly to the rest-frame U band. For GRB 080607, this is shifted all the way to approximately the observed J band. Therefore, taking advantage of the apparent lack of color change, we shift all other filters to the J-band light curve using our model fluxes, extending this curve back to the observed emission peak. This curve is corrected for Galactic extinction (only 0.02 mag), for host extinction (4.94 mag), and for the difference in luminosity distance between $z = 1$ and $z = 3.036$ using standard cosmological parameters ($h = 0.7$, $\Omega_M = 0.3$, $\Omega_\Lambda = 0.7$). A small K correction is then applied to match the spectrum exactly with the $z = 1$ R band, and the light curve is scaled (undilated) to $z = 1$.

The result is plotted in Figure 6.6, compared with the light curves of GRB 080319B and the three next most luminous events (from Figure 7 of Bloom et al. 2009), and with the peak luminosities of a large sample of well-studied *Swift* bursts (from Figure 7 of Kann et al. 2010). At the beginning of observations GRB 080607 is comparable in luminosity to GRB 080319B (and at early times was likely brighter), but the prompt optical flaring of GRB 080319B pushes that burst to a higher luminosity over the next several minutes. GRB 080607 remains among the five most luminous bursts for the rest of its observed evolution. This illustrates the remarkable attributes of this burst that allowed it to provide such a detailed analysis of its environment. In terms of the afterglow (external-shock) emission alone, GRB 080607 may yet be the most luminous: the peak of GRB 080319B appears to correlate with its prompt emission and fades particularly rapidly when the prompt emission ends; the origin of its early-time optical emission is still debated (Racusin et al. 2008). The optical light curve of GRB 080607 bears no relation to the prompt emission and is certainly external-shock dominated at all times.

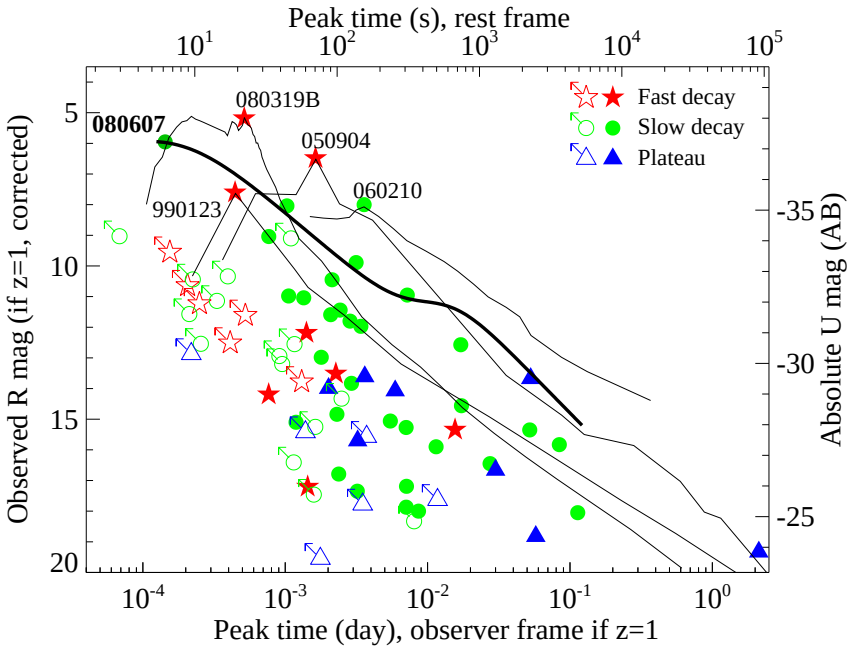

Figure 6.6 Near-UV luminosity of GRB 080607 (bold curve) compared to several other prominent bursts, as well as to a large sample of rapidly observed *Swift* GRBs from Kann et al. (2010). Colored points indicate peak observed luminosities of the events described in that paper (unfilled points are events caught after the peak and therefore only lower limits on the peak luminosity). At peak, GRB 080607 is among the most luminous GRB known, peaking at $M_U \approx -37$ mag. At $z = 1$ it would peak at mag 6 if unobscured by dust.

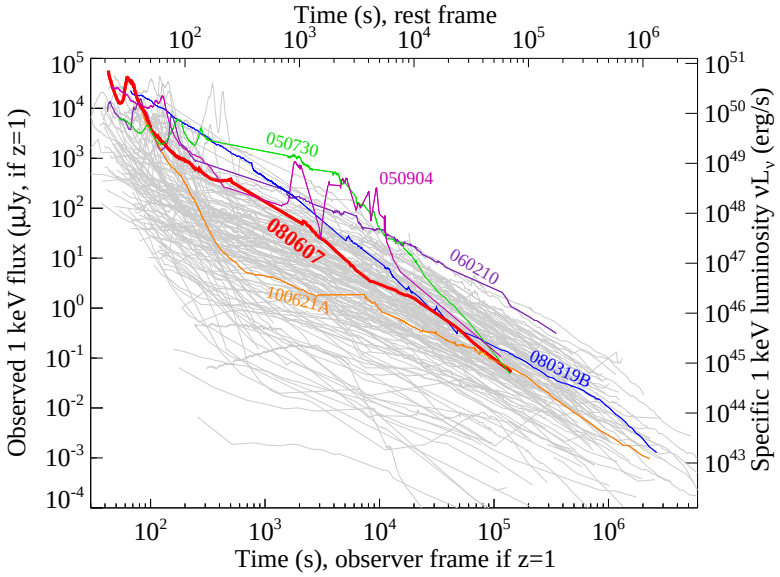

Figure 6.7 X-ray luminosity of GRB 080607 (bold red curve) compared to all other *Swift* -followed GRBs. Several other prominent bursts are also individually colored. GRB 080607 is among the most X-ray luminous bursts at peak, but fades quickly to an average luminosity by later times.

6.4.2 Physical Properties

Unfortunately, the physical properties responsible for making GRB 080607 so energetic remain mostly hidden from view. In the burst rest frame, our optical observations extend only to 10^3 s and the X-ray observations cease at $t \approx 1$ day, which does not usefully constrain the jet opening angle. Conservatively setting $t_{\rm jet} > 6 \times 10^4$ s using the X-ray light curve, following the standard equations for the jetting time (Sari & Piran 1999a; Frail et al. 2001) and fiducial values of density[6] $n = 100$ cm^{-3} and efficiency $\eta = 0.2$, we measure a jet opening angle of $\theta_{\rm jet} > 3.6\eta_{0.2}^{1/8} n_{100}^{1/8}$ degrees; the equivalent lower limit on the beaming-corrected gamma-ray energy release is $E_\gamma > 1.8 \times 10^{51} \eta_{0.2}^{1/4} n_{100}^{1/4}$ erg, a fairly typical value. It is therefore not clear whether the extreme apparent luminosity of this burst is attributable to intrinsically large energetics (Cenko et al. 2010c), favorable viewing angle (of a nonuniform, centrally concentrated jet, as was suggested for GRB 080319B by Racusin et al. 2008), an intrinsically narrowly concentrated (uniform) jet, or some combination of these parameters.

To a large extent, the optical luminosity is simply another reflection of the total energetics of the burst itself: both in theory (Sari et al. 1998) and observationally (Gehrels et al. 2008; Nysewander et al. 2009a; Kann et al. 2010), the inferred afterglow luminosity scales

[6]This is an unusually large value of n, motivated by the apparent low value of the cooling break ν_c and inference of a dense molecular environment along the line of sight, as discussed later in this section. Fortunately, the value of n only weakly affects the derived value of θ and E_γ.

approximately linearly with $E_{\rm iso}$, and if the optical light curve is extrapolated to late times the predicted optical flux is in the middle of the fluence-normalized distribution. However, there is more to the story: the X-ray light curve of this burst is not (except at the earliest times) particularly bright; when normalized to the burst fluence it is quite typical for a *Swift* burst at early times (and actually is unusually faint at late times, due to its rapid unbroken decay).

There are two broad ways to interpret this. The simplest interpretation is that the cooling-break frequency ν_c has a particularly low value compared to most GRBs, perhaps even below the optical band (the available data are marginally consistent with the X-ray and optical bands being on a single spectral power law). The obvious culprit for this involves the external density n: the X-ray flux should be independent of density (assuming that $\nu_{\rm X} > \nu_c$ for most bursts), but the cooling break and optical flux are sensitive to it ($\nu_c \propto n^{-1}$; below the cooling break $F \propto n^{1/2}$). An external density 10 or 100 times the "typical" *Swift* value would push the cooling break from its typical position between the optical and X-ray bands into or below the optical band at early times, increasing the optical luminosity. Indeed, after correcting for extinction the early-time broad-band SED appears to demand a low cooling-break frequency: the optical-to-X-ray index at only 300 s is $\beta_{\rm OX} = 1.1$, consistent with the X-ray spectral slope ($\beta_{\rm X} = 1.16 \pm 0.13$). The probable low value of the cooling break also helps explain why a similar extinction column is derived whether the optical data are considered alone (the most general case) or in conjunction with the X-ray data assuming an unbroken power law (which requires $\nu_c < \nu_{\rm opt}$), as demonstrated in §6.3.4. Unfortunately, the period of simultaneous temporal coverage between the optical and X-ray observations is too short to determine, via the light curve, whether a break is present between the bands. (The burst could also have exploded into a wind-stratified medium — one with variable density $n \propto r^{-2}$ — in which case ν_c rises with time and the optical flux fades more rapidly than the X-ray flux, as is observed.)

The alternative interpretation is that the optical flux originates from a separate emission component, the most obvious candidate being the reverse shock (Meszaros & Rees 1997). Several previous early fast-fading light curves have been associated with reverse shocks (e.g., Akerlof et al. 1999; Kobayashi & Zhang 2003; Perley et al. 2008e; Steele et al. 2009); qualitatively, the behavior of GRB 080607 appears similar to these events, although the decay is somewhat slower and there are no late-time observations to determine whether the light curve became forward-shock dominated as predicted. The factors determining the luminosity of the reverse shock (Zhang et al. 2003) are generally the same as for the forward shock (and so a high external density would similarly aid the production of a luminous afterglow), but can be further amplified if the magnetization $R_B = \epsilon_{B,r}/\epsilon_{B,f}$ of the reverse shock is high, due (for instance) to primordial fields in the ejecta (Gomboc et al. 2008).

Unfortunately, the lack of late-time observations (to search for the appearance of a forward shock) or radio data (to more directly constrain n) prevents us from distinguishing between these possibilities. Fortunately, we can speak more confidently about the other aspect of this burst's remarkable luminosity: the fact that it peaked so early (even if two bursts have similar energetics and late-time luminosities, the power-law nature of GRB light

curves ensures that the event with the earlier peak time will have significantly larger peak brightness, fleeting as it is).

The peak time (for $\nu > \nu_m$) is set by the deceleration timescale of the ejecta (Sari et al. 1999). Because the afterglow has already peaked and is fading at the start of our observations, the ejecta must have accumulated enough circumstellar matter to begin to decelerate and develop an external shock by this time: a mere 24 s after the BAT trigger (6 s in the rest frame), or more conservatively 32 s after the beginning of the prompt emission (8 s in the rest frame).

Such rapid deceleration generally requires a high initial Lorentz factor Γ, although a very high interstellar density also contributes. Using Equation 3 of Rykoff et al. (2009)[7], we estimate $\Gamma > 660\eta_{0.2}^{1/8} n_{100}^{-1/8}$, where $\eta_{0.2}$ and n_{100} indicate values of the efficiency and external density relative to fiducial values of 0.2 and 100 cm^{-3}, respectively (see also Molinari et al. 2007). Based on the preceding discussion of the late-time optical luminosity, we have chosen an unusually large value for the interstellar density; even in this case the constraint on Γ is at the top end of the afterglow-inferred range (if still somewhat below the pair-opacity limits recently provided by the *Fermi*-LAT: Abdo et al. 2009a). It is notable that both $E_{\rm iso}$ and Γ are exceptionally large for this burst, which could suggest that the properties may be correlated.

6.4.3 X-Ray and Optical Properties: the Environment of GRB 080607

The derivation of precise values for the extinction parameters along the GRB 080607 sightline (Table 6.4) gives us an additional means for learning about its host environment. Although the reason for the variation of these parameters is not well understood even within the Milky Way, some broad conclusions can be drawn.

First, we note the high value of $R_V \approx 4$ (or equivalently, since the parameters are tied in our modeling, the small value of c_2), indicating a relatively flat extinction curve. In the diffuse interstellar medium (in the MW and in other galaxies as well), R_V typically takes on lower values of 2–4. UV-flat extinction curves are generally restricted to denser sightlines, probably because grains are able to coagulate to larger sizes (Valencic et al. 2004). (However, dense regions can exhibit low values of R_V as well as high values.) The high R_V value is therefore suggestive of a dense environment — fully consistent with the conclusion from the atomic and molecular analysis that the sightline penetrates through a dark molecular cloud in its host.

Second, the value of c_3 is nonzero, indicating a significant 2175 Å absorption bump. This is one of only a few clear detections of this feature at cosmological distances (Motta et al.

[7]This equation is strictly valid only for the thin-shell scenario, in which the burst duration is less than the deceleration time (Sari et al. 1999; Mészáros 2006). This is not strictly true for this GRB, as prompt emission is observed to continue during the light-curve decline. However, as noted previously, the energetics are dominated by a single, bright pulse which ends well before the start of optical observations.

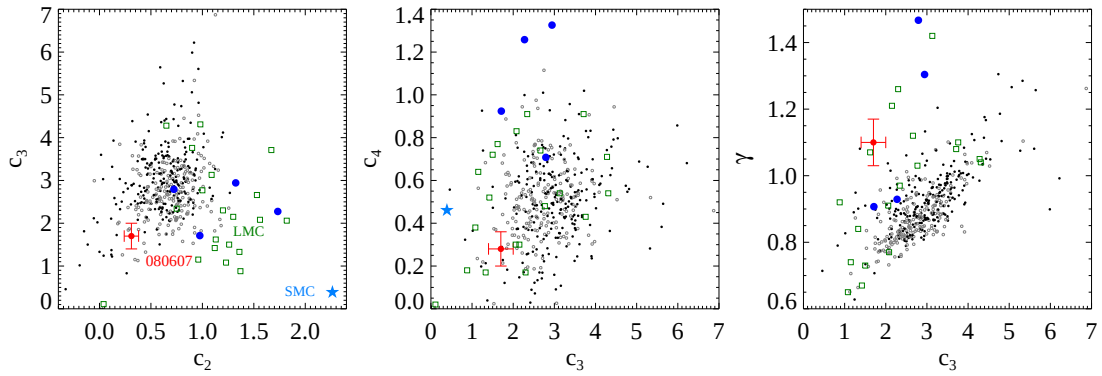

Figure 6.8 Extinction parameters for GRB 080607, compared to various MW and LMC sightlines from Valencic et al. (2004) and Misselt et al. (1999). Diffuse MW sightlines are indicated with small, gray open circles; dense sightlines are indicated with small, filled black circles. Peculiar MW sightlines incompatible with the standard CCM one-parameter family are identified as blue circles. LMC sightlines are indicated with rectangles; the SMC curve is plotted as a star. Extinction parameter c_2 is a measure of the UV slope (inverse greyness); c_3 is a measure of the strength of the 2175 Å bump and γ is a measure of its width; and c_4 indicates the strength of the far-UV rise. All parameter values (and all pairs of two values) are within the distribution seen locally, although there is no single example of a local sightline that is consistent with the extinction properties of the GRB 080607 sightline in all aspects.

2002; Junkkarinen et al. 2004; Ellison et al. 2006; Srianand et al. 2008; Krühler et al. 2008; Elíasdóttir et al. 2009; Noterdaeme et al. 2009; Zhou et al. 2010) and the highest-redshift detection of the feature yet. The identity of the carrier is still unknown (although polycyclic aromatic hydrocarbons and graphite are considered promising candidates; see Draine 2003 for a review) and the processes that cause it to be present or absent are similarly not yet certain: an evolved stellar population (Noll et al. 2007), metallicity (Fitzpatrick 2004), the strength of the UV radiation field (e.g., Gordon et al. 1997), and disturbance of the environment due to shocks (Seab & Shull 1983) have all been cited in explaining its absence. Generically, however, it seems to be present in almost all sightlines in the MW and LMC, and in nearby disk galaxies, but absent in more disturbed locations such as the SMC, nearby starburst galaxies (Gordon 2005), and at least one highly disturbed sightline within the MW (Valencic et al. 2003). This suggests that the interstellar medium of the host of GRB 080607 is a closer analog of the more quiescent environments found in the MW and LMC than of the extreme conditions of nearby galaxies having high specific star-formation rates. The determination of significant pre-existing stellar mass and relatively modest specific star-formation rate in our parallel study of the host galaxy (Chen et al. 2010) is in agreement with this expectation.

The strength of the bump is, however, weaker than in almost any sightline in either the MW or LMC (Figure 6.8). Furthermore, the degree to which the bump is weaker does *not* follow the local correlations: in the MW, very low values of c_3 tend to correlate with very low values of c_2 (weakly) and γ (strongly). In our case, a low c_2 is observed, but it is

still much higher than for the Orion Nebula sightlines in which the lowest values of c_3 are seen. This may be an indicator that a different phenomenon is suppressing this carrier than is in operation within the MW Galaxy. Metallicity is not likely the culprit: the molecular cloud giving rise to the observed extinction has near-solar metallicity despite being at $z > 3$ (Prochaska et al. 2009).

The strength of the FUV rise, c_4, is fairly typical for local sightlines. However, the origin of the rise is even less secure than that of the 2175 Å bump, and does not significantly constrain the environment.

The X-ray inferred host-galaxy equivalent hydrogen column of GRB 080607 was measured to be $N_{\rm H} = 2.7^{+0.8}_{-0.7} \times 10^{22}$ cm^{-2}, which is comparable to the neutral hydrogen column $N_{\rm HI} = 1.5^{+0.6}_{-0.5} \times 10^{22}$ derived from the damped Lyman-α line (Prochaska et al. 2009). This is a very large value, even considering the high extinction in this direction: the ratio of $N_{\rm H}/A_V = 8 \times 10^{21}$ cm^{-2} mag^{-1} is several times larger than observed in the MW, although quite typical of GRBs for which both values have been securely measured (e.g., Schady et al. 2010). It is possible that this arises for reasons unrelated to the molecular cloud — for example, if additional dust-free gas is located closer or further along the sightline relative to the molecular cloud that is responsible for the absorption. If intrinsic, this combination of a weak (but present) bump and a large $N_{\rm H}/A_V$ ratio is consistent with the correlation discussed by Elíasdóttir et al. (2009) and Gordon et al. (2003).

6.5 Conclusions

As one of the brightest and best-studied GRBs (at early times) of the *Swift* era, GRB 080607 holds particular potential for revealing the nature of GRBs and their environments at high redshift. While the relatively limited observed temporal range restricts our ability to study the intrinsic nature of this event, this is more than compensated by the abundant early-time optical/IR data that reveal the detailed properties of the dark-cloud sightline in its distant host.

The utility of this event is perhaps most evident in the context of the class of "dark" GRBs. Many factors, both intrinsic (high $E_{\rm iso}$, Γ, and n) and extrinsic (large but not extremely large A_V, a redshift placing the 2175 Å bump in the optical window, and the fortuitous ability to observe immediately with telescopes in both the continental US and Hawaii) had to conspire together to allow the dust properties of this GRB to be observable in such rich detail. Had this event been slightly less luminous ("only" comparable to GRB 990123, $\sim$2 mag fainter at most epochs), its afterglow would have been only marginally detected, and only at the earliest times; further decrease in luminosity would have rendered it undetectable with small telescopes. Even a modest increase in the amount of extinction (higher by $A_V \approx 1$–2 mag) or the presence of relatively UV-opaque SMC-like dust would have a similar impact, suppressing all of the optical measurements.

The literature contains many examples of such sources: GRBs with a large dust column but insufficient luminosity to shine through it. Some prominent cases include GRBs 970828

(Djorgovski et al. 2001), 060923A (Tanvir et al. 2008c), 061222A and 070521 (Cenko et al. 2009; Perley et al. 2009c), 070306 (Jaunsen et al. 2008), 081221 (Tanvir et al. 2008a), and 090709A (Cenko et al. 2010d). But even these objects were unusually bright or had particularly rapid or deep observations in their favor. A truly typical-luminosity *Swift* event without rapid or deep observations would completely escape notice in most cases, permitting only shallow limits on its extinction column. Therefore, there is every reason to think that very dusty environments like that of GRB 080607 are actually not uncommon among GRBs (if not necessarily ubiquitous). This is in agreement with our afterglow plus host survey with the P60 and Keck telescopes (Cenko et al. 2009; Perley et al. 2009c).

The extinction curve along the GRB 080607 sightline — a dark molecular cloud at $z = 3.036$ — is quite similar to that of our own Galaxy (with a significant 2175 Å bump), though there are differences in finer details. The success in modeling the extinction curve of this event within entirely locally developed models is in some ways heartening, giving us confidence that with sufficient knowledge we should be able to understand the absorption properties even out to these immense distances. As perhaps the most detailed determination of the extinction properties of a galaxy at cosmological redshift to date, we suggest that the extinction curve in this work may be of use to others attempting to take into account the effects of dust extinction in other galaxies at high redshift (see Appendix A). At the same time, some other GRBs and other techniques have also at times pointed to extinction curves that diverge dramatically from local templates, so the topic should continue to be addressed with caution.

Once corrected for extinction, GRB 080607 rivals the "naked eye burst" GRB 080319B as the most luminous known object in the Universe. This extreme early luminosity of GRB 080607 is likely the product of a variety of factors: it has one of the largest $E_{\rm iso}$ values to date, and its optical luminosity may have been further amplified by a large circumburst density in its host (or, alternatively, a bright reverse shock). Unlike GRB 080319B, GRB 080607 has a smooth optical peak and shows no correlation with prompt emission at that time. Events like GRB 080607 demonstrate the power of GRBs to illuminate the darkest corners of the Universe: not just the reionization era (on which much current attention is focused) but also the dustiest regions over the following several billion years when the global star formation rate — much of it occurring behind optically thick dust clouds — was at its maximum. Such dust-obscured regions are extremely difficult to study by other techniques, or even with most GRBs, as demonstrated by the class of "dark" bursts. The combination of early observations and extreme energetics of GRB 080607 were enough to overcome even this difficulty, and demonstrate the power of rare, individual events to illuminate these hard-to-study regions and improve our understanding of the early universe.

Acknowledgments

KAIT and its ongoing operation were made possible by donations from Sun Microsystems, Inc., the Hewlett-Packard Company, AutoScope Corporation, Lick Observatory, the NSF, the University of California, the Sylvia & Jim Katzman Foundation, and the TABASGO

Foundation. We thank S. Klose for additional computations that confirmed our luminosity results, and we are grateful for the H_2^* model developed by B. T. Draine and supplied by Y. Sheffer. We benefited from the excellent assistance of the staffs of the observatories at which we obtained observations.

Table 6.1: Host-Galaxy Limits

Instrument	Obs. date (UT)	Exp. time (s)	Filter	5σ limit (mag)
Keck I / LRIS	2009-02-19	2490	g	> 27.3
Keck I / LRIS	2009-02-19	2220	I	> 25.3
Keck I / NIRC	2009-05-31	3600	K_s	> 21.6

5σ limiting magnitudes on a host galaxy at the afterglow position from our ground-based optical and IR observations at the Keck Observatory. Magnitudes are in the SDSS (g), Vega (I), or 2MASS (K_s) systems and not corrected for Galactic extinction.

Table 6.2: Model Fluxes at $t = 300$ s

Filter	$\lambda_{\rm obs}$ (Å)	$F_{\rm obs}$ (μJy)	$m_{\rm obs}$ (mag)	$A_{\lambda,\rm Gal}$ (mag)	$\Delta m_{\rm lines}$ (mag)	$m_{\rm cont}$ (AB mag)	$F_{\rm cont}$ (μJy)	$A_{\lambda,\rm host}$ (mag)
X-ray	12.4	34.04						
V	5505	94.25 ± 11.4	18.98 ± 0.13	0.07	0.60	18.29 ± 0.13	174.6 ± 21.1	6.23
R	6588	200.6 ± 12.6	17.97 ± 0.07	0.06	0.21	17.88 ± 0.07	256.6 ± 16.1	5.76
i	7706	260.5 ± 16.6	17.86 ± 0.07	0.05	0.06	17.75 ± 0.07	287.5 ± 18.3	5.88
I	8060	214.0 ± 19.1	17.64 ± 0.10	0.04	0.07	17.97 ± 0.10	236.0 ± 21.0	6.05
z	9222	242.5 ± 21.4	17.96 ± 0.10	0.03	0	17.91 ± 0.10	249.8 ± 22.0	6.12
J	12350	867.4 ± 51.4	15.66 ± 0.06	0.02	0	16.54 ± 0.06	883.1 ± 52.3	4.94
H	16620	2296 ± 131	14.12 ± 0.06	0.01	0	15.48 ± 0.06	2322 ± 132	4.20
K_s	21590	5866 ± 337	12.64 ± 0.06	0.01	0	14.47 ± 0.06	5911 ± 339	3.30

Broad-band afterglow fluxes as determined by the light-curve model, interpolated to $t = 300$ s after the trigger. Observed magnitudes are not corrected for Galactic extinction and are in the Vega (VRI), SDSS (iz), or 2MASS (JHK_s) systems. Continuum magnitudes and fluxes have been corrected for both Galactic extinction (from NED) and line absorption (calculated using our optical Keck spectroscopy).

Table 6.3: Binned, Line-Interpolated Keck Spectroscopy

λ (Å)	$F_{\nu,\mathrm{cont}}$ [a] (μJy)
5448.56	157.73 ± 1.15
5670.14	180.13 ± 2.20
5842.98	197.47 ± 3.05
6112.85	248.35 ± 3.11
6235.50	241.48 ± 2.14
6476.67	260.41 ± 3.02
6776.25	287.44 ± 1.82
7099.05	296.41 ± 2.11
7281.72	293.54 ± 1.28
7483.82	284.98 ± 1.19
7774.03	262.52 ± 2.97
7997.30	240.04 ± 1.04
8181.51	230.34 ± 1.04
8411.10	222.31 ± 2.78
8607.66	203.17 ± 1.25
8759.01	189.30 ± 8.11
8892.83	186.93 ± 5.67
9044.91	200.48 ± 3.56
9175.62	195.13 ± 2.90

Uncertainties are photometric only and do not include any systematic term. Fluxes are corrected for H_2^* absorption in the host galaxy and for Galactic extinction.

Table 6.4: Extinction Fits

Model	A_V (mag)	R_V	c_1	c_2	c_3	c_4	γ	χ^2/dof
Average MW	1.25 ± 0.03	3.1	-0.07	0.70	3.23	0.41	0.99	127 / 24
Average LMC	1.09 ± 0.02	3.2	-1.28	1.11	2.73	0.64	0.91	275 / 24
LMC2	0.16 ± 0.03	2.6	-2.16	1.31	1.92	0.42	1.05	1143 / 24
SMC	0 ± 0.01	2.73	-4.96	2.26	0.37	0.46	0.99	1159 / 24
CCM	0.82 ± 0.06	2.41 ± 0.12						123 / 22
FM+tie	3.26 ± 0.31	4.17 ± 0.15	1.11 ± 0.12	0.31 ± 0.04	1.70 ± 0.29	0.28 ± 0.07	1.10 ± 0.06	24.2 / 20
FM+Reichart	3.52 ± 0.35	4.69 ± 0.19	1.29 ± 0.15	0.30 ± 0.05	1.66 ± 0.30	0.31 ± 0.07	1.07 ± 0.07	22.9 / 20
Li	1.70 ± 0.06		200	12.3 ± 0.6	14 ± 285	0.03 ± 0.01		38.7 / 20

Comparison of fits to the SED of GRB 080607 using a variety of extinction models, most of which cannot adequately fit the observations. Because the optical spectrum and photometry dominate the observations, most models converge to a low extinction value to try to accommodate the weak 2175 Å bump and seemingly flat spectrum. These models are not consistent with the red IR color. Both a high R_V and a low c_3 are required to explain the optical and IR data together, as reflected in the FM fits. Parameter uncertainties do not include the effect of the uncertain intrinsic spectral index β (a value of 0.7 is assumed).

Table 6.5: FM Extinction Parameters for GRB 080607

Parameter	Optical alone value	Optical + X-ray value
β	0.70 ± 0.26	1.08 ± 0.05
E_{B-V}	0.78 ± 0.09	0.68 ± 0.04
A_V	3.26 ± 0.35	3.07 ± 0.32
R_V	4.17 ± 0.25	4.52 ± 0.23
c_1	1.11 ± 0.20	1.37 ± 0.15
c_2	0.31 ± 0.07	0.22 ± 0.05
c_3	1.70 ± 0.30	1.82 ± 0.32
c_4	0.28 ± 0.08	0.37 ± 0.08
γ	1.10 ± 0.07	1.07 ± 0.06
x_0	4.596	

Final FM extinction parameters for GRB 080607. The values in the left column incorporate only the optical data and include the effect of unknown intrinsic spectral index. Values at right assume an unbroken power law between the optical and X-rays. The values of c_1 and R_V are tied to c_2 as described in the text; the best-fit value of A_V is likewise dependent on this tie, although all other parameters are independent of R_V. The resulting R_V is significantly higher (i.e., c_2 is lower) than the average MW or LMC curves but has a typical value for dense sightlines. The 2175 Å bump (strength given by c_3), ubiquitous in the MW but nearly absent in the SMC, is present but weaker than in the MW or LMC.

Chapter 7

The *Swift*/Keck GRB Host Project: Deep Observations of 146 GRB Host Galaxies

Abstract

I present the first data release of the Keck Observatory GRB Host Survey, a large, multi-year project to discover GRB host galaxies and characterize their properties in large numbers, focusing in particular on events of significant community interest and on poorly-understood GRB subpopulations including short GRBs, XRFs, dark GRBs, and GRBs with detected GeV emission. We have imaged a total of 135 different host-galaxy fields, most in multiple filters, in imaging observations totaling over 100 hours of effective on-source integration time. Likely host galaxies are detected consistent with the afterglow position in 80 of these cases, the majority of which have not previously been reported in the literature. We also present low-resolution spectroscopy of 46 fields, successfully measuring the redshifts of 21 hosts or host candidates. Fourteen of these were previously unknown before our observations, 8 of which have not been previously reported in the literature. The long GRB hosts in the sample are almost universally blue, star-forming galaxies, but their colors are less universally red than Lyman-break galaxies. Several interesting and exotic objects are found, including numerous line-of-sight near-superpositions with foreground galaxies, a low-luminosity burst from an H II region in a grand-design low-redshift spiral galaxy, and a probable short GRB originating from the halo of a ULIRG.

7.1 Introduction

The *Swift* satellite (Gehrels et al. 2004) has transformed the study of gamma-ray bursts in significant ways. Until 2004, a well-localized gamma-ray burst was an infrequent event:

the early satellites Beppo-SAX (Boella et al. 1997) and HETE-2 (Ricker et al. 2003) detected only about one GRB per month on average, and years of concerted follow-up were needed to build even a modest sample of events. Furthermore, the distribution of a precise GRB position to ground-based observers normally took at least several hours, during which time the afterglow had inevitably faded significantly. In recent years, however, the situation has changed dramatically: *Swift* detects a new GRB every ∼4 days on average and is able to follow the large majority of them immediately (starting within a few minutes) with its on-board X-ray and UV/optical cameras, the XRT and UVOT (Burrows et al. 2005c; Roming et al. 2005). The XRT in particular has proven to be a phenomenally successful afterglow-detection machine: except in the (relatively uncommon) situation where observing constraints prevent immediate follow-up, its success at detecting long gamma-ray bursts is nearly 100%[1].

This brings both opportunities and challenges for the GRB observer. For the first time, the afterglow catalog is large enough that one can produce a statistically meaningful sample not just for GRBs as a whole but for less common subpopulations: for example, X-ray flashes (very soft bursts, with $E_{\rm peak} < 30$ keV; Heise et al. 2001), short gamma-ray bursts (with or without extended emission; see Chapter 1), dark bursts (bursts with faint optical afterglow; Groot et al. 1998; Jakobsson et al. 2004a), low-redshift bursts, and so on.

However, the productivity of *Swift* is a double-edged sword: this order-of-magnitude improvement in the burst detection rate has not been matched by an equivalent improvement in the capabilities for large-aperture, late-time ground-based follow-up. To be sure, the number of rapid follow-up instruments has exploded; many of these facilities were similarly motivated by and dedicated to GRB science. But the scarce resource of big telescopes is significantly more challenging to come by, and searching for hosts in particular is an unavoidably aperture-intensive process: the typical *Swift* GRB is at a redshift of $z > 2$ (Jakobsson et al. 2006); a typical host is $R = 26$ mag and often fainter. So while most pre-*Swift* GRBs with afterglow localizations also have known host galaxies, the number of published hosts in the *Swift* era remains paltry, especially in comparison to the number of GRBs that have occurred since the *Swift* launch (over 600). Host spectroscopy is even more challenging to acquire.

This is unfortunate, because direct imaging of the host provides a wealth of information that cannot be gleaned by other means. An afterglow spectrum, when available, can provide highly detailed information about the burst sightline (Vreeswijk et al. 2007; Prochaska et al. 2007a,b; Fynbo et al. 2009), but the integrated properties of the galaxy (mass, luminosity, and so on) can be inferred only from its emitted starlight. Understanding the place of GRBs within the zoo of high-z galaxies inferred from the large strides made by recent ground- and space-based fields surveys can place strong constraints on the nature of GRBs and galaxies alike, but is only possible if the hosts are themselves directly studied.

[1]Of > 400 LGRBs *Swift* has detected and rapidly (within 5 minutes) slewed the XRT to the position, only three have no detected X-ray afterglow (GRBs 070126, 061218, and 060728: Vetere et al. 2007; Zane et al. 2006; Pagani et al. 2006). All three are extremely faint events, and in fact the detected signal from two of the three are so faint that the reality of the burst itself is ambiguous.

Furthermore, for a significant fraction of bursts, the information provided by the afterglow is minimal in the first place, leaving study of the host galaxy as the only way to understand the burst environment in any detail. In particular, a redshift has never been derived from a short burst afterglow directly (aside from the highly ambiguous case of GRB 090426). Similarly, "dark" gamma-ray bursts lack (by definition) a bright afterglow and are similarly challenging to understand directly. Any information about the redshift distribution, progenitors, and stellar populations giving rise to these classes of transients therefore is particularly dependent on host-galaxy follow-up.

Although host follow-up in the *Swift* era is challenging, it is certainly not impossible. Starting in 2005 (not long after the launch of *Swift* itself), we have been continuously conducting deep observations of gamma-ray burst positions to produce a legacy sample of gamma-ray burst host galaxies that is both *large* enough to expand on pre-*Swift* results in a meaningful way and *diverse* enough to incorporate not just "ordinary" bright long-duration bursts but also to enable the detailed study of interesting GRB subclasses that were hardly constrained by pre-*Swift* studies at all.

In this chapter, I outline our host discovery program, summarizing the data acquisition process, reductions, host-galaxy identification, and photometry of each field, as well as our small-aperture calibration program. Beyond general remarks, we do not address in detail the properties of any of the events or underlying science, which will be presented in the next chapter and in subsequent future work.

7.2 Survey Characteristics

7.2.1 Goals and Target Selection

It is important to note from the outset that our survey is *not*, as a whole, uniform, and so the properties of the resulting burst catalog should not be taken as statistically representative of those of all GRBs. We proposed for time on a semester-by-semester basis over a five-year period, and our goals have evolved throughout the program in parallel with our evolving understanding of GRBs in general. These goals have included improving constraints on the GRB redshift distribution, elucidating the origins of dark GRBs, studying the hosts of X-ray flashes (XRFs) and short gamma-ray bursts (SHBs), constraining late-time supernova emission from bursts at lower redshifts, discovering host galaxies at high redshifts $z > 5$, and characterizing the host galaxies of GRBs showing strong DLAs (e.g., Chen et al. 2009) or intervening Mg II absorption (Pollack et al. 2009) in their afterglows. Many other bursts were targeted on the basis of other interesting aspects of the prompt emission or afterglow, especially if these events did not have known redshift—after an afterglow has faded, the host galaxy represents the only method of constraining the redshift of a GRB. Overall, with only a few exceptions, our goals of this program generally revolved around the identification and (where possible) redshift measurement of *new* host galaxies: we generally did not extensively re-observe events with previously reported host galaxies and emission-line redshifts.

7.2.2 Instrument Description

Almost all optical imaging was conducted with the Low Resolution Imaging Spectrometer (LRIS; Oke et al. 1995) on the Keck I 10-meter telescope. LRIS is a dual-channel optical instrument operating at the Cassegrain focus of the telescope, capable of seeing-limited optical imaging (in two bands simultaneously) as well as low-resolution ($R \sim 700$) spectroscopy covering the entire visible range of approximately $3200-10000$ Å. Both longslit and slit-mask spectroscopy are supported by the instrument, but only longslit spectroscopy was used in this program.

Since 2000, the LRIS backend has consisted of two cameras with different characteristics. LRIS-Blue or LRISB, the "blue side" (McCarthy et al. 1998), is a 2K×4K Marconi E2V CCD with 15μm pixels and an on-sky pixel resolution of 0.135 $''$/px. The sensitivity of the CCD is optimized for the 3500–6000 Å range in which this camera normally operates. Until early 2009, the LRIS "red side" (LRIS-Red I or LRISR1) consisted of a Tektronix 24μm pixel camera, with an on-sky resolution of 0.214 $''$/px. This camera had very limited quantum efficiency redward of 9000Å, and was replaced in the spring of 2009 with LRIS-Red II (LRISR2), a deep depletion CCD manufactured at LBNL with 15μm pixels and an on-sky resolution nearly identical to the blue side (0.135 $''$/px). This new camera (Rockosi et al. 2010) offered significantly-improved sensitivity at >9000Å, although at the expense of being much more adversely affected by cosmic rays and a slightly longer readout time. Unfortunately, in the following months the performance of this camera rapidly degraded and it was replaced by a nearly-identical copy (LRIS-Red III or LRISR3) in early 2011 (see §7.5.1 for more on the impact of this degradation on the observations). The two cameras are fed separately by a dichroic, allowing observations to be taken on both the red and blue sides simultaneously. Since 2007, LRIS has also been equipped with a Cassegrain Anti-Dispersion Compensator (ADC; Phillips et al. 2006), enabling observations to be taken far from the parallactic angle without large slit losses.

A small number of imaging observations were taken with ESI, the Echelle Spectrograph and Imager (Sheinis et al. 2002), instead of LRIS. ESI is mounted on Keck II and uses a single Lincoln Labs CCD with 15 μm pixels for an on-sky resolution of 0.154$''$/px.

7.2.3 Observing Procedure

Imaging

All LRIS cameras except for LRISR1 have a chip gap that runs through the center of the observable field. As a result, objects were typically centered on the "LRIS-B" position (located on "right" blue chip, near the chip gap horizontally but centered vertically) in the first exposure and dithered away from the gap in subsequent frames. Exposure times varied greatly for different fields depending on conditions and the anticipated flux of the target, but a representative strategy was to first take an "acquisition" frame of $30-60$ s on each side to confirm the field and for later photometric calibration of bright stars (which would otherwise saturate), then proceed to take five exposures of 300 s each on the red side and 330 s each

on the blue side (the longer blue-side exposure was to take advantage of the shorter read-out time compared to the red side). We would then proceed to the next field.

We had no single standard filter combination; the choice of filters depended on anticipated characteristics of the target, the filters available in the instrument, and considerations based on other science needs from the same night. Most typically we imaged with g and R simultaneously, but also frequently used g and I, or V and I.

Spectroscopy

We attempted to follow up most objects whose redshifts were previously unknown but which had "bright" host galaxies ($R \lesssim 24$ mag) with LRIS spectroscopy during subsequent runs.

In all cases, the faintness of the host galaxy required blind-offset spectroscopy. Using previously-acquired LRIS imaging (or occasionally imaging from other sources), we calculated the positional offset of the host galaxy from a nearby bright star. In most cases we attempted to choose a position angle to place another, brighter object on the slit for reference, but especially before the installation of the ADC this was not always possible as we also (at that time) attempted to observe at or near the parallactic angle to minimize slit losses (Filippenko 1982). We slewed to the field, identified the offset star on the guider camera, centered this at the "SLIT-B" position, and then performed the pre-calculated offset and began integration. We usually acquired two or three exposures on each source, of typically $900 - 1800$s each. We dithered along the slit by a few arcseconds between exposures.

The redshift of the target was almost never known in advance, and we therefore took full advantage of the spectral range of LRIS by using (in nearly all cases) the combination of the 600/4000 grating on the blue side (spectral range $3010 - 5600$ Å) and 400/8500 grating on the red side (tunable spectral range spanning 4762 Å at $1.16''$/px for LRISR2/LRISR3, or 3788 Å at $1.85''$/px for LRISR1). We used the $1.0''$ slit in almost all cases, although during nights of poor seeing the $1.5''$ slit was employed, and in one night of good seeing we used the $0.7''$ slit. For the standard $1''$slit, this setup affords a resolution of approximately 4.0 Å on the blue side and 6.9 Å on the red side.

7.3 Data Reduction

7.3.1 Imaging

We developed a fully-automated pipeline for end-to-end reduction of LRIS imaging, using a combination of IDL and python[2] routines. For observations taken in standard conditions, the pipeline performs all standard CCD reduction procedures, including bias subtraction, flat-fielding, fringe correction, cosmic ray removal, astrometry/alignment, and final combining of the frames. This was successful in most cases, although a variety of different

[2] `http://python.org`

instrument issues on certain nights or fields complicated the fully automatic reduction and required special procedures. These will be described in §7.5.1. The general data reduction procedure is described below.

Bias subtraction and gain correction

The instrument bias is removed using the overscan region on the two chips. Before the LRIS upgrade, this is performed using a custom routine that takes the median of each data row and subtracts it from the image. After the LRIS upgrade, we use the IDL routine `readmhdufits.pro` (supplied by Keck Observatory) to perform the overscan subtraction automatically by essentially the same procedure. Each amp is divided by a gain correction constant. Provisional astrometry is also added at this step and bad pixels are masked, and the two halves of the LRISB and LRISR2/3 CCD chips are separated into individual files.

Flatfielding

The quality of flat-fields acquired varied from run to run and filter to filter. Dome flats were always acquired (except for U-band, for which dome flats have insufficient signal), but flat-fielding solely with dome flats leaves some low-level residual variations in the field. Twilight flats were sometimes taken, but because of the long readout time on the red side and lengthy time to switch filters and dichroics, and the fact that twilight time was often used for spectroscopic calibrations and/or bright auxiliary science targets such as low-z supernovae, these sky flats are not available for most nights. Super-sky flats, made using a large number of different science exposures, are often possible, but scattered light from brighter stars in the field typically creates large "halos" up to arcminutes in size that are present in most images, and it requires observations of many different fields (ideally, at least five per filter) to ensure these variations do not affect the final flatfield. In the future, we will attempt to mask the halos as well using catalog positions of bright stars.

Even after gain correction and flatfielding, the LRISR1 chip often shows a "jump" between the sky level of its two amplifiers. Despite extensive tests we have been unable to conclusively identify the source of this issue although it appears to be most prominent when sky levels are low. We fix this jump by calculating the difference in medians across the amplifer gap and simply add the difference to all pixels on one amplifier.

In general, we attempted to acquire flats in the same filter+dichroic combination in which the observations were taken. On some runs this was not possible, and flats taken in the same filter but different dichroic were used instead. Testing shows that this has generally negligible impact on the quality of the flat-fields and subsequent photometric accuracy.

Fringe correction

Observations with the original LRIS I-band filter[3] or $RG850$ filters exhibit strong fringing across the LRISR1 chip. We build a fringe frame by taking the median of the exposure-normalized individual frames in this filter throughout the night. (This fringe frame is susceptible to the same challenges with bright stars as are super-sky flats, which unfortunately are unavoidable.) We then fringe-correct all images in each filter by iteratively fitting the fringe frame multiplied by a constant to minimize the absolute deviation of the sky (masking out stars, galaxies, and haloes to the extent possible).

Cosmic ray removal

Like other deep-depletion CCDs, the LRISR2 and LRISR3 cameras are severely affected by cosmic rays and other radiation events. Although the overall cosmic ray rate is not conspicuously higher than on other CCDs, a typical event produces a charge trail that may affect 100 pixels or more, streaking or curling across the image (see Smith et al. 2002 for a description of the effects of different radiation events and their effects on this CCD type); 1% of image pixels or more may be affected by radiation events in a long exposure. Ordinary cosmic ray removal tools, which usually assume that a cosmic ray will occupy only one or two pixels and that they have amplitudes of many times the sky level, struggle to remove these signatures. Instead, I developed my own cosmic ray detection and removal tool, `pzap`, which uses a variety of different algorithms to identify cosmic ray pixels in an image. In brief, this routine works by repeatedly scanning the image with a special filter that attempts to robustly estimate the flux in a given pixel *without knowledge* of any of its neighbors by taking the median of several different models combining interpolation vertically, diagonally, etc. Pixels that are sufficiently discrepant relative to the model are flagged and removed, being replaced with the model value. This procedure iterates several times, and finally a "percolation" step is employed to flag additional pixels along the cosmic ray trail even if they are only slightly above the level of noise in the image. A mask file is then written out, such that any pixels that were affected by cosmic rays are not included when stacking the image in later steps. (This same procedure is used on the LRISR1 and LRISB images as well: although the complex algorithm is somewhat overkill for the simpler cosmic ray properties evident there, it is equally effective in these more straightforward cases.) A demonstration of an LRISR2 cosmic ray before and after `pzap` processing is given in Figure 7.1.

While the `pzap` routine is nearly 100% effective when optimized individually for each image, in good seeing conditions it is capable of mistakenly flagging brighter stars (which would be severely problematic, since these are needed for calibration later). To avoid overzealous removal of pixels I chose very conservative values for the input parameters, ensuring stars are never mistakenly flagged at the risk of ocassionally missing some cosmic rays (these are later removed by median combination of the frames). In the future, I anticipate being able

[3]This original filter, available until July 2007, was only a long-pass filter and is described as $I_{\rm long}$ in our data tables; the newer I filter installed in 2008 has a long-wavelength cutoff that prevents most fringing.

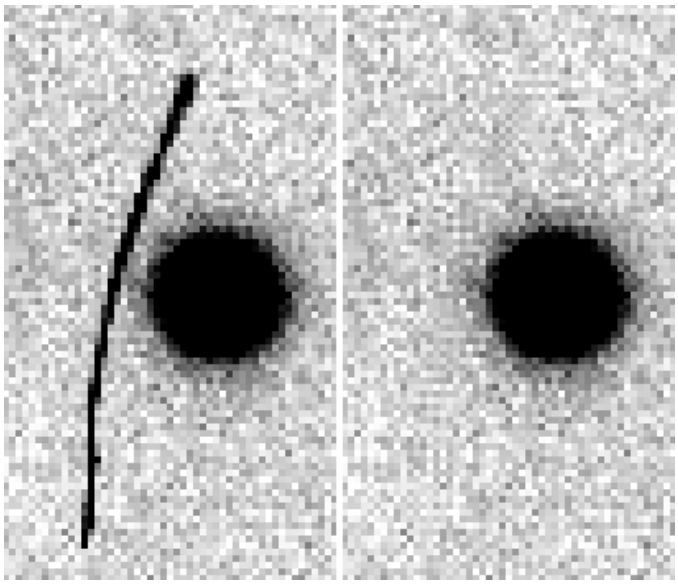

Figure 7.1 Illustration of a long, muon-trailed LRISR-2 cosmic-ray removal by the automated `pzap` routine.

to reject more zealously and reliably reject essentially all cosmic ray pixels (with no adverse effects on bright stars) by iteratively and automatically "training" on a set of LRIS images to optimize the numerous hard-coded parameters that control the algorithm's behavior.

Astrometry and alignment

Astrometry is performed on individual images using a custom Python routine, `autoastrometry.py`. This code uses SEXtractor (Bertin & Arnouts 1996) to calculate the XY and RA/dec positions of all sources in the image, and then attempts to find matching asterisms against a list of RA/dec positions from a catalog, allowing the routine to calculate and apply rotational and translational corrections to the image. (Distortion parameters are *not* yet fit for: fortunately, the distortions in LRIS are minor albeit not entirely negligible, about $0.4''$ RMS across the field. Future reductions and releases will address this.) This procedure is illustrated in Figure 7.2. For each field, the reduction pipeline first chooses *one* image and performs astrometry relative to a reference catalog (SDSS DR7 if available, otherwise USNO B1.0). SExtractor is then used to produced a source catalog from this image, and all other images of the same field are aligned relative to this image.

Stacking

Finally, individual frames on a single source are combined using SWarp (Bertin et al. 2002). We resample the images to a single grid (the default LANCZOS3 resampling algorithm is used) and subtract a median sky-filter (which helps to remove artifacts due to

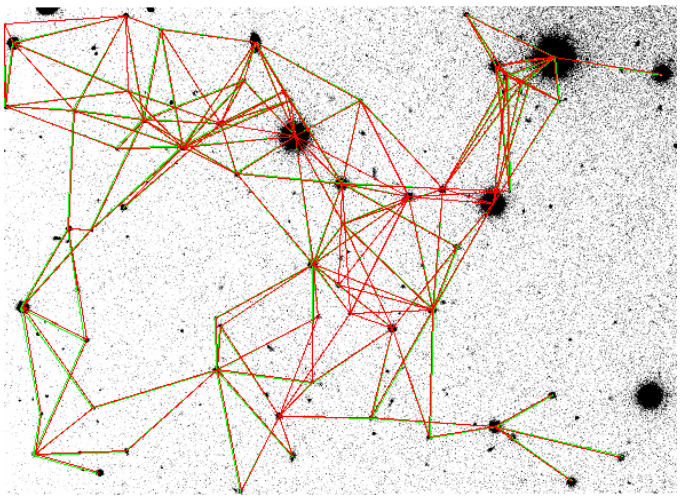

Figure 7.2 Illustration of the automatic alignment procedure on an LRISB image (dimensions $5.4 \times 3.8''$). Star asterisms (clusters of distance-pairs radiating from an individual star) are pattern-matched between the catalog and the image, creating a mesh of overlapping asterims shown in the diagram. In this figure, the red lines indiate the asterisms in image coordinates (lines radiate from the measured centroids) and the green lines in the reference catalog frame (lines radiate from the centroids of where the stars "should" be, according to the catalog.)

bad flatfielding from dome flats, etc., although this somewhat oversubtracts the sky around galaxy and star haloes); the images are normalized based on the exposure time and median-combined, producing the final image. A final `autoastrometry.py` run is then performed on the stack relative to SDSS or USNO. Our stacks generally incorporate only the "right" half of each of the two-chip LRISB and LRISR2 CCDs to ensure that stars near the chip gap are not misaligned due to discontinuity of this unfit distortion correction near the chip edges (which might later adversely affect photometry).

ESI

ESI data are reduced using essentially the same procedure under a modified version of the LRIS pipeline. Additionally, since most of the ESI filters strongly vignette the instrument field of view (usually in a non-rectagonal pattern), we used a mask to flag the vignetted pixels and use only the "good" region of each image without having to crop unnecessarily.

7.3.2 Spectroscopy

The spectroscopic data are reduced using several procedures in common with imaging. Bias subtraction is identical. Flat-fielding is performed using dome flats in all cases. Unfortunately, there is no clear way to remove fringing on the LRISR1 chip given the small changes in the wavelength range that occur when slewing the telescope between different

targets.

We use a modified version of `pzap` to simultaneously remove the sky and any cosmic rays affecting the spectrum. This procedure works in a similar way to `pzap` itself, but also simultaneously builds a model of the sky spectrum (by median across column) and slit profile (median filter across rows) in addition to the smaller-scale cosmic ray filter. The sky is subtracted off and cosmic rays are interpolated over using the model. This routine is essentially 100% effective in all spectra (it does oversubtract the sky around bright emission lines on extended objects, which does not affect the science here).

With a few rare exceptions, all host galaxies studied in this program are extremely faint, with $S/N \lesssim 1$/pix, and usually have unknown redshift. Spectral analysis therefore is largely a search for line signatures against a continuum trace that is itself marginally detected. Given this, I do not generally flux-calibrate the data by default, as it is easier to identify lines if the S/N is constant across the chip (which is generally the case outside sky lines, since spectroscopic observations are close to read-noise dominated.) Line candidates are searched for primarily in the 2D spectrum to better distinguish real lines from outliers (sky line and cosmic-ray residuals and the effects of bad pixels) and when possible are verified by checking for their continued presence in multiple frames (for most sources we take two frames, typically dithered by a few arcseconds). Spectra are then extracted using a simple custom IDL routine and wavelength-calibrated using the positions of the night sky lines. Once the wavelengths of the known lines are determined, I then search for other, fainter emission lines elsewhere in the 1D spectrum based on the expected locations of additional lines at different possible redshifts.

The LRISR1 chip suffers from severe fringing redward of $\sim$ 7700 Å that is not easily removed by flatfielding. However, during photometric nights the fringing signature—and sky-lines generally—can be removed fairly effectively by subtracting two dithered, scaled exposures (at the expense of somewhat increased read-noise). When necessary, we have employed this as an alternate 2D reduction technique for identifying line candidates.

The analysis of the spectroscopy is, at this stage, provisional, and further reductions will be necessary to better constrain the existence of low-EW emission lines in spectra and to flux-calibrate the observations and quantify the line fluxes in most cases.

7.4 Data Analysis Procedures

7.4.1 Host Identification

Identifying a host galaxy from ground-based imaging ranges from relatively straightforward to extremely challenging, depending on the accuracy of the position, brightness of the host galaxy, and the density of stars and galaxies in the field.

In the best circumstances, a ground-based optical afterglow position is available; the positional accuracy possible (in principle) from most ground-based detectors is usually at least $0.5''$ and often much better, depending on the instrument pixel scale and depth of the image

relative to a reference catalog. (Positions from the Chandra X-ray Observatory or radio telescopes, while much less common, also provide <0.5″accuracy.) In such cases the host ID can usually be done unambiguously since essentially the entire error circle overlaps the flux of a detected source in our Keck imaging. However, positions quoted in the GCN circulars (where afterglow discoveries are first announced) are often necessarily done in haste without the opportunity to perform accurate astrometry. Usually, the report of sub-arcsecond astrometric uncertainty is indicative of a reliable position fit against a reference catalog and is straightforward to interpret, but when no uncertainty is specified it is not always clear how to interpret the position: the position may actually be quite precise (but the uncertainty was omitted in the circular) or it may be approximate at the level of several arcseconds. In the latter case (and even, in some cases, where an uncertainty is specified), we attempt to confirm or improve the position via direct access to the imaging (small cutouts in posted figures on the web or in published papers are usually sufficient).

Otherwise, we must rely on *Swift* itself to supply the afterglow coordinates. A *Swift*-UVOT position, taken from Roming et al. (2009) and usually accurate to about 0.6″, can usually unambiguously identify the host galaxy. Significantly more uncertainty in the identification results when only an X-ray position is available. In these cases, we employ the UVOT-calibrated ("UVOT-enhanced") XRT positions of Goad et al. (2007) and Evans et al. (2009) in addition to the DSS/SDSS-calibrated XRT positions of Butler (2007). These positions have typical accuracy of 1.5″-2.5″ (90% confidence containment radius), which is often sufficient to identify the host to reasonable confidence (a single object is contained within the error circle), but in other cases the host identification is more ambiguous. The most obvious such circumstance occurs when more than one detected source is consistent with the error circle, but several others are often encountered, in particular when the two positions disagree by a nontrivial amount (and a host galaxy is consistent with one, but not the other), or when a relatively bright host candidate is visible slightly (but entirely) oustide both 90% confidence error circles.

A different sort of uncertainty is often encountered in dealing with SGRBs, for which there is theoretical and observational precedent (e.g., Bloom et al. 1999, 2007b; Stratta et al. 2007; Church et al. 2011) for considering "host" candidates that are far from the actual afterglow site: if the SGRB progenitor is an old, degenerate star in at least some cases, such an object could be flung far from its host by a natal systematic kick (or at the very least exist in places such as the outer stellar halo or intracluster medium on occasion.) In these cases, host identification is intrinsically uncertain regardless of how precise the on-sky localization is made, and whether or not to call a nearby galaxy a "host" is at best a probabilistic assessment.

In this work, we generally do not call an object a host galaxy (and include it in our statistical host analyses at the end of this Chapter) unless its detected light at least overlaps a $< 2''$ XRT error circle and any other available reliable positions. When multiple sources fulfill this basic criterion, we choose the one that is most consistent with all available positions (i.e., both XRT error circles); if multiple objects seem close to equally consistent with the afterglow positions (only a few cases) we generally remain agnostic about the choice of host

identification and consider both as host "candidates", but do not tag one as a host galaxy.

Of course, in such cases we must remain open to the possibility of incorrect identification. In fact, it must be noted that in a sample of this size, some false coincidences are unavoidable even with a perfect position. Following the calculations of Bloom et al. (2002), the probability that a faint galaxy ($R \sim 25$ mag, unresolved in $0.7''$ seeing) will be consistent with a $0.5''$ circle placed randomly on the sky is approximately 2%; for a $2''$ XRT circle it is as high as 12%. These probabilities may be further amplified somewhat by gravitational lensing or small-to-large-scale clustering effects (e.g., another galaxy in the same group seen in projection with the host). While we may therefore have reasonable confidence that any individual source in isolation is correctly identified, in a sample of hundreds of bursts (as presented here) it is evident that there should certainly several false matches among numerous accurate associations (Cobb et al. 2006; Cobb & Bailyn 2008). In a few cases, additional data (such as afterglow spectroscopy) allows us to clearly identify cases where a source that would appear to be a nearly-unambiguous host is in fact unassociated with the burst (e.g., GRB 060512 and GRB 080319C, discussed in §7.5.2). Several other cases where a brighter galaxy is observed within 1–$2''$ of the true host (061111A, 060111B, 060428B) further illustrate the perils of host identification. Nevertheless, these represent a minority of cases (and are not necessarily surprising in an imaging sample of well over 100 objects, given the probabilities above); we expect that in bulk we have identified the host correctly a large majority of the time.

In Table C.1 we present a complete list of all positions which were employed to identify the host galaxy and are showin in Figures 7.8–7.16 (occasionally some of the less accurate positions are omitted when more precise positions are available). Note that while we often use the same images used to derive existing positions in the literature, our coordinates are expected to be more accurate and with better-constrained uncertainty.

We describe the host identification process for each individual object in the sample in §7.5.2.

7.4.2 Photometric Calibration

Accurately calibrating the data for this survey is challenging. Observations were taken in a variety of conditions, and only about half of runs were photometric according to our notes and the CFHT SkyProbe archives[4]. Because of the depth of the Keck observations, fields are inevitably crowded at the faint level, while bright stars saturate and are unusable for photometry.

We use at least one of several different techniques to calibrate each field, in order of precedence:

- *SDSS DR7 calibration.* Many fields overlap the footprint of the last imaging release of the Sloan Digital Sky Survey (Abazajian et al. 2009), which provides the simplest

[4] `http://www.cfht.hawaii.edu/Instruments/Elixir/skyprobe/home.html`

way of calibrating the observations. To maximize the number of usable stars involved in the calibration, for fields where a "short" initial exposure is available (see §7.2.3) we first perform photometry of all unsaturated stars in this exposure to extend the SDSS calibration to fainter magnitudes. This produces an "extended" star catalog can then be used to directly calibrate the full stack (in which more of the original SDSS stars are saturated.) For measurements in the $BVRI$ filters we employ the SDSS filter transforms from Lupton (2005)[5]. $RG850$ is calibrated to z-band and treated as z.

- *Landolt photometry.* On photometric nights, we observed at least one (usually two or three) different standard fields from Landolt (2009), sometimes repeatedly. We calibrate our observations relative to these observations in a standard way, correcting the instrumental magnitude to an "infinite" aperture (actually, because all observed fields are quite crowded, we treat $5''$ as "infinite"; typical Keck seeing is 0.7–1.1$''$), performing an airmass correction (generally using archival airmass constants), and then inverting the procedure for a set of secondary standards in each field.

- *Nickel photometry.* For non-SDSS fields on non-photometric nights, we acquired calibration data using the Nickel 1m telescope at Lick Observatory over a series of runs between March and December of 2009. During these runs (all of which were photometric), we observed each GRB field for typically 3 exposures of 300 s each at least twice in each relevant filter, observing Landolt standards frequently throughout the night. This was used to calibrate secondary standards in the field using the same standard technique in the previous paragraph, except that it was normally possible to solve robustly for the airmass term in each filter for each night due to the much larger of standard-star observations possible. Because the Nickel imaging is shallow, we extend the calibration to fainter magnitudes using the first, short LRIS exposure (when available) using the same procedure as for SDSS stars.

Crosschecks of the various techniques on photometric nights suggest that the three calibrations are constistent to within 5% for most fields (with most exceptions being attributable to brief nonphotometric conditions.) In interpreting the photometry given later in this chapter, a systematic uncertainty of <5% is therefore reasonable for SDSS fields, increasing to $\sim 5 - 10\%$ for Landolt and Nickel fields due to the extra calibration step.

An important exception concenrs imaging with the LRISR2 CCD. On all four program nights (all of which were photometric) we identify a significant systematic offset (of about 0.2–0.6 mag) between fields calibrated using local standards (SDSS or Nickel standards) and what would be inferred from the standard stars. We have not conclusively identified the origin of this discrepancy. Possibilities include a shutter error in the red camera (although none has been reported), nonlinear behavior (the most likely cause, although the discrepancy is comparable between I-band observations, where the sky level is quite low, and $RG850$ observations where the sky was close to 30000 counts per frame), or (in the case of the

[5] `http://www.sdss.org/dr7/algorithms/sdssUBVRITransform.html#Lupton2005`

final run when the CCD problems had developed) CTE-related flux losses. As a result, we were unable to use the Landolt calibrations. In their place, we used fields with SDSS observations to establish the zeropoints in the science frames, and apply these on other science fields without SDSS data. (Comparing SDSS fields, this assumption appears to be valid to $\pm \sim 0.15$ mag.)

For a few fields, none of the above calibration techniques were available. In these cases we use USNO or other means to provide a provisional calibration. The calibration method is given in Table C.5.

Calibration was accomplished by means of an automatic pipeline (written in IDL, and relying in particular on the `aper` photometry procedure in the GSFC IDL package) which automatically performs star-galaxy separation and ensures that aperture corrections are not affected by crowding and that the calibration is not varying significantly from image to image. The end product of the calibration procedures is a list of nonsaturated standards suitable for direct comparison to the host galaxy using an arbitrary aperture radius in the stacked images.

7.4.3 Host Photometry

Finally, we calculate the flux of the host galaxy (and any other sources of interest in the field). The host photometry procedure is also automatic, calculating the instrumental magnitudes of secondary standards and galaxy targets in the stacked image using `aper` and calibrating them using the calibrations above. The aperture radius is $1''$ for images with good seeing (even if the effective seeing is much less than this, due to the possibility of subtle extension), or 1.1 times the seeing FWHM otherwise. If the host is noticeably extended, we increase the aperture radius manually. In a few cases, due to nearby blending objects we *decrease* the aperture size slightly to avoid contamination. (However, note that in such cases, the table values should not be relied upon exclusively.) The results are presented in the Appendix (Table C.5).

Several additional caveats are in order in interpreting the photometry presented in this table. Due to the large number of fields and filters (approximately 300), the photometry has *not* been extensively cross-checked. Although the results given by our automated procedure are generally reliable, given the challenges in bridging deep Keck images (in which most fainter objects are extended and brighter objects saturate) with fainter catalogs, systematic deviations in the calibration beyond the expected $5 - 10\%$ are possible in rare cases. Particular caution is warranted when the source is extended or when image quality differs between the observed filters or observing epochs. As a result, we recommend that users who require precision analysis of individual analysis (e.g., input into photo-zs) perform photometry manually against the images using a fixed, specified aperture. For coarser purposes, however, the calibrations should be reliable.

7.5 Observations and Host Galaxies

7.5.1 Log of Observations

Table 7.1: Table of Keck Runs

UT date	half[a]	Instrument	Program[b]	Observer[c]	Photometric?[d]	Avg. seeing
2005-06-05		LRIS	CIT	Kulkarni	yes	1.0″
2005-08-04		ESI	UCB	Bloom	no	0.7″
2005-12-04	2	LRIS1	UCB	Bloom	yes	0.6″
2006-05-30		LRIS1	UCB	Bloom	yes	1.0″
2006-05-31		LRIS1	UCB	Bloom	yes	1.4″
2006-07-25		LRIS1	UCB	Bloom	yes	1.0″
2006-07-26		LRIS1	UCB	Bloom	yes	1.0″
2006-09-21		LRIS1	UCB	Perley	yes	1.0″
2006-11-21		LRIS1	UCB	Perley	before 2AM	0.7″
2006-12-19		LRIS1	CIT	Kulkarni	yes	1.1″
2007-04-16		LRIS1	UCB	Perley	yes	1.6″
2007-05-21		LRIS1	TOO	Stanford	no	0.8″
2007-07-18		LRIS1-ADC	UCB	Perley	yes	0.8″
2007-08-11		LRIS1-ADC	UCB	Bloom	yes	1.0″
2007-08-12		LRIS1-ADC	CIT	Cenko	yes	0.7″
2007-10-09	1	LRIS1-ADC	UCB	Perley	yes	0.9″
2007-10-10	1	LRIS1-ADC	UCB	Perley	no	1.0″
2007-10-11		LRIS1-ADC	UCB	Perley	after 2AM	1.0″
2007-12-11		LRIS1-ADC	CIT	Kasliwal	no	1.3″
2007-12-12	2	LRIS1-ADC	UCB	Perley	unknown[e]	
2007-12-13	2	LRIS1-ADC	UCB	Perley	yes[e]	1.2″
2008-02-12		LRIS1-ADC	UCB	Perley	after 1AM	1.0″
2008-06-07		LRIS1-ADC	UCB	Perley	before 3AM	0.9″
2008-08-02	2	LRIS1-ADC	UCB	Perley	yes	0.8″
2008-08-03	2	LRIS1-ADC	UCB	Perley	no	0.9″
2008-12-23		LRIS1-ADC	TOO	Kalirai	yes	1.0″
2009-02-19		LRIS1-ADC	UCB	Perley	no	0.8″
2009-06-25		LRIS2-ADC	UCB	Perley	yes	0.7″
2010-02-07		LRIS2-ADC	UCB	Perley	yes	1.4″
2010-07-08		LRIS2-ADC	UCB	Perley	yes	1.0″
2010-10-31		LRIS2-ADC	CIT	Kasliwal	(no imaging)	
2010-11-07		LRIS2-ADC	UCB	Perley	yes	0.8″
2011-03-07		LRIS3-ADC	PTF	Filippenko	(no imaging)	
2011-06-03		LRIS3-ADC	PTF	Filippenko	no	1.0″

[a]Denotes a half-night (1 = first half, 2 = second half).

[b]UCB indicates our primary host program. CIT includes various Caltech programs.

[c]In most cases more than one observer was present. Only the primary observer is given here.

[d]For partially photometric nights, the start/end of photometric conditions is given in local time.

[e]Due to the apparent vignetting of the primary seen during focusing, these observations should be treated as nonphotometric.

A summary of our observations is given in Table 7.1, including the cameras installed and primary observer. Most of these observing runs are formally part of our program under the UCB group and devoted mostly to GRBs; however, some additional data was included from the Caltech transient program or from target-of-opportunity observations of dark bursts (since no afterglow was found, the latter are equally useful as host-galaxy constraints using X-ray or radio positions). These supplementary nights generally only involved observations of a small number of host targets during the night, as opposed to the official UCB nights which were largely dedicated to host science.

Several runs were adversely affected by instrumental issues—most of which were minor but others were more significant. In our reductions we have attempted to remove these artifacts from the final data products where possible. Nevertheless, an observer rereducing the data from scratch should be aware of issues apparent in some frames. A detailed report on instrument conditions during the program nights follows:

2005-08-04 (ESI) — No persistent data quality issues observed. However, for most of the night we were discouraged from attempting to switch from spectroscopy to imaging mode due to concerns about the decker becoming stuck (this had occurred the previous night). As this was also the first night of the program (no pre-imaging), we attempted echelle spectroscopy blindly at several afterglow locations, generally without success. Late in the night we did switch to imaging and experienced no difficulties.

2005-12-04 — Most V-band frames were taken with the D560 dichroic, whose spectral cutoff falls near the center of the filter response curve. As a result the thoroughput was approximately halved and the spectral response is narrower and bluer than a standard V-band observation. Observations in this mode were reduced normally, but due to the difference in spectral response are marked V_{560} in future output tables.

2006-05-30 — No persistent data quality issues observed.

2006-07-25/26 — The R-band filter was improperly installed by the support staff at the start of the night (a different filter was installed in its place) and a few frames were accidentally taken in an order-blocking filter before the problem was noticed and the correct filter installed. Most frames taken during the second night are severely out of focus, with a distorted PSF. Many frames show scattered light.

2006-09-21 — No persistent data quality issues observed.

2006-11-21 — Poor focus is evident on some blue-side images.

2007-04-16 — This run was afflicted by numerous problems. The telescope guiding system frequently lost the guide star and dramatically overcorrected, causing the telescope to jump randomly by several arcseconds while exposing, and exposures suffering from this problem (half or more on some fields) had to be thrown out. During the night, the blue-side shutter broke, forcing subsequent observations to be taken using the instrument trapdoor in

place of the camera shutter. Finally, for unknown reasons images taken with the blue camera are highly vignetted, with a vignetting pattern that changes dramatically from exposure to exposure (fortunately, this only affects the edges of the image). The seeing was also very poor and highly variable.

2007-07-18 — Towards the end of the night, during a routine instrument change the I-band filter shattered inside the filter wheel. Examination of the instrument the next day found small fragments of the filter elsewhere in the instrument, causing LRIS to be offline for several days following. Surprisingly, inspection of the data does not show any artifacts or data quality issues even after this event occurred. (Complications likely associated with this event did briefly cause the blue camera to go offline, but it was restored by software fixes.)

2007-08-11 — Poor focus is evident on some red-side images.

2007-10-09/10/11 — No persistent data quality issues.

2007-12-12 — During the mirror-segment alignment procedure ("mira") the image of the primary mirror was observed to be noticeably vignetted. Further investigation was unable to determine the source of the problem, although the data quality was not significantly affected aside from some possible loss of thoroughput.

2008-02-11 — No persistent data quality issues.

2008-06-07 — No persistent data quality issues.

2008-08-02 — No persistent data quality issues.

2009-02-19 — One of the amplifiers on the blue side failed before this run. This would normally affect the half of the left chip nearest the chip gap, but the readout method was reconfigured to read out the near side of the chip at the expense of the far side—however, in the raw fits images these pixels appear on the far side of the chip. (Since only the right side of the CCD is fully reduced, this does not affect our current imaging products.) A few images on both sides exhibit poor focus.

2009-06-25 — Most images on the red side exhibit variable focus across the field, with good focus close to the field center but degraded PSFs towards the edges, especially in I and z-bands. This appears to have affected our automatic photometry procedure (there is no straightforward way to aperture-correct) and so photometry from this night should be used with caution.

2010-02-07 — LRIS developed significant charge transfer efficiency (CTE) problems in the months prior to this run, with the different amplifiers degrading to different degrees. Half of the left CCD chip was effectively unusuable and reduction of this chip was ignored. Half of the right CCD chip (the half further from the central chip gap) also suffered from smaller CTE problems in the standard readout mode, but switching to a single-amplifier readout mode for our imaging observations removed this issue (at the expense of significantly

lengthened readout time). Only the

2010-07-08 — Data quality issues were similar to the previous run and the left chip was not used. To speed red-side readout we chose to use the standard readout mode, causing the far half of the right chip to exhibit limited CTE problems. The near half of the right chip, where the source falls in both imaging and spectroscopy mode, was not affected.

2010-11-07 — By this run LRIS-2 had developed significant CTE problems on all amplifiers, including the primary one. Examination of cosmic rays showed that while trailing is apparent in dark frames its affects on science data are likely limited (i.e., almost all flux remained contained within the PSF and background noise was not significantly altered). Nevertheless, observations from this run should be used with caution. (These same considerations apply to the single spectrum taken on 2010-10-31.) To help mitigate this problem, we used a different spectroscopic setup with a lower-resolution blue-side grism (300/5000) and the D680 dichroic to shift more of the light onto the blue camera during spectroscopy. The grating temporarily became stuck in the red side at the end of the night, preventing acquisition of Landolt standard observations, but due to the problems discussed above we are unable to use our Landolt observations for LRISR2 anyway.

Additional non-persistent data quality issues are also evident on several different runs. On some images scattered light is evident on one or both cameras, usually for several exposures in a row on a field (with the pattern changing with each exposure) before disappearing for the rest of the night.

No novel problems not listed here occurred on any of the non-program nights, although some problems (poor focus, scattered light) did occur on some frames of those nights also.

7.5.2 GRB Host Galaxies

All fields imaged during our program are presented in Figures 7.8–7.16. We describe the conventions used in coloring and labeling these images below.

Images are colorized using the RGB channels of DS9 (Joye & Mandel 2003). Most of our imaging is two-color only and so the green channel image is constructed by combination of the other two channels in such cases (usually by a weighted linear combination.) Even when three colors are available, if one image is of notably lower quality we occasionally still favor the interpolated color map. It is important to note that the colors in these images are only meaningful in a relative sense within an image, and cannot be precisely compared between images (the scaling is not directly tied to the photometric calibration or any other factor, and furthermore many different filter combinations are employed). Furthermore, for clarity in displaying faint objects we allow the pixel values to saturate towards white even for fluxes that are not particularly large.

Afterglow positions are shown by thin, colored lines. The color indicates the wavelength and/or instrument: blue indicates X-ray, purple indicates UV (or UVOT B- or V-band); orange indicates ground-based optical; red indicates ground-based NIR; yellow indicates

radio or millimeter. The X-ray positions are further divided into shades of blue by calibration method: "cyan" is a UVOT-calibrated position while "sky blue" indicates a DSS-calibrated position. A darker shade of blue indicates either an uncalibrated (boresight) XRT position or an X-ray position from another satellite such as XMM-Newton or Chandra. The size of these error circles is based on the quoted uncertainty in the original source, if specified (almost always 90% for *Swift* UVOT/XRT error circles; the confidence is almost never specified in all other situations).

Identified objects of interest are shown by thick, dashed lines with a letter caption. An object which we associate with the GRB host is designated by an "H", other objects of interest are usually denoted "A", "B", "C", etc. although sometimes other conventions are used to try to retain consistency with the object identifiers chosen in previous studies of the same field. If the photometry aperture radius was manually forced to a value other than the default value (either $1.0''$ or $1.1\times$ the seeeing FWHM, whichever is larger) this is shown; in other cases a $1.0''$ radius circle is plotted regardless of the value used for photometry (which means for images with poor seeing the aperture is often larger than shown).

In the remainder of this section, we describe each field individually, including (where possible) some of the notable properties of the burst. As the X-ray afterglow behavior is often of interest (especially in the context of interpreting an optical nondetection), we frequently refer to *Swift* XRT light curves; these are taken from the automated analyses of Evans et al. (2007) and Butler & Kocevski (2007a). Other works are cited where appropriate.

GRB 041219A

This was only the second GRB detected by *Swift*, and remains one of the brightest events of the entire mission. The afterglow is very red due to strong extinction by Galactic dust, given its Galactic latitude of $b = 0.1°$ (an extinction of $E_{B-V} = 1.80$ mag is given by the dust maps of Schlegel et al. 1998, corresponding to $A_R \sim 6$ mag), although it was detected by several small telescopes at early times and has an unusual early light curve (Blake et al. 2005; Vestrand et al. 2005). In spite of this formidable extinction, a host galaxy with $R = 25.0$ mag (uncorrected) is actually detected in a relatively shallow ESI image underlying the PAIRITEL position. The object is clearly extended in the N-S direction in the image, suggesting it is not a foreground star. Given the anticipated extinction-corrected brightness ($R \sim 20$ mag), this host is likely at quite low redshift, although we have not attempted spectroscopic observations.

GRB 041223

This early *Swift* GRB was the first to be observed by the XRT, although it was not slewed to rapidly; it was also imaged in the NIR by the VLT on several epochs (Burrows et al. 2005c). Our ESI imaging of this field is significantly hindered by stray light, and the problem is particularly bad at around the GRB location with wide bands of scattered light crossing the GRB position in three of five exposures. No source is detected in either the

total combined image or the sum of the two unaffected exposures at the well-determined IR position.

GRB 050124

The afterglow of this event was detected only at IR wavelengths (Berger et al. 2005b) and in X-rays, making it a candidate dark burst. Several sources are detected in our imaging consistent with the original XRT error circle, and significant ambiguity exists among the reported positions (although the UVOT-enhanced position would favor object "B", which is also noted as a potential host candidate by Pellizza et al. 2006a). We aligned the small finding-chart image posted online by Berger & Kulkarni 2005 directly against our Keck imaging to determine the most accurate position of the afterglow—which, surprisingly, turns out to be consistent with none of these objects, suggesting that the true host is quite faint.

GRB 050126

The afterglow of GRB was also detected only at IR wavelengths and is quite faint in these observations (Berger et al. 2005b), although optical limits are shallow and the X-ray afterglow is also faint. The position reported in that work is consistent with the location of a bright ($R = 22.2$ mag), red ($B - R = 2.5$ mag) source in our imaging; ESI spectroscopy of this object already reported by Berger et al. identifies the redshift as z =1.29. The ESI imaging presented here has not previously been published.

XRF050215B

This GRB was the first X-ray flash discovered by *Swift* and the subject of the study of Levan et al. (2006e). The position reported in that work simply repeats the GCN position of Tanvir et al. 2005, for which no uncertainty is quoted—nevertheless, it is sufficient to unambiguously identify the host galaxy in our Keck imaging. The host is well-detected in both filters and is fairly blue, with $B - R = 0.9$ mag. Our spectroscopy of this event was interrupted by the occurrence of GRB 061121 (Page et al. 2006b) during the second of two planned exposures, but even so we detect a clear, strong emission line in both the completed exposure and the interrupted exposure at the blue end of the spectrograph, which we identify as Lyman α at a redshift of $z = 2.62$. (An alternative redshift would be $z = 0.18$ if the emission were due to [O II], which would both make this galaxy remarkably underluminous and predict the presence of other emission lines in the red spectrum which we do not observe.) This one of few probable Lyman-α detections in our study. Another nearby object placed on the slit, object "A", is unrelated; a single emission line is visible that we associate with [O II] at $z = 1.00$.

GRB 050319

This was one of the first bright GRBs of the *Swift* era and has been extensively studied by many groups. It is at moderately high redshift, $z = 3.24$ (Fynbo et al. 2005). Given this redshift, we unsurprisingly do not detect any source consistent with any of the reported afterglow positions in our relatively shallow imaging observations.

GRB 050401

This well-studied GRB is notable for its very strong spectroscopic DLA and clear evidence of dust extinction in the GRB afterglow, suggesting it occurred in a relatively large, gas-rich host galaxy (Watson et al. 2006). Indeed, despite the absorption redshift of $z = 2.899$, we marginally detect a very faint ($R \sim 27$ mag) host galaxy in our imaging, underlying the optical position. A second, much brighter object appears at an offset of $\sim 2''$ and could correspond to the absorber identified in the spectrum at $z = 2.5$. This result was previously reported by our group in Chen et al. (2009).

GRB 050408

This X-ray-rich gamma-ray burst was detected by HETE-2, but the afterglow was followed by *Swift* and many ground-based observers. The afterglow is significantly dust-extinguished, and the optical spectrum shows numerous unusual absorption lines (Foley et al. 2006). We detect a relatively bright, blue, and noticeably extended host galaxy centered just slightly south of the optical position of Aslan et al. (2005); this galaxy was previously reported by De Ugarte Postigo et al. (2007).

GRB 050412

Owing to the faintness of the X-ray afterglow only a relatively poor position is available, which contains several host candidates. The brightest of these ("A") is a red object with $R = 22.4$ mag; despite this brightness and good signal-to-noise we identify no clear emission lines in our spectroscopy, which may suggest it is a quiescent galaxy. Three other, much fainter objects in the field have magnitudes of $R \sim 25$ mag (because of the poor seeing experienced during the imaging of this field, they are only marginally detected). Because of its brightness, object A is a statistically significant association and represents a plausible host, whereas the appearance of several fainter objects in an error circle this large is expected due to random chance. Based on these host properties and the remarkable X-ray faintness of this object, this source may be an unusual example of a "naked" long-duration GRB (Vetere et al. 2008, see also Chapter 2) generated by an older progenitor, although there is no firm evidence proving this case. This was the first object in the P60 sample, and will be discussed in more detail in the next chapter (which focuses on dark P60 events and their hosts specifically).

GRB 050416B

The initially reported XRT afterglow for this event (Kennea et al. 2005) was later retracted (Parola et al. 2005), and no verified counterpart was detected at optical/NIR wavelengths, so there is no position available to identify the host in our imaging.

GRB 050502A

This high-redshift burst was detected by INTEGRAL; afterglow spectroscopy using the HIRES echelle spectrograph identified a redshift of $z = 3.793$ (Prochaska et al. 2005). Unsurprisingly, considering this redshift, we do not detect any host-galaxy counterpart at the afterglow position to deep limits of $V > 26.3$ mag, $I > 25.4$ mag.

GRB 050502B

This GRB is perhaps best-known for the spectacular X-ray flare that appeared in its light curve at ~ 12 minutes after the gamma-ray trigger (Falcone et al. 2006), the fluence of which was comparable to that of the GRB itself. However, it is also notable for its faint and notably red optical counterpart (Cenko et al. 2005). In our Keck imaging, no source is identified consistent with either the optical or X-ray positions, unambiguously ruling out a bright host galaxy. The host is likely highly reddened and undetectable at optical wavelengths, small and underluminous, or at high redshift. Future IR imaging will be necessary to distinguish these hypotheses. The high-redshift model was favored by Afonso et al. (2011), who estimate a redshift of $z = 5.2 \pm 0.3$ from the afterglow colors.

SGRB 050509B

As the first short-duration GRB with a detected afterglow, this event has been the subject of intense study by many groups around the world (Bloom et al. 2006f; Gehrels et al. 2005; Hjorth et al. 2005a). The environment of this event is remarkable: the XRT positions are within with the halo of a luminous, red elliptical galaxy at redshift $z = 0.2248$; the galaxy is a bright member of a cluster and has almost no star formation ($< 0.1 M_{\odot}$/yr).

A comprehensive report of Keck imaging of this field and spectroscopy of the putative host has already been given by our group in Bloom et al. (2006f). The imaging data presented here is not the same as that which was presented in that work (it was acquired one month later) but was taken with the same instrument and filters, and is of generally comparable depth and quality. Since the publication of those early works, the improvements to the XRT astrometric calibration have somewhat refined the error circle further, but remained generally compatible with the original positions; the updated circles are shown in Figure 7.8. This revision does not qualitatively change any features of this system–the position remains in the outer parts of the bright elliptical galaxy G0 but is also consistent a number of faint, blue sources that probably represent background galaxies.

GRB 050603

The luminous afterglow of this event was detected by the UVOT and Very Large Array (VLA) as well as numerous ground-based telescopes; it is one of the brightest events of the *Swift* era (Grupe et al. 2006) despite a redshift of $z = 2.821$ (Berger & Becker 2005). The optical position of Berger & McWilliam (2005) is significantly offset from the VLA position of Cameron (2005a) and the UVOT position, but in this case it does not matter: there is no detection of a host galaxy at any of these locations to $R > 26.1$ mag.

GRB 050607

This was a relatively faint *Swift* burst, and had only a faint optical afterglow. Unfortunately, the afterglow position is very close ($3''$) to a bright, blue foreground star, making identification of a host difficult. (There is some hint of excess emission below the optical position above the wings of the stellar PSF, but the star is highly saturated and we have been unable to model the PSF sufficiently well to demonstrate this unambiguously.) A conservative limit for any host is $R > 24.5$ mag. Further details of this source are given in the next chapter.

SGRB 050709

This was the first short burst with an optical counterpart; it was localized to the outer regions of a dwarf galaxy at $z = 0.16$ with only modest current star-formation (Fox et al. 2005b; Villasenor et al. 2005; Hjorth et al. 2005b). We measure $R = 21.2$ mag for this galaxy in our imaging. This host galaxy has already been studied extensively with HST and other major facilities and is only mentioned here for completeness.

GRB 050712

This GRB was noted for its rapid early variability in both the XRT and UVOT (De Pasquale et al. 2006). We detect a faint, blue host galaxy at the UVOT afterglow position ($V = 24.6$ mag, $V - I = 0.5$ mag). The host appears marginally resolved in the NW-SE direction. We attempted spectroscopy of this source and detect a faint continuum, but no absorption or emission lines are observed over the spectral range.

GRB 050713A

This was a bright GRB, notable for extensive X-ray flaring also detected in BAT and ground-based detections with several rapid follow-up telescopes (Guetta et al. 2007; Morris et al. 2007). This field was imaged with both ESI and LRIS. Although the LRIS integration was longer, scattered light from a nearby very bright ($\sim$6 mag) star is vastly worse in the LRIS image and only the ESI image is usable for photometry. We detect a host galaxy near the detection threshold of this image.

GRB 050713B

This event had a bright X-ray afterglow but no optical detection despite early follow-up (Lin et al. 2005). We imaged this event in g and I with LRIS (an ESI R-band epoch unfortunately was offset from the OT location) and detect a probable faint host galaxy at the center of the UVOT-enhanced XRT position. This galaxy is, however, inconsistent with the DSS-enhanced XRT position and we therefore consider the association tentative pending resolution of this discrepancy.

XRF050714B

This faint, soft XRF had no detected optical afterglow; although several afterglow candidates were reported, none of them faded in subsequent follow-up; nor are any of them consistent with the current UVOT-enhanced and DSS-enhanced XRT afterglow position (Covino et al. 2005; D'Avanzo et al. 2005). However, a faint, blue host galaxy is marginally detected in both g and R-bands in our imaging at a position consistent with both of these XRT positions that we consider a likely host galaxy. (Note that this does not correspond to any of the objects mentioned as possible hosts by Covino et al. or D'Avanzo et al.; although it is just north of their source "A" as seen in Figure 7.8.) We acquired a spectrum of this source; but no trace, and no sign of emission lines, are detected at the host location. The nearby object A was also placed on the slit; it is well-detected and is a Galactic star.

GRB 050716

The infrared position of this GRB from Rol et al. (2007b) places it only $2''$ from a foreground star, again greatly complicating the host identification. However, a clear flux excess is visible at this location above the level of the PSF wing. The nearby star is faint enough for the wings to be subtracted by measuring the PSF of an isolated elsewhere in the image at similar or greater flux level, scaling, shifting, and subtracting, removing the stellar contamination and cleanly isolating the host galaxy. The host is faint and moderately red in the observed optical bands. NIRC K-band imaging of this object (Perley et al. in prep) also detects the source after subtraction of the stellar PSF; its color is characteristic of an extremely red object (ERO).

GRB 050730

This GRB is another very luminous event at high redshift ($z = 3.967$); absorption spectroscopy shows a clear damped Lyman-alpha system with complex velocity structure (D'Elia et al. 2007). In previous work (Chen et al. 2009), we reported no detection of a host galaxy or other source near the afterglow position. The improved reductions of the same data presented here above reveal two very faint objects at the detection threshold very close to the OT positions. These could, in principle, be part of an extended host-galaxy complex—however, they are well-detected in g band, with a very blue observed color, even

though at $z = 3.967$ Lyman-α is redshifted well past the g-band. More likely, they represent one of the three absorbing systems known for this system at z=2.262, z=2.253, or z=1.772.

GRB 050803

This GRB had no detected optical afterglow in early follow-up—most of it relatively shallow, although no variable source is detected in Magellan imaging 18 hours after the burst (Berger et al. 2005a). We previously presented spectroscopy of a host candidate in the original XRT error circle, which is a star-forming galaxy at redshift $z = 0.422$ (Bloom et al. 2005b). This galaxy, however, is well outside the final XRT position and is therefore unlikely to be related to the burst. No bright sources are consistent with the improved XRT positions, but a faint source ($R = 26.0$) is marginally detected at the southwest edge of the error circle ($23^{\rm h}22^{\rm m}37\overset{\rm s}{.}826$, $+05^\circ47'08\overset{''}{.}81$). This could be an afterglow (our imaging was conducted starting 23.8 hours after the GRB) or a faint host galaxy; a hint of extension suggests the later. In either case, the lack of a bright afterglow counterpart identifies this as a dark GRB.

GRB 050814

The afterglow of this event was well-detected in I- and R-bands but absent in V, suggesting a photometric dropout and leading Jakobsson et al. (2006) to claim a photometric redshift of $z = 5.3 \pm 0.3$. Consistent with this hypothesis, we find no host galaxy candidate in a deep R-band integration to $R > 26.5$ mag. We were unable to calibrate the g-band frame directly, but there is no detection in this frame either (assuming similar relative image depths to other images, we estimate at least $g > 27$ mag).

XRF050819

This weak, soft X-ray flash had only minimal ground-based follow-up and no optical or UV detections. The UVOT-enhanced error circle contains a single, bright object that we consider a likely host candidate. The simultaneous R-band imaging of this field was significantly affected by stray light in the field and should be used with caution; but the galaxy is well-detected in this imaging as well. Despite the relative brightness of this source ($\sim$24 mag), LRIS spectroscopy shows no lines over the spectral range.

GRB 050820A

This was an extremely bright and energetic early *Swift* burst, well-observed from early through late times with many different telescopes. Two sources of about equal brightness are consistent with the published coordinates of this object, which do not robustly distinguish between them (the ground position of Fox & Cenko (2005) and Cenko et al. (2006h) in particular is aboud mid-way between these objects.) Fortunately, this field was observed by HST 37 days after the burst, and the GRB afterglow is still visible in this imaging, which

shows it to be unambiguously associated with what appears to be a projection extending $\sim 0.2''$ north from source "B", although it is not clear if the sources are truly associated or if source "B" is coincidentlly aligned with the fainter disk of the host (for more details, see Chen et al. 2009). Unfortunately, the R-band imaging of this field was highly compromised by the focus issue (§7.5.1), and given the blending with source A and other nearby objects we cannot reliably extract the host flux. Even the g-band imaging cannot distinguish between the host disk/projection and source B, but the combined magnitude of the sources is $g = 25.63 \pm 0.08$ mag.

GRB 050826

The optical afterglow position for this object is coincident with the brightest object of a complex of several bright, extended sources. We identify this source as the low-redshift host galaxy also noted by Mirabal et al. (2007); our spectroscopy confirms their redshift measurement of $z = 0.296$. The host is quite red, with $V - I = 2.3$ mag — this is due partly to foreground extinction ($E_{V-I} = 0.8$ mag), but the host is nevertheless surprisingly red for an LGRB host. The spectroscopic properties of this host are also unusual: in particular, Levesque et al. (2010a) report a metallicity of approximately Solar, consistent with the strong [O III] and [N II] observed in our own spectroscopy. The resolved imaging of this object suggests that the host may be interacting with a companion (object "A"); the configuration of the two objects is reminiscent of disks connected by a tidal bridge. Interestingly, our longslit spectroscopy reveals no emission lines (and only an extremely faint continuum trace) at in the spectrum of object A (the slit was aligned to cover both objects). In particular, we see no evidence of emission lines at the same redshift as the host galaxy: this object may be at a different redshift, or it may be very gas-poor and not undergoing active star-formation as a result of interaction with the host.

GRB 050827

Follow-up of this burst identified no counterpart at optical or IR wavelengths (e.g., Halpern 2005), although the foreground extinction is significant. We imaged this field only briefly before being stymied by cloud cover; no source is detected to the very shallow limits that were attained.

GRB 050915A

Only a single object is consistent with the XRT position of this object: a faint blue, unresolved source. An infrared position is available from our PAIRITEL imaging as well (the only detection of this burst); this position is nearly but not precisely coincident with the optical disk. This is somewhat surprising, considering that the apparent size of this image is likely inflated by the seeing and the true size of the host is even smaller than it appears (it is unresolved in seeing of $0.8''$). Nevertheless, the GRB could be occuring in a low-surface brightness extension of the host not apparent in the imaging; the sub-arcsecond positional

coincidence is quite unlikely to appear by chance. Deep spectroscopy of this object was performed by the VLT GRB host survey, which after several hours of integration measured an emission redshift of $z = 0.444$ (Hjorth et al., priv. communication). We also acquired our own spectroscopy of this source: the observations occurred during thin cloud cover, but a faint trace is detected. Our provisional analysis shows no clear line detections throughout the spectrum; however, low-significance [O III] lines are indeed seen at $z = 0.443$ after inspection of the expected locations. Considering the faintness of this object ($V = 25.0$), this is a quite underluminous galaxy.

GRB 050922B

No optical afterglow was reported for this object despite significant ground-based follow-up (in particular, a limit of $r > 22.5$ mag at 0.57 days: Guziy et al. 2005b). A relatively short integration shows no clear host galaxy, although an object is very marginally detected (at < 2 sigma) within the XRT error circle. A deeper integration would be necessary to confirm the reality of this source.

GRB 050922C

This bright and luminous GRB was one of the best-studied of the early part of the *Swift* era; high-resolution spectroscopy of the afterglow showed a wealth of absorption lines at $z = 2.199$ as well as several intervening systems at slightly lower redshift (Piranomonte et al. 2008a). As previously reported in Chen et al. 2009, we detect no host galaxy at the position of the optical counterpart to deep limits.

GRB 051001

Rapid follow-up of this object at optical wavelengths (Tristram et al. 2005) identified no optical counterpart to moderately deep limits, although the X-ray afterglow is also faint. Two sources are evident near the X-ray positions; the northern, extend source ("H") is much brighter than the marginally-detected southern source ("A"); this second source is also inconsistent with the more precise (in this case) DSS-enhanced afterglow position, and therefore we identify the northern source as the likely host. The object is well-detected and fairly blue.

GRB 051006

A possible optical counterpart of this burst was noted by Rumyantsev et al. (2005a); however, this object is well outside both the DSS-enhanced and UVOT-enhanced final error circles, and appears to be a persistent, extended object in our Keck imaging. However, the UVOT-enhanced error circle (which is far more precise for this field) does include another, unresolved source of similar magnitude that we identify as a likely host galaxy. We attempted spectroscopy of this object, although seeing conditions were poor during the integration. No

trace is seen at the expected position of the host galaxy in the 2D spectrum; we searched for emission lines at this position and found none.

GRB 051008

The afterglow of GRB 051008 was not detected in deep early follow-up. A possible optical candidate was presented by Rumyantsev et al. (2005b), but this source is clearly resolved into a pair of bright, interacting galaxies in our Keck imaging, and furthermore it is well outside the final XRT error circles. A fainter source is detected inside the XRT circle that we do identify as the likely host galaxy. The source is quite blue, with $g - R = 0.7$ mag. We also acquired spectroscopy of this source (three exposures of 900 s each); a possible, marginally-resolved line signature suggestive of the [O II] doublet appears at a wavelength of 7123 Å in the sum of the exposures, but it is very faint and not clearly seen in any spectrum individually. If this is real, the redshift of this host would be $z = 0.91$. Further spectroscopy would be required to confirm the association—however, we note that if this were a correct association, we would expect to see [O III] lines elsewhere in the spectrum which are not observed. No other line candidates are observed over our spectral range. Further study of this object will be presented by Pozanenko et al. in upcoming work. (Note that our imaging of this field was significantly affected by a diffraction spike from a very bright star in the field, which passed through the GRB location during the images, but we were able to completely remove this artifact by masking out pixels affected by the diffraction spike during data reduction.)

GRB 051109A

This is another well-observed bright GRB from early in the *Swift* era with a bright, flaring optical afterglow (Yost et al. 2007); the spectroscopic afterglow redshift is $z = 2.326$ (Quimby et al. 2005). Our observations identify a bright ($R \sim 23$ mag) and noticeably extended galaxy at the afterglow position, indicating a very luminous host—indeed, unless this is a foreground absorber (none is noted in the spectroscopy of Quimby et al.), this host is among the most luminous in our entire sample.

GRB 051109B

GRB 051109B is one of the most remarkable events in the entire sample. The GRB and its X-ray afterglow are faint and unremarkable; sparse ground-based follow-up reported no optical afterglow detection to relatively shallow limits (e.g., Huang et al. 2005). However, our Keck imaging reveals a well-resolved grand-design spiral near the X-ray position with a diameter of about 20″; the X-ray position lies directly on top of the northern arm, consistent with a point source. An extremely faint tidal bridge connects this galaxy to another edge-on spiral 35″ to the north.

We acquired spectra of this system at two positions: a short integration across the putative host galaxy's nucleus, and a longer integration over the point-source at the XRT

position. The galaxy itself is at $z = 0.080$ and composed mostly of old stars, with very faint emission lines. Spectroscopy of the point-source reveals it to be at the same redshift, with strong emission lines superimposed on a faint continuum. Evidently, this is a star-forming region within a largely quiescent (despite an ongoing tidal interaction) galaxy. At this redshift, the $14.1''$ offset between the burst position and the galaxy nucleus corresponds to an offset of 20.9 kpc: as can also be seen in the imaging directly, this event occurred in the far outer regions of this galaxy.

Our imaging was acquired 9 months after the GRB, when a supernova component should still be easily detectable at this redshift. Nebular SN emission features are, however, not observed in the spectrum. Furthermore, a second epoch one year later at showed no change in flux of this source down to approximately $R > 25$ mag, at least 2 mag fainter than would be expected for a 1998bw-like supernova at this epoch. This suggests that, similar to GRB 060505 a year later (which also occurred in a star-forming region within spiral galaxy at $z \sim 0.08$; Fynbo et al. 2006b), this was a long-duration GRB which failed to produce a bright supernova.

This unusual association (and the lack of a detectable supernova) raises the question of whether this may simply be a chance coincidence of a distant, background object with a foreground spiral galaxy (see also Cobb et al. 2006). Simple $P_{\rm chance}$ arguments (Bloom et al. 2002) begin to break down in such cases, because the morphology and physical size of the galaxy become significantly more important than the angular offset for evaluating an association. To test this robustly, we chose 2000 positions randomly out of the SDSS footprint and manually inspected all of them for coincidence with the light of a resolved galaxy. Only two objects in this sample showed such an association, indicating a $P_{\rm chance}$ of ~ 0.001. Based on this argument, such an association would be exceedingly unlikely to be due to chance coincidence. On the other hand, there have now been close to 700 GRBs observed to date with $< 10''$ afterglow positions, so the appearance of a coincidence of this sort is not impossible (another such case, which we do associate with a chance coindicence of exactly this sort, is GRB 070412[6]. At the same time, in addition to the broad localization to the spiral, this object is also much more precisely localized to a star-forming knot (within $2''$ within a galaxy with relatively few such features) and does not have an underlying distant host or other signifying feature of being in the distant background. The unusual GRB 980425 (Galama et al. 1998) also offers a strong (if, as yet, singlar) precedent for associations of exactly this sort. We therefore argue that this association is much more likely to be physical than coincidental—unfortunately, it is impossible to be sure.

GRB 051111

GRB 051111 is another bright, well-studied *Swift* GRB; and is one of the few with a high-resolution echelle spectrum (Penprase et al. 2006). The afterglow is at least mildly dust-extinguished (Butler et al. 2006; Guidorzi et al. 2007b). We detect a faint, blue probable host

[6]Another possible example would be GRB 990705, which was seen in close projection with the Large Magellanic Cloud (Djorgovski et al. 1999).

in our LRIS imaging consistent with the UVOT and optical positions; the object appears marginally extended N-S. Two other sources are observed close to the optical afterglow position; these may correspond to the two line-of-sight absorbers observed in the GRB spectrum at $z = 1.19$ and $z = 0.83$.

GRB 051117A

This *Swift* burst had an exceptionally bright, flaring X-ray afterglow (Goad et al. 2007), although the UVOT afterglow was much fainter and ground-based follow-up nonexistent (until very late times; Kann et al. 2006b), so no redshift was determined. No object is detected in our Keck imaging at the UVOT or XRT positions, with the possible exception of a very marginal object detected at about the 2-σ level g-band slightly outside the UVOT error circle at $g \approx 27.6$ mag.

GRB 051117B

No optical counterpart was detected for this faint *Swift* burst. An extended object at the edge of the XRT circle was noted by Chen et al. (2005) and Thöne et al. (2005); this is clearly detected in our deep Keck imaging ("A" in Figure 7.10), as is a fainter, bluer neighboring object ("B"). Both of these only skirt the most recent XRT error circles and are plausible host galaxy candidates, although object B is well outside the UVOT-calibrated XRT position.

We acquired longslit spectroscopy across these two objects; object "A" is much brighter and is well-detected on both sides; seeing conditions were poor and source "B" is barely detected on either side. A clear emission line is visible on the LRISB chip just blueward of the dichroic cutoff; it is marginally resolved as a doublet and we identify it as [O II] at a redshift of $z = 0.4805$. We also detect Ca H+K absortpion features and modest Hβ and [O III] at the same redshift further to the red, suggesting that this is a relatively evolved galaxy. It would be an unusual GRB host. Unfortunately, the other object consistent with the error circle ("B") has no clear line detections over the spectral range.

GRB 051211B

This GRB was detected by INTEGRAL; its position is low towards the Galactic plane but has a detected optical afterglow (Jelnek et al. 2005), as well as a likely radio afterglow (Frail 2005). Jelnek et al. (2005) also mention the existence of an object in pre-explosion DSS imaging which they speculate may be an underlying host galaxy. Our imaging clearly detects this object; it is consistent with a point-source with no evidence of extension towards the optical position (offset by $1.3''$ from the object centroid). Indeed, spectroscopy verifies it to be a Galactic star with absorption lines at $z = 0$.

GRB 060105

This GRB had a very bright X-ray afterglow but no optical detections (a possible UVOT candidate was retracted; Schady et al. 2006). Although extinction towards this direction is not particularly large ($E_{B-V} = 0.17$ mag), the field is crowded and the burst location is sandwiched between three bright stars in a region of variable background. There is a faint hint of flux excess above this resulting background in R-band only just north of the XRT error circle which could represent a faint host at the image detection level, although it is not statistically signficant.

GRB 060109

No optical counterpart was identified for this burst, although there was no early ground-based follow-up. A single, faint source is present at the edge of the DSS-enhanced XRT error circle, although it is inconsistent with the UVOT-enhanced XRT error circle. This could be a host galaxy, but the distance from the UVOT-enhanced circle offers reason for caution. We acquired a spectrum of this source and observe no lines over the spectral range.

GRB 060111A

The afterglow of this event was detected by UVOT and several ground-based telescopes. A nearby extended source was reported by Khamitov et al. (2006a) and presented as a possible host-galaxy. Our LRIS imaging clearly resolves this object (denoted "G1" in the Figures) into a disk-like galaxy with what appears to be an associated companion. However, the available UVOT and XRT positions are clearly separate from this structure, but is consistent with a much fainter, physically separated source that is not obviously associated with the brighter object.

Indeed, spectroscopy shows the two sources to be at highly disparate redshifts. The extended source G1 shows a bright, marginally resolved emission line (with rotational velocity structure) at a wavelength of 4366 Å, which we identify as the [O II] doublet at $z = 0.171$. No emission is observed at the location of the host galaxy at this wavelength. However, a clear, unresolved emission line is visible blueward of this at 4042 Å. This likely represents Lyman-α at $z = 2.32$: the only other plausible line identification would be [O II] at $z = 0.08$, which would predict several other emission lines to be present on the blue side which are not observed. This is the highest-redshift host emission line in our sample and given the relatively bright host ($R = 23.6$ mag) indicates a very luminous galaxy.

GRB 060111B

Much like the other burst from the same day, the Keck imaging of this position shows a bright, extended source (claimed as a possible host by Khamitov et al. 2006b) offset from the afterglow position as well as a fainter source directly underlying the optical afterglow (almost certainly the true host galaxy). As usual, we acquired spectroscopy of both objects

by placing the LRIS slit at the appropriate angle. The nearby galaxy dispays several emission and absorption lines establishing it as an older galaxy at $z = 0.239$. Unfortunately, the host galaxy does not show any clear emission or absorption features with which to establish its redshift, although the lack of any features at the same redshift as the nearby galaxy suggests that it is a background source and not a companion. The analysis of this object is discussed in more detail by Stratta et al. (2009); it likely falls within the approximate redshift range $z = 1 - 2$.

GRB 060123

This was an extremely long (T_{90} = 900 s), faint burst detected by *Swift* (Cummings et al. 2006). There was no early rapid follow-up and the UVOT did not detect an afterglow. Previously, Butler & Bloom (2006) claimed in a GCN circular that the XRT error circle included a bright galaxy visible in SDSS; spectroscopy of this galaxy was presented by Berger et al. (2006) who suggested a redshift of $z = 1.099$ (or possibly 0.193 or 0.562, depending on line identification.) We did not re-image this field, but did acquire spectroscopy of this source using the much wider wavelength coverage of LRIS. We confirm both of the possible emission lines presented by Berger et al. and also detect a third line further to the blue (outside their spectral range) at 5821 Å. This identifies this object as a star-forming galaxy at redshift $z = 0.562$, case (3) presented by Berger et al. However, the most recent DSS-enhanced error circle no longer includes this SDSS galaxy; nor does the UVOT-enhanced error circle of Evans et al. (2009). Most likely, this object is not associated. Without imaging of this field, we cannot yet constrain a fainter host inside the XRT error circle.

GRB 060124

This was a well-observed burst, notable for its precursor flash almost 10 minutes before the GRB itself (Romano et al. 2006). Spectroscopy of the afterglow places the redshift at $z = 2.297$ (Cenko et al. 2006a). The afterglow position overlaps with the PSF wing of a bright nearby star. There is no detection of a host galaxy in our imaging.

GRB 060202

This GRB was imaged at early times by LRIS and with NIRI at Gemini-North. A bright source was immediately identified in the XRT error circle that appeared to be an afterglow candidate (Cenko et al. 2006b), but subsequent imaging indicated that it did not fade (Wang et al. 2006b); the nondetection of any transient emission in any of these images (which are not included in our sample) identifies this GRB as an unambiguous dark burst. This position of this object remains (marginally) consistent with the improved XRT positions and is a likely host candidate. It is clearly extended in our LRIS imaging and has a relatively blue $g - R$ color. (However, the bright IR magnitudes reported by Wang et al. 2006a and Schmidt et al. 2006 suggest that this is actually quite a red source in a broader sense, or alternatively a red afterglow was dominating the host flux at the early times of those reports.) Spectroscopy

of this object reveals a single line on the red side, consistent with the [O II] doublet at $z = 0.785$. At this redshift the other expected lines are in heavily fringed regions of the chip.

GRB 060203

The optical afterglow of this GRB was detected by many ground-based telescopes; it is particularly bright at IR wavelengths and has a red color of $V - K \sim 6$ mag (e.g., Bloom et al. 2006a; Bikmaev et al. 2006). No source is identified in our Keck imaging consistent with the optical or IR counterparts to deep limits ($R > 25.9$ mag, $g > 26.9$ mag).

GRB 060204B

The optical position for this object lies slightly outside the XRT error circle and no positional uncertainty is supplied (Guidorzi et al. 2006a), but this position lines up within $0.2''$ of the centroid of a relatively bright, blue host candidate in our late-time Keck imaging. Although the source is relatively bright, we have not yet attempted spectroscopic follow-up.

GRB 060210

This high-redshift ($z = 3.91$; Cucchiara et al. 2006) GRB was one of the most luminous events of the *Swift* era, considering its bright detection to numerous small telescopes despite its redshift (Kann et al. 2010). The event may be even more luminous if it was moderately dust-extinguished as some evidence suggests (Cenko et al. 2008a). Remarkably, despite the high redshift we firmly detect a likely host galaxy underlying the optical position, even in a relatively short R-band integration; its conspicuous nondetection in much deeper g-band observations supports the assertion that the galaxy is at the GRB redshift. This is a rare example of a luminous Lyman-break galaxy hosting a GRB. Spectroscopy of this event was acquired in the hope of detecting a highly redshifted Lyman-α line, without success; an approximate flux limit for this line is $\lesssim 2 \times 10^{-17}$ erg/cm^2/s.

XRF060219

A bright, extended galaxy is visible in the LRIS imaging just outside the XRT error circles (it is also visible in SDSS pre-imaging; Moretti 2006). Its position is not formally consistent with either error circle, and its association with the GRB is therefore uncertain, although still plausible. We see no other sources in the XRT error circle or near the galaxy—including, conspicuously, any source that might correspond to the faint source reported by Rol et al. (2006), which may confirm the fading of that source (unfortunately, no position is given for this putative afterglow). Spectroscopy of this object reveals a single, moderately strong emission line at 6748 Å which we associate with [O II] at $z = 0.810$ (other possible redshift line IDs are not consistent with the lack of other nondetections; at $z = 0.810$ the other strong lines should lie far to the red in fringed sky-line regions.)

GRB 060306

This event is a clear dark burst, given the early, moderately deep NIR nondetections (Lamb et al. 2006). We imaged this field on two occasions; conditions were extremely poor during the first integration (thick clouds) and no source was detected, but a clear host galaxy candidate is detected during the second integration consistent with both reported XRT positions. We acquired spectroscopy of this object on two different occasions (acquiring a single, long spectrum in each case); we detected a faint, marginal flux excess on the first blue spectrum that could be Lyα at $z = 2.66$ but it does not appear to be confirmed in the second spectrum. The redshift of this system therefore remains unknown.

GRB 060312

There was no optical afterglow detection of this GRB, although follow-up was very shallow. No source is visible inside the DSS-enhanced XRT error circle (no UVOT-enhanced position is available), although the edge of the error circle overlaps a relatively bright, blue source that represents a plausible host. No other objects are visible near the position.

GRB 060319

The only reported long-wavelength detection of this GRB came at infrared wavelengths with the WHT (Tanvir et al. 2006b), even though the burst was observed to deep limits at optical wavelengths as well (D'Avanzo et al. 2006b) and the XRT afterglow is reasonably bright. The position given by Tanvir et al. is significantly offset from the final XRT positions (nothing is detected at the quoted position in our imaging), but no uncertainty was specified and the position was quoted as "approximate" in the circular. The afterglow magnitude was estimated at $K = 19$ mag; in our imaging, no source in or near the original XRT error circle (Beardmore et al. 2006) or the reported IR position unless it was exceptionally red. We therefore consider it likely that Tanvir et al. did detect an IR afterglow but slightly misreported the position.

Using the XRT positions as the best available constraint on the source location, we detect a bright source near the center of the UVOT-enhanced position (and at the edge of the DSS-enhanced position) that is a likely host galaxy, a few arcseconds east of a bright star (fortunately, contamination from the stellar PSF is negilible.) We acquired spectroscopy of this object and detected a single, bright emission line in the red half of the spectrum. Associating this with the [O II] doublet indicates a redshift of $z = 1.172$.

GRB 060413

This GRB was only one degree from the Galactic plane and the foreground extinction is very high ($E_{B-V} = 1.97$ mag). No afterglow is detected at optical or NIR wavelengths (e.g., French et al. 2006), but the limits are shallow and given the exinction the observations are not at all constraining. A bright, red source is detected in R-band (and weakly detected in

g-band), but its profile is pointlike and given its brightness and the large extinction in this direction it is almost certainly a foreground star.

GRB 060418

The afterglow of GRB 060418 at $z = 1.491$ was exceptionally well-observed and is notable for the excellent echelle spectrum acquired on UVES on the VLT (Ellison et al. 2006) that showed evidence of time-variable absorption lines due to the energy input from the burst itself (Vreeswijk et al. 2007). Notably, the afterglow shows absorption by three different Mg II systems at redshifts of z=0.603, z=0.656, and z=1.107. Its host environment has also been extensively studied by our collaboration using observations from HST and LGS observations at Keck (Pollack et al. 2009). Our LRIS observations of this object (both imaging and spectroscopy) were previously published in that work. We identify the host galaxy as a faint, extended object in between several other sources ("A", "B", and "C" in this figure, defined following Pollack et al.) The host is not resolved by our imaging, although HST imaging shows it to actually be a complex of three objects (perhaps a small interacting system). Our spectrum was aligned with the slit covering object A and B, as well as the faint host H. Object A is a star-forming galaxy at z=0.656, and likely associated with the absorber of the same redshift in the afterglow spectrum. No clear emission or absorption lines are visible for the other objects along the slit in our observations. Pollack at al. proposed (based on photometric arguments) that object "B" is associated with the z=0.603 absorber.

GRB 060424

Swift was not able to slew to this object and there are no X-ray observations, but ground follow-up in I-band identified an optical afterglow (Thöne et al. 2006e). We downloaded the finding chart image presented in this circular and are able to refine the optical position by direct comparison to our deep Keck imaging, which localizes the GRB position to the outer part of one of two moderately bright, extended sources. We also acquired spectroscopy of this object with the slit aligned to also include a brighter source visible to the west (but not coincident with the afterglow position). Only a faint trace is seen at the putative host galaxy, with no significant emission lines. The nearby object shows a single bright emission feature that we associate with [O II] at $z = 0.922$.

XRF060428B

Our study of this system was previously presented in Perley et al. (2007a). An optical counterpart for this event was detected by several ground-based facilities and the UVOT. Even in the small-aperture ground observations, a source is evident within about 2″ of the transient; our Keck imaging reveals this to be a clearly extended, bright disk galaxy. Spectroscopy of this source reveals it to be an early-type galaxy at $z = 0.35$ with very little star formation. If physically associated with this object, this would be an exceptional example of a long-duration gamma-ray burst occurring in the outskirts of a galaxy dominated by old

stars (the afterglow offset and the magnitude and redshift of this putative host are reminiscent of some short GRB host associations, such as GRB 050509B). However, deep imaging of the field reveals a faint, blue underlying source directly below the optical afterglow position which likely represents the true host galaxy. This galaxy is far too faint for spectroscopy ($g = 26.6$ mag). This host could be a satellite galaxy of the early-type object (several other, brighter objects in the field are indeed at similar redshift, suggesting a group association), or (perhaps more likely) could be a more distant background host. In the latter case, is is possible that the host (and burst) is strongly gravitationally lensed by the foreground early-type galaxy.

SGRB 060502B

Our study of this object was previously published in Bloom et al. (2007b). This was a short-duration GRB detected by *Swift* with a very faint afterglow; consequently only a relatively poor XRT localization was possible, and no optical counterpart was identified. Our imaging identifies several faint sources, all just outside the edge of the DSS-refined XRT error circle. These could be plausible host candidates (see also Berger 2010a and Church et al. 2011). On the other hand, a bright and luminous early-type galaxy ("G*") is visible about $15''$ to the south in our imaging; we previously argued in Bloom et al. (2007b) that this was the true host galaxy of this system and that the progenitor was probably ejected from that system sometime in the distant past. G* is a luminous post-starburst galaxy with relatively limited current star-formation activity at $z = 0.287$.

GRB 060505

The afterglow position of this GRB is consistent with an HII region in the outer part of a low-redshift ($z = 0.089$) spiral galaxy (Fynbo et al. 2006b). We first imaged this object 25 days after the GRB, when a bright supernova expected to be associated with such a low-redshift burst should have been peaking. However, no point source is identified at the afterglow position in this imaging; image subtraction between this initial epoch and a subsequent image taken at LRIS two months later demonstrated no object down to at least $R > 25.2$ mag (compared to an anticipated SN magnitude of $R = 18 - 20$ mag, based on shifting the observed light curves of SN1998bw and SN2006aj to the appropriate distance). Unless this object is seen in projection with a large, resolved foreground object by chance (as also discussed for GRB 051109B earlier in this section) supernova associated with this object must therefore be extremely underluminous. This analysis was previously included in Fynbo et al. (2006b).

GRB 060510B

At the time of discovery, this was the fourth-highest redshift burst known with a Lyman-break afterglow redshift of $z = 4.9$ (Price 2006). The source was observed to very deep levels in g and R filters. This would be a poor filter choice to actually identify the host galaxy,

since the Lyman break redshift is at the red edge of the R-band transmission function; indeed, consistent with this expectation we detect no source at our improved afterglow position (measured using data from the Gemini Science Archive) to deep limits of $g > 27.1$ mag, $R > 25.9$ mag. However, the deep nondetection in both filters offers supporting evidence to the Spitzer host galaxy detection reported by Chary et al. (2007) at the afterglow position. They report an afterglow flux of 0.23 ± 0.04 μJy at 3.6 μm, corresponding to an AB magnitude of 25.5 ± 0.2. The resulting color constraint ($g - m_{3.6} > 1.6$ AB mag) rules out only relatively blue interloper galaxies, but does bolster the identification of the Spitzer source as the GRB host. If that association is correct, this is the highest-known GRB with a detected host galaxy.

XRF060512

We imaged this event on two occasions. The first epoch was carried out 28 days after the GRB in the g and R filters; the second was acquired two months later for comparison with the first epoch (however, seeing conditions were exceptionally poor during the second epoch, and the red imaging was mistakenly taken in the OG580 filter and was not usable; see §7.5.1 for more details). A moderately bright ($g = 25$ mag), extended object is detected underlying the UVOT and optical positions. Spectroscopy of this source, previously announced in Bloom et al. (2006c), detects numerous emission lines, showing it to be a star-forming galaxy at a redshift of $z = 0.4428$. Ordinarily, the close positional association and brightness of this source would unambigiously associate it as the GRB host galaxy. However, such an association is disputed by other observations of the afterglow of this GRB: in particular, careful re-analysis of the TNG afterglow spectrum presented in Fynbo et al. (2009) identified what appears to be a strong Lyman-α absorption line corresponding to a redshift of $z \sim 2.1$. If this is correct, the low-redshift galaxy we observe in emission cannot be associated with the GRB.

The morphology of this coincident object is somewhat suggestive of the superposition of two sources (indeed, a profile across the long axis of this object is marginally bimodal, and Figure 7.11 shows a hint of a color gradient as well), and it therefore may actually represent a chance alignment between of the true, distant host with a brighter foreground source. We attempted to verify this possibility by analyzing the spectrum for the presence of a Lyman-α emission line at the expected location on the spectrum, but did not see any excess emission at this wavelength.

GRB 060607A

This was a well-studied *Swift* GRB with a bright afterglow detected at UV through IR wavelengths. Echelle spectroscopy from the VLT (Ledoux et al. 2006) identified a weak Lyman-α line at z=3.082 and two intervening absorbers at slightly lower redshifts ($z = 3.050$ and $z = 2.937$). We detect no sources consistent with the afterglow in either filter. Unfortunately, the R-band imaging of this field was somewhat compromised due to poor

focus.

GRB 060805A

Analysis of this field was previously presented in Perley et al. (2009c). No optical afterglow was detected for this GRB despite rapid and deep follow-up, but its X-ray afterglow is exceedingly faint and these limits do not strongly constrain the broadband SED of the burst. Two objects are detected at opposite edges of the X-ray position; one of these is likely to be the host galaxy, although we cannot definitively establish which of the two objects (if either.) Note that a faint diffraction spike from a nearby star mildly affects the R-band imaging observations. We acquired spectroscopy of this source on two epochs, but detect no lines in either case. Object A shows no lines down to the atmospheric cutoff, while the trace of object B is too faint to detect.

GRB 060807

A very red afterglow for this GRB was presented by Malesani & Piranomonte (2006a), establishing it as a candidate dark burst. Thöne et al. (2006c) presented imaging between 13 and 15 days following the burst showing the detection of a probable host candidate; this source is evident in our imaging also, centered almost exactly on the optical position reported by Fynbo et al. (2006a). We measure a V-band magnitude consistent with that given Thoene et al.; however, the I-band magnitude is much fainter ($I_{AB} = 24.6 \pm 0.2$ mag in our imaging vs. $i = 22.1 \pm 0.2$ mag in Thoene et al.) If the value of Thoene et al. is accurate, this suggests that two weeks after the GRB an extremely red source was still present at the GRB position—perhaps a low-redshift supernova. Unfortunately, we cannot test this without direct access to the early imaging. Our spectroscopy of this source shows no clear line signatures.

GRB 060814A

No variable optical counterpart to this GRB was detected despite deep early imaging (e.g., Malesani & Patat 2006) and a bright X-ray afterglow. However, several reports note the presence of a bright, extended object inside the XRT error circle (Levan et al. 2006c; Malesani 2006; Cenko et al. 2006d; Ofek & Cenko 2006) showing some evidence for fading in the NIR Levan et al. (2006b). This source is optically blue ($V - I \sim 0.9$ mag). Spectroscopy of this source shows it to apparently be a star-forming galaxy at a redshift of $z = 0.84$, as previously announced in Thöne et al. (2007b).

However, the connection of this source to the GRB is not unambiguous. Although no obvious color gradient is evident across the host, the 2D spectrum shows the emission lines to be localized to the eastern half of the object, suggesting that it may be an unresolved blend of two different sources, likely at different redshifts (however, as the western component shows no clear lines at all, we cannot irrefutably confirm this.) If the western source is at different redshift, the strong detection of uninterruped continuum down to the atmospheric cut-off at

$\sim$3730Å, indicates $z \lesssim 2$. The positional accuracy of the X-ray afterglow is not sufficient to distinguish which source the GRB occurred in.

GRB 060904A

GRB 060904A had no optical counterpart despite early observations and a relatively bright X-ray afterglow (e.g., Cenko & Rau 2006). No source is detected consistent with the X-ray position in our Keck imaging, although seeing conditions were poor during the observation and limits are not deep.

GRB 060904B

GRB 060904B had a bright afterglow followed by many groups, and detected by the UVOT in all filters including UVW2, indicating a low to moderate redshift, confirmed by an afterglow spectrum taken by Fugazza et al. (2006) that showed numerous absorption lines at a reshift of $z = 0.703$. We acquired imaging and spectroscopy of this source seventeen days after the event (at which time the afterglow and possibly SN components may still contribute somewhat), plus additional imaging several years later.

We detect a bright, compact source at the transient location; our measurement of $R = 22.99 \pm 0.03$ mag is significantly brighter than an extrapolation of earlier afterglow data points to this epoch or the expected supernova brightness at this redshift, suggesting it is host-dominated. Indeed, a later epoch shows the source to still be present to years later with no significant change in flux; the corresponding 3σ limit on any transient emission a tthe first epoch is $R > 24.9$ mag). Spectroscopy of this object shows it to be a bright, star-forming galaxy at the same redshift inferred from the absorption spectrum.

GRB 060906

This was a relatively faint *Swift* burst with an optical afterglow followed by several groups (e.g., Cenko 2006; Li & Bloom 2006). No source is detected at the optical afterglow location in our Keck imaging (note that the more precise KAIT position has been corrected for an apparent typo in the degrees value for the declination [39 versus 30] versus the reported position.) A faint red, extended source is marginally detected in the DSS-calibrated error circle, but is not likely to be associated with the burst.

GRB 060923A

This bright GRB is one of the best-studied "dark" bursts, and was the subject of the study of Tanvir et al. (2008c); we also present further analysis of this source in Chapter 8. The field of this burst was observed to deep limits in a large number of filters ($BgVRIZ$) but only marginally detected in any of them (combining filters together—as shown in Figure 7.12—generates a more secure but still weak detection). The host is not particularly red in these optical measurements, although the NIR detection from Tanvir et al. (2008c) and

Spitzer observations of this GRB (Perley et al. in prep) detect the host at a surprisingly bright flux level, suggesting it is actually quite massive and/or dusty.

GRB 060923C

This event is another dark burst; its afterglow was detected only in the infrared at Gemini and the VLT despite early I-band observations at Keck (Rau et al. 2006; Covino et al. 2006a; Fox 2006; D'Avanzo et al. 2006a). We downloaded the NIRI K-band imaging from Gemini Science Archive and matched it to our Keck images to localize the burst precisely in our imaging. Intriguingly, this position lies directly between two bright, red galaxies (these galaxies are also visible in the K imaging directly) in a region of faint, diffuse emission that may represent a tidal bridge connecting the objects (or possibly an unrelated source, but its color resembles the red nature of objects A and B more than it does the numerous faint ($g \sim 26$ mag), blue sources just south of these objects. Due to the LRIS2 short-exposure problem (§7.5.1) we have not yet been able to reliably calibrate the I-band image.

GRB 060927

GRB 060927 was the second-highest redshift GRB known at the time of its discovery, with $z = 5.47$ (Ruiz-Velasco et al. 2007). To search for a host galaxy we imaged the field for almost two hours in V and I-bands, achieving limits of $V > 27.3$ mag, $I > 25.8$ mag. Two objects are detected in this imaging just outside the UVOT-enhanced XRT error circle, but neither is consistent with the optical position of Ruiz-Velasco et al. (2007). No hint of emission is detected at this location.

GRB 060929

This was a relatively faint burst with a large X-ray flare detected at $t \sim 500$ s. No optical afterglow was detected from this object to (relatively shallow) limits. A faint ($R = 25.0$ mag), red ($g - R = 1.8$ mag) host candidate is detected in our Keck imaging, comfortably inside both reported X-ray error circles.

GRB 061021

Initial analysis of the afterglow spectrum reported in the GCN circulars (Thöne et al. 2008a) showed no clear absorption lines, although further analysis by (Fynbo et al. 2009) identified faint Mg II lines that established a redshift of $z = 0.3463$ for this GRB. Consistent with this, we detect a faint, extended source at the afterglow position in our LRIS imaging; given the low redshift the host is evidently quite underluminous. As with GRB 050915A, we do not identify any clear lines on examination of our 2D or 1D spectra. However, inspection of the appropriate wavelength regions given the redshift does identify a faint (2σ) line consistent with $[\mathrm{O\ III}]_{5007}$ at this redshift, but no other lines.

GRB 061028

This faint, long GRB was detected by *Swift* as an image trigger[7]. Several early optical afterglow candidates lie outside the refined XRT error circles and remain bright and point-like in our Keck observations, and are unlikely to be associated with the GRB, as also concluded by Cenko et al. 2006e, suggesting that the optical afterglow was undetected to moderately deep early limits (Bloom et al. 2006b; Cenko et al. 2006f). We detect no host candidate within the XRT error circles. Our integration on this field was during a period of variable transmission due to intermittent thin clouds at the end of an otherwise photometric night, and the Landolt calibration of the upper limit may be uncertain to up to 1 mag.

GRB 061110A

We imaged this field only 11 days after the burst, and detect a faint, red point-like object consistent with the optical position inferred from re-analysis of the acquisition data from an epoch of VLT spectroscopy taken 11 hours after the burst (Thöne et al. 2006b). This could represent the host galaxy or the optical counterpart, or some combination, although the fact that it is not much fainter than the reported magnitudes ($R \sim 22 - 23$ mag at 11 hr. vs. an interpolated $R \sim 24 - 25$ mag in our observation a factor of 24 in time later) suggests that is probably not afterglow-dominated (although afterglow emission may still contribute). Indeed, the VLT spectrum shows bright emission lines present at $z = 0.756$ on top of the continuum (Fynbo et al. 2007), suggesting the presence of a bright host. In this context, the red color of the host ($V - I = 2.6$ mag) may be a reflection of the 4000Å break at this redshift, or could reflect the contribution of a reddened afterglow (the color reported by Thöne et al. 2006d is quite red). A faint, blue source is also visible a few arcseconds to the north.

GRB 061121

This is a bright well-studied *Swift* burst, notable for its precursor event that enabled the XRT to be observing throughout the primary episode of prompt emission. The burst occurred near the end of one of our program nights, and we established the redshift of $z = 1.314$ via LRIS spectroscopy of the afterglow starting 13 minutes after the GRB as a target-of-opportunity interrupt of our observations of GRB 050215B (Bloom et al. 2006d).

Given this redshift, the host is exceedingly bright ($I = 21.9$ mag) and blue (this bright host was also mentioned in the study of Page et al. 2006a). We acquired spectroscopy of

[7] *Swift* image triggers are GRBs identified by a special on-board algorithm designed to identify long, faint bursts which never increase the total instrument count rate significantly above the background level at any given time (but are recognizable in a time-integrated, spatially-resolved sense). Because of the effects of time dilation and the faintness expected for bursts at extreme distances, the detection of an event as an image trigger has been taken to be possibly indicative of a high-redshift burst. This was seemingly confirmed by the detection of image-trigger GRB 050904 at $z = 6.28$, although some of the highest-z GRBs have had surprisingly short observed durations and were standard rate-triggers (e.g., Zhang et al. 2009)

this object with LRISR2 and detected an emission line far to the red, confirming the host association. The emission line is spectacularly bright, given this redshift: the equivalent width of the line is ∼250 Å, corresponding to a total flux of 5×10^{-16} erg/cm^2/s and an inferred unobscured star formation rate of 50 $M_\odot$/yr (Kewley et al. 2004).

GRB 061122

This was an INTEGRAL burst relatively close to the Galactic plane; an optical afterglow was detected starting 18 hours after the burst (Halpern & Armstrong 2006). A faint, blue host galaxy is detected underlying this position in our Keck imaging, just north of a blue, extended object. We placed the LRIS slit over both sources. The nearby object shows a well-detected trace, but no clear lines are evident over the spectral range. The host galaxy trace is only weakly detected, and also shows no lines.

SGRB 061217

This was an unambiguous short-duration burst with a T_{90} of 0.3 s and no evidence of extended emission (Barthelmy et al. 2006). No UVOT-enhanced or prompt-ground (SPER)[8] XRT position exists for this burst, and so the only available *Swift*-team position is the boresight-calibrated GCN position with a quoted uncertainty of 6.0 ″ (Evans et al. 2006). The brightest object inside this error circle ("G1") was claimed as a possible host galaxy by Berger (2006) and studied by Leibler & Berger (2010). A more precise, DSS-enhanced position is also available (initially presented as a GCN circular, Butler 2006, but unchanged in the current catalog). Although Butler et al. note in this circular that this position favors G1 as a host candidate, G1 is actually shown to be outside this XRT error circle in our Keck imaging (acquired as a ToO observation two days after the event). The only detected source within the astrometrically-aligned error circle is source "A" in Figure 7.12. Given its faintness and the size of the XRT error circle, its association with the event is unclear.

GRB 061222A

GRB 061222A is among the most dramatic dark bursts (in terms of $\beta_{\rm OX}$: Jakobsson et al. 2004a and Chapter 8) of the *Swift* era, and its host galaxy is among the most curious objects in our sample. The GRB extremely luminous in gamma-rays and X-rays, but despite deep and rapid follow-up it was only detected at a faint level in deep NIRI K-band imaging. We acquired this imaging from the Gemini archive and aligned it with our Keck image to produce the IR position shown in Figure 7.12; it is located on top of a faint blue object that appears at first glance to be part of an interacting pair. Surprisingly, however, the two sources are at different redshifts: spectroscopy places the host at z=1.151 (based on a likely [O II] line near the red end of the spectrum) and neighboring object B at $z = 2.088$ (based on a bright, probable Lyman-alpha detection at the blue end of the spectrum). The optical

[8] `http://www.swift.ac.uk/sper/index.php`

colors of this event rank it among the bluest objects in our sample, and this extends all the way through to the NIR and Spitzer bands (Perley et al. in prep); evidently only a very small fraction of the star-formation in this galaxy is dust-obscured. This event is further discussed in the next chapter.

GRB 070103

GRB 070103 is another dark burst, given nondetections in early optical (Malesani et al. 2007c; Chen et al. 2007b) and NIR (Updike et al. 2007) observations, although its X-ray afterglow is not particularly bright. A single faint, blue object, weakly extended east-west, is visible in our Keck imaging at the edge of both UVOT- and DSS-enhanced X-ray positions, likely to be the GRB host galaxy.

GRB 070219

GRB 070219 is also a dark burst on account on the deep, early optical limit provided by early TNG observations of D'Avanzo et al. (2007). A very faint source is weakly detected in both the g and I filters near the center of the UVOT-enhanced XRT error circle. This object is quite red, with $g - I \sim 2.8$ mag. We do not yet have NIR observations of this source, but given the optical color it is likely to be quite bright and probably represents a luminous, dusty GRB host of the class being found in ongoing work. We hope to test this hypothesis with future followup.

GRB 070224

GRB 070224 is a relatively ordinary *Swift* burst, although its optical afterglow had an unusual plateau phase of very little fading during the first day (Chen et al. 2007a; Thöne et al. 2007a). We detect a faint, blue host galaxy in our imaging directly underlying the optical afterglow position.

GRB 070311

This GRB had a bright afterglow from early through late times, and is particularly notable for significant rebrightening ($\sim$1 mag) observed in the optical light curve 2 days after the event (Guidorzi et al. 2007a). This field was observed during during a period of exceptionally poor seeing (2–3″). We remained on the burst position for only a few minutes and observations were taken in g-band only (actually, some data was also taken in the R-band in a 2×2 binning mode, but given the difficulties in reducing and calibrating these observations we do not present it here.) No host is detected to a (shallow) limit of $g > 25.3$ mag.

GRB 070412

GRB 070412 is another prime example of a dark burst (deep, early limits are placed by several reports: Rol et al. 2007a; Perley et al. 2007b; Prieto et al. 2007) in a highly unusual field: an exceptionally large, bright ($r \sim 13$ mag), extended galaxy (first noted by Ofek & Berger 2007) is present approximately $45''$ from the burst position. This is a large elliptical-type galaxy with a boxy morphology; stellar emission from its outer portions extends well past the location of the GRB. Subtraction of the host light reveals no object at the XRT error circle location, with the exception of a very faint, unresolved source detected in I-band only. This imaging was acquired only four days after the GRB, but the same source is also visible in R-band imaging from Prieto et al. (2007), suggesting it is probably not transient.

This event remains a puzzle. A physical association with the bright elliptical seems unlikely: although the $P_{\rm chance}$ value for association is actually better than the large majority of hosts in this sample (at 4×10^{-4}), given the hundreds of GRBs now localized to a precision of a few arcseconds, it is not necessarily surprising that one or two so far (GRB 070521 is also curiously close to a bright, low-z elliptical galaxy) appear close to, or even within the light of, highly extended low-redshift galaxies on the sky. A more conservative interpretation is that the GRB originated from background galaxy, perhaps the reported I-band source.

GRB 070419A

GRB 070419A is a fairly typical *Swift* burst with a well-observed optical afterglow. The absorption redshift is $z = 0.97$ (Cenko et al. 2007b and Fynbo et al. 2009). Given this low redshift a bright host galaxy might be expected, but we detect no source at the optical position down to $R > 25$ mag, $g > 26.3$ mag, suggesting an underluminous host similar to that of GRB 080319B. (Note that, for this field, all three reported optical positions are centered far outside either XRT position.) The R-band background is slightly elevated due to the halo of a bright red star just outside the field to the west.

GRB 070429A

This is another GRB without a detected afterglow despite early, rapid observations. Afterglow candidates were reported by Garnavich et al. (2007a) and Postigo et al. (2007); both of these objects remain visible in our imaging ("A" and "B", respectively, in Figure 7.13), although due to the poor seeing they are blended and appear as a single, extended object. (Unfortunately, neither report provided a magnitude, and we are unable to determine whether either object contains a fading counterpart.) Both objects lie inside the UVOT-enhanced XRT error circle. A third, fainter source appears at the edge of the DSS-enhanced XRT error circle but is far outside the UVOT-enhanced circle. It is not clear which of these three objects is the host galaxy. We acquired spectroscopy of objects A and B with LRIS; they do indeed appear to be at different redshifts. A bright line is visible on the trace of source B; although unresolved the absence of other lines on either the red or blue sides suggests that it is likely [O II] at $z = 0.931$. This line is not visible on the trace of the

adjacent source A. For this object, a possible line at 7575 Å sits directly on top of a sky line and is therefore uncertain, but it appears to be present in both exposures. It is narrow: possibly too narrow to be marginally resolved [O II] at $z = 1.031$, although other likely associations predict the appearance of other lines elsewhere in the spectrum that are not observed.

SGRB 070429B

GRB 070429B is a clear short-duration GRB with $T_{90} = 0.5$ seconds and no obvious extended emission (Tueller et al. 2007). No optical afterglow was reported, although the online table accompanying (Roming et al. 2009) does report a UVOT position just outside the UVOT-enhanced XRT error circle. (Outside this table, this position has never been formally reported in any publication to our knowledge.) The only object visible in this area of the field is an isolated, bright, moderately red galaxy; it is located inside the UVOT-enhanced error circle and is slightly offset from the possible UVOT position. This seems to be a likely host candidate. Spectroscopy of this source was previously reported by Perley et al. (2007c); we detect a single emission line blended with a bright sky line that we associate with OII at $z = 0.904$. The host association and redshift were independently reported by Cenko et al. (2008b).

GRB 070518

A bright host galaxy was reported for this event from observations at the Large Binocular Telescope (Garnavich et al. 2007c). Given this, we did not attempt imaging observations of our own at Keck, although we did acquire our own imaging at Lick Observatory to produce a finding chart for spectroscopic observations with LRIS, confirming the presence of a bright host galaxy underlying the UVOT afterglow position. In our spectroscopy, we detect a single, bright emission line in the red camera at 8075Å; it is marginally resolved and consistent with [O II] at $z = 1.161$. The brighter, neighboring object is a Galactic star.

GRB 070612

This unusual GRB had both a bright optical afterglow and a bright radio counterpart (Horst et al. 2007), although it was not observed in X-rays due to a Sun constraint. A SDSS galaxy is reported at the GRB position, with a photometric redshift of $z = 0.1$ (Cenko et al. 2007c) (an alternative redshift solution is $z = 0.4$; Malesani et al. 2007b); subsequently a Gemini host spectrum taken under poor conditions and while the afterglow was still present identified a line at 6229 Å which they identified as [O II] at $z = 0.617$ (Cenko et al. 2007a).

Several years later we acquired an LRIS spectrum of this object with a position angle of 149 degrees on-sky. In the 2D spectrum, the SDSS object (which is marginally resolved in the SDSS public imaging) resolves into two objects at different redshifts. Within the trace of the brighter, northern object we confirm the presence of a strong emission line at 6229 Å, and also identify additional lines corresponding to Hβ, and [O III] (5007) at the same

redshift of $z = 0.62$. Based on our slit orientation, this object is more consistent with the afterglow position given by Cenko et al. (2007c) ad is the likely host galaxy. However, the nearby object shows a different set of emission features: this fainter object shows [O II], Hβ, [O III], Hα, [N II] at a common redshift of $z = 0.385$.

GRB 070520A

No optical afterglow was identified for this GRB in deep, early observations (e.g., Ishimura et al. 2007; Rumyantsev et al. 2007). A faint z-band source ($z \sim 24$ mag) was reported by Hattori et al. (2007a) in Subaru observations 18 hours after the GRB and no constraints on its variability were provided. This same source is visible in our Keck imaging also; our observations were taken in g and R filters and cannot be directly compared to Subaru, but the magnitudes and colors we observe suggest it has probably not faded greatly since the Subaru epoch. This object is near the center of the DSS-enhanced error circle and is a likely host-galaxy (it is just outside the much larger UVOT-enhanced error circle.)

GRB 070521

GRB 070521 is one of the darkest GRBs of the *Swift* era, being undetected in early, deep P60 imaging and in early NIRI observations (Cenko et al. 2009). As a result, no precise position is available, but an optically dim, very red source is present inside the UVOT-enhanced XRT error circle. This source has been imaged with a variety of different instruments (including at NIR wavelengths) and the SED is well-constrained; we discuss this source in much more detail in the next chapter. It appears to be a moderately evolved, moderately dust-extinguished galaxy at $z \sim 1.35$. Curiously, like GRB 070412, this GRB occured at a location positionally coincident with the far outskirts of a highly extended low-redshift elliptical galaxy.

GRB 070621

This event is another prominent dark burst, with no afterglow detection despite follow-up by many different ground-based instruments (including, notably, adaptive optics imaging with Keck: Bloom et al. 2007a). No clear host is evident in our imaging, although some faint host candidates are visible just outside the XRT error circle.

XRF070714A

Follow-up of this event was significantly hindered by a TDRSS[9] outage which delayed the relay of the GRB coordinates for several hours; no ground-based follow-up was attempted. Only one source is consistent with the UVOT-enhanced XRT circle ("A" in Figure 7.13, which we identify as the probable host, but given a slightly brighter object (B) somewhat outside

[9]The Tracking and Data Relay Satellite System is the

this position (and more consistent with the DSS-enhanced position) this determination is far from secure. Our R-band imaging of this field is affected by a bleeding spike from a bright star elsewhere from the image; it does not affect photometry of the putative host but nearby object B overlaps the bleeding spike.

We placed the LRIS slit across these two objects. The putative host (A) shows a single, bright emission line well towards the red end of the LRISR2 spectral coverage; associating this with [O II] gives a redshift of $z \sim 1.579$. (No other emission lines are observed at the locations expected if the line corresponds to other common emission features.) The nearby bright object (B) shows several emission lines at a common redshift of $z = 0.55$.

SGRB 070714B

This is a short-duration burst with extended emission. An afterglow was detected by the Liverpool 2m telescope (Melandri 2007); underlying the position is a faint host galaxy previously reported by Graham et al. (2009) and Cenko et al. (2008b). Spectroscopy by these groups establishes a redshift of $z = 0.92$. As also noted by these authors, the galaxy has a blue color and is a star-forming object notably unlike the low-redshift ellipticals hosting the first few short GRBs.

XRF070721A

The UVOT position is unusually poor due to the contamination by a nearby star. Fortunately, the star is cleanly separated in our imaging from the apparent host galaxy: a single, bright source at a position consistent with all three *Swift*-based positions. This source was also noted by Malesani et al. (2007a). We acquired a spectrum of this object with LRIS; although a strong trace is detected in both cameras no identifying lines are detected.

SGRB 070724A

Our study of this object was previously published in Kocevski et al. (2010). This short-duration burst occurred positionally coincident with a large, extended host shown spectroscopically to be a moderately star-forming galaxy at $z = 0.457$. We acquired spectroscopy of many other objects in the field along the slit or in separate observations; many but not all are at similar redshift, suggesting that this galaxy is part of a group (however, the lack of X-ray emission suggests it is not in a full-scale cluster.) Surprisingly, IR follow-up by another group (Berger et al. 2009) identified a faint infrared counterpart in the southern region of the galaxy, indicating that the afterglow was likely strongly extinguished.

SGRB 070729

This was a short-duration GRB with no detected extended emission. No optical or NIR counterpart was found in ground-based follow-up observations the same night (Berger & Kaplan 2007; Berger & Murphy 2007), although Berger & Kaplan report the detection of

an extended $K \sim 18.2$ mag object in the field. This source is visible in our imaging also as a red, extended object ("B"), although it is far from the UVOT-enhanced XRT position. Only one object ("A", a much bluer galaxy that may be part of a complex of neighboring sources) overlaps the XRT error circle, and no other notable galaxies are located nearby in the field.

GRB 070808

This is another dark burst, with no afterglow detection in early ground observations (e.g., Melandri et al. 2007). Several objects are identified in or near the XRT error circles; source "A" is a bright, extended object just outside both the UVOT- and DSS- enhanced positions; source "B" is within the DSS-enhanced position but outside the UVOT-enhanced position and is much fainter. Source A is the more likely host candidate, although it is highly unclear whether any of these sources truly represent the host of this event.

SGRB 070809

This event was a short-duation burst, although its $T_{90} = 1.3 \pm 0.1$ s (Krimm et al. 2007) is long enough to still be consistent with the long-duration population. The optical afterglow of this burst was discovered by our LRIS imaging the night of the event (Perley et al. 2007g,f); the images presented here were acquired much later, after the transient had faded. We detect no source at the afterglow location, although there are two nearby sources: an edge-on spiral $5.8''$ northwest of the optical transient (possibly with a faint companion at its north end), and a faint, marginally resolved object $2.0''$ to the southeast. (There is red object to the southwest is a star. Another, much brighter star is present even further to the southwest out of the field.)

On two separate epochs, we obtained 2×900s of spectroscopy of the spiral galaxy G at a slit orientation aligned with the axis of the galaxy (however, the source was extremely low during the first epoch and the spectra are of poor quality). Two bright emission lines are detected - one at 4542 Å and one at 6100 Å. Associating these lines with [O II] and [O III], respectively, the redshift of this galaxy is $z = 0.2187$. No other emission lines are significantly detected. No spectroscopy is available of the other galaxy closer to the afterglow position, which is much fainter ($R = 24.9$ mag).

The association of the transient with either of these galaxies is not clear; the source is not coincident with the light of either of them, and while the association is suggestive the $P_{\rm chance}$ values are far from definitive (~ 0.1). Recent observational experience has demonstrated that short GRBs can indeed sometimes occur at significant offset from their host galaxies and may even be kicked out into the intracluster medium; this may represent another example of such a case. However, intriguingly, Fruchter (2010) has reported a weak possible detection of an exceedingly faint source underlying the afterglow position in deep HST imaging, although the detection is marginal and further imaging will be required to characterize it.

GRB 070810A

Our imaging of this object was acquired only 28.6 hours after the burst itself occurred. While this GRB had a bright afterglow at early times (e.g., Swan et al. 2007), it had already faded to quite a faint level by the time of these observations, although we do see a source at the afterglow position in our imaging. Interestingly, this object is closely blended with another, redder source about $1.2''$ to the northwest, which could represent part of an underlying host galaxy. Further imaging would be necessary to determine this unambiguously.

SGRB 070810B

This clearly short-duration ($T_{90} = 0.08$ s) event occurred shortly before our run; we acquired several epochs of deep imaging to search for an optical counterpart. Image subtraction of the frames reveals no such source Kocevski et al. (2007a). No afterglow was detected by the *Swift* XRT either, and so there is no position with which to look for a host galaxy in this imaging.

GRB 071021

The host galaxy of this event is part of a "chain" of three very faint objects running through the image in a line (Figure 7.14); all three objects are quite faint (V ranging from 25.6–26.8 mag). The optical afterglow position of Castro-Tirado et al. (2007a) is consistent only with the northwestern object, which we identify as the host galaxy. We placed the LRIS slit through all three objects. Unfortunately, only G1 is detected clearly on the slit; the other objects are too faint to even show a trace, and do not show visible emission lines over the spectral range at their expected position on the slit. G1 is an older galaxy with weak star formation lines at $z = 0.45$.

GRB 071025

GRB 071025 is a luminous, high-redshift $z \sim 5$ burst; its afterglow is studied in extensive detail in §7.14. Since no spectroscopic confirmation of this high redshift was available, we conducted deep imaging of this field with LRIS. Consistent with the high-redshift origin, we detect no source at the position of the afterglow to deep limits.

GRB 080207

GRB 080207 is a prominent *Swift* dark burst; our study of this object is presented in detail in Svensson et al. (2011). (The recently published study of Hunt et al. 2011 has also come to similar conclusions.) The afterglow was not detected in deep ground-based images by several groups, including in deep NIR observations the first night (Fugazza et al. 2008). A grouping of three marginally-detected sources are located in or near the UVOT-enhanced; only the southwestern source (the faintest of the three) is also consistent with the

DSS position. The precise Chandra localization of in Svensson et al. (2011) confirms this is the host galaxy. This object is not particularly red in our optical measurements, but it is extremely bright in the NIR and is among the brightest GRBs ever imaged by Spitzer, showing it to be an extremely red object; properties which strongly differ from most GRB hosts studied to a similar level of detail to date. The photometric redshift of this object is $z = 2.1$.

GRB 080210

This was a *Swift* GRB with a bright optical afterglow; our imaging of this field was conducted only two days after the burst, when the afterglow was still dominating the flux. Spectroscopy from the VLT (Jakobsson et al. 2008) identified a redshift of $z = 2.641$ and suggested Lyα may be present in the afterglow spectrum, which would likely indicate a bright, luminous host galaxy. No extension or nearby sources suggesting an underlying host galaxy are detected. The afterglow magnitude (including any underlying host) is $R = 24.12$ mag, which is still consistent with the possible presence (or absence) of a luminous galaxy at this redshift.

GRB 080229A

Deep, early limits on an optical afterglow inside the XRT location were presented by Berger (2008). Unfortunately, this location falls very close ($3''$) to an extremely bright ($R \sim 13$ mag) star. A bleeding spike from the star completely washes out the XRT position in the red imaging. Even in the blue imaging, the complicated outer PSF of this star overwhelms the signature of any possible faint host galaxy at this location. Given the highly variable background and noise properties within the XRT region we do not present any limit on a host in Table C.5 for this object.

GRB 080307

Although an optical afterglow was detected for this burst, it is significantly fainter than might be expected given the X-ray afterglow; this afterglow also appears reddened given the colors presented in Page et al. (2009). Underlying the optical position presented in that work, we identify a moderately faint, blue galaxy.

GRB 080310

GRB 080310 was a bright GRB with an afterglow followed by many telescopes; the absorption redshift is $z = 2.4266$ (Prochaska et al. 2008b). The red-side imaging of this field is affected by variable background due to charge-transfer effects on the LRISR2 chip from two nearby stars; an $R \sim 15$ mag star $13''$ due-south produces a faint trail running through the UV position, and an $R \sim 11$ mag star $40''$ to the west produces a large "curtain" that

creates an obvious gradient through the image. (The blue side is not susceptible to these issues.) No source is evident at the UV position.

GRB 080319A

While overshadowed by the much brighter event that happened nearby shortly after this burst, GRB 080319A was also observed rapidly by a number of telescopes, and a faint optical afterglow was detected (Cenko 2008). As described in more detail in Chapter 8, we detect a modestly bright, blue, slightly host galaxy at the optical position which we identify as the GRB host galaxy. We attempted spectroscopy of this object with LRIS and detect no line signatures across the spectral range. We do detect several emission features from the neighboring object "A" to the west, which place this unrelated galaxy at $z = 0.428$.

GRB 080319C

GRB 080319C is an intriguing case, and another reminder of the perils of host association with large data-sets. This event had a bright afterglow, established by absorption spectroscopy to be at a likely redshift of $z = 1.9492$ (Fynbo et al. 2009) based on absorption by several metal lines. An intervening Mg II absorber is also observed in the spectrum at a redshift of $z = 0.8104$.

A bright ($R = 22.5$ mag), extended object is seen in our imaging of this burst very close to the optical position. This would, at first glance, appear to be the host galaxy, which given the redshift of the burst would have to be exceptionally luminous. Indeed, we originally claimed this to be the host in the study of (Perley et al. 2009c). We acquired spectroscopy with the slit aligned with the long axis of this object with LRIS and notably do *not* confirm this association: in fact, we observe a series of bright emission lines ([O II], Hβ, [O III]) at a redshift of $z = 0.810$, indicating that this object is actually the foreground absorber!

Given the extended size of the object, we examined the 2D spectrum to determine whether or not this might actually be a complex of sources at varying redshift, as observed for several other objects in this survey (the burst position is consistent only with the outer part of the northeastern lobe.) The emission lines are indeed strongly concentrated towards the opposite, southwestern portion of the object, which may suggest that this source is a superposition of the host and a foreground absorber (or background object), but seeing during the spectroscopy was poor and we cannot definitively determine whether or not these lines are intrinsically absent in the fainter part of the object. No emission lines are found in the northeastern corner exclusively. Likely, HST or similarly high-resolution observations would be required to unambiguously resolve this question.

GRB 080319D

GRB 080319D was detected by the *Swift* UVOT, GROND (the Gamma-Ray Burst Optical Near-Infrared Detector; Greiner et al. 2008), and several other telescopes. Inside the XRT error circle is a single, bright, likely-extended source. This is presumably the same

source posited as a possible host in the GROND observations of Clemens et al. (2008), although they give a slightly different position and claim that the source is coincident with the UVOT error circle, which is not the case in our imaging. We suspect the GROND position may be a blend of the late-time afterglow and this nearby source in approximately equal quantities, giving a position approximately intermediate between the two. Given the UVOT position, this object does not appear to be a natural host galaxy. No host is detected underlying the UVOT position.

GRB 080320

The afterglow of this event was extremely faint in r-band but reasonably bright in I and redder filters, tentatively suggesting a relatively high redshift of $z \sim 5$, as we suggested previously in Perley et al. (2009c). A high-redshift association is further bolstered by the nondetection of a bright host galaxy in our imaging. Further discussion of this object is presented in Chapter 8.

In the improved imaging reductions presented here, while we continue to detect no source in g-band, there is in fact a 5σ detection of an object underlying the optical position in the I-band imaging at at a level of $I \sim 23.4$ mag. If this source is indeed at $z \sim 5$, as originally claimed, this would represent a very luminous Lyman-break galaxy. Alternatively, it could be an exceptionally red lower-redshift host galaxy. Infrared imaging will be required to distinguish these possibilities.

GRB 080325

GRB 080325 is a dark burst; its red afterglow and host galaxy were previously studied by (Hashimoto et al. 2010). It appears to be a luminous, dusty object at $z \sim 1.9$. Independently of that effort, we also identified the host galaxy in our Keck observations; it is an extended and seemingly rather blue source (although much brighter in the near-infrared and very bright in the Spitzer bands—further study of this and other dark bursts will be provided in upcoming work). We attempted spectroscopy of this object but detected no trace or lines.

XRF080330

GRB 080330 was an X-ray flash with a moderately bright optical afterglow; echelle spectroscopy was presented by D'Elia et al. (2009b) that established the redshift of $z = 1.51$. Line-of-sight absorbers are also observed in the spectrum at redshifts of $z = 1.017$ and $z = 0.822$. The ground-based positions disagree slightly with the UVOT position, but there is no detection of an underlying host at either location down to deep limits. Several faint objects are located a few arcseconds away in each direction that represent possible candidates for the Mg II absorbers, the most interesting of which is a highly extended, diffuse blob spanning at least $4''$ in diameter, the closest part of which is $2''$ from the afterglow position.

GRB 080430

This is a relatively low-redshift *Swift* burst with a faint, low-luminosity optical afterglow; absorption spectroscopy identified a redshift of $z = 0.767$ (Cucchiara & Fox 2008), although this is based only on metal lines. We identify a blue, relatively bright galaxy closely underlying the afterglow position that we identify as the host galaxy.

GRB 080507

This AGILE (Astro-rivelatore Gamma a Immagini Leggero, and italian high-energy satellite; Feroci et al. 2007; Tavani et al. 2009) GRB initially came to our attention due to its close proximity to the red elliptical galaxy NGC5969 (Lapshov et al. 2008); centered $90''$ from the afterglow position (although there is no galaxy flux anywhere near the GRB location; the slight background gradient seen in Figure 7.15 is due to a bright star just north of the image.) Our photometry gives $g = 25.1$ mag, $R = 24.7$ mag, suggesting a fairly bright and blue object, although we caution that the R-band values may be affected by contamination from a diffraction spike from the bright star.

GRB 080514B

GRB 080514B was (also) detected by Super-AGILE, including by its high-energy GRID detector. The ground position is consistent with bright blue object which we identify as the host galaxy. Our observations were previously published in Rossi et al. (2008) (who also present a photometric afterglow redshift of $z \sim 1.8$); the host is a blue, luminous object.

XRF080515

The position of the source reported in Updike et al. (2008a) disagrees with that of the X-ray afterglow; we acquired this imaging and measured the position of the transient directly; this corrected position is within the (relatively large) DSS-enhanced XRT error circle. The optical position is also consistent with the northern of two nearby sources in the outer PSF of a bright foreground star; we identify this as the GRB host galaxy.

We placed the LRIS slit over both of these nearby sources. The host galaxy may be at very low redshift: in both of our longslit spectra we identify a marginally resolved line profile well in the blue that is consistent with [O II] at $z = 0.132$. We also see what could be Hβ at the same redshift near the dichroic cutoff, but do not clearly recognize any lines in the red side, notably including Hα. However, the issue is somewhat confused due to possible blending with the other source in the 2D spectrum. This neighboring object ("A") shows a very bright line at an observed wavelength of 5510Å the same wavelength as Hβ at the putative host redshift). For object A, this line correspond unambiguously to [O II] at $z = 0.478$, as we identify weak lines corresponding to Hβ and [O III]$_5$007 at the same redshift.

If the host is indeed at $z = 0.132$, our imaging would have occurred while an associated supernova would have been quite bright—similar to the magnitudes which were actually observed. We do not yet have a subsequent epoch of observations to check for fading. Regardless of whether supernova light contributes to the observed flux or not, however, if this redshift is correct the galaxy must be exceptionally underluminous: $M_V \sim -13.6$ mag, less luminous than the SMC by a factor of $2 - 3$.

GRB 080603A

This GRB was detected by INTEGRAL. Its afterglow is optically bright and was followed by several ground-based telescopes, including a spectrum triggered at Gemini-North which established the GRB redshift as $z = 1.68742$ and revealed two strong Mg II absorbers at $z = 1.2714$ and $z = 1.5636$. Those data have been previously presented, in combination with the late-time Keck observations of the host environment, in the comprehensive study of Guidorzi et al. (2011). A grouping of several sources underlies the optical afterglow position; this position is consistent only with the northernmost object of the group (this is not clear from the *Swift* XRT or UVOT positions alone, but the ground-based position by Guidorzi et al. places it squarely on this putative host. Furthermore, the afterglow is actually detected in our first epoch of Keck imaging.)

We also acquired three spectroscopic observations across this complex; in the first two spectra we aligned the slit to cover the host galaxy and the southern object "B"; in the third we aligned the slit horizontally to cover object "B" and a red object visible at the east edge of Figure 7.15. All four sources show well-detected traces in the 2D spectra, but none of them shows an obvious emission line. Only the lowest-redshift absorber is expected to show an emission line in the spectral range (the [O II] doublet at 8465 Å), but is expected location falls within a group of strong sky lines, so these observations do not rule out any of these objects being absorbers.

GRB 080607

In a stroke of exceptionally good fortune, GRB 080607 occurred and was immediately observable during one of our host galaxy observing runs. This was not the first such case to occur during our program (GRBs 061121 and 071011 also occurred under these circumstances)—however, GRB 080607 is an unusually interesting GRB: as reported in Chapter 6, this was a phenomenally luminous event in an extremely unusual environment. As reported in that Chapter and in the works of Prochaska et al. (2009) and Sheffer et al. (2009), GRB 080607 occurred in or behind a dark molecular cloud in its host galaxy, highly obscuring the afterglow (by $A_V \sim 3$ mag, or $A_{R,\mathrm{obs}} \sim 5$ mag). A "typical" (in terms of luminosity) GRB would be completely undetectable under such circumbstances, but GRB 080607 was so brilliant as to shine through the cloud and still be detected by numerous small-aperture telescopes at $z = 3.036$. This molecular cloud imprinted a veritable chemical forest of emission lines on the afterglow spectrum.

Well after the afterglow had faded, we returned to the field to conduct deep imaging. The host galaxy is faint, but nevertheless well-detected in both g- and I-band; we also observed this position in the NIR with NIRC and using Spitzer. Analysis of the host galaxy was presented in Chen et al. (2010) [see also the erratum at Chen et al. 2011]. The host itself is a dusty, rapidly star-forming galaxy with very red broadband colors. As with the hosts of GRB 080207, GRB 060923, and other prominent dark bursts, this host represents a class of obscured galaxy rarely or never seen hosting GRBs until recently.

GRB 080701

This object had no detected optical afterglow in early ground-based observations, although in part this is likely due to the influence of a relatively large extinction in this direction of $E_{B-V} = 0.51$ mag. Seeing conditions were poor during our imaging of this field. Two sources are detected just outside the UVOT-enhanced error circle; a bright, red source and a fainter, blue source. It is not clear which (if either) of these objects is the host galaxy.

SGRB 080702A

This was a short GRB in a region of relatively high extinction in spite of its moderate distance from the Galactic plane ($E_{B-V} = 0.66$ mag at $b = 17°$). No optical counterpart was reported. Interestingly, the background in and around this region is quite variable, showing faint nebular emission. We do not detect any source consistent with the XRT localization; nor any notably bright or extended galaxies nearby.

GRB 080710

This otherwise rather ordinary GRB was notable for its slow, steady brightening out to 2000 s after the event, reaching a peak of $r = 16.3$ mag before fading (Krühler et al. 2009b). The relatively low afterglow redshift of $z = 0.8454$ was discovered by our group (Perley et al. 2008b).

A bright double star is located 18″ southwest of the burst position and two diffraction spikes are visible in the imaging very close to these objects (although neither directly intersects our targets, caution should be used in interpreting photometry of this field). A faint source is observed at a position consistent with the XRT and UVOT positions that we identify as a low-luminosity host galaxy.

SGRB 081211B

GRB 081211B is a notable event. The burst was first discovered in the *Swift*-BAT slew survey (Copete et al. 2008), which (due to the slewing of the telescope) observed only the end of the event. Konus-Wind observed the entire event (Golenetskii et al. 2008b) and observed a short, intense spike of harder radiation shortly before the *Swift* detection; putting these two reports together suggests that this GRB was actually a short burst with extended emission

(an SGRB). *Swift* later slewed to the location and detected a faint, fading X-ray transient. However, the GRB localization lies within a visual galaxy overdensity in SDSS archival imaging, and near the centers of several reported clusters in the literature, which likely correspond to the same physically extended structure: ZW 3893, Abell 1196, and MaxBCG J168.22310+53.83028. Redshifts from the Sloan Digital Sky Survey of the brightest two apparent cluster members place this cluster at a probable redshift of $z = 0.216$.

No host galaxy underlying the most recent UVOT-enhanced XRT position is availble in our imaging down to a limit of $R > 25$ mag, although a faint extended object is visible just west of the error circle. In context with the possible cluster associations of several other SGRBs (790613, 050509B, 050813, 051210, 061201: Gal-Yam et al. 2008; Berger et al. 2007b; Prochaska et al. 2006b; Berger & Fox 2005a; Stratta et al. 2007), this result seems to suggest that this GRB in fact originated in the intracluster medium, perhaps after being kicked out of another cluster member.

GRB 081221

This was an exceptionally bright GRB without a detected optical afterglow. A NIR afterglow was detected in a deep NIRI image reported by Tanvir et al. (2008a). We acquired this image from the Gemini Science Archive and aligned it with our Keck observations, which conclusively shows the IR transient to be coincident with the edge of a faint, extended object in the image. We placed the LRIS slit through this object and nearby source "A" on the slit. This nearby source is well-detected and shows a single, marginally resolved line in the red consistent with the [O II] doublet at $z = 1.345$. However, the host itself is very faint, with only a marginal detection on the slit and no lines evident over our spectral range.

XRF090111

GRB 090111 was a relatively faint *Swift* GRB, not observed by any ground-based telescopes. The high-energy burst spectrum is quite soft, and the Baysean analysis of Butler (2007) suggests that it is an XRF ($E_{\rm peak} = 22^{+12}_{-21}$ keV). In our imaging of this field we detect a bright ($R = 24$ mag) host galaxy at the center of the UVOT-enhanced error circle.

GRB 090113

This GRB was followed, and not detected, by several ground-based observatories including GROND (Olivares et al. 2009a). Given the X-ray afterglow, the limits are below the $\beta_{\rm OX} = 0.5$ threshold and designate this to be a dark burst. A single source is detected just outside the UVOT-enhanced XRT error circle; a target-of-opportunity Chandra observation (A. Levan, private communication) identifies it as the GRB host galaxy. We took a spectrum of this object, but no lines or other spectral features were detected.

GRB 090404

Reflecting the increased focus of our program in the last two years on obscured events, GRB 090404 is also a dark GRB. Our images were previously reported in Perley et al. (2009a). The GRB position is in a complex environment, near two resolved, seemingly interacting galaxies connected by a thin bridge. The millimeter position of Castro-Tirado et al. (2009), the most precise available, is about an arcsecond west of this system, on top of a region of increased flux that we refer to as the host galaxy, though this host may—or may not—be a part of the other nearby components of the system. A brighter point-like concentration is seen further to the north in the g-band image (this source blended into a single diffuse component in I-band, where the image quality is poorer.)

GRB 090407

GRB 090407 is another dramatic dark burst, not detected in any ground-based observations despite significant early follow-up. Its environment is quite simple: only a single source is detected at a position consistent with the XRT positions, with no other sources nearby. The source is moderately red in the optical (but extremely red in the IR.)

SGRB 090515

This is an unambiguous short-duration GRB detected by *Swift*. Its X-ray afterglow is quite bright considering the low gamma-ray fluence (only 2×10^{-8} erg/cm^2; Barthelmy et al. 2009) and exhibits some curious features, in particular a sudden drop in flux at 200 s that motivated the work of Rowlinson et al. (2010), who suggest that this feature may result from with spindown emission from a newly-formed millisecond pulsar.

Consistent with the late-time Gemini imaging in that work after the optical counterpart disappeared, our imaging of the field shows no source at the optical afterglow position or anywhere else in the XRT error circle (note that the true optical afterglow location is not at the coordinates specified by Rowlison et al., which actually correspond a cosmic ray that was not properly flagged by the Gemini reduction routines).

GRB 090618

GRB 090618 was a very bright *Swift* burst with a bright afterglow followed by many different groups. Spectroscopy by our group established a redshift of $z = 0.54$, making it one of the lowest-redshift *Swift* events to date. A host galaxy was previously known from SDSS (Malesani 2009); a bright, unresolved source is visible in this position in our imaging as well. Our imaging was conducted only 7 days after the event and may include significant afterglow contribution, although the magnitude is already similar to the reported SDSS magnitudes and no fading is reported by Khamitov et al. (2009) in observations taken between 7.7–9.7 days after the burst.

GRB 090709A

GRB 090709A was an extremely bright *Swift* burst; its afterglow was only marginally detected in a few early optical/NIR observations before fading from view. The inference of quasiperiodicity in the GRB light curve (Markwardt et al. 2009; Golenetskii et al. 2009; Gotz et al. 2009) led to some early speculation that this might be a flare from a Galactic magnetar (although the position of this object is far from the Galactic plane). We argued in Cenko et al. (2010d) that this is more likely a highly-extinguished event at moderate redshift (a similar conclusion was also reached by de Luca et al. 2010). In that study we had not yet imaged the source to deep limits (except with adaptive optics, which is not particularly sensitive to the presence of extended sources), but in subsequent Keck observations (and in NIRI IR imaging and Spitzer imaging as well) we detect a faint, red source underlying the OT position. The colors of this object are consistent with a luminous, dust-obscured galaxy at moderate to high redshift, further bolstering the extragalactic hypothesis and identifying this host as another member of the class of dust-obscured GRB host galaxies.

GRB 090902B

GRB 090902B is an extremely bright burst detected by GBM (Gamma-Ray Burst Monitor; Meegan et al. 2009) and, notably, the LAT (Large Area Telescope Atwood et al. 2009) on Fermi, which provided evidence for high-energy spectral excess in the prompt emission (Abdo et al. 2009b). The redshift is $z = 1.822$ (Cucchiara et al. 2009). We imaged this source on two epochs, although seeing conditions during the first epoch were exceptionally poor. A faint host galaxy is detected in the second epoch (taken during good conditions); it directly lies directly under our own position provided by reanalysis of the Nickel afterglow discovery imaging (Pandey et al. 2010). The host is faint and blue, although note that the R-band photometry might be slightly compromised by the CTE trail from a star elsewhere in the image.

SGRB 100117A

We identified the host galaxy candidates for this short-duration GRB from CFHT pre-imaging (Cenko et al. 2010b). Of the sources listed there, one source ("S3", here designated "H") was shown to be variable; the analysis of Fong et al. (2011) resolved this source into an optical counterpart offset by about $1''$ to the west of the centroid of a quiescent object. We did not repeat this imaging, but acquired a spectrum with LRIS across all three targets several days later. Observations were conducted at high airmass during twilight as the field was setting, and seeing was poor throughout the night in general. As a result the spectrum is of poor quality, and we are unable to recognize the possible weak absorption signatures from which Fong et al. (2011) associated this event with an older galaxy at a redshift of $z = 0.911$.

GRB 100205A

GRB 100205A is a candidate very-high-redshift GRB, as its afterglow was detected only in deep H and K imaging (Cucchiara et al. 2010) and the X-ray column density is consistent with the Galactic value (Racusin et al. 2010). We imaged this source for over an hour in the g and R filters and detect no source to the image limits of $R > 26.6$ mag, $g > 27$ mag, supporting the high-redshift interpretation.

SGRB 100206A

This was another *Swift* short burst. We identified a bright host candidate (Miller et al. 2010) in DeepSky Palomar pre-imaging of the field, and proceeded directly to spectroscopy. The host trace is extremely red, with several visible lines present only in the red part of the spectrum; the wavelengths of the observed lines are consistent with Hα and [N II] at $z = 0.41$. Remarkably, this galaxy is detectable in JHK filters even to the 1.3 m PAIRITEL IR telescope, and is detected by WISE as well (Wright et al. 2010; source designation J030839.15+130929.0) with given magnitudes of $W1 = 15.7$, $W2 = 15.14$, $W3 = 11.2$. Modeling the IR SED as a young star-forming galaxy extinguished by a dust screen, the inferred bolometric luminosity is at least $2 \times 10^{11}\ L_\odot$ (identifying this object as a luminous infrared galaxy), but the total bolometric flux may be much larger if significant star formation is occurring in totally obscured regions.

Although the nominal XRT position does not exactly coincide with the host, the separation is only $7''$ (35 kpc in projection), a separation closer than that of SGRB 050509B to its putative host galaxy. This would, again, seem to be a compelling case for an SGRB ejected by a massive galaxy—but in this case, one which is still very actively star-forming.

We did not image this field at Keck, but an additional source is reported within the XRT error circle by Levan et al. (2010c) and Berger et al. (2010) which could, alternatively, represent a fainter background host galaxy. Nevertheless, as with GRB 050509B (and, to a lesser extent, 060502B) the proximity of association with such a remarkable object provides strong evidence for an association with the brighter galaxy at larger offset: the space density of LIRGs and ULIRGs is very low in the nearby universe (Kim & Sanders 1998). From querying the WISE data base, the sky density of sources with $W3 < 11.2$ mag is only ~ 0.04 per square arcminute; the inferred $P_{\rm chance}$ is 4×10^{-4} — likely much smaller than the chance of association with the object inside the XRT error circle if its magnitude is typical. This further increases our confidence that the association is real.

GRB 100413A

GRB 100413A is another dark burst; no afterglow was detected with any optical/NIR facility, although a detection was secured with the EVLA (the Expanded VLA). The EVLA position and XRT position are both consistent with two sources with different properties: a red, northern source and a blue southern source (a third, brighter red source is also visible further to the south but is not consistent with either position.) Likely, one of these two faint

objects represents the host galaxy; the EVLA position seems to slightly favor the northern source, which we tentatively ID as the host here. Further refinement of the position will be necessarily to establish this identification more definitively.

GRB 100414A

GRB 100414A was another Fermi GRB detected by the LAT. Its redshift is known from absorption spectroscopy to be $z = 1.368$ (Cucchiara & Fox 2010). Our Keck imaging shows a moderately faint, compact blue source underlying the optical afterglow position which we identify as the GRB host galaxy.

GRB 100420A

The afterglow of this GRB was detected only in K-band with NIRI on Gemini-North (Levan et al. 2010b), although the GRB itself, and its X-ray afterglow, are relatively faint and the constraints on absorption are modest. Unfortunately, the first two blue exposures were unusable due to bleeding from a bright star elsewhere in the field (the position angle was subsequently rotated to alleviate this), while two of four red exposures placed the NIR position near a diffraction spike and in the third it was hit by a cosmic ray. Nevertheless, there is a significant detection of a faint extended source underlying the NIR position in the R-band image. The source is detected only at low significance in the g-band image.

GRB 100424A

GRB 100424A is another dark burst, with no detection in a variety of moderately deep ground observations during the first night (Huang et al. 2010; Levan et al. 2010a; Olivares et al. 2010). Imaging by our group with NIRI revealed a red NIR optical afterglow that faded in subsequent observations. Consistent with the NIR position, we identify a faint optical source in our deep Keck imaging.

GRB 100526A

As with GRB 100424, the highly reddened NIR afterglow of GRB 100526A was discovered by our observations at NIRI on Gemini-North. Again, a faint optical source is identified underlying the IR position. An extended neighboring source is also seen just to the southwest: it is not clear whether not the object is physically connected with the GRB—the two sources, and in fact two other sources further two the south, may form a large complex, extended object or simply be a superposition of unrelated sources, the relatively poor seeing of our observations is not sufficient to resolve the issue.

GRB 100614A

No afterglow was detected for this burst even in early NIR observations (it is another dark burst). We do not detect any source consistent with the X-ray afterglow position in our optical imaging.

GRB 100628A

This was a short-hard gamma-ray burst detected by *Swift*. No optical counterpart was ever identified, and the X-ray error circle was modified several times (the first two possible X-ray counterparts were shown to not be fading; Immler et al. 2010). The final X-ray afterglow is only a marginal detection (seven counts) and as a result, the error circle is quite large and contains several different sources. The brightest of these are the extended source "G7" (using the identifier of Berger 2010b) and "S8", a more pointlike object that G7 may be interacting with.

GRB 100823A

This GRB was another possible dark burst, given the apparent nondetection at optical wavelengths and faint detection at IR wavelengths (Levan et al. 2010d), although the issue is somewhat confused by reports of a UVOT detection (Chester et al. 2010). We detect a faint optical source at the IR location which we associate with the GRB host galaxy. This is just south of a much brighter galaxy.

GRB 100905A

This event was imaged by UKIRT within only 17 minutes of the trigger and only a faint source was detected, suggesting a dim or dark GRB (Im et al. 2010). No coordinates of this reported source were given, so we have only the XRT positions with which to determine limits on the host galaxy: nevertheless, even in the relatively large XRT error circles we do not identify any host galaxy candidates.

7.6 Results

An in-depth analysis of the results of this survey—detailed study of various sub-classes of GRBs (XRFs and short bursts) and further study of a handful of interesting objects—will be presented in future work. I summarize a few general results below.

7.6.1 Detection Statistics

Although our integrations were not particularly deep (by 10 m telescope standards: only rarely did we image a field for more than 30 minutes) we were able to successfully detect a host galaxy for a large fraction of our objects. To quantify this statement, I will consider all

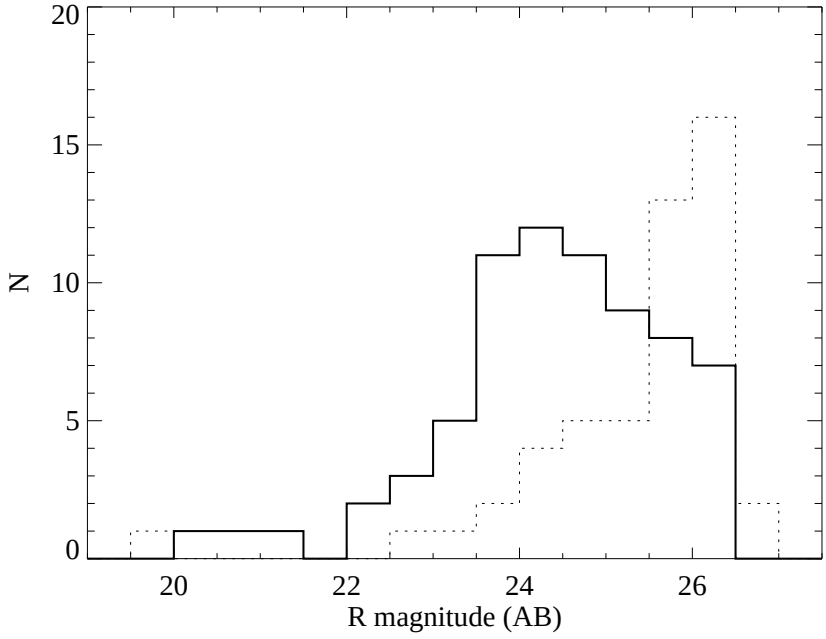

Figure 7.3 Histogram of AB magnitudes (solid line) and magnitude limits (dotted line) of GRB hosts in the survey, corrected for Galactic extinction. We detect about 65% of all burst hosts observed to moderately deep limits.

fields observed in R-band or in filters bracketing R-band (all imaging fields except for two). Excluding a relatively small number of shallow nondetections ($R < 24.5$ mag) that resulted from poor conditions or foreground extinction, this sample constitues a total of 126 fields observed; 12 of these are SGRBs. Among the 114 long GRB fields, we detect a total of 73 objects—or 64% of the total. For SGRBs, host identification is often ambiguous and it is difficult to trivially identify a host in most fields—especially when a faint X-ray afterglow provides the only available position. Nevertheless, we identify a promising host candidate in 8 of these cases (67% success rate).

A histogram of R-band magnitudes (the R-band is interpolated from neighboring filters if this filter was not used directly) for LGRBs is presented in Figure 7.3. Few hosts are brighter than $R < 23.5$, but the distribution is relatively flat after that point (the apparent dropoff is likely at least in part due to nondetections.) While we detect most objects, significant fraction (about one third) of *Swift*-era LGRBs are evidently fainter than $R > 26.5$ mag and are much more challenging to find.

Before interpreting this, we again caution that this was not a uniform survey: some galaxies were specifically selected on the basis of intrinsic brightness, faintness, or other anticipated features of interest, and the magnitude distribution (or any other broad statistic encompassing the entire sample) is not necessarily fully representative of all GRBs. Nevertheless, selection criteria were broad enough and the sample large enough that it is not

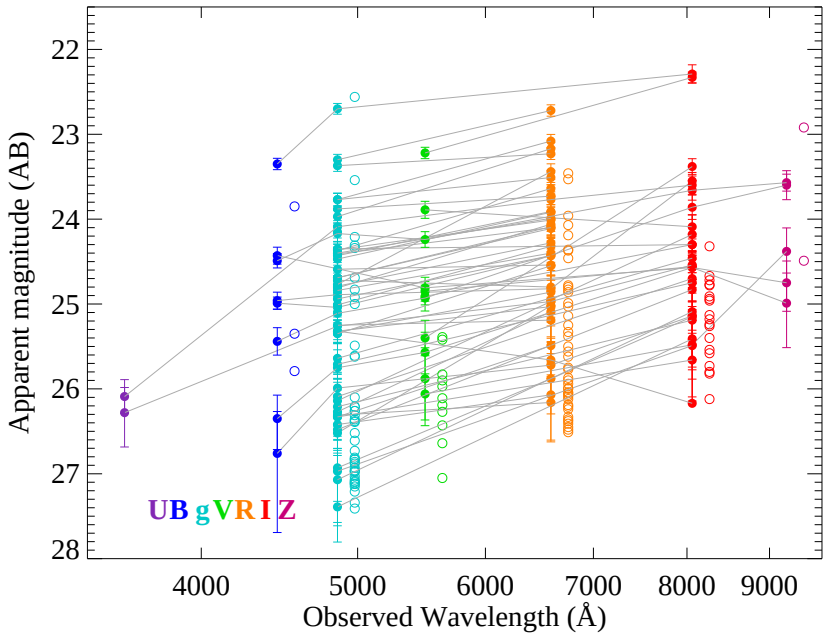

Figure 7.4 Composite of observer-frame photometry and SEDs for all LGRBs in the sample. (Upper limits are shifted slightly to the right for clarity.) The consistency of the spectral index for most of these objects is notable.

unreasonable to consider this as reflective of a broader statement that deep ($R_{\rm lim} > 26$ mag) imaging surveys are in fact detecting a majority of the star-formation[10] in the volume of the universe being probed by GRBs (primarily $0.5 < z < 4$: see the following Chapter)—while fainter galaxies must exist, they do not dominate the star-formation rate in this redshift range. This is consistent with the star-formation rate inferred by extrapolating of the luminosity function (Reddy & Steidel 2009). If GRBs occur preferentially in small galaxies with low metallicity, as has been suggested (see Chapter 1), this would only strengthen this conclusion.

7.6.2 Colors

The large majority of our fields were imaged in multiple colors, allowing us to also speak about the colors of typical GRB hosts. Moving beyond the R-band, then, in Figure 7.4 we show the magnitudes of all detections in all of the filters employed. Most other bands show a similar distribution in magnitudes as R, with the bluer filters offset slightly lower and the redder filters slightly higher. The grey lines connect observations of the same host galaxy: note the general consistency of this slope in all but a few of these objects. We can express this more quantitatively in terms of the color: in Figure 7.5 I have plotted a

[10] Or at least, the type of star-formation which causes GRBs.

histogram of the $g - R$ color (interpolating to g-band or R-band where necessary using the same procedure outlined above in the cases where other filters were used). If the burst is at sufficiently high redshift for the Balmer break to be redshifted beyond these bands ($z \sim 1$), this color is proportional to the UV spectral index, normally defined in this context in terms of wavelength as $f_\lambda \propto \lambda^\beta$ (as this is a different convention than is used elsewhere in this dissertation; I use the subscript λ—i.e., β_λ — to distinguish this spectral index from the more conventional definition in terms of f_ν.)

This index is a useful probe of conditions in star-forming galaxies. In the local universe, the smallest and most intensely star-forming galaxies have $\beta_\lambda \sim -2$ to -2.5 with more typical galaxies being redder than this (larger β) (Robertson et al. 2010); Lyman-break galaxies (LBGs) at higher redshift cluster between -2 and -1, again with more typical galaxies with larger evolved populations skewing redder than this (Bouwens et al. 2009). Galaxies with $\beta < -2.5$ are essentially unknown at low redshift (ordinary stellar populations simply are not blue enough) although may exist in the very high-z universe (Bouwens et al. 2010).

Our sample is basically consistent with this picture. Most of the objects in the sample have a spectral index β_λ between -2 and 0, and none have $\beta_\lambda < -2.5$. These are blue colors and indicate a star-forming population with relatively little dust ($E_{B-V} < 0.5$ mag) and no unexpectedly blue objects. However, the population overall is significantly redder than what is observed for LBGs—indicating the ability of GRBs to select a different, perhaps more representative, sample of high-redshift galaxies than what is possible from color-break techniques.

A small number of galaxies form a tail towards the right indicating relatively red objects; these may be older or dust-reddened, or at lower redshift (where $g-R$ may bracket the 4000Å break; note that we do not have redshifts for most of our objects). Such objects clearly only make up a small fraction of the sample, consistent with the idea that very few GRB hosts are significantly dust-obscured. However, it is important to note that this sample only incorporates observer frame optical colors. Since most galaxies in the sample are near our detection limit to begin with (see Figure 7.3), it is difficult to tightly constrain the presence of strongly unusual colors with only these data. Observations in the infrared are necessary to search for truly unusual SEDs. Such a program is currently ongoing and will be discussed in future work.

7.6.3 Luminosities

Most objects in our sample do not have known redshift, even after spectroscopic observations (see next section). Nevertheless, this represents a significant number of objects; for these events it is possible to convert our observed magnitudes to rest-frame magnitudes and luminosities. This is shown in Figure 7.6.

Unsurprisingly, the results vary with redshift. (Although redshift is not shown on the plot explicitly, since all imaging was conducted in the optical bands the redshift shifts from low to high from right to left on the plot.) The relatively small number of low-redshift GRBs observed are mostly faint, with absolute magnitudes of $M_{AB} < 20.5$. Moving to

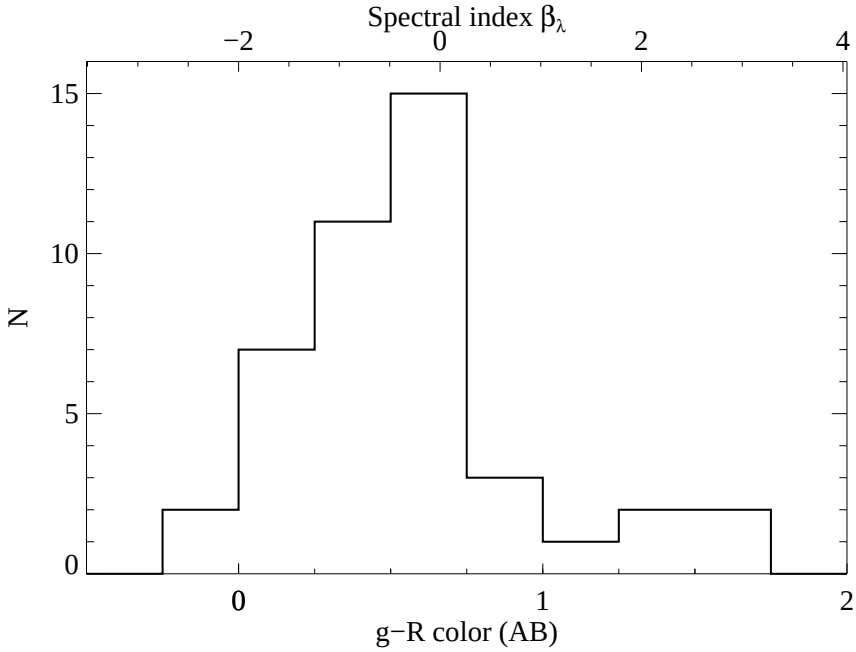

Figure 7.5 Histogram of observed or interpolated $g - R$ colors for LGRBs in the sample. Almost all SEDs in the sample are consistent with SED of a star-forming galaxy with relatively little dust, though skew slightly redder than LBGs.

high redshift, these galaxies become undetectable to our typical depths, but a population of luminous objects appears instead. Still, all galaxies in the survey are sub-L_* ($M^*_{\rm UV}$ at $z = 2 - 3$ is approximately -21 AB mag) with the notable exception of a few powerhouses: GRB 060210 at $z = 3.94$, GRB 061121 at $z = 1.314$, GRB 051109A at $z = 2.346$, and GRB 060111A (probably a Lyman-α emitter at $z = 2.32$).

7.6.4 GRB subclasses

A detailed examination of intrinsic differences between the various classes of GRBs examined in this survey is beyond of the scope of this Chapter. In particular, because we have aimed to not duplicate observations made previously at other telescopes and only present here our optical observations, However, a few general remarks are in order.

SGRBs show a surprising diversity of environments and are difficult to quantify. Among just the objects in this survey, we have noted an SGRB apparently originating from the outer halo of a bright elliptical (050509B), an SGRB from the outskirts of a small, star-forming galaxy (050709), an SGRB at a large offset from a bright post-starburst galaxy (060502B), an SGRB from the intracluster medium (081211B), SGRBs from faint star-forming galaxies at $z \sim 1$ (070429B, 070714B), and an SGRB from the halo of a luminous infrared galaxy (100206A); earlier in this thesis (Chapter 2) we also presented a probable

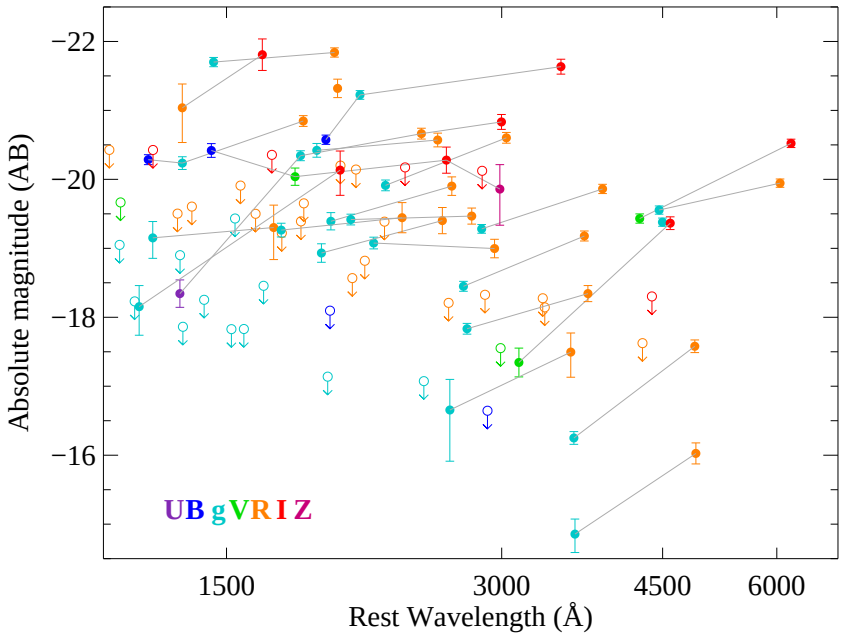

Figure 7.6 Host-frame SEDs of all LGRBs with known redshift observed in the program. Color indicates the observed filter, as shown in the legend.

SGRB in intergalactic space. This diversity of origins may point to a complex history, or even multiple classes of progenitor.

XRFs tend to show very similar host galaxies as LGRBs, at least in the cases where their host can be determined unambiguously: these galaxies are generally blue and show bright emission lines. Only the case of XRF 060428B, localized within the outer regions of a red elliptical galaxy, would seem to contest this paradigm, and this event is just as easily associated with the faint, blue probable background galaxy. Interestingly, our detection rate for XRF hosts is quite high: 10 out of 11 objects show a source in or very near the optical locations.

Dark burst hosts, based solely on the data here, look generally quite similar to the hosts of GRBs generally in most cases: with occasional exeptions, they are optically faint, blue galaxies usually unresolved in our ground-based imaging and detected at similar rates as GRBs generally. While comparing detection statistics precisely is difficult without a more detailed study (since in most cases only an XRT position is available), in a large number of cases—including some of the most notable dark events such as 061222A—a host galaxy is identified. This strongly suggests that most of these events cannot be at high redshift. Seen in optical colors alone, the hosts often look unremarkable: like other GRB hosts, they are consistent with blue, star-forming galaxies. The subject of the dark bursts, and their connection to the overall GRB redshift distribution, will be the subject of the final chapter of this thesis.

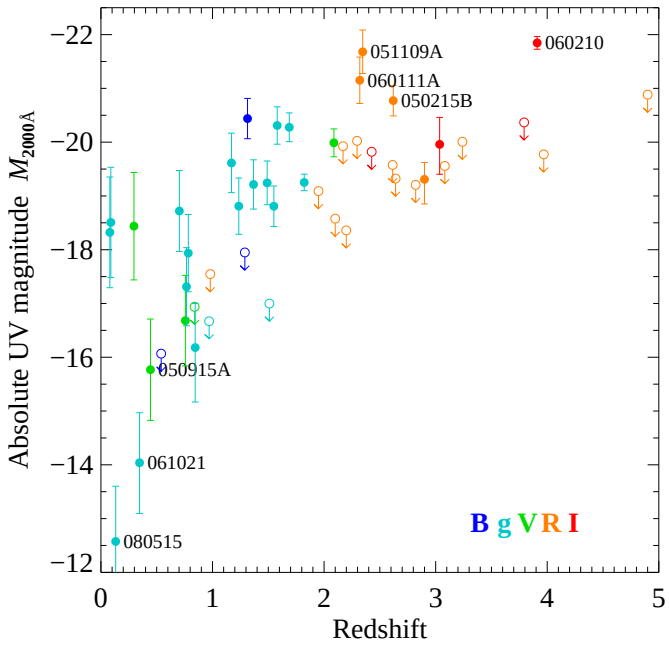

Figure 7.7 Absolute ultraviolet (2000 Å) magnitudes of observed GRB host galaxies as a function of redshift. To calculate the absolute magnitude, we identify the observed filter nearest to 2000 Å in the GRB rest frame and scale from its central wavelength to 2000 Å using a k-correction assuming a host spectrum with $\beta_\lambda \sim -1$, a typical color for the galaxies in our program (see Figure 7.5). GRB host galaxies span an impressive range of luminosities, from extremely underluminous galaxies barely detectable to Keck despite their relative proximity (at $z < 0.5$), up to super-L_* galaxies. The characteristic UV magnitude M_* varies from about -18 in the nearby universe (Budavári et al. 2005) to a peak of -21 at $z \sim 2-3$ (Reddy et al. 2008) before probably declining again at even higher redshifts (Bouwens et al. 2006).

7.7 Conclusions

With almost 150 objects included, the work presented here represents the largest sample of GRB host galaxies published to date by more than a factor of three. We hope that its completion will provide a launching point for a variety of further investigations in the subject—both of specific individual objects of interest as well as of the broader population of GRBs generally. Although we have not attempted to address any of the science of the survey in detail in this chapter, further work enabled by this sample (beginning with the next Chapter) will fully exploit the potential for these observations to address the motivating science goals in detail. Especially when merged with other large efforts (parallel optical surveys at Gemini, the VLT, and elsewhere, as well as programs at different wavelengths such as recent observations at IR wavelengths), we expect that these results will help bring an answer to open questions in the field about the range of galaxies in which GRBs inhabit, the types of stars which produce them, and their cosmic utility for understanding the evolution of star formation and the chemical enrichment of the universe. Of course, in addition to the general conclusions about larger classes of objects provided by a sample of this size, a major goal of this survey has been to identiful rare, possibly unique examples of GRBs that may point to new phenomena or other novel science—as illustrated by the cases of GRBs 051109B, 060428B, and 100206A.

Whether these ideals are fully realized depends, in part, on the accessibility of the observations to the general scientific community. To this end, we intend to make all observations publicly available in the near future, enabling users to perform their own detailed studies of individual object (e.g., using customized aperture sizes and field calibrations other than those chosen by our automated software) or to perform spectroscopy of hosts of interest using our imaging as a finding chart.

7.8 GRB Host Mosaic Images

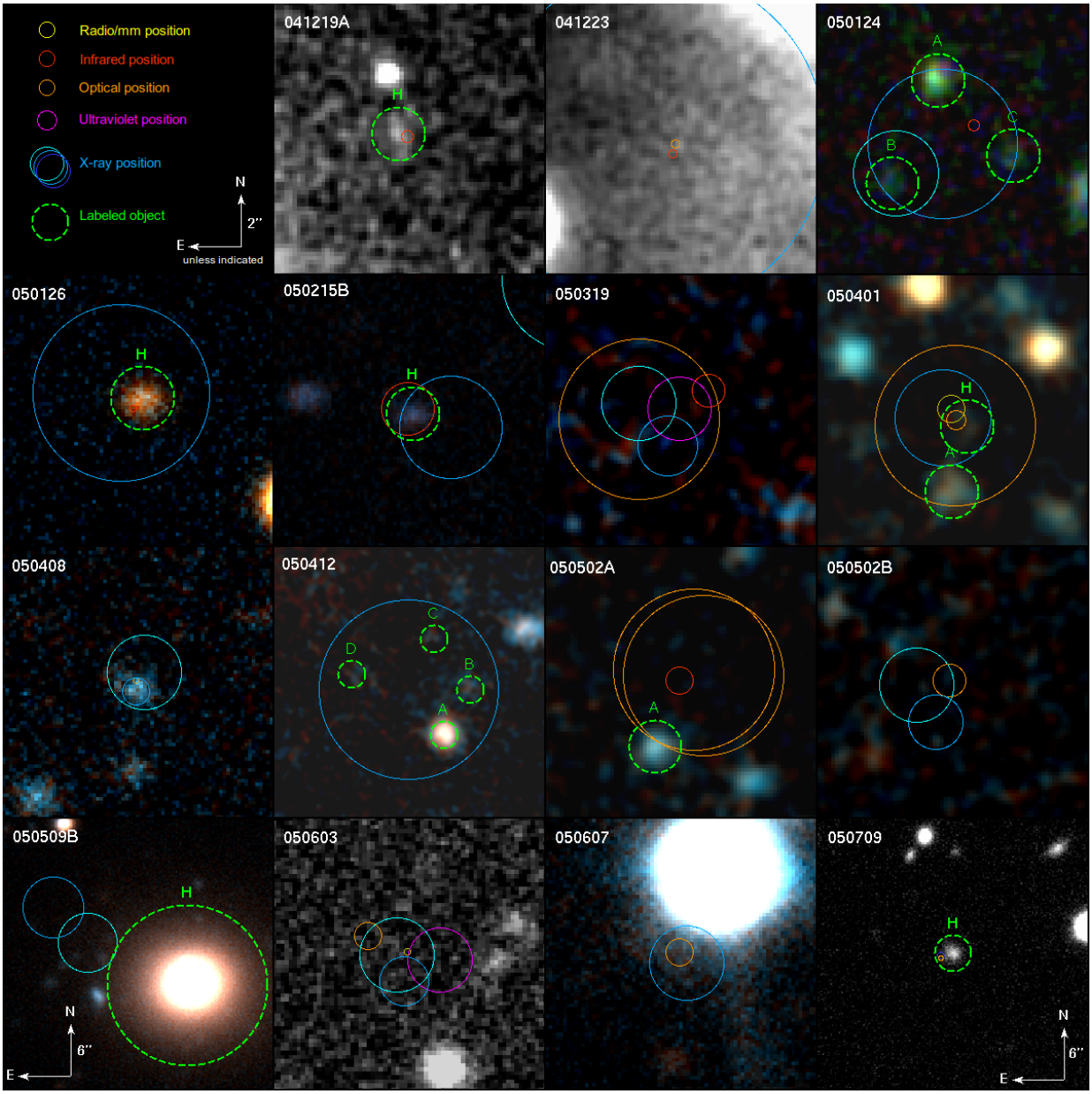

Figure 7.8 Mosaic #1 of GRB imaging from the survey. Thin, solid circles represent afterglow positions; thick dashed circles represent objects of interest. More information about the images and overlaid captions are given in §7.5.2

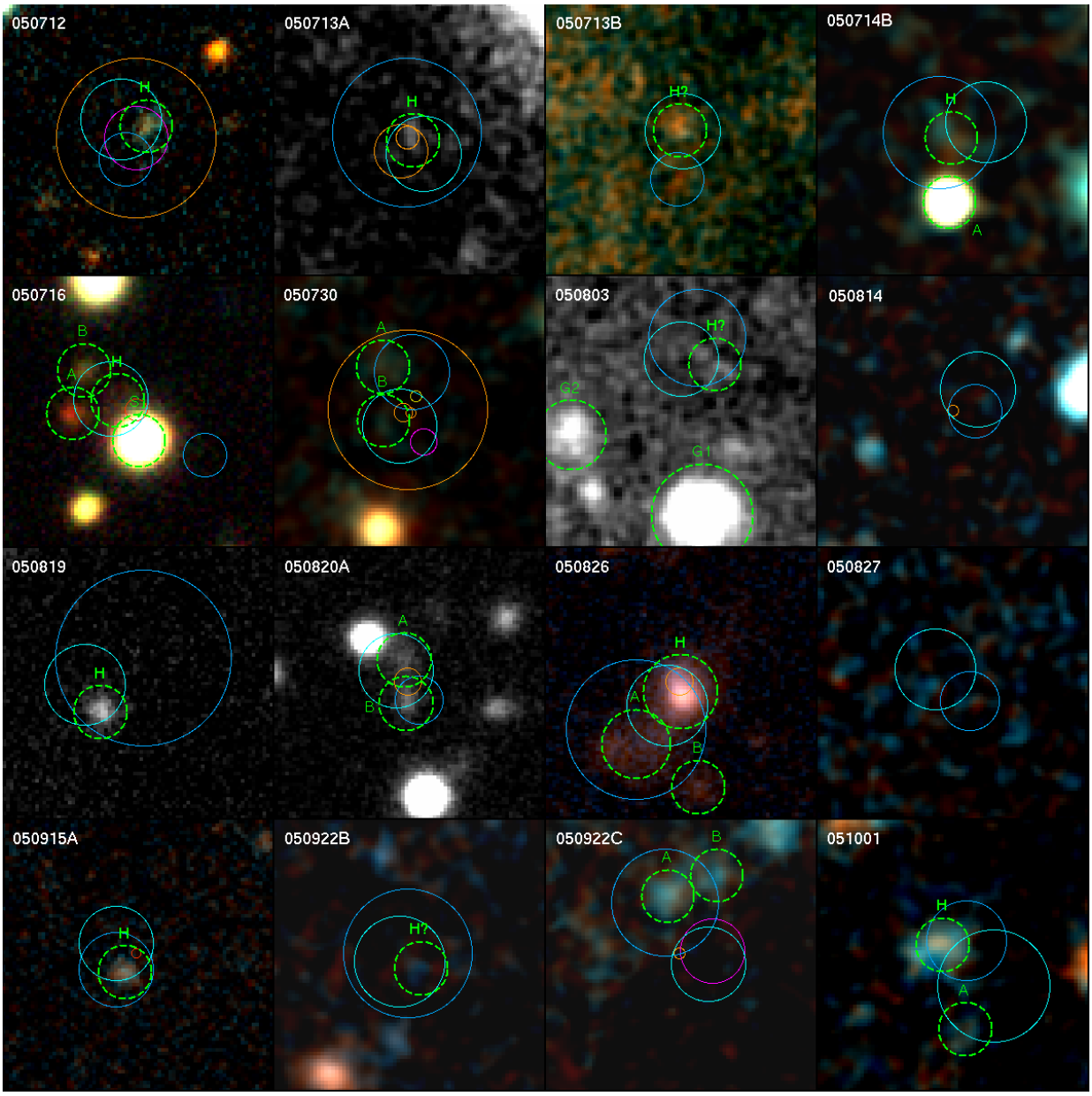

Figure 7.9 Mosaic #2 of GRB imaging from the survey.

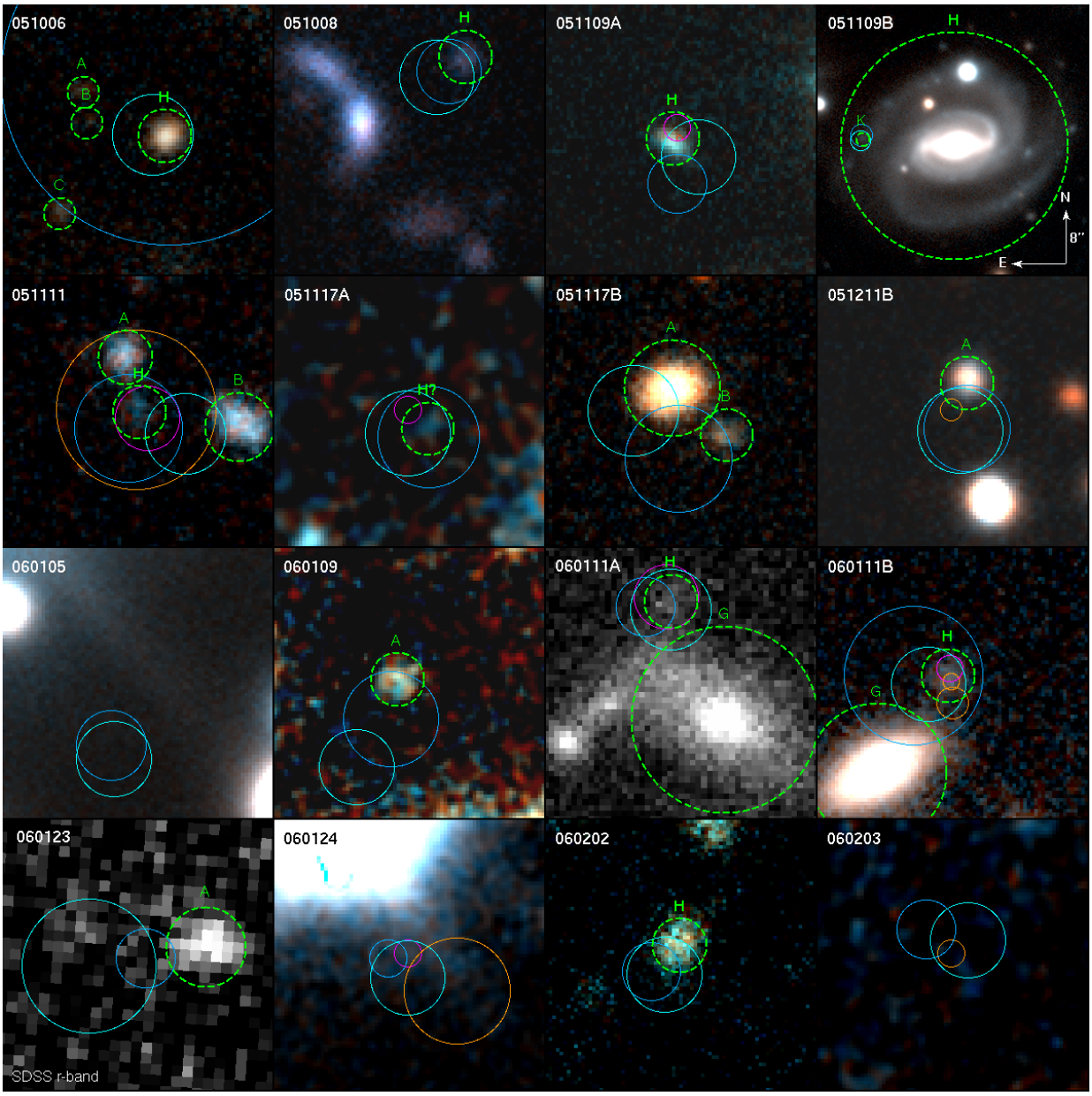

Figure 7.10 Mosaic #3 of GRB imaging from the survey.

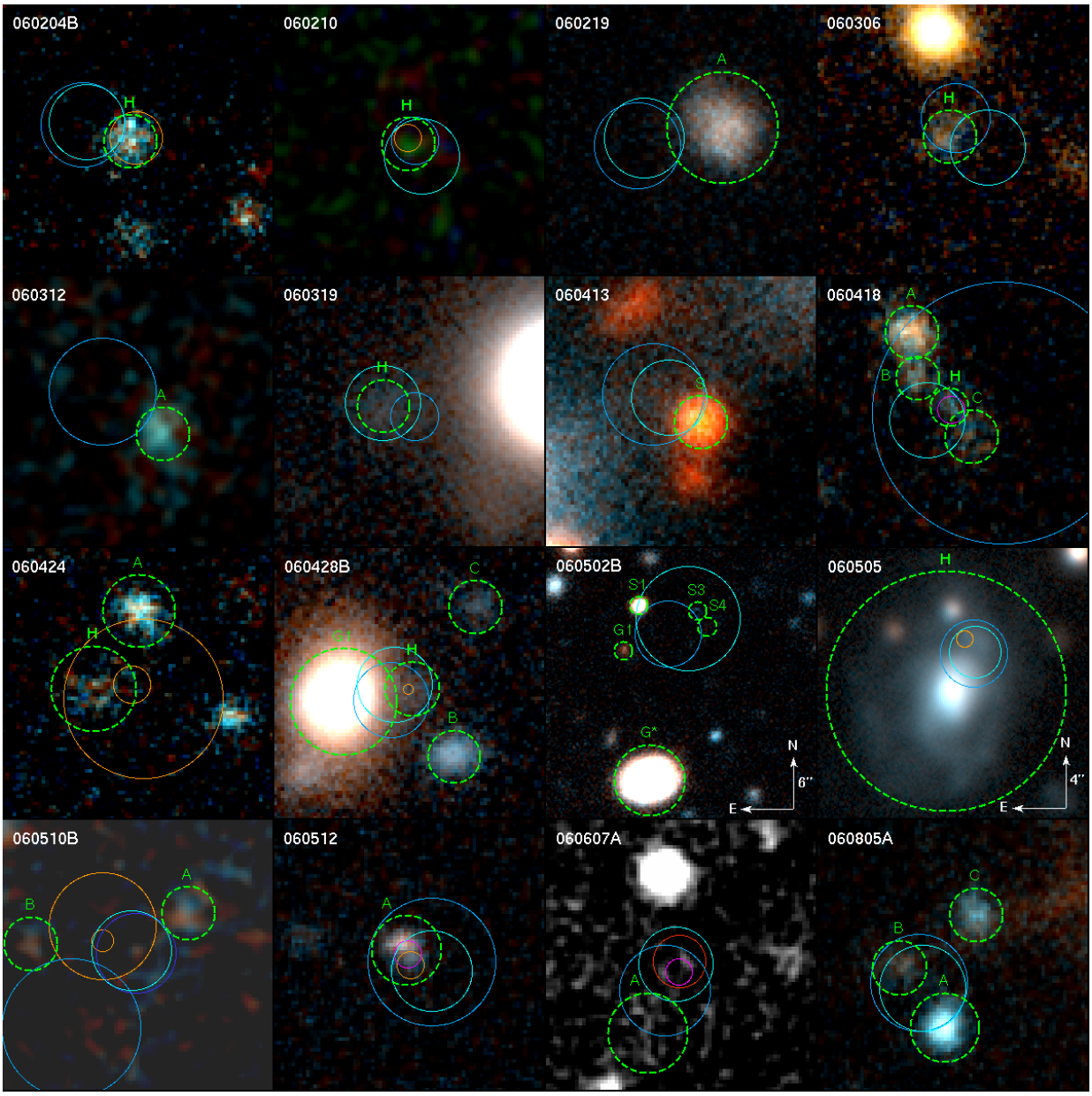

Figure 7.11 Mosaic #4 of GRB imaging from the survey.

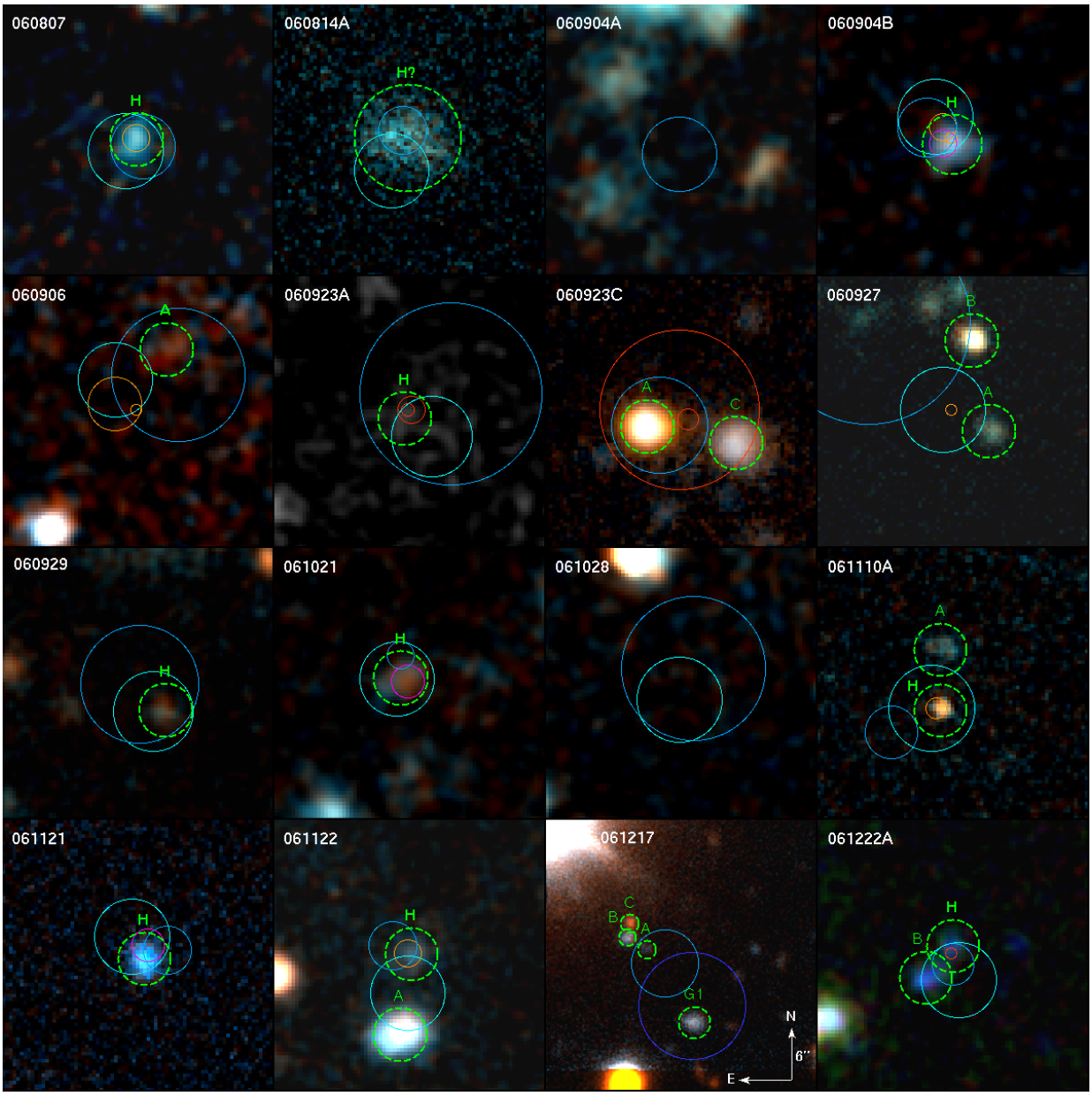

Figure 7.12 Mosaic #5 of GRB imaging from the survey.

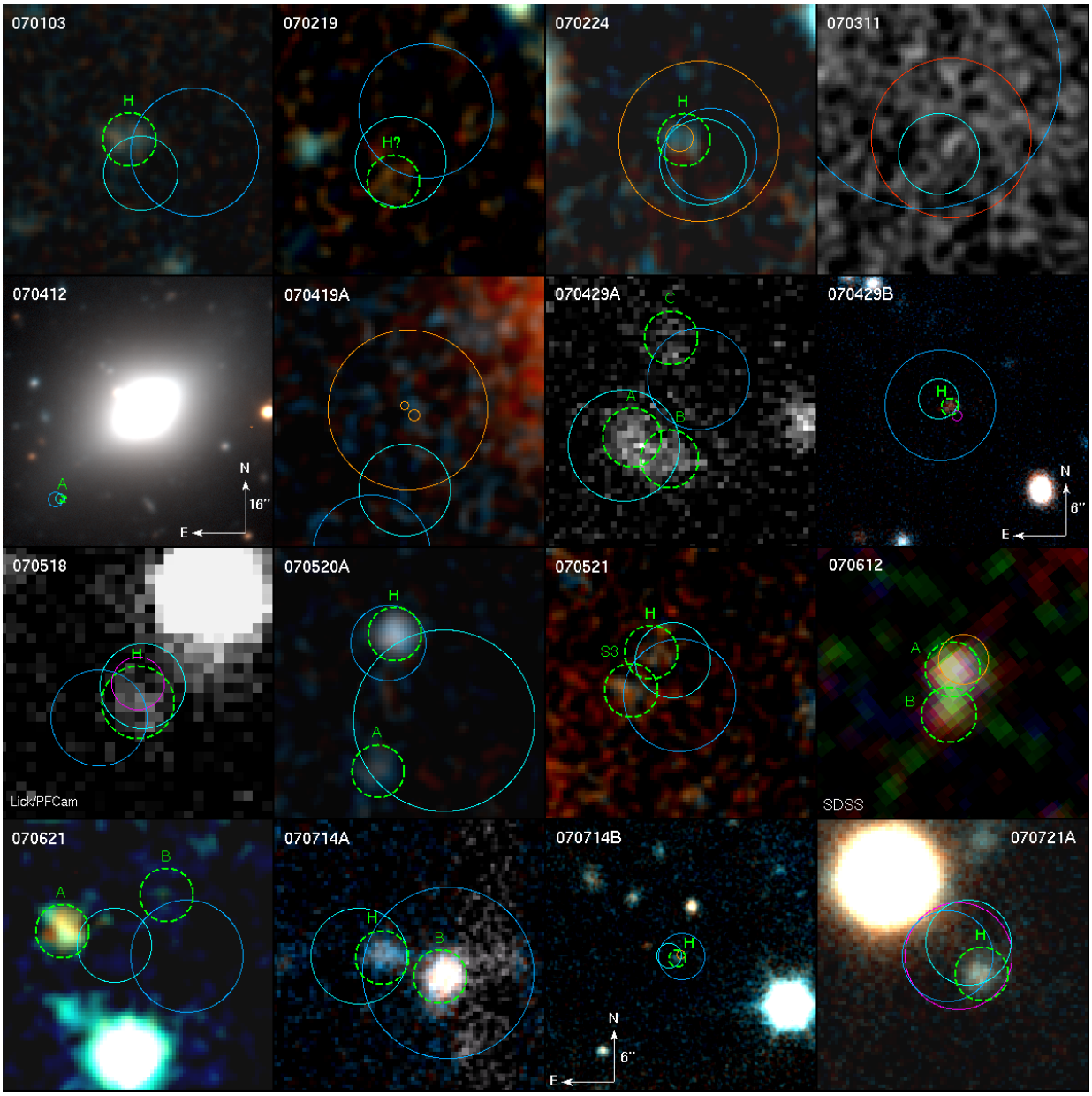

Figure 7.13 Mosaic #6 of GRB imaging from the survey.

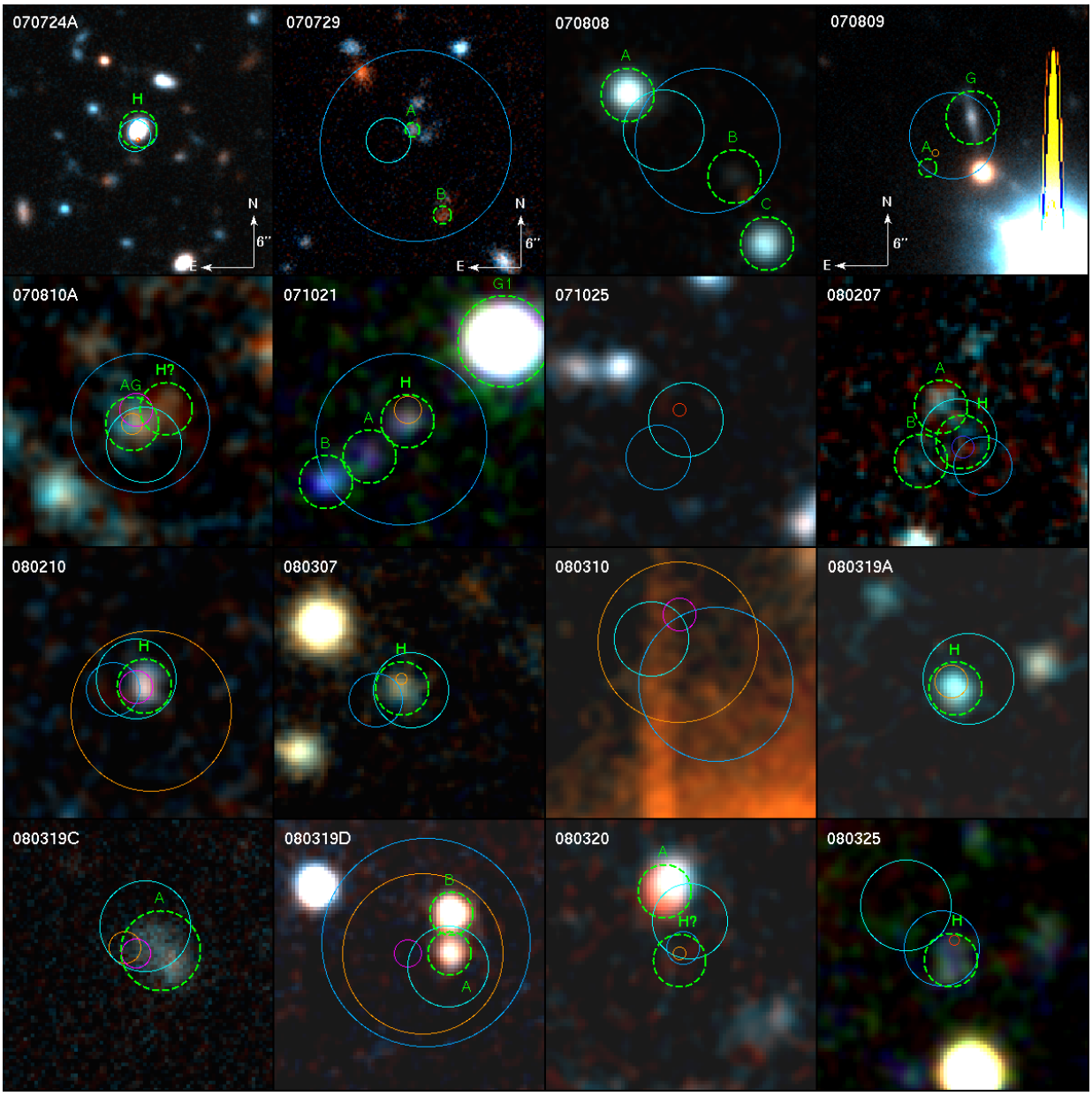

Figure 7.14 Mosaic #7 of GRB imaging from the survey.

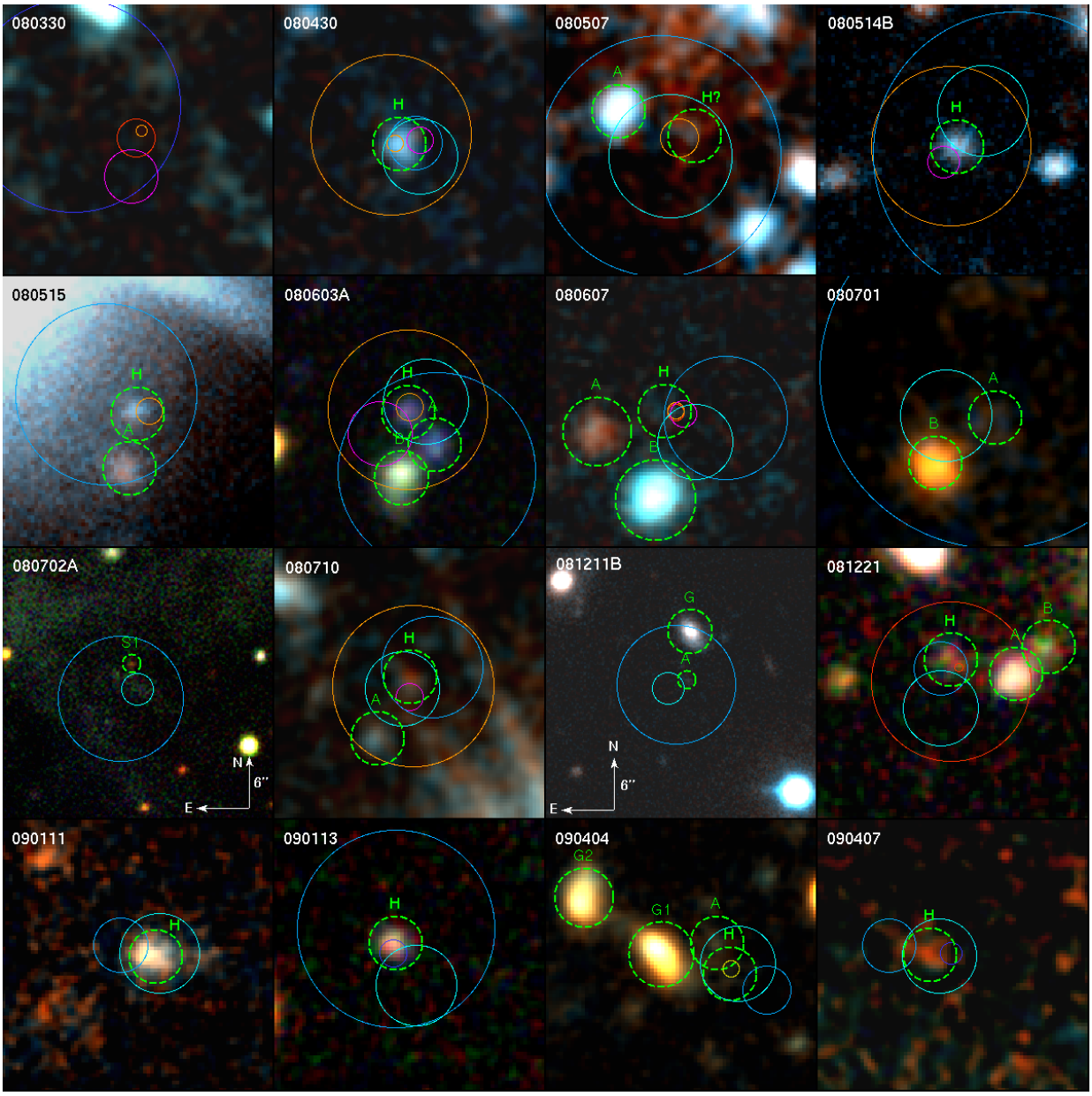

Figure 7.15 Mosaic #8 of GRB imaging from the survey.

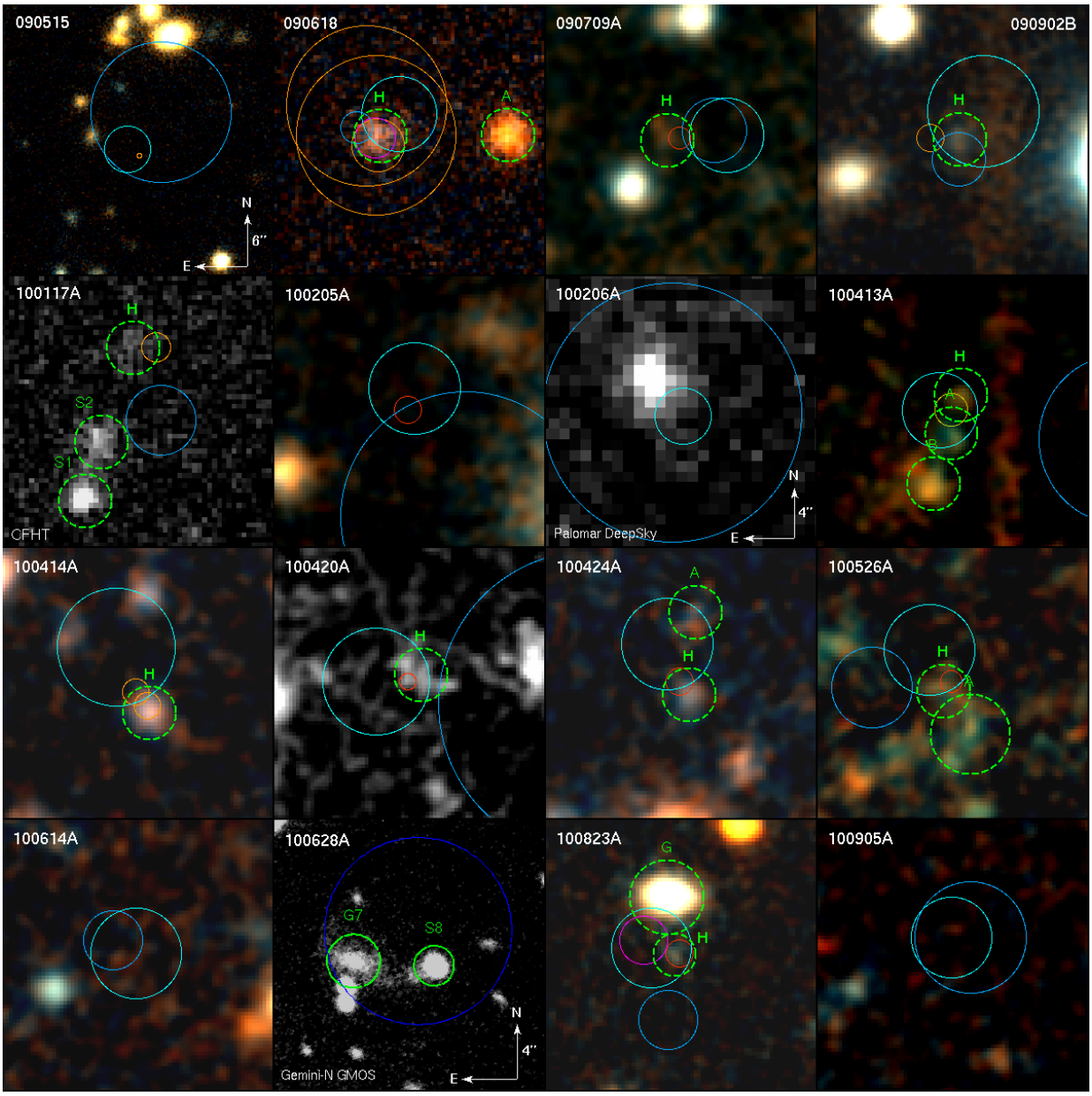

Figure 7.16 Mosaic #9 of GRB imaging from the survey.

Chapter 8

The Host Galaxies of Dark Gamma-Ray Bursts: Observational Constraints on Highly Obscured and Very High-Redshift GRBs

An earlier version of this chapter was previously published as AJ 138:1690–1708[1].

Abstract

In this Chapter we present the first results of our imaging campaign at Keck Observatory to identify the host galaxies of "dark" gamma-ray bursts (GRBs), events with no detected optical afterglow or with detected optical flux significantly fainter than expected from the observed X-ray afterglow. We find that out of a uniform sample of 29 *Swift* bursts rapidly observed by the Palomar 60-inch telescope through March 2008 (14 of which we classify as dark), all events have either a detected optical afterglow, a probable optical host-galaxy detection, or both. Our results constrain the fraction of *Swift* GRBs coming from very high redshift ($z > 7$), such as the recent GRB 090423, to between 0.2–7 percent at 80% confidence. In contrast, a significant fraction of the sample requires large extinction columns (host-frame $A_V \gtrsim 1$ mag, with several events showing $A_V > 2 - 6$ mag), identifying dust extinction as the dominant cause of the dark GRB phenomenon. We infer that a significant fraction of GRBs (and, by association, of high-mass star formation) occurs in highly obscured regions. However, the host galaxies of dark GRBs seem to have normal optical colors, suggesting that the source of obscuring dust is local to the vicinity of the GRB progenitor or highly unevenly distributed within the host galaxy.

8.1 Introduction

The prevalence of "dark" gamma-ray bursts (GRBs) remains one of the most persistent mysteries of the field, twelve years after the discovery of GRB afterglows (van Paradijs et al. 1997; Costa et al. 1997). While we now know that GRBs are frequently accompanied by extremely luminous afterglows (sometimes spectacularly so: e.g., Akerlof et al. 1999; Bloom et al. 2009; Racusin et al. 2008) an optical detection is reported in only about half of cases since the launch of *Swift* [2].

In contrast, an X-ray detection is nearly always reported for *Swift* bursts (Gehrels 2008). Partly this is due to observational constraints: the limitations of ground-based observing prevent a significant fraction of GRBs from being observed with terrestrial optical telescopes at all. Furthermore, the Ultra-Violet/Optical Telescope (UVOT; Roming et al. 2005) on-board *Swift* has a typical limiting magnitude that is shallower than the equivalent X-Ray Telescope (XRT; Burrows et al. 2005c) X-ray flux limit for a typical broadband afterglow spectrum, in particular when filters are applied. Galactic extinction, stellar crowding, and proximity to the Sun or Moon, which do not significantly affect the X-ray band, also often complicate optical follow-up. Estimates for the intrinsic frequency of optically dim GRBs vary and likely depend on the sensitivity of the detecting satellite, but for *Swift* events Akerlof & Swan (2007) have estimated that approximately 30% of GRBs have an optical magnitude > 22 at only 1000 s after the trigger, and 15–20% have an optical magnitude > 24 at this time. Detecting an optical afterglow from such an event requires a rapid response by a large-aperture telescope and is rare.

It is noteworthy that most of the conclusions about GRBs to date are based on a limited subsample of well-studied events that tends to exclude this large population of faint afterglows. For example, evidence of a GRB-SN connection can only be established for known low-redshift events targeted for intensive photometric and spectroscopic follow-up (but c.f. Levan et al. 2005). Likewise, conclusions based on the nature of GRB host galaxies (Bloom et al. 2002; Fruchter et al. 2006; Wainwright et al. 2007) require accurate (generally sub-1″) positions. Only a handful of pre-*Swift* events without optical counterparts had sufficiently precise positions for later follow-up work of this nature. Therefore the specific scrutiny of optically dark events is vital to understanding the entire GRB demography.

Key in the study of dark bursts has been the progression from a wholly observational definition of darkness to the physically motivated $\beta_{\rm OX}$ criterion of Jakobsson et al. (2004a), who define a dark burst on the basis of the flux ratio between X-ray and optical bandpasses in the afterglow at 11 hr after the burst. Here the parameter $\beta_{\rm OX}$ is the observed spectral index (defined using the convention $F_\nu \propto \nu^{-\beta}$) between the X-ray and optical bands, after correcting for Galactic extinction: $\beta_{\rm OX} = \log(F_{\rm X}/F_{\rm opt})/\log(\lambda_{\rm X}/\lambda_{\rm opt})$. Jakobsson defines a dark burst as one with $\beta_{\rm OX} < 0.5$, motivated by the prediction from the synchrotron model in which, once the afterglow begins to fade, the intrinsic spectrum is given by $F \propto \nu^{-(p-1)/2}$ (for $\nu < \nu_c$) or $F \propto \nu^{-p/2}$ (for $\nu > \nu_c$), implying $\beta_{\rm OX} \geq 0.5$ if $p > 2$. [3]

[2] See, for example, `http://www.mpe.mpg.de/~jcg/grbgen.html` and `http://grbox.net`.

[3] In addition to assuming $p > 2$, this definition is meaningful only if the synchrotron model is assumed

The availability and uniformity of X-ray follow-up in the *Swift* era makes this definition of darkness particularly appropriate for a survey of *Swift* bursts. Even so, a purely optically defined criterion is still relevant: optical detection versus non-detection (rather than the flux ratio) is an essential factor determining the nature of further follow-up of the event: sensitive searches for host-galaxy dust, spectroscopic redshifts and measurements of the host ISM properties, and (to a lesser extent) accurate host identification require bright optical afterglows, making this likely the dominant selection bias affecting our current understanding of GRB afterglows and their origins.

The implications of dark bursts are potentially far-reaching, and the importance of folding them into our understanding of the GRB population as a whole is great, as—depending on the cause(s) of their optical faintness—there are reasons to suspect that their nature or environments may differ from those of the optically brighter GRBs which underpin our understanding of the field. Some of the possibilities include (e.g., Fynbo et al. 2001):

1. **Extinction.** Dust in the GRB host galaxy (or elsewhere along the line of sight) can strongly obscure the rest-frame optical and ultraviolet light, dimming and reddening the afterglow (e.g., Djorgovski et al. 2001; Lazzati et al. 2002a; Reichart & Price 2002). While previous (largely optically selected) samples have shown little evidence for widespread dust along GRB sightlines (e.g., Kann et al. 2006a, 2010; Schady et al. 2007), recent cases such as GRB 080607 ($A_V = 3.2$ mag[4], Chapter 6) have demonstrated that very large dust columns can and do occur. A bias against dusty galaxies in the current sample could easily mislead us in conclusions about, for example, mean GRB host metallicities and luminosities (Fruchter et al. 2006; Wolf & Podsiadlowski 2007).

2. **High redshift.** GRBs have now been observed out to $z = 8.3$ (Tanvir et al. 2009; Salvaterra et al. 2009). At $z \gtrsim 6$, photons which would be redshifted into the optical bandpass are absorbed by neutral hydrogen in the host galaxy and IGM, suppressing the observed optical flux almost entirely (Gunn & Peterson 1965; Fan et al. 2006b). The redshift distribution of GRBs beyond $z \sim 6$ (and its implications on the star-formation history of the universe) cannot be observationally constrained without incorporating the dark burst population.

3. **Low luminosity.** It is well-established (e.g., Gehrels et al. 2008; Nysewander et al. 2009a) that GRB fluence and afterglow flux are positively correlated (that is, underluminous bursts tend to also have underluminous afterglows). Due to a wide distribution both in the depth of optical follow-up as well as in the gamma-ray fluence of observed GRBs, many nondetections could simply be attributed to follow-up that was not deep enough to constrain the predicted optical afterglow for a relatively faint GRB, without need to invoke absorption effects.

to be a complete description of the afterglow SED at these wavelengths. We will make these assumptions throughout the Chapter, but see Chapter 4 for a possible counterexample.

[4]Throughout this Chapter, A_V refers to extinction in the host galaxy rest-frame V-band.

4. **Low-density medium.** However, it is physically possible to have a energetic event without a luminous afterglow. The afterglow phenomenon, which is thought to originate from shocks in the surrounding medium (Paczyński & Rhoads 1993), critically depends on the presence of circumstellar gas at sufficient density to excite bright synchrotron radiation. GRBs exploding in galaxy halos or the intergalactic medium are predicted to have afterglows orders of magnitude fainter than those occurring in galactic disks (e.g., Kumar & Panaitescu 2000).

To some extent, these various possibilities can be disentangled via broadband observations of the afterglows of the events alone. For example, a low-density medium will result in a dim afterglow at all wavelengths, extinction will suppress both the optical and the near-IR flux as well as soft X-rays (to different and characteristic extents), and a high redshift will suppress only the optical flux. As a result, we will give attention in the subsequent discussion to the nature of the afterglows at all wavelengths. However, extensive broadband follow-up is not always available (and the decision to trigger multi-wavelength observations carries its own selection biases), and in some cases the two possibilities are difficult to disentangle.

The remaining degeneracies can largely be broken via deep imaging of the host galaxy of a GRB. In particular, high-redshift bursts should not have optically observable host galaxies, and the detection of a host can rule out the high-redshift hypothesis for that event. Secondarily, study of the host galaxies themselves can determine whether our existing sample of pre-*Swift* host galaxies is in fact typical, or if we are missing (for example) a large population of red, dusty ULIRGs.

8.2 The Palomar 60-inch Sample

The Palomar 60-inch telescope (P60; Cenko et al. 2006h) is a robotic facility designed for moderately fast ($t \lesssim 3$ minutes) and sustained ($R \lesssim 23$ mag) observations of GRB afterglows and other transient events. Fully operational since 2004 September, the P60 now routinely interrupts regular queue-scheduled observations in response to electronic notification of transient events. The standard P60 response to *Swift* GRB alerts results in a sequence of multi-color ($gR_{\rm C}i'z'$) observations for approximately the first hour after the trigger. Subsequent observations are then triggered manually based on the properties of the afterglow in observations to that point.

The first catalog of P60 GRB observations was presented by Cenko et al. (2009). The P60 follow-up program is fully robotic and the GRBs presented in that sample were selected entirely based on whether an event was rapidly followed-up. P60 automatically follows up all *Swift* GRB triggers that are observable, and therefore this catalog constitutes an effectively uniform sample of *Swift* events to date, and should not be affected by any afterglow-related biases. Other advantages of this population include a high afterglow detection efficiency (75%, thanks to the relatively large aperture of the telescope and red filter sequence) and a large fraction with spectroscopic redshifts (60%).

In total, the P60 sample contains 29 events (Table 8.1). Of these, 7 were undetected with the P60 (to a typical limiting magnitude of $R > 20 - 23$, depending on conditions) at 1000 seconds. No event that was undetected at 1000 s was detected at earlier times. This is approximately consistent with the results of previous studies which have attempted to correct for the shallow follow-up of most *Swift* GRBs in determining the true afterglow brightness function: in particular that of Akerlof & Swan (2007), which estimates (Figure 6 of that work) that 30% of afterglows are fainter than 22nd magnitude at 1000 s. These events are "dark" by the simple nondetection criterion, although the rapid response, large aperture, and nearly uniform depth of P60 makes a nondetection significantly more meaningful than is typical for *Swift* bursts (many of which have no optical follow-up at all, or follow-up only from the UVOT and small-aperture ground-based telescopes.) Four of the seven events have optical or infrared afterglows detected by other telescopes (typically with larger apertures and/or a redder wavelength response.)

We include a handful of additional events as "dark" via application of the $\beta_{\rm OX} < 0.5$ criterion of Jakobsson et al. (2004a), though we apply it at 1000 s instead of 11 hr, given that late-time imaging is not always available and that our non-detection cutoff is also at 1000 s. [5] There are 12 such events that satisfy this criterion: 5 of which are also P60 nondetections and 7 events which are detected by P60, but at a flux level that is less than a simple $\beta = 0.5$ extrapolation of the 2 keV X-ray flux as determined by Table 3 in Cenko et al. (2009). [6] Therefore our full "dark" sample defined by the union of both criteria consists of 14 events in all, approximately half of the P60 sample. All 14 fields were imaged to deep limits at Keck Observatory, as discussed in the next section.

[5]This involves some risks: there are occasional cases in which X-ray rebrightenings or strong spectral evolution is observed after 1000 s, indicating the contribution of additional prompt-like emission (X-ray flares) which have much harder spectra than a typical afterglow (Butler & Kocevski 2007a) and could generate "pseudo-dark" events at early times which would look normal in later observations. We will discuss the possibility of this contribution in the next section in the few cases where there appears to be evidence of extended activity at this time, but conclude that it is not a significant contaminant of our dark burst sample.

[6]Two events are listed with $\beta_{\rm OX} < 0.5$ at 1000s in Cenko et al. (2009) which we do not include in our sample: GRB 050820A and GRB 071003. In both cases, the *Swift* XRT was not observing the source at 1000s and the actual spectral index at that time is unknown; the estimate in Cenko et al. (2009) was based on an extrapolation from other epochs. This is difficult, since GRB 050820A shows extensive early-time X-ray flaring while GRB 071003 experiences a dramatic rebrightening at around 1 day when XRT observations begin. Late-time observations in both cases (Cenko et al. 2006g; Perley et al. 2008d) show that the spectral index is quite normal at late times, strongly indicating that neither event is a genuine dark burst by either of our criteria (these are, in fact, among the two brightest bursts of the *Swift* era.)

Table 8.1: P60 GRBs

GRB	S_γ[a] (10^{-7} erg cm^{-2})	F_X[b] (μJy)	R[c,d] (mag)	NIR[c,d,e] (mag)	β_{OX}[f]	Reason for dark classification
050412	6.18	0.27	> 21.4		< 0.49	P60 nondet.
050416A	3.67	1.95	20.31		0.35	low β_{OX}
050607	5.92	0.45	~ 22.1[i]		~ 0.33	P60 nondet.
050713A	51.1	14.51	18.45		0.31	low β_{OX}
050915A	8.5	0.72	> 20.7	$H \sim 18$	< 0.44	P60 nondet. + low β_{OX}
060210	76.6	12.23	18.2		0.37	low β_{OX}
060510B	40.7	15.09	~ 20.4[j]		0.04	low β_{OX}
060805A	0.72	0.17	> 19.9		< 0.76	P60 nondet.
060923A	8.69	0.92	> 22.0[k]	$K \sim 18$[k]	< 0.24	P60 nondet. + low β_{OX}
061222A	79.9	7.82	> 22.1	$K \sim 18$	< -0.19[m]	P60 nondet. + low β_{OX}
070521	80.1	4.40	> 22.9[l]	$K > 18.7$	< -0.10	P60 nondet. + low β_{OX}
080319A	48	1.19	20.43		0.41	low β_{OX}
080319C	36	11.68	18.32		0.36	low β_{OX}
080320	2.7	1.37	> 21.0	$z' = 20.0$	< 0.31	low β_{OX}
050820A	34.4	~ 150[g]	15.21		$\sim$0.4	(not dark)
050908	0.51	0.12	19.17		0.91	...
060110	15.7	7.42	15.46		0.80	...
060502A	23.1	1.22	19.50		0.53	...
060906	22.1	0.20	18.84		0.88	...
060908	28.0	0.92	17.59		0.82	...
070208	47.7	0.88	19.74		0.54	...
070419A	5.58	0.17	19.02		0.87	...
071003	83	_[h]	17.06		_[h]	...
071010A	2.0	2.11	16.18		0.89	...
071011	0.22	8.06	16.42		0.66	...
071020	23	6.91	17.66		0.52	...
071122	5.8	0.34	20.02		0.64	...
080310	23	2.19	16.88		0.79	...
080319B	810	265.8	13.69		0.52	...

[a] $15 - 150$ keV fluenced; taken from the BAT GRB table.

[b] Absorbed X-ray flux at 2 keV; calculated using the *Swift* XRT Repository (Evans et al. 2007).

[c] Calculated at 1000 s.

[d] Vega mag; corrected for Galactic extinction.

[e] Specified only in the case of R-band nondetections.

[f] Between R-band and 2 keV. From Cenko et al. (2009), modified include deeper non-P60 upper limits (where available) and revised XRT light curves.

[g] The XRT was not observing this burst at 1000 s, and earlier observations were dominated by rapid flaring (see footnote in text).

[h] The XRT did not slew to this burst until 22000 sec after the BAT trigger (see footnote in text).

[i] Rhoads (2005a)

[j] Based on extrapolation from later times: the burst was not detected in R-band at 1000s.

[k] Tanvir et al. (2008c)

[l] Interpolated between P60 measurements and Rau et al. (2007).

[m] Cenko & Fox (2006a)

8.3 Observations

8.3.1 The Keck Imaging Campaign

Observations of the P60 GRB host galaxies were conducted as part of the Berkeley Keck GRB Host Project, as described in Chapter 7. As this study was initially published prior to the completion of that survey, however, some of the details differ. In particular, we used a different imaging reduction pipeline (using Python and IRAF instead of IDL) and a different set of field calibrations (the Nickel calibration was not yet available, but as all fields were observed with the P60, often photometric calibrations from P60 were available for fields lacking SDSS imaging (an exception is the field of GRB 060210, which was was calibrated to USNO directly.) Photometry was performed using the `phot` task in IRAF and nearly exclusively using a 1″radius regardless of seeing. Finally, because all bursts in this section were observed by P60, our own optical position was always available, allowing direct registration and alignment with the Keck data to determine the position accurately. Of course, for bursts with no optical afterglow, we again relied on external positions; although in the case of GRB 050915A we were able to align our PAIRITEL discovery image with the Keck image. A list of all observations and exposure times is presented in Table 8.2.

Table 8.2: Keck Imaging Observations of P60 Dark Bursts

GRB Field	Obs. Date (UT)	Filter	Int.[a] (s)	Seeing (″)	Cal. Sys.	Cal. Unc. (mag)	5σ Limit[b] (mag)	E_{B-V} (mag)
050412	2007-12-13	g	690	1.4	SDSS[c]	0.03	25.8	0.02
		R	600	1.2		0.17	24.5	
050416A	2005-06-05	g	960	0.9	SDSS	0.03	26.2	0.03
		R	960	0.9		0.02	25.4	
050607	2007-10-09	g	960	1.0	Landolt[d]	0.3[g]	24.4	0.156
		R	870	1.0		0.3	23.7	
050713A	2008-08-02	g	990	0.8	P60/USNO[e]	0.25	25.7	0.414
		R	870	0.7		0.27	24.7	
050915A	2005-12-04	V	2280	0.7	Landolt	0.05	25.8	0.026
		I	1539	0.8		0.02	24.9	
	2005-10-31	g	1680	1.0	P60/USNO	0.25	25.5	
		R	1500	1.0		0.35	24.5	
060210	2007-08-13	R	540	0.7	USNO[f]	0.35	23.6	0.093
	2009-02-19	g	1680	0.8		0.35	24.4	
		I	1530	1.0		0.14	23.5	
060510B	2006-05-31	g	3840	1.4	Landolt	0.02	25.8	0.039
		R	3660	1.4		0.02	25.5	
060805A	2008-02-12	g	1080	1.0	SDSS	0.04	26.3	0.024
		R	1260	1.0		0.10	24.8	
060923A	2007-04-16	V	1560	1.4	SDSS	0.04	25.2	0.060
		I	1590	1.2		0.06	23.8	
	2007-08-12	B	1500	0.8		0.07	26.4	
		$RG850$	1500	0.6		0.09	23.6	
061222A	2007-07-18	V	710	0.8	Landolt	0.05	24.7	0.099

Continued on Next Page...

GRB Field	Obs. Date (UT)	Filter	Int.[a] (s)	Seeing (″)	Cal. Sys.	Cal. Unc. (mag)	5σ Limit[b] (mag)	E_{B-V} (mag)
		I	600	0.7		0.05	23.7	
	2007-08-12	B	1500	0.7	P60/USNO	0.12	25.9	
		$RG850$	1500	0.6		0.27	23.6	
	2009-05-31	H	900	0.5	2MASS	0.06	21.6	
		K	1800	0.5		0.09	21.7	
070521	2007-05-21	V	1500	0.7	SDSS	0.05	24.8	0.027
		I	1500	0.8		0.03	24.3	
	2009-06-25	V	1440	0.7	SDSS	0.05	26.2	
		$RG850$	1260	0.8		0.15	24.6	
080319A	2009-02-19	g	1070	0.6	SDSS	0.07	26.4	0.015
		R	960	0.7		0.04	25.0	
080319C	2009-02-19	g	1530	0.9	SDSS	0.05	25.6	0.026
		R	1380	0.7		0.13	24.5	
080320	2009-02-19	g	990	1.0	SDSS	0.18	25.8	0.014
		I	810	1.3		0.09	24.1	

8.3.2 Host Identification

Until recently, the same biases that made pre-*Swift* host searches difficult without optical positions have applied to *Swift* as well: early XRT positions were accurate to only 4–6″, an error region sufficiently large as to normally contain numerous faint galaxies. However, by using optical sources to register the field (Butler 2007; Goad et al. 2007; Evans et al. 2009), the *Swift* XRT now routinely produces afterglow positions to better than 2″ (90% confidence). Furthermore, thanks to the proliferation of small- to medium-sized telescopes and the improving ability of larger apertures to respond relatively quickly, all but three of the *P*60-followed bursts in our sample are detected in the optical or IR. In all cases where a host candidate is identified in or near the error circle, we follow the prescription in Bloom et al. (2002) to estimate $P_{\rm chance}$. Formally, this parameter is an estimate of the probability that one or more galaxies with an observed magnitude brighter than m will be centered within a randomly chosen region on the sky with solid angle $\pi\theta^2$. This probability is given by:

[a] Total integration time. For this work, the short (30-60s) exposures were included in the final stacks, which they were not in the reductions described in Chapter 7, resulting in a small difference in exposure times.

[b] As measured over a 1″ aperture and averaged over the field; not corrected for extinction. $BVRI$ magnitudes are in the Vega system. The $RG850$ filter is calibrated to the SDSS z-band.

[c] Sloan Digital Sky Survey: Adelman-McCarthy et al. (2008)

[d] Landolt (1992)

[e] P60 calibration, based on USNO B1.0 catalog (Monet et al. 2003)

[f] Direct calibration to USNO B1.0 catalog.

[g] The two standard star observations during the 2007-10-09 run are not consistent with each other, indicating that this night may not have been photometric.

$$P_{\rm ch} = 1 - \exp(\pi\theta^2\sigma_{\leq m})$$

Where $\sigma_{\leq m}$ is the average sky surface density of galaxies with apparent magnitude brighter than m, taken in this case from Hogg et al. (1997). The values for m and θ for each burst-host association are chosen as in Bloom et al. (2002), with two exceptions. Because we do not have access to space-based imaging and the size of a typical host galaxy is significantly smaller than the seeing disk, we conservatively use the visible extent of the optical disk in the ground-based imaging rather than the half-light radius. We also use the 90% confidence radius, rather than 3σ, which is slightly less conservative. We treat this value as an estimate of the probability that, for a given burst, the association with the nearest host galaxy is incorrect.

Some additional caution is warranted before interpreting $P_{\rm chance}$ this way. In particular, this probability applies to a single event treated in isolation only: it is not necessarily appropriate for events chosen from a larger sample which includes both detections and non-detections (a shallow survey of a very large number of well-localized objects would find many individual low-$P_{\rm chance}$ galaxies even if the positions were chosen completely randomly). Fortunately, in our case we identify good host galaxy candidates for most of our objects: 11 out of 14 fields contain at least one object with $P_{\rm chance} \leq 0.1$ consistent with the error circle. Nevertheless, given the number of fields observed, we must recognize that the chance of a misidentification being present somewhere in the full sample is not insignificant. A basic Monte Carlo analysis (including the nondetections) suggests that the probability of at least one chance coincidence being present in our host sample is an appreciable 48%, and the probability of two or more is about 15%.

The $P_{\rm chance}$ calculation also assumes that lines of sight toward GRBs, and in particular toward dark GRBs, are randomly sampled among all sightlines in the universe. One possible interpretation of the overabundance of Mg II absorbers in GRB spectra relative to QSOs (Prochter et al. 2006b) is that this assumption is incorrect and observed GRBs preferentially cluster along lines of sight near low-z galaxies, perhaps due to gravitational lensing. This interpretation is generally disfavored (Prochter et al. 2006b), and for the few cases of galaxy-associated Mg II systems in GRB spectra to date (Masetti et al. 2003; Jakobsson et al. 2004b; Pollack et al. 2009) there has been no clear demonstration that the number and offset distribution of these galaxies implies a significant excess of what is expected from chance. Another possibility which could affect our results is if dark GRBs are due to extinction in unrelated field galaxies along the light of sight (rather than in the host galaxy) and therefore more likely to fall close to a line-of-sight galaxy: such an effect was studied as a possible interpretation of the GRB-QSO discrepancy in terms of a selection bias (Sudilovsky et al. 2007). Were this the case, dark GRB sight lines would be biased towards dusty foreground sources, and $P_{\rm chance}$ would be quite inappropriate for this sample. However, given the highly confined distribution of dust in local galaxies and the observed density of galaxies on the sky, it would be surprising if a large fraction of GRB sightlines turned out to be attenuated; indeed, more detailed analysis by Sudilovsky et al. (2009) has also recently shown that it

cannot explain the GRB/QSO discrepancy either.

For the purposes of this work, we will assume no particular bias in GRB or dark GRB sightlines. We shall return to this issue when discussing the implications of our large putative detection fraction in §8.6.

8.3.3 Host Photometry

We used aperture photometry within IRAF to measure the flux of all candidate host galaxies, using a 1.0″ aperture in all cases except for GRB 080319C, whose candidate host is highly extended and a 2.0″ aperture was used. In a few cases, the afterglow position was within the outer point-spread function (PSF) of a bright star, which was subtracted prior to photometry using various techniques (depending on proximity and brightness, discussed below) to avoid the complication of a variable sky background as discussed in the relevant sections below. The resulting aperture magnitudes are presented in Table 8.3. A false-color mosaic of all imaging observations is presented in Figure 8.1.

8.3.4 Infrared Observations

Two events in the sample, GRBs 061222 and 070521A, are of particular interest. Both events were extremely X-ray bright, were not detected optically, and were observed at infrared wavelengths with large telescopes within a few hours after the burst.

GRB 061222A was observed (Cenko & Fox 2006a) to have a faint, fading IR afterglow. We returned to this field on 2009-05-31 with NIRC on Keck I and integrated for 10 exposures of 100s each in H- and K-bands. (5 sec $\times$ 20 coadds). Images were processed and stacked using a modified Python/pyraf script originally written by D. Kaplan and aligned to our LRIS imaging. The field was calibrated using a single Two-Micron All Sky Survey (2MASS) star within the NIRC field of view (2MASS J23530271+4632187). We detect a faint source near the detection limit close to but not coincident with the infrared afterglow (likely a foreground galaxy very near the line of sight: see 8.4.10). No source coincident with the IR transient is detected. Measurements and limits are reported in Table 8.3.

GRB 070521 was observed less than two hours after the burst by NIRI on Gemini-North (Cenko et al. 2007d) and the lack of an IR detection imposes the deepest limit on a counterpart of any event in our sample. The final UVOT-calibrated XRT position contains a red source (well-detected in K and H, weakly detected in $RG850$, I and V) near the eastern edge. To rule out variability of this source, we acquired 24 $\times$ 60 s exposures in K-band and 18 $\times$ 60 s exposures in H-band on Gemini-North on 2009-02-01 (UT), 2.5 years after the burst. The object is still detected in this imaging with no evidence for fading photometrically or in image subtraction of the frames. The final IR photometry is presented alongside the optical photometry in Table 8.3.

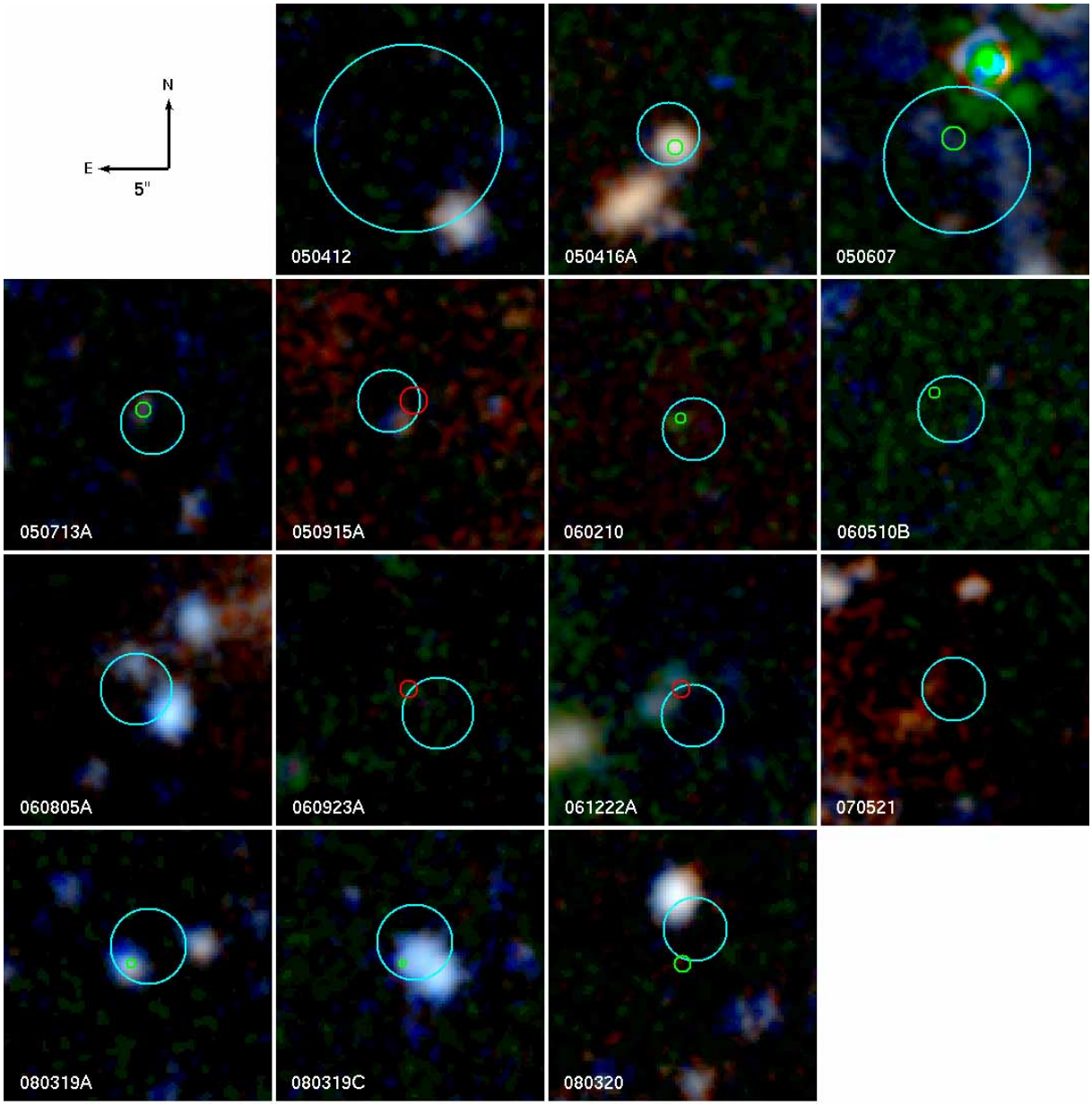

Figure 8.1 False-color mosaic of all 14 dark GRB host fields using our Keck LRIS imaging acquired between 2005 and 2009. The 90% confidence afterglow positions overplotted in each case. X-Ray (XRT) error circles are cyan-colored, optical positions are green, and infrared positions are red. All images are 11.8″ on each side with north towards the top and east to the left. See Table 8.2 for filter information. In most cases images are constructed using two filters, with the green channel interpolated using a geometric mean.

Table 8.3: Photometry of P60 Host Candidates

GRB field	Source	$P_{\rm chance}$	Magnitude [a]	AB Magnitude [b]	
050412	A	0.06	g	24.11 ± 0.04	24.04 ± 0.04
			R	22.14 ± 0.02	22.26 ± 0.02
	B	0.45	g	25.82 ± 0.18	25.75 ± 0.18
			R	25.08 ± 0.33	25.20 ± 0.33
	C	0.52	g	25.91 ± 0.18	25.84 ± 0.18
			R	25.34 ± 0.39	25.46 ± 0.39
	D	0.40	g	> 27.05	> 26.98
			R	24.85 ± 0.24	24.97 ± 0.24
050416A		0.005	g	24.11 ± 0.03	24.00 ± 0.03
			R	23.10 ± 0.02	23.19 ± 0.02
050607			g	> 25.0	> 24.44
			R	> 24.8	> 24.58
050713A		0.006	g	25.73 ± 0.22	24.24 ± 0.22
			R	24.68 ± 0.16	23.81 ± 0.16
050915A		0.03	g	25.56 ± 0.18	25.47 ± 0.18
			V	25.07 ± 0.06	24.97 ± 0.06
			R	24.58 ± 0.42	24.68 ± 0.42
			I	24.25 ± 0.08	24.63 ± 0.08
060210		0.008	g	> 25.6	> 25.27
			R	24.33 ± 0.24	24.27 ± 0.24
			I	24.14 ± 0.20	24.40 ± 0.20
060510B			g	> 26.0	> 25.86
			R	> 26.0	> 26.07
060805A	A	0.05	g	25.46 ± 0.04	25.37 ± 0.04
			R	24.45 ± 0.07	24.56 ± 0.07
	B	0.06	g	23.63 ± 0.01	23.54 ± 0.01
			R	23.46 ± 0.04	23.57 ± 0.04
	C	0.22	g	24.63 ± 0.04	24.54 ± 0.04
			R	23.97 ± 0.05	24.08 ± 0.05
060923A		0.06	B	> 27.2	> 26.82
			V	26.19 ± 0.30	25.98 ± 0.30
			I	24.67 ± 0.24	24.99 ± 0.24
			z	> 25.23	> 25.12
061222A	A	0.03	B	24.84 ± 0.06	24.30 ± 0.06
			V	24.55 ± 0.10	24.22 ± 0.10
			I	24.71 ± 0.22	24.96 ± 0.22
			z	25.26 ± 0.35	25.10 ± 0.35
			H	> 22.16	> 23.48
			K	> 22.23	> 24.03
	B	0.02	B	24.41 ± 0.04	23.87 ± 0.04
			V	24.30 ± 0.07	23.97 ± 0.07
			I	24.21 ± 0.13	24.46 ± 0.13
			z	24.92 ± 0.26	24.76 ± 0.26
			H	21.84 ± 0.30	23.16 ± 0.30
			K	21.91 ± 0.29	23.71 ± 0.29
070521		0.10	V	26.29 ± 0.20	26.18 ± 0.20

Continued on Next Page...

GRB field	Source	$P_{\rm chance}$	Magnitude [a]	AB Magnitude [b]	
			I	25.08 ± 0.33	25.46 ± 0.33
			i	25.25 ± 0.17	25.20 ± 0.17
			z	24.10 ± 0.16	24.04 ± 0.16
			J	22.52 ± 0.20	23.40 ± 0.20
			H	21.58 ± 0.09	22.94 ± 0.09
			K	20.95 ± 0.10	22.78 ± 0.10
080319A		0.03	g	24.63 ± 0.03	24.58 ± 0.03
			R	23.85 ± 0.06	23.98 ± 0.06
080319C		0.01	g	23.08 ± 0.03	22.99 ± 0.03
			R	22.22 ± 0.03	22.32 ± 0.03
080320			g	> 27.25	> 27.20
			I	> 25.3	> 25.70

8.3.5 Spectroscopy

In several cases bright host candidates without afterglow absorption redshifts available were suitable for spectroscopic follow-up. All spectroscopic integrations were conducted with longslit spectroscopy on LRIS, using the 400/8500 grating (red side) and 600/4000 grism (blue side) with the D560 dichroic, giving continuous spectroscopic coverage from the atmospheric cutoff to 9200 Å (using the old LRIS red chip) or out to 10400Å (using the new LRIS red chip, which has greater quantum efficiency beyond 9000 Å and improved spectral range). The exposures were reduced in IRAF using standard techniques and flux-calibrated using observations of standard stars BD+262606 and BD+174708 (red side) and BD+284211 (blue side) at similar airmass. Absolute flux scales were then derived using the photometry derived from our previous imaging. A summary of these observations is presented in Table 8.4.

Table 8.4: LRIS Spectroscopy of P60 GRBs

Field	Obs. Date (UT)	Exp.	Air-mass	Slit ($''$)	PA (deg)	λ (Å)
050412	2007-12-13	2×900	1.16	1.0	142.85	3500–9150
060805A	2009-06-25	2×900	1.21	0.7	30.40	3500–10400
061222A	2007-10-09	2×1800	1.12	1.0	142.19	3500–9350
080319A	2009-06-25	2×900	1.31	0.7	105.10	3500–10400
080319C	2010-02-07	2×600	1.5	1.60	58.44	3500–10400

[a] Not corrected for Galactic extinction.
[b] Corrected for Galactic extinction.

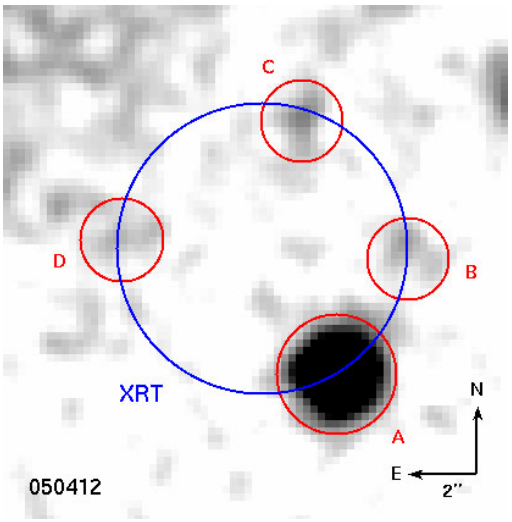

Figure 8.2 Keck/LRIS R-band image of the vicinity of GRB 050412 showing the four host galaxy candidates near the edge of the error circle. The XRT error circle is relatively large; only object A is a statistically significant association ($P_{\rm chance} < 0.1$).

8.3.6 Photometric redshift limits

Even in the absence of spectroscopy, it is possible to place limiting a redshift on host galaxy candidates using the color observed our optical imaging. Absorption of host-galaxy continuum light from hydrogen gas in the ISM at either the Lyman break (912 Å) or Lyman-α (1216 Å; Gunn & Peterson 1965) will strongly suppress the observed flux once these features enter the g-band at about $z = 3.4$ and $z = 2.3$, respectively, greatly reddening the $g - R$ color and allowing us to translate an observed color into a limiting redshift. We assume a strongly star-forming galaxy template (the Irr template from *hyperz* [Bolzonella et al. 2000], which due to its intrinsic blueness provides the most conservative choice) with no internal extinction, then apply a simple IGM attenuation correction from Madau (1995) to measure how its observed $g - R$ color evolves with redshift. At sufficiently high redshifts, the Lyman-α forest and Lyman break sufficiently redden the galaxy light enough to be inconsistent with observations, generating a simple limiting photo-z. If the redshift is known or well-constrained, a similar procedure can also be used to limit the internal extinction A_V.

8.4 Dark Bursts and Host Galaxies

8.4.1 GRB 050412

The gamma-ray light curve of GRB 050412 shows no unusual features with a single peak and a long tail, and the prompt emission fluence (15–200 keV) is 9.6×10^{-7} erg cm^{-2} (Tueller et al. 2005), near the median value for *Swift* bursts. The X-ray counterpart, however,

is highly unusual. *Swift* slewed to the position after only 99 s, and detected a fading source inside the BAT location. However, the X-ray flux (after decaying slowly in the first 100 s of the exposure) plummeted abruptly starting around 300 s, with a decay index (defined by $F \propto t^{-\alpha}$) of $\alpha \sim 3$, and was not detected after about 1200 s (Mineo et al. 2007). A Chandra X-ray Observatory Target of Opportunity observation at 5 d (Berger & Fox 2005b) failed to detect the counterpart.

This burst was relatively well-positioned for ground-based follow-up, and was tracked by several telescopes including P60, all of which failed to identify a fading counterpart. Two additional observations deserve particular note: a Subaru integration at 2.3 hr which identified no afterglow to $R > 24.9$ mag (Kosugi et al. 2005), and rapid PAIRITEL follow-up which identified no infrared afterglow in observations starting at 175 seconds after the burst trigger. Nondetections at such early times are rare among PAIRITEL-followed bursts (B. Cobb et al., in preparation).

Mineo et al. (2007) speculate that the lack of afterglow flux of GRB 050412 might be the result of an extremely low-density environment suppressing the afterglow flux: a "naked" burst. In this case, the X-ray afterglow is interpreted as being completely absent, with the sharply-decaying light curve attributed to photons from high latitude from the burst itself whose arrival at Earth is delayed by the curvature effect (Kumar & Panaitescu 2000). A handful of other similar events exist in the literature, as discussed by Vetere et al. (2008). However, such events are very rare (at most a few percent of *Swift* bursts): plotting gamma-ray fluence versus X-ray flux (Gehrels et al. 2008; Nysewander et al. 2009a; Perley et al. 2009b), 050412 is one of only a handful of outliers with extremely low X-ray to gamma-ray ratios. The optical and IR nondetections are quite consistent with this picture—indeed, in terms of $\beta_{\rm OX}$, the available constraint of $\beta \lesssim 0.5 - 1.0$ is nothing unusual. The darkness appears to be intrinsic, not due to absorption.

Presumably because of the weak and short-lived X-ray detection, the error circle of this event is large. A UVOT-corrected XRT position is not available, so the best available position is the one reported by Moretti et al. (2006): $\alpha = 12{:}04{:}25.19$, $\delta = -01{:}12{:}00.4$ (unc. $4.2''$)[7].

A total of four sources are located within this region in our imaging, all of which are on the edge of the error circle (Figure 8.2). The first object (A), which was reported by several groups in the GCN circulars (Jensen et al. 2005; Fox et al. 2005a), is bright ($R_{\rm AB} = 22.3 \pm 0.17$)[8] and very red ($g - R_{\rm AB} \approx 1.8$) with no clear emission lines over our spectral range in spite of its continuum brightness, which may suggest that it is an old galaxy with little star formation at moderate redshift (alternatively, it may also be an extremely luminous galaxy at $2.3 > z > 1.4$). Fitting line templates to the spectrum results in a best-fit redshift of $z \sim 0.6$, but this is based on low-S/N absorption features. In spite of the large XRT error circle, the brightness of the source gives a low $P_{\rm chance}$ of 0.06, making this a probable (though

[7]All positional uncertainties in this Chapter are reported as 90% confidence error circles.

[8]All reported host AB magnitudes and colors are corrected for Galactic extinction. Afterglow magnitudes or those quoted from other sources are in the original reference system (Vega if $BVRI$, SDSS if $griz$) and are not corrected for extinction.

by no means definitive) host candidate.

Several additional, much fainter objects are also present near the edge of the XRT error circle. One neighboring source (B) is not reported in any circular (likely because it was outside the original XRT error circle in the GCN circulars). It is marginally detected in both filters ($R_{\rm AB} = 25.2 \pm 0.4$) and has a rather typical color. A third source (C) was noted in the Subaru imaging of Kosugi et al. (2005) as being near the center of the original GCN XRT error circle. It is weakly detected in our g-band imaging ($g = 25.84 \pm 0.18$) and marginally detected in our R-band imaging ($R_{\rm AB} = 25.46 \pm 0.39$) which is consistent with the report of a marginal detection with $R \approx 26.0$ in the Subaru imaging. Finally, a fourth source (D) is at the top of the error circle and is detected with significance greater than 2σ in R-band only. It is very red, with $g - R_{\rm AB} > 2$ mag. All three of these additional sources have $P_{\rm chance}$ values of order unity.

The large XRT error circle, and the fact that all available host candidates are near its edge, makes host assignment particularly difficult in this case. The only object whose presence in or near the error circle cannot be attributed to a chance alignment with probability of order unity is the brightest one (source A), but especially given that the original XRT position did not even include this source there is plenty of reason to be skeptical about the association. If this is indeed the associated object, the combination of its red color, lack of lines, and perhaps even the fact that it is nearly outside the XRT error circle is particularly intriguing given the possibility of a very low circumburst density indicated by the X-ray light curve.

8.4.2 GRB 050416A

GRB 050416A (actually an XRF) is the second-lowest-redshift event in the P60 sample. This GRB did have an optical afterglow that was detected by P60 and many other telescopes — including the UVOT in its ultraviolet filters, suggesting that while this is a dark burst, it is perhaps a borderline case. Indeed, in terms of $\beta_{\rm OX}$ (equal to 0.37 for this burst) this event is only slightly under the Jakobsson criterion.

The afterglow of GRB 050416A has been studied in detail by many authors (Holland et al. 2007; Mangano et al. 2007; Soderberg et al. 2007) and the presence of line-of-sight dust which may contribute to its optical faintness is, in principle, well-constrained. Soderberg et al. (2007) estimate $A_V \sim 0.87$ (using a Milky Way template), which compared to the majority of GRBs is already quite high, although Holland et al. (2007) derive a significantly lower value of $A_V = 0.24$. This lower value is also favored by Kann et al. (2010).

The host galaxy color is moderately red: $g - R_{\rm AB} = 0.8$; in part this is likely due to the presence of the 4000 Å break between the g and R bands at the emission redshift of $z = 0.6535$. Soderberg et al. (2007) detected the host in the *HST F775W* filter and estimate $I = 22.7 \pm 0.1$, corresponding to a significantly bluer color of $(R - I)_{\rm AB} \sim 0.15$. Neither of these values constrain the host extinction strongly. However, on the basis of the observed emission line ratio of $H_\gamma / H_\beta = 0.3 \pm 0.1$, they conclude that the host galaxy does likely harbor significant extinction.

8.4.3 GRB 050607

GRB 050607 is at the faint end of *Swift* GRBs, with a fluence of 8.9×10^{-7} erg cm^{-2} (Retter et al. 2005). Unfortunately, optical follow-up of this burst was greatly complicated by the presence of a bright ($R \approx 16$) star only $4''$ away from the burst location. As a result, the P60 imaging of this burst is quite shallow, and no afterglow was detected in any filter. However, even if stellar contamination were not a problem it is unlikely that P60 would have detected the afterglow, since much deeper observations with the KPNO 4m telescope (Rhoads 2005a) do detect a transient with $I = 21.5$ at 10 minutes, below the typical P60 limit even in an uncrowded field. Rhoads (2005a) also note that the optical color is quite red, with $\beta_{\rm opt} > 1.5$: suggesting either substantial dust extinction or a high redshift ($z = 3$–4).

The bright nearby star that complicated the P60 followup causes substantial difficulties for host follow-up also. The star is saturated in our imaging, making PSF subtraction difficult, and the crowded field leaves no bright isolated template stars with which to accurately measure the PSF. We fit and subtract the PSF of the nearby star (excluding the saturated core) using `galfit` (Peng et al. 2002), and identify no obvious source at the position of the optical transient. Therefore we are unable to strongly distinguish between the extinction and high-redshift possibilities, though the B-band afterglow detection imposes a limit of about $z < 4$.

8.4.4 GRB 050713A

GRB 050713A is another well-studied burst—mainly at X-ray and higher energies (Morris et al. 2007; Guetta et al. 2007; Albert et al. 2006), as unfortunately the optical coverage is much more limited. It is bright, near the top end of the *Swift* sample in both gamma-ray and X-ray flux. The associated optical afterglow, however, is quite faint: RAPTOR triggered on this burst and observed the event towards the end of the gamma-ray emission, but even at that point the event was only marginally detected with a peak magnitude of $R \approx 18.4$ (Wren et al. 2005). Several prompt-emission flares at this time are seen in the X-ray and not the optical, but even after the X-ray flaring subsides the optical-to-X-ray index remains shallow at $\beta_{\rm OX} \sim 0.3$. Unfortunately, this afterglow was detected in only R and I filters[9] and as a result the optical slope is only poorly constrained ($\beta_{\rm opt} = 1.4 \pm 1.0$) and on its own does not constrain the redshift of or extinction towards this GRB.

The position of this GRB is within the outer halo of a extremely bright star ($1.1'$ from HD 204408, $V \sim 6.6$ mag). As a result, the region of the GRB is mildly compromised by a variable background, which we remove by applying a median filter over the region of the image around the GRB position. After this step a source coincident with the optical position is clearly visible in R and marginally detected in g. The color of $g - R_{\rm AB} = 0.4 \pm 0.3$ does not constrain the nature of the galaxy given the unknown redshift. It does limit

[9]Detections in JHK filters have been reported by Hearty et al. 2005 but the photometry has not been made public.

the redshift to $z < 3.6$, ruling out any contribution of Lyman absorption to the observed afterglow faintness.

8.4.5 GRB 050915A

GRB 050915A is genuinely dark by all definitions. It was followed up rapidly by several instruments, but only detected by one: the robotic infrared telescope PAIRITEL, which marginally detected a transient in H-band only ($H = 18.25 \pm 0.16$). This is contemporaneous with R and I-band nondetections with the P60 that require an afterglow spectral index of about $\beta_{\rm opt} > 1.45$, outside the range observed for typical unextinguished afterglows but only weakly constraining on the rest-frame extinction without additional constraints on the redshift and spectral index. Furthermore, although this is not a particularly bright event in X-rays or gamma-rays, $\beta_{\rm OX}$ is clearly below the canonical dark value of 0.5. There is no evidence of X-ray flaring or a flat energy reinjection phase after about 100s.

A faint galaxy, previously discovered by Ovaldsen et al. (2007), is well-detected consistent with the XRT position in all filters in which it was observed (g, V, R, and I). It is somewhat offset (by about $1.1''$) from the IR position, although because of the relatively low-significance detection of the infrared afterglow the 90% confidence circle is large and its edge skirts that of the optical disk. While $P_{\rm chance}$ is still low (0.06), we admit that this is one of the more tenuous associations in the sample.

While the optical detection of the host alone rules out a high-redshift origin, VLT spectroscopy of this galaxy (P. Jakobsson et al. in preparation) has revealed a surprisingly low redshift of $z \sim 0.4$, indicating an extremely underluminous system ($M_{V(AB)} \approx -17.4$) and requiring a significant (though not, in this case, particularly large) dust column to explain the redness of optical afterglow. Consistency of the combined X-ray and optical data requires $A_V \gtrsim 0.5$ mag independent of extinction law.

The blue colors of this galaxy indicate a young population free of widespread dust (global $A_V \lesssim 1.0$ mag from our template modeling). This limit is not inconsistent with the relatively modest minimum extinction inferred from the afterglow.

8.4.6 GRB 060210

GRB 060210 provides significant insight into the dark burst phenomenon. The optical afterglow of this burst was fairly bright, but only in the reddest bands (R and I), peaking around 19.5 mag at a relatively late time of 600s following an extended episode of X-ray and optical flaring. Afterglow spectroscopy by Cucchiara et al. (2006) confirmed that this is a (moderately) high-redshift event at $z = 3.91$, explaining the steep fall-off towards the optical bands. In addition, there is significant evidence for high-redshift dust, given that even optical filters redward of Lyman-α are significantly suppressed (Curran et al. 2007). Cenko et al. (2009) estimate $A_V = 1.21^{+0.16}_{-0.12}$ mag (in agreement with Kann et al. 2010), which at the burst redshift corresponds to ~ 4 mag of extinction in the observed R-band using an SMC template.

We imaged the field on two occasions; a relatively short R integration followed by deeper g and I observations. Unsurprisingly, nothing is detected in g-band, which falls below the wavelength of Lyman-α and is likely to be heavily obscured. However, a bright source is detected at the OT position in R and I.[10] The offset between this object and the OT is less than $0.5''$ ($P_{\rm chance} < 0.01$) and the association is further bolstered by the g-band nondetection. This therefore likely represents among the highest-redshift GRB host galaxies detected to date, as well as among the most luminous ($M_R < -20.2$ for a starburst template). In spite of the optical extinction, redward of Lyman-α the color of the object is quite blue, with $(R-I)_{\rm AB} = 0.1 \pm 0.3$ (the large uncertainty is dominated by the poor calibration of this field using USNO standards). Given that the R and I bands correspond to wavelengths well into the ultraviolet at this redshift (1300–1700 Å) where dust absorption is extremely efficient, this suggests that the average observed extinction cannot be high, though given the lack of knowledge about the extinction law it is difficult to constrain this formally. For an assumed SMC-like extinction law, the host extinction is $A_V = 0.25 \pm 0.25$, which is certainly much less than the inferred extinction from the afterglow.

8.4.7 GRB 060510B

The spectroscopic redshift of this event ($z = 4.941$, Price 2006; Price et al. 2007) is the highest in the sample and among the highest for any burst to date. At this redshift the Lyman-α transition is shifted well into the optical band, and consistent with this the flux in the P60 R and i bands is strongly suppressed. Blueward of R-band the OT is not detected. Unfortunately, this is one of the few bursts which displays clear flaring activity in the X-ray band as late as 1000 seconds after the GRB, making a consistent estimate of $\beta_{\rm OX}$ difficult, though as measured in R-band the burst is clearly dark for almost any assumption of the X-ray afterglow behavior.

Optically, coverage of this burst was sparse, and both R and i filters are affected by Lyman-α absorption, making it difficult to estimate the extinction. However, the $z - J_{\rm AB}$ color of 0.0 ± 0.4 (based on the J-band point of Price et al. 2006) requires $A_V < 0.5$ for $\beta_{opt} > 0$ and SMC-like extinction. In addition, the late-time $\beta_{\rm IR-X}$ (using the J-band point) is actually ~ 1.0 and entirely normal, giving further evidence that the extinction is negligible. Because of the known high redshift, our integration on this source was particularly long (approximately one hour), though the quality of the images is poor due to bad seeing ($1.4''$). No object was detected at the P60 position or anywhere inside of XRT and *XMM* X-ray error circles in either the R or g filters to 26th magnitude.

The host galaxy of this burst was imaged by the Spitzer Space Telescope in a study conducted by Chary et al. (2007), and successfully detected with a flux level of 0.23 ± 0.04 μJy. Our g-band nondetection can be interpreted as support of this association (a detection of a galaxy blueward of the expected Lyman break in or near the optical position would

[10] This is not the object mentioned in Hearty et al. 2006, which according to that note is 2-3$''$ north of the XRT position. No source is detected at that position in our imaging.

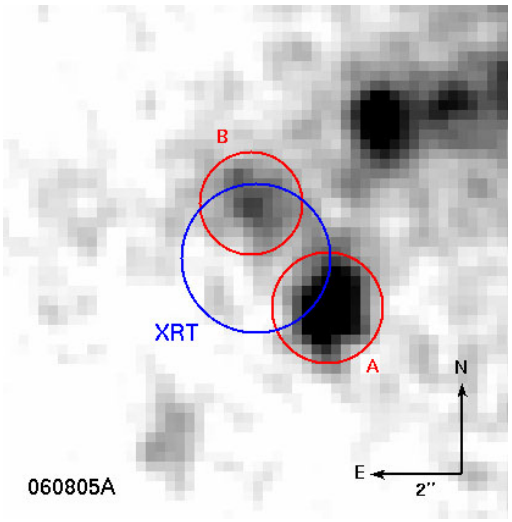

Figure 8.3 R-band imaging of the field around GRB 060805A. Two galaxies are located inside the XRT error circle with additional objects nearby.

indicate that the Spitzer source was actually an intervening source at lower redshift). Given the high redshift, the R nondetection is not surprising either; our limit of $R > 26$ corresponds to a luminosity of $M_R > -20.5$, which is still consistent with the luminosities of the majority of GRB hosts which have been observed to date (Fruchter et al. 2006) and with the sub-L_* nature of the reported Spitzer host (Chary et al. 2007).

8.4.8 GRB 060805A

GRB 060805A was an extremely faint *Swift* burst, with a fluence value in the bottom 3 percent of all *Swift* long GRBs (the burst was not detected at all above 100 keV). The X-ray afterglow is extremely faint: $\approx 3 \times 10^{-4}$ mJy even at 100 seconds.

From this perspective it is no surprise that P60 (and all other optical instruments) failed to detect an optical afterglow, and indeed the limit on the optical to X-ray slope is effectively nonconstraining at $\beta_{\rm OX} < 0.7$. The low observed flux and fluence suggest an intrinsically low-luminosity event, though a typical-luminosity GRB at sufficiently high redshift could also appear faint simply because of its great distance. Our imaging observations favor the former interpretation: two host galaxy candidates are present within the XRT error circle: one bright object (object "A" of Figure 8.3, $R_{\rm AB} \sim 23.6$) at the southwestern edge and a second, fainter source (object "B", $R_{\rm AB} \sim 24.6$) slightly northeast of center. The colors are significantly different: the brighter source is blue with $g - R_{\rm AB} \approx 0$; the fainter one is redder with $g - R_{\rm AB} \approx 0.8$. Unfortunately, we are not able to distinguish which is the correct host given the size of the XRT error circle.

Our spectroscopic observation of this source used a slit angle covering both sources (A and B). Only the brighter object (A) shows a noticeable continuum trace in our 2D

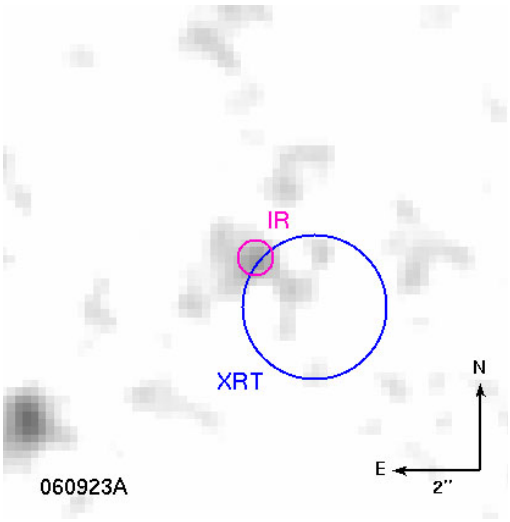

Figure 8.4 Stacked V- and I-band image of the field near GRB 060923A. A faint galaxy is marginally detected coincident with the brightest, central region of the galaxy as also noted by Tanvir et al. (2008c). A projection from the galaxy appears to extend towards the southwest.

spectra. No line features are observed over the spectral range down to the atmospheric cutoff; the nondetection of Lyman alpha or associated absorption features implies approximately $z < 1.8$. The nondetection of Lyman alpha at the position of object A may impose a similar redshift constraint on this object also, but this conclusion is less robust. The redshift limit implied by the $g - R$ color is $z < 3.8$.

8.4.9 GRB 060923A

One of the clearest examples of a dark burst in the sample is GRB 060923A. Though not a particularly high-fluence event in gamma-rays or in X-rays, this burst was observed very early in the NIR (< 1 hr) using UKIRT (Tanvir et al. 2006a) and shortly thereafter with both Keck and Gemini (Fox et al. 2006). A transient was detected in K-band in all of these observations, but not in any bluer filter including J or H. One possible explanation for this would be an extremely luminous event at high redshift ($z > 15$). However, later optical follow-up by Tanvir et al. (2008c) identified a host galaxy exactly coincident with the IR location, marginally detected in our imaging as well in V- and I-bands (Figure 8.4). It is not detected in B or $RG850$. Tanvir et al. (2008c) estimate that for $z = 2.8$ about $A_V \approx 2.6$ would be sufficient to explain the inferred absorption.

The host galaxy is fairly but not remarkably red in the observed-frame optical: $(B - V)_{\rm AB} \gtrsim 0.5$ and $(V - I)_{\rm AB} = 1.0 \pm 0.4$. A nondetection in $RG850$ rules out continuation of this trend further to the red, implying that the spectral energy distribution (SED) flattens towards the rest-frame optical, inconsistent with a highly dust-obscured source. [Tanvir et al.

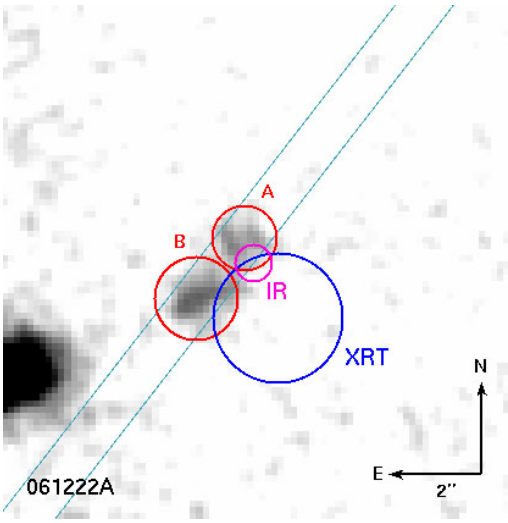

Figure 8.5 V-band image of the field near GRB 061222A. Two objects with similar magnitudes and colors are slightly blended; only the northern object (A) is consistent with the Gemini infrared afterglow position (Cenko & Fox 2006b). The position of the slit used in acquiring spectroscopy of the two sources is also shown.

(2008c) additionally report $(R-K)_{\rm AB} \sim 2.1$, which is not unusual for moderate-redshift galaxies. We attempted to fit model SEDs using the combined $BVRIzK$ photometry, but due to the poor detections in all filters no reliable model converged. Further, only a redshift limit of $z < 4.4$ is possible from our photometry, though Tanvir et al. 2008c conclude that $z < 4.0$ based on the combined properties of the X-ray and optical afterglows.] Additional photometry will be necessary to reliably constrain the extent of extinction and other properties of the host, but as with most other galaxies in our sample the host-galaxy photometry does not demand large amounts of dust.

8.4.10 GRB 061222A

At high energies, GRB 061222A is among the brightest events in the sample. The gamma-ray light curve contains numerous separate pulses and extensive flaring out to ∼100 s, and the X-ray flux is also bright, well-detected by the XRT out to 10^6 s. As measured at ~ 11 hr the X-ray flux from this event is in the top 2% of all *Swift* GRBs.

Several other telescopes in addition to the P60 observed this event at early times, generally obtaining relatively shallow limits. However, NIRI was triggered at Gemini in K-band only (Cenko & Fox 2006b), and a faint source was identified that later faded, confirming this to be an infrared afterglow (Cenko & Fox 2006a). Unfortunately no deep imaging was acquired in other filters. However, this event was also detected in radio using the VLA (Chandra & Frail 2007).

Two blended but seemingly distinct sources are observed near the afterglow position

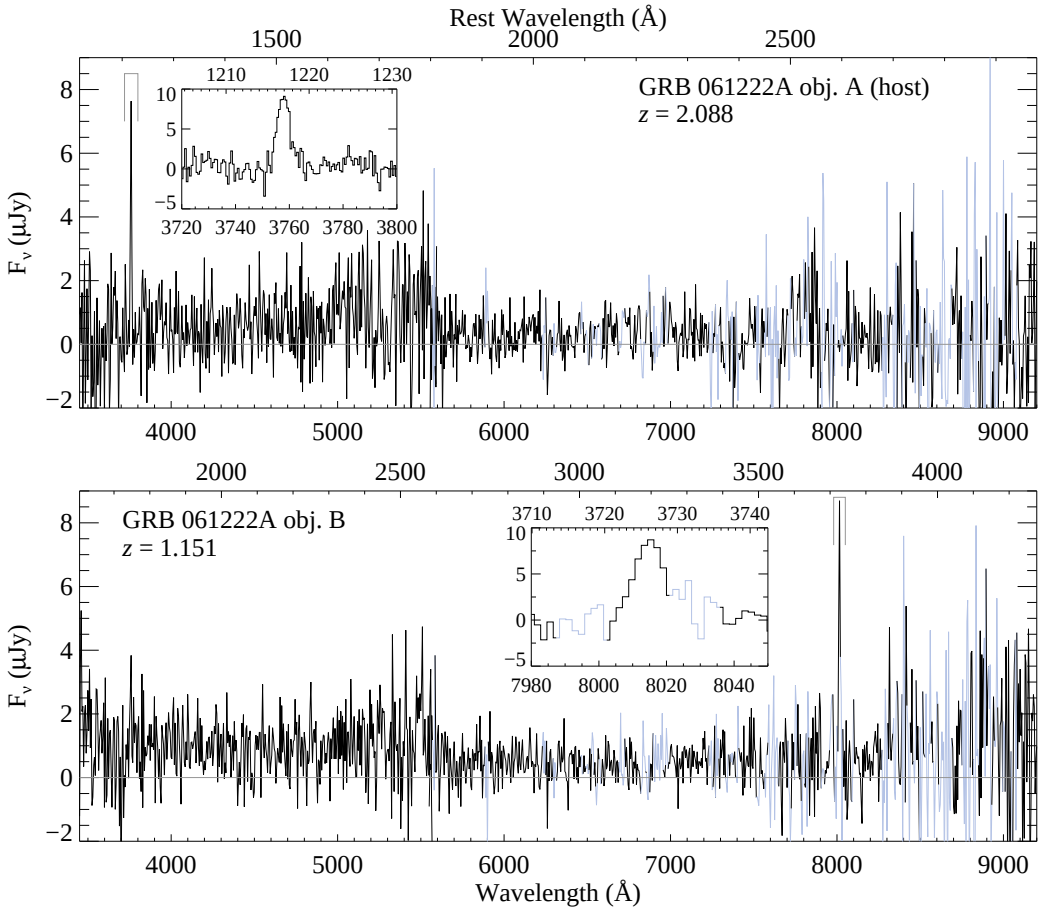

Figure 8.6 LRIS red-side spectrum of the host galaxy GRB 061222A and a nearby (in projection) object placed along the slit (Figure 8.5) with insets showing detected emission lines. A strong line is observed in the host galaxy (object A; top) at 3758Å which we interpret as Lyman-α at a redshift of $z = 2.088$. No other objects are observed over our spectral range. Despite the small offset and similar broadband color, object B is not at the same redshift. No flux is observed at the location of the putative Lyman-α line; instead, we detect a single line at 8015Å which we interpret as the [OII]3727 doublet at a redshift of $z = 1.151$.

(Figure 8.5): one (source A) coincident with the IR transient and a second (source B) offset by about $1''$ to the southeast. We identify the former as the host galaxy. The two objects have similar colors, though photometry is complicated by the close blending, especially in the redder filters where neither object is well-detected. Both galaxies are quite blue, with $(B-V)_{\rm AB} \sim 0.0$ mag, $(V-I)_{\rm AB} \sim 0.5$ mag, $(I-z)_{\rm AB} \sim 0.3$ mag. Only object B is detected in the infrared, but both galaxies are clearly very blue in IR colors as well: for object A, $(I-K)_{\rm AB} < 1.0$ mag; for object B, $(I-K)_{\rm AB} = 0.8 \pm 0.3$ mag.

Our LRIS longslit spectroscopic observation placed both objects along the $1''$ slit for two exposures of 1800s each. The telescope was dithered $5''$ between the exposures. The blue-side exposure was reduced normally, though the severe fringing on the red side was only removed effectively by subtracting the two exposures, which cleanly removed the fringe pattern. We extracted spectra separately for both sources (A and B) along the slit near the afterglow position. Interestingly, despite similar colors these galaxies are not at the same redshift. The fainter, northern object (A), which we identify as the host galaxy, has a strong emission line at 3758 Å. No flux is observed at this position in the southern object (B). At the same time, between two sky lines on the red side another bright emission line is clearly observed at 8014 Å in this case consistent only with the position of object B. The spectra and putative lines of both objects are shown in Figure 8.6.

The strong line in the blue part of the host-galaxy spectrum strongly suggests Lyman-α at a redshift of $z = 2.088$. An alternate possibility is [OII] at $z = 0.008$, but this would require an extraordinarily small and underluminous galaxy as well as imply the presence of Hα at 6617 Å, which is not observed. Galaxy B cannot be at this redshift—its solitary line, if interpreted as [OII], indicates $z = 1.151$. (Alternatively, the line could be associated with Hα at $z = 0.22$, but this would predict the presence of [OII] at 4550 Å which is not observed.)

At the observed redshift, any suppression of the bright optical afterglow predicted by the bright X-ray counterpart must be due to dust extinction. The darkness of this burst is truly extreme: even in the observed K-band, approximately 4 mag of extinction are necessary if we assume the minimum synchrotron intrinsic spectral index of $\beta_{\rm OX} = 0.5$. At the observed host-galaxy redshift of $z = 2.088$, this corresponds to approximately $A_V > 5.0$ mag (nearly independent of the choice of extinction law).[11]

Given the enormous amount of extinction inferred from the faint infrared afterglow, one might expect that the relative amount of extinction in the observed optical bandpasses should be even greater—yet the host candidate is relatively bright ($V \sim 24$ mag) and extremely blue, showing no signs of reddening at all: the broadband color strictly limits the host-galaxy $A_V < 0.5$ mag.

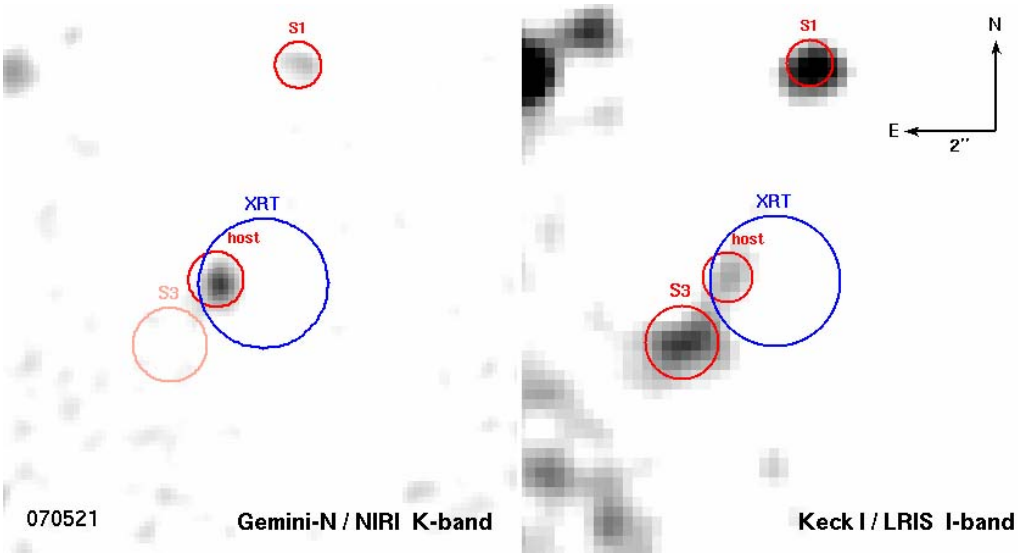

Figure 8.7 K-band imaging of the host galaxy of 070521 from NIRI on Gemini-North alongside I-band imaging from Keck. S1 and S3 are nearby, unassociated objects that were proposed as possible hosts in the GCN circulars (Hattori et al. 2007b; Perley et al. 2007d).

8.4.11 GRB 070521

Like GRB 061222A, GRB 070521 was a bright GRB with a bright X-ray counterpart. In addition to the standard P60 follow-up, observations commenced at P200 within 1 hr (Rau et al. 2007) and at both Keck and Gemini (including, in the latter case, JHK_s IR imaging: Minezaki & Price 2007) within 2 hr. As described in §8.3.4, no transient source within or near the XRT error circle was identified in any of this imaging despite the rapidity, depth, and relatively long wavelengths of these observations, making this burst the darkest in the sample.

In our observations, the most recent UVOT-enhanced XRT error circle includes a red, pointlike object near its eastern edge (Figure 8.7). It is strongly detected in the NIR filters (except J, which was a relatively short exposure). However, in I-band it is only marginally detected, slightly blended with another source located outside the XRT error circle, and was only detected in our V-band imaging after a second visit to the field: uniquely among the host-galaxy candidates in this sample, this object is quite red. No other objects are present within the error circle at either optical or infrared wavelengths.

Thanks to the large suite of broadband photometry available for this object, we have been able to model the host SED and estimate an approximate photometric redshift. Using the package *hyperz* (Bolzonella et al. 2000), the SED is well fit by a late-type galaxy template

[11]It is conceivable that the foreground object may also contribute to the extinction, but the blue colors of both this foreground object and the host (which would be reddened by a similar degree as the afterglow) make it unlikely to be a large contributing factor to the large absorption demanded by the afterglow.

at a redshift of $z = 1.35^{-0.16}_{+0.32}$ with a stellar age of 360 Myr and an extinction of only $A_V = 0.4$ mag. The apparent redness is, therefore, more likely to be due to the presence of the 4000Å break rather than dust: indeed, the JHK SED redward of this break is quite normal. Therefore, as with the other host galaxies in our sample, little dust extinction is demanded by the host data.

The amount of extinction required by the afterglow of this burst is as phenomenal as for 061222A. Assuming an intrinsic afterglow $\beta_{\rm OX} > 0.5$ at 10^4 sec, the deep Gemini limit requires an extinction of at least 4.7 mag in the observed K-band. At the putative host redshift of $z = 1.35$ this corresponds to a limit of $A_V > 9$ mag (over the 95% confidence redshift range of $z = 0.95 - 2.05$, the constraint is $A_V > 6$ mag). A similarly large amount of extinction in the host SED is ruled out by our template modeling.

8.4.12 GRB 080319A

GRB 080319A was a relatively bright GRB, though both its X-ray and optical afterglows are unremarkable, and the observational coverage sparse—likely as a result of the intense focus on GRB 080319B which occurred only 27 minutes afterward in the same part of the sky. *Swift*'s initial slew to this burst was also delayed by 500 s due to an Earth constraint (in total, the XRT observed for only two epochs—at ~ 1 ksec and briefly at 4 ks). Optically, the afterglow is detected by P60 in Riz filters and in a single epoch with the UVOT at approximately 600 s. PAIRITEL also successfully detected the afterglow in JHK before slewing to 080319B. The IR color is also red and consistent with the optical color, for an overall optical-NIR spectral index of $\beta = 1.5$. This is suggestive of significant extinction.

A relatively bright galaxy is located coincident with the P60 optical afterglow position. As with other galaxies in our sample, the optical color is not unusual ($g - R_{\rm AB} = 0.60 \pm 0.06$). While this single color does not strongly constrain host extinction, as with other bursts the relative brightness of the host combined with the lack of obvious redness does not give any reason to suspect its presence. Spectroscopy reveals no line features over our spectral range redward of the atmospheric cutoff, limiting the redshift to $z < 2.2$. At this redshift and assuming an intrinsic spectral slope $\beta < 1.2$, the lower limit on the extinction implied by the photometric SED is $A_V \sim 0.25$ mag (SMC extinction). Any deviation from these assumptions (lower redshift, shallower intrinsic slope, or other standard extinction laws) would require additional extinction, implying a lower limit on the extinction of $A_V > 0.25$ mag.

8.4.13 GRB 080319C

GRB 080319C was a bright, hard burst, and triggered several satellites in addition to *Swift* including Suzaku, Konus, and Agile (Marisaldi et al. 2008; Golenetskii et al. 2008a; Onda et al. 2008). The afterglow is relatively unremarkable at late times, and was detected by the UVOT in filters as blue as U and so clearly is not as "dark" as other objects in this sample ($\beta_{\rm OX} = 0.36$). The burst was in fact bright enough for an absorption redshift

(Wiersema et al. 2008) to be acquired, placing the event at $z = 1.95$. However, as is the case with the other bursts in the sample, the observed optical fluxes are suppressed relative to the X-ray flux and show evidence of reddening, which can be estimated with precision thanks to the known redshift and large numbers of filters ($A_V = 0.67 \pm 0.06$ mag, consistent with Kann et al. 2010). The optical and X-ray afterglows both show a dramatic flare around 200 s, after which the afterglow appears to decay relatively uniformly, though coverage is sparse.

In the original version of this study, we had not yet acquired spectroscopy of this system and noted that if this object were indeed the host galaxy, at the redshift of this system it would have to be tremendously luminous ($\sim 4L_*$). However, we did eventually acquire spectroscopy of this object and, as noted in Chapter 7, this galaxy is in fact not at the host redshift but is associated with the line-of-sight MgII absorber at $z = 0.810$. It is possible that this galaxy is blended with the true host: in the 2D spectrum the line emission is restricted to the brightest clump of the object and does not extend to the fainter, western edge where the afterglow position is. Higher-resolution imaging will be required to distinguish whether we have detected a host in the imaging or not, or what its nature is.

8.4.14 GRB 080320

GRB 080320 is a relatively faint *Swift* burst with a mostly featureless light curve, though the X-ray light curve shows significant flaring ending at around 1000 s. Due to the nearly full moon and the attention towards the previous night's GRB080319B, the optical afterglow was observed only sparsely. This makes it difficult to accurately construct an SED of this event. However, assuming no dramatic color changes or late-time optical flaring, all data are consistent with a very red afterglow color: using contemporaneous or near-contemporaneous epochs we estimate $i - r > 1.1$ mag, $z - i \approx 0.8 \pm 0.2$ mag, and $J_{\rm AB} - i \approx 2.2$ mag. Alone, these observations are not sufficient to distinguish between a highly extinguished or high-redshift counterpart, though there is suggestion that both probably contribute: the SED is red across many filters, which is characteristic of extinction but less so of a Lyman break. However, the J-band is probably not strongly suppressed relative to the X-rays ($\beta_{\rm OX} \approx 0.5$ as measured from J-band), and furthermore our early-time PAIRITEL limits on this event show no evidence for a bright K-band afterglow that may be expected if this redness carried into the optical. The i-band detection imposes an upper limit on the redshift of $z < 7$.

Consistent with this interpretation, we do not detect any host galaxy at the position of the optical transient to deep limits, although our latest reduction indicates a possible marginal detection in I-band only. While in principle this could simply be the result of a low-luminosity host, the N_H column measured by the XRT is relatively low in comparison with the dark bursts in our sample for which we infer large absorption columns, offering additional support of a moderately high-redshift origin (X-ray absorption is strongly wavelength-dependent, with the same column absorbing much more efficiently at lower energies: at higher redshift these lower energies are shifted out of the XRT sensitivity window and swamped by the Galactic absorption signature—see also Grupe et al. 2007.) Of course,

a small host would predict a relatively low absorption column as well, though significant dust extinction in such a system would not be expected. Nevertheless, we cannot rule out this scenario and can formally only place an upper limit on the redshift.

8.5 Results

8.5.1 Redshift limits and the implications for high-z GRBs

An afterglow detection in any optical (I-band or blueward) filter immediately rules out a high-redshift origin.[12] So does an optical detection of the host (assuming we have a proper identification). Using the combination of these two factors we can place an upper limit on the number of bursts in our sample which could have originated from very high redshift ($z > 7$).

In fact, *no* events of our sample are consistent with such a high-redshift origin. If we assume our proposed host associations are all correct, *all* 29 events in the P60 sample have either an optical transient or an optical host candidate, suggesting that—in spite of *Swift*'s sensitivity and customized trigger software—it detects few events beyond the range that has already been probed by optical spectroscopy. Under this assumption, all events in the sample are constrained to $z < 7$ and all but one (GRB 080320) to $z < 5$.

Because the P60 sample is uniformly drawn from all *Swift* events, we can convert this observational statement to a limit on the intrinsic high-redshift fraction among *Swift* bursts. We perform a simple Monte Carlo simulation in which 29 events are repeatedly drawn from a source population with the intrinsic high-z fraction treated as an input parameter. To convert this to a 90% confidence upper limit, we then vary this input parameter until zero high-z are events are drawn in exactly 10% of the simulated 29-event samples (for $z > 7$) or zero or one event is drawn in exactly 10% of the samples (for $z > 5$). We conclude that, if all of our supposed associations are correct, at most 13 percent of *Swift* events are at $z > 5$ and at most 7 percent are at $z > 7$ to within 90% confidence. (This procedure can be generalized to lower redshifts also with appropriate assumptions—see Figure 8.8.)

These estimates have neglected the possibility that some of our host associations may be chance alignments with foreground galaxies. To take into account the possibility of foreground galaxy contamination, we assumed that 10% of high-z events in our simulation would be wrongly associated with a low redshift host ($P_{\rm chance} = 0.1$ is the largest observed in any of our possible host associations) and performed the simulation again, varying the true high-z fraction until zero *apparently* high-z events are present in 10% of the samples (for $z > 7$), or zero or one apparently high-z events are present in 10% of the samples (for $z > 5$). In fact, this changes our constraints only slightly (by about one tenth of each percentage value). We therefore conclude that, within 90% confidence, **at most 14 percent of all**

[12]Some measurable flux could be detected blueward of the Gunn-Peterson trough from a sufficiently luminous event at $5 < z < 7$, though such an event would show a clear photometric break. We find no evidence for such an event in the P60 sample among GRBs with unknown redshifts.

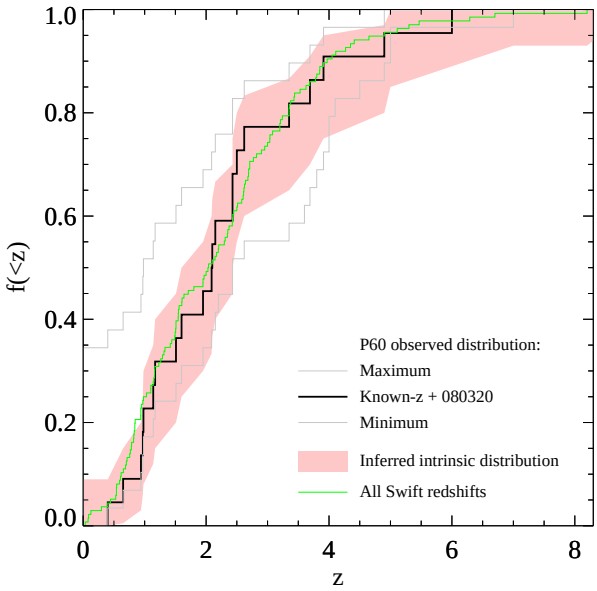

Figure 8.8 Cumulative redshift distribution of *Swift* GRBs inferred from the uniform P60 sample. The two solid gray lines show the absolute maximum and minimum observed redshift distribution in the entire sample (that is, assuming all GRBs with unknown redshift are at the maximum possible [see Table 8.5] or the minimum possible [$z = 0$] redshift). The thick black line is the distribution omitting non-dark ($\beta_{\rm OX} > 0.5$) or potentially dark $z < 4$ events with no measured redshift (these events are, as a population, not likely to significantly deviate from the redshift distribution of *Swift* events in general) and conservatively assumes GRB080320 to be at $z = 6$. Based on this assumption, the salmon region then represents statistical limits on the cumulative fraction of *Swift* GRBs originating at or below a given redshift as a function of z permissible to be consistent with the observed distribution (10–90% confidence limits). The inferred distribution is generally consistent with the observed distribution of spectroscopic redshifts for all *Swift* events to date, indicating that there are no strong redshift biases—except possibly at the highest-z end, where the observed and intrinsic rate are not as well-constrained.

***Swift* GRBs are at $z > 5$ and at most 7 percent are at $z > 7$.**

As our most conservative assumption, we may choose to reject two host associations completely (in spite of the low $P_{\rm chance}$). Specifically, suppose we reject two of the six host associations for events with no optical detection (for events with optical detections whether or not we have identified the host correctly does not significantly impact our conclusions about the redshift distribution)—that is, we assume a 33% contamination rate, which is much higher than that anticipated by chance. In this case, the data are consistent at 90% confidence with up to 23% of GRBs at $z > 5$ and up to 18% at $z > 7$. However, we point out that the "weaker" associations (where error circles and/or offsets are large: 050412, 050915A, 060805A) are consistent with simply being underluminous in all bands and no more likely to be at high-redshift than any other burst even if their claimed host galaxies are unassociated. The one exception, GRB 070521, has independent confirming evidence for a highly-absorbed, low-z nature in the form of a large X-ray $N_{\rm H}$ column (as do the statistically firmer associations of GRB 061222A and GRB 060923A; see also Figure 8.9).

The recent detection of GRB 090423 at $z = 8.2$ also allows us to place a (relatively non-constraining) lower limit on the high-redshift fraction. While the P60 sample in this Chapter was cut off at the end of March 2008, P60 triggered rapidly on GRB 090423 and detected no afterglow to limits comparable to those discussed in this work. GRB 090423 was the 42nd *Swift* GRB on which P60 triggered rapidly. We perform a simple Monte Carlo simulation in which bursts are sampled from an intrinsic population with a user-specified high-z rate, which is varied until a high-z event occurs as or earlier than the 42nd event 10% of the time. Only a rate of 0.2% is necessary to fulfill this criterion. Therefore, the detection of GRB 090423 requires (to >90% confidence) only that a minimum of 0.2% of all *Swift* events originate from $z > 7$, which is fully consistent with our maximum value inferred from the sample discussed in this Chapter. Our overall constraint on the $z > 7$ burst fraction for *Swift* is therefore 0.2–7 percent (to within 80% confidence). This estimate is consistent with other recent observational limits on the high-z fraction, such as that of Ruiz-Velasco et al. 2007 ($\leq$ 19% at $z > 6$), Grupe et al. 2007 ($\leq$ 7% at $z > 6$), and Jakobsson et al. 2005b ($7 - 40$% at $z > 5$).

Our results strongly constrain some theoretical models of the evolution of the GRB rate with cosmic time. For example, Bromm & Loeb (2002) predicted that 50% of all GRBs and 25% of *Swift* GRBs originate at $z > 5$, which we rule out. It is consistent with some more recent models that predict a low high-z GRB rate based on star formation rate (SFR) models (Bromm & Loeb 2006; Le & Dermer 2007), luminosity indicators (Li 2008), and limits on the GRB production efficiency of Population III stars (Belczynski et al. 2007; Naoz & Bromberg 2007)—though some of these models predict high-z fractions close to our maximum value, which a larger sample may be able to confirm or refute.

Table 8.5: Redshift and extinction constraints on P60 GRBs

GRB	$\beta_{\rm OX}^a$	Bluest AG det.	Bluest host det.	z	$A_V^{b,c}$ (mag)	$N_{\rm H}$ excess $(z=0)^d$ (10^{20} cm^{-2})
050412	< 0.49	none	g?	<4.5?		<93.2
050416A	0.35	UVW2	g	0.6535[e]	0.87	24.0±6.0
050607	~ 0.33	B	none	<4		<15.0
050713A	0.31	R	g	<3.6		<28.3
050915A	< 0.44	H	g	∼0.4	> 0.5	<14.4
060805A	< 0.76	none	g	<3.8		<38.0
060210	0.37	R	R	3.91	1.21	8.7±2.1
060923A	< 0.24	K	V	<4	∼2.5	22.1±9.2
061222A	< -0.19	K	B	2.088[e]	> 5.0	34.6±2.8
060510B	0.04	R	3.6μ	4.941	< 0.5	<14.6
070521	< -0.10	none	V	~ 1.35	> 6	44.1±12.7
080319A	0.41	r	g	<2.2	> 0.25	<17.3
080319C	0.36	U	g	1.95	0.67	<32.6
080320	< 0.31	i	none	<7	-	8.7± 3.3
050820A		UVW1	g	2.615	< 0.1	3.4±1.5
050908		V		3.35	< 0.55	<19.3
060110		R		<5	< 0.3	—
060502A		B		1.51	0.53	<5.5
060906		R		3.685	0.2	<31.2
060908		UVW1	V	1.884[h]	< 0.1	<12.6
070208		R		1.165	0.96	<38.8
070419A		g	r?[g]	0.97	0.70	<35.8
071003		U		1.60435	< 0.26	<13.9
071010A		g		0.98	0.60	<37.0
071011		V		<5		<60.7
071020		R		2.145	< 0.35	<16.1
071122		white		1.14	0.58	<10.6
080310		UVW1		2.43	0.10	<7.9
080319B		UVW2	g	0.937	0.07	4.4± 2.2
090423[f]	< 0.5	J	none	8.3	0.1	<10.6

[a] Only listed for bursts identified as "dark" in the sample.

[b] Extinction in the host-frame V-band along the line of sight inferred from the afterglow, generally assuming SMC extinction and $\beta_{\rm opt} \sim 0.6$.

[c] A_V references: Cenko et al. (2009); Soderberg et al. (2007); Covino et al. (2008); Bloom et al. (2009)

[d] Equivalent $z = 0$ hydrogen column density in excess of the Galactic value inferred from the X-ray spectrum, fit using the procedure of Butler & Kocevski (2007b). Only detections of $> 2\sigma$ excess are shown; other events are displayed as upper limits (see Figure 8.9 for a less conservative assessment of N_H columns for bursts in the sample.) All objects for which we infer large amounts of dust extinction in the optical band also have unambiguous detection of excess X-ray absorption columns; no event with low or negligible dust extinction shows this signature. Since X-ray absorption is more efficient at low redshifts, this offers additional support to our association of these objects with moderate-z hosts.

8.5.2 Constraints on dust extinction

In Table 8.5 and in Figure 8.10 we have summarized the extinction constraints derived based on our host-galaxy redshift constraints and the properties of the afterglow. For most bursts in the full P60 sample, there is little extinction: the median A_V is about 0.5, within the range of values typically seen in previous studies of optically well-studied bursts (e.g., Kann et al. 2006a). However, large extinction columns are common: six bursts (out of 22 in which useful constraints can be derived) have $A_V > 0.8$ mag and three have $A_V \gtrsim 2.5$ mag. In comparison, only two events have R-band fluxes that are suppressed by hydrogen absorption at high redshift. Thanks to the uniform nature of this sample, we therefore are able to assert with reasonable confidence that the predominant cause of the dark burst phenomenon is dust extinction. Even an extinction of $A_V \sim 1$ mag translates to large R-band extinction values at typical *Swift* redshifts (> 3 mag at redshifts of $z > 2$).

Unfortunately, the nature of this dust remains a mystery. The hosts of highly extinguished events tend to be unremarkable objects—often optically bright and with no evidence for large amounts of intrinsic reddening, and in a few cases with blue colors that appear to directly contradict the expectation of extremely red objects. In no case are the optical colors indicative of a ULIRG-like highly extinguished object, which some theoretical models (e.g., Ramirez-Ruiz et al. 2002) predict should be common among the GRB host population. This result is not peculiar to our study: other dark burst hosts have, in the large majority of cases which have been studied to date, also been relatively blue objects without clear photometric evidence for extinction (Jaunsen et al. 2008; Rol et al. 2007b; Castro-Tirado et al. 2007b; Pellizza et al. 2006b; Gorosabel et al. 2003; Djorgovski et al. 2001), though a few counterexamples of very red hosts do exist as well (Levan et al. 2006a; Berger et al. 2007a).

The results can be interpreted in several ways. One possibility is that these apparently blue galaxies are concealing their true natures: if the distribution of dust is sufficiently patchy, it is conceivable that what looks like a normal object in the optical and NIR bands could harbor a massive starburst obscured from view by the same dust concealing the afterglow, allowing the (blue) emission from the optically thin regions to dominate the SED even if they contribute little to the total SFR. Alternatively, there could be relatively little dust in

[e] Emission-line redshift.

[f] While not formally in our sample, the recent GRB 090423 is presented for reference as an example of a confirmed $z > 7$ event. Notably, this event has no host galaxy to $z > 26$ and no significant excess $N_{\rm H}$ column (Tanvir et al. 2009).

[g] Dai et al. (2008).

[h] Revised redshift from Fynbo et al. 2009.

the galaxy overall, but the GRB itself could be located deep within a relatively small dusty patch, such as a young molecular cloud, though this region would have to be sufficiently large to escape the destructive influence of the burst itself (Waxman & Draine 2000). A third, more exotic possibility is that our templates for modeling high-redshift dust are incorrect, and high-redshift GRB hosts are dominated by grey extinction laws that redden their stellar populations relatively little (Chen et al. 2006; Li et al. 2008a; Perley et al. 2008e). Unfortunately, the available data do not allow us to distinguish between these possibilities.

In any case, however, our results suggest that a significant fraction of GRBs (and, by association, of high-mass star formation) must occur within dusty regions not being probed by traditional optically-selected redshift surveys. Based on our inferred distribution of A_V, we estimate that approximately $\sim$50% of the rest-frame near-UV emission from *Swift* GRB afterglows is absorbed by dust. This value is quite similar to the fraction of obscured star formation inferred at high redshift based on far-infrared and millimeter studies (Chary & Elbaz 2001; Le Floc'h et al. 2005) and may suggest that the potential for GRBs to serve as tracers of the high-redshift star-formation rate (Blain & Natarajan 2000) is finally being realized. Nevertheless, there is still need for caution: in addition to the possibility that the extinction may be a unique property of the GRB site hinted at by the blue observed colors of the host galaxies in our observations, there is evidence that metallicity or other biases result in a GRB host population strongly favoring subluminous galaxies in the local universe (e.g., Modjaz et al. 2008) and possibly at higher redshifts as well (Fruchter et al. 2006; Le Floc'h et al. 2003; cf. Fynbo et al. 2008)—which could skew the GRB positional distribution significantly away from that of high-z star formation in general.

8.6 Conclusions

Twelve years after the discovery of a class of "dark" GRBs lacking optical afterglows (Groot et al. 1998), we claim that the mystery surrounding the relative importance of the varying hypothesis for their apparent optical faintness is largely resolved. Of 14 dark events (out of 29 events in the full P60 sample):

- Seven or more events (070521, 061222A, 060923A, 060210, 080319C, 050416A, 080319A, plus likely 050915A and perhaps 050713A) are significantly suppressed by dust extinction (at least 1 magnitude in the observed R-band and typically much more) in their $z < 4$ host galaxies.

- Two events are probably suppressed due to Lyman absorption at redshift of $z > 4.5$: GRB 060510B at $z = 4.941$ and GRB 080320 (at unknown redshift, but $z < 7$).

- Three events appear to be simply underluminous: not at high redshift, but because they were either intrinsically underenergetic (050607 and 060805A) or because little energy was coupled to the afterglow (050412, which may be a "naked" long GRB). Although no optical afterglow was detected for any of these events, they would not be classified as dark using the Jakobsson et al. (2004a) criterion.

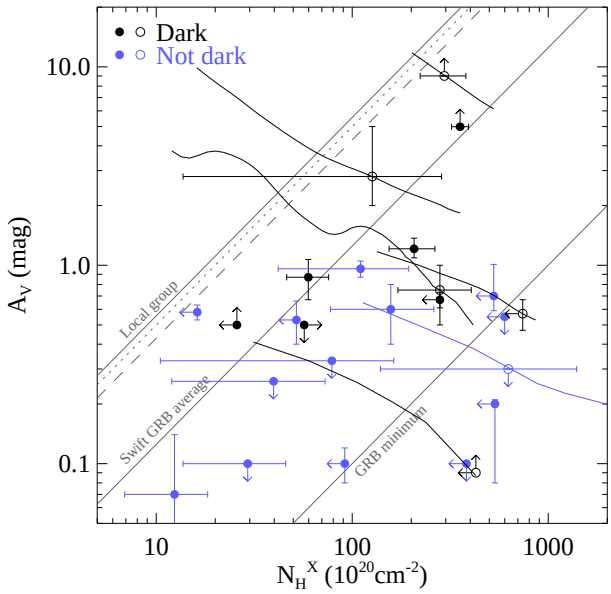

Figure 8.9 Rest-frame dust extinction A_V versus N_H as calculated from absorption in the X-ray spectrum due to light metal ions (assuming Solar metallicity) for 24 of 29 bursts in the P60 sample (five events, four dark and one non-dark, have been excluded due to the absence of meaningful constraints on either parameter). Bursts with known redshift are shown as solid points; bursts with unknown z are shown as open points at their most likely redshift (if only an upper limit is available, we plot the burst at a redshift of $z \sim 2$ or, in the case of GRB 080320, $z \sim 5$). A "track" line then shows the evolution of the best-fit measurement or limit at different redshifts between $z = 0.5$ and the maximum host or afterglow redshift in Table 8.5. The majority of events have a ratio of A_V/N_H substantially lower than seen in Local Group galaxies, consistent with observations of other GRBs. (Milky Way, SMC, and LMC relations are plotted as lines using the values in Schady et al. 2007, along with the average value for bursts in that paper and the minimum A_V/N_H in the pre-*Swift* sample of Kann et al. 2006a). The high-A_V events in our sample ($A_V > 2$), while not clearly inconsistent with the low A_V/N_H relation observed previously, may suggest a trend towards more 'normal' dust-to-gas ratios.

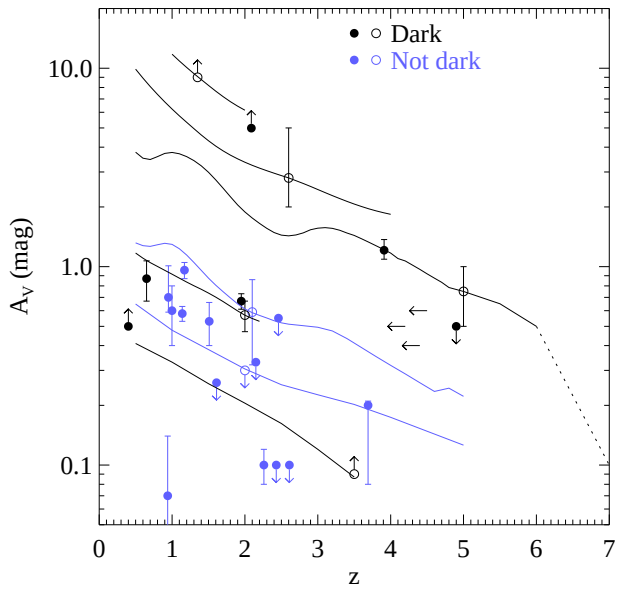

Figure 8.10 Constraints on rest-frame dust extinction (A_V) and redshift (z) inferred for all 29 bursts in the full P60 sample. As in Figure 8.9, bursts with known redshift are solid points; bursts with unknown z are shown as a redshift "track" showing the evolution of the best-fit A_V or limit with z; an open circle is plotted at a representative value. For a few bursts A_V is unconstrained; redshift limits are plotted as arrows at an arbitrary A_V with no circle. For clarity, the redshifts of two events have been adjusted slightly (less than 0.1) to prevent overlap of points. All bursts are constrained to $z < 7$ and all but one to $z < 5$ (for the exception, GRB 080320, extinction is not constrained above $z \sim 6$, as shown by the dotted line). However, many events show large extinction values, with a distribution skewed towards noticeably higher A_V than previous, nonuniform samples (e.g., Kann et al. 2010).

We conclude that the dark burst phenomenon is predominantly the result of extinction at moderate redshifts ($1 < z < 5$), with underluminous afterglows (otherwise normal events which are too faint for the sensitivity of a small telescope) also contributing significantly in an amount depending on the detection threshold—consistent with, but more constraining than, the results of pre-*Swift* dark burst studies (e.g., De Pasquale et al. 2003). In particular, a large fraction of high-redshift GRBs is not needed, and in fact is ruled out—providing observational evidence limiting the ability of Population III stars to efficiently produce GRBs and in agreement with most recent models of the high-redshift star formation rate. Furthermore, our methods suggest that even if the discovery of very high-z events continues to be extremely challenging (although the recent discovery of GRB 090423 at $z = 8.2$ has now demonstrated that such events do exist and can be recognized), complementary host-galaxy searches can impose useful constraints on the high-redshift bursting rate free of selection biases, and we encourage continued host-galaxy follow-up of other medium-aperture robotic telescope samples and of dark bursts in general. (A much larger, though not uniformly sampled, broadband survey of *Swift*-era dark bursts is in progress.)

The location and nature of this high-redshift dust remains unknown: although our wavelength coverage is limited, no galaxy in our sample shows evidence of significant dust extinction. In these cases, the line of sight to the afterglow must be passing through a much larger extinction column than the light from the observed young stars in the galaxy which dominate its rest-frame near-UV flux. The solution likely requires that the dust is nonuniformly distributed—either closely linked with the GRB site itself, or widespread but sufficiently patchy to conceal its effects. Although we cannot firmly resolve this question at this stage, it is clear that GRBs still have much to teach us about the structure of galaxies at high redshift and the importance of obscuration in the early universe.

Fortunately, the answers to these lingering questions may not be far off. Longer-wavelength observations (near- and mid-infrared, sub-mm, radio) of these and other dark burst hosts would clarify the picture, piercing through the inferred dust screen or even detecting the reradiated emission from any postulated highly-extinguished population directly. Such studies of the (limited) pre-*Swift* dark burst host sample (Barnard et al. 2003; Berger et al. 2003a) indicate a population that differs little from GRB hosts in general—consistent with a patchy dust distribution in all GRB hosts, where the location of the GRB within its host (rather than the type of host) is the determining factor in the observed darkness of a given burst. However, the obscuration rates derived from these radio and sub-mm studies are surprisingly high (typical radio/mm-derived host SFRs are 20–50 times the optically inferred values) and the non-detection of most such sub-mm sources in a recent survey by the *Spitzer Space Telescope* (Le Floc'h et al. 2006) may call this conclusion of very high obscuration into some doubt. The sample of Le Floc'h et al. (2006) includes three "dark" GRBs, one of which (GRB 970828) is indeed associated with a strongly obscured galaxy (one of only two identified in their sample of 16 objects). We suggest that more work in the long-wavelength regime is necessary to fully understand the nature of GRB host galaxies, especially of the most highly-extinguished events.

However, continued study in the optical band promises to be useful as well. High-resolution space-based imaging could constrain the morphologies of dark GRB host galaxies, including any possible difference between the burst site and the rest of the galaxy. (For example, studies of the host of pre-*Swift* dark GRB 970828 seem to indicate a dust lane running through the afterglow position [Djorgovski et al. 2001].) The most luminous bursts are capable of shining through even very thick dust columns, allowing for detailed study of the material along their lines of sight. Recently, spectroscopy and infrared photometry of the extremely bright GRB 080607 at $z = 3.036$ revealed a strongly extinguished ($A_V = 3.2 \pm 0.5$) event, showing a clear 2175Å bump and an abundance of molecular and ionic lines associated with a nearby molecular cloud with Solar-like metallicity (Prochaska et al. 2009 and Chapter 6). Similarly, *Swift* bursts GRB 050401 (Watson et al. 2006) and GRB 070802 (Krühler et al. 2008) were also "dark" events that were nevertheless sufficiently optically luminous to enable multiband photometry and optical spectroscopy, confirming the link between optical suppression (darkness), reddening, and dust absorption. Such events, while rare, illustrate the need for continued observational effort on as many fronts as possible (including both spectroscopy and photometry, of both afterglow and host galaxies, and at all available wavelength regimes) to make further progress on the environments of gamma-ray bursts and their connection to star formation in the early universe.

Acknowledgments

We thank D. A. Kann and the anonymous referee for helpful comments and suggestions on the original manuscript, and also thank Derek Fox as well as Pall Jakobsson and collaborators for sharing additional data on bursts within our sample.

Chapter 9

Conclusions

In this final chapter, I will attempt to bring together the different chapters of this dissertation by tersely summarizing some of the major scientific results presented throughout this work, organized by scientific theme.

9.1 Summary of Major Results

9.1.1 The Environments of Short-Duration Bursts and the Role of Extended Emission

The environments of SGRBs are remarkably—perhaps surprisingly—diverse. Combining the existing literature (e.g., Prochaska et al. 2006b; Fong et al. 2010; Berger 2009) with our survey (Chapter 7), it is possible to find convincing evidence of SGRBs from a tremendous diversity of environments: ellipticals, spirals, distant star-forming galaxies, the intracluster medium, and intergalactic space. Perhaps the most convincing example of the last of these comes from the analysis, provided in Chapter 2, of GRB 080503. The faint and late-rising X-ray afterglow of this GRB is consistent with the occurrence of this burst in an extremely low-density environment, and deep HST imaging uncovered no static source underlying the afterglow position.

It is particularly notable that this conclusion comes from an event with a bright extended-emission component (with 30 times the fluence of the initial short-duration spike, as measured by the *Swift* BAT). Before the publication of this work, a study by Troja et al. (2008) had pointed towards a tentative association between the occurrence of extended emission itself and the burst environment: namely, that events with extended emission occurred only in or near the centers of their host galaxies, while events without extended emission could occur anywhere. This interesting result, if confirmed in a larger sample, would have several possible important ramifications: it would either suggest a further split in progenitor populations between extended-emission events (sometimes called "SGRBEEs") and the "true" short-duration bursts, or alternatively suggest that the extended emission itself some-

how owes to interaction of the progenitor with its environment (a much less likely case). However, GRB 080503 is a striking counter-example to the Troja correlation, demonstrating that SGRBEEs can occur outside host galaxies. The production of extended-emission may therefore not be indicative of the progenitor (or environment) after all.

It is interesting to note that we have *not* yet unambiguously identified a Swift-localized short-duration GRB from a galaxy in the "local" (Virgo cluster or closer) Universe. For canonical SGRBs, this is certainly no surprise at all: at an apparent observed rate of only a few per year out to a redshift of $z \sim 0.5 - 1.0$, only a negligible rate is expected within the nearest 30 Mpc (or even the nearest 300 Mpc). However, the 2004 megaflare from SGR 1806-20 would have been detectable to *Swift* from as far away as the Virgo group, and depending on the assumed rate of similar events the observed SGR megaflare rate should be at least a few percent (and perhaps as much as 15-20%) of the total short burst rate (e.g., Hurley et al. 2005). The lack of clear galaxy associations in our sample or in the literature would therefore seem to favor values on the low end of this scale.

9.1.2 The Faint End of the Host Galaxy Luminosity Distribution

While this disseration has a heavy emphasis on the use of (L)GRBs to probe dust extinction and obscured stellar populations, GRBs are also important probes of star formation in other hard-to-study locations, such as in small low-luminosity galaxies. Such galaxies are difficult to detect beyond the nearby universe, and the contribution of small galaxies to the total star-formation (or stellar mass) in the Universe generally has to be extrapolated based on relations established from brighter fluxes. In conjunction with the study of GRB 071025 by Cenko et al. (2008a), our analysis of GRB 071003 in Chapter 3 suggests that the contribution of these small galaxies to massive star formation is, at least, nontrivial. Extremely weak Mg II absorption seen in the burst afterglow is consistent with a very small host system, and while the proximity of the burst to a bright foreground star makes the search for a coincident host galaxy in emission difficult, no diffuse host emission is in evidence in NIR adaptive optics imaging. We have also discovered surprisingly faint hosts for some low-redshift GRBs in our broader host survey, such as the hosts of 050915A and 080515.

9.1.3 The (Lack) of Gamma Ray / Optical Emission Coupling

Several GRBs studied in the course of this work were observed simultaneously in the gamma-rays, X-rays, and optical or near-infrared during the latter phases of the detectable prompt emission. The exact mechanism that produces prompt emission radiation is still not known, and both correlations (e.g., Blake et al. 2005; Vestrand et al. 2005, 2006) and non-correlations (Yost et al. 2007; Rykoff et al. 2009) between light curves at different wavelengths have been previously reported. Our own observations show no correlations: for all of these events (GRB 071003 in Chapter 3, GRB 061126 in Chapter 4, GRB 071025 in Chapter 5, and GRB 080607 in Chapter 6) we observe no optical/IR counterpart to the gamma-ray

pulses and flares, nor any gamma-ray counterpart to the subtler optical light curve "bumps" often seen at early times.

These results do not rule out the existence of such a correlation, though—merely that, in the cases observed, any simultaneous correlated signal is drowned out by a much brighter and relatively non-variable "standard" afterglow that had already emerged by the time our observations began. Earlier (and perhaps more sensitive) observations, preceding the rise of the afterglow, appear to be necessary to study optical prompt emission the majority of cases. The few correlated signals which have been reported are associated either with rare bursts where a faint precursor had allowed follow-up telescopes to slew to the burst position (Vestrand et al. 2005; Blake et al. 2005), or (in one case) an extremely bright event that could be detected by wide-angle telescopes which did not have to slew (Racusin et al. 2009; Beskin et al. 2010).

We also observe no *color* evolution that can clearly be associated with dust destruction by either the prompt emission or the afterglow (a possible model for early-rising optical emission is that the optical flash is "burning" its way through an enshrouding dust cloud; Klotz et al. 2008b). Our multicolor observations of GRB 071025 in particular, which began at 30 s in the rest-frame during the initial rise of the afterglow, provide some of the most constraining limits on this phenomenon yet reported: see in particular Figure 5.4.

9.1.4 Extinction Properties of GRB Host Galaxies

GRBs 071025 and 080607 (the subjects of Chapters 5 and 6, respectively) were both strongly affected by extinction within the host galaxy: their SEDs are clearly deviant from a power-law. Given the high redshifts of these bursts ($z > 3$), our observations of these events provide an invaluable opportunity to help understand the evolution of interstellar dust in the early universe and its differences from the dust observed locally. Interestingly, despite its great distance, the extinction curve of $z = 3.04$ GRB 080607 (which is tightly constrained by the combination of our photometric and spectroscopic observations) is qualitatively quite similar to that in our own Milky Way—it shows a prominent 2175 Åabsorption bump (although its relative strength appears weaker than within our Galaxy) and significantly greater opacity at shorter wavelengths than longer ones. While its properties do not correspond directly with any single known Local Group sightline, its properties would not appear markedly unusual if placed within our Galaxy. On the other hand, GRB 071025 at $z \sim 5$ is remarkably different from local extinction curves with no 2175 Åbump and a peculiar flattening of the opacity curve around 2000 Å. It is, however, modeled well by a supernova-produced dust profile first developed to explain observations of a $z > 6$ quasar (Maiolino et al. 2004). This may provide tentative evidence of a transition between dust produced at $z \gtrsim 5$ and $z \lesssim 5$ (possibly related to stellar evolution timescales of stars producing supernovae and AGB stars, respectively), although at present such claims remain speculative. More observations of high-redshift GRBs (and QSOs) will be required to confirm this tantalizing suggestion.

GRB 061126 (Chapter 4) may also have been affected by dust extinction, although this

event is much more challenging to understand—its UV-optical-IR SED is an excellent fit to a power-law, yet all these fluxes are much fainter than would be expected (under standard synchrotron-models) given its bright X-ray flux. This may indicate the presence of unusual "gray" dust in the system with weak wavelength dependence. However, it could also simply represent a failing of the simple model and require the presence of a separate SED component boosting the X-ray flux.

9.1.5 The Swift Redshift Distribution and the Dusty Origins of Dark Bursts

The fraction of GRBs coming from very high redshift is of obvious interest: afterglows are bright enough to be easily detected by small NIR telescopes at these redshifts (e.g., Bloom et al. 2009), and their rate should be directly controlled by the star-formation history of the very early universe. While the directly-confirmed high-redshift GRB rate is small (only a handful of spectrosopically, or even photometrically, confirmed $z > 6$ events are known despite years of searching: GRBs 050904, 080913, and 090423; Kawai et al. 2006; Greiner et al. 2009b; Tanvir et al. 2009; Salvaterra et al. 2009), many more events could exist: a large population of "dark" GRBs (defined vaguely as events with unusually faint optical afterglow, or more specifically in Chapter 8 using, e.g., the criterion of Jakobsson et al. 2004a) has been a mystery almost since the discovery of GRBs themselves, and high-redshift GRBs are indeed expected to be optically dark. By combining the afterglow catalog of (Cenko et al. 2009) with deep Keck imaging of GRB host galaxies, we have provided (also in Chapter 8) a nearly-complete redshift distribution of a uniformly-selected sample representative of all detected *Swift* bursts. Almost every dark event in the sample has a high-probability host-galaxy candidate detected in our Keck optical observations, ruling out a high-redshift origin. In fact, among all P60-triggering *Swift* GRBs to date, *only* GRB 090423 (known spectroscopically to be at $z = 8.2$) is consistent with a redshift of $z > 7$. The high-z fraction must therefore be quite low (< 13 percent at $z > 5$ and < 7 percent at $z > 7$ for *Swift*GRBs, to 90% confidence). Instead, on the basis of reddened afterglows and elevated X-ray absorption columns, we suggest that most dark P60 events are the result of large amounts of dust extinction within the host galaxies. Even though few well-studied GRBs show significant dust extinction (Kann et al. 2010), when the hard-to-study dark events are considered, we conclude that dust is actually fairly common among GRB sightlines. The GRB obscuration fraction in the rest-frame UV is comparable to that inferred for star-forming galaxies generally.

9.1.6 The Host Galaxies of Dust-Obscured Bursts

If the optical faintness of "dark" bursts is predominantly the result of dust extinction, this might imply that the existing host galaxy sample is strongly biased—because optical afterglows of these events are challenging to detect and optical positions are often used to

identify the host galaxy, hosts for these events may have been missing (or at least, underrepresented) in the pre-*Swift* sample. This is an important point, since it has been previously claimed that GRB hosts themselves are unusually low-luminosity, metal- and dust-poor population (e.g., Le Floc'h et al. 2003, 2006).

The host galaxies of some dark bursts do not appear obviously unusual: the host of GRB 061222A, for example, is a very blue Lyman-alpha emitter, and while the host of GRB 070521 is redder than those of most LGRBs it is not clearly heavily dust-suppressed. But the hosts of GRBs 060923A, 080207 and 080607 do appear to be massive and dust-obscured, and there are tentative suggestions that this may be the case for several other dark events as well. In any event, submillimeter galaxies (e.g., Blain et al. 2002) show that the rest-frame UV is not necessarily representative of the whole stellar population in dusty galaxies (Smail et al. 2004), and further observations (particularly in the near-IR, mid-IR, and longer wavelengths), will be necessary to resolve this question unambiguously. Such a program is already underway: answering this question will be the primary focus of my research for the next several years.

9.1.7 Unusual Host Galaxies and Environments

Finally, in the course of our survey (Chapter 7), we have discovered an array of intriguing individual objects that, prior to this survey, were nearly unprecedented. GRBs 051109B and 060505 occurred in star-forming regions of low-redshift spirals and lacked corresponding supernovae. XRF 060428B is a long GRB which occurred in close proximity to a low-redshift elliptical and may have been gravitationally lensed. SGRB 100206A likely originated from the halo of a dust-enshrouded low-redshift starburst.

9.2 Final Remarks

I have chosen a relatively simple title for this dissertation to encapsulate what is ultimately a complex result: the environments of GRBs are not easily generalized, spanning the full range of observable redshifts and galaxies across the Hubble sequence (and occasionally from intergalactic space). Yet, trends do appear. Conspicuous differences between the LGRB and SGRB host populations are indicative of what appears to be a marked physical separation in their progenitor populations: a massive star for the former class and (likely) some sort of degenerate binary system for the latter. Furthermore, the fact that GRBs occur in a wide variety of galaxy types does not mean that they must do so uniformly, offering a path to determine what, if anything, is "special" about the production of GRBs (and of specific types of GRBs) compared to formation other astronomical objects and transients. Given this, it is clear that future approaches to the subject of GRB host galaxies and environments will have to be addressed systematically, with an understanding of the entire range of GRB classes, their range environments, and the selection effects that factor into our ability to measure them. The dark and dusty bursts and their hosts are of particular

interest: this population is not small, and is of clear importance for the understanding of the cosmic history of the universe, since much of the cosmic story occurs in regions enshrouded from our view by dust. Therefore in addition to the variety of results summarized above, I hope that the most prominent legacy of my work will be to point the way forward for the next generation of large, integrative studies of GRBs and their environments—enabling us to finally unravel Nature's recipe for producing these objects, and with that knowledge, to use these events better understand the grand cosmic story of the birth and evolution of the Universe that continues today.

Bibliography

Abazajian, K. N., et al. 2009, ApJS, 182, 543
Abbott, B., e. 2004, Nucl. Instrum. Methods, A517
—. 2008, ApJ, 681, 1419
Abdo, A. A., et al. 2009a, Nature, 462, 331
—. 2009b, ApJ, 706, L138
—. 2009c, Science, 323, 1688
Acernese, F. e. 2004, Astroparticle Physics, 21, 1
Adelberger, K. L., & Steidel, C. C. 2000, ApJ, 544, 218
Adelman-McCarthy, J. K., et al. 2006, ApJS, 162, 38
—. 2008, ApJS, 175, 297
Afonso, P., et al. 2011, A&A, 526, A154+
Akerlof, C., et al. 1999, Nature, 398, 400
Akerlof, C. W., & Swan, H. F. 2007, ApJ, 671, 1868
Akerlof, C. W., et al. 2003, PASP, 115, 132
Alard, C., & Lupton, R. H. 1998, ApJ, 503, 325
Albert, J., et al. 2006, ApJ, 641, L9
Amati, L., et al. 2002, A&A, 390, 81
Aschenbach, B. 1985, Reports on Progress in Physics, 48, 579
Aslan, Z., et al. 2005, GCN Circular 3198
Atteia, J.-L., et al. 1987, ApJS, 64, 305
Atwood, W. B., et al. 2009, ApJ, 697, 1071
Band, D., et al. 1993, ApJ, 413, 281
Barnard, V. E., et al. 2003, MNRAS, 338, 1
Barris, B. J., Tonry, J. L., Novicki, M. C., & Wood-Vasey, W. M. 2005, AJ, 130, 2272
Barthelmy, S. D., Butterworth, P., Cline, T. L., Gehrels, N., Fishman, G. J., Kouveliotou, C., & Meegan, C. A. 1995, Ap&SS, 231, 235
Barthelmy, S. D., Norris, J., & Ziaeepour, H. 2006, GCN Circular 5931
Barthelmy, S. D., et al. 1994, in American Institute of Physics Conference Series, Vol. 307, Gamma-Ray Bursts, ed. G. J. Fishman, 643
Barthelmy, S. D., et al. 2005, Space Sci. Rev., 120, 143
—. 2009, GCN Circular 9364
Basu, Baidyanath. 2003, An Introduction to Astrophysics (Published by PHI Learning Pvt.

Ltd.)
Beardmore, A. P., Page, K. L., Kennea, J. A., Burrows, D. N., & Ziaeepour, H. 2006, GCN Circular 4895
Belczynski, K., Bulik, T., Heger, A., & Fryer, C. 2007, ApJ, 664, 986
Berger, E. 2006, GCN Circular 5949
—. 2008, GCN Circular 7344
—. 2009, ApJ, 690, 231
—. 2010a, ApJ, 722, 1946
—. 2010b, GCN Circular 10943
Berger, E., & Becker, G. 2005, GCN Circular 3520
Berger, E., Cenko, S. B., Fox, D. B., & Cucchiara, A. 2009, ApJ, 704, 877
Berger, E., Chornock, R., Tanvir, N., Levan, A. J., Fox, D., Cucchiara, A., Fruchter, A., & Graham, J. 2010, GCN Circular 10395
Berger, E., Cowie, L. L., Kulkarni, S. R., Frail, D. A., Aussel, H., & Barger, A. J. 2003a, ApJ, 588, 99
Berger, E., & Fox, D. 2005a, GCN Circular 4316
Berger, E., & Fox, D. B. 2005b, GCN Circular 3291
Berger, E., Fox, D. B., Kulkarni, S. R., Frail, D. A., & Djorgovski, S. G. 2007a, ApJ, 660, 504
Berger, E., Geha, M., & Thompson, I. 2005a, GCN Circular 3753
Berger, E., & Kaplan, D. L. 2007, GCN Circular 6680
Berger, E., & Kulkarni, S. R. 2005, GCN Circular 2978
Berger, E., & McWilliam, A. 2005, GCN Circular 3511
Berger, E., & Murphy, D. 2007, GCN Circular 6686
Berger, E., Price, P. A., & Fox, D. B. 2006, GCN Circular 4622
Berger, E., Shin, M.-S., Mulchaey, J. S., & Jeltema, T. E. 2007b, ApJ, 660, 496
Berger, E., et al. 2002, ApJ, 581, 981
—. 2003b, Nature, 426, 154
—. 2005b, Nature, 438, 988
—. 2005c, ApJ, 629, 328
—. 2007c, ApJ, 664, 1000
Bertin, E., & Arnouts, S. 1996, A&AS, 117, 393
Bertin, E., Mellier, Y., Radovich, M., Missonnier, G., Didelon, P., & Morin, B. 2002, in Astronomical Society of the Pacific Conference Series, Vol. 281, Astronomical Data Analysis Software and Systems XI, ed. D. A. Bohlender, D. Durand, & T. H. Handley, 228
Beskin, G., Karpov, S., Bondar, S., Greco, G., Guarnieri, A., Bartolini, C., & Piccioni, A. 2010, ApJ, 719, L10
Beuermann, K., et al. 1999, A&A, 352, L26
Bikmaev, I., et al. 2006, GCN Circular 4652
Blain, A. W., & Natarajan, P. 2000, MNRAS, 312, L35
Blain, A. W., Smail, I., Ivison, R. J., Kneib, J.-P., & Frayer, D. T. 2002, Phys. Rep., 369, 111

Blake, C., & Bloom, J. S. 2005, GCN Circular 3327
Blake, C. H., Bloom, J. S., Latham, D. W., Szentgyorgyi, A. H., Skrutskie, M. F., Falco, E. E., & Starr, D. S. 2008, PASP, 120, 860
Blake, C. H., et al. 2005, Nature, 435, 181
Blandford, R. D., & McKee, C. F. 1976, Physics of Fluids, 19, 1130
Blinnikov, S. I., Novikov, I. D., Perevodchikova, T. V., & Polnarev, A. G. 1984, Soviet Astronomy Letters, 10, 177
Bloom, J. S. 2005, GCN Circular 3990
—. 2007, GCN Circular 6989
Bloom, J. S., Alatalo, K., & Blake, C. 2006a, GCN Circular 4648
Bloom, J. S., Blake, C. H., Starr, D., & Alatalo, K. 2005a, GCN Circular 4216
Bloom, J. S., Butler, N. R., & Perley, D. A. 2008, in American Institute of Physics Conference Series, Vol. 1000, American Institute of Physics Conference Series, ed. M. Galassi, D. Palmer, & E. Fenimore, 11–15
Bloom, J. S., Charbonneau, D., Holman, M. J., Falco, E. E., & Chen, H. W. 2006b, GCN Circular 5768
Bloom, J. S., Foley, R. J., Koceveki, D., & Perley, D. 2006c, GCN Circular 5217
Bloom, J. S., Kulkarni, S. R., & Djorgovski, S. G. 2002, AJ, 123, 1111
Bloom, J. S., Perley, D., Foley, R., Prochaska, J. X., Chen, H. W., & Starr, D. 2005b, GCN Circular 3758
Bloom, J. S., Perley, D. A., & Chen, H. W. 2006d, GCN Circular 5826
Bloom, J. S., Pollack, L., & Perley, D. A. 2007a, GCN Circular 6572
Bloom, J. S., Sigurdsson, S., & Pols, O. R. 1999, MNRAS, 305, 763
Bloom, J. S., & Starr, D. L. 2008, GCN Circular 7542
Bloom, J. S., Starr, D. L., Blake, C. H., Skrutskie, M. F., & Falco, E. E. 2006e, in ASP Conf. Ser. 351: Astronomical Data Analysis Software and Systems XV, ed. C. Gabriel, C. Arviset, D. Ponz, & S. Enrique, 751
Bloom, J. S., et al. 2004, GCN Circular 2893
—. 2006f, ApJ, 638, 354
—. 2007b, ApJ, 654, 878
—. 2009, ApJ, 691, 723
—. 2011, Science, 333, 203
Boella, G., Butler, R. C., Perola, G. C., Piro, L., Scarsi, L., & Bleeker, J. A. M. 1997, A&AS, 122, 299
Boër, M., Atteia, J. L., Damerdji, Y., Gendre, B., Klotz, A., & Stratta, G. 2006, ApJ, 638, L71
Bolzonella, M., Miralles, J.-M., & Pelló, R. 2000, A&A, 363, 476
Bonnell, J. 1995, http://apod.nasa.gov/htmltest/jbonnell/www/grbhist.html
Bouwens, R. J., Illingworth, G. D., Blakeslee, J. P., & Franx, M. 2006, ApJ, 653, 53
Bouwens, R. J., Illingworth, G. D., Franx, M., & Ford, H. 2007, ApJ, 670, 928
Bouwens, R. J., et al. 2009, ApJ, 705, 936
—. 2010, ApJ, 708, L69

Brecher, K., & Morrison, P. 1974, ApJ, 187, L97
Bromm, V., & Loeb, A. 2002, ApJ, 575, 111
—. 2006, ApJ, 642, 382
Brown, P. J., & Mao, J. 2008, GCN Circular 7675
Budavári, T., et al. 2005, ApJ, 619, L31
Burrows, D. N., Roming, P. W. A., Fox, D. B., Herter, T. L., Falcone, A., Bilén, S., Nousek, J. A., & Kennea, J. A. 2010, in Presented at the Society of Photo-Optical Instrumentation Engineers (SPIE) Conference, Vol. 7732, Society of Photo-Optical Instrumentation Engineers (SPIE) Conference Series
Burrows, D. N., et al. 2005a, Science, 309, 1833
—. 2005b, ApJ, 622, L85
—. 2005c, Space Sci. Rev., 120, 165
Butler, N. 2006, GCN Circular 5953
Butler, N., & Bloom, J. S. 2006, GCN Circular 4600
Butler, N. R. 2007, AJ, 133, 1027
Butler, N. R., Bloom, J. S., & Poznanski, D. 2010, ApJ, 711, 495
Butler, N. R., & Kocevski, D. 2007a, ApJ, 663, 407
—. 2007b, ApJ, 668, 400
Butler, N. R., Kocevski, D., & Bloom, J. S. 2009, ApJ, 694, 76
Butler, N. R., Kocevski, D., Bloom, J. S., & Curtis, J. L. 2007, ApJ, 671, 656
Butler, N. R., et al. 2005, ApJ, 621, 884
—. 2006, ApJ, 652, 1390
Calzetti, D., Armus, L., Bohlin, R. C., Kinney, A. L., Koornneef, J., & Storchi-Bergmann, T. 2000, ApJ, 533, 682
Cameron, P. B. 2005a, GCN Circular 3513
—. 2005b, GCN Circular 3761
Campana, S., & DeLuca, A. 2006, GCN Circular 5157
Campana, S., et al. 2006, A&A, 454, 113
Cappellaro, E., Evans, R., & Turatto, M. 1999, A&A, 351, 459
Cappellaro, E., Turatto, M., Tsvetkov, D. Y., Bartunov, O. S., Pollas, C., Evans, R., & Hamuy, M. 1997, A&A, 322, 431
Cardelli, J. A., Clayton, G. C., & Mathis, J. S. 1989, ApJ, 345, 245
Caroli, E., Stephen, J. B., Di Cocco, G., Natalucci, L., & Spizzichino, A. 1987, Space Sci. Rev., 45, 349
Cash, W. 1976, A&A, 52, 307
Castro-Tirado, A. J., et al. 1998, Science, 279, 1011
—. 2003, A&A, 411, L315
—. 2005, A&A, 439, L15
—. 2007a, GCN Circular 6971
—. 2007b, A&A, 475, 101
—. 2009, GCN Circular 9100
Cavallo, G., & Rees, M. J. 1978, MNRAS, 183, 359

Cenko, S. B. 2005, GCN Circular 3807
—. 2006, GCN Circular 5531
—. 2008, GCN Circular 7429
—. 2009, GCN Circular 9513
Cenko, S. B., Berger, E., & Cohen, J. 2006a, GCN Circular 4592
Cenko, S. B., Bloom, J. S., Perley, D. A., Morgan, A. N., Cobb, B. E., & Levan, A. J. 2010a, GCN Circular 10692
Cenko, S. B., & Fox, D. B. 2006a, GCN Circular 5978
—. 2006b, GCN Circular 5975
Cenko, S. B., Fox, D. B., Cucchiara, A., Schmidt, B. P., Berger, E., Price, P. A., & Roth, K. C. 2007a, GCN Circular 6556
Cenko, S. B., Fox, D. B., Rich, J., Schmidt, B., Christiansen, J., & Berger, E. 2005, GCN Circular 3358
Cenko, S. B., Gezari, S., Small, T., Fox, D. B., & Berger, E. 2007b, GCN Circular 6322
Cenko, S. B., Moon, D. ., & Schmidt, B. P. 2006b, GCN Circular 4636
Cenko, S. B., Ofek, E. O., & Fox, D. B. 2006c, GCN Circular 5529
—. 2007c, GCN Circular 6525
Cenko, S. B., Ofek, E. O., Gelino, D., Thompson, T., Price, P. A., & Berger, E. 2006d, GCN Circular 5457
Cenko, S. B., Ofek, E. O., & Kasliwal, M. 2006e, GCN Circular 5772
—. 2006f, GCN Circular 5770
Cenko, S. B., Perley, D. A., Bloom, J. S., Cobb, B. E., & Morgan, A. N. 2010b, GCN Circular 10339
Cenko, S. B., Price, P. A., & Berger, E. 2007d, GCN Circular 6450
Cenko, S. B., & Rau, A. 2006, GCN Circular 5512
Cenko, S. B., et al. 2006g, ApJ, 652, 490
—. 2006h, PASP, 118, 1396
—. 2008a, ApJ, 677, 441
—. 2008b, ArXiv e-prints, 0802.0874
—. 2009, ApJ, 693, 1484
—. 2010c, ApJ, 711, 641
—. 2010d, AJ, 140, 224
—. 2011, ApJ, 732, 29
Chandra, P., & Frail, D. A. 2007, GCN Circular 5997
Chandra, P., et al. 2008, ApJ, 683, 924
Chary, R., Berger, E., & Cowie, L. 2007, ApJ, 671, 272
Chary, R., & Elbaz, D. 2001, ApJ, 556, 562
Chen, H. ., Glazebrook, K., & Bloom, J. S. 2007a, GCN Circular 6148
Chen, H.-W., Dembicky, J., York, D., Lamb, D., McMillan, R., Ketzeback, B., & Saurage, G. 2007b, GCN Circular 5996
Chen, H.-W., Glazebrook, K., & Bloom, J. S. 2007c, GCN Circular 6145
Chen, H.-W., Prochaska, J. X., & Gnedin, N. Y. 2007d, ApJ, 667, L125

Chen, H.-W., et al. 2009, ApJ, 691, 152
—. 2010, ApJ, 723, L218
—. 2011, ApJ, 727, L53
Chen, S. L., Li, A., & Wei, D. M. 2006, ApJ, 647, L13
Chen, Y. T., Huang, K. Y., Ip, W. H., Urata, Y., Qiu, Y., & Lou, Y. Q. 2005, GCN Circular 4285
Chester, M. M., Koch, T. S., Hoversten, E. A., & Mangano, V. 2010, GCN Circular 11148
Chevalier, R. A. 2007, in 070228: The Next Decade of Gamma-Ray Burst Afterglows, ed. R. A. M. J. Wijers, L. Kaper, & H. J. van Eerten, Conference Proceedings of 070228: The Next Decade of Gamma-Ray Burst Afterglows
Chevalier, R. A., & Li, Z.-Y. 1999, ApJ, 520, L29
Chincarini, G., et al. 2007, ApJ, 671, 1903
Chornock, R., Foley, R. J., Li, W., & Filippenko, A. V. 2008a, GCN Circular 7381
Chornock, R., Li, W., & Filippenko, A. V. 2007, GCN Circular 6304
Chornock, R., Perley, D., Li, W., & Filippenko, A. V. 2008b, GCN Circular 7789
Chornock, R., et al. 2010, ArXiv e-prints, 1004.2262
Christensen, L., Hjorth, J., & Gorosabel, J. 2004, A&A, 425, 913
Church, R. P., Levan, A. J., Davies, M. B., & Tanvir, N. 2011, MNRAS, 413, 2004
Clemens, C., Klose, S., Greiner, J., Yoldas, A. K., Yoldas, A., Kruehler, T., Szokoly, G., & Garching), M. 2008, GCN Circular 7503
Cline, T. L., Desai, U. D., Klebesadel, R. W., & Strong, I. B. 1973, ApJ, 185, L1
Cline, T. L., et al. 1999, A&AS, 138, 557
Cobb, B. E., & Bailyn, C. D. 2008, ApJ, 677, 1157
Cobb, B. E., Bailyn, C. D., van Dokkum, P. G., & Natarajan, P. 2006, ApJ, 651, L85
Cohen, M., Wheaton, W. A., & Megeath, S. T. 2003, AJ, 126, 1090
Colgate, S. A. 1968, Canadian Journal of Physics, 46, 476
—. 1974, ApJ, 187, 333
Conconi, P., et al. 2004, in Presented at the Society of Photo-Optical Instrumentation Engineers (SPIE) Conference, Vol. 5492, Society of Photo-Optical Instrumentation Engineers (SPIE) Conference Series, ed. A. F. M. Moorwood & M. Iye, 1602–1612
Cool, R. J. 2006, GCN Circular 5985
Cool, R. J., et al. 2006, GCN Circular 5863
Copete, A., Grindlay, J., Markwardt, C., & Gehrels, N. 2008, GCN Circular 8661
Costa, E., et al. 1997, Nature, 387, 783
Covino, S., D'Avanzo, P., Malesani, D., Israel, G. L., Piranomonte, S., Tagliaferri, G., Chincarini, G., & Stella, L. 2005, GCN Circular 3616
Covino, S., Malesani, D., & Tagliaferri, G. 2006a, GCN Circular 5604
Covino, S., et al. 2004, in Presented at the Society of Photo-Optical Instrumentation Engineers (SPIE) Conference, Vol. 5492, Society of Photo-Optical Instrumentation Engineers (SPIE) Conference Series, ed. A. F. M. Moorwood & M. Iye, 1613–1622
Covino, S., et al. 2006b, GCN Circular 5234
—. 2006c, A&A, 447, L5

—. 2007, GCN Circular 6190
—. 2008, MNRAS, 388, 347
Cucchiara, A. 2010, GCN Circular 10608
Cucchiara, A., & Fox, D. B. 2008, GCN Circular 7654
Cucchiara, A., Fox, D. B., & Berger, E. 2006, GCN Circular 4729
Cucchiara, A., Fox, D. B., Tanvir, N. R., Levan, A. J., Cobb, B. E., Berger, E., & Chornock, R. 2010, GCN Circular 10374
Cucchiara, A., et al. 2011, ArXiv e-prints
Cucchiara, N., & Fox, D. B. 2010, GCN Circular 10606
Cucchiara, N., Fox, D. B., Tanvir, N., & Berger, E. 2009, GCN Circular 9873
Cummings, J., et al. 2006, GCN Circular 4608
Curran, P. A., et al. 2007, A&A, 467, 1049
Dai, X., et al. 2008, ApJ, 682, L77
Dai, Z. G., & Lu, T. 1999, ApJ, 519, L155
Dai, Z. G., Wang, X. Y., Wu, X. F., & Zhang, B. 2006, Science, 311, 1127
D'Avanzo, P., Covino, S., Israel, G. L., Piranomonte, S., Malesani, D., Tagliaferri, G., Chincarini, G., & Stella, L. 2005, GCN Circular 3644
D'Avanzo, P., Covino, S., Malesani, D., & Tagliaferri, G. 2006a, GCN Circular 5609
D'Avanzo, P., Israel, G. L., & Cosentino, R. 2006b, GCN Circular 4890
D'Avanzo, P., Magazzu, A., de Gurtubai, A. G., & Antonelli, L. A. 2007, GCN Circular 6108
de Luca, A., Esposito, P., Israel, G. L., Götz, D., Novara, G., Tiengo, A., & Mereghetti, S. 2010, MNRAS, 402, 1870
De Pasquale, M., et al. 2003, ApJ, 592, 1018
—. 2006, A&A, 455, 813
De Ugarte Postigo, A., et al. 2007, A&A, 462, L57
D'Elia, V., et al. 2007, A&A, 467, 629
—. 2009a, ApJ, 694, 332
—. 2009b, A&A, 503, 437
Della Valle, M., et al. 2006, Nature, 444, 1050
Dermer, C. D., Chiang, J., & Mitman, K. E. 2000, ApJ, 537, 785
Dessauges-Zavadsky, M., Chen, H.-W., Prochaska, J. X., Bloom, J. S., & Barth, A. J. 2006, ApJ, 648, L89
Dickey, J. M., & Lockman, F. J. 1990, ARA&A, 28, 215
Djorgovski, S. G., Frail, D. A., Kulkarni, S. R., Bloom, J. S., Odewahn, S. C., & Diercks, A. 2001, ApJ, 562, 654
Djorgovski, S. G., et al. 1999, GCN Circular 368
Dolphin, A. E. 2000, PASP, 112, 1397
Draine, B. T. 2003, ARA&A, 41, 241
Draine, B. T. 2009, in Astronomical Society of the Pacific Conference Series, Vol. 414, Cosmic Dust - Near and Far, ed. T. Henning, E. Grün, & J. Steinacker, 453
Draine, B. T., & Hao, L. 2002, ApJ, 569, 780

Dwek, E., Galliano, F., & Jones, A. P. 2007, ApJ, 662, 927
Eddington, A. S. 1926, The Internal Constitution of the Stars (Cambridge University Press)
Eichler, D., & Granot, J. 2006, ApJ, 641, L5
Eichler, D., Livio, M., Piran, T., & Schramm, D. N. 1989, Nature, 340, 126
Elias-Rosa, N., et al. 2006, MNRAS, 369, 1880
Elíasdóttir, Á., et al. 2009, ApJ, 697, 1725
Ellison, S. L., et al. 2006, MNRAS, 372, L38
Evans, P. A., Page, K. L., & Kennea, J. A. 2006, GCN Circular 5947
Evans, P. A., et al. 2007, A&A, 469, 379
—. 2009, MNRAS, 397, 1177
—. 2010, A&A, 519, A102
Evans, W. D., et al. 1980, ApJ, 237, L7
Faber, S. M., et al. 2007, ApJ, 665, 265
Falcone, A. D., et al. 2006, ApJ, 641, 1010
Fan, X., Carilli, C. L., & Keating, B. 2006a, ARA&A, 44, 415
Fan, X., et al. 2006b, AJ, 132, 117
Fenimore, E. E., in 't Zand, J. J. M., Norris, J. P., Bonnell, J. T., & Nemiroff, R. J. 1995, ApJ, 448, L101
Fenimore, E. E., Madras, C. D., & Nayakshin, S. 1996, ApJ, 473, 998
Feroci, M., et al. 1998, A&A, 332, L29
—. 2007, Nuclear Instruments and Methods in Physics Research A, 581, 728
Filippenko, A. V. 1982, PASP, 94, 715
Filippenko, A. V. 2005, in Astronomical Society of the Pacific Conference Series, Vol. 332, The Fate of the Most Massive Stars, ed. R. Humphreys & K. Stanek, 33
Filippenko, A. V., Li, W. D., Treffers, R. R., & Modjaz, M. 2001, in Astronomical Society of the Pacific Conference Series, Vol. 246, IAU Colloq. 183: Small Telescope Astronomy on Global Scales, ed. B. Paczyński, W.-P. Chen, & C. Lemme, 121
Firmani, C., Ghisellini, G., Avila-Reese, V., & Ghirlanda, G. 2006, MNRAS, 370, 185
Fishman, G. J., & Meegan, C. A. 1995, ARA&A, 33, 415
Fishman, G. J., Meegan, C. A., Wilson, R. B., Paciesas, W. S., & Pendleton, G. N. 1992, in NASA Conference Publication, Vol. 3137, NASA Conference Publication, ed. C. R. Shrader, N. Gehrels, & B. Dennis, 26–34
Fitzpatrick, E. L. 1999, PASP, 111, 63
Fitzpatrick, E. L. 2004, in Astronomical Society of the Pacific Conference Series, Vol. 309, Astrophysics of Dust, ed. A. N. Witt, G. C. Clayton, & B. T. Draine, 33
Fitzpatrick, E. L., & Massa, D. 1990, ApJS, 72, 163
Flewelling-Swan, H., et al. 2006, in Bulletin of the American Astronomical Society, Vol. 38, Bulletin of the American Astronomical Society, 134
Foley, R. J., et al. 2006, ApJ, 645, 450
Fong, W., Berger, E., & Fox, D. B. 2010, ApJ, 708, 9
Fong, W., et al. 2011, ApJ, 730, 26
Fox, D. B. 2006, GCN Circular 5607

Fox, D. B., & Cenko, S. B. 2005, GCN Circular 3829
—. 2006, GCN Circular 4723
Fox, D. B., Cenko, S. B., Berger, E., & Morrell, N. 2005a, GCN Circular 3244
Fox, D. B., Rau, A., & Ofek, . E. O. 2006, GCN Circular 5597
Fox, D. B., et al. 2005b, Nature, 437, 845
Frail, D. A. 2005, GCN Circular 4350
Frail, D. A., & Fox, D. 2010, GCN Circular 10611
Frail, D. A., Kulkarni, S. R., Nicastro, L., Feroci, M., & Taylor, G. B. 1997, Nature, 389, 261
Frail, D. A., et al. 2001, ApJ, 562, L55
Frederiks, D. D., Palshin, V. D., Aptekar, R. L., Golenetskii, S. V., Cline, T. L., & Mazets, E. P. 2007, Astronomy Letters, 33, 19
Freiburghaus, C., Rosswog, S., & Thielemann, F.-K. 1999, ApJ, 525, L121
French, J., et al. 2006, GCN Circular 4960
Fruchter, A., Krolik, J. H., & Rhoads, J. E. 2001, ApJ, 563, 597
Fruchter, A. S. 2010, in Bulletin of the American Astronomical Society, Vol. 42, American Astronomical Society Meeting Abstracts 215, 303.06
Fruchter, A. S., et al. 2006, Nature, 441, 463
Fryer, C. L., & Heger, A. 2005, ApJ, 623, 302
Fryer, C. L., Woosley, S. E., & Hartmann, D. H. 1999, ApJ, 526, 152
Fugazza, D., D'Elia, V., D'Avanzo, P., Covino, S., & Tagliaferri, G. 2008, GCN Circular 7293
Fugazza, D., et al. 2006, GCN Circular 5513
—. 2007, GCN Circular 6851
Fynbo, J. P. U., Djupvik, A., Rol, E., & Jaunsen, A. 2006a, GCN Circular 5420
Fynbo, J. P. U., Hjorth, J., Jensen, B. L., Jakobsson, P., Moller, P., & Naranen, J. 2005, GCN Circular 3136
Fynbo, J. P. U., Prochaska, J. X., Sommer-Larsen, J., Dessauges-Zavadsky, M., & Møller, P. 2008, ApJ, 683, 321
Fynbo, J. P. U., Thöne, C. C., Malesani, D., Hjorth, J., Vreeswijk, P. M., & Jakobsson, P. 2007, GCN Circular 6759
Fynbo, J. P. U., et al. 2006b, Nature, 444, 1047
—. 2009, ApJS, 185, 526
Fynbo, J. U., et al. 2001, A&A, 369, 373
Gal-Yam, A., et al. 2006, Nature, 444, 1053
—. 2008, ApJ, 686, 408
Galama, T. J., et al. 1998, Nature, 395, 670
Gallerani, S., Salvaterra, R., Ferrara, A., & Choudhury, T. R. 2008, MNRAS, 388, L84
Garnavich, P., et al. 2007a, GCN Circular 6351
—. 2007b, GCN Circular 6406
—. 2007c, GCN Circular 6462
Garnavich, P. M., Loeb, A., & Stanek, K. Z. 2000, ApJ, 544, L11

Gaskell, C. M., Goosmann, R. W., Antonucci, R. R. J., & Whysong, D. H. 2004, ApJ, 616, 147
Gehrels, N. 2007, GCN Circular 6760
Gehrels, N. 2008, in American Institute of Physics Conference Series, Vol. 968, Astrophysics of Compact Objects, ed. Y.-F. Yuan, X.-D. Li, & D. Lai, 3–8
Gehrels, N., Ramirez-Ruiz, E., & Fox, D. B. 2009, ARA&A, 47, 567
Gehrels, N., et al. 2004, ApJ, 611, 1005
—. 2005, Nature, 437, 851
—. 2006, Nature, 444, 1044
—. 2008, ApJ, 689, 1161
George, K., Banerjee, D. P. K., Chandrasekhar, T., & Ashok, N. M. 2006, ApJ, 640, L13
Ghirlanda, G., Ghisellini, G., & Lazzati, D. 2004, ApJ, 616, 331
Giacconi, R. 1972, ApJ, 173, L79+
Goad, M. R., et al. 2007, A&A, 476, 1401
Godet, O., et al. 2006, A&A, 452, 819
Golenetskii, S., Aptekar, R., Mazets, E., Pal'shin, V., Frederiks, D., & Cline, T. 2007, GCN Circular 6849
—. 2008a, GCN Circular 7487
Golenetskii, S., Aptekar, R., Mazets, E., Pal'shin, V., Frederiks, D., Oleynik, P., Ulanov, M., & Svinkin, D. 2009, GCN Circular 9647
Golenetskii, S., et al. 2008b, GCN Circular 8676
—. 2008c, GCN Circular 7682
Gomboc, A., Steele, I. A., Monfardini, A., Mottram, C. J., Guidorzi, C., Bode, M. F., & Mundell, C. G. 2005a, GCN Circular 3325
Gomboc, A., et al. 2005b, GCN Circular 3706
—. 2008, ApJ, 687, 443
Gordon, K. D. 2005, in American Institute of Physics Conference Series, Vol. 761, The Spectral Energy Distributions of Gas-Rich Galaxies: Confronting Models with Data, ed. C. C. Popescu & R. J. Tuffs, 134–140
Gordon, K. D., Calzetti, D., & Witt, A. N. 1997, ApJ, 487, 625
Gordon, K. D., Clayton, G. C., Misselt, K. A., Landolt, A. U., & Wolff, M. J. 2003, ApJ, 594, 279
Gorosabel, J., et al. 2003, A&A, 400, 127
—. 2006, A&A, 450, 87
Gotz, D., Mereghetti, S., von Kienlin, A., & Beck, M. 2009, GCN Circular 9649
Gou, L.-J., Fox, D. B., & Mészáros, P. 2007, ApJ, 668, 1083
Graham, J. F., et al. 2009, ApJ, 698, 1620
Granot, J. 2005, ApJ, 631, 1022
Granot, J., Königl, A., & Piran, T. 2006, MNRAS, 370, 1946
Granot, J., & Kumar, P. 2006, MNRAS, 366, L13
Granot, J., Nakar, E., & Piran, T. 2003, Nature, 426, 138
Granot, J., Panaitescu, A., Kumar, P., & Woosley, S. E. 2002, ApJ, 570, L61

Granot, J., & Sari, R. 2002, ApJ, 568, 820
Greiner, J., et al. 2008, PASP, 120, 405
—. 2009a, ApJ, 693, 1912
—. 2009b, ApJ, 693, 1610
—. 2009c, A&A, 498, 89
Grindlay, J. E., & Fazio, G. G. 1974, ApJ, 187, L93
Groot, P. J., et al. 1998, ApJ, 493, L27
Grupe, D., et al. 2006, ApJ, 645, 464
—. 2007, ApJ, 662, 443
Guetta, D., et al. 2007, A&A, 461, 95
Guidorzi, C., et al. 2006a, GCN Circular 4661
—. 2006b, GCN Circular 5633
—. 2007a, A&A, 474, 793
—. 2007b, A&A, 463, 539
—. 2009, A&A, 499, 439
—. 2011, "MNRAS accepted"
Gunn, J. E., & Peterson, B. A. 1965, ApJ, 142, 1633
Guziy, S., Castro-Tirado, A. J., Postigo, A. d. U., Gorosabel, J., Cruz, J. d. L., Bogdanov, O., & Jelnek, M. 2005a, GCN Circular 3584
Guziy, S., Jelinek, M., Gorosabel, J., Castro-Tirado, A. J., Postigo, A. d. U., Flores, E. R., & Vijanen, K. 2005b, GCN Circular 4025
Haislip, J. B., et al. 2006, Nature, 440, 181
Hakkila, J., Giblin, T. W., Norris, J. P., Fragile, P. C., Bonnell, J. T., & Wells, M. 2008, in American Institute of Physics Conference Series, Vol. 1000, American Institute of Physics Conference Series, ed. M. Galassi, D. Palmer, & E. Fenimore, 109–112
Halpern, J. P. 2005, GCN Circular 3900
Halpern, J. P., & Armstrong, E. 2006, GCN Circular 5849
Halpern, J. P., & Mirabal, N. 2006, GCN Circular 4749
Harrison, F. A., et al. 2001, ApJ, 559, 123
Hartmann, D. H., & Woosley, S. E. 1995, Advances in Space Research, 15, 143
Hartmann, D. H., et al. 2009, in Astronomy, Vol. 2010, astro2010: The Astronomy and Astrophysics Decadal Survey, 115
Harwit, M., & Salpeter, E. E. 1973, ApJ, 186, L37
Hashimoto, T., et al. 2010, ApJ, 719, 378
Hattori, T., Aoki, K., & Kawai, N. 2007a, GCN Circular 6441
—. 2007b, GCN Circular 6444
Hawking, S. W. 1974, Nature, 248, 30
Hearty, F., Bayliss, M., Lamb, D. Q., McMillan, R., Ketzeback, B., Barentine, J., Dembicky, J., & York, D. G. 2006, GCN Circular 4753
Hearty, F., et al. 2005, GCN Circular 3583
Heise, J., in't Zand, J., Kippen, R. M., & Woods, P. M. 2001, in Gamma-ray Bursts in the Afterglow Era, ed. E. Costa, F. Frontera, & J. Hjorth, 16

Heng, K., Lazzati, D., Perna, R., Garnavich, P., Noriega-Crespo, A., Bersier, D., Matheson, T., & Pahre, M. 2008, ApJ, 681, 1116
Hillenbrand, L. A., Foster, J. B., Persson, S. E., & Matthews, K. 2002, PASP, 114, 708
Hinshaw, G., et al. 2009, ApJS, 180, 225
Hirschi, R., Meynet, G., & Maeder, A. 2005, A&A, 443, 581
Hjorth, J., et al. 2003, Nature, 423, 847
—. 2005a, ApJ, 630, L117
—. 2005b, Nature, 437, 859
Hogg, D. W., Pahre, M. A., McCarthy, J. K., Cohen, J. G., Blandford, R., Smail, I., & Soifer, B. T. 1997, MNRAS, 288, 404
Holland, S. T., et al. 2003, AJ, 125, 2291
—. 2007, AJ, 133, 122
Horst, A. J. v. d., Wijers, R. A. M. J., Wiersema, K., & Rol, E. 2007, GCN Circular 6549
Hoyle, F., & Clayton, D. D. 1974, ApJ, 191, 705
Huang, F. Y., Huang, K. Y., Ip, W. H., Urata, Y., Qiu, Y., & Lou, Y. Q. 2005, GCN Circular 4231
Huang, K. Y., Urata, Y., & Tsai, P. 2010, GCN Circular 10692
Huang, Y. F., Cheng, K. S., & Gao, T. T. 2006, ApJ, 637, 873
Hudec, R., Borovicka, J., Peresty, R., Danis, S., & Franc, V. 1988, Advances in Space Research, 8, 665
Hudec, R., Peresty, R., & Motch, C. 1990, A&A, 235, 174
Hunt, L., Palazzi, E., Rossi, A., Savaglio, S., Cresci, G., Klose, S., Michalowski, M., & Pian, E. 2011, ArXiv e-prints
Hurley, K., et al. 2005, Nature, 434, 1098
Im, M., Choi, C., Jun, H., Kang, E., Urata, Y., Choi, P., Sakamoto, T., & Gehrels, N. 2010, GCN Circular 11222
Immler, S., Starling, R. L. C., Evans, P. A., Barthelmy, S. D., & Sakamoto, T. 2010, GCN Reports, 273.1, GCN Report 273.1
Ishimura, T., Shimokawabe, T., Vasquez, N., Yatsu, Y., Kudou, Y., & Kawai, N. 2007, GCN Circular 6430
Izzard, R. G., Ramirez-Ruiz, E., & Tout, C. A. 2004, MNRAS, 348, 1215
Jakobsson, P., Hjorth, J., Fynbo, J. P. U., Watson, D., Pedersen, K., Björnsson, G., & Gorosabel, J. 2004a, ApJ, 617, L21
Jakobsson, P., Paraficz, D., Telting, J., Fynbo, J. P. U., Jensen, B. L., Hjorth, J., & Ceron, J. M. C. 2005a, GCN Circular 4015
Jakobsson, P., Vreeswijk, P. M., Malesani, D., Jaunsen, A. O., Fynbo, J. P. U., Hjorth, J., & Tanvir, N. R. 2008, GCN Circular 7286
Jakobsson, P., et al. 2003, A&A, 408, 941
—. 2004b, A&A, 427, 785
—. 2005b, MNRAS, 362, 245
—. 2006, A&A, 447, 897
Janka, H.-T., Eberl, T., Ruffert, M., & Fryer, C. L. 1999, ApJ, 527, L39

Jaunsen, A. O., et al. 2008, ApJ, 681, 453
Jelínek, M., Tristram, P., Postigo, A. d. U., Gorosabel, J., Hale, F., Gilmore, A., Kilmartin, P., & Castro-Tirado, A. J. 2007, GCN Circular 6338
Jelinek, M., et al. 2008, GCN Circular 7648
Jelnek, M., et al. 2005, GCN Circular 4358
Jensen, B. L., Gorosabel, J., Laursen, P., Jakobsson, P., Watson, D., Fynbo, J. P. U., & Hjorth, J. 2005, GCN Circular 3243
Jester, S., et al. 2005, AJ, 130, 873
Jordi, K., Grebel, E. K., & Ammon, K. 2006, A&A, 460, 339
Joye, W. A., & Mandel, E. 2003, in Astronomical Society of the Pacific Conference Series, Vol. 295, Astronomical Data Analysis Software and Systems XII, ed. H. E. Payne, R. I. Jedrzejewski, & R. N. Hook, 489–+
Junkkarinen, V. T., Cohen, R. D., Beaver, E. A., Burbidge, E. M., Lyons, R. W., & Madejski, G. 2004, ApJ, 614, 658
Kanbach, G., et al. 1988, Space Sci. Rev., 49, 69
Kann, D. A. 2006, GCN Circular 4577
Kann, D. A., Klose, S., & Zeh, A. 2006a, ApJ, 641, 993
Kann, D. A., Masetti, N., & Klose, S. 2007, AJ, 133, 1187
Kann, D. A., Palazzi, E., Masetti, N., & Maiorano, E. 2006b, GCN Circular 5025
Kann, D. A., et al. 2010, ApJ, 720, 1513
—. 2011, ApJ, 734, 96
Kasliwal, M. M., et al. 2008, ApJ, 678, 1127
Katz, J. I. 1994, ApJ, 422, 248
Katz, J. I., & Canel, L. M. 1996, ApJ, 471, 915
Kawai, N., et al. 2006, Nature, 440, 184
Kennea, J. A., Hurkett, C. P., Burrows, D. N., Mangano, V., Sakamoto, T., & Gehrels, N. 2005, GCN Circular 3295
Kennicutt, Jr., R. C. 1998, ARA&A, 36, 189
Kewley, L. J., Geller, M. J., & Jansen, R. A. 2004, AJ, 127, 2002
Khamitov, I., et al. 2006a, GCN Circular 4494
—. 2006b, GCN Circular 4493
—. 2009, GCN Circular 9597
Kim, D.-C., & Sanders, D. B. 1998, ApJS, 119, 41
Klebesadel, R., et al. 1982, ApJ, 259, L51
Klebesadel, R. W., Strong, I. B., & Olson, R. A. 1973, ApJ, 182, L85
Klotz, A., Boer, M., & Atteia, J. L. 2006, GCN Circular 4495
—. 2008a, GCN Circular 7280
Klotz, A., Gendre, B., Atteia, J. L., Boër, M., Coward, D. M., & Imerito, A. C. 2009, ApJ, 697, L18
Klotz, A., et al. 2008b, A&A, 483, 847
Kluzniak, W., & Lee, W. H. 1998, ApJ, 494, L53
Kobayashi, S. 2000, ApJ, 545, 807

Kobayashi, S., Piran, T., & Sari, R. 1997, ApJ, 490, 92
Kobayashi, S., & Zhang, B. 2003, ApJ, 582, L75
Kobayashi, Y., et al. 2003, in Presented at the Society of Photo-Optical Instrumentation Engineers (SPIE) Conference, Vol. 4837, Society of Photo-Optical Instrumentation Engineers (SPIE) Conference Series, ed. J. M. Oschmann & L. M. Stepp, 954–964
Kocevski, D., Bloom, J. S., Thöne, C. C., & Prochaska, J. 2007a, GCN Circular 6771
Kocevski, D., Butler, N., & Bloom, J. S. 2007b, ApJ, 667, 1024
Kocevski, D., et al. 2010, MNRAS, 404, 963
Kosugi, G., Kawai, N., Aoki, K., Hattori, T., Ohta, K., & Yamada, T. 2005, GCN Circular 3263
Kouveliotou, C., Meegan, C. A., Fishman, G. J., Bhat, N. P., Briggs, M. S., Koshut, T. M., Paciesas, W. S., & Pendleton, G. N. 1993, ApJ, 413, L101
Kouveliotou, C., et al. 1994, ApJ, 422, L59
Krimm, H., et al. 2007, GCN Circular 6732
Krühler, T., et al. 2008, ApJ, 685, 376
—. 2009a, ApJ, 697, 758
—. 2009b, A&A, 508, 593
Kulkarni, S. R. 2005, ArXiv e-prints, 0510256
Kulkarni, S. R., et al. 1998, Nature, 393, 35
—. 1999, Nature, 398, 389
Kumar, P., & Granot, J. 2003, ApJ, 591, 1075
Kumar, P., & Panaitescu, A. 2000, ApJ, 541, L51
—. 2008, MNRAS, 391, L19
Kumar, P., & Piran, T. 2000a, ApJ, 535, 152
—. 2000b, ApJ, 532, 286
Küpcü Yoldaş, A., Krühler, T., Greiner, J., Yoldaş, A., Clemens, C., Szokoly, G., Primak, N., & Klose, S. 2008, in American Institute of Physics Conference Series, Vol. 1000, American Institute of Physics Conference Series, ed. M. Galassi, D. Palmer, & E. Fenimore, 227–231
Kurucz, R. L. 1979, ApJS, 40, 1
Lamb, D. Q. 1995, PASP, 107, 1152
Lamb, D. Q., Nysewander, M., Hearty, F., Chen, H. ., & Reichart, D. E. 2006, GCN Circular 5079
Lamb, D. Q., & Reichart, D. E. 2000, ApJ, 536, 1
Landolt, A. U. 1992, AJ, 104, 340
—. 2009, AJ, 137, 4186
Lapshov, I., et al. 2008, GCN Circular 7697
Laros, J. G. 1988, Nature, 333, 124
Laros, J. G., et al. 1981, ApJ, 245, L63
—. 1987, ApJ, 320, L111
Lattimer, J. M., & Schramm, D. N. 1976, ApJ, 210, 549
Laursen, L. T., & Stanek, K. Z. 2003, ApJ, 597, L107
Lazzati, D., Covino, S., & Ghisellini, G. 2002a, MNRAS, 330, 583

Lazzati, D., & Perna, R. 2007, MNRAS, 375, L46
Lazzati, D., Rossi, E., Covino, S., Ghisellini, G., & Malesani, D. 2002b, A&A, 396, L5
Le, T., & Dermer, C. D. 2007, ApJ, 661, 394
Le Floc'h, E., Charmandaris, V., Forrest, W. J., Mirabel, I. F., Armus, L., & Devost, D. 2006, ApJ, 642, 636
Le Floc'h, E., et al. 2003, A&A, 400, 499
—. 2005, ApJ, 632, 169
Ledoux, C., Vreeswijk, P., Smette, A., Jaunsen, A., & Kaufer, A. 2006, GCN Circular 5237
Lee, W. H., & Ramirez-Ruiz, E. 2007, New Journal of Physics, 9, 17
Lee, W. H., Ramirez-Ruiz, E., & Granot, J. 2005a, ApJ, 630, L165
Lee, W. H., Ramirez-Ruiz, E., & Page, D. 2004, ApJ, 608, L5
—. 2005b, ApJ, 632, 421
Leibler, C. N., & Berger, E. 2010, ApJ, 725, 1202
Levan, A., et al. 2005, ApJ, 624, 880
—. 2006a, ApJ, 647, 471
Levan, A. J., Copperwheat, C., Breedt, E., & Malesani, D. 2010a, GCN Circular 10672
Levan, A. J., Cucchiara, A., Tanvir, N. R., & Fox, D. 2010b, GCN Circular 10706
Levan, A. J., Rol, E., Tanvir, N. R., Fruchter, A., Rhoads, J., Davis, C., & Adamson, A. 2006b, GCN Circular 5461
Levan, A. J., Tanvir, N. R., Rol, E., Fruchter, A., & Adamson, A. 2006c, GCN Circular 5455
Levan, A. J., Tanvir, N. R., Wiersema, K., Niederste-Ostholt, M., Malesani, D., Leloudas, G., & Xu, D. 2010c, GCN Circular 10386
Levan, A. J., Wiersema, K., Tanvir, N., & Copperwheat, C. 2010d, GCN Circular 11145
Levan, A. J., et al. 2006d, ApJ, 648, L9
—. 2006e, ApJ, 648, 1132
—. 2011, Science, 333, 199
Levesque, E. M., Kewley, L. J., Berger, E., & Zahid, H. J. 2010a, AJ, 140, 1557
Levesque, E. M., et al. 2010b, MNRAS, 401, 963
Levinson, A., & Eichler, D. 2000, Physical Review Letters, 85, 236
Li, A., Liang, S. L., Kann, D. A., Wei, D. M., Klose, S., & Wang, Y. J. 2008a, ApJ, 685, 1046
Li, L.-X. 2008, MNRAS, 388, 1487
Li, L.-X., & Paczyński, B. 1998, ApJ, 507, L59
Li, W. 2006, GCN Circular 4725
Li, W., & Bloom, J. 2006, GCN Circular 5532
Li, W., Chornock, R., Filippenko, A. V., & Berkeley, U. o. C. a. 2008b, GCN Circular 7441
Li, W., Chornock, R., Perley, D. A., & Filippenko, A. V. 2008c, GCN Circular 7959
Li, W., Filippenko, A. V., Chornock, R., & Jha, S. 2003a, ApJ, 586, L9
—. 2003b, PASP, 115, 844
Li, W., Jha, S., Filippenko, A. V., Bloom, J. S., Pooley, D., Foley, R. J., & Perley, D. A. 2006, PASP, 118, 37
Li, W. D., et al. 2000, in American Institute of Physics Conference Series, Vol. 522, American

Institute of Physics Conference Series, ed. S. S. Holt & W. W. Zhang, 103–106
Li, Y., Li, A., & Wei, D. M. 2008d, ApJ, 678, 1136
Li, Z.-Y., & Chevalier, R. A. 2003, in Lecture Notes in Physics, Berlin Springer Verlag, Vol. 598, Supernovae and Gamma-Ray Bursters, ed. K. Weiler, 419–444
Liang, S. L., & Li, A. 2009, ApJ, 690, L56
Lin, R. P., et al. 2002, Sol. Phys., 210, 3
Lin, Z. Y., Huang, K. Y., Ip, W. H., Urata, Y., Qiu, Y., & Lou, Y. Q. 2005, GCN Circular 3593
Lipkin, Y. M., et al. 2004, ApJ, 606, 381
Lisenfeld, U., Israel, F. P., Stil, J. M., & Sievers, A. 2002, A&A, 382, 860
MacFadyen, A. I., Ramirez-Ruiz, E., & Zhang, W. 2005, ArXiv e-prints, 0510192
MacFadyen, A. I., & Woosley, S. E. 1999, ApJ, 524, 262
Madau, P. 1995, ApJ, 441, 18
Maiolino, R., Schneider, R., Oliva, E., Bianchi, S., Ferrara, A., Mannucci, F., Pedani, M., & Roca Sogorb, M. 2004, Nature, 431, 533
Malesani, D. 2006, GCN Circular 5456
Malesani, D. 2009, GCN Circular 9526
Malesani, D., D'Avanzo, P., Palazzi, E., Israel, G. L., Chincarini, G., Stella, L., & Pedani, M. 2005, GCN Circular 3582
Malesani, D., Fynbo, J. P. U., Vreeswijk, P. M., & Ilyn, I. 2007a, GCN Circular 6674
Malesani, D., Hjorth, J., Fynbo, J. P. U., Sollerman, J., Olofsson, G., Paraficz, D., & Durant, M. 2007b, GCN Circular 6555
Malesani, D., & Patat, F. 2006, GCN Circular 5450
Malesani, D., & Piranomonte, S. 2006a, GCN Circular 5422
—. 2006b, GCN Circular 4645
Malesani, D., Stempels, E., Fynbo, J. P. U., & Hjorth, J. 2007c, GCN Circular 5990
Malesani, D., et al. 2004, ApJ, 609, L5
Mangano, V., et al. 2007, A&A, 470, 105
Mao, J., & Guidorzi, C. 2008, GCN Circular 7583
Marisaldi, M., et al. 2008, GCN Circular 7457
Markwardt, C. B., Gavriil, F. P., Palmer D. M. Baumgartner, W. H., & Barthelmy, S. 2009, GCN Circular 9645
Masetti, N., et al. 2003, A&A, 404, 465
Matzner, C. D. 2003, MNRAS, 345, 575
Mazets, E. P., et al. 1981, Ap&SS, 80, 3
—. 2008, ApJ, 680, 545
McCarthy, J. K., et al. 1998, in Presented at the Society of Photo-Optical Instrumentation Engineers (SPIE) Conference, Vol. 3355, Society of Photo-Optical Instrumentation Engineers (SPIE) Conference Series, ed. S. D'Odorico, 81–92
McLean, I. S., et al. 1993, in Presented at the Society of Photo-Optical Instrumentation Engineers (SPIE) Conference, Vol. 1946, Society of Photo-Optical Instrumentation Engineers (SPIE) Conference Series, ed. A. M. Fowler, 513–533

McLean, I. S., et al. 1994, in Presented at the Society of Photo-Optical Instrumentation Engineers (SPIE) Conference, Vol. 2198, Society of Photo-Optical Instrumentation Engineers (SPIE) Conference Series, ed. D. L. Crawford & E. R. Craine, 457–466
McNaught, R., & Price, P. A. 2005, GCN Circular 3163
McQuinn, M., Lidz, A., Zaldarriaga, M., Hernquist, L., & Dutta, S. 2008, MNRAS, 388, 1101
Meegan, C., et al. 2009, ApJ, 702, 791
Melandri, A. 2007, GCN Circular 6621
Melandri, A., et al. 2007, GCN Circular 6727
Mészáros, P. 2002, ARA&A, 40, 137
—. 2006, Reports on Progress in Physics, 69, 2259
Meszaros, P., & Rees, M. J. 1992, ApJ, 397, 570
—. 1993, ApJ, 405, 278
—. 1997, ApJ, 476, 232
Metzger, B. D., Piro, A. L., & Quataert, E. 2008a, MNRAS, 390, 781
—. 2009, MNRAS, 396, 304
Metzger, B. D., Quataert, E., & Thompson, T. A. 2008b, MNRAS, 385, 1455
Metzger, M. R., Djorgovski, S. G., Kulkarni, S. R., Steidel, C. C., Adelberger, K. L., Frail, D. A., Costa, E., & Frontera, F. 1997, Nature, 387, 878
Miller, A. A., Perley, D. A., Bloom, J. S., Cenko, S. B., & Nugent, P. E. 2010, GCN Circular 10377
Mineo, T., et al. 2007, A&A, 469, 663
Minezaki, T., & Price, P. A. 2007, GCN Circular 6456
Mirabal, N., & Halpern, J. P. 2006, GCN Circular 5097
Mirabal, N., Halpern, J. P., & O'Brien, P. T. 2007, ApJ, 661, L127
Misra, K., Pandey, S. B., Roy, R., & Castro-Tirado, A. J. 2007, GCN Circular 6840
Misselt, K. A., Clayton, G. C., & Gordon, K. D. 1999, ApJ, 515, 128
Mochkovitch, R., Hernanz, M., Isern, J., & Martin, X. 1993, Nature, 361, 236
Modjaz, M., Kewley, L., Bloom, J. S., Filippenko, A. V., Perley, D., & Silverman, J. M. 2011, ApJ, 731, L4
Modjaz, M., et al. 2008, AJ, 135, 1136
—. 2009, ApJ, 702, 226
Molinari, E., et al. 2007, A&A, 469, L13
Monet, D. G., et al. 2003, AJ, 125, 984
Moretti, A. 2006, GCN Circular 4801
Moretti, A., et al. 2006, A&A, 448, L9
Morgan, A. N., Bloom, J. S., & Klein, C. R. 2009, GCN Circular 9635
Morgan, H. L., & Edmunds, M. G. 2003, MNRAS, 343, 427
Morris, D. C., et al. 2007, ApJ, 654, 413
Morsony, B. J., Lazzati, D., & Begelman, M. C. 2010, ApJ, 723, 267
Motch, C., Ilovaisky, S. A., Chevalier, C., Pedersen, H., Hurley, K., & Pizzichini, G. 1985, A&A, 145, 201

Motta, V., et al. 2002, ApJ, 574, 719
Mundell, C. G., & Steele, I. A. 2006, GCN Circular 5119
Mundell, C. G., et al. 2006, GCN Circular 4726
Nakar, E. 2007, Phys. Rep., 442, 166
Nakar, E., Gal-Yam, A., & Fox, D. B. 2006, ApJ, 650, 281
Nakar, E., & Granot, J. 2007a, MNRAS, 380, 1744
—. 2007b, MNRAS, 380, 1744
Nakar, E., & Piran, T. 2002, ApJ, 572, L139
—. 2003, ApJ, 598, 400
Nakar, E., Piran, T., & Granot, J. 2003, New Astronomy, 8, 495
Naoz, S., & Bromberg, O. 2007, MNRAS, 380, 757
Narayan, R., Paczyński, B., & Piran, T. 1992, ApJ, 395, L83
Nestor, D. B., Turnshek, D. A., & Rao, S. M. 2005, ApJ, 628, 637
Noll, S., Pierini, D., Pannella, M., & Savaglio, S. 2007, A&A, 472, 455
Norris, J. P. 1995, Ap&SS, 231, 95
Norris, J. P., & Bonnell, J. T. 2006, ApJ, 643, 266
Norris, J. P., Cline, T. L., Desai, U. D., & Teegarden, B. J. 1984, Nature, 308, 434
Norris, J. P., Marani, G. F., & Bonnell, J. T. 2000, ApJ, 534, 248
Noterdaeme, P., Ledoux, C., Srianand, R., Petitjean, P., & Lopez, S. 2009, A&A, 503, 765
Nousek, J. A., et al. 2006, ApJ, 642, 389
Nysewander, M., Fruchter, A. S., & Pe'er, A. 2009a, ApJ, 701, 824
Nysewander, M., Reichart, D. E., Crain, J. A., Foster, A., Haislip, J., Ivarsen, K., Lacluyze, A., & Trotter, A. 2009b, ApJ, 693, 1417
Nysewander, M. C., et al. 2006, ApJ, 651, 994
Oates, S. R., et al. 2007, MNRAS, 380, 270
—. 2009, MNRAS, 395, 490
O'Brien, P. T., et al. 2006, ApJ, 647, 1213
Odewahn, S. C., et al. 1998, ApJ, 509, L5
Ofek, E. O., & Berger, E. 2007, GCN Circular 6275
Ofek, E. O., & Cenko, S. B. 2006, GCN Circular 5458
Ofek, E. O., Cenko, S. B., Gal-Yam, A., Peterson, B., Schmidt, B. P., Fox, D. B., & Price, P. A. 2006, GCN Circular 5123
Ohno, M., et al. 2008, PASJ, 60, 361
Oke, J. B. 1974, ApJS, 27, 21
Oke, J. B., et al. 1995, PASP, 107, 375
Olivares, F., Kruehler, T., & Greiner, J. 2010, GCN Circular 10676
Olivares, F., Rossi, A., Greiner, J., Yoldas, A., & Yoldas, A. K. 2009a, GCN Circular 8812
Olivares, F., et al. 2009b, GCN Circular 9874
Omodei, N. 2008, GCN Circular 8407
Onda, K., et al. 2008, GCN Circular 7508
Ovaldsen, J.-E., et al. 2007, ApJ, 662, 294
Paciesas, W. S., et al. 1999, ApJS, 122, 465

Paczyński, B. 1991, Acta Astronomica, 41, 257
—. 1995, PASP, 107, 1167
Paczyński, B., & Rhoads, J. E. 1993, ApJ, 418, L5
Pagani, C., Morris, D., & Burrows, D. N. 2006, GCN Circular 5393
Pagani, C., Racusin, J. L., Kuin, N. P. M., Holland, S. T., Barthelmy, S. D., & Gehrels, N. 2007, GCN Reports, 97.1, GCN Report 97.1
Page, D. N., & Hawking, S. W. 1976, ApJ, 206, 1
Page, K. L., et al. 2006a, ApJ, 637, L13
—. 2006b, GCN Circular 5823
—. 2007, ApJ, 663, 1125
—. 2009, MNRAS, 395, 328
Panaitescu, A. 2007, MNRAS, 379, 331
Panaitescu, A., Meszaros, P., & Rees, M. J. 1998, ApJ, 503, 314
Panaitescu, A., & Vestrand, W. T. 2008, MNRAS, 387, 497
Pandey, S. B., et al. 2010, ApJ, 714, 799
Parola, V. L., Mangano, V., Kennea, J. A., Burrows, D. N., Sakamoto, T., Hurkett, C. P., & Gehrels, N. 2005, GCN Circular 3362
Pei, Y. C. 1992, ApJ, 395, 130
Pellizza, L. J., Duc, P. ., Floc'h, E. L., & Mirabel, I. F. 2006a, GCN Circular 5269
Pellizza, L. J., et al. 2006b, A&A, 459, L5
Peng, C. Y., Ho, L. C., Impey, C. D., & Rix, H.-W. 2002, AJ, 124, 266
Peng, F., Königl, A., & Granot, J. 2005, ApJ, 626, 966
Penprase, B. E., et al. 2006, ApJ, 646, 358
Perley, D., & Kemper, Y. 2008, in American Institute of Physics Conference Series, Vol. 1000, American Institute of Physics Conference Series, ed. M. Galassi, D. Palmer, & E. Fenimore, 631–634
Perley, D. A. 2009, GCN Circular 9514
—. 2010, GCN Circular 10806
Perley, D. A., & Bloom, J. S. 2007, GCN Circular 6091
Perley, D. A., Bloom, J. S., Butler, N. R., Li, W., & Chen, H.-W. 2007a, in American Institute of Physics Conference Series, Vol. 937, Supernova 1987A: 20 Years After: Supernovae and Gamma-Ray Bursters, ed. S. Immler, K. Weiler, & R. McCray, 526–529
Perley, D. A., Bloom, J. S., Foley, R. J., & Kocevski, D. 2007b, GCN Circular 6465
Perley, D. A., Bloom, J. S., Modjaz, M., Miller, A. A., Shiode, J., Brewer, J., Starr, D., & Kennedy, R. 2008a, GCN Circular 7889
Perley, D. A., Bloom, J. S., Modjaz, M., Poznanski, D., & Thöne, C. C. 2007c, GCN Circular 7140
Perley, D. A., Bloom, J. S., Prochaska, J. X., Stanford, S., Brodwin, M., & Butler, N. R. 2007d, GCN Circular 6451
Perley, D. A., Cenko, S. B., & Bloom, J. S. 2009a, GCN Circular 9873
Perley, D. A., Chornock, R., & Bloom, J. S. 2008b, GCN Circular 7962
Perley, D. A., Chornock, R., Bloom, J. S., Fassnacht, C., & Auger, M. W. 2007e, GCN

Circular 6850
Perley, D. A., Foley, R. J., Bloom, J. S., & Butler, N. R. 2006, GCN Circular 5387
Perley, D. A., Prochaska, J. X., & Hennawi, J. 2008c, GCN Circular 7706
Perley, D. A., Thöne, C. C., & Bloom, J. S. 2007f, GCN Circular 6774
Perley, D. A., Thöne, C. C., Cooke, J., Bloom, J. S., & Barton, E. 2007g, GCN Circular 6739
Perley, D. A., et al. 2008d, ApJ, 688, 470
—. 2008e, ApJ, 672, 449
—. 2009b, ApJ, 696, 1871
—. 2009c, AJ, 138, 1690
—. 2010, MNRAS, 406, 2473
Perna, R., & Lazzati, D. 2002, ApJ, 580, 261
Perna, R., Lazzati, D., & Fiore, F. 2003, ApJ, 585, 775
Phillips, A. C., Miller, J., Cowley, D., & Wallace, V. 2006, in Presented at the Society of Photo-Optical Instrumentation Engineers (SPIE) Conference, Vol. 6269, Ground-based and Airborne Instrumentation for Astronomy. Edited by McLean, Ian S.; Iye, Masanori. Proceedings of the SPIE, Volume 6269, pp. 62691O (2006).
Pian, E., et al. 2006, Nature, 442, 1011
Piran, T. 1999, Phys. Rep., 314, 575
—. 2000, Phys. Rep., 333, 529
Piran, T., Shemi, A., & Narayan, R. 1993, MNRAS, 263, 861
Piranomonte, S., et al. 2008a, A&A, 492, 775
—. 2008b, A&A, 491, 183
Podsiadlowski, P., Mazzali, P. A., Nomoto, K., Lazzati, D., & Cappellaro, E. 2004, ApJ, 607, L17
Pollack, L. K., Chen, H.-W., Prochaska, J. X., & Bloom, J. S. 2009, ApJ, 701, 1605
Popham, R., Woosley, S. E., & Fryer, C. 1999, ApJ, 518, 356
Postigo, A. d. U., Aceituno, F., Castro-Tirado, A. J., & Kubanek, P. 2006, GCN Circular 5509
Postigo, A. d. U., Castro-Tirado, A. J., Jelinek, M., Kubanek, P., Cunniffe, R., Vitek, S., Gorosabel, J., & Skillen, I. 2007, GCN Circular 6361
Pozanenko, A., Shulga, A., Volnova, A., Hafizov, B., Asfandiyarov, I., & Ibrahimov, M. 2007, GCN Circular 6407
Price, P. A. 2006, GCN Circular 5104
Price, P. A., Cenko, S. B., & Fox, D. B. 2006, GCN Circular 5101
Price, P. A., et al. 2002, ApJ, 572, L51
—. 2003, Nature, 423, 844
—. 2007, ApJ, 663, L57
Prieto, J., et al. 2007, GCN Circular 6374
Prochaska, J. X. 2006, ApJ, 650, 272
Prochaska, J. X., Chen, H.-W., & Bloom, J. S. 2006a, ApJ, 648, 95
Prochaska, J. X., Chen, H.-W., Dessauges-Zavadsky, M., & Bloom, J. S. 2007a, ApJ, 666,

267
Prochaska, J. X., Chen, H.-W., Wolfe, A. M., Dessauges-Zavadsky, M., & Bloom, J. S. 2008a, ApJ, 672, 59
Prochaska, J. X., Ellison, S., Foley, R. J., Bloom, J. S., & Chen, H. . 2005, GCN Circular 3332
Prochaska, J. X., Foley, R. J., Holden, B., Magee, D., Cooper, M., & Dutton, A. 2008b, GCN Circular 7397
Prochaska, J. X., et al. 2006b, ApJ, 642, 989
—. 2007b, ApJS, 168, 231
—. 2009, ApJ, 691, L27
Prochter, G. E., Prochaska, J. X., & Burles, S. M. 2006a, ApJ, 639, 766
Prochter, G. E., et al. 2006b, ApJ, 648, L93
Quimby, R., Fox, D., Hoeflich, P., Roman, B., & Wheeler, J. C. 2005, GCN Circular 4221
Quimby, R. M., et al. 2006, ApJ, 640, 402
Racusin, J., Starling, R. L. C., Hoversten, E., & Sakamoto, T. 2010, GCN Reports, 273.1, GCN Report 273.1
Racusin, J. L., et al. 2008, Nature, 455, 183
—. 2009, ApJ, 698, 43
Ramaprakash, A. N., et al. 1998, Nature, 393, 43
Ramirez-Ruiz, E., Granot, J., Kouveliotou, C., Woosley, S. E., Patel, S. K., & Mazzali, P. A. 2005, ApJ, 625, L91
Ramirez-Ruiz, E., Merloni, A., & Rees, M. J. 2001, MNRAS, 324, 1147
Ramirez-Ruiz, E., Trentham, N., & Blain, A. W. 2002, MNRAS, 329, 465
Rau, A., Kasliwal, M. M., & Cenko, S. B. 2007, GCN Circular 6436
Rau, A., Ofek, E. O., & Fox, D. B. 2006, GCN Circular 5598
Rauch, M. 1998, ARA&A, 36, 267
Reddy, N. A., & Steidel, C. C. 2009, ApJ, 692, 778
Reddy, N. A., Steidel, C. C., Pettini, M., Adelberger, K. L., Shapley, A. E., Erb, D. K., & Dickinson, M. 2008, ApJS, 175, 48
Reed, S. G., Van Atta, R. H., & Deitchman, S. J. 1990, DARPA Technical Accomplishments: An Historical Review of Selected DARPA Projects, Volume I, Vol. 1 (Defense Advanced Research Projects Agency)
Rees, M. J. 1999, A&AS, 138, 491
Rees, M. J., & Meszaros, P. 1992, MNRAS, 258, 41P
—. 1994, ApJ, 430, L93
—. 1998, ApJ, 496, L1
Reichart, D. E. 2001, ApJ, 553, 235
Reichart, D. E., & Price, P. A. 2002, ApJ, 565, 174
Retter, A., et al. 2005, GCN Circular 3525
Rhoads, J. 2005a, GCN Circular 3531
—. 2005b, GCN Circular 3527
Rhoads, J. E. 1997, ApJ, 487, L1

Rich, J., Schmidt, B., & Christiansen, J. 2005, GCN Circular 3338
Ricker, G. R., et al. 2003, in American Institute of Physics Conference Series, Vol. 662, Gamma-Ray Burst and Afterglow Astronomy 2001: A Workshop Celebrating the First Year of the HETE Mission, ed. G. R. Ricker & R. K. Vanderspek, 3–16
Rinner, C., & Kugel, F. 2008, GCN Circular 7670
Robertson, B. E., Ellis, R. S., Dunlop, J. S., McLure, R. J., & Stark, D. P. 2010, Nature, 468, 49
Rockosi, C., et al. 2010, in Presented at the Society of Photo-Optical Instrumentation Engineers (SPIE) Conference, Vol. 7735, Society of Photo-Optical Instrumentation Engineers (SPIE) Conference Series
Rodgers, C. T., Canterna, R., Smith, J. A., Pierce, M. J., & Tucker, D. L. 2006, AJ, 132, 989
Rol, E., Tanvir, N., Levan, A., & Fuhrman, L. 2007a, GCN Circular 6294
Rol, E., Tanvir, N., & Mundell, C. 2006, GCN Circular 4855
Rol, E., et al. 2007b, ApJ, 669, 1098
—. 2007c, MNRAS, 374, 1078
Romano, P., et al. 2006, A&A, 456, 917
Roming, P. W. A., et al. 2005, Space Sci. Rev., 120, 95
—. 2009, ApJ, 690, 163
Rossi, A., et al. 2008, A&A, 491, L29
Rossi, E. M., & Begelman, M. C. 2009, MNRAS, 392, 1451
Rosswog, S. 2007, MNRAS, 376, L48
Rosswog, S., Liebendörfer, M., Thielemann, F.-K., Davies, M. B., Benz, W., & Piran, T. 1999, A&A, 341, 499
Rosswog, S., & Ramirez-Ruiz, E. 2003, MNRAS, 343, L36
Rosswog, S., Ramirez-Ruiz, E., & Davies, M. B. 2003, MNRAS, 345, 1077
Rowlinson, A., et al. 2010, MNRAS, 409, 531
Ruderman, M. A., & Sutherland, P. G. 1975, ApJ, 196, 51
Ruiz-Velasco, A. E., et al. 2007, ApJ, 669, 1
Rujopakarn, W., Guver, T., Pandey, S. B., & Yuan, F. 2009, GCN Circular 9515
Rujopakarn, W., Swan, H., Rykoff, E. S., & Schaefer, B. 2005, GCN Circular 4247
Rumyantsev, V., Biryukov, V., Pozanenko, A., & Ibrahimov, M. 2005a, GCN Circular 4094
—. 2005b, GCN Circular 4087
Rumyantsev, V., & Pozanenko, A. 2008, GCN Circular 7891
Rumyantsev, V., Shakhovskoy, D., Biryukov, V., & Pozanenko, A. 2007, GCN Circular 6484
Rykoff, E. S., et al. 2004, ApJ, 601, 1013
—. 2006, ApJ, 638, L5
—. 2009, ApJ, 702, 489
Sakamoto, T., et al. 2006, in American Institute of Physics Conference Series, Vol. 836, Gamma-Ray Bursts in the Swift Era, ed. S. S. Holt, N. Gehrels, & J. A. Nousek, 43–47
Sakamoto, T., et al. 2011, ApJS, 195, 2
Salvaterra, R., et al. 2009, Nature, 461, 1258

Sari, R., & Esin, A. A. 2001, ApJ, 548, 787
Sari, R., & Piran, T. 1995, ApJ, 455, L143+
—. 1997, ApJ, 485, 270
—. 1999a, ApJ, 520, 641
—. 1999b, A&AS, 138, 537
Sari, R., Piran, T., & Halpern, J. P. 1999, ApJ, 519, L17
Sari, R., Piran, T., & Narayan, R. 1998, ApJ, 497, L17
Savaglio, S., & Fall, S. M. 2004, ApJ, 614, 293
Savaglio, S., Fall, S. M., & Fiore, F. 2003, ApJ, 585, 638
Sbarufatti, B., et al. 2006, GCN Reports, 16.2, GCN Report 16.2
Schady, P., & Mangano, V. 2008, GCN Circular 7858
Schady, P., Page, M., Cucchiara, A., Marshall, F., & Gehrels, N. 2006, GCN Circular 4437
Schady, P., et al. 2007, MNRAS, 377, 273
—. 2010, MNRAS, 401, 2773
Schaefer, B. E. 1981, Nature, 294, 722
Schaefer, B. E. 1992, in Gamma-Ray Bursts - Observations, Analyses and Theories, ed. Ho, C., Epstein, R. I., & Fenimore, E. E., 107–112
—. 2007, ApJ, 660, 16
Schaefer, B. E., Yost, S. A., & Yuan, F. 2006, GCN Circular 5629
Schaefer, B. E., et al. 1984, ApJ, 286, L1
Schlegel, D. J., Finkbeiner, D. P., & Davis, M. 1998, ApJ, 500, 525
Schmidt, B., Berger, E., Kakazu, Y., Cowie, L., & Cenko, B. 2006, GCN Circular 4639
Schmidt, B. P., et al. 1998, ApJ, 507, 46
Seab, C. G., & Shull, J. M. 1983, ApJ, 275, 652
Shao, L., & Dai, Z. G. 2005, ApJ, 633, 1027
Sheffer, Y., Prochaska, J. X., Draine, B. T., Perley, D. A., & Bloom, J. S. 2009, ApJ, 701, L63
Sheinis, A. I., Bolte, M., Epps, H. W., Kibrick, R. I., Miller, J. S., Radovan, M. V., Bigelow, B. C., & Sutin, B. M. 2002, PASP, 114, 851
Shen, R.-F., Willingale, R., Kumar, P., O'Brien, P. T., & Evans, P. A. 2009, MNRAS, 393, 598
Shih, C. Y., Lee, Y. H., Urata, Y., & Huang, K. Y. 2007, GCN Circular 6846
Skrutskie, M. F., et al. 2006, AJ, 131, 1163
Skvarc, J. 2006, GCN Circular 5511
Sloan, G. C., et al. 2009, Science, 323, 353
Smail, I., Chapman, S. C., Blain, A. W., & Ivison, R. J. 2004, ApJ, 616, 71
Smith, A. R., et al. 2002, in Presented at the Society of Photo-Optical Instrumentation Engineers (SPIE) Conference, Vol. 4669, Society of Photo-Optical Instrumentation Engineers (SPIE) Conference Series, ed. M. M. Blouke, J. Canosa, & N. Sampat, 172–183
Soderberg, A. M. 2005, GCN Circular 3187
Soderberg, A. M., et al. 2005, ApJ, 627, 877
—. 2007, ApJ, 661, 982

—. 2008, Nature, 453, 469
Sofia, S., & van Horn, H. M. 1974, ApJ, 194, 593
Sommer, M., et al. 1994, ApJ, 422, L63
Sota, A., Castro-Tirado, A. J., Guziy, S., Jelnek, M., Postigo, A. d. U., Gorosabel, J., Bodganov, A., & Ramrez, M. D. P. 2005, GCN Circular 3705
Srianand, R., Gupta, N., Petitjean, P., Noterdaeme, P., & Saikia, D. J. 2008, MNRAS, 391, L69
Stanek, K. Z., et al. 2003, ApJ, 591, L17
—. 2006, Acta Astron., 56, 333
Steele, I. A., Mundell, C. G., Smith, R. J., Kobayashi, S., & Guidorzi, C. 2009, Nature, 462, 767
Stetson, P. B. 1987, PASP, 99, 191
Stone, R. P. S. 1977, ApJ, 218, 767
Stratta, G., Perna, R., Lazzati, D., Fiore, F., Antonelli, L. A., & Conciatore, M. L. 2005, A&A, 441, 83
Stratta, G., et al. 2007, A&A, 474, 827
—. 2009, A&A, 503, 783
Sturner, S. J., Seifert, H., Shrader, C., & Teegarden, B. J. 2000, in American Institute of Physics Conference Series, Vol. 510, American Institute of Physics Conference Series, ed. M. L. McConnell & J. M. Ryan, 814
Sudilovsky, V., Savaglio, S., Vreeswijk, P., Ledoux, C., Smette, A., & Greiner, J. 2007, ApJ, 669, 741
Sudilovsky, V., Smith, D., & Savaglio, S. 2009, ApJ, 699, 56
Sugita, S., et al. 2008, in American Institute of Physics Conference Series, Vol. 1000, American Institute of Physics Conference Series, ed. M. Galassi, D. Palmer, & E. Fenimore, 354–357
Svensson, K. M., et al. 2011, MNRAS submitted
Swan, H., Schaefer, B. E., & Rykoff, E. S. 2007, GCN Circular 6734
Tagliaferri, G., et al. 2005, A&A, 443, L1
Tanvir, N., Levan, A., Jarvis, M., & Wold, T. 2006a, GCN Circular 5587
Tanvir, N., et al. 2005, GCN Circular 3031
Tanvir, N. R., Levan, A. J., Cucchiara, A., Fox, D., Cobb, B. E., & Mason, R. 2010, GCN Circular 10366
Tanvir, N. R., Levan, A. J., Wiersema, K., Fruchter, A. S., & Graham, J. 2008a, GCN Circular 8698
Tanvir, N. R., Rol, E., & Stephens, A. 2008b, GCN Circular 7488
Tanvir, N. R., Rol, E., Wiersema, K., Starling, R., & O'Mahoney, N. 2006b, GCN Circular 4897
Tanvir, N. R., et al. 2008c, MNRAS, 388, 1743
—. 2009, Nature, 461, 1254
Tavani, M., et al. 2009, A&A, 502, 995
Thöne, C., et al. 2005, GCN Circular 4291

Thöne, C. C., Cia, A. D., Malesani, D., & Vreeswijk, P. M. 2008a, GCN Circular 7587
Thöne, C. C., Fynbo, J. P. U., & Jakobsson, P. 2006a, GCN Circular 5747
Thöne, C. C., Fynbo, J. P. U., Jakobsson, P., Vreeswijk, P. M., & Hjorth, J. 2006b, GCN Circular 5812
Thöne, C. C., Henriksen, C., & Wiersema, K. 2006c, GCN Circular 5672
Thöne, C. C., Kann, D. A., Augusteijn, T., & Reyle-Laffont, C. 2007a, GCN Circular 6154
Thöne, C. C., Malesani, D., Fynbo, J. P. U., Henriksen, C., & Sharapov, D. 2006d, GCN Circular 5799
Thöne, C. C., Nilsson, K., Jensen, B. L., & Fynbo, J. 2006e, GCN Circular 5003
Thöne, C. C., Perley, D. A., & Bloom, J. S. 2007b, GCN Circular 6663
Thöne, C. C., et al. 2008b, ApJ, 676, 1151
Tosti, G., et al. 2004, in Presented at the Society of Photo-Optical Instrumentation Engineers (SPIE) Conference, Vol. 5492, Society of Photo-Optical Instrumentation Engineers (SPIE) Conference Series, ed. A. F. M. Moorwood & M. Iye, 689–700
Totani, T., Kawai, N., Kosugi, G., Aoki, K., Yamada, T., Iye, M., Ohta, K., & Hattori, T. 2006, PASJ, 58, 485
Tristram, P., Jelinek, M., Castro-Tirado, A. J., Postigo, A. d. U., Guziy, S., Gorosabel, J., & Yock, P. 2005, GCN Circular 4055
Troja, E., King, A. R., O'Brien, P. T., Lyons, N., & Cusumano, G. 2008, MNRAS, 385, L10
Tueller, J., et al. 2005, GCN Circular 3251
—. 2007, GCN Circular 6365
Uhm, Z. L., & Beloborodov, A. M. 2007, ApJ, 665, L93
Updike, A. C., Bryngelson, G., & Hartmann, D. H. 2008a, GCN Circular 7765
Updike, A. C., Hartmann, D. H., Klose, S., & Fruchter, A. 2007, GCN Circular 5994
Updike, A. C., et al. 2008b, ApJ, 685, 361
Valencic, L. A., Clayton, G. C., & Gordon, K. D. 2004, ApJ, 616, 912
Valencic, L. A., Clayton, G. C., Gordon, K. D., & Smith, T. L. 2003, ApJ, 598, 369
Van Dam, M. A., Le Mignant, D., & Macintosh, B. A. 2004, Applied Optics, 43, 5458
van Paradijs, J., Kouveliotou, C., & Wijers, R. A. M. J. 2000, ARA&A, 38, 379
van Paradijs, J., et al. 1997, Nature, 386, 686
Vestrand, W. T., et al. 2002, in Presented at the Society of Photo-Optical Instrumentation Engineers (SPIE) Conference, Vol. 4845, Advanced Global Communications Technologies for Astronomy II. Edited by Kibrick, Robert I. Proceedings of the SPIE, Volume 4845, pp. 126-136 (2002)., ed. R. I. Kibrick, 126–136
Vestrand, W. T., et al. 2005, Nature, 435, 178
—. 2006, Nature, 442, 172
Vetere, L., Burrows, D. N., Gehrels, N., Meszaros, P., Morris, D. C., & Racusin, J. L. 2008, in American Institute of Physics Conference Series, Vol. 1000, American Institute of Physics Conference Series, ed. M. Galassi, D. Palmer, & E. Fenimore, 191–195
Vetere, L., Racusin, J., Burrows, D. N., & Pagani, C. 2007, GCN Circular 6068
Vietri, M., & Stella, L. 1999, ApJ, 527, L43
Villasenor, J. S., et al. 2005, Nature, 437, 855

Vrba, F. J., et al. 2000, ApJ, 528, 254
Vreeswijk, P. M., et al. 2007, A&A, 468, 83
Wainscoat, R. J., & Cowie, L. L. 1992, AJ, 103, 332
Wainwright, C., Berger, E., & Penprase, B. E. 2007, ApJ, 657, 367
Walker, M. A. 1998, MNRAS, 294, 307
—. 2001, MNRAS, 321, 176
Wang, W., Kakazu, Y., Schmidt, B. P., & Cowie, L. L. 2006a, GCN Circular 4637
Wang, W.-H., Kakazu, Y., Schmidt, B. P., Cowie, L. L., Cenko, S. B., & Moon, D.-S. 2006b, GCN Circular 4653
Wang, X., Wang, L., Pain, R., Zhou, X., & Li, Z. 2006c, ApJ, 645, 488
Watson, D., et al. 2006, ApJ, 652, 1011
Waxman, E., & Draine, B. T. 2000, ApJ, 537, 796
Wei, D. M. 2003, A&A, 402, L9
Weingartner, J. C., & Draine, B. T. 2001, ApJ, 548, 296
Wiersema, K., Tanvir, N., Vreeswijk, P., Fynbo, J., Starling, R., Rol, E., & Jakobsson, P. 2008, GCN Circular 7517
Williams, G. G., Milne, P. A., Park, H. S., Barthelmy, S. D., Hartmann, D. H., Updike, A., & Hurley, K. 2008, in American Institute of Physics Conference Series, Vol. 1000, American Institute of Physics Conference Series, ed. M. Galassi, D. Palmer, & E. Fenimore, 535–538
Williams, G. G., et al. 2004, in American Institute of Physics Conference Series, Vol. 727, American Institute of Physics Conference Series, ed. E. Fenimore, 723–727
Wolf, C., & Podsiadlowski, P. 2007, MNRAS, 375, 1049
Woods, P. M., & Thompson, C. 2006, in Compact stellar X-ray sources, ed. Lewin, W. H. G. & van der Klis, M. (Cambridge University Press), 547–586
Woosley, S. E. 1993, ApJ, 405, 273
Woosley, S. E., & Bloom, J. S. 2006, ARA&A, 44, 507
Woosley, S. E., & Heger, A. 2006, ApJ, 637, 914
Woźniak, P. R., Vestrand, W. T., Panaitescu, A. D., Wren, J. A., Davis, H. R., & White, R. R. 2009, ApJ, 691, 495
Woźniak, P. R., Vestrand, W. T., Wren, J. A., White, R. R., Evans, S. M., & Casperson, D. 2006, ApJ, 642, L99
Wren, J., Vestrand, W. T., Wozniak, P., White, R., & Evans, S. 2005, GCN Circular 3604
Wright, E. L., et al. 2010, AJ, 140, 1868
Xin, L.-P., et al. 2011, MNRAS, 410, 27
Yanagisawa, K., Toda, H., & Kawai, N. 2006, GCN Circular 4496
Yonetoku, D., Murakami, T., Nakamura, T., Yamazaki, R., Inoue, A. K., & Ioka, K. 2004, ApJ, 609, 935
Yoon, S., & Langer, N. 2005, A&A, 443, 643
Yoshii, Y. 2002, in New Trends in Theoretical and Observational Cosmology, ed. Sato, K. and Shiromizu, T., New Trends in Theoretical and Observational Cosmology (Universal Academy Press), 235
Yoshii, Y., Kobayashi, Y., & Minezaki, T. 2003, in Bulletin of the American Astronomical

Society, Vol. 35, American Astronomical Society Meeting Abstracts #202, 752
Yost, S. A., Harrison, F. A., Sari, R., & Frail, D. A. 2003, ApJ, 597, 459
Yost, S. A., et al. 2007, ApJ, 657, 925
Zafar, T., Watson, D. J., Malesani, D., Vreeswijk, P. M., Fynbo, J. P. U., Hjorth, J., Levan, A. J., & Michałowski, M. J. 2010, A&A, 515, A94
Zane, S., et al. 2006, GCN Circular 5936
Zeh, A., Kann, D. A., Klose, S., Manning, A., & Riddle, C. 2005, GCN Circular 3646
Zerbi, R. M., et al. 2001, Astronomische Nachrichten, 322, 275
Zhang, B., Fan, Y. Z., Dyks, J., Kobayashi, S., Mészáros, P., Burrows, D. N., Nousek, J. A., & Gehrels, N. 2006, ApJ, 642, 354
Zhang, B., Kobayashi, S., & Mészáros, P. 2003, ApJ, 595, 950
Zhang, B., Zhang, B.-B., Liang, E.-W., Gehrels, N., Burrows, D. N., & Mészáros, P. 2007, ApJ, 655, L25
Zhang, B., et al. 2009, ApJ, 703, 1696
Zhou, H., Ge, J., Lu, H., Wang, T., Yuan, W., Jiang, P., & Shan, H. 2010, ApJ, 708, 742
Zwicky, F. 1974, Ap&SS, 28, 111
Zytkow, A. N. 1990, ApJ, 359, 138

Appendix A

Afterglow Light Curve Fitting Methodology

The explosion of a gamma-ray burst into a gaseous medium creates a bright broadband electromagnetic *afterglow*, as discussed in detail in Section 1.2. The characteristics of this short-lived transient emission—in particular, its spectral energy distribution (SED) and temporal evolution (light curve) have been successfully described, at least in broader terms, by the basic model of synchrotron emission from a relativistic shockwave first described by Paczyński & Rhoads (1993) and Meszaros & Rees (1997), and further refined by Sari et al. (1998) and numerous later works after this predicted emission was actually detected.

While a GRB afterglow provides a wealth of information, the unpredictability and short-lived nature of a GRB afterglow makes it challenging to study. Different telescopes spaced around the world observe an afterglow at different times, in different filters, and to different image depths, often resulting in highly non-uniform and irregular coverage. Interpretation of such data is not always straightforward: the signatures of interesting physical processes can be subtle and are easily glossed over in basic analysis of such a complicated data set; even fairly basic measurements (such as the construction of an instantaneous spectral energy distribution) can be subject to significant errors if not handled properly. In particular, it is often standard practice to assume that GRB light curves are fully achromatic, or to dismiss color changes based on little more than visual inspection of the data — yet, theory predicts should afterglows should strongly evolve in color under certain conditions.

In the course of my thesis work, I developed a semi-empirical procedure for modeling GRB light curves in a way that explicitly incorporates the possiblity of complex temporal evolution and color change within the surprisingly diverse early-to-late-time light curves of these remarkable events. Essentially all of the afterglows presented throughout this work were modeled with this tool, which is implemented as the code `lcurve` within IDL. I present a brief, unified description of the fitting procedure, relevant to all of Chapters 2–6, below.

A.1 Assumed Input Data Properties

While usable in principle to describe the evolution of a GRB afterglow at any wavelength, the fitting procedure and codes were designed to fit optical data (I define optical here in the broader sense of the full UV-visible-NIR range between 1000–25000Å.) These observations consist of, usually, a table of values with two dependent variables (frequency and time) and one independent variable (magnitude, which is translated to a flux F_ν. This is subsequently written simply as "Flux" in this Appendix to avoid confusion with the flux-scaling parameters $F_{c,f}$ and to avoid conflicting use of subscripts). The distribution of times can be arbitrary—it does not matter whether or not exposures were simultaneous; however, it is assumed that the "frequencies" are distributed over only a relatively small number of specific, recognized filters. The number of unique filters must be significantly less than the number of data points to avoid underconstraining the problem (since among the fitted parameters is a single flux-scaling parameter for each filter, $F_{c,f}$).

A.2 Mathematical Model

Both theoretical motivation and observational precendent demonstrate that almost any GRB light curve can be described as a broken power-law. On short timescales, the observed flux varies as Flux $\propto (t - t_0)^{-\alpha}$, where α is the power-law "decay index" (note the negative sign convention, which we employ throughout this thesis) and $t0$ is usually the start time of the GRB prompt emission. On longer timescales, the decay index α may change: a period of slow decay may steepen to fast decay, or a fast-decaying component may be subsumed by a slower-decaying component. To allow for the former case, we employ the Beuermann function (from Beuermann et al. 1999). This function describes a smoothly-broken power-law; i.e., a power-law that gently rolls from one index α_b to another index α_a (the subscripts stand for "before" and "after" the break time $t_{\rm break}$):

$$\text{Flux} \propto \left(0.5\,(\frac{t}{t_{\rm break}})^{-s\alpha_b} + 0.5\,(\frac{t}{t_{\rm break}})^{-s\alpha_a} \right)^{-\frac{1}{s}} \tag{A.1}$$

This function includes a "sharpness" parameter s that describes how sharp (large values of s) or smooth (small values of s) the break is. (As s approaches zero, the broken power-law approaches a single power-law, so unbroken power-laws are implemented by setting s to zero.) The value of s is usually not very well-constrained unless there is excellent data sampling near the break-time and is typically fixed to 1 in the modeling.

A single Beuermann function allows only for a steepening decay index ($\alpha_a > \alpha_b$), including a rising light curve that peaks and then falls. A curve with a steep-to-shallow transition can modeled by summing a series of Beuermann components, i.e.:

$$\begin{aligned}\text{Flux}_f &= +F_{0,f}\left(\left(\tfrac{t-t0_0}{t_{\text{break0},\nu}}\right)^{-s_0\alpha_{0,b}} + \left(\tfrac{t-t0_0}{t_{\text{break0,f}}}\right)^{-s_0\alpha_{0,a}}\right)^{-\frac{1}{s_0}} \\ &\quad +F_{1,f}\left(\left(\tfrac{t-t0_1}{t_{\text{break1},\nu}}\right)^{-s_1\alpha_{1,b}} + \left(\tfrac{t-t0_1}{t_{\text{break1,f}}}\right)^{-s_1\alpha_{1,a}}\right)^{-\frac{1}{s_1}} \\ &\quad +F_{2,f}\left(\left(\tfrac{t-t0_2}{t_{\text{break2},\nu}}\right)^{-s_2\alpha_{2,b}} + \left(\tfrac{t-t0_2}{t_{\text{break2,f}}}\right)^{-s_2\alpha_{2,a}}\right)^{-\frac{1}{s_2}} \\ &\quad +...\end{aligned} \tag{A.2}$$

Or, in series notation:

$$\text{Flux}_f = \sum_{c=0}^{n} F_{c,f}\left(\left(\frac{t-t0_c}{t_{c,f}}\right)^{-s_c\alpha_{c,b}} + \left(\frac{t-t0_c}{t_{\text{c},f}}\right)^{-s_c\alpha_{c,a}}\right)^{-\frac{1}{s_c}} \tag{A.3}$$

All summed components (c indicates the integer component index) are permitted to have different sharpnesses s_c and even different start times $t0_c$ (typically, $t0$ is fixed to 0 for all parameters, but this can be changed or fitted). The break times can depend on the filter f as well as on the component, allowing arbitrary color change between all different sections of the power-law. Many types of complicated light curves, including those with features like, flares, bumps, wiggles, etc. can be fit to remarkable precision with this model, although we note that the model conspicuously *cannot* yet handle a light curve that steepens twice (becomes steeper, and then steepens further with no breaks in between), though such a behavior would not be overly difficult to implement in the future. (Such a light curve has yet to come up in my own modeling, though it has been seen in some GRBs analyzed elsewhere.)

As described, this model has too many parameters to be applicable to real light curves without further constraints in almost any real case, since we usually do not have good measurements at all frequencies during each different segment of the light curve: we are forced to make some simplifying behaviors about the behavior of the SED.

Basic afterglow theory dictates that, when the afterglow is not in the middle of a spectral and temporal break such as a cooling break, the SED should also obey a simple power-law: i.e., over a limited range in frequency space the intrinsic spectrum of an afterglow follows the form:

$$F_\nu \propto t^{-\alpha}\nu^{-\beta}$$

It would be tempting to make β a free parameter in the fit in addition to α. However, the SED is also subject to the influence of intervening gas and dust (both within our Galaxy and within the host galaxy) that makes the SED which is actually observed very different from a power-law. While in principle the modeling of this extinction and absorption could be handled at the same time as the light curve modeling, it is more convenient from a practical and presentational standpoint to separate the problem into two parts: first, to model the detailed temporal properties of the light curve and construct an idealized observed SED at a single epoch (that is, the SED that would be observed if all observations were exactly simultaneous), and then as a separate to fit that SED using a wide range of different dust models.

The goal, then, is to construct a model that both allows for a completely arbitrary observed SED, but explicitly modeles the spectral *evolution* using a small number of meaningful parameters. I do this by restricting the color evolution to a change in the *underlying intrinsic spectral index* between components, and that the non-power-law absorption remains fixed throughout. Suppose that the intrinsic spectrum (the $F_{c,f}$ parameters) of component 0 can be described as:

$$F_{0,f} = A_f(\frac{\nu}{\nu_{\rm ref}})^{\beta_0}$$

where A_f represents the extinction and absorption factors (or any other completely arbitrary non-power-law behavior in the SED.) Then, similarly, we can write the flux parameters of component 1 as:

$$F_{1,f} = A_f S_1(\frac{\nu}{\nu_{\rm ref}})^{\beta_1}$$

(S_1 is an overall flux-scaling factor, and $\nu_{\rm ref}$ is the frequency of an arbitrary reference filter, such as R-band.)

By calculating the ratio, the unevolving (and non-power-law) term (A_ν) drops out, and β_0 and β_1 merge into a single parameter indicating the color change:

$$\frac{F_{1,f}}{F_{0,f}} = S_1(\frac{\nu}{\nu_{\rm ref}})^{-\beta_0+\beta_1} = S_1(\frac{\nu}{\nu_{\rm ref}})^{-\Delta\beta_{0,1}} \tag{A.4}$$

In this model, then, the vector of free flux parameters over each filter $F_{1,f}$ is reduced to only two parameters, regardless of the number of filters: a color-change parameter $\Delta\beta_{0,1}$ and a flux-scaling factor S_1. Additional components have $\Delta\beta_{0,2}$ and S_2, $\Delta\beta_{0,3}$ and S_3, etc. Component "0" is designated the reference component.

In addition to permitting color change between the summed components (i.e. during a steep-to-shallow transition), I wish to allow the color to change across a temporal break (i.e. during a shallow-to-steep transition or a peak in the light curve.) This is only slightly more complicated to implement. Instead of constraining the flux terms directly, instead I tie the frequency/filter-dependent *peak time* appropriately (in order for the color of a component to change across a break, the different frequencies must peak at different times: for example, for a red-to-blue transition, the red components must peak first and therefore begin fading before the blue filters.) Mathematically, this constraint is expressed (for the peaks at frequencies $\nu_f 0$ and $\nu_f 1$) and as:

$$(\frac{t_{\rm break0}, f0}{t_{\rm break1}, f1}) = (\frac{\nu_y}{\nu_x})^{\Delta\beta_{0,b-a}/(\alpha_{0,b}-\alpha_{0,a})} \tag{A.5}$$

This reduces the vector of filter-dependent break time parameters for a component (component 0, in this case) to a single parameter $\Delta\beta_{0,b-a}$.

A demonstration of the types of color-change fitted is given in Figure A.1. In this test example, the data were constructed artificially (with noise added) using the parameters given

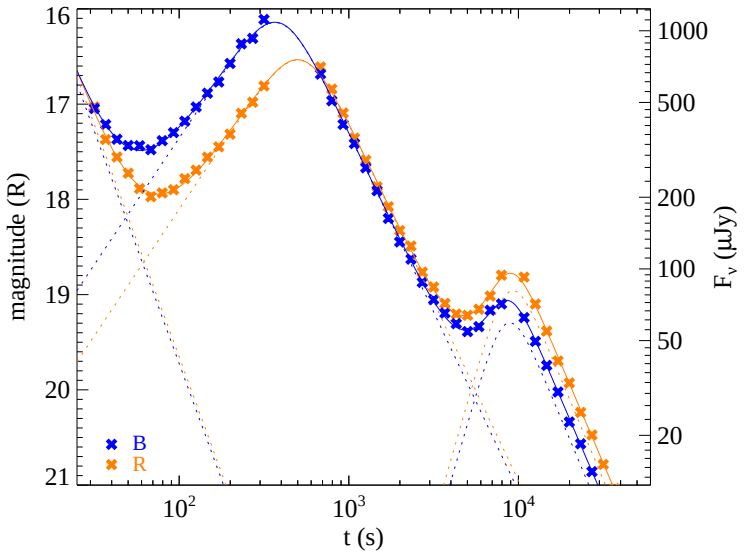

Figure A.1 Illustration of a fit to an artificial GRB afterglow with highly chromatic behavior. The software implemented can accurately deal with power-law color evolution between different components and across a break in the light-curve.

in Table A.1. The "afterglow" changes with each power-law segment, a feature which which is reproduced accurately by the data.

A.3 Implementation and Usage

The numerical light-curve fitter is incorporated into a broader program called `lcurve`, implemented in IDL, which also reads the light curve data from disk and makes customizable, publication-ready plots of the data and fitted curves.

Within `lcurve`, the photometric data table is input as an arbitrarily-formatted text file. Lines starting with a special character (the percent sign %) are used to indicate table headings, allowing the table format (order and nature of input columns) to be customized, and even changed repeatedly throughout the input file. This allows data to be copied and pasted directly from external tables using different formats without having to manually re-order columns.

The actual numerical implementation of the fitting i handled by the `mpfit` library[1] using a Levenberg-Marquardt least-squares algorithm. The fitting function can involve involve an arbitrary number of summed components, and the various fitting variables can be fixed by the user—an exercise that is almost always necessary, since even with the constraints above, some components cannot always be well-constrained by the data and must be fixed. An

[1] `http://cow.physics.wisc.edu/~craigm/idl/idl.html`

Table A.1 Test fit results

Input parameter	Fitted parameter
$\alpha_0 = 2.0$	$\alpha_0 = 1.95 \pm 0.09$
$\alpha_{1,b} = -1.0$	$\alpha_{1,b} = -1.06 \pm 0.03$
$\alpha_{1,a} = 1.5$	$\alpha_{1,a} = 1.50 \pm 0.02$
$\alpha_{2,b} = -2.0$	$\alpha_{2,b} = -2.48 \pm 0.12$
$\alpha_{2,a} = 1.7$	$\alpha_{2,a} = 1.70 \pm 0.01$
$\beta_0 = 0$	
$\beta_{1,a} - \beta_0 = 0.0$	$\Delta\beta_{0,1} = 0.09 \pm 0.08$
$\beta_{1,a} - \beta_{1,b} = 2.0$	$\Delta\beta_{1,b-a} = 2.02 \pm 0.05$
$\beta_{1,a} - \beta_0 = 0.7$	$\Delta\beta_{0,2} = 0.81 \pm 0.08$
$\beta_{2,a} - \beta_{2,b} = 0.4$	$\Delta\beta_{2,b-a} = 0.45 \pm 0.09$

Results of a fit to the simplified test data shown in Figure A.1. Because in normal cases the true intrinsic values of the SED are masked by extinction and other effects, the light curve fitter solves for the difference in the spectral indices β. All input parameters are reproduced with values close to the input values, though larger-than-expected deviation is seen for $\alpha_{2,b}$.

Table A.2 All light curve fitting parameters

Parameter	Description
F_f	Flux in each filter at f at component 0 break time
S_c	Flux in reference filter at component c break time
$\alpha_{c,b}$	Pre-break decay index
$\alpha_{c,a}$	Post-break decay index
$t0_c$	Power-law reference time
s_c	Sharpness
$t_{\mathrm{break},c}$	Break time in reference filter
$\Delta\beta_{0,c}$	Change in spectral index versus component 0
$\Delta\beta_{c,b-a}$	Change in spectral index across break

Summary of all free parameters in the final light curve fit. The subscript f indicates the filter and the subscript c indicates the model component; as a result all quantities are vectors. The F_f is of length N_{filters}; all other parameters are of length $N_{\mathrm{components}}$ with the exception of $\Delta\beta_{0,c}$ (which is one element shorter than this because $\Delta\beta_{0,0}$ is fixed to zero by definition) and S_c (which is similarly one element shorter because S_0 is fixed to 1 to avoid degeneracy with F_f.) Because of the effects of the smooth break and a numerical scaling factor, the flux terms (F_f and S_c) do above not exactly specify the flux exactly at the break time as specified, but are multiplied by a constant of order unity that depends on s_c.

additional input text file is used to specify the number of components desired and the choice of starting parameters. Given the large number of possible parameters in the model, it is rare (unless the behavior of the light curve is intrinsically quite simple) for the software to converge to the "correct" result on the first try, and so a few user iterations are usually necessary to reach a satisfactory fit. Upon each fit, the program outputs a new file containing the best-fit values of that fit; this can be modified by the user and fed back into the program. Typically, the user will begin with a basic model (describing only the dominant components and with color change fixed to zero) and add additional terms until a satisfactory fit without excess residuals is reached.

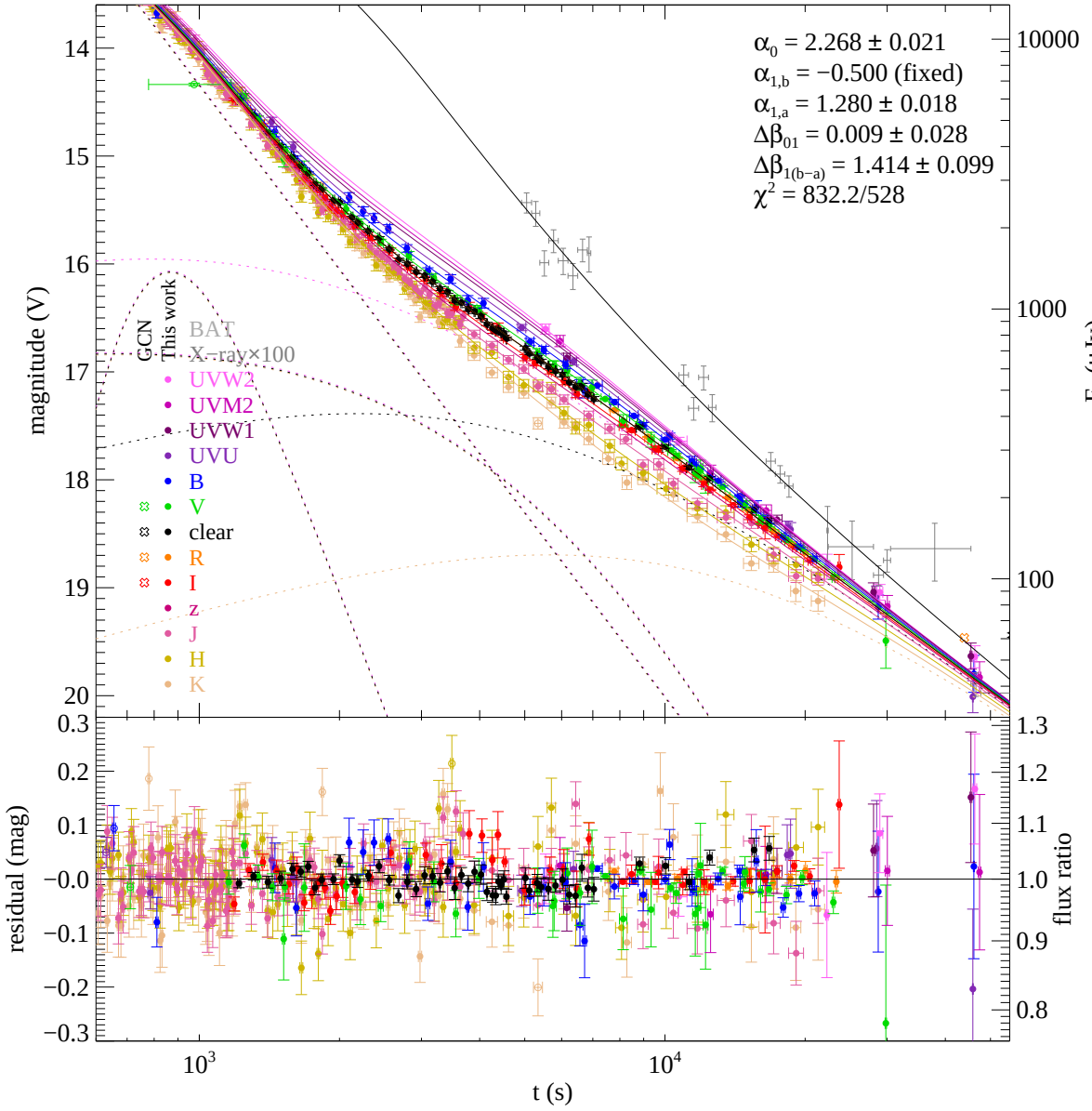

Figure A.2 Real-world example of a GRB (the naked eye burst, GRB 080319B) showing complex behavior and strong color change during its evolution, as fit by `lcurve`. The afterglow spectrum, initially quite red, hardens dramatically between 2000–20000 seconds after the burst before reverting nearly back to its original color at later times. This behavior, as well as the shallowing-out of the decay and several subtle wiggles in the light curve, are fit very well by the model, leaving no visible trend in the residuals over this time range. This behavior is difficult to interpret, although it could be the fading of a reverse shock as the forward shock reaches its synchrotron peak. Figure is modified from Bloom et al. (2009).

Appendix B

LGRB Afterglow Photometry

Table B.1: Photometry of GRB 061126

Telescope	$t_{\rm mid}$[a] sec	Filter	Exp. time sec	Mag.[b]	Flux[c] μJy
GCN	36.3	R		12.930 ± 0.200^{x}	30900 ± 5210^{x}
GCN	258.3	R		15.970 ± 0.050^{x}	1880 ± 84.7^{x}
GCN	626.4	I	120.0	17.100 ± 0.200^{x}	467 ± 78.6^{x}
GCN	806.1	I	120.0	17.000 ± 0.200^{x}	512 ± 86.1^{x}
GCN	2820.1	R		18.800 ± 0.200^{x}	139 ± 23.4^{x}
GCN	5880.4	R		19.300 ± 0.500^{x}	87.6 ± 32.3^{x}
GCN	8939.8	R		19.400 ± 0.300^{x}	79.9 ± 19.3^{x}
GCN	34367.3	R		21.500 ± 0.250^{x}	11.6 ± 2.38^{x}
GCN	152064	R		22.850 ± 0.060^{x}	3.33 ± 0.179^{x}
GCN	156381	R		23.690 ± 0.170^{x}	1.54 ± 0.223^{x}
GCN	39225.6	R		21.160 ± 0.040^{x}	15.8 ± 0.572^{x}
GCN	51235.2	R		21.650 ± 0.080^{x}	10.1 ± 0.715^{x}
GCN	35424.0	R		20.980 ± 0.100	1.86 ± 1.64
GCN	36288.0	R		21.040 ± 0.090	1.76 ± 1.40
GCN	42336.0	R		21.340 ± 0.100	1.34 ± 1.18
GCN	48384.0	R		21.490 ± 0.100	1.17 ± 1.03
PAIRITEL	64.8	J	4.3	11.720 ± 0.017	37423.2 ± 581.4
PAIRITEL	72.0	J	4.0	11.957 ± 0.019	30084.4 ± 521.9
PAIRITEL	80.0	J	4.0	12.099 ± 0.020	26396.2 ± 481.8
PAIRITEL	100.8	J	4.5	12.384 ± 0.025	20302.1 ± 462.1
PAIRITEL	109.0	J	4.0	12.494 ± 0.028	18346.0 ± 467.1
PAIRITEL	117.0	J	4.0	12.599 ± 0.032	16654.9 ± 483.7
PAIRITEL	136.7	J	4.5	12.795 ± 0.045	13904.0 ± 564.5
PAIRITEL	145.0	J	4.0	12.935 ± 0.058	12221.9 ± 635.8
PAIRITEL	153.0	J	4.0	13.081 ± 0.071	10684.2 ± 676.3
PAIRITEL	174.0	J	4.0	13.290 ± 0.043	8813.3 ± 342.2
PAIRITEL	182.0	J	4.0	13.263 ± 0.041	9035.3 ± 334.8
PAIRITEL	190.0	J	4.0	13.465 ± 0.045	7501.4 ± 304.6
PAIRITEL	210.0	J	4.0	13.491 ± 0.045	7323.9 ± 297.3

Continued on Next Page...

Telescope	$t_{\rm mid}$[a] sec	Filter	Exp. time sec	Mag.[b]	Flux[c] μJy
PAIRITEL	218.0	J	4.0	13.555 ± 0.045	6904.6 ± 280.3
PAIRITEL	226.0	J	4.0	13.661 ± 0.051	6262.4 ± 287.4
PAIRITEL	246.7	J	4.5	13.821 ± 0.052	5404.3 ± 252.7
PAIRITEL	254.2	J	3.5	13.871 ± 0.053	5161.1 ± 245.9
PAIRITEL	262.0	J	4.0	13.847 ± 0.045	5276.4 ± 214.2
PAIRITEL	282.8	J	4.5	13.989 ± 0.050	4629.6 ± 208.4
PAIRITEL	291.0	J	4.0	14.049 ± 0.057	4380.7 ± 224.0
PAIRITEL	308.4	J	24.0	14.260 ± 0.056	3607.0 ± 181.3
PAIRITEL	330.9	J	12.0	14.361 ± 0.067	3286.6 ± 196.7
PAIRITEL	358.9	J	12.0	14.555 ± 0.077	2748.8 ± 188.2
PAIRITEL	380.6	J	24.0	14.559 ± 0.055	2738.7 ± 135.3
PAIRITEL	402.9	J	12.0	14.835 ± 0.057	2123.9 ± 108.6
PAIRITEL	441.8	J	40.5	14.978 ± 0.045	1861.8 ± 75.6
PAIRITEL	489.5	J	41.0	15.193 ± 0.059	1527.4 ± 80.8
PAIRITEL	537.4	J	40.0	15.374 ± 0.075	1292.8 ± 86.3
PAIRITEL	587.5	J	40.0	15.295 ± 0.056	1390.4 ± 69.9
PAIRITEL	634.9	J	41.0	15.589 ± 0.067	1060.6 ± 63.5
PAIRITEL	694.8	J	68.5	15.720 ± 0.060	940.0 ± 50.5
PAIRITEL	767.1	J	68.0	15.797 ± 0.063	875.7 ± 49.4
PAIRITEL	839.6	J	69.0	15.905 ± 0.066	792.8 ± 46.8
PAIRITEL	912.2	J	68.0	15.934 ± 0.066	771.9 ± 45.5
PAIRITEL	984.4	J	68.0	16.149 ± 0.077	633.2 ± 43.4
PAIRITEL	1074.4	J	105.0	16.138 ± 0.065	639.6 ± 37.2
PAIRITEL	1183.0	J	104.9	16.321 ± 0.075	540.4 ± 36.1
PAIRITEL	1291.8	J	104.0	16.264 ± 0.071	569.6 ± 36.1
PAIRITEL	1400.8	J	105.9	16.443 ± 0.080	483.0 ± 34.3
PAIRITEL	1510.1	J	103.9	16.703 ± 0.113	380.1 ± 37.6
PAIRITEL	1625.7	J	84.5	16.959 ± 0.126	300.3 ± 32.9
PAIRITEL	1727.9	J	113.0	16.398 ± 0.144	503.4 ± 62.5
PAIRITEL	262.0	H	4.0	12.885 ± 0.047	7813.4 ± 331.0
PAIRITEL	282.8	H	4.5	13.146 ± 0.061	6143.9 ± 335.7
PAIRITEL	380.6	H	24.0	13.561 ± 0.060	4192.2 ± 225.4
PAIRITEL	402.9	H	12.0	13.838 ± 0.063	3248.2 ± 183.1
PAIRITEL	441.8	H	40.5	14.002 ± 0.046	2792.8 ± 115.9
PAIRITEL	483.5	H	33.0	14.200 ± 0.077	2327.2 ± 159.3
PAIRITEL	544.8	H	20.5	14.267 ± 0.081	2188.0 ± 157.3
PAIRITEL	587.5	H	40.0	14.410 ± 0.071	1918.0 ± 121.4
PAIRITEL	634.9	H	41.0	15.093 ± 0.110	1022.5 ± 98.5
PAIRITEL	694.8	H	68.5	14.843 ± 0.073	1287.2 ± 83.7
PAIRITEL	767.1	H	68.0	14.863 ± 0.073	1263.7 ± 82.2
PAIRITEL	839.6	H	69.0	14.754 ± 0.066	1397.1 ± 82.4
PAIRITEL	912.2	H	68.0	15.116 ± 0.080	1001.0 ± 71.1
PAIRITEL	984.4	H	68.0	15.338 ± 0.098	815.9 ± 70.4
PAIRITEL	1074.4	H	105.0	15.273 ± 0.074	866.2 ± 57.1
PAIRITEL	1184.9	H	104.9	15.599 ± 0.107	641.6 ± 60.2
PAIRITEL	1291.8	H	104.0	15.730 ± 0.109	568.6 ± 54.3
PAIRITEL	1400.8	H	105.9	15.628 ± 0.102	624.7 ± 56.0

Continued on Next Page...

Telescope	$t_{\rm mid}$[a] sec	Filter	Exp. time sec	Mag.[b]	Flux[c] μJy
PAIRITEL	1505.1	H	103.9	15.497 ± 0.104	704.8 ± 64.4
PAIRITEL	1613.1	H	97.0	15.789 ± 0.126	538.6 ± 59.0
PAIRITEL	1714.8	H	77.0	15.242 ± 0.137	891.3 ± 105.7
PAIRITEL	136.7	K	4.5	11.011 ± 0.055	27852.9 ± 1375.8
PAIRITEL	145.0	K	4.0	11.071 ± 0.069	26355.4 ± 1622.8
PAIRITEL	153.0	K	4.0	11.060 ± 0.080	26623.8 ± 1891.2
PAIRITEL	174.0	K	4.0	11.376 ± 0.045	19900.7 ± 808.0
PAIRITEL	182.0	K	4.0	11.591 ± 0.049	16325.6 ± 720.4
PAIRITEL	190.0	K	4.0	11.602 ± 0.045	16161.1 ± 656.1
PAIRITEL	210.0	K	4.0	11.655 ± 0.050	15391.1 ± 692.7
PAIRITEL	218.0	K	4.0	11.852 ± 0.052	12837.2 ± 600.3
PAIRITEL	226.0	K	4.0	11.773 ± 0.049	13806.1 ± 609.2
PAIRITEL	246.7	K	4.5	12.027 ± 0.058	10926.2 ± 568.4
PAIRITEL	254.2	K	3.5	12.132 ± 0.059	9919.0 ± 524.6
PAIRITEL	262.0	K	4.0	12.114 ± 0.051	10084.9 ± 462.8
PAIRITEL	282.8	K	4.5	12.452 ± 0.065	7387.0 ± 429.3
PAIRITEL	291.0	K	4.0	12.358 ± 0.068	8055.1 ± 489.0
PAIRITEL	308.4	K	24.0	12.509 ± 0.058	7009.2 ± 364.6
PAIRITEL	330.9	K	12.0	12.492 ± 0.070	7119.8 ± 444.5
PAIRITEL	358.9	K	12.0	12.763 ± 0.077	5547.1 ± 379.8
PAIRITEL	371.0	K	4.0	12.827 ± 0.100	5229.6 ± 460.2
PAIRITEL	402.9	K	12.0	13.070 ± 0.060	4180.9 ± 224.8
PAIRITEL	441.8	K	40.5	13.260 ± 0.048	3509.7 ± 151.8
PAIRITEL	489.5	K	41.0	13.344 ± 0.063	3248.4 ± 183.1
PAIRITEL	537.4	K	40.0	13.610 ± 0.077	2542.6 ± 174.1
PAIRITEL	587.5	K	40.0	13.693 ± 0.072	2355.4 ± 151.1
PAIRITEL	634.9	K	41.0	13.801 ± 0.070	2132.4 ± 133.1
PAIRITEL	694.8	K	68.5	13.966 ± 0.065	1831.8 ± 106.4
PAIRITEL	767.1	K	68.0	14.082 ± 0.069	1646.2 ± 101.4
PAIRITEL	839.6	K	69.0	14.303 ± 0.084	1343.0 ± 100.0
PAIRITEL	912.2	K	68.0	14.276 ± 0.083	1376.8 ± 101.3
PAIRITEL	984.4	K	68.0	14.333 ± 0.083	1306.4 ± 96.1
PAIRITEL	1074.4	K	105.0	14.548 ± 0.082	1071.7 ± 78.0
PAIRITEL	1181.7	K	97.0	14.688 ± 0.113	942.0 ± 93.1
PAIRITEL	1291.8	K	104.0	14.685 ± 0.092	944.6 ± 76.7
PAIRITEL	1399.2	K	105.9	14.633 ± 0.107	991.0 ± 93.0
PAIRITEL	1504.5	K	56.5	14.601 ± 0.129	1020.6 ± 114.3
PAIRITEL	1617.8	K	104.9	14.972 ± 0.137	725.2 ± 86.0
PAIRITEL	1707.6	K	77.0	14.357 ± 0.174	1277.8 ± 189.2
PAIRITEL	83357.5	J	8367.0	20.170 ± 0.400	15.60 ± 4.81
PAIRITEL	83220.5	H	8367.0	≥ 18.98	≤ 28.50
PAIRITEL	83221.0	K	8367.0	≥ 18.04	≤ 42.98
UVOT	2152.0	UVU	967.5	$18.643 \pm 0.112^{\rm x}$	$112.9 \pm 11.1^{\rm x}$
UVOT	2114.0	B	809.5	$19.049 \pm 0.117^{\rm x}$	$194.1 \pm 19.8^{\rm x}$
UVOT	2178.0	V	809.5	$18.431 \pm 0.141^{\rm x}$	$260.0 \pm 31.7^{\rm x}$
UVOT	8862.0	V	902.0	$20.511 \pm 0.316^{\rm x}$	$38.28 \pm 9.67^{\rm x}$
UVOT	7700.3	UVU	196.6	$19.752 \pm 0.187^{\rm x}$	$40.65 \pm 6.43^{\rm x}$

Continued on Next Page...

Telescope	$t_{\rm mid}$[a] sec	Filter	Exp. time sec	Mag.[b]	Flux[c] μJy
UVOT	15119.5	UVU	295.1	20.329 ± 0.379^{x}	23.89 ± 7.04^{x}
UVOT	2807.3	B	196.6	19.517 ± 0.124^{x}	126.1 ± 13.6^{x}
UVOT	7905.3	B	196.6	20.612 ± 0.260^{x}	46.01 ± 9.80^{x}
UVOT	3421.3	V	196.6	19.066 ± 0.227^{x}	144.9 ± 27.3^{x}
GCNR	1802.0	UVW1	39.0	19.280 ± 0.800	52.36 ± 27.30
GCNR	2355.0	UVW1	97.0	≥ 18.78	≤ 82.99
GCNR	5665.0	UVW1	280.0	19.340 ± 0.370	49.55 ± 14.31
GCNR	14515.0	UVW1	886.0	≥ 21.26	≤ 8.453
GCNR	42531.0	UVW1	2374.0	≥ 20.77	≤ 13.27
GCNR	1935.0	UVM2	39.0	19.560 ± 0.700	56.03 ± 26.62
GCNR	2251.0	UVM2	39.0	18.850 ± 0.540	107.7 ± 42.2
GCNR	3103.0	UVM2	236.0	19.980 ± 0.590	38.06 ± 15.95
GCNR	11695.0	UVM2	1149.0	≥ 20.50	≤ 23.57
GCNR	44049.0	UVM2	3386.0	≥ 20.89	≤ 16.46
GCNR	5108.0	UVW2	510.0	≥ 20.18	≤ 20.64
GCNR	43319.0	UVW2	4752.0	≥ 21.48	≤ 6.233
GCNR	1655.0	White	98.0	18.500 ± 0.110	170.4 ± 16.4
GCNR	1789.0	White	10.0	18.160 ± 0.290	233.0 ± 54.6
GCNR	1947.0	White	10.0	18.560 ± 0.400	161.2 ± 49.7
GCNR	2105.0	White	10.0	18.790 ± 0.460	130.4 ± 45.0
GCNR	2263.0	White	10.0	19.320 ± 0.720	80.06 ± 38.81
GCNR	2421.0	White	10.0	19.070 ± 0.570	100.8 ± 41.2
GCNR	2579.0	White	10.0	19.380 ± 0.770	75.75 ± 38.48
GCNR	3013.0	White	197.0	18.870 ± 0.120	121.2 ± 12.7
GCNR	8111.0	White	197.0	19.720 ± 0.220	55.39 ± 10.16
Nickel	3336.0	R	300.0	18.860 ± 0.050	131.4 ± 5.9
Nickel	3664.0	R	300.0	18.920 ± 0.050	124.3 ± 5.6
Nickel	4092.0	R	300.0	19.150 ± 0.060	100.6 ± 5.4
Nickel	4420.0	R	300.0	19.130 ± 0.060	102.5 ± 5.5
Nickel	4747.0	R	300.0	19.270 ± 0.070	90.08 ± 5.62
Nickel	5073.0	R	300.0	19.130 ± 0.080	102.5 ± 7.3
Nickel	5402.0	R	300.0	19.420 ± 0.100	78.46 ± 6.90
Nickel	5729.0	R	300.0	19.340 ± 0.230	84.46 ± 16.12
KAIT	366.0	clear	20.0	16.290 ± 0.120	1401.6 ± 146.7
KAIT	520.5	clear	45.0	16.650 ± 0.060	1006.1 ± 54.1
KAIT	726.0	clear	60.0	17.270 ± 0.070	568.4 ± 35.5
KAIT	1044.0	clear	120.0	17.660 ± 0.060	396.9 ± 21.3
KAIT	1561.0	clear	240.0	18.100 ± 0.060	264.6 ± 14.2
KAIT	2309.0	clear	360.0	18.460 ± 0.060	190.0 ± 10.2
KAIT	2839.0	clear	600.0	18.650 ± 0.060	159.5 ± 8.6
KAIT	5017.0	clear	180.0	19.150 ± 0.060	100.6 ± 5.4
KAIT	5239.0	clear	180.0	19.190 ± 0.070	96.97 ± 6.05
KAIT	5461.0	clear	180.0	19.130 ± 0.070	102.5 ± 6.4
KAIT	5683.0	clear	180.0	19.260 ± 0.070	90.92 ± 5.68
KAIT	5905.0	clear	180.0	19.240 ± 0.070	92.61 ± 5.78
KAIT	409.5	V	45.0	17.250 ± 0.120	771.6 ± 80.7
KAIT	584.0	V	60.0	17.540 ± 0.120	590.7 ± 61.8

Continued on Next Page...

Telescope	$t_{\rm mid}$[a] sec	Filter	Exp. time sec	Mag.[b]	Flux[c] μJy
KAIT	465.5	I	45.0	16.240 ± 0.110	1031.1 ± 99.4
KAIT	655.0	I	60.0	16.640 ± 0.110	713.4 ± 68.7
KAIT	880.0	I	120.0	17.050 ± 0.110	489.0 ± 47.1
KAIT	1277.0	I	240.0	17.290 ± 0.080	392.0 ± 27.8
KAIT	1905.0	I	360.0	17.740 ± 0.110	259.0 ± 25.0
NMSU	52.3	I	10.0	12.526 ± 0.003	31544.1 ± 87.1
NMSU	96.8	R	10.0	14.222 ± 0.006	9415.4 ± 51.9
NMSU	148.8	V	20.0	15.324 ± 0.007	4547.6 ± 29.2
NMSU	213.2	B	40.0	16.428 ± 0.009	2169.9 ± 17.9
NMSU	302.9	U	60.0	16.673 ± 0.025	911.4 ± 20.7
NMSU	374.3	I	10.0	15.814 ± 0.025	1526.6 ± 34.7
NMSU	418.8	R	10.0	16.677 ± 0.028	981.4 ± 25.0
NMSU	470.7	V	20.0	17.266 ± 0.025	760.3 ± 17.3
NMSU	535.1	B	40.0	17.982 ± 0.024	518.6 ± 11.3
NMSU	624.6	U	60.0	17.675 ± 0.052	362.1 ± 16.9
NMSU	696.4	I	10.0	16.792 ± 0.060	620.2 ± 33.3
NMSU	740.7	R	10.0	17.405 ± 0.050	501.9 ± 22.6
NMSU	792.8	V	20.0	18.031 ± 0.045	375.8 ± 15.3
NMSU	857.0	B	40.0	18.668 ± 0.045	275.7 ± 11.2
NMSU	946.4	U	60.0	18.189 ± 0.088	225.6 ± 17.6
NMSU	1017.9	I	10.0	17.068 ± 0.080	481.0 ± 34.2
NMSU	1062.5	R	10.0	18.031 ± 0.091	282.0 ± 22.7
NMSU	1114.5	V	20.0	18.317 ± 0.062	288.8 ± 16.0
NMSU	1178.6	B	40.0	18.935 ± 0.055	215.6 ± 10.6
NMSU	1268.5	U	60.0	18.407 ± 0.104	184.5 ± 16.9
NMSU	1340.0	I	10.0	17.430 ± 0.108	344.6 ± 32.6
NMSU	1384.5	R	10.0	18.230 ± 0.112	234.8 ± 23.0
NMSU	1436.4	V	20.0	18.624 ± 0.080	217.7 ± 15.5
NMSU	1500.9	B	40.0	19.168 ± 0.063	174.0 ± 9.8
NMSU	1590.8	U	60.0	19.208 ± 0.213	88.24 ± 15.72
NMSU	1667.2	I	20.0	17.653 ± 0.083	280.6 ± 20.7
NMSU	1721.8	R	20.0	18.410 ± 0.071	198.9 ± 12.6
NMSU	1789.0	V	40.0	18.849 ± 0.059	176.9 ± 9.4
NMSU	1883.2	B	80.0	19.473 ± 0.054	131.4 ± 6.4
NMSU	2022.8	U	120.0	19.329 ± 0.133	78.94 ± 9.10
NMSU	2129.2	I	20.0	17.761 ± 0.089	254.0 ± 20.0
NMSU	2183.7	R	20.0	18.568 ± 0.088	172.0 ± 13.4
NMSU	2250.8	V	40.0	19.151 ± 0.073	134.0 ± 8.7
NMSU	2344.8	B	80.0	19.591 ± 0.058	117.8 ± 6.1
NMSU	2484.6	U	120.0	19.402 ± 0.163	73.81 ± 10.29
NMSU	2590.9	I	20.0	18.699 ± 0.207	107.1 ± 18.6
NMSU	2645.2	R	20.0	18.761 ± 0.104	144.0 ± 13.1
NMSU	2712.8	V	40.0	19.308 ± 0.090	115.9 ± 9.2
NMSU	2807.4	B	80.0	19.947 ± 0.091	84.89 ± 6.82
NMSU	2946.9	U	120.0	19.359 ± 0.125	76.79 ± 8.35
NMSU	3053.0	I	20.0	18.133 ± 0.123	180.4 ± 19.3
NMSU	3107.7	R	20.0	19.034 ± 0.128	112.0 ± 12.5

Continued on Next Page...

Telescope	$t_{\rm mid}$[a] sec	Filter	Exp. time sec	Mag.[b]	Flux[c] μJy
NMSU	3174.7	V	40.0	19.586 ± 0.104	89.74 ± 8.20
NMSU	3268.9	B	80.0	19.958 ± 0.072	84.03 ± 5.39
NMSU	3408.5	U	120.0	19.584 ± 0.175	62.41 ± 9.29
NMSU	3515.1	I	20.0	18.380 ± 0.153	143.7 ± 18.9
NMSU	3569.6	R	20.0	19.422 ± 0.184	78.31 ± 12.21
NMSU	3636.6	V	40.0	19.799 ± 0.127	73.75 ± 8.14
NMSU	3730.9	B	80.0	20.134 ± 0.093	71.46 ± 5.87
NMSU	3870.4	U	120.0	19.195 ± 0.142	89.31 ± 10.95
RAPTOR	23.4	clear	5.0	12.260 ± 0.010	57364.0 ± 525.9
RAPTOR	32.3	clear	5.0	12.660 ± 0.020	39686.2 ± 724.3
RAPTOR	41.1	clear	5.0	13.080 ± 0.030	26955.0 ± 734.6
RAPTOR	49.8	clear	5.0	13.360 ± 0.040	20827.6 ± 753.3
RAPTOR	58.5	clear	5.0	13.710 ± 0.050	15088.3 ± 679.1
RAPTOR	67.2	clear	5.0	13.810 ± 0.060	13760.7 ± 739.8
RAPTOR	75.9	clear	5.0	14.400 ± 0.140	7991.7 ± 966.8
RAPTOR	84.6	clear	5.0	14.300 ± 0.090	8762.7 ± 697.1
RAPTOR	93.3	clear	5.0	14.400 ± 0.090	7991.7 ± 635.7
RAPTOR	107.2	clear	10.0	14.540 ± 0.060	7024.9 ± 377.7
RAPTOR	119.8	clear	10.0	14.520 ± 0.040	7155.5 ± 258.8
RAPTOR	132.4	clear	10.0	14.670 ± 0.060	6232.2 ± 335.1
RAPTOR	145.0	clear	10.0	14.740 ± 0.070	5843.1 ± 364.8
RAPTOR	157.6	clear	10.0	14.810 ± 0.100	5478.2 ± 482.0
RAPTOR	170.3	clear	10.0	15.120 ± 0.150	4117.6 ± 531.3
RAPTOR	182.9	clear	10.0	14.970 ± 0.110	4727.6 ± 455.5
RAPTOR	195.5	clear	10.0	15.330 ± 0.160	3393.4 ± 465.0
RAPTOR	208.1	clear	10.0	15.450 ± 0.110	3038.4 ± 292.7
RAPTOR	220.8	clear	10.0	15.460 ± 0.130	3010.5 ± 339.7
RAPTOR	233.4	clear	10.0	15.470 ± 0.060	2982.9 ± 160.4
RAPTOR	246.1	clear	10.0	15.670 ± 0.070	2481.1 ± 154.9
RAPTOR	258.7	clear	10.0	15.700 ± 0.090	2413.5 ± 192.0
RAPTOR	271.3	clear	10.0	16.030 ± 0.230	1780.9 ± 340.0
RAPTOR	283.9	clear	10.0	15.990 ± 0.120	1847.7 ± 193.3
RAPTOR	296.5	clear	10.0	16.000 ± 0.100	1830.8 ± 161.1
RAPTOR	309.1	clear	10.0	15.950 ± 0.120	1917.1 ± 200.6
RAPTOR	321.7	clear	10.0	16.060 ± 0.140	1732.4 ± 209.6
RAPTOR	334.3	clear	10.0	16.060 ± 0.130	1732.4 ± 195.5
RAPTOR	347.3	clear	10.0	16.340 ± 0.170	1338.6 ± 194.0
RAPTOR	372.7	clear	30.0	16.400 ± 0.130	1266.6 ± 142.9
RAPTOR	408.2	clear	30.0	16.610 ± 0.140	1043.9 ± 126.3
RAPTOR	443.5	clear	30.0	16.310 ± 0.140	1376.1 ± 166.5
RAPTOR	479.0	clear	30.0	16.390 ± 0.170	1278.3 ± 185.3

[a]Exposure mid-time, measured from the *Swift* trigger.
[b]Observed value; not corrected for Galactic extinction
[c]Corrected for Galactic extinction ($E_{B-V} = 0.182$ mag)
[x]Point not used in modeling

Table B.2: Photometry of GRB 071003

Telescope	$t_{\rm mid}$[a] sec	Filter	Exp. time sec	Mag.[b]	Flux[c] μJy
P60	206.0	R	60.0	14.570 ± 0.060	6391.1 ± 343.6
P60	462.0	R	60.0	16.030 ± 0.070	1665.6 ± 104.0
P60	719.0	R	60.0	16.880 ± 0.090	761.3 ± 60.6
P60	291.0	i	60.0	15.080 ± 0.050	4347.9 ± 195.7
P60	548.0	i	60.0	16.410 ± 0.070	1277.3 ± 79.7
P60	805.0	i	60.0	17.120 ± 0.100	664.2 ± 58.4
P60	377.0	z	60.0	15.370 ± 0.070	3186.0 ± 198.9
P60	633.0	z	60.0	16.430 ± 0.080	1200.2 ± 85.3
P60	890.0	z	60.0	17.020 ± 0.110	697.0 ± 67.2
P60	1369.0	z	120.0	17.920 ± 0.200	304.3 ± 51.2
P60	1951.0	z	120.0	18.670 ± 0.280	152.5 ± 34.7
P60	1514.0	g	120.0	18.710 ± 0.100	197.0 ± 17.3
P60	2097.0	g	120.0	19.330 ± 0.150	111.3 ± 14.4
P60	2678.0	g	120.0	19.440 ± 0.200	100.6 ± 16.9
KAIT	107.0	V	20.0	14.465 ± 0.027	9201.3 ± 226.0
KAIT	198.0	V	20.0	14.916 ± 0.034	6073.6 ± 187.3
KAIT	289.0	V	20.0	15.409 ± 0.035	3857.0 ± 122.4
KAIT	380.0	V	20.0	16.034 ± 0.107	2168.9 ± 203.6
KAIT	472.0	V	20.0	16.853 ± 0.200	1020.1 ± 171.6
KAIT	44.5	clear	5.0	12.791 ± 0.019	32898.4 ± 570.7
KAIT	51.5	clear	5.0	12.999 ± 0.024	27162.8 ± 593.9
KAIT	57.5	clear	5.0	13.193 ± 0.021	22718.3 ± 435.2
KAIT	63.5	clear	5.0	13.321 ± 0.024	20191.8 ± 441.4
KAIT	69.5	clear	5.0	13.500 ± 0.019	17122.8 ± 297.0
KAIT	167.0	clear	20.0	14.382 ± 0.031	7599.3 ± 213.9
KAIT	259.0	clear	20.0	14.750 ± 0.023	5414.7 ± 113.5
KAIT	350.0	clear	20.0	15.401 ± 0.024	2972.9 ± 65.0
KAIT	441.0	clear	20.0	16.239 ± 0.082	1374.0 ± 99.9
KAIT	532.0	clear	20.0	16.749 ± 0.091	859.0 ± 69.1
KAIT	605.0	clear	20.0	16.849 ± 0.097	783.4 ± 67.0
KAIT	664.0	clear	20.0	17.041 ± 0.089	656.4 ± 51.7
KAIT	787.7	clear	128.0	17.362 ± 0.121	488.4 ± 51.5
KAIT	1010.0	clear	260.0	17.711 ± 0.147	354.1 ± 44.8
KAIT	1422.3	clear	440.0	18.103 ± 0.154	246.8 ± 32.6
KAIT	138.0	I	20.0	13.919 ± 0.032	8331.3 ± 242.0
KAIT	229.0	I	20.0	14.121 ± 0.022	6916.9 ± 138.7
KAIT	320.0	I	20.0	14.578 ± 0.030	4540.6 ± 123.7
KAIT	411.0	I	20.0	15.478 ± 0.063	1982.0 ± 111.7
KAIT	502.0	I	20.0	15.977 ± 0.069	1251.7 ± 77.1
KAIT	575.0	I	20.0	16.255 ± 0.077	969.0 ± 66.3
KAIT	634.0	I	20.0	16.364 ± 0.106	876.4 ± 81.5
KAIT	749.1	I	138.0	16.830 ± 0.113	570.6 ± 56.4
KAIT	1007.7	I	280.0	17.314 ± 0.148	365.4 ± 46.6
KAIT	1464.6	I	440.0	17.473 ± 0.135	315.6 ± 36.9
AEOS	568.6	clear		16.708 ± 0.016	892.0 ± 13.1

Continued on Next Page...

Telescope	$t_{\rm mid}$[a] sec	Filter	Exp. time sec	Mag.[b]	Flux[c] μJy
AEOS	681.3	clear		17.046 ± 0.018	653.4 ± 10.7
AEOS	794.0	clear		17.337 ± 0.020	499.8 ± 9.1
AEOS	906.8	clear		17.573 ± 0.020	402.1 ± 7.3
AEOS	1019.6	clear		17.766 ± 0.020	336.6 ± 6.1
AEOS	1132.3	clear		17.940 ± 0.020	286.8 ± 5.2
AEOS	1245.1	clear		18.101 ± 0.020	247.3 ± 4.5
AEOS	1357.9	clear		18.229 ± 0.023	219.8 ± 4.6
AEOS	1470.7	clear		18.339 ± 0.025	198.6 ± 4.5
AEOS	1583.5	clear		18.454 ± 0.026	178.6 ± 4.2
AEOS	1696.3	clear		18.545 ± 0.028	164.3 ± 4.2
AEOS	1809.1	clear		18.640 ± 0.034	150.5 ± 4.6
AEOS	1922.0	clear		18.724 ± 0.033	139.3 ± 4.2
AEOS	2034.8	clear		18.814 ± 0.040	128.2 ± 4.6
AEOS	2147.6	clear		18.865 ± 0.037	122.3 ± 4.1
AEOS	2260.3	clear		18.924 ± 0.042	115.9 ± 4.4
AEOS	2373.1	clear		18.941 ± 0.048	114.1 ± 4.9
AEOS	2485.9	clear		18.941 ± 0.064	114.1 ± 6.5
AEOS	2598.7	clear		19.042 ± 0.044	103.9 ± 4.1
AEOS	2711.4	clear		19.087 ± 0.049	99.72 ± 4.40
AEOS	2824.2	clear		19.104 ± 0.050	98.17 ± 4.42
AEOS	2937.0	clear		19.109 ± 0.054	97.72 ± 4.74
AEOS	3049.7	clear		19.142 ± 0.054	94.79 ± 4.60
AEOS	3162.5	clear		19.150 ± 0.052	94.10 ± 4.40
AEOS	3275.3	clear		19.160 ± 0.056	93.23 ± 4.69
AEOS	3388.2	clear		19.169 ± 0.055	92.46 ± 4.57
AEOS	3501.0	clear		19.158 ± 0.050	93.41 ± 4.20
AEOS	3613.8	clear		19.139 ± 0.056	95.05 ± 4.78
AEOS	3726.5	clear		19.185 ± 0.055	91.11 ± 4.50
AEOS	3839.3	clear		19.206 ± 0.056	89.37 ± 4.49
AEOS	4062.4	clear		19.188 ± 0.056	90.86 ± 4.57
AEOS	4175.3	clear		19.196 ± 0.055	90.19 ± 4.46
AEOS	4288.1	clear		19.194 ± 0.057	90.36 ± 4.62
AEOS	4401.0	clear		19.208 ± 0.051	89.20 ± 4.09
AEOS	4513.8	clear		19.167 ± 0.054	92.63 ± 4.49
AEOS	4626.6	clear		19.150 ± 0.053	94.10 ± 4.48
AEOS	4739.4	clear		19.163 ± 0.065	92.98 ± 5.40
AEOS	4852.2	clear		19.160 ± 0.057	93.23 ± 4.77
AEOS	5002.6	clear		19.145 ± 0.050	94.53 ± 4.25
Keck	9523.7	clear		18.590 ± 0.250	157.6 ± 32.4
Keck	517510	u		24.000 ± 0.120	1.699 ± 0.178
Keck	682211	u		24.860 ± 0.250	0.7695 ± 0.1583
Keck	76891.8	g		20.320 ± 0.070	44.72 ± 2.79
Gemini-S	231174	g		22.330 ± 0.200	7.023 ± 1.182
Keck	516250	g		23.560 ± 0.300	2.262 ± 0.546
Keck	605144	g		24.050 ± 0.400	1.441 ± 0.444
Keck	682211	V		23.560 ± 0.400	2.118 ± 0.653
Keck	77044.0	R		19.430 ± 0.060	72.71 ± 3.91

Continued on Next Page...

Telescope	$t_{\rm mid}$[a] sec	Filter	Exp. time sec	Mag.[b]	Flux[c] μJy
Keck	515855	R		22.610 ± 0.300	3.887 ± 0.938
Keck	604978	R		23.060 ± 0.500	2.568 ± 0.948
Keck	682940	R		23.400 ± 0.600	1.877 ± 0.797
Gemini-S	233056	z		21.350 ± 0.400	12.92 ± 3.98
Gemini-S	232000	R		21.750 ± 0.250	8.582 ± 1.765
Gemini-S	231000	I		21.090 ± 0.370	11.28 ± 3.26
Keck	1374489	K'	1800.0	21.580 ± 0.030	1.635 ± 0.045

Table B.3: Photometry of GRB 071025

Telescope	$t_{\rm mid}$[a] sec	Filter	Exp. time sec	Mag.[b]	Flux[c] μJy
Magnum	10206.0	J	600.0	17.760 ± 0.059	132.4 ± 7.0
Magnum	10326.0	R	600.0	21.850 ± 0.390	6.628 ± 2.000
Magnum	11526.0	Y	300.0	18.408 ± 0.183	96.43 ± 14.96
Magnum	11526.0	I	600.0	19.880 ± 0.140	30.49 ± 3.69
Magnum	12846.0	K	480.0	16.491 ± 0.086	172.9 ± 13.2
Magnum	12846.0	R	600.0	≥ 21.28	≤ 11.20
Magnum	14106.0	H	540.0	17.597 ± 0.082	96.87 ± 7.05
Magnum	14106.0	I	600.0	20.220 ± 0.200	22.29 ± 3.75
Magnum	15366.0	J	540.0	18.320 ± 0.103	79.08 ± 7.16
Magnum	15366.0	R	600.0	≥ 21.36	≤ 10.41
Magnum	16506.0	Y	540.0	19.750 ± 0.430	28.02 ± 9.16
Magnum	16506.0	I	600.0	20.460 ± 0.280	17.87 ± 4.06
Kuiper	5098.5	I	1055.0	18.452 ± 0.085	113.6 ± 8.6
Kuiper	11260.0	I	2176.0	19.798 ± 0.010	32.88 ± 0.30
Kuiper	15382.0	I	3530.0	≥ 19.65	≤ 37.68
Kuiper	18584.5	I	2701.0	≥ 19.23	≤ 55.48
Kuiper	1824.8	R	261.7	19.290 ± 0.040	70.05 ± 2.53
Kuiper	2613.5	R	1225.9	19.790 ± 0.040	44.20 ± 1.60
Kuiper	3887.7	R	1259.3	20.300 ± 0.060	27.63 ± 1.49
Kuiper	8647.0	R	2940.0	≥ 20.85	≤ 16.65
Super-LOTIS	134.5	R	50.0	≥ 19.46	≤ 59.89
Super-LOTIS	244.2	R	100.0	$19.180 \pm 0.240^{\rm x}$	$77.51 \pm 15.37^{\rm x}$
Super-LOTIS	478.7	R	300.0	$19.700 \pm 0.240^{\rm x}$	$48.02 \pm 9.52^{\rm x}$
Super-LOTIS	813.7	R	300.0	18.910 ± 0.120	99.40 ± 10.40
Super-LOTIS	1315.1	R	600.0	19.520 ± 0.160	56.67 ± 7.77
Super-LOTIS	1983.3	R	600.0	19.390 ± 0.180	63.88 ± 9.76
REM/NTT	377.0	J	91.0	15.220 ± 0.200	1374.2 ± 231.2
REM/NTT	1085.0	J	181.0	15.570 ± 0.160	995.5 ± 136.4
REM/NTT	2304.0	J	331.0	15.350 ± 0.110	1219.1 ± 117.5

Continued on Next Page...

[a] Exposure mid-time, measured from the *Swift* trigger.
[b] Observed value; not corrected for Galactic extinction
[c] Corrected for Galactic extinction ($E_{B-V} = 0.151$ mag)
[x] Point not used in modeling

Telescope	$t_{\rm mid}$[a] sec	Filter	Exp. time sec	Mag.[b]	Flux[c] μJy
REM/NTT	185.0	H	82.0	16.131 ± 0.690	373.7 ± 175.8
REM/NTT	666.0	H	181.0	13.890 ± 0.050	2944.3 ± 132.5
REM/NTT	1623.0	H	331.0	14.380 ± 0.080	1874.9 ± 133.2
REM/NTT	2795.0	H	81.0	≥ 14.90	≤ 1161.4
REM/NTT	275.0	K	82.0	13.430 ± 0.130	2899.2 ± 327.2
REM/NTT	890.0	K	212.0	12.900 ± 0.070	4723.6 ± 294.9
REM/NTT	470.0	Y	81.0	15.620 ± 0.240	1257.2 ± 249.3
REM/NTT	1281.0	Y	181.0	15.700 ± 0.190	1167.9 ± 187.5
REM/NTT	2653.0	Y	332.0	16.280 ± 0.330	684.6 ± 179.4
REM/NTT	81101.0	J	5104.0	20.780 ± 0.270	8.204 ± 1.806
REM/NTT	81672.0	H	4938.0	19.340 ± 0.200	19.45 ± 3.27
REM/NTT	168032	H	2187.0	≥ 19.80	≤ 12.73
REM/NTT	82061.0	K	4960.0	18.780 ± 0.200	21.00 ± 3.53
GROND	80533.0	I		$22.748 \pm 0.400^{\rm x}$	$2.172 \pm 0.669^{\rm x}$
GROND	80533.0	J		$20.460 \pm 0.240^{\rm x}$	$11.02 \pm 2.18^{\rm x}$
GROND	80533.0	H		$19.230 \pm 0.340^{\rm x}$	$21.53 \pm 5.79^{\rm x}$
GROND	80533.0	K		$19.150 \pm 0.800^{\rm x}$	$14.94 \pm 7.79^{\rm x}$
Lick	2714.0	J	210.0	15.817 ± 0.030	792.9 ± 21.6
Lick	2997.0	J	210.0	15.938 ± 0.030	709.3 ± 19.3
Lick	3279.0	J	210.0	16.135 ± 0.030	591.6 ± 16.1
Lick	3562.0	J	210.0	16.227 ± 0.030	543.6 ± 14.8
Lick	3846.0	J	210.0	16.378 ± 0.030	473.0 ± 12.9
Lick	4129.0	J	210.0	16.504 ± 0.030	421.2 ± 11.5
Lick	4413.0	J	210.0	16.558 ± 0.030	400.7 ± 10.9
Lick	4698.0	J	210.0	16.684 ± 0.030	356.8 ± 9.7
Lick	2714.0	K	210.0	$14.143 \pm 0.100^{\rm x}$	$1503.4 \pm 132.3^{\rm x}$
Lick	2997.0	K	210.0	$14.321 \pm 0.100^{\rm x}$	$1276.1 \pm 112.3^{\rm x}$
Lick	3279.0	K	210.0	$14.384 \pm 0.100^{\rm x}$	$1204.1 \pm 106.0^{\rm x}$
Lick	3562.0	K	210.0	$14.518 \pm 0.100^{\rm x}$	$1064.3 \pm 93.6^{\rm x}$
Lick	3846.0	K	210.0	$14.583 \pm 0.100^{\rm x}$	$1002.5 \pm 88.2^{\rm x}$
Lick	4129.0	K	210.0	$14.650 \pm 0.100^{\rm x}$	$942.5 \pm 82.9^{\rm x}$
Lick	4413.0	K	210.0	$14.818 \pm 0.100^{\rm x}$	$807.4 \pm 71.0^{\rm x}$
RAPTOR	119.5	clear	76.4	≥ 16.94	≤ 608.9
RAPTOR	290.4	clear	252.5	17.187 ± 0.159	485.9 ± 66.2
RAPTOR	526.3	clear	207.7	16.793 ± 0.118	698.5 ± 71.9
RAPTOR	739.6	clear	208.0	16.792 ± 0.111	699.2 ± 67.9
RAPTOR	953.3	clear	208.1	16.761 ± 0.112	719.4 ± 70.5
RAPTOR	1167.1	clear	207.5	17.517 ± 0.236	358.6 ± 70.1
RAPTOR	1381.1	clear	208.7	17.012 ± 0.140	570.9 ± 69.1
RAPTOR	1594.9	clear	207.5	17.096 ± 0.156	528.4 ± 70.7
RAPTOR	1808.7	clear	208.9	17.186 ± 0.170	486.4 ± 70.5
RAPTOR	2022.3	clear	207.9	17.216 ± 0.172	473.1 ± 69.3
RAPTOR	2235.6	clear	207.6	17.691 ± 0.281	305.5 ± 69.7
RAPTOR	2448.6	clear	207.6	17.429 ± 0.227	388.8 ± 73.4
RAPTOR	2662.1	clear	208.0	18.050 ± 0.372	219.5 ± 63.7
RAPTOR	2875.7	clear	208.1	18.097 ± 0.413	210.2 ± 66.5
RAPTOR	3124.9	clear	278.9	17.793 ± 0.265	278.1 ± 60.2

Continued on Next Page...

Telescope	$t_{\rm mid}$[a] sec	Filter	Exp. time sec	Mag.[b]	Flux[c] μJy
PAIRITEL	174.6	J	23.4	16.160 ± 0.452	578.2 ± 196.9
PAIRITEL	209.9	J	23.4	15.448 ± 0.153	1113.9 ± 146.4
PAIRITEL	246.0	J	23.4	15.486 ± 0.160	1075.6 ± 147.4
PAIRITEL	282.1	J	23.4	15.300 ± 0.141	1276.6 ± 155.5
PAIRITEL	318.4	J	23.4	15.083 ± 0.143	1559.0 ± 192.4
PAIRITEL	354.6	J	23.4	14.814 ± 0.126	1997.3 ± 218.8
PAIRITEL	390.9	J	23.4	14.797 ± 0.117	2028.8 ± 207.3
PAIRITEL	427.0	J	23.4	15.058 ± 0.129	1595.3 ± 178.7
PAIRITEL	463.3	J	23.4	14.624 ± 0.091	2379.3 ± 191.3
PAIRITEL	499.4	J	23.4	14.669 ± 0.084	2282.7 ± 169.9
PAIRITEL	553.7	J	46.8	14.600 ± 0.064	2432.5 ± 139.2
PAIRITEL	626.1	J	46.8	14.801 ± 0.083	2021.4 ± 148.8
PAIRITEL	698.4	J	46.8	14.758 ± 0.073	2103.0 ± 136.8
PAIRITEL	770.8	J	46.8	14.677 ± 0.059	2265.9 ± 119.8
PAIRITEL	844.2	J	46.8	14.799 ± 0.088	2025.1 ± 157.7
PAIRITEL	916.6	J	46.8	14.942 ± 0.083	1775.2 ± 130.6
PAIRITEL	989.0	J	46.8	14.982 ± 0.083	1711.0 ± 125.9
PAIRITEL	1079.6	J	70.2	15.359 ± 0.099	1209.1 ± 105.4
PAIRITEL	1188.2	J	70.2	15.374 ± 0.078	1192.5 ± 82.7
PAIRITEL	1297.9	J	70.2	15.161 ± 0.080	1450.9 ± 103.1
PAIRITEL	1407.1	J	70.2	15.247 ± 0.066	1340.4 ± 79.1
PAIRITEL	1516.1	J	70.2	15.086 ± 0.052	1554.7 ± 72.7
PAIRITEL	1624.7	J	70.2	15.064 ± 0.052	1586.5 ± 74.2
PAIRITEL	1733.1	J	70.2	15.176 ± 0.052	1431.0 ± 66.9
PAIRITEL	1841.8	J	70.2	15.193 ± 0.052	1408.8 ± 65.9
PAIRITEL	1950.4	J	70.2	15.227 ± 0.054	1365.4 ± 66.2
PAIRITEL	2058.9	J	70.2	15.302 ± 0.063	1274.2 ± 71.8
PAIRITEL	2168.5	J	70.2	15.434 ± 0.066	1128.4 ± 66.5
PAIRITEL	2277.1	J	70.2	15.543 ± 0.078	1020.6 ± 70.7
PAIRITEL	2385.7	J	70.2	15.637 ± 0.066	935.9 ± 55.2
PAIRITEL	2494.4	J	70.2	15.644 ± 0.071	929.9 ± 58.9
PAIRITEL	2603.9	J	70.2	15.602 ± 0.082	966.6 ± 70.3
PAIRITEL	2712.4	J	70.2	15.848 ± 0.087	770.6 ± 59.3
PAIRITEL	2857.2	J	117.0	15.985 ± 0.094	679.3 ± 56.3
PAIRITEL	3075.0	J	163.8	16.004 ± 0.070	667.5 ± 41.7
PAIRITEL	3347.1	J	187.2	16.168 ± 0.075	573.9 ± 38.3
PAIRITEL	3655.8	J	210.6	16.314 ± 0.082	501.7 ± 36.5
PAIRITEL	10770.8	J	2152.8	17.680 ± 0.154	142.6 ± 18.9
PAIRITEL	14884.5	J	2269.8	18.344 ± 0.228	77.35 ± 14.65
PAIRITEL	174.6	H	23.4	15.933 ± 0.768	448.5 ± 227.4
PAIRITEL	209.9	H	23.4	14.898 ± 0.198	1163.5 ± 194.0
PAIRITEL	246.0	H	23.4	14.589 ± 0.143	1546.6 ± 190.9
PAIRITEL	282.1	H	23.4	14.299 ± 0.103	2020.1 ± 182.8
PAIRITEL	318.4	H	23.4	14.072 ± 0.124	2489.9 ± 268.7
PAIRITEL	354.6	H	23.4	13.987 ± 0.112	2692.7 ± 263.9
PAIRITEL	390.9	H	23.4	13.956 ± 0.110	2770.6 ± 267.0
PAIRITEL	427.0	H	23.4	14.065 ± 0.117	2506.0 ± 256.0

Continued on Next Page...

Telescope	$t_{\rm mid}$[a] sec	Filter	Exp. time sec	Mag.[b]	Flux[c] μJy
PAIRITEL	463.3	H	23.4	13.817 ± 0.086	3149.1 ± 239.8
PAIRITEL	499.4	H	23.4	13.885 ± 0.082	2957.9 ± 215.2
PAIRITEL	553.7	H	46.8	13.774 ± 0.064	3276.3 ± 187.5
PAIRITEL	626.1	H	46.8	13.884 ± 0.071	2960.6 ± 187.4
PAIRITEL	698.4	H	46.8	13.913 ± 0.069	2882.6 ± 177.5
PAIRITEL	770.8	H	46.8	13.871 ± 0.057	2996.3 ± 153.2
PAIRITEL	844.2	H	46.8	13.977 ± 0.083	2717.6 ± 200.0
PAIRITEL	916.6	H	46.8	14.250 ± 0.083	2113.4 ± 155.5
PAIRITEL	989.0	H	46.8	14.100 ± 0.076	2426.5 ± 164.0
PAIRITEL	1079.6	H	70.2	14.466 ± 0.087	1732.1 ± 133.4
PAIRITEL	1188.2	H	70.2	14.355 ± 0.061	1918.6 ± 104.8
PAIRITEL	1297.9	H	70.2	14.384 ± 0.078	1868.0 ± 129.5
PAIRITEL	1407.1	H	70.2	14.443 ± 0.063	1769.2 ± 99.7
PAIRITEL	1516.1	H	70.2	14.257 ± 0.056	2099.8 ± 105.6
PAIRITEL	1624.7	H	70.2	14.351 ± 0.061	1925.7 ± 105.2
PAIRITEL	1733.1	H	70.2	14.405 ± 0.056	1832.2 ± 92.1
PAIRITEL	1841.8	H	70.2	14.452 ± 0.054	1754.6 ± 85.1
PAIRITEL	1950.4	H	70.2	14.527 ± 0.059	1637.5 ± 86.6
PAIRITEL	2058.9	H	70.2	14.564 ± 0.066	1582.6 ± 93.3
PAIRITEL	2168.5	H	70.2	14.573 ± 0.063	1569.6 ± 88.5
PAIRITEL	2277.1	H	70.2	14.702 ± 0.066	1393.7 ± 82.2
PAIRITEL	2385.7	H	70.2	14.763 ± 0.066	1317.6 ± 77.7
PAIRITEL	2494.4	H	70.2	14.927 ± 0.078	1132.9 ± 78.5
PAIRITEL	2603.9	H	70.2	14.959 ± 0.087	1100.0 ± 84.7
PAIRITEL	2712.4	H	70.2	15.039 ± 0.087	1021.8 ± 78.7
PAIRITEL	2857.2	H	117.0	15.100 ± 0.084	966.0 ± 71.9
PAIRITEL	3075.0	H	163.8	15.211 ± 0.072	872.1 ± 56.0
PAIRITEL	3347.1	H	187.2	15.455 ± 0.084	696.6 ± 51.9
PAIRITEL	3655.8	H	210.6	15.420 ± 0.075	719.4 ± 48.0
PAIRITEL	10770.8	H	2152.8	17.196 ± 0.226	140.1 ± 26.3
PAIRITEL	14884.5	H	2269.8	17.462 ± 0.245	109.7 ± 22.2
PAIRITEL	174.6	K	23.4	14.098 ± 0.413	1567.0 ± 495.8
PAIRITEL	209.9	K	23.4	13.751 ± 0.195	2157.1 ± 354.6
PAIRITEL	246.0	K	23.4	13.397 ± 0.138	2988.6 ± 356.7
PAIRITEL	282.1	K	23.4	13.259 ± 0.119	3393.7 ± 352.3
PAIRITEL	318.4	K	23.4	13.070 ± 0.131	4039.0 ± 459.1
PAIRITEL	354.6	K	23.4	12.905 ± 0.136	4701.9 ± 553.6
PAIRITEL	390.9	K	23.4	12.884 ± 0.110	4793.7 ± 461.9
PAIRITEL	427.0	K	23.4	12.854 ± 0.112	4928.0 ± 483.0
PAIRITEL	463.3	K	23.4	12.835 ± 0.098	5015.0 ± 432.8
PAIRITEL	499.4	K	23.4	12.606 ± 0.079	6192.6 ± 434.6
PAIRITEL	553.7	K	46.8	12.630 ± 0.064	6057.2 ± 346.7
PAIRITEL	626.1	K	46.8	12.919 ± 0.080	4641.7 ± 329.7
PAIRITEL	698.4	K	46.8	12.858 ± 0.073	4909.9 ± 319.3
PAIRITEL	770.8	K	46.8	13.007 ± 0.073	4280.3 ± 278.3
PAIRITEL	844.2	K	46.8	12.875 ± 0.095	4833.6 ± 405.0
PAIRITEL	916.6	K	46.8	13.136 ± 0.090	3800.8 ± 302.4

Continued on Next Page...

Telescope	$t_{\rm mid}$[a] sec	Filter	Exp. time sec	Mag.[b]	Flux[c] μJy
PAIRITEL	989.0	K	46.8	13.111 ± 0.095	3889.3 ± 325.8
PAIRITEL	1079.6	K	70.2	13.417 ± 0.094	2934.1 ± 243.3
PAIRITEL	1188.2	K	70.2	13.355 ± 0.075	3106.5 ± 207.3
PAIRITEL	1297.9	K	70.2	13.330 ± 0.090	3178.9 ± 252.9
PAIRITEL	1407.1	K	70.2	13.311 ± 0.075	3235.0 ± 215.9
PAIRITEL	1516.1	K	70.2	13.296 ± 0.068	3280.0 ± 199.1
PAIRITEL	1624.7	K	70.2	13.465 ± 0.075	2807.2 ± 187.4
PAIRITEL	1733.1	K	70.2	13.435 ± 0.073	2885.9 ± 187.7
PAIRITEL	1841.8	K	70.2	13.528 ± 0.073	2649.0 ± 172.2
PAIRITEL	1950.4	K	70.2	13.554 ± 0.082	2586.3 ± 188.1
PAIRITEL	2058.9	K	70.2	13.525 ± 0.082	2656.3 ± 193.2
PAIRITEL	2168.5	K	70.2	13.739 ± 0.094	2181.1 ± 180.9
PAIRITEL	2277.1	K	70.2	13.775 ± 0.097	2110.0 ± 180.3
PAIRITEL	2385.7	K	70.2	13.713 ± 0.087	2234.0 ± 172.0
PAIRITEL	2494.4	K	70.2	13.887 ± 0.101	1903.2 ± 169.1
PAIRITEL	2603.9	K	70.2	14.111 ± 0.125	1548.4 ± 168.4
PAIRITEL	2712.4	K	70.2	14.006 ± 0.118	1705.6 ± 175.6
PAIRITEL	2857.2	K	117.0	14.081 ± 0.116	1591.7 ± 161.3
PAIRITEL	3075.0	K	163.8	14.078 ± 0.089	1596.2 ± 125.6
PAIRITEL	3347.1	K	187.2	14.405 ± 0.111	1181.1 ± 114.8
PAIRITEL	3655.8	K	210.6	14.415 ± 0.108	1170.2 ± 110.8
PAIRITEL	10770.8	K	2152.8	16.074 ± 0.228	253.9 ± 48.1
PAIRITEL	14884.5	K	2269.8	16.564 ± 0.324	161.7 ± 41.7

Table B.4: Photometry of GRB 080607

Telescope	$t_{\rm mid}$[a] sec	Filter	Exp. time sec	Mag.[b]	Flux[c] μJy
PAIRITEL	89.0	J	23.4	13.766 ± 0.107	5048.6 ± 475.4
PAIRITEL	89.0	H	23.4	12.050 ± 0.109	15657.3 ± 1501.3
PAIRITEL	89.0	K	23.4	10.750 ± 0.139	33681.7 ± 4058.1
PAIRITEL	125.5	J	23.4	14.195 ± 0.110	3400.4 ± 327.1
PAIRITEL	125.5	H	23.4	12.569 ± 0.112	9704.1 ± 954.9
PAIRITEL	125.5	K	23.4	11.432 ± 0.141	17967.8 ± 2189.1
PAIRITEL	161.0	J	23.4	14.739 ± 0.112	2059.3 ± 201.3
PAIRITEL	161.0	H	23.4	13.013 ± 0.111	6449.1 ± 624.1
PAIRITEL	161.0	K	23.4	11.419 ± 0.143	18176.7 ± 2243.9
PAIRITEL	197.0	J	23.4	14.976 ± 0.115	1655.9 ± 166.4
PAIRITEL	197.0	H	23.4	13.567 ± 0.113	3871.3 ± 381.3
PAIRITEL	197.0	K	23.4	12.117 ± 0.145	9562.1 ± 1193.1
PAIRITEL	233.5	J	23.4	15.311 ± 0.123	1216.2 ± 130.4

Continued on Next Page...

[a]Exposure mid-time, measured from the *Swift* trigger.
[b]Observed value; not corrected for Galactic extinction
[c]Corrected for Galactic extinction ($E_{B-V} = 0.074$ mag)
[x]Point not used in modeling

Telescope	$t_{\rm mid}$[a] sec	Filter	Exp. time sec	Mag.[b]	Flux[c] μJy
PAIRITEL	233.5	H	23.4	13.928 ± 0.114	2776.7 ± 277.7
PAIRITEL	233.5	K	23.4	12.297 ± 0.134	8098.3 ± 937.6
PAIRITEL	269.5	J	23.4	15.444 ± 0.126	1076.5 ± 117.8
PAIRITEL	269.5	H	23.4	13.915 ± 0.117	2808.4 ± 287.9
PAIRITEL	269.5	K	23.4	12.240 ± 0.147	8535.6 ± 1081.3
PAIRITEL	305.5	J	23.4	15.626 ± 0.134	909.7 ± 105.4
PAIRITEL	305.5	H	23.4	14.006 ± 0.118	2582.8 ± 266.5
PAIRITEL	305.5	K	23.4	12.577 ± 0.140	6255.4 ± 757.7
PAIRITEL	360.0	J	46.8	16.032 ± 0.113	626.3 ± 62.2
PAIRITEL	360.0	H	46.8	14.356 ± 0.089	1872.6 ± 147.3
PAIRITEL	360.0	K	46.8	12.906 ± 0.106	4621.6 ± 431.3
PAIRITEL	450.5	J	70.2	16.312 ± 0.109	483.8 ± 46.3
PAIRITEL	450.5	H	70.2	14.718 ± 0.083	1341.6 ± 98.2
PAIRITEL	450.5	K	70.2	13.223 ± 0.092	3452.5 ± 279.3
PAIRITEL	577.5	J	93.6	16.519 ± 0.111	399.7 ± 39.0
PAIRITEL	577.5	H	93.6	15.189 ± 0.087	869.0 ± 66.8
PAIRITEL	577.5	K	93.6	13.589 ± 0.086	2464.5 ± 188.3
PAIRITEL	758.5	J	140.4	17.004 ± 0.126	255.9 ± 28.0
PAIRITEL	758.5	H	140.4	15.729 ± 0.098	528.7 ± 45.8
PAIRITEL	758.5	K	140.4	14.068 ± 0.092	1585.4 ± 128.2
PAIRITEL	1013.5	J	187.2	17.139 ± 0.131	225.9 ± 25.7
PAIRITEL	1013.5	H	187.2	15.804 ± 0.096	493.4 ± 41.7
PAIRITEL	1013.5	K	187.2	14.280 ± 0.088	1303.9 ± 101.7
PAIRITEL	1266.5	J	329.6	17.402 ± 0.109	177.4 ± 17.0
PAIRITEL	1266.5	H	329.6	15.937 ± 0.063	436.4 ± 24.5
PAIRITEL	1266.5	K	329.6	14.497 ± 0.065	1067.8 ± 61.7
PAIRITEL	1882.0	J	470.9	17.807 ± 0.133	122.1 ± 14.0
PAIRITEL	1882.0	H	470.9	16.124 ± 0.081	367.2 ± 26.4
PAIRITEL	1882.0	K	400.2	14.727 ± 0.071	863.8 ± 54.9
PAIRITEL	3475.5	J	1601.0	18.021 ± 0.161	100.3 ± 13.9
PAIRITEL	3485.5	H	1608.8	16.522 ± 0.092	254.6 ± 20.6
PAIRITEL	3485.5	K	1491.1	15.064 ± 0.084	633.6 ± 47.3
KAIT	188.0	clear	20.0	17.501 ± 0.055	326.0 ± 16.1
KAIT	279.0	clear	20.0	18.094 ± 0.087	188.8 ± 14.5
KAIT	370.0	clear	20.0	18.413 ± 0.114	140.7 ± 14.0
KAIT	466.0	clear	20.0	18.883 ± 0.168	91.28 ± 13.09
KAIT	557.0	clear	20.0	19.358 ± 0.270	58.93 ± 12.98
KAIT	741.5	clear	207.0	19.773 ± 0.216	40.21 ± 7.25
KAIT	1156.0	clear	480.0	19.648 ± 0.154	45.12 ± 5.97
KAIT	1687.0	clear	438.0	20.080 ± 0.227	30.31 ± 5.72
KAIT	2237.5	clear	585.0	20.488 ± 0.293	20.81 ± 4.92
KAIT	3241.5	clear	615.0	20.262 ± 0.236	25.63 ± 5.01
KAIT	4105.0	clear	1034.0	21.361 ± 0.501	9.315 ± 3.443
KAIT	4914.5	clear	507.0	≥ 21.53	≤ 7.994
KAIT	7192.5	clear	3793.0	≥ 21.97	≤ 5.330
KAIT	158.0	I	20.0	16.582 ± 0.094	587.2 ± 48.7
KAIT	250.0	I	20.0	17.322 ± 0.170	297.0 ± 43.0

Continued on Next Page...

Telescope	$t_{\rm mid}$[a] sec	Filter	Exp. time sec	Mag.[b]	Flux[c] μJy
KAIT	341.0	I	20.0	17.995 ± 0.332	159.8 ± 42.1
KAIT	436.0	I	20.0	17.929 ± 0.308	169.8 ± 41.9
KAIT	527.0	I	20.0	18.439 ± 0.487	106.2 ± 38.4
KAIT	712.0	I	206.0	18.926 ± 0.456	67.79 ± 23.25
KAIT	1126.5	I	481.0	19.529 ± 0.567	38.90 ± 15.83
KAIT	1957.0	I	1038.0	19.628 ± 0.417	35.51 ± 11.33
KAIT	3778.0	I	1748.0	≥ 20.36	≤ 18.06
KAIT	6137.5	I	1755.0	≥ 20.32	≤ 18.71
KAIT	128.0	V	20.0	17.538 ± 0.142	379.9 ± 46.6
KAIT	219.0	V	20.0	18.517 ± 0.315	154.2 ± 38.8
KAIT	310.0	V	20.0	19.187 ± 0.585	83.19 ± 34.65
KAIT	449.0	V	116.0	19.540 ± 0.531	60.10 ± 23.25
KAIT	727.0	V	298.0	≥ 19.91	≤ 42.74
KAIT	1187.0	V	480.0	≥ 20.06	≤ 37.23
ROTSE	24.5	clear	5.0	14.920 ± 0.040	3512.1 ± 127.0
ROTSE	31.4	clear	5.0	15.210 ± 0.060	2688.8 ± 144.6
ROTSE	38.4	clear	5.0	15.200 ± 0.050	2713.7 ± 122.1
ROTSE	45.3	clear	5.0	15.520 ± 0.080	2021.0 ± 143.6
ROTSE	52.2	clear	5.0	15.590 ± 0.080	1894.8 ± 134.6
ROTSE	59.1	clear	5.0	15.830 ± 0.080	1519.0 ± 107.9
ROTSE	66.1	clear	5.0	15.700 ± 0.080	1712.2 ± 121.6
ROTSE	73.0	clear	5.0	15.870 ± 0.100	1464.1 ± 128.8
ROTSE	80.0	clear	5.0	16.060 ± 0.120	1229.0 ± 128.6
ROTSE	87.0	clear	5.0	16.270 ± 0.120	1012.9 ± 106.0
ROTSE	112.2	clear	20.0	16.540 ± 0.080	789.9 ± 56.1
ROTSE	141.4	clear	20.0	16.810 ± 0.110	616.0 ± 59.3
ROTSE	170.5	clear	20.0	17.190 ± 0.120	434.1 ± 45.4
ROTSE	215.0	clear	49.3	17.660 ± 0.170	281.6 ± 40.8
ROTSE	273.5	clear	49.3	17.980 ± 0.190	209.7 ± 33.7
ROTSE	346.3	clear	78.4	18.350 ± 0.180	149.1 ± 22.8
ROTSE	563.0	clear	337.0	19.130 ± 0.210	72.71 ± 12.79
ROTSE	1082.3	clear	683.1	19.630 ± 0.270	45.87 ± 10.10
ROTSE	1969.9	clear	1073.3	19.640 ± 0.240	45.45 ± 9.01
ROTSE	3655.6	clear	2273.5	20.520 ± 0.370	20.21 ± 5.84
SuperLOTIS	40.8	R		15.060 ± 0.059	3087.2 ± 163.7
SuperLOTIS	57.9	R		15.412 ± 0.077	2232.4 ± 153.0
SuperLOTIS	75.2	R		15.596 ± 0.092	1884.4 ± 153.1
SuperLOTIS	91.9	R		15.961 ± 0.097	1346.4 ± 114.8
SuperLOTIS	109.1	R		16.267 ± 0.118	1015.7 ± 104.5
SuperLOTIS	130.7	R		16.508 ± 0.146	813.5 ± 102.4
SuperLOTIS	157.9	R		16.917 ± 0.213	558.2 ± 99.5
SuperLOTIS	184.6	R		17.326 ± 0.296	383.0 ± 91.3
SuperLOTIS	211.2	R		17.786 ± 0.440	250.7 ± 83.5
SuperLOTIS	238.4	R		17.920 ± 0.490	221.6 ± 80.5
SuperLOTIS	285.0	R		17.973 ± 0.128	211.0 ± 23.4
SuperLOTIS	352.2	R		18.159 ± 0.152	177.8 ± 23.2
SuperLOTIS	418.9	R		18.559 ± 0.199	123.0 ± 20.6

Continued on Next Page...

Telescope	$t_{\rm mid}$[a] sec	Filter	Exp. time sec	Mag.[b]	Flux[c] μJy
SuperLOTIS	486.1	R		18.400 ± 0.192	142.4 ± 23.1
SuperLOTIS	586.3	R		18.988 ± 0.226	82.86 ± 15.57
SuperLOTIS	720.1	R		19.295 ± 0.301	62.45 ± 15.10
P60	234.8	R	60.0	17.524 ± 0.014	319.1 ± 4.1
P60	320.3	R	60.0	18.122 ± 0.020	184.0 ± 3.4
P60	577.6	R	60.0	19.115 ± 0.050	73.72 ± 3.32
P60	748.9	R	60.0	19.566 ± 0.066	48.66 ± 2.87
P60	1005.8	R	60.0	19.717 ± 0.079	42.34 ± 2.97
P60	1262.8	R	60.0	19.837 ± 0.091	37.91 ± 3.05
P60	1579.4	R	120.0	19.959 ± 0.068	33.88 ± 2.06
P60	2161.9	R	120.0	20.053 ± 0.078	31.07 ± 2.15
P60	2744.3	R	120.0	20.263 ± 0.095	25.61 ± 2.15
P60	406.1	i	60.0	18.359 ± 0.022	171.1 ± 3.4
P60	834.5	i	60.0	19.538 ± 0.060	57.76 ± 3.11
P60	1091.4	i	60.0	19.621 ± 0.067	53.51 ± 3.20
P60	1348.3	i	60.0	19.570 ± 0.062	56.08 ± 3.11
P60	1725.0	i	120.0	19.892 ± 0.055	41.69 ± 2.06
P60	2307.5	i	120.0	19.899 ± 0.062	41.42 ± 2.30
P60	2889.9	i	120.0	20.280 ± 0.086	29.16 ± 2.22
P60	491.8	z	60.0	18.694 ± 0.092	127.3 ± 10.3
P60	920.0	z	60.0	19.725 ± 0.222	49.25 ± 9.11
P60	1177.0	z	60.0	19.936 ± 0.299	40.55 ± 9.76
P60	1433.8	z	60.0	19.880 ± 0.248	42.69 ± 8.72
P60	1870.7	z	120.0	20.133 ± 0.211	33.82 ± 5.97
UKIRT	8451000	K	360.0	14.624 ± 0.025	949.7 ± 21.6
UKIRT	10058400	K	360.0	14.768 ± 0.025	831.8 ± 18.9
UKIRT	11651400	K	360.0	14.987 ± 0.026	679.8 ± 16.1
UKIRT	15233400	J	180.0	18.470 ± 0.054	66.29 ± 3.22
UKIRT	16286400	H	180.0	17.060 ± 0.035	155.1 ± 4.9
UKIRT	17337600	J	180.0	18.609 ± 0.060	58.33 ± 3.14
UKIRT	18390600	K	180.0	15.784 ± 0.029	326.3 ± 8.6
UKIRT	19468800	J	180.0	18.817 ± 0.066	48.16 ± 2.84
UKIRT	20529000	H	180.0	17.480 ± 0.042	105.4 ± 4.0
UKIRT	21618000	J	180.0	19.169 ± 0.085	34.82 ± 2.62
UKIRT	22674600	K	180.0	16.220 ± 0.031	218.4 ± 6.1
UKIRT	23729400	J	180.0	19.335 ± 0.089	29.89 ± 2.35
UKIRT	24458400	H	180.0	18.014 ± 0.053	64.43 ± 3.07
UKIRT	25835400	J	180.0	19.634 ± 0.116	22.69 ± 2.30
UKIRT	26888400	K	180.0	16.526 ± 0.033	164.7 ± 4.9
UVOT/CrAO	190.9	White		19.790 ± 0.130	31.21 ± 3.52
UVOT/CrAO	45453.3	R		≥ 22.20	≤ 4.301
UVOT/CrAO	51710.4	R		≥ 22.50	≤ 3.263

[a]Exposure mid-time, measured from the *Swift* trigger.
[b]Observed value; not corrected for Galactic extinction
[c]Corrected for Galactic extinction ($E_{B-V} = 0.023$ mag)
[x]Point not used in modeling

Appendix C

GRB Host Galaxy Data

Table C.1: Afterglow Positions

GRB	Telescope	RA (J2000)	Declination	Unc. $''$	Reference
041219A	Keck/NIRC	00:24:27.68	+62:50:33.501	0.228	Bloom et al. 2004
041223	XRT-DSS	06:40:47.39	−37:04:22.6	6.4	(b)
	LCO40	06:40:47.323	−37:04:22.77	0.15	Berger et al. 2005c
	VLT	06:40:47.33	−37:04:23.14	0.16	Burrows et al. 2005b
050124	XRT-Enhanced	12:51:30.55	+13:02:39.5	1.6	(a)
	XRT-DSS	12:51:30.43	+13:02:40.6	2.8	(b)
	NIRC	12:51:30.35	+13:02:41.3	0.2	Berger et al. 2005c
050126	XRT-DSS	18:32:27.22	+42:22:14.2	3.3	(b)
	NIRC	18:32:27.18	+42:22:13.6	0.12	Berger et al. 2005c
050215B	XRT-Enhanced	11:37:47.35	+40:47:50.5	2.7	(a)
	XRT-DSS	11:37:47.76	+40:47:44.9	1.9	(b)
	UKIRT	11:37:47.90	+40:47:45.6	–	Tanvir et al. 2005
050319	XRT-Enhanced	10:16:47.90	+43:32:55.1	1.4	(a)
	XRT-DSS	10:16:47.80	+43:32:53.5	1.1	(b)
	UVOT	10:16:47.76	+43:32:54.9	1.2	(c)
	ROTSE	10:16:47.9	+43:32:54.5	–	Quimby et al. 2006
	MAIT	10:16:47.66	+43:32:55.6	0.6	George et al. 2006
050401	XRT-DSS	16:31:28.84	+02:11:14.5	1.8	(b)
	VLA	16:31:28.82	+02:11:14.83	0.5	Soderberg 2005
	Siding Spring	16:31:28.81	+02:11:14.2	–	McNaught & Price 2005
	VLT acquisition	16:31:28.807	+02:11:14.41	0.35	this work
050408	XRT-Enhanced	12:02:17.29	+10:51:09.7	1.4	(a)
	XRT-DSS	12:02:17.31	+10:51:09.0	0.5	(b)
	RTT150	12:02:17.31	+10:51:9.4	0.1	Aslan et al. 2005
050412	XRT-DSS	12:04:25.19	−01:12:01.0	6.7	(b)
050416B	No afterglow position available				
050502A	PAIRITEL	13:29:46.33	+42:40:27.3	0.5	Blake & Bloom 2005
	AAVSO	13:29:46.28	+42:40:27.7	–	
	Liverpool 2m	13:29:46.25	+42:40:27.50	–	Gomboc et al. 2005a

Continued on Next Page...

GRB	Telescope	RA (J2000)	Declination	Unc. $''$	Reference
050502B	XRT-Enhanced	09:30:10.11	+16:59:47.9	1.4	(a)
	XRT-DSS	09:30:10.06	+16:59:46.5	1.0	(b)
	ANU 1m	09:30:10.024	+16:59:48.07	–	Rich et al. 2005
050509B	XRT-Enhanced	12:36:13.76	+28:59:03.2	3.3	(a)
	XRT-DSS	12:36:14.06	+28:59:07.2	3.4	(b)
050603	XRT-Enhanced	02:39:56.92	−25:10:54.7	1.4	(a)
	XRT-DSS	02:39:56.90	−25:10:55.7	0.9	(b)
	UVOT	02:39:56.8	−25:10:54.9	1.2	(c)
	LCO 100-inch	02:39:57	−25:10:54	0.5	Berger & McWilliam 2005
	VLA	02:39:56.891	−25:10:54.6	0.1	Cameron 2005a
050607	XRT-DSS	20:00:42.77	+09:08:31.1	1.4	(b)
	KPNO 4m	20:00:42.79	+09:08:31.5	0.5	Rhoads 2005b
050709	La Silla 1.5m	23:01:26.957	−38:58:39.76	0.25	Hjorth et al. 2005b
	Chandra	23:01:26.96	−38:58:39.5	0.4	Fox et al. 2005b
050712	XRT-Enhanced	05:10:48.19	+64:54:48.3	1.5	(a)
	XRT-DSS	05:10:48.16	+64:54:46.8	1.0	(b)
	UVOT	05:10:48.1	+64:54:47.6	1.2	(c)
	Tautenburg	05:10:48.1	+64:54:47.6	–	Zeh et al. 2005
050713A	XRT-Enhanced	21:22:9.35	+77:04:28.9	1.4	(a)
	XRT-DSS	21:22:09.54	+77:04:29.7	2.8	(b)
	NOT	21:22:09.53	+77:04:29.5	0.4	Guziy et al. 2005a
	TNG	21:22:09.6	+77:04:29	1	Malesani et al. 2005
050713B	XRT-Enhanced	20:31:15.56	+60:56:43.7	1.4	(a)
	XRT-DSS	20:31:15.59	+60:56:41.9	1.0	(b)
050714B	XRT-Enhanced	11:18:47.63	−15:32:48.9	1.5	(a)
	XRT-DSS	11:18:47.75	−15:32:49.3	2.1	(b)
	UVOT	11:18:48.26	−15:32:50.87	1.2	(c)
050716	XRT-Enhanced	22:34:20.81	+38:41:04.0	1.4	(a)
	XRT-DSS	22:34:20.51	+38:41:01.9	0.8	(b)
	UKIRT	22:34:20.73	+38:41:03.6	0.4	Rol et al. 2007c
050730	XRT-Enhanced	14:08:17.15	−03:46:18.3	1.4	(a)
	XRT-DSS	14:08:17.12	−03:46:16.3	1.4	(b)
	UVOT	14:08:17.09	−03:46:18.9	0.5	(c)
	OSN 1.5m	14:08:17.14	−03:46:17.8	0.35	Sota et al. 2005
	Liverpool 2m	14:08:17.13	−03:46:17.7	–	Gomboc et al. 2005b
	VLA	14:08:17.11	−03:46:17.2	0.2	Cameron 2005b
	VLT	14:08:17.122	−03:46:17.82	0.2	this work
050803	XRT-Enhanced	23:22:37.91	+05:47:09.0	1.4	(a)
	XRT-DSS	23:22:37.87	+05:47:09.8	1.8	(b)
050814	XRT-Enhanced	17:36:45.30	+46:20:22.4	1.4	(a)
	XRT-DSS	17:36:45.31	+46:20:21.6	1.0	(b)
	P60	17:36:45.39	+46:20:21.6	0.2	Cenko 2005
050819	XRT-Enhanced	23:55:01.65	+24:51:38.9	1.5	(a)
	XRT-DSS	23:55:01.49	+24:51:39.9	3.3	(b)
050820A	XRT-Enhanced	22:29:38.14	+19:33:37.5	1.4	(a)
	XRT-DSS	22:29:38.08	+19:33:36.4	0.9	(b)
	P60	22:29:38.11	+19:33:37.1	0.5	Fox & Cenko 2005

Continued on Next Page...

GRB	Telescope	RA (J2000)	Declination	Unc. $''$	Reference
050826	XRT-Enhanced	05:51:01.61	−02:38:36.7	1.5	(a)
	XRT-DSS	05:51:01.69	−02:38:37.6	2.6	(b)
	MDM 1.3m	05:51:01.58	−02:38:35.8	0.5	Halpern & Mirabal 2006
050827	XRT-Enhanced	04:17:9.61	+18:12:01.0	1.5	(a)
	XRT-DSS	04:17:09.52	+18:11:59.8	1.1	(b)
050915A	XRT-Enhanced	05:26:44.86	−28:00:58.9	1.4	(a)
	XRT-DSS	05:26:44.86	−28:00:59.9	1.4	(b)
	PAIRITEL	05:26:44.804	−28:00:59.27	0.18	Bloom 2005
050922B	XRT-Enhanced	00:23:13.39	−05:36:18.0	1.7	(a)
	XRT-DSS	00:23:13.37	−05:36:17.7	2.4	(b)
050922C	XRT-Enhanced	21:09:33.01	−08:45:30.6	1.4	(a)
	XRT-DSS	21:09:33.12	−08:45:28.3	2.0	(b)
	UVOT	21:09:33.0	−08:45:30.1	1.2	(c)
	NOT	21:09:33.083	−08:45:30.2	0.2	Jakobsson et al. 2005a
051001	XRT-Enhanced	23:23:48.65	−31:31:25.0	2.1	(a)
	XRT-DSS	23:23:48.73	−31:31:23.3	1.5	(b)
051006	XRT-Enhanced	07:23:14.13	+09:30:20.1	1.5	(a)
	XRT-DSS	07:23:14.09	+09:30:22.3	6.3	(b)
051008	XRT-Enhanced	13:31:29.59	+42:05:53.1	1.4	(a)
	XRT-DSS	13:31:29.55	+42:05:53.3	1.2	(b)
051109A	XRT-Enhanced	22:01:15.25	+40:49:22.6	1.4	(a)
	XRT-DSS	22:01:15.32	+40:49:21.6	1.1	(b)
	UVOT	22:01:15.32	+40:49:23.7	0.5	(c)
	PAIRITEL	22:01:15.313	+40:49:23.31	0.1	Bloom et al. 2005a
051109B	XRT-Enhanced	23:01:50.33	+38:40:46.5	1.5	(a)
	XRT-DSS	23:01:50.32	+38:40:47.3	1.6	(b)
051111	XRT-Enhanced	23:12:33.07	+18:22:28.2	1.5	(a)
	XRT-DSS	23:12:33.22	+18:22:28.4	2.0	(b)
	UVOT	23:12:33.17	+18:22:28.80	1.2	(c)
	ROTSE	23:12:33.2	+18:22:29.1	–	Rujopakarn et al. 2005
051117A	XRT-Enhanced	15:13:34.09	+30:52:11.8	1.6	(a)
	XRT-DSS	15:13:34.03	+30:52:11.7	1.9	(b)
	UVOT	15:13:34.09	+30:52:12.7	0.5	(c)
051117B	XRT-Enhanced	05:40:43.38	−19:16:26.9	1.7	(a)
	XRT-DSS	05:40:43.26	−19:16:28.7	2.0	(b)
051211B	XRT-Enhanced	23:02:41.53	+55:04:50.7	1.6	(a)
	XRT-DSS	23:02:41.50	+55:04:50.8	1.6	(b)
	OSN 1.5m	23:02:41.57	+55:04:51.5	0.4	Jelnek et al. 2005
060105	XRT-Enhanced	19:50:00.68	+46:20:55.4	1.4	(a)
	XRT-DSS	19:50:00.69	+46:20:55.9	1.3	(b)
060109	XRT-Enhanced	18:50:43.65	+31:59:26.5	1.4	(a)
	XRT-DSS	18:50:43.55	+31:59:28.3	1.8	(b)
060111A	XRT-Enhanced	18:24:49.12	+37:36:14.0	1.5	(a)
	XRT-DSS	18:24:49.20	+37:36:14.1	1.1	(b)
	UVOT	18:24:49.132	+37:36:14.47	1.2	(c)
060111B	XRT-Enhanced	19:05:42.64	+70:22:33.0	1.4	(a)
	XRT-DSS	19:05:42.75	+70:22:33.3	2.6	(b)

Continued on Next Page...

GRB	Telescope	RA (J2000)	Declination	Unc. $''$	Reference
	UVOT	19:05:42.48	+70:22:33.6	0.5	(c)
	MITSuME	19:05:42.47	+70:22:33.1	0.3	Yanagisawa et al. 2006
	TAROT	19:05:42.46	+70:22:32.3	0.6	Klotz et al. 2006
060124	XRT-Enhanced	05:08:25.86	+69:44:26.5	1.4	(a)
	XRT-DSS	05:08:26.00	+69:44:27.2	0.7	(b)
	Tautenburg	05:08:25.5	+69:44:26	2	Kann 2006
	UVOT	05:08:25.859	+69:44:27.41	0.5	Romano et al. 2006
060202	XRT-Enhanced	02:23:22.97	+38:23:03.1	1.4	(a)
	XRT-DSS	02:23:23.01	+38:23:03.2	1.1	(b)
060203	XRT-Enhanced	06:54:03.72	+71:48:38.9	1.4	(a)
	XRT-DSS	06:54:04.05	+71:48:39.3	1.1	(b)
	Asiago	06:54:03.85	+71:48:38.4	0.5	Malesani & Piranomonte 2006b
060204B	XRT-Enhanced	14:07:15.04	+27:40:37.0	1.4	(a)
	XRT-DSS	14:07:15.05	+27:40:36.9	1.6	(b)
	FTN	14:07:14.9	+27:40:36.4	–	Guidorzi et al. 2006a
060210	XRT-Enhanced	03:50:57.33	+27:01:33.7	1.4	(a)
	XRT-DSS	03:50:57.35	+27:01:34.3	0.9	(b)
	FTN	03:50:57.37	+27:01:34.40	0.5	Mundell et al. 2006
	P60	03:50:57.41	+27:01:34.4	2	Fox & Cenko 2006
	KAIT	03:50:57.35	+27:01:34.1	–	Li 2006
060219	XRT-Enhanced	16:07:21.52	+32:18:57.6	1.5	(a)
	XRT-DSS	16:07:21.54	+32:18:57.3	1.6	(b)
060306	XRT-Enhanced	02:44:22.83	−02:08:55.1	1.4	(a)
	XRT-DSS	02:44:22.91	−02:08:54.0	1.3	(b)
060312	XRT-DSS	03:03:05.92	+12:50:02.0	2.0	(b)
060319	XRT-Enhanced	11:45:33.05	+60:00:39.6	1.4	(a)
	XRT-DSS	11:45:32.89	+60:00:39.1	0.9	(b)
060413	XRT-Enhanced	19:25:07.87	+13:45:30.0	1.4	(a)
	XRT-DSS	19:25:07.91	+13:45:30.1	1.9	(b)
060418	XRT-Enhanced	15:45:42.66	−03:38:20.4	1.4	(a)
	XRT-DSS	15:45:42.47	−03:38:20.1	4.9	(b)
	UVOT	15:45:42.60	−03:38:20.0	0.5	(c)
060424	NOT	00:29:25.8	+36:47:58.7	–	Thöne et al. 2006e
	NOT	00:29:25.837	+36:47:59.23	0.7	this work
060428B	XRT-Enhanced	15:41:25.70	+62:01:30.2	1.4	(a)
	XRT-DSS	15:41:25.72	+62:01:29.6	1.4	(b)
	KAIT	15:41:25.628	+62:01:30.02	0.2	Perley et al. 2007a
060502B	XRT-Enhanced	18:35:45.28	+52:37:54.7	5.8	(a)
	XRT-DSS	18:35:45.53	+52:37:52.9	3.7	(b)
060505	XRT-Enhanced	22:07:03.38	−27:48:52.9	1.9	(a)
	XRT-DSS	22:07:03.39	−27:48:53.0	2.5	(b)
	Gemini-S GMOS	22:07:03.44	−27:48:51.9	–	Ofek et al. 2006
060510B	XRT-Enhanced	15:56:29.25	+78:34:12.1	1.5	(a)
	XRT-DSS	15:56:30.02	+78:34:09.2	2.6	(b)
	XMM-Newton	15:56:29.2	+78:34:12.0	1.5	Campana & DeLuca 2006
	MDM 1.3m	15:56:29.615	+78:34:13.02	2	Mirabal & Halpern 2006
	Gemini-N GMOS	15:56:29.621	+78:34:12.47	0.4	this work

Continued on Next Page...

GRB	Telescope	RA (J2000)	Declination	Unc. $''$	Reference
060512	XRT-Enhanced	13:03:05.73	+41:11:26.6	1.5	(a)
	XRT-DSS	13:03:05.73	+41:11:26.9	2.4	(b)
	UVOT	13:03:05.81	+41:11:27.2	0.5	(c)
	Liverpool 2m	13:03:05.8	+41:11:26.8	0.5	Mundell & Steele 2006
060607A	XRT-Enhanced	21:58:50.41	−22:29:47.1	1.4	(a)
	XRT-DSS	21:58:50.44	−22:29:48.1	1.7	(b)
	UVOT	21:58:50.4	−22:29:47.4	0.5	(c)
	REM	21:58:50.4	−22:29:47	–	Covino et al. 2006b
060805A	XRT-Enhanced	14:43:43.45	+12:35:11.6	1.6	(a)
	XRT-DSS	14:43:43.46	+12:35:11.8	1.8	(b)
060807	XRT-Enhanced	16:50:02.63	+31:35:30.2	1.4	(a)
	XRT-DSS	16:50:02.58	+31:35:30.4	1.2	(b)
	NOT	16:50:02.6	+31:35:30.7	0.5	Fynbo et al. 2006a
060814A	XRT-Enhanced	14:45:21.32	+20:35:09.2	1.4	(a)
	XRT-DSS	14:45:21.29	+20:35:10.7	0.9	(b)
060904A	XRT-DSS	15:50:54.50	+44:59:09.2	1.4	(b)
060904B	XRT-Enhanced	03:52:50.56	−00:43:30.1	1.4	(a)
	XRT-DSS	03:52:50.58	−00:43:30.5	1.1	(b)
	UVOT	03:52:50.54	−00:43:31.1	0.5	(c)
	Crni Vrh	03:52:50.52	−00:43:30.9	0.2	Skvarc 2006
	BOOTES	03:52:50.54	−00:43:30.5	0.5	Postigo et al. 2006
060906	XRT-Enhanced	02:43:00.90	+30:21:43.0	1.4	(a)
	XRT-DSS	02:43:00.72	+30:21:43.2	2.5	(b)
	P60	02:43:00.9	+30:21:42.12	–	Cenko et al. 2006c
	KAIT	02:43:00.84	+30:21:41.9	0.2	Li & Bloom 2006
060923A	XRT-Enhanced	16:58:28.10	+12:21:37.9	1.5	(a)
	XRT-DSS	16:58:28.05	+12:21:39.5	3.4	(b)
	Gemini-N NIRI	16:58:28.15	+12:21:38.9	0.5	Fox et al. 2006
	UKIRT	16:58:28.16	+12:21:38.9	0.25	Tanvir et al. 2008c
060923C	XRT-DSS	23:04:28.36	+03:55:28.4	1.8	(b)
	VLT	23:04:28.31	+03:55:29.0	–	Covino et al. 2006a
	Gemini-N NIRI	23:04:28.288	+03:55:28.63	0.4	this work
060927	XRT-Enhanced	21:58:12.04	+05:21:48.9	1.6	(a)
	XRT-DSS	21:58:12.23	+05:21:52.2	3.8	(b)
	ROTSE	21:58:11.93	+05:21:50.32	–	Schaefer et al. 2006
	FTS	21:58:12.0	+05:21:49	–	Guidorzi et al. 2006b
	VLT	21:58:12.02	+05:21:48.9	0.2	Ruiz-Velasco et al. 2007
060929	XRT-Enhanced	17:32:28.94	+29:50:06.7	1.5	(a)
	XRT-DSS	17:32:28.98	+29:50:07.7	2.2	(b)
061021	XRT-Enhanced	09:40:36.15	−21:57:05.3	1.4	(a)
	XRT-DSS	09:40:36.14	−21:57:04.4	0.5	(b)
	UVOT	09:40:36.12	−21:57:05.4	0.6	(c)
061028	XRT-Enhanced	06:28:54.66	+46:17:56.3	1.6	(a)
	XRT-DSS	06:28:54.61	+46:17:57.5	2.7	(b)
061110A	XRT-Enhanced	22:25:9.85	−02:15:31.0	1.6	(a)
	XRT-DSS	22:25:09.95	−02:15:31.9	1.0	(b)
	VLT	22:25:09.838	−02:15:31.00	0.4	this work

Continued on Next Page...

GRB	Telescope	RA (J2000)	Declination	Unc. $''$	Reference
061121	XRT-Enhanced	09:48:54.59	−13:11:42.1	1.4	(a)
	XRT-DSS	09:48:54.50	−13:11:42.6	0.9	(b)
	UVOT	09:48:54.55	−13:11:42.4	0.6	(c)
061122	XRT-Enhanced	20:15:19.84	+15:31:01.0	1.4	(a)
	XRT-DSS	20:15:19.88	+15:31:02.8	0.9	(b)
	MDM 2.4m	20:15:19.84	+15:31:02.5	0.5	Halpern & Armstrong 2006
061217	XRT-DSS	10:41:39.32	−21:07:22.1	3.8	(b)
	XRT	10:41:39.10	−21:07:26.9	6.0	Evans et al. 2006
061222A	XRT-Enhanced	23:53:03.39	+46:31:57.6	1.4	(a)
	XRT-DSS	23:53:03.41	+46:31:58.2	0.8	(b)
	Gemini-N NIRI	23:53:03.419	+46:31:58.60	0.2	Cenko & Fox 2006a
070103	XRT-Enhanced	23:30:13.75	+26:52:34.0	1.4	(a)
	XRT-DSS	23:30:13.60	+26:52:34.8	2.4	(b)
070219	XRT-Enhanced	17:20:46.08	+69:22:12.2	1.7	(a)
	XRT-DSS	17:20:45.90	+69:22:14.1	2.5	(b)
070224	XRT-Enhanced	11:56:06.59	−13:19:49.7	1.6	(a)
	XRT-DSS	11:56:06.57	−13:19:49.4	1.7	(b)
	NOT	11:56:06.65	−13:19:48.8	0.5	Thöne et al. 2007a
	Gemini-S GMOS	11:56:06.6	−13:19:48.9	–	Chen et al. 2007c
070311	XRT-Enhanced	05:50:08.24	+03:22:29.7	1.5	(a)
	XRT-DSS	05:50:08.28	+03:22:32.8	5.1	(b)
	REM	05:50:08.21	+03:22:30.3	–	Covino et al. 2007
070412	XRT-Enhanced	12:06:10.06	+40:08:35.6	1.5	(a)
	XRT-DSS	12:06:10.18	+40:08:35.3	2.2	(b)
070419A	XRT-Enhanced	12:10:58.83	+39:55:30.9	1.7	(a)
	XRT-DSS	12:10:58.94	+39:55:28.5	2.2	(b)
	MAO 1.5m	12:10:58.83	+39:55:34.06	0.15	Pozanenko et al. 2007
	KAIT	12:10:58.82	+39:55:33.9	–	Chornock et al. 2007
	LBT	12:10:58.80	+39:55:33.71	0.2	Garnavich et al. 2007b
070429A	XRT-Enhanced	19:50:48.93	−32:24:17.6	2.1	(a)
	XRT-DSS	19:50:48.71	−32:24:15.1	1.9	(b)
070429B	XRT-Enhanced	21:52:03.85	−38:49:41.7	2.3	(a)
	XRT-DSS	21:52:03.84	−38:49:42.4	6.2	(b)
	UVOT	21:52:03.68	−38:49:43.6	0.6	(c)
070520A	XRT-Enhanced	12:53:26.06	+74:59:23.4	3.4	(a)
	XRT-DSS	12:53:26.60	+74:59:26.3	1.4	(b)
070521	XRT-Enhanced	16:10:38.62	+30:15:22.6	1.4	(a)
	XRT-DSS	16:10:38.60	+30:15:21.3	2.1	(b)
070621	XRT-Enhanced	21:35:10.16	−24:49:02.8	1.4	(a)
	XRT-DSS	21:35:09.96	−24:49:03.2	2.1	(b)
070714A	XRT-Enhanced	02:51:43.36	+30:14:34.8	1.8	(a)
	XRT-DSS	02:51:43.10	+30:14:34.2	3.2	(b)
070714B	XRT-Enhanced	03:51:22.30	+28:17:51.3	1.4	(a)
	XRT-DSS	03:51:22.19	+28:17:51.2	2.6	(b)
	Liverpool	03:51:22.2	+28:17:51.4	0.5	Graham et al. 2009
070721A	XRT-Enhanced	00:12:39.19	−28:33:00.2	1.6	(a)
	XRT-DSS	00:12:39.25	−28:33:00.7	1.7	(b)

Continued on Next Page...

GRB	Telescope	RA (J2000)	Declination	Unc. $''$	Reference
	UVOT	00:12:39.22	−28:33:00.7	2.0	(c)
070724A	XRT-Enhanced	01:51:14.09	−18:35:39.0	1.8	(a)
	XRT-DSS	01:51:14.03	−18:35:38.6	1.6	(b)
	Gemini-N NIRI	01:51:14.071	−18:35:39.33	0.15	Berger et al. 2009
	Gemini-N NIRI	01:51:14.066	−18:35:39.34	0.18	Berger et al. 2009
070729	XRT-Enhanced	03:45:16.05	−39:19:20.3	2.5	(a)
	XRT-DSS	03:45:15.79	−39:19:20.9	10.7	(b)
070808	XRT-Enhanced	00:27:03.40	+01:10:35.1	1.5	(a)
	XRT-DSS	00:27:03.29	+01:10:34.7	2.7	(b)
070809	XRT-DSS	13:35:04.41	−22:08:28.9	4.8	(b)
	Keck LRIS	13:35:04.55	−22:08:30.8	0.4	Perley et al. 2007g
070810A	XRT-Enhanced	12:39:51.20	+10:45:03.0	1.4	(a)
	XRT-DSS	12:39:51.21	+10:45:03.8	2.6	(b)
	UVOT	12:39:51.22	+10:45:04.3	0.6	(c)
	Keck LRIS	12:39:51.230	+10:45:03.77	0.4	this work
070810B	No afterglow position available				
071021	XRT-DSS	22:42:34.33	+23:43:05.4	3.2	(b)
	TNG+NOT	22:42:34.31	+23:43:06.5	0.5	Castro-Tirado et al. 2007a
071025	XRT-Enhanced	23:40:17.06	+31:46:42.5	1.4	(a)
	XRT-DSS	23:40:17.14	+31:46:41.1	1.2	(b)
	PAIRITEL	23:40:17.078	+31:46:42.87	0.25	Bloom 2007
080207	XRT-Enhanced	13:50:02.99	+07:30:07.8	1.4	(a)
	XRT-DSS	13:50:02.93	+07:30:06.7	1.1	(b)
	Chandra	13:50:02.98	+07:30:07.4	0.4	MNRAS submitted
080210	XRT-Enhanced	16:45:04.01	+13:49:36.2	1.5	(a)
	XRT-DSS	16:45:04.07	+13:49:35.8	1.0	(b)
	UVOT	16:45:04.01	+13:49:35.9	0.6	(c)
	TAROT	16:45:03.97	+13:49:35	–	Klotz et al. 2008a
080229A	XRT-Enhanced	15:12:52.29	−14:42:16.2	1.4	(a)
	XRT-DSS	15:12:52.44	−14:42:14.9	2.0	(b)
080307	XRT-Enhanced	09:06:30.77	+35:08:19.7	1.4	(a)
	XRT-DSS	09:06:30.88	+35:08:19.3	1.0	(b)
	Gemini-N GMOS	09:06:30.80	+35:08:20.1	0.2	Page et al. 2009
080310	XRT-Enhanced	14:40:13.87	−00:10:30.5	1.4	(a)
	XRT-DSS	14:40:13.71	−00:10:32.2	2.9	(b)
	UVOT	14:40:13.80	−00:10:29.6	0.6	(c)
	KAIT	14:40:13.81	−00:10:30.6	–	Chornock et al. 2008a
080319A	XRT-Enhanced	13:45:19.95	+44:04:48.7	1.7	(a)
	XRT-DSS	13:45:19.94	+44:04:47.6	6.5	(b)
	P60	13:45:20.01	+44:04:48.6	–	Cenko 2008
080319C	XRT-Enhanced	17:15:55.45	+55:23:31.6	1.7	(a)
	XRT-DSS	17:15:56.15	+55:23:32.5	3.0	(b)
	UVOT	17:15:55.49	+55:23:30.6	0.53	(c)
	KAIT	17:15:55.54	+55:23:30.8	–	Li et al. 2008b
080319D	XRT-Enhanced	06:37:53.49	+23:56:33.7	1.5	(a)
	XRT-DSS	06:37:53.55	+23:56:34.6	3.9	(b)
	UVOT	06:37:53.6	+23:56:34.2	0.5	(c)

Continued on Next Page...

GRB	Telescope	RA (J2000)	Declination	Unc. ″	Reference
	GROND	06:37:53.56	+23:56:34.2	–	Clemens et al. 2008
080320	XRT-Enhanced	11:50:56.38	+57:09:25.1	1.4	(a)
	XRT-DSS	11:50:56.41	+57:09:24.1	0.6	(b)
	Gemini-N GMOS	11:50:56.427	+57:09:23.90	0.25	Tanvir et al. 2008b
080325	XRT-Enhanced	18:31:34.38	+36:31:26.1	1.7	(a)
	XRT-DSS	18:31:34.27	+36:31:24.5	1.4	(b)
	Subaru	18:31:34.23	+36:31:24.8	0.2	Hashimoto et al. 2010
080330	XRT-DSS	11:17:02.08	+30:37:26.8	3.8	(b)
	UVOT	11:17:04.51	+30:37:22.1	1.0	(c)
	XRT	11:17:04.68	+30:37:24.78	4.0	Mao & Guidorzi 2008
	PAIRITEL	11:17:04.496	+30:37:23.53	0.7	Bloom & Starr 2008
	Liverpool 2m	11:17:04.48	+30:37:23.8	0.2	Guidorzi et al. 2009
080430	XRT-Enhanced	11:01:14.66	+51:41:07.8	1.4	(a)
	XRT-DSS	11:01:14.68	+51:41:08.3	1.0	(b)
	UVOT	11:01:14.66	+51:41:08.4	0.5	(c)
	Chante-Perdix	11:01:14.76	+51:41:08.3	0.3	Rinner & Kugel 2008
	BOOTES-1	11:01:14.777	+51:41:08.61	–	Jelinek et al. 2008
080507	XRT-Enhanced	15:34:43.43	+56:26:07.6	2.3	(a)
	XRT-DSS	15:34:43.48	+56:26:07.6	4.5	(b)
	Keck LRIS	15:34:43.39	+56:26:08.28	0.7	Perley et al. 2008c
080514B	XRT-Enhanced	21:31:22.61	+00:42:29.9	1.7	(a)
	XRT-DSS	21:31:22.53	+00:42:28.3	5.3	(b)
	UVOT	21:31:22.71	+00:42:28.	0.60	(c)
	IAC80 0.8m	21:31:22.69	+00:42:28.6	–	Rossi et al. 2008
080515	XRT-DSS	00:12:39.49	+32:34:46.1	3.4	(b)
	KPNO 4m	00:12:39.362	+32:34:45.46	0.5	this work
080603A	XRT-Enhanced	18:37:37.96	+62:44:39.6	1.6	(a)
	XRT-DSS	18:37:37.90	+62:44:37.0	3.7	(b)
	UVOT	18:37:38.21	+62:44:38.40	1.2	(c)
	KAIT	18:37:38.06	+62:44:39.3	–	Chornock et al. 2008b
	FTN	18:37:38.05	+62:44:39.4	0.5	MNRAS submitted
080607	XRT-Enhanced	12:59:47.17	+15:55:09.7	1.4	(a)
	XRT-DSS	12:59:47.09	+15:55:10.6	2.3	(b)
	UVOT	12:59:47.20	+15:55:10.74	0.5	(c)
	KAIT	12:59:47.221	+15:55:10.86	0.3	this work
	PAIRITEL	12:59:47.219	+15:55:10.79	0.3	this work
080701	XRT-Enhanced	03:03:21.37	+75:28:29.1	1.7	(a)
	XRT-DSS	03:03:20.88	+75:28:30.7	6.6	(b)
080702A	XRT-Enhanced	20:52:12.20	+72:18:46.5	1.8	(a)
	XRT-DSS	20:52:12.63	+72:18:45.4	7.0	(b)
080710	XRT-Enhanced	00:33:05.67	+19:30:05.6	1.4	(a)
	XRT-DSS	00:33:05.59	+19:30:06.4	1.9	(b)
	UVOT	00:33:05.65	+19:30:05.3	0.5	(c)
	KAIT	00:33:05.64	+19:30:05.7	–	Li et al. 2008c
081211B	XRT-Enhanced	11:13:03.37	+53:49:47.4	1.8	(a)
	XRT-DSS	11:13:03.26	+53:49:47.8	6.7	(b)
081221	XRT-Enhanced	01:03:10.22	−24:32:53.2	1.4	(a)

Continued on Next Page...

GRB	Telescope	RA (J2000)	Declination	Unc. $''$	Reference
	XRT-DSS	01:03:10.22	−24:32:51.7	1.0	(b)
	Gemini-N NIRI	01:03:10.19	−24:32:52.2	–	Tanvir et al. 2008a
	Gemini-N NIRI	01:03:10.168	−24:32:51.67	0.15	this work
090111	XRT-Enhanced	16:46:42.08	+00:04:38.2	1.5	(a)
	XRT-DSS	16:46:42.18	+00:04:38.5	1.0	(b)
090113	XRT-Enhanced	02:08:13.71	+33:25:42.2	1.5	(a)
	XRT-DSS	02:08:13.77	+33:25:44.3	3.7	(b)
	Chandra	02:08:13.78	+33:25:43.4	0.5	priv. comm.
090404	XRT-Enhanced	15:56:57.50	+35:30:57.7	1.4	(a)
	XRT-DSS	15:56:57.41	+35:30:56.7	0.9	(b)
	PdbI	15:56:57.52	+35:30:57.5	0.3	Castro-Tirado et al. 2009
090407	XRT-Enhanced	04:35:55.01	−12:40:45.6	1.4	(a)
	XRT-DSS	04:35:55.14	−12:40:45.2	1.0	(b)
	Chandra	04:35:54.98	−12:40:45.5	0.4	priv. comm.
090515	XRT-Enhanced	10:56:36.20	+14:26:30.0	2.6	(a)
	XRT-DSS	10:56:35.94	+14:26:34.1	7.9	(b)
	Gemini-N GMOS	10:56:36.105	+14:26:29.26	0.3	this work
090618	XRT-Enhanced	19:35:58.40	+78:21:25.2	1.4	(a)
	XRT-DSS	19:35:58.92	+78:21:24.7	0.6	(b)
	UVOT	19:35:58.69	+78:21:24.3	0.74	(c)
	P60	19:35:58.68	+78:21:24.4	–	Cenko 2009
	KAIT	19:35:58.80	+78:21:25.5	–	Perley 2009
	ROTSE	19:35:58.65	+78:21:24.03	1	Rujopakarn et al. 2009
090709A	XRT-Enhanced	19:19:42.40	+60:43:39.4	1.4	(a)
	XRT-DSS	19:19:42.46	+60:43:39.6	1.2	(b)
	PAIRITEL	19:19:42.64	+60:43:39.3	0.4	Morgan et al. 2009
090902B	XRT-Enhanced	17:39:45.26	+27:19:28.1	2.1	(a)
	XRT-DSS	17:39:45.33	+27:19:26.3	1.0	(b)
	GROND	17:39:45.41	+27:19:27.1	0.5	Olivares et al. 2009b
	Nickel	17:39:45.347	+27:19:26.61	0.4	this work
100205A	XRT-Enhanced	09:25:33.00	+31:44:25.8	1.7	(a)
	XRT-DSS	09:25:32.85	+31:44:21.0	4.7	(b)
	Gemini-N NIRI	09:25:33.02	+31:44:25.0	0.5	Tanvir et al. 2010
100413A	XRT-Enhanced	17:44:53.19	+15:50:03.2	1.4	(a)
	XRT-DSS	17:44:52.71	+15:50:02.1	3.2	(b)
	EVLA	17:44:53.16	+15:50:03.2	0.6	Frail & Fox 2010
100414A	XRT-Enhanced	12:48:27.01	+08:41:36.6	2.2	(a)
	Gemini-N GMOS	12:48:26.96	+08:41:34.91	0.5	Cucchiara 2010
100420A	XRT-Enhanced	19:44:30.71	+55:46:10.0	2.0	(a)
	XRT-DSS	19:44:29.76	+55:46:09.2	5.7	(b)
	Gemini-N NIRI	19:44:30.57	+55:46:10.0	0.3	Levan et al. 2010b
100424A	XRT-Enhanced	13:57:47.46	+01:32:20.3	1.7	(a)
	XRT-DSS	13:57:47.49	+01:32:16.4	7.3	(b)
	Gemini-N NIRI	13:57:47.43	+01:32:18.9	0.5	Cenko et al. 2010a
100526A	XRT-Enhanced	15:23:04.54	+25:37:56.4	1.7	(a)
	XRT-DSS	15:23:04.70	+25:37:55.0	1.5	(b)
	Gemini-N NIRI	15:23:04.480	+25:37:55.23	0.4	Perley 2010

Continued on Next Page...

GRB	Telescope	RA (J2000)	Declination	Unc. $''$	Reference
100614A	XRT-Enhanced	17:33:59.82	+49:14:03.6	1.7	(a)
	XRT-DSS	17:33:59.91	+49:14:04.1	1.1	(b)
100823A	XRT-Enhanced	01:22:49.01	+05:50:06.1	1.5	(a)
	XRT-DSS	01:22:48.97	+05:50:03.4	1.1	(b)
	UVOT	01:22:49.03	+05:50:06.4	0.9	(c)
	WHT LIRIS	01:22:48.94	+05:50:05.9	0.5	Levan et al. 2010d
100905A	XRT-Enhanced	02:06:12.06	+14:55:46.5	1.5	(a)
	XRT-DSS	02:06:12.01	+14:55:46.5	2.1	(b)

(a): Evans et al. (2009), taken from `http://www.swift.ac.uk/xrt_positions/index.php`
(b): Butler (2007), taken from `http://astro.berkeley.edu/~nat/swift/xrt_pos.html`
(c): Roming et al. (2009), taken from `http://heasarc.nasa.gov/docs/swift/results/uvot_grbcat/`

Table C.2: Log of imaging observations

GRB field	UT date	Inst.	Filter	T_{int} sec	$N_{\rm exp}$	Airmass	Seeing	3σ limit $''$
041219A	2005-08-04	ESI	R	240	1	1.43	0.65	25.4
041223	2005-03-05	ESI	$R_{\rm Ellis}$	1500	5	1.84	1.60	24.9
050124	2005-03-05	ESI	$R_{\rm Ellis}$	1920	4	1.01	0.78	24.9
		ESI	I	360	2	1.01	0.92	24.9
	2005-12-04	LRISB	V	840	3	1.49	1.07	26.2
		LRISR1	$I_{\rm long}$	750	3	1.49	0.94	25.1
050126	2005-03-05	ESI	$B_{\rm Ellis}$	480	1	1.33	0.94	26.1
		ESI	$R_{\rm Ellis}$	1500	5	2.34	1.36	25.5
050215B	2005-06-05	LRISB	g	960	2	1.17	1.15	27.0
		LRISR1	R	960	2	1.17	1.30	25.8
	2005-12-04	LRISB	B	1260	2	1.39	0.93	27.5
		LRISR1	R	1200	2	1.39	1.08	26.5
050319	2005-06-05	LRISB	g	960	2	1.35	1.57	26.7
		LRISR1	R	960	2	1.35	1.84	25.6
050401	2005-06-05	LRISB	g	960	2	1.07	1.05	27.2
		LRISR1	R	960	2	1.07	0.91	26.1
	2006-05-30	LRISB	g	2480	4	1.41	1.22	26.9
		LRISR1	R	2400	4	1.41	1.13	26.2
050408	2005-06-05	LRISB	g	960	2	1.13	1.08	26.8
		LRISR1	R	960	2	1.13	1.27	25.9
050412	2007-12-13	LRISB	g	600	2	1.35	1.51	26.3
		LRISR1	R	540	2	1.35	1.43	25.3
050416B	2005-12-04	LRISB	$V_{\rm D560}$	960	4	1.07	0.77	26.3
		LRISR1	$I_{\rm long}$	880	4	1.07	0.73	24.8
050502A	2005-06-05	LRISB	g	1391	3	1.40	1.11	26.8
		LRISR1	R	1391	3	1.40	1.11	26.2
	2005-12-04	LRISB	V	1400	5	1.54	1.43	26.3
		LRISR1	$I_{\rm long}$	1250	5	1.53	0.99	25.2
050502B	2005-12-04	LRISB	V	840	3	1.00	0.72	26.5
		LRISR1	$I_{\rm long}$	750	3	1.00	0.77	25.4

Continued on Next Page...

GRB field	UT date	Inst.	Filter	T_{int} sec	$N_{\rm exp}$	Airmass	Seeing $''$	3σ limit
050509B	2005-06-05	LRISB	g	1920	4	1.14	0.91	27.0
		LRISR1	R	1920	4	1.14	1.28	24.6
050603	2005-08-04	ESI	R	720	3	1.78	0.71	26.1
050607	2007-10-09	LRISB	g	960	4	1.33	1.16	26.1
		LRISR1	R	840	4	1.33	1.13	25.1
050709	2005-08-04	ESI	R	120	1	1.93	0.84	24.4
050712	2005-12-04	LRISB	$V_{\rm D560}$	1050	5	1.45	1.10	26.3
		LRISR1	$I_{\rm long}$	900	5	1.45	0.68	25.1
050713A	2005-08-04	ESI	R	600	3	1.86	0.91	25.1
	2008-08-02	LRISB	g	900	3	1.86	0.86	25.7
		LRISR1	R	810	3	1.86	0.79	25.2
050713B	2005-08-04	ESI	R	720	3	1.40	0.66	25.7
	2009-06-25	LRISB	g	500	2	1.33	0.75	26.7
		LRISR2	I	720	3	1.33	1.08	25.2
050714B	2009-02-19	LRISB	g	630	2	1.51	0.80	26.8
		LRISR1	R	600	2	1.51	0.77	25.6
050716	2005-08-04	ESI	R	480	2	1.13	0.89	25.7
	2010-07-08	LRISB	g	970	4	1.11	0.84	26.9
		LRISR2	I	870	4	1.11	0.98	24.5
050730	2006-05-30	LRISB	g	2100	7	1.13	1.11	26.7
		LRISR1	R	3600	12	1.16	1.14	25.6
050803	2005-08-04	ESI	R	480	2	1.05	0.76	25.9
050814	2007-08-12	LRISB	g	1500	5	1.40	0.86	27.3
		LRISR1	R	1500	5	1.40	0.87	26.3
050819	2008-08-02	LRISB	g	630	2	1.00	0.83	27.1
050820A	2006-07-26	LRISB	g	2750	5	1.01	0.70	27.6
		LRISR1	R	2500	5	1.01	1.79	25.6
050826	2005-12-04	LRISB	$V_{\rm D560}$	1260	6	1.13	0.70	26.3
		LRISR1	$I_{\rm long}$	1080	6	1.13	0.63	24.5
050827	2008-02-12	LRISB	g	420	2	1.30	1.22	25.6
		LRISR1	R	360	2	1.30	1.08	24.7
050915A	2005-12-04	LRISB	$V_{\rm D560}$	1960	9	1.49	0.82	26.8
		LRISR1	$I_{\rm long}$	1510	8	1.49	0.82	25.5
050922B	2008-08-03	LRISB	g	720	2	1.11	1.04	27.1
		LRISR1	R	690	2	1.11	1.03	26.0
050922C	2006-07-25	LRISB	g	3780	6	1.15	1.24	27.5
		LRISR1	R	3540	6	1.15	1.29	26.5
051001	2006-09-21	LRISB	g	1080	3	1.66	1.39	26.6
		LRISR1	R	990	3	1.66	1.19	25.2
051006	2005-12-04	LRISB	$V_{\rm D560}$	720	3	1.02	0.60	26.3
		LRISR1	$I_{\rm long}$	660	3	1.02	0.77	25.3
051008	2008-02-12	LRISB	g	690	4	1.11	1.00	26.6
		LRISR1	R	600	4	1.11	0.85	25.4
051109A	2007-08-12	LRISB	g	1500	5	1.07	0.74	26.9
		LRISR1	R	1500	5	1.07	0.73	26.3
051109B	2006-07-25	LRISB	g	630	1	1.07	0.83	26.8
		LRISR1	R	600	1	1.07	1.05	26.6

Continued on Next Page...

GRB field	UT date	Inst.	Filter	T_{int} sec	$N_{\rm exp}$	Airmass	Seeing $''$	3σ limit
	2007-07-18	LRISB	g	900	3	1.06	0.86	26.7
		LRISR1	R	810	3	1.06	0.83	25.5
051111	2006-07-25	LRISB	g	1320	4	1.01	1.05	27.2
		LRISR1	R	1200	4	1.01	1.26	25.9
051117A	2008-02-12	LRISB	g	990	3	1.04	0.92	27.2
		LRISR1	R	930	3	1.04	0.89	25.9
051117B	2005-12-04	LRISB	$V_{\rm D560}$	420	2	1.33	0.81	26.1
		LRISR1	$I_{\rm long}$	360	2	1.33	0.70	24.8
051211B	2006-09-21	LRISB	g	450	3	1.25	1.02	26.0
		LRISR1	R	360	3	1.25	0.97	25.0
060105	2006-05-30	LRISB	g	660	1	1.12	1.33	25.3
		LRISR1	R	600	1	1.13	1.31	24.6
060109	2006-05-30	LRISB	g	330	1	1.11	1.01	26.6
		LRISR1	R	300	1	1.11	1.08	25.5
060111A	2007-07-18	LRISR1	R	480	2	1.30	1.19	24.9
060111B	2006-07-25	LRISB	g	1260	2	1.62	1.13	27.1
		LRISR1	R	1200	2	1.62	1.09	26.0
060124	2007-12-11	LRISB	g	1500	5	1.65	1.14	26.1
		LRISR1	R	1500	5	1.64	1.12	25.0
060202	2006-07-25	LRISB	g	1260	2	1.46	1.15	27.0
		LRISR1	R	1200	2	1.46	1.30	25.9
060203	2007-10-11	LRISB	g	1200	4	1.66	1.00	27.1
		LRISR1	R	1085	4	1.66	1.19	26.0
060204B	2006-05-30	LRISB	g	1200	2	2.17	1.46	26.7
		LRISR1	R	1200	2	2.17	1.81	25.6
060210	2007-08-12	LRISR1	R	540	3	1.09	0.92	25.0
	2009-02-19	LRISB	g	1650	8	1.32	0.85	26.6
		LRISR1	I	1440	8	1.32	1.40	24.5
060219	2006-05-30	LRISB	g	660	1	1.59	1.31	26.5
		LRISR1	R	600	1	1.59	1.25	25.4
060306	2008-02-12	LRISB	g	930	4	1.21	1.35	23.4
		LRISR1	R	810	4	1.21	1.29	24.9
	2008-08-02	LRISB	g	150	1	1.28	0.99	25.6
		LRISR1	R	150	1	1.28	0.84	22.9
	2010-11-07	LRISB	B	990	3	1.18	0.71	26.7
		LRISR2	I	850	3	1.18	1.22	24.6
060312	2008-08-02	LRISB	g	90	1	1.27	1.19	25.5
		LRISR1	R	60	1	1.27	1.08	24.5
060319	2007-04-16	LRISB	g	1355	6	1.35	2.23	26.4
		LRISR1	R	1380	7	1.34	1.96	25.2
060413	2006-05-31	LRISB	g	660	1	1.02	1.78	25.6
		LRISR1	R	600	1	1.02	1.52	24.5
060418	2006-05-30	LRISB	g	1800	3	1.33	1.15	26.7
		LRISR1	R	600	1	1.38	1.06	25.6
	2007-08-11	LRISB	g	660	2	1.34	0.98	27.0
		LRISR1	R	600	2	1.34	1.35	25.7
060424	2006-09-21	LRISB	g	1320	4	1.12	1.12	27.0

Continued on Next Page...

GRB field	UT date	Inst.	Filter	T_{int} sec	$N_{\rm exp}$	Airmass	Seeing $''$	3σ limit
		LRISR1	R	1200	4	1.12	1.02	26.9
060428B	2006-05-30	LRISB	g	600	2	1.37	1.58	26.0
		LRISR1	R	600	2	1.37	1.88	25.1
	2006-09-21	LRISB	g	4410	7	1.99	1.17	26.9
		LRISR1	R	4200	7	1.99	1.07	25.7
060502B	2006-05-30	LRISB	g	1040	3	1.27	1.13	26.9
		LRISR1	R	900	3	1.27	1.22	25.7
060505	2006-05-30	LRISB	g	330	1	1.62	1.20	24.3
		LRISR1	R	300	1	1.62	1.10	23.9
	2006-07-25	LRISB	g	660	2	1.49	1.28	24.8
		LRISR1	R	600	2	1.49	1.21	24.0
060510B	2006-05-31	LRISB	g	3780	6	2.14	1.59	27.1
		LRISR1	R	3600	6	2.14	1.48	25.9
060512	2006-05-30	LRISB	g	660	2	1.15	0.90	27.1
		LRISR1	R	600	2	1.15	0.77	26.1
	2006-07-25	LRISB	g	990	3	1.44	1.93	25.9
060607A	2006-07-26	LRISB	g	2520	4	1.36	0.97	27.4
		LRISR1	R	2400	4	1.36	1.58	26.0
060805A	2008-02-12	LRISB	g	990	3	1.12	1.11	27.0
		LRISR1	R	1200	4	1.14	1.05	26.0
060807	2007-04-16	LRISB	V	1260	6	1.02	1.40	26.3
		LRISR1	$I_{\rm long}$	1080	6	1.02	1.22	25.0
060814A	2007-04-16	LRISB	V	630	3	1.05	1.75	25.6
		LRISR1	$I_{\rm long}$	690	4	1.06	1.86	24.3
060904A	2007-04-16	LRISB	V	1050	5	1.15	1.67	26.0
		LRISR1	$I_{\rm long}$	900	5	1.15	1.54	24.5
060904B	2006-09-21	LRISB	g	630	1	1.22	1.03	26.9
		LRISR1	R	600	1	1.22	1.09	25.8
	2009-02-19	LRISB	g	990	3	1.88	1.04	25.8
		LRISR1	R	900	3	1.88	1.19	24.5
060906	2007-12-11	LRISB	g	1500	5	1.02	1.02	26.8
		LRISR1	R	1500	5	1.02	0.95	25.7
060923A	2007-04-16	LRISB	V	1650	8	1.04	1.80	26.6
		LRISR1	$I_{\rm long}$	1260	7	1.03	1.49	24.5
	2007-06-13	LRISB	g	1960	3	1.42	1.43	26.6
		LRISR1	R	1800	3	1.42	1.30	25.7
	2007-08-12	LRISB	B	1500	5	1.04	0.82	26.5
		LRISR1	$RG850$	1500	5	1.04	0.72	24.6
060923C	2007-08-12	LRISB	B	1500	5	1.12	0.71	24.2
		LRISR1	$RG850$	1500	5	1.12	0.71	23.0
	2010-11-07	LRISB	g	1880	6	1.29	0.97	26.5
		LRISR2	I	1800	6	1.29	0.98	24.9
060927	2006-11-21	LRISB	V	5100	17	1.25	0.81	27.3
		LRISR1	$I_{\rm long}$	4590	17	1.25	0.81	25.8
060929	2008-06-07	LRISB	g	1290	4	1.05	1.12	27.4
		LRISR1	R	1200	4	1.05	0.92	26.4
061021	2007-12-13	LRISB	g	1800	6	1.45	1.54	26.9

Continued on Next Page...

GRB field	UT date	Inst.	Filter	T_{int} sec	$N_{\rm exp}$	Airmass	Seeing $''$	3σ limit
		LRISR1	R	1650	6	1.45	1.41	26.0
061028	2006-11-21	LRISB	V	3000	10	1.16	1.21	27.1
		LRISR1	$I_{\rm long}$	2970	11	1.15	0.66	25.6
061110A	2006-11-21	LRISB	V	600	2	1.53	0.86	27.1
		LRISR1	$I_{\rm long}$	540	2	1.53	0.82	25.0
061121	2009-02-19	LRISB	B	150	1	1.24	0.88	26.6
		LRISB	g	290	1	1.23	0.83	27.0
		LRISR1	I	180	1	1.24	1.56	23.5
061122	2007-10-09	LRISB	g	930	3	1.32	0.99	26.9
		LRISR1	R	840	3	1.32	0.98	25.8
061217	2006-12-19	LRISB	g	1500	5	1.33	1.11	27.1
		LRISR1	R	1500	5	1.33	1.04	26.0
061222A	2007-07-18	LRISB	V	630	3	1.14	1.00	26.5
		LRISR1	$I_{\rm long}$	540	3	1.14	0.86	25.1
	2007-08-12	LRISB	B	1500	5	1.12	0.64	26.6
		LRISR1	$RG850$	1500	5	1.12	0.67	25.0
070103	2008-08-02	LRISB	g	1770	5	1.01	0.88	27.3
		LRISR1	R	330	1	1.01	0.70	25.8
070219	2009-06-25	LRISB	g	1300	4	1.73	0.83	27.2
		LRISR2	I	1200	4	1.73	1.24	25.0
070224	2007-12-13	LRISB	g	1200	4	1.39	1.27	26.8
		LRISR1	R	1110	4	1.39	1.31	25.9
070311	2007-04-16	LRISB	g	510	2	1.53	2.58	25.4
070412	2007-04-16	LRISB	V	3570	17	1.23	1.83	25.5
		LRISR1	R	60	1	1.11	2.36	23.4
		LRISR1	$I_{\rm long}$	3600	20	1.29	1.97	23.9
070419A	2009-02-19	LRISB	g	630	2	1.09	0.96	26.3
		LRISR1	R	600	2	1.09	1.01	25.0
070429A	2007-07-18	LRISR1	R	600	2	1.87	1.46	25.3
070429B	2007-07-18	LRISB	g	810	3	1.92	1.40	26.3
		LRISR1	R	720	3	1.92	1.34	25.2
070520A	2008-02-12	LRISB	g	960	3	1.76	1.33	26.6
		LRISR1	R	900	3	1.76	1.26	25.7
070521	2007-05-21	LRISB	V	1500	5	1.33	0.92	26.5
		LRISR1	$I_{\rm long}$	1500	5	1.33	0.91	24.9
	2009-06-25	LRISB	V	1380	5	1.39	0.73	26.7
		LRISR2	$RG850$	1200	6	1.39	1.13	24.6
070621	2007-07-18	LRISB	V	1680	8	1.46	1.39	26.0
		LRISR1	$I_{\rm long}$	1440	8	1.46	1.23	24.4
070714A	2007-07-18	LRISB	g	600	2	1.38	1.07	26.5
		LRISR1	R	540	2	1.38	0.91	25.7
070714B	2007-07-18	LRISB	g	810	3	1.67	0.94	26.1
		LRISR1	R	720	3	1.67	0.72	25.3
070721A	2007-10-09	LRISB	g	900	3	1.53	1.14	26.6
		LRISR1	R	810	3	1.53	1.00	25.4
070724A	2007-08-11	LRISB	g	2220	4	1.31	0.90	26.6
		LRISR1	R	2400	4	1.31	1.07	25.6

Continued on Next Page...

GRB field	UT date	Inst.	Filter	T_{int} sec	$N_{\rm exp}$	Airmass	Seeing $''$	3σ limit
	2008-08-02	LRISB	g	1290	4	1.34	0.93	26.4
		LRISR1	R	1200	4	1.34	0.82	25.3
070729	2007-12-11	LRISB	g	540	3	2.25	1.35	26.3
		LRISR1	R	540	3	2.25	1.17	24.6
070808	2007-08-11	LRISB	g	660	2	1.15	0.78	26.9
		LRISR1	R	600	2	1.15	0.75	25.9
070809	2008-02-12	LRISB	g	2640	8	1.35	1.04	27.1
		LRISR1	R	2430	8	1.35	1.14	25.8
070810A	2007-08-11	LRISB	g	420	2	3.78	1.43	25.6
		LRISR1	R	360	2	3.79	1.36	24.7
070810B	2007-08-11	LRISB	g	1980	6	1.22	1.82	26.7
		LRISR1	R	1800	6	1.22	1.31	27.2
	2007-08-12	LRISB	g	3000	10	1.46	1.08	27.2
		LRISR1	R	3000	10	1.45	0.84	26.5
071021	2008-08-03	LRISB	g	970	3	1.03	0.91	27.2
		LRISR1	$I_{\rm long}$	900	3	1.04	0.91	25.3
	2010-11-07	LRISB	B	830	4	1.18	0.91	26.9
		LRISB	V	640	3	1.12	0.88	26.2
		LRISR2	$RG850$	1440	8	1.16	0.89	25.1
071025	2008-08-02	LRISB	g	1050	3	1.05	0.85	27.2
		LRISR1	R	990	3	1.05	0.75	26.5
080207	2009-02-19	LRISB	g	1640	5	1.19	0.80	27.3
		LRISR1	I	1500	5	1.19	1.13	25.2
080210	2008-02-12	LRISB	g	600	2	1.16	1.21	26.7
		LRISR1	R	540	2	1.16	1.05	25.9
080229A	2008-06-07	LRISB	g	960	3	1.49	1.53	27.2
		LRISR1	R	900	3	1.49	1.33	26.3
080307	2010-02-07	LRISB	g	600	2	1.07	1.17	26.4
		LRISR2	I	600	2	1.07	1.26	25.2
080310	2009-06-25	LRISB	g	1260	4	1.79	0.85	27.0
		LRISR2	I	910	3	1.79	1.29	24.6
080319A	2009-02-19	LRISB	g	980	3	1.16	1.29	26.9
		LRISR1	R	900	3	1.16	0.77	25.7
080319C	2009-02-19	LRISB	g	1440	5	1.44	0.98	26.3
		LRISR1	R	1320	5	1.44	0.92	25.2
080319D	2009-02-19	LRISB	g	600	2	1.01	0.92	26.3
		LRISR1	R	570	2	1.01	0.84	25.3
080320	2009-02-19	LRISB	g	900	3	1.32	1.15	26.8
		LRISR1	I	810	3	1.32	1.69	24.3
080325	2008-06-07	LRISB	g	600	2	1.05	1.04	27.1
		LRISR1	R	600	2	1.05	0.90	26.2
	2008-08-03	LRISB	U	1070	4	1.68	1.04	26.6
		LRISR1	$I_{\rm long}$	960	4	1.68	0.91	25.1
080330	2009-02-19	LRISB	g	1080	3	1.11	0.76	27.1
		LRISR1	R	990	3	1.11	0.77	25.9
080430	2009-02-19	LRISB	g	600	2	1.21	0.98	27.0
		LRISR1	R	540	2	1.21	0.87	25.8

Continued on Next Page...

GRB field	UT date	Inst.	Filter	T_{int} sec	$N_{\rm exp}$	Airmass	Seeing $''$	3σ limit
080507	2008-06-07	LRISB	g	1320	4	1.43	1.12	27.1
		LRISR1	R	1230	4	1.43	1.07	26.1
080514B	2008-06-07	LRISB	g	990	3	1.18	1.25	27.0
		LRISR1	R	900	3	1.18	0.87	26.1
080515	2008-08-02	LRISB	g	660	2	1.03	0.91	26.7
		LRISR1	R	630	2	1.03	0.87	25.8
080603A	2008-08-02	LRISB	g	1020	3	1.58	0.86	26.5
		LRISR1	R	930	3	1.58	1.01	26.0
	2008-08-03	LRISB	U	720	3	2.00	0.93	26.9
		LRISR1	$I_{\rm long}$	660	3	2.00	1.00	26.0
080607	2009-02-19	LRISB	g	2400	8	1.15	0.86	27.5
		LRISR1	I	2160	8	1.15	1.20	25.2
080701	2010-02-07	LRISB	g	930	3	2.46	1.83	26.0
		LRISR2	R	900	3	2.46	1.81	25.2
080702A	2008-08-02	LRISB	g	2660	8	1.79	0.92	27.4
		LRISR1	R	960	3	1.66	1.02	25.2
	2008-08-03	LRISR1	$I_{\rm long}$	1500	5	1.80	0.92	25.7
080710	2008-08-02	LRISB	g	660	2	1.01	0.95	26.2
		LRISR1	R	600	2	1.01	1.06	25.8
081211B	2009-02-19	LRISB	g	900	3	1.27	0.89	26.3
		LRISR1	R	810	3	1.27	0.85	25.0
081221	2008-12-23	LRISB	g	3300	10	1.41	1.02	27.6
		LRISR1	I	3000	10	1.41	1.79	24.6
	2010-11-07	LRISB	B	1000	5	1.51	0.88	26.7
		LRISB	V	1000	5	1.45	0.82	26.0
		LRISR2	$RG850$	1800	10	1.49	1.11	24.6
090111	2010-07-08	LRISB	g	1200	4	1.25	1.16	26.9
		LRISR2	R	1040	4	1.25	1.13	25.6
090113	2010-02-07	LRISB	g	1070	5	1.98	1.25	26.2
		LRISR2	I	1000	5	1.97	1.23	24.6
	2010-11-07	LRISB	B	800	4	1.08	0.74	27.0
		LRISB	V	770	4	1.10	0.76	26.4
		LRISR2	$RG850$	1440	8	1.09	0.82	25.3
090404	2009-06-25	LRISB	g	1610	5	1.30	0.59	27.1
		LRISR2	I	1500	5	1.30	1.13	25.1
090407	2010-02-07	LRISB	g	1910	6	1.58	1.94	26.4
		LRISR2	I	1800	6	1.59	1.77	24.8
090515	2010-02-07	LRISB	g	940	3	1.03	1.16	26.6
		LRISR2	R	900	3	1.02	1.12	26.0
090618	2009-06-25	LRISB	B	260	2	2.10	1.04	25.8
		LRISR2	R	125	1	2.10	1.30	24.4
090709A	2010-11-07	LRISB	g	2880	9	1.74	1.02	27.2
		LRISR2	I	2590	9	1.74	0.91	25.5
090902B	2010-02-07	LRISB	g	820	4	1.39	1.81	25.1
		LRISR2	I	600	3	1.36	1.54	24.0
	2010-07-08	LRISB	g	1180	4	1.23	0.91	27.1
		LRISR2	R	1080	4	1.23	0.95	25.7

Continued on Next Page...

GRB field	UT date	Inst.	Filter	T_{int} sec	$N_{\rm exp}$	Airmass	Seeing $''$	3σ limit
100205A	2010-02-07	LRISB	g	3940	13	1.02	1.48	27.0
		LRISR2	R	3740	13	1.02	1.46	26.3
100413A	2010-07-08	LRISB	g	2000	7	1.36	0.98	27.1
		LRISR2	I	1680	7	1.36	0.92	25.2
100414A	2010-07-08	LRISB	g	1860	7	1.78	1.17	26.7
		LRISR2	R	1570	6	1.84	1.02	25.8
100420A	2011-06-03	LRISB	g	600	2	1.29	0.89	25.7
		LRISR3	R	1120	4	1.28	1.10	25.5
100424A	2010-07-08	LRISB	g	2100	7	1.64	1.26	26.7
		LRISR2	I	1939	7	1.64	1.23	25.0
100526A	2010-07-08	LRISB	g	2400	8	1.28	1.12	27.1
		LRISR2	I	2180	8	1.28	1.25	25.4
100614A	2010-07-08	LRISB	g	2100	7	1.27	1.03	27.3
		LRISR2	I	1670	6	1.28	1.08	25.3
100823A	2010-11-07	LRISB	g	690	3	1.10	0.73	26.4
		LRISR2	I	640	3	1.10	0.84	24.5
100905A	2010-11-07	LRISB	g	670	3	1.03	0.70	26.6
		LRISR2	I	580	3	1.03	0.81	24.9

Table C.3: Log of spectroscopic observations

GRB field	Object on slit	UT date	Sky PA (°)	Exp. time (s)	Slit width ($''$)	Airmass
050215B	H,A	2006-11-21	260.52	1200+353	1.0	1.37
050412	A	2007-12-12	142.85	2×900	1.0	1.16
050712	H	2006-11-21	228.79	2×1200	1.0	1.45
050714B	H,A	2010-02-07	0.00	3×600	1.5	1.25
050819	H	2009-06-25	193.45	2×600+900	1.0	1.18
050826	H,A	2006-09-21	-43.82	1×660	1.0	1.16
050915A	H	2008-02-11	257.95	2×1200	1.0	1.51
051006	H	2007-04-16	69.22	(2959)	1.5	1.58
051008	H	2009-06-25	202.00	3×900	0.7	1.19
051109B	K	2006-07-26	168.74	2×300+1000	1.0	1.08
	H	2006-07-26	199.00	1×120	1.0	1.11
051117B	A,B	2007-12-12	227.10	2×1200	1.5	1.29
051211B	A	2006-09-21	341.45	2×600	1.0	1.30
060109	A	2006-09-21	96.21	2×1200	1.0	1.18
060202	H	2006-09-21	68.42	1400+1500	1.0	1.30
060210	H	2010-11-07	95.80	2×550	1.0	1.23
060111A	H,G	2007-08-11	20.00	2×1800	1.0	1.14
060111B	G,H	2006-07-26	143.40	2×1200	1.5	1.62
060123	A	2006-05-30	147.30	2×900	1.0	1.12
060219	A	2006-05-31	33.12	2×600	1.0	1.03
060306	H	2009-02-19	190.0	1200	1.0	1.54
	H	2010-11-07	190.0	2×850	1.0	1.32
060319	H	2007-07-18	233.63	2×1200	1.5	1.86

Continued on Next Page...

GRB field	Object on slit	UT date	Sky PA (°)	Exp. time (s)	Slit width (″)	Airmass
060418	A,B,H,C	2006-05-31	33.59	2×1200	1.0	1.11
	C,H	2006-07-26	187.00	1×1800	1.5	1.66
060424	H,B	2006-11-21	80.94	2×1200	1.0	1.20
060428B	G,H	2006-07-26	96.4	1×900	1.5	1.92
060502B	G*	2006-05-31	10.80	1×600	1.0	1.36
060512	A	2006-05-31	122.17	2×1200	1.0	1.13
	A	2006-05-31	90.0	2×1800	1.0	1.85
060805A	A,B	2009-02-19	40.5	2×900	1.0	1.06
060805A	A,B	2009-06-25	30.4	2×900	0.7	1.21
060807	H	2007-07-18	94.00	3×1800	1.0	1.17
060814	H	2007-07-18	257.35	2×1200	1.5	1.22
060904B	H	2006-09-21	134.82	4×1800	1.0	1.11
061021	H	2008-02-11	188.85	3×1200	1.0	1.35
061121	H	2010-02-07	186.85	3×600	1.5	1.23
061122	H,A	2007-10-11	169.79	2×1500	1.0	1.03
061222A	H,B	2007-10-11	142.19	2×1800	1.0	1.12
070721A	H	2010-07-08	-23.75	600+580	1.0	1.73
070724A	H,others[a]	2007-08-11	20.00	1×900	1.0	1.43
	others[a]	2007-10-10	-24.00	(3436)	1.0	1.42
	others[a]	2007-10-10	69.00	2×1700	1.0	1.40
	others[a]	2007-10-11	-24.00	2×1320	1.0	1.28
	others[a]	2007-10-11	12.00	1200+1800	1.0	1.31
070429A	A,B	2007-10-09	236.04	2×1800	2.0	1.70
070429B	H	2007-10-11	88.00	2×1500	1.0	1.92
070518	A	2007-07-18	47.04	1×1200	1.0	1.23
	H+B	2007-07-18	47.04	2×1000	1.0	1.27
070612	A,B	2009-02-19	149.2	1×900	1.0	1.05
070714A	H+B	2010-02-07	72.50	2×600	1.0	1.28
070809	G	2007-08-11	10.73	2×900	1.0	2.20
	G	2008-06-07	11.00	2×900	1.0	1.87
071021	H,A,B,G	2009-06-25	130.00	900+1000	1.0	1.11
080307	H	2010-11-07	50.80	4×560+600	1.0	1.12
	H	2011-03-09	322.50	1160+1190	1.0	1.06
080319A	H,A	2009-06-25	105.1	2×900	0.7	1.32
080319C	A	2010-02-07	58.44	2×600	1.5	1.60
080325	H	2008-08-02	66.50	1200	1.0	1.44
080515	H,A	2010-07-08	171.00	2×990	1.0	1.22
080603A	H,B	2008-06-07	171.45	850+2×900	1.0	1.45
	A	2008-06-07	90.46	630	1.0	1.45
081221	H,A	2010-07-08	255.00	900+990	1.0	1.72
090113	H	2010-11-01	11.0	2×600+2×500	1.0	1.22
100117A	H	2010-02-07	162.60	600+2×900	1.5	1.83
100206A	G	2010-02-07	18.20	2×600	1.0	1.15
100628A	G7	2010-07-08	257.50	2×900	1.0	1.62
	S8	2010-07-08	-67.00	900	1.0	1.64

[a] See Kocevski et al. 2010

Table C.4: Lines and redshifts identified in the spectroscopic sample

GRB field	Object ID	Redshift	Detected lines
050215B	H	2.62	Lyα
	B	1.00	[O II]
050412	A		none
050712	H		none
050714B	A	0	Na D
	H		none
050819	H		none
050826	H	0.296	[O II], Hβ, [O III], Hα, [N II], [S II]
	A		none
050915	H	(0.443)	([O III]$_{5007}$)
051006	H		none
051008	H	0.913?	[O II]?
051109B	K	0.080	[O II], [O III], Hβ, Hα, [N II]
	H	0.080	Hγ^a, Hβ^a, Hα^a, Ca H+K
051117B	A	0.480	[O II], Hβ, [O III]$_{5007}$, Ca H+K
	B		no trace/lines
051211B	A	0	Na D
060111A	H	2.32	Lyα
	G	0.17	[O II], Ca H+K, [O III], Hα
060111B	H		none
	G	0.239	[O II], Ca H+K, Hα
060123	H	0.56	[O II], Hβ, [O III]
060219	A	0.810	[O II]
060306	H		
060319	H	1.172	[O II]
060418	A	0.655	[O II], Hβ, [O III]
	B		none
	C		none
	H		none
060424	H		none
	B	0.922	[O II]
060428B	G	0.350	[O II], Ca H+K, Ca G, Hγ^aHβ^a, Hα^a, Mg I, Na D, [Si II]
060502B	H	0.287	[O II], Ca H+K, Hδ^a, Hβ^a, Mg I
060512	A	0.443	[O II], Hβ, [O III]
060814	HE	0.828	[O II], Hβ, [O III]
	HW		none
060805A	A,B		none
060807	H		none
060904B	H	0.703	[O II], [O III], Hβ, Hγ
061021	H	(0.346)	([O III])
061121	H	1.315	[O II]
061122	H		none
	A		none
061222A	H	2.088	Lyα
	B	1.151	[O II]

Continued on Next Page...

GRB field	Object ID	Redshift	Detected lines
070429A	A	1.03	[O II], $[O\ III]_{5007}$
	B	0.931	[O II]
070429B	H	0.904	[O II]
070724A	H	0.457	[O II], Ca H+K, Hγ, Hβ, [O III]
	others	various	see Kocevski et al. 2010
070518	H	1.161	[O II]
	A	0	
070612	A	0.385	[O II], Hβ, [O III], Hα, [N II]
	B	0.671	[O II], Hβ, $[O\ III]_{5007}$
070714A	H	1.58	[O II]
	B	0.55	[O II], Hγ, Hδ, Hβ[O III], Hα, [N II]
070721	H		none
070809	G	0.219	[O II], [O III]
071021	H		none
	G	0.45	[O II], Hβ
080319A	H		none
	A	0.428	[O II]
080319C	A	0.81	[O II], Hβ, Hγ, Ca H+K
080325	H		none
080515	H	0.132?	[O II], Hβ?
	A	0.478	[O II], Hβ, [O III]
080603A	H		no lines
	A		no lines
	B		no lines
081221	H		none
	A	1.345	[O II]
090113	H		none
100117A	H		none
100206A	G		Hα, [N II]
100628A	G7	0.102	[O II], [O III], Hβ, Hα
	S8		

[a] denotes a line seen in absorption.

Table C.5: Photometry of GRB hosts and other objects of interest

GRB field	Source	Filt.		Magnitude	AB Mag.	Aperture ($''$)	Seeing ($''$)	Cal. Sys.	UT date
041219A	H	R		$25.00^{-0.23}_{+0.29}$	20.40	1.00	0.65	USNO	2005-08-04
041223	limit	R	$>$	24.92	24.80	1.76	1.60	USNO	2005-03-05
050124	limit	V	$>$	26.23	26.11	1.16	1.06	SDSS	2005-12-04
		R	$>$	26.27	26.36	1.00	0.78	SDSS	2005-03-05
		I	$>$	24.87	25.25	1.12	1.02	SDSS	2005-03-05
		I	$>$	25.16	25.54	1.02	0.92	SDSS	2005-12-04
	A	V		25.31 ± 0.16	25.19	1.16	1.06	SDSS	2005-12-04
		R		24.34 ± 0.06	24.43	1.00	0.78	SDSS	2005-03-05
		I		23.72 ± 0.13	24.10	1.12	1.02	SDSS	2005-03-05

Continued on Next Page...

GRB field	Source	Filt.		Magnitude	AB Mag.	Aperture (″)	Seeing (″)	Cal. Sys.	UT date
		I		23.70 ± 0.09	24.08	1.02	0.92	SDSS	2005-12-04
	B	V		$25.88^{-0.23}_{+0.29}$	25.76	1.16	1.06	SDSS	2005-12-04
		R		$26.04^{-0.25}_{+0.33}$	26.13	1.00	0.78	SDSS	2005-03-05
		I		$25.31^{-0.44}_{+0.74}$	25.69	1.12	1.02	SDSS	2005-03-05
		I		$26.12^{-0.61}_{+1.54}$	26.50	1.02	0.92	SDSS	2005-12-04
	C	V		$25.82^{-0.24}_{+0.31}$	25.70	1.16	1.06	SDSS	2005-12-04
		R		25.45 ± 0.16	25.54	1.00	0.78	SDSS	2005-03-05
		I		$24.60^{-0.27}_{+0.36}$	24.98	1.12	1.02	SDSS	2005-03-05
		I		$25.45^{-0.38}_{+0.59}$	25.83	1.02	0.92	SDSS	2005-12-04
050126	limit	B	$>$	26.14	25.79	1.03	0.94	SDSS	2005-03-05
		R	$>$	25.52	25.56	1.50	1.36	SDSS	2005-03-05
	H?	B		24.73 ± 0.11	24.38	1.20	0.94	SDSS	2005-03-05
		R		22.24 ± 0.02	22.28	1.20	1.36	SDSS	2005-03-05
050215B	H	B		25.21 ± 0.04	24.99	1.06	0.96	SDSS	2005-12-04
		g		25.11 ± 0.07	25.04	1.23	1.12	SDSS	2005-06-05
		R		24.52 ± 0.11	24.64	1.45	1.32	SDSS	2005-06-05
		R		24.31 ± 0.05	24.43	1.02	0.93	SDSS	2005-12-04
050319	limit	g	$>$	26.65	26.61	1.42	1.29	SDSS	2005-06-05
		R	$>$	25.61	25.75	1.64	1.49	SDSS	2005-06-05
050401	H	g		$26.55^{-0.23}_{+0.29}$	26.31	1.21	1.10	Landolt	2005-06-05
		g		$28.13^{-0.62}_{+1.57}$	27.89	1.36	1.23	Landolt	2006-05-30
		R		$26.16^{-0.32}_{+0.46}$	26.16	1.02	0.93	Landolt	2005-06-05
		R		$27.06^{-0.60}_{+1.46}$	27.06	1.28	1.17	Landolt	2006-05-30
	A	g		26.07 ± 0.16	25.83	1.21	1.10	Landolt	2005-06-05
		g		26.04 ± 0.12	25.80	1.36	1.23	Landolt	2006-05-30
		R		25.01 ± 0.12	25.01	1.02	0.93	Landolt	2005-06-05
		R		24.72 ± 0.09	24.72	1.28	1.17	Landolt	2006-05-30
050408	H	g		24.81 ± 0.06	24.72	1.14	1.04	SDSS	2005-06-05
		R		24.70 ± 0.12	24.80	1.30	1.18	SDSS	2005-06-05
050412	limit	g	$>$	26.28	26.21	1.58	1.44	SDSS	2007-12-13
		R	$>$	25.26	25.38	1.55	1.41	SDSS	2007-12-13
	A	g		23.82 ± 0.04	23.75	1.58	1.44	SDSS	2007-12-13
		R		22.37 ± 0.02	22.49	1.55	1.41	SDSS	2007-12-13
	B	g		25.14 ± 0.15	25.07	1.58	1.44	SDSS	2007-12-13
		R		$24.98^{-0.23}_{+0.29}$	25.10	1.55	1.41	SDSS	2007-12-13
	C	g	$>$	26.31	26.24	1.58	1.44	SDSS	2007-12-13
		R		$25.32^{-0.29}_{+0.40}$	25.44	1.55	1.41	SDSS	2007-12-13
	D	g		$25.97^{-0.24}_{+0.31}$	25.90	1.58	1.44	SDSS	2007-12-13
		R		$25.29^{-0.29}_{+0.39}$	25.41	1.55	1.41	SDSS	2007-12-13
050416B	limit	V	$>$	26.31	26.19	1.00	0.80	SDSS	2005-12-04
		I	$>$	24.80	25.18	1.00	0.73	SDSS	2005-12-04
050502A	limit	g	$>$	26.85	26.81	1.24	1.13	SDSS	2005-06-05
		V	$>$	26.32	26.27	1.24	1.13	SDSS	2005-12-04
		R	$>$	26.19	26.33	1.21	1.10	SDSS	2005-06-05
		I	$>$	25.16	25.58	1.06	0.97	SDSS	2005-12-04

Continued on Next Page...

GRB field	Source	Filt.		Magnitude	AB Mag.	Aperture (″)	Seeing (″)	Cal. Sys.	UT date
	A	g		25.03 ± 0.06	24.99	1.24	1.13	SDSS	2005-06-05
		V		24.78 ± 0.08	24.73	1.24	1.13	SDSS	2005-12-04
		R		24.89 ± 0.11	25.03	1.21	1.10	SDSS	2005-06-05
		I		24.16 ± 0.13	24.58	1.06	0.97	SDSS	2005-12-04
050502B	limit	V	$>$	26.54	26.43	1.00	0.72	SDSS	2005-12-04
		I	$>$	25.43	25.82	1.00	0.82	SDSS	2005-12-04
050509B	H	g		19.14	19.07	9.00	0.95	SDSS	2005-06-05
		R		17.60	17.72	9.00	1.22	SDSS	2005-06-05
050603	limit	R	$>$	26.09	26.19	1.00	0.71	USNO	2005-08-04
050607	limit	g	$>$	26.19	25.62	1.25	1.13	SDSS	2007-10-09
		R	$>$	25.08	24.86	1.20	1.09	SDSS	2007-10-09
050709	H	R		21.22 ± 0.02	21.36	2.00	0.84	USNO	2005-08-04
050712	H	V		24.61 ± 0.08	23.89	1.21	1.10	Nickel	2005-12-04
		I		24.06 ± 0.13	24.09	1.00	0.70	Nickel	2005-12-04
050713A	H	g		$25.89^{-0.37}_{+0.56}$	24.43	1.00	0.89	P60	2008-08-02
		R		$24.77^{-0.23}_{+0.30}$	23.91	1.01	0.91	P60	2005-08-04
		R		$24.97^{-0.26}_{+0.35}$	24.10	1.00	0.83	P60	2008-08-02
050713B	limit	g	$>$	26.66	24.92	1.00	0.76	Nickel	2009-06-25
		I	$>$	25.21	24.77	1.01	0.92	Nickel	2009-06-25
	H?	g		$26.81^{-0.34}_{+0.49}$	25.07	1.00	0.76	Nickel	2009-06-25
		I		24.54 ± 0.17	24.10	1.01	0.92	Nickel	2009-06-25
050714B	H	g		$26.47^{-0.25}_{+0.32}$	26.27	1.00	0.81	Nickel	2009-02-19
		R		$25.06^{-0.23}_{+0.29}$	25.09	1.00	0.78	Nickel	2009-02-19
	A	g		23.77 ± 0.02	23.57	1.00	0.81	Nickel	2009-02-19
		R		21.77 ± 0.01	21.80	1.00	0.78	Nickel	2009-02-19
	U	g		23.50 ± 0.02	23.30	1.00	0.81	Nickel	2009-02-19
		R		22.62 ± 0.03	22.65	1.00	0.78	Nickel	2009-02-19
050716	H	g		$27.32^{-0.41}_{+0.68}$	26.93	0.85	0.83	Nickel	2010-07-08
		R		$25.97^{-0.29}_{+0.41}$	25.88	0.85	0.89	Nickel	2005-08-04
		I		$24.91^{-0.34}_{+0.50}$	25.15	0.85	0.95	Nickel	2010-07-08
	A	g		$26.82^{-0.29}_{+0.40}$	26.43	1.00	0.83	Nickel	2010-07-08
		R		24.41 ± 0.09	24.32	1.00	0.89	Nickel	2005-08-04
		I		22.68 ± 0.05	22.92	1.04	0.95	Nickel	2010-07-08
	B	g		$26.62^{-0.27}_{+0.35}$	26.23	1.00	0.83	Nickel	2010-07-08
		R		24.21 ± 0.09	24.12	1.00	0.89	Nickel	2005-08-04
		I		23.05 ± 0.08	23.29	1.04	0.95	Nickel	2010-07-08
	S1	g		24.49 ± 0.04	24.10	1.00	0.83	Nickel	2010-07-08
		R		23.60 ± 0.04	23.51	1.00	0.89	Nickel	2005-08-04
		I		$24.29^{-0.21}_{+0.27}$	24.53	1.04	0.95	Nickel	2010-07-08
050730	limit	g	$>$	27.16	26.98	1.28	1.16	Landolt	2006-05-30
		R	$>$	26.47	26.51	1.22	1.11	Landolt	2006-05-30
	A	g		26.26 ± 0.17	26.08	1.28	1.16	Landolt	2006-05-30
		R		$26.18^{-0.24}_{+0.30}$	26.22	1.22	1.11	Landolt	2006-05-30
	B	g		$27.86^{-0.55}_{+1.17}$	27.68	1.28	1.16	Landolt	2006-05-30

Continued on Next Page...

GRB field	Source	Filt.		Magnitude	AB Mag.	Aperture (″)	Seeing (″)	Cal. Sys.	UT date
		R		$26.95^{-0.49}_{+0.90}$	26.99	1.22	1.11	Landolt	2006-05-30
050803	limit	R	$>$	25.89	25.87	1.00	0.76	USNO	2005-08-04
	H?	R		$25.97^{-0.26}_{+0.35}$	25.95	1.00	0.76	USNO	2005-08-04
	G1	R		22.16 ± 0.02	22.14	1.90	0.76	USNO	2005-08-04
	G2	R		23.92 ± 0.06	23.90	1.30	0.76	USNO	2005-08-04
050814	limit	g	$>$	27.31	27.21	1.10	1.00	zeropt.	2007-08-12
		R	$>$	26.35	26.45	1.09	0.99	zeropt.	2007-08-12
050819	H	g		24.57 ± 0.04	24.15	1.00	0.81	SDSS	2008-08-02
050820A	limit	g	$>$	27.57	27.41	1.00	0.74	Landolt	2006-07-26
		R	$>$	25.56	25.62	1.97	1.79	Landolt	2006-07-26
	A	g		25.34 ± 0.06	25.18	1.00	0.74	Landolt	2006-07-26
		R		22.03 ± 0.01	22.09	1.97	1.79	Landolt	2006-07-26
	B	g		25.63 ± 0.08	25.47	1.00	0.74	Landolt	2006-07-26
		R		23.41 ± 0.05	23.47	1.97	1.79	Landolt	2006-07-26
050826	H	V		23.10 ± 0.03	21.21	1.40	0.72	Nickel	2005-12-04
		I		20.83 ± 0.01	20.12	1.40	0.59	Nickel	2005-12-04
	A	V		24.58 ± 0.09	22.69	1.30	0.72	Nickel	2005-12-04
		I		22.39 ± 0.03	21.68	1.30	0.59	Nickel	2005-12-04
	B	V		$26.41^{-0.26}_{+0.34}$	24.52	1.00	0.72	Nickel	2005-12-04
		I		23.62 ± 0.09	22.91	1.00	0.59	Nickel	2005-12-04
050827	limit	g	$>$	25.57	23.54	1.28	1.17	Landolt	2008-02-12
		R	$>$	24.65	23.46	1.14	1.04	Landolt	2008-02-12
050915A	H	V		25.01 ± 0.08	24.91	1.00	0.83	Nickel	2005-12-04
		I		23.91 ± 0.07	24.30	1.00	0.82	Nickel	2005-12-04
050922B	limit	g	$>$	27.1	27.0	1.4	1.3	relative	2008-08-03
		R	$>$	25.97	26.05	1.34	1.22	zeropt.	2008-08-03
	H?	g	$\sim$	27	26.9	1.4		relative	2008-08-03
		R		$26.16^{-0.37}_{+0.56}$	26.24	1.34	1.22	zeropt.	2008-08-03
050922C	limit	g	$>$	27.46	27.12	1.35	1.22	Nickel	2006-07-25
		R	$>$	26.47	26.38	1.34	1.22	Nickel	2006-07-25
	A	g		26.46 ± 0.14	26.12	1.35	1.22	Nickel	2006-07-25
		R		$26.04^{-0.22}_{+0.28}$	25.95	1.34	1.22	Nickel	2006-07-25
	B	g		26.83 ± 0.23	26.49	1.35	1.22	Nickel	2006-07-25
		R		$26.09^{-0.24}_{+0.31}$	26.00	1.34	1.22	Nickel	2006-07-25
051001	H	g		24.86 ± 0.07	24.81	1.58	1.44	Landolt	2006-09-21
		R		23.93 ± 0.11	24.06	1.39	1.26	Landolt	2006-09-21
	A	g		$26.74^{-0.36}_{+0.54}$	26.69	1.58	1.44	Landolt	2006-09-21
		R		$25.48^{-0.41}_{+0.66}$	25.61	1.39	1.26	Landolt	2006-09-21
051006	H	V		23.44 ± 0.03	23.22	1.00	0.60	Nickel	2005-12-04
		I		22.01 ± 0.02	22.33	1.00	0.73	Nickel	2005-12-04
	A	V		26.37 ± 0.23	26.15	0.60	0.60	Nickel	2005-12-04
		I		24.60 ± 0.12	24.92	0.60	0.73	Nickel	2005-12-04
	B	V		$26.78^{-0.28}_{+0.38}$	26.56	0.60	0.60	Nickel	2005-12-04
		I		$25.41^{-0.24}_{+0.31}$	25.73	0.60	0.73	Nickel	2005-12-04

Continued on Next Page...

GRB field	Source	Filt.		Magnitude	AB Mag.	Aperture (″)	Seeing (″)	Cal. Sys.	UT date
	C	V		25.68 ± 0.12	25.46	0.60	0.60	Nickel	2005-12-04
		I		24.43 ± 0.10	24.75	0.60	0.73	Nickel	2005-12-04
051008	H	g		24.51 ± 0.04	24.47	1.10	1.00	Landolt	2008-02-12
		R		23.78 ± 0.07	23.92	1.00	0.85	SDSS	2008-02-12
051109A	H	g		24.07 ± 0.03	23.37	1.00	0.75	zeropt.	2007-08-12
		R		23.54 ± 0.03	23.23	1.00	0.76	zeropt.	2007-08-12
051109B	K	g		25.39 ± 0.13	24.79	1.00	0.86	Nickel	2006-07-25
		g		25.44 ± 0.14	24.85	1.00	0.87	Nickel	2007-07-18
		R		24.46 ± 0.20	24.21	1.19	1.08	Nickel	2006-07-25
		R		24.23 ± 0.14	23.98	1.00	0.82	Nickel	2007-07-18
051111	H	g		25.89 ± 0.12	25.33	1.08	0.98	SDSS	2006-07-25
		R		25.10 ± 0.18	24.86	1.31	1.19	SDSS	2006-07-25
	A	g		24.84 ± 0.04	24.28	1.08	0.98	SDSS	2006-07-25
		R		24.18 ± 0.06	23.94	1.31	1.19	SDSS	2006-07-25
	B	g		24.26 ± 0.02	23.70	1.30	0.98	SDSS	2006-07-25
		R		23.88 ± 0.05	23.64	1.30	1.19	SDSS	2006-07-25
051117A	limit	g	$>$	27.21	27.12	1.04	0.95	SDSS	2008-02-12
		R	$>$	26.13	26.24	1.00	0.85	SDSS	2008-02-12
	H?	g		$27.58^{-0.42}_{+0.68}$	27.49	1.04	0.95	SDSS	2008-02-12
		R		27.99	28.10	1.00	0.85	SDSS	2008-02-12
051117B	limit	V	$>$	26.10	25.90	1.00	0.79	Nickel	2005-12-04
		I	$>$	24.79	25.13	1.00	0.64	Nickel	2005-12-04
	A	V		22.11 ± 0.02	21.91	1.80	0.79	Nickel	2005-12-04
		I		20.45 ± 0.01	20.79	1.80	0.64	Nickel	2005-12-04
	B	V		24.13 ± 0.06	23.93	1.00	0.79	Nickel	2005-12-04
		I		23.44 ± 0.12	23.78	1.00	0.64	Nickel	2005-12-04
051211B	limit	g	$>$	26.04	24.31	1.14	1.03	Nickel	2006-09-21
		R	$>$	24.96	23.96	1.07	0.97	Nickel	2006-09-21
		R	$>$	24.90	23.90	1.07	0.97	Nickel	2006-09-21
	A	g		22.38 ± 0.01	20.65	1.14	1.03	Nickel	2006-09-21
		R		21.04 ± 0.01	20.04	1.07	0.97	Nickel	2006-09-21
		R		21.14 ± 0.01	20.14	1.07	0.97	Nickel	2006-09-21
060105	limit	g	$>$	25.30	24.69	1.49	1.35	Landolt	2006-05-30
		R	$>$	24.62	24.36	1.45	1.32	Landolt	2006-05-30
060109	limit	g	$>$	26.62	26.10	1.13	1.03	Landolt	2006-05-30
		R	$>$	25.46	25.25	1.22	1.11	Landolt	2006-05-30
	A	g		25.24 ± 0.10	24.72	1.13	1.03	Landolt	2006-05-30
		R		24.34 ± 0.13	24.13	1.22	1.11	Landolt	2006-05-30
060111A	H	R		23.63 ± 0.12	23.73	1.28	1.16	Nickel	2007-07-18
	G	R		21.11 ± 0.02	21.21	3.50	1.16	Nickel	2007-07-18
060111B	H	g		25.09 ± 0.06	24.69	1.23	1.12	Landolt	2006-07-25
		R		24.22 ± 0.08	24.11	1.18	1.07	Landolt	2006-07-25
	G	g		21.80 ± 0.01	21.40	2.60	1.12	Landolt	2006-07-25
		R		20.13	20.02	2.60	1.07	Landolt	2006-07-25
060124	limit	g	$>$	26.0	25.5	1.3		relative	2007-12-11

Continued on Next Page...

GRB field	Source	Filt.		Magnitude	AB Mag.	Aperture (″)	Seeing (″)	Cal. Sys.	UT date
		R	>	25.00	24.83	1.28	1.17	USNO	2007-12-11
060202	H	g		24.54 ± 0.04	24.37	1.28	1.16	Nickel	2006-07-25
		R		23.59 ± 0.04	23.64	1.37	1.25	Nickel	2006-07-25
060203	limit	g	>	27.09	26.52	1.10	1.00	Landolt	2007-10-11
		R	>	25.98	25.77	1.25	1.14	Landolt	2007-10-11
060204B	H	g		24.42 ± 0.05	24.36	1.57	1.43	SDSS	2006-05-30
		R		23.88 ± 0.07	24.01	1.51	1.37	SDSS	2006-05-30
060210	H	g		$27.13^{-0.47}_{+0.86}$	26.79	1.01	0.91	Nickel	2009-02-19
		R		$25.02^{-0.34}_{+0.50}$	24.95	1.00	0.90	Nickel	2007-08-12
		I		23.91 ± 0.22	24.18	1.43	1.30	Nickel	2009-02-19
060219	limit	g	>	26.50	26.38	1.46	1.33	SDSS	2006-05-30
		R	>	25.41	25.50	1.43	1.30	SDSS	2006-05-30
	A	g		22.73 ± 0.01	22.61	2.10	1.33	SDSS	2006-05-30
		R		21.50 ± 0.01	21.59	2.10	1.30	SDSS	2006-05-30
060306	H	B		25.24 ± 0.08	24.96	1.00	0.77	Landolt	2010-11-07
		g		25.02 ± 0.18	24.89	1.13	1.02	Nickel	2008-08-02
		g	>	23.45	23.32	1.48	1.34	Nickel	2008-02-12
		R		$24.74^{-0.25}_{+0.33}$	24.82	1.09	0.99	Nickel	2008-08-02
		R	>	22.86	22.94	1.42	1.29	Nickel	2008-02-12
		I		23.17 ± 0.08	23.55	1.26	1.14	zeropt.	2010-11-07
060312	limit	g	>	25.46	24.83	1.31	1.19	Nickel	2008-08-02
		R	>	24.46	24.19	1.28	1.16	Nickel	2008-08-02
	A	g		23.85 ± 0.09	23.22	1.31	1.19	Nickel	2008-08-02
		R		23.18 ± 0.11	22.91	1.28	1.16	Nickel	2008-08-02
060319	H	g		23.86 ± 0.05	23.77	2.56	2.33	SDSS	2007-04-16
		R		22.97 ± 0.05	23.08	2.14	1.94	SDSS	2007-04-16
060413	limit	g	>	25.61	18.19	2.01	1.83	SDSS	2006-05-31
		R	>	24.51	19.79	1.68	1.53	SDSS	2006-05-31
	S	g		$26.18^{-0.54}_{+1.14}$	18.76	2.01	1.83	SDSS	2006-05-31
		R		21.19 ± 0.02	16.47	1.68	1.53	SDSS	2006-05-31
060418	H	g		25.60 ± 0.11	24.79	0.70	1.22	Landolt	2006-05-30
		g		26.03 ± 0.16	25.22	0.70	1.01	Landolt	2007-08-11
		R		24.82 ± 0.17	24.42	0.70	1.12	Landolt	2006-05-30
		R		24.68 ± 0.12	24.28	0.70	1.34	Landolt	2007-08-11
	C	g		25.60 ± 0.09	24.79	1.00	1.22	Landolt	2006-05-30
		g		25.33 ± 0.09	24.52	1.00	1.01	Landolt	2007-08-11
		R		24.45 ± 0.12	24.05	1.00	1.12	Landolt	2006-05-30
		R		24.30 ± 0.08	23.90	1.00	1.34	Landolt	2007-08-11
	A	g		24.71 ± 0.04	23.90	1.00	1.22	Landolt	2006-05-30
		g		24.57 ± 0.04	23.76	1.00	1.01	Landolt	2007-08-11
		R		23.32 ± 0.04	22.92	1.00	1.12	Landolt	2006-05-30
		R		23.31 ± 0.03	22.91	1.00	1.34	Landolt	2007-08-11
	B	g		25.56 ± 0.09	24.75	0.80	1.22	Landolt	2006-05-30
		g		25.40 ± 0.09	24.59	0.80	1.01	Landolt	2007-08-11
		R		24.26 ± 0.10	23.86	0.80	1.12	Landolt	2006-05-30

Continued on Next Page...

GRB field	Source	Filt.		Magnitude	AB Mag.	Aperture (″)	Seeing (″)	Cal. Sys.	UT date
		R		24.45 ± 0.09	24.05	0.80	1.34	Landolt	2007-08-11
060424	H	g		25.57 ± 0.12	25.32	1.60	1.09	Nickel	2006-09-21
		R		25.03 ± 0.22	25.03	1.60	0.97	Nickel	2006-09-21
	A	g		25.13 ± 0.06	24.88	1.35	1.09	Nickel	2006-09-21
		R		24.32 ± 0.09	24.32	1.35	0.97	Nickel	2006-09-21
060428B	H	g	$>$	26.0 ± 0.14	24.98	1.45	1.32	SDSS	2006-05-30
		g		26.7 ± 0.2	24.77	1.23	1.12	SDSS	2006-09-21
		R	$>$	25.1 ± 0.07	23.44	1.36	1.23	SDSS	2006-05-30
		R		26.9 ± 0.3	23.85	1.14	1.03	SDSS	2006-09-21
	G1	g		21.72 ± 0.01	21.67	2.00	1.32	SDSS	2006-05-30
		g		21.70 ± 0.01	21.65	2.00	1.12	SDSS	2006-09-21
		R		19.81	19.94	2.00	1.23	SDSS	2006-05-30
		R		19.82 ± 0.01	19.95	2.00	1.03	SDSS	2006-09-21
	B	g		24.22 ± 0.05	24.17	1.45	1.32	SDSS	2006-05-30
		g		24.20 ± 0.03	24.15	1.23	1.12	SDSS	2006-09-21
		R		23.87 ± 0.11	24.00	1.36	1.23	SDSS	2006-05-30
		R		23.79 ± 0.06	23.92	1.14	1.03	SDSS	2006-09-21
	C	g		25.42 ± 0.13	25.37	1.45	1.32	SDSS	2006-05-30
		g		25.69 ± 0.07	25.64	1.23	1.12	SDSS	2006-09-21
		R		$25.58^{-0.35}_{+0.52}$	25.71	1.36	1.23	SDSS	2006-05-30
		R		25.23 ± 0.15	25.36	1.14	1.03	SDSS	2006-09-21
060502B	limit	g	$>$	26.88	26.73	1.32	1.20	Landolt	2006-05-30
		R	$>$	25.65	25.71	1.37	1.24	Landolt	2006-05-30
	G*	g		20.40	20.25	4.00	1.20	Landolt	2006-05-30
		R		18.76	18.82	4.00	1.24	Landolt	2006-05-30
	S1	g		23.47 ± 0.02	23.32	1.32	1.20	Landolt	2006-05-30
		R		21.76 ± 0.01	21.82	1.37	1.24	Landolt	2006-05-30
	G1	g		25.84 ± 0.13	25.69	1.32	1.20	Landolt	2006-05-30
		R		23.95 ± 0.06	24.01	1.37	1.24	Landolt	2006-05-30
	S3	g		26.24 ± 0.18	26.09	1.32	1.20	Landolt	2006-05-30
		R		$25.64^{-0.24}_{+0.31}$	25.70	1.37	1.24	Landolt	2006-05-30
	S4	g		$26.56^{-0.22}_{+0.27}$	26.41	1.32	1.20	Landolt	2006-05-30
		R		$25.83^{-0.27}_{+0.36}$	25.89	1.37	1.24	Landolt	2006-05-30
060505	H	g		18.47	18.40	9.00	1.25	Landolt	2006-05-30
		g		18.52	18.45	9.00	1.38	Landolt	2006-07-25
		R		17.89	18.01	9.00	1.20	Landolt	2006-05-30
		R		17.91	18.03	9.00	1.25	Landolt	2006-07-25
060510B	limit	g	$>$	27.10	26.96	1.70	1.54	Landolt	2006-05-31
		R	$>$	25.87	25.94	1.64	1.49	Landolt	2006-05-31
	A	g		26.44 ± 0.21	26.30	1.70	1.54	Landolt	2006-05-31
		R		25.12 ± 0.18	25.19	1.64	1.49	Landolt	2006-05-31
	B	g		$28.01^{-0.63}_{+1.69}$	27.87	1.70	1.54	Landolt	2006-05-31
		R		$26.31^{-0.45}_{+0.78}$	26.38	1.64	1.49	Landolt	2006-05-31
060512	limit	g	$>$	27.09	27.03	1.00	0.89	SDSS	2006-05-30
		g	$>$	26.14	26.08	2.08	1.89	SDSS	2006-07-25
		R	$>$	25.91	26.04	1.00	0.78	SDSS	2006-05-30

Continued on Next Page...

GRB field	Source	Filt.		Magnitude	AB Mag.	Aperture (″)	Seeing (″)	Cal. Sys.	UT date
	A	g		24.72 ± 0.05	24.66	1.30	0.89	SDSS	2006-05-30
		g		24.96 ± 0.12	24.90	1.30	1.89	SDSS	2006-07-25
		R		23.52 ± 0.05	23.65	1.30	0.78	SDSS	2006-05-30
060607A	limit	g	$>$	27.44	27.34	1.08	0.99	Landolt	2006-07-26
		R	$>$	25.97	26.07	1.74	1.58	Landolt	2006-07-26
	A	g		$27.09^{-0.31}_{+0.43}$	26.99	1.50	0.99	Landolt	2006-07-26
		R		$26.28^{-0.33}_{+0.48}$	26.38	1.50	1.58	Landolt	2006-07-26
060805A	limit	g	$>$	26.95	26.86	1.20	1.10	SDSS	2008-02-12
		R	$>$	25.98	26.09	1.13	1.03	SDSS	2008-02-12
	A	g		23.66 ± 0.02	23.57	1.30	1.10	SDSS	2008-02-12
		R		23.29 ± 0.04	23.40	1.30	1.03	SDSS	2008-02-12
	B	g		25.17 ± 0.08	25.08	1.20	1.10	SDSS	2008-02-12
		R		24.33 ± 0.09	24.44	1.13	1.03	SDSS	2008-02-12
	C	g		24.52 ± 0.04	24.43	1.20	1.10	SDSS	2008-02-12
		R		23.88 ± 0.06	23.99	1.13	1.03	SDSS	2008-02-12
060807	H	V		24.96 ± 0.10	24.85	1.54	1.40	SDSS	2007-04-16
		I		24.17 ± 0.17	24.56	1.25	1.13	SDSS	2007-04-16
060814A	limit	V	$>$	25.56	25.42	2.00	1.82	SDSS	2007-04-16
		I	$>$	24.30	24.67	1.98	1.80	SDSS	2007-04-16
	H?	V		22.92 ± 0.03	22.78	2.00	1.82	SDSS	2007-04-16
		I		22.06 ± 0.04	22.43	2.00	1.80	SDSS	2007-04-16
060904A	limit	V	$>$	26.05	25.97	1.86	1.69	SDSS	2007-04-16
		I	$>$	24.53	24.94	1.71	1.56	SDSS	2007-04-16
060904B	H	g		23.90 ± 0.02	23.30	1.10	1.03	SDSS	2006-09-21
		g		24.05 ± 0.07	23.45	1.10	1.09	SDSS	2009-02-19
		R		22.99 ± 0.03	22.72	1.10	0.91	SDSS	2006-09-21
		R		22.95 ± 0.08	22.68	1.10	1.24	SDSS	2009-02-19
060906	limit	g	$>$	26.8	26.00	1.12	1.02	SDSS	2007-12-11
		R	$>$	25.0	24.70	1.05	0.95	SDSS	2007-12-11
	A	g		$27.17^{-0.48}_{+0.88}$	26.43	1.00	1.02	SDSS	2007-12-11
		R		$25.06^{-0.22}_{+0.28}$	24.72	1.00	0.95	SDSS	2007-12-11
060923A	H	B		$27.14^{-0.49}_{+0.93}$	26.76	1.00	0.84	gcn	2007-08-12
		g		$26.21^{-0.23}_{+0.29}$	25.99	1.56	1.42	gcn	2007-06-13
		V		$26.08^{-0.36}_{+0.55}$	25.88	2.17	1.97	gcn	2007-04-16
		R		$25.70^{-0.31}_{+0.43}$	25.72	1.47	1.34	gcn	2007-06-13
		I		$24.81^{-0.38}_{+0.60}$	25.14	1.84	1.67	gcn	2007-04-16
		z	$>$	24.60	24.49	1.00	0.76	gcn	2007-08-12
060923C	limit	B	$>$	24.24	23.85	1.00	0.87	zeropt.	2007-08-12
		g	$>$	26.54	26.31	1.06	0.96	Landolt	2010-11-07
		I	$>$	24.94	25.26	1.29	1.17	zeropt.	2010-11-07
		z	$>$	23.03	22.92	1.00	0.77	zeropt.	2007-08-12
	A	B		19.87 ± 0.01	19.48	1.00	0.87	zeropt.	2007-08-12
		g		22.36 ± 0.01	22.13	1.06	0.96	Landolt	2010-11-07
		I		20.43 ± 0.01	20.75	1.29	1.17	zeropt.	2010-11-07
		z		19.11 ± 0.01	19.00	1.00	0.77	zeropt.	2007-08-12

Continued on Next Page...

GRB field	Source	Filt.		Magnitude	AB Mag.	Aperture ($''$)	Seeing ($''$)	Cal. Sys.	UT date
	C	B		20.54 ± 0.01	20.15	1.00	0.87	zeropt.	2007-08-12
		g		23.27 ± 0.01	23.04	1.06	0.96	Landolt	2010-11-07
		I		22.02 ± 0.02	22.34	1.29	1.17	zeropt.	2010-11-07
		z		20.73 ± 0.03	20.62	1.00	0.77	zeropt.	2007-08-12
060927	limit	V	$>$	27.26	27.05	1.00	0.81	SDSS	2006-11-21
		I	$>$	25.79	26.12	1.00	0.73	SDSS	2006-11-21
	A	V		25.12 ± 0.04	24.91	1.00	0.81	SDSS	2006-11-21
		I		23.85 ± 0.06	24.18	1.00	0.73	SDSS	2006-11-21
	B	V		24.25 ± 0.03	24.04	1.00	0.81	SDSS	2006-11-21
		I		22.55 ± 0.03	22.88	1.00	0.73	SDSS	2006-11-21
060929	H	g		26.69 ± 0.17	26.52	1.17	1.06	SDSS	2008-06-07
		R		24.97 ± 0.08	25.02	1.00	0.88	SDSS	2008-06-07
061021	H	g		$26.35^{-0.21}_{+0.26}$	26.14	1.62	1.48	Nickel	2007-12-13
		R		24.94 ± 0.14	24.97	1.46	1.32	Nickel	2007-12-13
061028	limit	V	$>$	27.14	26.64	1.27	1.15	Landolt	2006-11-21
		I	$>$	25.64	25.80	1.00	0.62	Landolt	2006-11-21
061110A	H	V		25.70 ± 0.20	25.40	1.00	0.81	Nickel	2006-11-21
		I		23.11 ± 0.07	23.38	1.00	0.79	Nickel	2006-11-21
	A	V		24.88 ± 0.09	24.58	1.00	0.81	Nickel	2006-11-21
		I		23.92 ± 0.15	24.19	1.00	0.79	Nickel	2006-11-21
061121	H	B		23.67 ± 0.03	23.35	1.00	0.89	Nickel	2009-02-19
		g		22.86 ± 0.02	22.70	1.00	0.91	Nickel	2009-02-19
		I		21.93 ± 0.09	22.29	1.93	1.76	Nickel	2009-02-19
061122	H	g		25.49 ± 0.09	24.84	1.08	0.99	Nickel	2007-10-09
		R		24.69 ± 0.13	24.40	1.07	0.97	Nickel	2007-10-09
	A	g		23.57 ± 0.02	22.92	1.08	0.99	Nickel	2007-10-09
		R		22.74 ± 0.02	22.45	1.07	0.97	Nickel	2007-10-09
061217	limit	g	$>$	27.11	26.95	1.32	1.20	Landolt	2006-12-19
		R	$>$	26.00	26.05	1.18	1.07	Landolt	2006-12-19
	A	g		25.44 ± 0.09	25.28	1.32	1.20	Landolt	2006-12-19
		R		24.48 ± 0.09	24.53	1.18	1.07	Landolt	2006-12-19
	B	g		24.24 ± 0.03	24.08	1.32	1.20	Landolt	2006-12-19
		R		23.33 ± 0.04	23.38	1.18	1.07	Landolt	2006-12-19
	C	g		25.28 ± 0.07	25.12	1.32	1.20	Landolt	2006-12-19
		R		23.12 ± 0.03	23.17	1.18	1.07	Landolt	2006-12-19
	G1	g		23.63 ± 0.02	23.47	1.80	1.20	Landolt	2006-12-19
		R		22.77 ± 0.02	22.82	1.80	1.07	Landolt	2006-12-19
061222A	H	B		24.95 ± 0.08	24.43	1.00	0.71	P60	2007-08-12
		V		25.13 ± 0.11	24.81	1.04	0.95	Nickel	2007-07-18
		I		24.31 ± 0.18	24.57	1.00	0.80	Nickel	2007-07-18
		z		$25.15^{-0.35}_{+0.52}$	24.99	1.00	0.63	P60	2007-08-12
	B	B		24.39 ± 0.05	23.87	1.00	0.71	P60	2007-08-12
		V		24.73 ± 0.07	24.41	1.04	0.95	Nickel	2007-07-18
		I		24.39 ± 0.21	24.65	1.00	0.80	Nickel	2007-07-18
		z		$25.14^{-0.32}_{+0.46}$	24.98	1.00	0.63	P60	2007-08-12

Continued on Next Page...

GRB field	Source	Filt.		Magnitude	AB Mag.	Aperture (″)	Seeing (″)	Cal. Sys.	UT date
070103	H	g		25.25 ± 0.05	25.01	1.00	0.89	Nickel	2008-08-02
		R		24.32 ± 0.07	24.32	1.00	0.73	Nickel	2008-08-02
070219	limit	g	$>$	27.23	27.10	1.00	0.83	SDSS	2009-06-25
		I	$>$	25.02	25.40	1.26	1.15	SDSS	2009-06-25
	H?	g		$27.54^{-0.41}_{+0.67}$	27.41	1.00	0.83	SDSS	2009-06-25
		I		$24.77^{-0.25}_{+0.33}$	25.15	1.26	1.15	SDSS	2009-06-25
070224	H	g		$26.62^{-0.27}_{+0.36}$	26.42	1.39	1.26	Nickel	2007-12-13
		R		$26.04^{-0.35}_{+0.53}$	26.07	1.36	1.24	Nickel	2007-12-13
070311	limit	g	$>$	25.35	22.56	2.46	2.24	SDSS	2007-04-16
070412	limit	V	$>$	25.48	25.39	2.03	1.84	SDSS	2007-04-16
		R	$>$	23.42	23.53	2.72	2.47	SDSS	2007-04-16
		I	$>$	23.92	24.32	1.76	1.60	SDSS	2007-04-16
	A	V		25.15 ± 0.23	25.06	2.03	1.84	SDSS	2007-04-16
		R		$23.95^{-0.47}_{+0.86}$	24.06	2.72	2.47	SDSS	2007-04-16
		I		23.41 ± 0.19	23.81	1.76	1.60	SDSS	2007-04-16
070419A	limit	g	$>$	26.31	26.21	1.01	0.92	SDSS	2009-02-19
		R	$>$	25.04	25.14	1.09	0.99	SDSS	2009-02-19
070429A	limit	R	$>$	25.30	25.03	1.60	1.45	Landolt	2007-07-18
	A	R		23.43 ± 0.06	23.16	1.10	1.45	Landolt	2007-07-18
	B	R		23.63 ± 0.07	23.36	1.10	1.45	Landolt	2007-07-18
	C	R		$24.70^{-0.22}_{+0.28}$	24.43	1.60	1.45	Landolt	2007-07-18
070429B	H	g		24.79 ± 0.14	24.69	2.1	1.40	Landolt	2007-07-18
		R		23.15 ± 0.06	23.25	1.56	1.41	Landolt	2007-07-18
070520A	H	g		24.77 ± 0.07	24.69	1.48	1.34	Landolt	2008-02-12
		R		23.98 ± 0.08	24.09	1.39	1.26	Landolt	2008-02-12
	A	g		25.66 ± 0.15	25.58	1.48	1.34	Landolt	2008-02-12
		R		$26.54^{-0.58}_{+1.31}$	26.65	1.39	1.26	Landolt	2008-02-12
070521	H	V		$26.16^{-0.23}_{+0.30}$	26.06	1.01	0.92	SDSS	2007-05-21
		V		$26.67^{-0.30}_{+0.41}$	26.57	1.00	0.73	SDSS	2009-06-25
		I		$25.09^{-0.41}_{+0.66}$	25.48	1.00	0.87	SDSS	2007-05-21
		z		$24.44^{-0.27}_{+0.36}$	24.38	1.44	1.31	zeropt.	2009-06-25
	S3	V		$26.56^{-0.31}_{+0.43}$	26.46	1.01	0.92	SDSS	2007-05-21
		V		26.10 ± 0.20	26.00	1.00	0.73	SDSS	2009-06-25
		I		24.29 ± 0.23	24.68	1.00	0.87	SDSS	2007-05-21
		z		$24.42^{-0.29}_{+0.39}$	24.36	1.44	1.31	zeropt.	2009-06-25
070621	limit	V	$>$	26.00	25.83	1.53	1.39	Landolt	2007-07-18
		I	$>$	24.43	24.78	1.35	1.23	Landolt	2007-07-18
	A	V		25.38 ± 0.18	25.21	1.53	1.39	Landolt	2007-07-18
		I		23.01 ± 0.08	23.36	1.35	1.23	Landolt	2007-07-18
	B	V		$26.06^{-0.27}_{+0.37}$	25.89	1.53	1.39	Landolt	2007-07-18
		I	$>$	24.70	25.05	1.35	1.23	Landolt	2007-07-18
070714A	H	g		24.58 ± 0.08	23.88	1.13	1.03	Landolt	2007-07-18
		R		24.03 ± 0.08	23.73	1.00	0.89	Landolt	2007-07-18
	B	g		23.85 ± 0.04	23.15	1.13	1.03	Landolt	2007-07-18

Continued on Next Page...

GRB field	Source	Filt.		Magnitude	AB Mag.	Aperture (″)	Seeing (″)	Cal. Sys.	UT date
		R		22.45 ± 0.02	22.15	1.00	0.89	Landolt	2007-07-18
	C	g		25.18 ± 0.14	24.48	1.13	1.03	Landolt	2007-07-18
070714B	H	g		25.24 ± 0.16	24.72	1.04	0.94	Nickel	2007-07-18
		R		24.66 ± 0.21	24.47	1.00	0.72	Nickel	2007-07-18
070721A	H	g		24.02 ± 0.04	23.97	1.28	1.16	Landolt	2007-10-09
		R		23.03 ± 0.04	23.17	1.13	1.03	Landolt	2007-10-09
070724A	H	g		21.63	21.58	2.10	0.79	Landolt	2007-08-11
		g		21.64 ± 0.01	21.59	2.10	0.84	Landolt	2008-08-02
		R		20.52	20.66	2.10	0.93	Landolt	2007-08-11
		R		20.53	20.67	2.10	0.89	Landolt	2008-08-02
070729	limit	g	$>$	26.35	26.29	1.49	1.35	Landolt	2007-12-11
		R	$>$	24.64	24.77	1.34	1.22	Landolt	2007-12-11
	A	g		24.29 ± 0.05	24.23	0.80	1.35	Landolt	2007-12-11
		R		23.23 ± 0.08	23.36	0.80	1.22	Landolt	2007-12-11
	B	g		25.13 ± 0.12	25.07	1.49	1.35	Landolt	2007-12-11
		R		22.83 ± 0.06	22.96	1.34	1.22	Landolt	2007-12-11
070808	limit	g	$>$	26.92	26.83	1.00	0.80	SDSS	2007-08-11
		R	$>$	25.88	25.99	1.00	0.70	SDSS	2007-08-11
	A	g		23.31 ± 0.01	23.22	1.00	0.80	SDSS	2007-08-11
		R		22.47 ± 0.01	22.58	1.00	0.70	SDSS	2007-08-11
	B	g		$26.50^{-0.21}_{+0.27}$	26.41	1.00	0.80	SDSS	2007-08-11
		R		24.65 ± 0.11	24.76	1.00	0.70	SDSS	2007-08-11
	C	g		23.75 ± 0.02	23.66	1.00	0.80	SDSS	2007-08-11
		R		23.02 ± 0.02	23.13	1.00	0.70	SDSS	2007-08-11
070809	limit	g	$>$	27.13	26.80	1.16	1.06	Nickel	2008-02-12
		R	$>$	25.77	25.71	1.19	1.08	Nickel	2008-02-12
	A	g		26.00 ± 0.13	25.67	1.16	1.06	Nickel	2008-02-12
		R		24.80 ± 0.14	24.74	1.19	1.08	Nickel	2008-02-12
	G	g		22.62 ± 0.02	22.29	3.00	1.06	Nickel	2008-02-12
		R		21.73 ± 0.02	21.67	3.00	1.08	Nickel	2008-02-12
070810A	limit	g	$>$	25.57	25.49	1.57	1.43	SDSS	2007-08-11
		R	$>$	24.66	24.78	1.53	1.39	SDSS	2007-08-11
	AG	g		24.43 ± 0.13	24.35	1.57	1.43	SDSS	2007-08-11
		R		23.62 ± 0.15	23.74	1.53	1.39	SDSS	2007-08-11
	H?	g		$25.18^{-0.22}_{+0.28}$	25.10	1.57	1.43	SDSS	2007-08-11
		R		23.49 ± 0.12	23.61	1.53	1.39	SDSS	2007-08-11
070810B	limit	g	$>$	26.70	26.52	1.91	1.74	Landolt	2007-08-11
		g	$>$	27.16	26.97	1.20	1.09	Landolt	2007-08-12
		R	$>$	26.16	26.20	1.35	1.22	Landolt	2007-08-11
		R	$>$	26.47	26.51	1.00	0.85	Landolt	2007-08-12
071021	H	B		$26.75^{-0.27}_{+0.36}$	26.35	1.02	0.92	SDSS	2010-11-07
		g		25.98 ± 0.11	25.75	1.04	0.94	SDSS	2008-08-03
		V		$25.79^{-0.23}_{+0.29}$	25.57	1.00	0.90	SDSS	2010-11-07
		I		24.25 ± 0.13	24.57	1.00	0.87	SDSS	2008-08-03
		z		$24.86^{-0.25}_{+0.33}$	24.75	1.00	0.87	SDSS	2010-11-07

Continued on Next Page...

GRB field	Source	Filt.		Magnitude	AB Mag.	Aperture (″)	Seeing (″)	Cal. Sys.	UT date
	A	B		26.42 ± 0.23	26.02	1.02	0.92	SDSS	2010-11-07
		g		26.08 ± 0.13	25.85	1.04	0.94	SDSS	2008-08-03
		V		$26.29^{-0.34}_{+0.50}$	26.07	1.00	0.90	SDSS	2010-11-07
		I		$24.84^{-0.25}_{+0.33}$	25.16	1.00	0.87	SDSS	2008-08-03
		z		$25.61^{-0.46}_{+0.81}$	25.50	1.00	0.87	SDSS	2010-11-07
	B	B		25.57 ± 0.10	25.17	1.02	0.92	SDSS	2010-11-07
		g		25.25 ± 0.05	25.02	1.04	0.94	SDSS	2008-08-03
		V		25.17 ± 0.14	24.95	1.00	0.90	SDSS	2010-11-07
		I		24.56 ± 0.19	24.88	1.00	0.87	SDSS	2008-08-03
		z	$>$	25.14	25.03	1.00	0.87	SDSS	2010-11-07
	G1	B		23.01 ± 0.02	22.61	1.70	0.92	SDSS	2010-11-07
		g		22.56 ± 0.01	22.33	1.70	0.94	SDSS	2008-08-03
		V		22.09 ± 0.02	21.87	1.70	0.90	SDSS	2010-11-07
		I		20.47 ± 0.01	20.79	1.70	0.87	SDSS	2008-08-03
		z		20.76 ± 0.01	20.65	1.70	0.87	SDSS	2010-11-07
071025	limit	g	$>$	27.24	26.97	1.00	0.85	Nickel	2008-08-02
		R	$>$	26.50	26.48	1.00	0.74	Nickel	2008-08-02
080207	H	g		$27.05^{-0.26}_{+0.35}$	26.97	1.00	0.81	SDSS	2009-02-19
		I		$25.09^{-0.29}_{+0.39}$	25.49	1.22	1.11	SDSS	2009-02-19
	A	g		26.64 ± 0.20	26.56	1.00	0.81	SDSS	2009-02-19
		I		24.38 ± 0.17	24.78	1.22	1.11	SDSS	2009-02-19
	B	g		$27.05^{-0.26}_{+0.35}$	26.97	1.00	0.81	SDSS	2009-02-19
		I		$25.83^{-0.57}_{+1.29}$	26.23	1.22	1.11	SDSS	2009-02-19
080210	limit	g	$>$	26.69	26.39	1.31	1.19	Nickel	2008-02-12
		R	$>$	25.93	25.90	1.05	0.96	Nickel	2008-02-12
	AG	g		25.19 ± 0.09	24.89	1.31	1.19	Nickel	2008-02-12
		R		24.12 ± 0.07	24.09	1.05	0.96	Nickel	2008-02-12
080307	H	g		24.44 ± 0.06	24.35	1.27	1.16	SDSS	2010-02-07
		I		23.91 ± 0.11	24.30	1.13	1.03	SDSS	2010-02-07
080310	limit	g	$>$	27.02	26.88	1.00	0.83	SDSS	2009-06-25
		I	$>$	24.59	24.96	1.44	1.31	SDSS	2009-06-25
080319A	H	g		24.46 ± 0.04	24.41	1.00	0.90	SDSS	2009-02-19
		R		23.96 ± 0.08	24.10	1.00	0.80	SDSS	2009-02-19
080319C	limit	g	$>$	26.35	26.26	1.08	0.99	SDSS	2009-02-19
		R	$>$	25.23	25.33	1.00	0.88	SDSS	2009-02-19
	A	g		23.14 ± 0.02	23.05	1.50	0.99	SDSS	2009-02-19
		R		22.49 ± 0.04	22.59	1.50	0.88	SDSS	2009-02-19
080319D	limit	g	$>$	26.28	25.61	1.00	0.85	Nickel	2009-02-19
		R	$>$	25.29	24.99	1.00	0.79	Nickel	2009-02-19
	A	g		24.59 ± 0.06	23.92	0.80	0.85	Nickel	2009-02-19
		R		22.53 ± 0.03	22.23	0.80	0.79	Nickel	2009-02-19
	B	g		23.67 ± 0.02	23.00	0.80	0.85	Nickel	2009-02-19
		R		21.66 ± 0.01	21.36	0.80	0.79	Nickel	2009-02-19
080320	limit	g	$>$	26.78	26.73	1.24	1.12	SDSS	2009-02-19
		I	$>$	24.31	24.72	1.84	1.68	SDSS	2009-02-19

Continued on Next Page...

GRB field	Source	Filt.		Magnitude	AB Mag.	Aperture (″)	Seeing (″)	Cal. Sys.	UT date
	H	g	$>$	26.77	26.72	1.24	1.12	SDSS	2009-02-19
		I		23.43 ± 0.16	23.84	1.84	1.68	SDSS	2009-02-19
	A	g		23.85 ± 0.02	23.80	1.24	1.12	SDSS	2009-02-19
		I		21.82 ± 0.03	22.23	1.84	1.68	SDSS	2009-02-19
080325	H	u		$26.55^{-0.29}_{+0.40}$	26.28	1.15	1.04	Nickel	2008-08-03
		g		25.49 ± 0.09	25.26	1.11	1.01	Nickel	2008-06-07
		R		24.97 ± 0.12	24.97	1.00	0.87	Nickel	2008-06-07
		I		24.22 ± 0.16	24.54	1.01	0.92	Nickel	2008-08-03
080330	limit	g	$>$	27.13	27.07	1.00	0.73	SDSS	2009-02-19
		R	$>$	25.87	26.00	1.00	0.76	SDSS	2009-02-19
080430	H	g		24.98 ± 0.05	24.94	1.07	0.97	SDSS	2009-02-19
		R		24.29 ± 0.10	24.43	1.00	0.87	SDSS	2009-02-19
080507	limit	g	$>$	27.13	27.09	1.24	1.13	SDSS	2008-06-07
		R	$>$	26.06	26.21	1.14	1.04	SDSS	2008-06-07
	H	g	$>$	27.10	27.06	1.24	1.13	SDSS	2008-06-07
		R		$25.93^{-0.27}_{+0.37}$	26.08	1.14	1.04	SDSS	2008-06-07
	A	g		25.06 ± 0.05	25.02	1.24	1.13	SDSS	2008-06-07
		R		24.66 ± 0.09	24.81	1.14	1.04	SDSS	2008-06-07
080514B	H	g		24.61 ± 0.04	24.40	1.21	1.10	SDSS	2008-06-07
		R		23.96 ± 0.05	23.99	1.00	0.88	SDSS	2008-06-07
080515	H	g		25.40 ± 0.21	25.25	1.00	0.80	Nickel	2008-08-02
		R		$25.12^{-0.34}_{+0.50}$	25.19	1.00	0.72	Nickel	2008-08-02
	A	g		24.29 ± 0.07	24.14	1.00	0.80	Nickel	2008-08-02
		R		23.49 ± 0.08	23.56	1.00	0.72	Nickel	2008-08-02
080603A	H	u		26.25 ± 0.19	26.09	1.03	0.94	Nickel	2008-08-03
		g		24.25 ± 0.04	24.09	1.00	0.86	Nickel	2008-08-02
		R		23.71 ± 0.05	23.77	1.08	0.98	Nickel	2008-08-02
		I		23.24 ± 0.09	23.60	1.09	0.99	Nickel	2008-08-03
	A	u		25.51 ± 0.09	25.35	1.03	0.94	Nickel	2008-08-03
		g		23.93 ± 0.04	23.77	1.00	0.86	Nickel	2008-08-02
		R		23.36 ± 0.03	23.42	1.08	0.98	Nickel	2008-08-02
		I		22.68 ± 0.05	23.04	1.09	0.99	Nickel	2008-08-03
	B	u		25.69 ± 0.11	25.53	1.03	0.94	Nickel	2008-08-03
		g		23.52 ± 0.02	23.36	1.00	0.86	Nickel	2008-08-02
		R		22.42 ± 0.01	22.48	1.08	0.98	Nickel	2008-08-02
		I		21.76 ± 0.02	22.12	1.09	0.99	Nickel	2008-08-03
080607	H	g		$27.47^{-0.30}_{+0.41}$	27.39	1.00	0.86	SDSS	2009-02-19
		I		$25.01^{-0.27}_{+0.36}$	25.41	1.00	1.14	SDSS	2009-02-19
	A	g		26.35 ± 0.17	26.27	1.30	0.86	SDSS	2009-02-19
		I		23.25 ± 0.06	23.65	1.30	1.14	SDSS	2009-02-19
	B	g		23.60 ± 0.02	23.52	1.50	0.86	SDSS	2009-02-19
		I		22.53 ± 0.03	22.93	1.50	1.14	SDSS	2009-02-19
080701	limit	g	$>$	26.02	24.21	2.06	1.88	SDSS	2010-02-07
		R	$>$	25.17	24.07	1.96	1.78	SDSS	2010-02-07
	A	g		$25.64^{-0.23}_{+0.29}$	23.83	2.06	1.88	SDSS	2010-02-07

Continued on Next Page...

GRB field	Source	Filt.		Magnitude	AB Mag.	Aperture (″)	Seeing (″)	Cal. Sys.	UT date
		R		$25.24^{-0.33}_{+0.48}$	24.14	1.96	1.78	SDSS	2010-02-07
	B	g		24.90 ± 0.13	23.09	2.06	1.88	SDSS	2010-02-07
		R		22.55 ± 0.03	21.45	1.96	1.78	SDSS	2010-02-07
080702A	limit	g	$>$	27.40	25.00	1.19	1.08	zeropt.	2008-08-02
		R	$>$	25.96	24.46	1.13	1.03	zeropt.	2008-08-02
		I	$>$	25.69	24.91	1.00	0.90	zeropt.	2008-08-03
	S1	g	$>$	27.40	25.00	1.19	1.08	zeropt.	2008-08-02
		R		$26.96^{-0.66}_{+1.93}$	25.46	1.13	1.03	zeropt.	2008-08-02
		I		24.85 ± 0.15	24.07	1.00	0.90	zeropt.	2008-08-03
080710	H	g		$26.60^{-0.44}_{+0.74}$	26.33	1.00	0.79	Nickel	2008-08-02
		R		$25.51^{-0.27}_{+0.36}$	25.49	1.12	1.02	Nickel	2008-08-02
	A	g		25.65 ± 0.23	25.38	1.00	0.79	Nickel	2008-08-02
		R		$25.95^{-0.37}_{+0.58}$	25.93	1.12	1.02	Nickel	2008-08-02
081211B	limit	g	$>$	26.27	26.23	1.00	0.84	SDSS	2009-02-19
		R	$>$	24.99	25.13	1.00	0.88	SDSS	2009-02-19
	A	g		25.28 ± 0.15	25.24	1.00	0.84	SDSS	2009-02-19
		R		24.09 ± 0.15	24.23	1.00	0.88	SDSS	2009-02-19
	G	g		21.52 ± 0.01	21.48	2.50	0.84	SDSS	2009-02-19
		R		20.13 ± 0.01	20.27	2.50	0.88	SDSS	2009-02-19
081221	H	B		25.67 ± 0.15	25.44	1.14	1.04	Landolt	2010-11-07
		g		25.19 ± 0.05	25.11	1.14	1.04	Nickel	2008-12-23
		V		25.02 ± 0.14	24.93	1.07	0.97	Landolt	2010-11-07
		I		23.46 ± 0.13	23.86	2.04	1.85	Nickel	2008-12-23
		z		23.65 ± 0.16	23.60	1.29	1.17	zeropt.	2010-11-07
	A	B		24.27 ± 0.04	24.04	1.14	1.04	Landolt	2010-11-07
		g		24.07 ± 0.02	23.99	1.14	1.04	Nickel	2008-12-23
		V		23.97 ± 0.04	23.88	1.07	0.97	Landolt	2010-11-07
		I		22.63 ± 0.06	23.03	2.04	1.85	Nickel	2008-12-23
		z		22.55 ± 0.05	22.50	1.29	1.17	zeropt.	2010-11-07
	B	B		25.58 ± 0.12	25.35	1.14	1.04	Landolt	2010-11-07
		g		25.19 ± 0.06	25.11	1.14	1.04	Nickel	2008-12-23
		V		24.83 ± 0.11	24.74	1.07	0.97	Landolt	2010-11-07
		I		22.69 ± 0.08	23.09	2.04	1.85	Nickel	2008-12-23
		z		23.63 ± 0.13	23.58	1.29	1.17	zeropt.	2010-11-07
090111	H	g		24.33 ± 0.04	23.77	1.27	1.15	Landolt	2010-07-08
		R		23.73 ± 0.06	23.51	1.28	1.17	zeropt.	2010-07-08
090113	H	B		24.97 ± 0.06	24.49	1.00	0.75	Landolt	2010-11-07
		g		24.47 ± 0.07	24.17	1.49	1.36	Nickel	2010-02-07
		V		24.52 ± 0.07	24.24	1.00	0.79	Landolt	2010-11-07
		I		23.37 ± 0.10	23.66	1.35	1.22	Nickel	2010-02-07
		z		23.71 ± 0.08	23.57	1.00	0.80	zeropt.	2010-11-07
090404	H	g		$26.56^{-0.21}_{+0.27}$	26.48	1.00	0.57	SDSS	2009-06-25
		I		24.43 ± 0.19	24.83	1.24	1.13	SDSS	2009-06-25
	A	g		$26.56^{-0.24}_{+0.31}$	26.48	1.00	0.57	SDSS	2009-06-25
		I		23.81 ± 0.11	24.21	1.24	1.13	SDSS	2009-06-25
	G1	g		23.85 ± 0.02	23.77	1.20	0.57	SDSS	2009-06-25

Continued on Next Page...

GRB field	Source	Filt.		Magnitude	AB Mag.	Aperture (″)	Seeing (″)	Cal. Sys.	UT date
		I		21.61 ± 0.01	22.01	1.20	1.13	SDSS	2009-06-25
	G2	g		23.89 ± 0.02	23.81	1.10	0.57	SDSS	2009-06-25
		I		21.95 ± 0.02	22.35	1.10	1.13	SDSS	2009-06-25
090407	H	g		$26.33^{-0.28}_{+0.38}$	26.09	1.95	1.77	Nickel	2010-02-07
		I		$24.38^{-0.22}_{+0.27}$	24.70	1.67	1.52	Nickel	2010-02-07
090515	limit	g	$>$	26.57	26.49	1.24	1.13	SDSS	2010-02-07
		R	$>$	25.97	26.09	1.12	1.02	SDSS	2010-02-07
090618	H/O	B		23.94 ± 0.06	23.45	1.14	1.04	SDSS	2009-06-25
		R		22.47 ± 0.06	22.42	1.54	1.40	SDSS	2009-06-25
	A	B		24.52 ± 0.10	24.03	1.14	1.04	SDSS	2009-06-25
		R		21.68 ± 0.03	21.63	1.54	1.40	SDSS	2009-06-25
090709A	H	g		26.55 ± 0.22	26.21	1.15	1.05	Landolt	2010-11-07
		I		24.92 ± 0.22	25.19	1.06	0.96	zeropt.	2010-11-07
090902B	H	g		$25.20^{-0.34}_{+0.49}$	25.05	2.03	1.85	Landolt	2010-02-07
		g		25.47 ± 0.08	25.32	1.02	0.93	Landolt	2010-07-08
		R		25.08 ± 0.21	25.14	1.11	1.01	zeropt.	2010-07-08
		I		25.81	26.17	1.76	1.60	zeropt.	2010-02-07
100205A	limit	g	$>$	27.00	26.93	1.66	1.51	Landolt	2010-02-07
		R	$>$	26.29	26.41	1.54	1.40	SDSS	2010-02-07
100413A	H	g		26.74 ± 0.22	26.33	0.70	1.00	Landolt	2010-07-08
		I		$25.43^{-0.31}_{+0.43}$	25.66	0.70	0.97	zeropt.	2010-07-08
	A	g		25.95 ± 0.11	25.54	0.70	1.00	Landolt	2010-07-08
		I		26.91	27.14	0.70	0.97	zeropt.	2010-07-08
	B	g		26.03 ± 0.13	25.62	1.10	1.00	Landolt	2010-07-08
		I		24.13 ± 0.12	24.36	1.10	0.97	zeropt.	2010-07-08
100414A	H	g		24.68 ± 0.05	24.59	1.29	1.17	SDSS	2010-07-08
		R		24.43 ± 0.10	24.54	1.12	1.02	SDSS	2010-07-08
100420A	H	g		$25.76^{-0.32}_{+0.46}$	25.35	1.00	0.89	zeropt.	2011-06-03
		R		24.66 ± 0.16	24.55	1.21	1.10	USNO	2011-06-03
100424A	H	g		25.83 ± 0.16	25.71	1.37	1.25	SDSS	2010-07-08
		I		24.37 ± 0.21	24.75	1.33	1.21	SDSS	2010-07-08
	A	g		$26.33^{-0.23}_{+0.29}$	26.21	1.37	1.25	SDSS	2010-07-08
		I		24.44 ± 0.20	24.82	1.33	1.21	SDSS	2010-07-08
100526A	H	g		$27.23^{-0.34}_{+0.50}$	27.07	1.24	1.13	SDSS	2010-07-08
		I		24.73 ± 0.21	25.09	1.32	1.20	SDSS	2010-07-08
	A	g		25.93 ± 0.14	25.77	1.50	1.13	SDSS	2010-07-08
		I		24.71 ± 0.23	25.07	1.50	1.20	SDSS	2010-07-08
100614A	limit	g	$>$	27.26	27.15	1.16	1.06	Landolt	2010-07-08
		I	$>$	25.35	25.73	1.36	1.23	zeropt.	2010-07-08
100823A	H	g		25.77 ± 0.18	25.64	0.80	0.81	Landolt	2010-11-07
		I		24.09 ± 0.16	24.46	0.80	0.94	zeropt.	2010-11-07
	G	g		22.82 ± 0.02	22.69	1.40	0.81	Landolt	2010-11-07
		I		21.08 ± 0.01	21.45	1.40	0.94	zeropt.	2010-11-07
100905A	limit	g	$>$	26.57	26.36	1.00	0.70	SDSS	2010-11-07

Continued on Next Page...

GRB field	Source	Filt.		Magnitude	AB Mag.	Aperture (″)	Seeing (″)	Cal. Sys.	UT date
		I	$>$	24.91	25.24	1.00	0.80	SDSS	2010-11-07